"Solid state NMR spectroscopic studies of organic semiconductors for molecular electronics application"

Dissertation zur Erlangung des Grades "Doktor der Naturwissenschaften" im Promotionsfach Chemie

Am Fachbereich Chemie, Pharmazie, Geographie und Geowissenschaften der Johannes Gutenberg-Universität Mainz

Constantin Haese

Geb. am 04.07.1992 in Boppard am Rhein

Mainz, 2023

Betreuer: Prof. Dr. Paul W. M. Blom

Zweitbetreuer: Apl. Prof. Dr. Gerald Hinze

Dritter Prüfer: Prof. Dr. Pol Besenius

Prüfungsvorsitz: Prof. Dr. Sebastian Seiffert

Protokoll: Dr. Mihail Mondeshki

Tag der Prüfung:

Versicherung
für das Gesuch um Zulassung zur Promotion im Fachbereich 09 an der Johannes Gutenberg-Universität Mainz

Hiermit versichere ich _____

Name, Vorname

gemäß § 13 Abs. (3), 3-7 der Promotionsordnung vom 18.10.2021 i.d.F. vom 17.08.2022, dass:

- die eingereichte wissenschaftliche Arbeit noch an keiner anderen deutschen oder ausländischen Hochschule oder vergleichbaren Einrichtung zur Erlangung eines akademischen Grades eingereicht wurde

- ich noch kein Promotions- oder ein vergleichbares Graduierungsverfahren im Promotionsfach erfolglos beendet habe

- ich noch kein Promotions- oder ein vergleichbares Graduierungsverfahren im Fach der Promotion erfolgreich abgeschlossen habe

- die wissenschaftliche Arbeit selbstständig verfasst und ausschließlich die angegebenen Quellen und Hilfsmittel verwendet wurden

- keine entgeltliche Hilfe Dritter, insbesondere Promotionsberatung oder -vermittlung in Anspruch genommen wurde.

_____   _____
Datum   Unterschrift

Zusammenfassung

Die im Folgenden vorgestellte Dissertation wurde in einem Zeitraum von 3 Jahren und 10 Monaten am Max-Planck-Institut für Polymerforschung, Mainz in der Abteilung für molekulare Elektronik angefertigt und befasst sich mit der Strukturaufklärung, den Struktur-Eigenschafts Beziehungen sowie der chemischen Reaktivität von organischen Halbleitern, welche Forschungsinhalte im Bereich der molekularen Elektronik darstellen. Als analytische Methode wurde die kernmagnetische Resonanz Spektroskopie (NMR) gewählt. Der experimentelle Teil der Arbeit ist in zwei Hauptabschnitte gegliedert.

Im ersten Teil wurden neun Moleküle mit der Eigenschaft zur thermisch aktivierten, verzögerten Fluoreszenz (TADF) untersucht. Zunächst wurde eine Strukturanalyse in Lösung durchgeführt, mit deren Hilfe ^{1}H, ^{13}C und ^{19}F Resonanzen, welche mittels MAS-NMR erhalten wurden zugeordnet werden konnten. Für die verschiedenen Materialien wurden nach Sublimation unterschiedliche kristalline und amorphe Anteile gefunden, welche mittels der Analyse von transversalen Relaxationszeiten identifiziert wurden. Zusätzlich wurden heteronukleare, dipolare Kopplungen von C-H Paaren durch das Messen und Auswerten von NMR-Spektren welche auf Recoupling-Techniken basieren, bestimmt. Des Weiteren wurde ein Vergleich der strukturellen Daten nach Sublimation und Lösungsmittelkristallisation durchgeführt. Hierzu wurden ^{19}F MAS-NMR Spektren der Einkristalle aufgenommen und die Ergebnisse mit XRD Daten untermauert. Für einige Verbindungen wurden starke Unterschiede in der Nahordnung zwischen den sublimierten und kristallisierten Proben festgestellt, während für andere eine nahezu identische lokale Umgebung gefunden wurde. Um ein besseres Verständnis für die Nahordnung zu erhalten wurde eine NICS (nuclear-independent-chemical-shift) Simulation an einem Molekül als Modell durchgeführt welches eine Möglichkeit für die Anordnung zweier benachbarter TADF Emitter illustriert. Die aus den NMR- sowie XRD Daten bestimmten Strukturen wurden mit besonderem Augenmerk auf das Trapping von Ladungsträgern in Bezug auf die Leitfähigkeit der Materialien diskutiert, was wiederum mit computerbasierten Simulationen untermauert wurde. Hierzu wurden die Energielevel der amorphen sowie kristallinen Materialien mit und ohne Sauerstoff als potenzielle Elektronen-Trap simuliert (Andrienko et al.). Abschließend wurden zwei der untersuchten Materialien in eine Polystyrolmatrix eingebettet und die strukturellen Daten zu einer Diskussion der Änderung in der Photolumineszenz herangezogen.

Der zweite Teil der Arbeit behandelt die Polymer-Dopant Mischung P3HT:F$_4$TCNQ, welche als Modellsystem für organische Solarzellen dient. In diesem Abschnitt wurden Proben mit verschiedenen Mischungsverhältnissen der Materialien nach thermischer Behandlung untersucht. Hierbei wurden ^{1}H, ^{13}C und ^{19}F MAS-NMR Experimente durchgeführt um mögliche Reaktionsprodukte zu identifizieren, welche dann mit Hilfe von ^{19}F MAS-NMR Spektren quantifiziert wurden. Die thermisch behandelten

Proben wurden abschließend mittles PFGSE-NMR analysiert um Fragmente, welche als Resultat der chemischen Reaktion auftreten identifizieren zu können.

Abstract

The dissertation presented below was prepared over a period of 3 years and 10 months at the Max Planck Institute for Polymer Research, Mainz in the Department of Molecular Electronics and deals with the structure elucidation, structure-property relations and chemical reactivity of organic semiconductors, which represent research topics in the field of molecular electronics. Nuclear magnetic resonance spectroscopy (NMR) was chosen as the analytical method. The experimental part of the work is divided into two main sections.

In the first part, nine molecules with the property of thermally activated delayed fluorescence (TADF) were studied. First, a structural analysis in solution was performed, which allowed to assign ^{1}H, ^{13}C and ^{19}F resonances obtained by MAS-NMR. Different crystalline and amorphous fractions were found for the different materials after sublimation, which were identified by transverse relaxation time analysis. In addition, heteronuclear dipolar couplings of C-H pairs were determined by measuring and evaluating NMR spectra based on recoupling techniques. Furthermore, a comparison of structural data after sublimation and solvent crystallization was performed. For this purpose, ^{19}F MAS-NMR spectra of the single crystals were recorded and the results were compared with XRD data. For some compounds, strong differences in the close range order were found between the sublimed and crystallized samples, while for others a nearly identical local environment was found. To gain a better understanding of the close range order, a NICS (nuclear-independent-chemical-shift) simulation was performed on a molecule as a model illustrating one possibility for the arrangement of two adjacent TADF emitters. The structures determined from the NMR as well as XRD data were discussed with particular attention to the trapping of charge carriers in relation to the conductivity of the materials, which in turn was supported with computer-based simulations. For this purpose, the energy levels of the amorphous as well as crystalline materials were simulated with and without oxygen as potential electron traps (Andrienko et al.). Finally, two of the investigated materials were embedded in a polystyrene matrix and the structural data were used to discuss the change in their photoluminescence behaviour.

The second part of the work deals with the polymer-dopant mixture P3HT:F4TCNQ which serves as a model system for organic solar cells. In this section, samples with different blend ratios of the materials were studied after thermal treatment. Here, ^{1}H, ^{13}C and ^{19}F MAS-NMR experiments were performed to identify possible reaction products, which were then quantified using 19F MAS-NMR spectra. The thermally treated samples were finally analysed by PFGSE NMR to identify fragments that occur as a result of the chemical reaction.

Table of content

BaBa	–	**Ba**ck to **ba**ck
COSY	–	**CO**rrelation **S**pectroscop**Y**
CTC	–	**C**harge **T**ransfer **C**omplex
CP	–	**C**ross**P**olarization
CS	–	Chemical Shift
CSA	–	**C**hemical **S**hift **A**nisotropy
CV	–	**C**yclo**V**oltammerty
DCB	–	**D**i**C**hloro**B**enzene
DCM	–	**D**i**C**hlor**M**ethane
DOSY	–	**D**iffusion **O**rdered **S**pectroscop**Y**
EA	–	**E**lectron Affinity
HETCOR	–	**HET**eronuclear **COR**relation
HMBC	–	**H**eteronuclear **M**ultiple **B**ond **C**orrelation
HSQC	–	**H**eteronuclear **S**ingle **Q**uantum **C**oherence
ICT	–	**I**nteger **C**harge **T**ransfer
IE	–	**I**onization **E**nergy
j-mod	–	j-modulated (modulated via scalar coupling)
MAS	–	**M**agic **A**ngle **S**pinning
NOESY	–	**N**uclear **O**verhauser **E**ffect **S**pectroscop**Y**
P3HT	–	**P**oly-**3**-**H**exyl**T**hiophene
REPT-HDOR	–	**RE**coupled **P**olarization **T**ransfer **H**eteronuclear **D**ipolar **O**rder **R**otor encoding
SQ-DQ	–	**S**ingle **Q**uantum **D**ouble **Q**uantum
TADF	–	**T**hermally **A**ctivated **D**elayed **F**luorescence

1. Introduction

Nuclear magnetic resonance (NMR) spectroscopy is nowadays one of the most powerful analytical methods and widely used to gain information about the structure and dynamics of molecules in different scientific areas. The discovery of this technique goes back to the year 1946 and is based on the work of Purcell[1] and Bloch[2]. To prove the applicability of NMR spectroscopy to liquid and solid phases, proton resonances were used in the first experiments on water (l) and paraffin (s) samples, opening up two large research areas such as high-resolution NMR spectroscopy and solid-state NMR spectroscopy. In 1973, Lauterburg[3] and Mansfield[4] developed a third method known as magnetic resonance imaging, which is today widely used in medical diagnostics. All three techniques are considered as more or less independent.

Initially, the application of solid-state NMR spectroscopy was limited due to the lack of spectral resolution. The broadening of the resonances is thereby caused by several effects as anisotropic interactions of the chemical shift (CSA) due to different orientation of the spins in the sample as well as homo- and heteronuclear dipole-dipole interactions and quadrupolar couplings. To reduce those effects and improve the spectral resolution in solid-state NMR measurements, the magic angle spinning method was developed. By spinning the sample in cylinders (rotors) commonly made of zirconium dioxide, at an angle of 54.7° (magic angle) the contributions of the CSA, dipole and quadrupole interactions are averaged. In the first MAS experiments in 1958, rotation frequencies of 0.8 kHz were used, but with the technical development of new systems spinning speeds of around 30 kHz are more common nowadays.[5–7] For specific purposes even higher rotation frequencies up to 100 kHz and above can be achieved by the usage of special probe heads and small rotors with a diameter of 0.7 mm. The improvement of the resolution, however, comes along with the loss of information about the anisotropic and dipolar interactions. Therefore, so called recoupling techniques were developed to reintroduce the spectroscopic information of interest selectively. Such a method induces a counterrotation of the spins of the nuclear wave function and thus recouple the particular interactions.[8–10] In summary this means, that the modern solid state NMR spectrometers in combination with the right pulse sequences can offer manifold information about spectroscopic parameters as the chemical shift in combination with the detection of dipolar coupling strengths. This also opens the possibility of determining internuclear distances as well as bond angles and site specific molecular dynamics.

In the year 2000, Alan MacDiarmid, Hideki Shirakawa and Alan Heeger were awarded "for the discovery and development of conductive polymers" with a Nobel prize. Since back then, the engineering of organic electronics that offer properties for a commercial use became a magnifying research field for

lots of material scientist. The initial researches focused on the development of organic photovoltaic solar panels, however, these devices were underperforming and instable if compared with photovoltaic panels made from silicon. Additionally, the decreasing price of silicon makes this material more favourable in terms of commercial use. Therefore, the interest of organic electronics shifted towards the field of flexible and bioelectronics devices. The improvement of charge mobility and photo conversion of organic devices on a lab-scale level went through tremendous strides within the last two decades. Solid-state organization of the molecules, no matter if mono- or polymeric, can have a high impact on the device performance. One challenging task is to understand the relationship between composition, structure and processing which can be limited by the complexity of the molecular architecture as well as the solid-state structure. A characterization over different length scales is therefore crucial to understand the properties of devices made of organic molecules, especially for regions with semi-crystalline and amorphous arrangements. Therefore, a combination of solid-state NMR spectroscopy, which is capable of detecting local environments for specific nuclei and revealing dynamic processes, scattering experiments and macroscopic analysis should be applied to the materials to obtain a detailed understanding of the relationship between structure and properties.

1.2 Motivation

In the first section of this thesis, after a brief introduction of the applied NMR methods, solid state NMR is used to identify the solid-state structure of different TADF materials after vacuum sublimation. This is from particular interest since to the current state of knowledge external impurities can play a crucial role in charge carrier trapping of organic semiconductors.[11,12] It is considered, that residual water (hole-trapping) or oxygen (electron-trapping) molecules are the responsible molecular species for the trapping mechanism. The main goal of this work is to identify the arrangement of the TADF molecules in the solid state, which seems to provide potential self-protection against impurities. It is assumed that the acceptor part, which contains a triazine ring in all investigated materials, is sensitive towards interactions with oxygen and responsible for electron trapping. Therefore, a solid-state structure elucidation of the TADF emitters plays a crucial role in gaining a better understanding of the trapping mechanism. In this particular case, solid state NMR spectroscopy can provide information about the molecular order even in amorphous materials, which makes it a powerful tool to identify structural motifs and link them to the trapping behaviour of the respective samples.

The second section of this thesis deals with the thermal degradation of the polymer-dopant system P3HT:F_4TCNQ. To the current state of knowledge, the mechanism of degradation is poorly understood. However, it plays an important role in the design and research of organic semiconductors since one of the main challenges is the fabrication of devices that provide a long lifetime. To improve the performance of those devices, it is crucial to identify possible chemical reactions that occur after thermal treatment within the material. Although the system P3HT:F_4TCNQ has been studied by methods like cyclovoltammetry and IR-spectroscopy, the mechanism of degradation remains unclear. Since F_4TCNQ is a perfluorinated compound and P3HT contains no fluorine atoms, this system is pretty well suited for heteronuclear solid state NMR experiments, revealing correlations between the two species and thus allowing a deeper insight into the distribution of the dopant molecules within the polymer matrix. Additionally, electronical changes such as redox processes in the F_4TCNQ molecule can be monitored nicely through observable changes in the ^{19}F chemical shift, making solid state NMR spectroscopy a powerful method in identifying degradation processes in polymer-dopant blends.

2. Theoretical Background

2.1 Basics of NMR spectroscopy

The state of a single spin, which is measured in an NMR experiment, can be described by a time dependent wave function in case of a single spatial coordinate $\psi(x, t)$. If the system under study shows no time dependence, the wavefunction is the solution of the time independent Schrödinger equation, which is given with:

$$\hat{H}\,\psi(x) = E\,\psi(x) \tag{2.1.1}$$

The Hamiltonian operator $\hat{H}$ describes the potential and kinetic energy of the system. In an NMR experiment, radiofrequency pulses are used und thus, a time dependency is generated. Therefore equation [2.1.1] is insufficient to describe the system and the time dependent Schrödinger equation which is given by

$$\hat{H}(t)\psi(x, t) = -i\hbar \frac{\partial \psi(x,t)}{\partial t} \tag{2.1.2}$$

has to be solved. Here, the wavefunction $\psi(x, t)$ gives a full description of the electron and nuclear spins in the sample. The full time-dependent Schrödinger, however, is practically not soluble and therefore it is assumed that the nuclei experience the averaged magnetic and electric influences of the surrounding electrons. Note, that the majority of the descriptions used in the theoretical section of this work, are based on the work of Levitt[13] and Keeler[14], if not marked differently. Those two books are also recommended for further reading in terms of NMR basics.

2.1.2 Rotating frame

Since the time dependence, which is generated by radio frequency pulses makes the mathematical description of spin dynamics more complicated than just solving time independent equations of motion, a transformation is required to simplify the problem. This transformation is equivalent to viewing the spins from a reference frame work that is also called the rotating frame. If approximations are chosen properly, the Hamiltonian appears to be time independent in this rotating frame. The view of the spins from a frame, which rotates with the RF field makes it possible to see the RF field as if it was static.
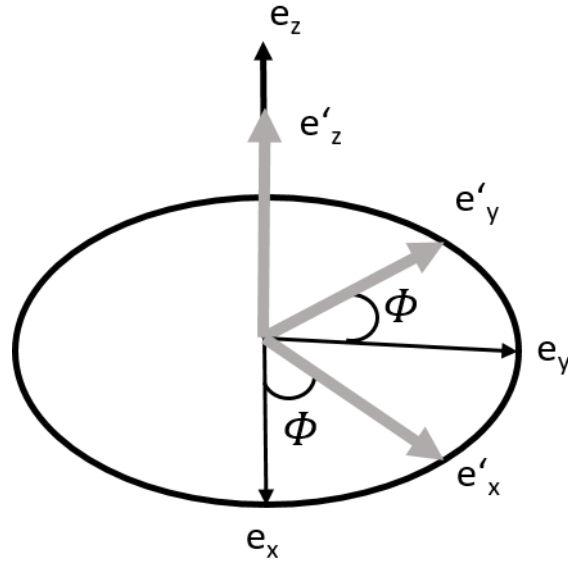
Figure 1 Schematic representation of the rotating frame.

In the rotating frame, the frame axes are related as:

$$e_x' = e_x \cos \Phi(t) + e_y \sin \Phi(t) \qquad \text{[2.1.3]}$$

$$e_y' = e_y \cos \Phi(t) - e_z \sin \Phi(t) \qquad \text{[2.1.4]}$$

$$e_z' = e_z \qquad \text{[2.1.5]}$$

In the equations [2.1.3]-[2.1.5], the parameter $\Phi(t)$ describes a time dependent angle between the laboratory- and the rotating frame axes. The relation of a spin state $|\psi\rangle$ that is viewed from a fixed frame and the same spin state viewed from the rotating frame, $|\tilde{\psi}\rangle$, can be written as:

$$|\tilde{\psi}\rangle = \hat{R}_z(-\Phi)|\psi\rangle \qquad \text{[2.1.6]}$$

In [2.1.6], $\hat{R}_z$ is called the rotation operator. After mathematical transformations, the Schrödinger-equation of the rotating frame is similar to equation [2.1.2]:

$$\frac{d}{dt}|\tilde{\psi}\rangle = -i\widehat{\tilde{H}}|\tilde{\psi}\rangle \qquad \text{[2.1.7]}$$

With the rotating frame spin Hamiltonian:

$$\widehat{\tilde{H}} = \hat{R}_z(-\Phi)\hat{H}\hat{R}_z(\Phi) - \omega_{ref}\hat{I}_z \qquad \text{[2.1.8]}$$

The first term on the right side of equation [2.1.8] describes the "usual" Hamilton operator, rotated about the z-axis by an angle Φ, which is the result of viewing the system from a frame that is rotating itself. The second term of [2.1.8] is a correction term and arises mainly due to the fact, that the frame is not executing a linear motion, but shows do to its rotation an acceleration. In the second term ω_{ref}

describes the constant rotation frequency of the rotating frame around the z-axis and $\hat{I}_z$ is the angular momentum operator. For a spin in the presence of an external magnetic field, the Hamiltonian can be simplified as follows:

$$\widehat{\widetilde{H}} = \omega^0 \hat{R}_z(-\Phi)\hat{I}_z\hat{R}_z(\Phi) - \omega_{ref}\hat{I}_z = \left(\omega^0 - \omega_{ref}\right)\hat{I}_z \qquad [2.1.9]$$

This simplification is possible, because the angular momentum operator $\hat{I}_z$ commutes with the rotation operator $\hat{R}_z$. The frequency $\omega^0 - \omega_{ref}$ is the difference between the Larmor frequency ω^0 and the reference frequency of the frame, which is called the resonance offset or offset frequency and is denoted Ω^0. Therefore, the Hamiltonian of a rotating frame spin in the presence of an external magnetic field has the form:

$$\widehat{\widetilde{H}} = \Omega^0 \hat{I}_z \qquad [2.1.10]$$

2.2 The density operator[15,16]

An NMR sample contains in good approximation about 10^{22} spins which influence each other through J (coupling via bond or scalar coupling)- and dipole-dipole couplings. Such a "collection" of independent but identical systems is often called ensemble and in this specific case an ensemble of isolated spins. At any given point, every spin has a different polarization state. Some of the spins are close to the state $|\alpha\rangle$, whereas another few are close to the state $|\beta\rangle$. However, the vast majority of the spins are in superposition states between $|\alpha\rangle$ and $|\beta\rangle$ and thus pointing towards all different directions in space, describing the total magnetization of the system. Although it is theoretically possible to calculate the contribution of each single spin and summarize the result as the total magnetization, the number of spins is simply too large, to make it a practicable procedure. However, an alternative is given by a method called the density operator, which describes the quantum state of the entire ensemble without referring to the individual spin states and is a fundamental tool in the description of NMR experiments, since the bulk magnetization which is measured in an NMR experiment is proportional to the coefficients of the eigenstates.

This density operator method is based on the expectation values of an observable. A single spin in a general superposition state can be described with:

$$|\psi\rangle = \begin{pmatrix} c_\alpha \\ c_\beta \end{pmatrix} \qquad [2.2.1]$$

And the expectation value of an operator $\hat{Q}$ is given by

$$\langle \hat{Q} \rangle = \langle \psi | \hat{Q} | \psi \rangle \qquad [2.2.2]$$

$$\langle \hat{Q} \rangle = (c_\alpha^*, c_\beta^*) \begin{pmatrix} Q_{\alpha\alpha} & Q_{\alpha\beta} \\ Q_{\beta\alpha} & Q_{\beta\beta} \end{pmatrix} \begin{pmatrix} c_\alpha \\ c_\beta \end{pmatrix} \qquad [2.2.3]$$

$$\langle \hat{Q} \rangle = c_\alpha c_\alpha^* Q_{\alpha\alpha} + c_\alpha c_\beta^* Q_{\alpha\beta} + c_\beta c_\alpha^* Q_{\beta\alpha} + c_\beta c_\beta^* Q_{\beta\beta} \qquad [2.2.4]$$

[2.2.4] is a quadratic product of the superposition coefficients. By multiplying column vector $|\psi\rangle$ and row vector $\langle\psi|$ a matrix containing these superposition coefficients can be formed:

$$|\psi\rangle\langle\psi| = \begin{pmatrix} c_\alpha \\ c_\beta \end{pmatrix} (c_\alpha^*, c_\beta^*) = \begin{pmatrix} c_\alpha c_\alpha^* & c_\alpha c_\beta^* \\ c_\beta c_\alpha^* & c_\beta c_\beta^* \end{pmatrix} \qquad [2.2.5]$$

The expectation value for $\hat{Q}$ can be extracted from the product $|\psi\rangle\langle\psi|$ and written as:

$$\langle \hat{Q} \rangle = \mathrm{Tr}\{|\psi\rangle\langle\psi|\hat{Q}\} \qquad [2.2.6]$$

Where Tr describes the trace operation of the matrix. As can be seen from [2.2.5], the state of the spin is described by four complex numbers. If there are two independent spins involved, with one being in the spin state $|\psi_1\rangle$ and the second one being in the spin state $|\psi_2\rangle$, the observed expectation value of $\hat{Q}$ is given by:

$$Q_{obs} = \mathrm{Tr}\{(|\psi_1\rangle\langle\psi_1| + |\psi_2\rangle\langle\psi_2|)\,\hat{Q}\} \qquad [2.2.7]$$

If the system contains a large number of spins (which it does in reality), a repetition of equation [2.2.7] gives

$$Q_{obs} = \mathrm{Tr}\{(|\psi_1\rangle\langle\psi_1| + |\psi_2\rangle\langle\psi_2| + \dots)\,\hat{Q}\} \qquad [2.2.8]$$

Where the sum displays all spins in the ensemble.

To obtain an average for all members of the ensemble the operator

$$\hat{p} = \mathbb{N}^{-1}(|\psi_1\rangle\langle\psi_1| + |\psi_2\rangle\langle\psi_2| + \dots) \qquad [2.2.9]$$

is defined, where $\mathbb{N}$ is the number of spins in the ensemble. This leads to a simplification for the macroscopic observation, $Q_{obs,macro}$.

$$Q_{obs,macro} = \mathbb{N}\mathrm{Tr}\{\hat{p}\hat{Q}\} \qquad [2.2.10]$$

This means, that the result of any macroscopic observation can be described by two spin operators, whereas the first one represents the measured observable and the second one the state of the entire

ensemble of spins – independent on the number of members. This reduces the individual description of ~10^{22} single spins in a sample to specifying the value of a single operator.

Considering a system of two coupled spins, the density operator also has to include the respective spin-spin interactions and can be written as follows:

$$\hat{p} = \begin{pmatrix} \overline{c_{\alpha\alpha}c_{\alpha\alpha}^*} & \overline{c_{\alpha\alpha}c_{\alpha\beta}^*} & \overline{c_{\alpha\alpha}c_{\beta\alpha}^*} & \overline{c_{\alpha\alpha}c_{\beta\beta}^*} \\ \overline{c_{\alpha\beta}c_{\alpha\alpha}^*} & \overline{c_{\alpha\beta}c_{\alpha\beta}^*} & \overline{c_{\alpha\beta}c_{\beta\alpha}^*} & \overline{c_{\alpha\beta}c_{\beta\beta}^*} \\ \overline{c_{\beta\alpha}c_{\alpha\alpha}^*} & \overline{c_{\beta\alpha}c_{\alpha\beta}^*} & \overline{c_{\beta\alpha}c_{\beta\alpha}^*} & \overline{c_{\beta\alpha}c_{\beta\beta}^*} \\ \overline{c_{\beta\beta}c_{\alpha\alpha}^*} & \overline{c_{\beta\beta}c_{\alpha\beta}^*} & \overline{c_{\beta\beta}c_{\beta\alpha}^*} & \overline{c_{\beta\beta}c_{\beta\beta}^*} \end{pmatrix} \qquad [2.2.11]$$

Here, a single element of the matrix represents one possible superposition of the spin eigenstates. The four elements on the diagonal describe the populations of the spins, whereas the other twelve elements are the coherences, which represent the possible transitions between the different populations. The coherences are characterized by the change in the multiplicity of the quantum number for two interacting spins. This allows a simplification of [2.2.11]:

$$\hat{p} = \begin{pmatrix} \alpha\alpha & +1 & +1 & +2 \\ -1 & \alpha\beta & +0 & +1 \\ -1 & -0 & \beta\alpha & +1 \\ -2 & -1 & -1 & \beta\beta \end{pmatrix} \qquad [2.2.12]$$

The transitions, which can be found symmetrically about the diagonal, are called coherence order p_{mn} where m and n describe the state of the respective spins.

If the transition between two states does not change the multiplicity ($p_{mn}=0$) it is called zero quantum transition, which is the case for a transition as $\alpha\beta \rightarrow \beta\alpha$. A change in the multiplicity by ±1, thus for a coherence as $\alpha\alpha \rightarrow \beta\alpha$, is called single quantum transition. The third possible transition in a system of two coupled spins is the double quantum coherence which is characterized by a change ±2 in the multiplicity of the quantum number, $\alpha\alpha \rightarrow \beta\beta$. A schematic representation of the different population levels and coherences is given in Figure 2.
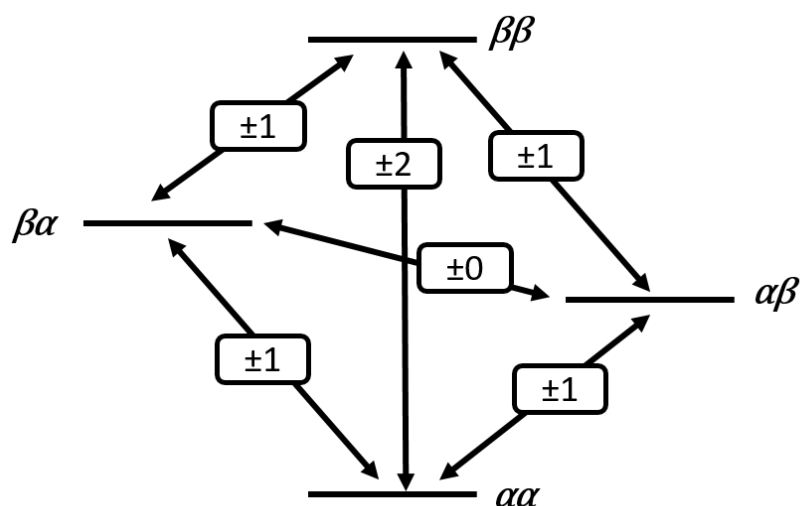
Figure 2 The four possible eigenstates of a spin pair α and β and the possible coherences between them. The symbol ±0 symbolises a zero quantum, ±1 a single quantum and ±2 a double quantum transition.

2.3 Interactions in NMR spectroscopy

As previously described, a sample contains a large quantity of spins from electrons as well as nuclei. The quantum state of an entire sample can be described by a wavefunction $|\psi_{full}\rangle$, containing information about the positions, velocities and spin state of all electrons and nuclei. In terms of NMR, the information about the spin states is the most interesting, which leads to the following expression

$$\frac{d}{dt}|\psi_{spin}(t)\rangle = -i\hat{H}_{spin}|\psi_{spin}(t)\rangle \qquad [2.3.1]$$

Where $|\psi_{spin}(t)\rangle$ describes the time dependent wavefunction of the spin states and $\hat{H}_{spin}$ the nuclear spin Hamiltonian, which contains only terms that describe the direction of the nuclear spin polarization. Therefore it is assumed, that the magnetic and electrical influences of the electrons are averaged. Furthermore, the energies of the nuclear spins are assumed to be way too small to influence the motions of electrons or even the whole molecules. This way of simplification is also known as the spin Hamiltonian hypothesis and is a secure concept for many systems at ordinary temperatures.

2.3.1 Zeeman interaction

A single spin in an external magnetic field B_0 conventionally describes the z-axis of the laboratory coordinate system. According to the quantum theory of angular momentum two angular momentum eigenstates, $|\alpha\rangle$ and $|\beta\rangle$, for a single spin ½ can be described:

$$|\alpha\rangle = |\tfrac{1}{2}, +\tfrac{1}{2}\rangle \qquad [2.3.2]$$

$$|\beta\rangle = |\tfrac{1}{2}, -\tfrac{1}{2}\rangle \tag{2.3.3}$$

Those eigenstate obey the following eigenequations:

$$\hat{I}_z|\alpha\rangle = +\tfrac{1}{2}|\alpha\rangle \tag{2.3.4}$$

$$\hat{I}_z|\beta\rangle = -\tfrac{1}{2}|\beta\rangle \tag{2.3.5}$$

Where $\hat{I}_z$ describes the angular momentum operator along the z-axis. $|\alpha\rangle$ is the eigenstate of the angular momentum along the z-axis with an eigenvalue of $+ \frac{1}{2}$ and is also called polarized along the z-axis. $|\beta\rangle$ on the other hand has an eigenvalue of $- \frac{1}{2}$ and is polarized along the –z-axis.

If the magnetic field along the z-axis has the magnitude B^0, the spin Hamiltonian is proportional to $\hat{I}_z$:

$$\widehat{H}^0_{spin} = \omega^0 \hat{I}_z \tag{2.3.6}$$

Where ω^0 is given with $\omega^0 = -\gamma B^0(1 + \delta)$ and describes the chemically shifted Larmor frequency. $\pm\omega^0$ are the eigenvalues of the energies of the two states $|\alpha\rangle$ and $|\beta\rangle$. The energies of those state are well-defined and can be shown in an energy diagram. The splitting between the energy levels is known as the Zeeman splitting, which is equal to the Larmor frequency.
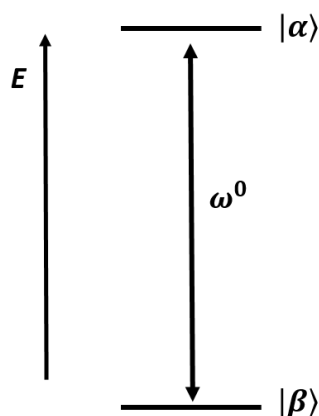

Figure 3 Energy diagram for the two possible eigen states of a ½ spin. The energy difference between the two states is described by the Larmor frequency ω^0. The population of the different states is described by the Boltzmann statistics.

This diagram displays the energy levels for a spin with a negative gyromagnetic ratio γ and hence a positive Larmor frequency. The population ratio between the two spin states is described by the Boltzmann distribution:

$$\frac{N_\alpha}{N_\beta} = e^{-\frac{\Delta E}{kT}} \tag{2.3.7}$$

in which k is the Boltzmann constant.

2.3.2 Radio frequency pulse interactions

The external magnetic field B_0, is the strongest magnetic field which is applied in an NMR experiment. However, due to technical issues, it is common to not detect the nuclear spin magnetization along the z-axis of the laboratory frame, which makes it necessary to flip the magnetization to the xy-plane. A much higher accuracy is achieved when measuring the time dependence of the coherent non-equilibrium states instead of measuring the equilibrium energy splitting. The flip of the magnetization into the transverse plane can be realized by applying an radio frequency (RF) pulse, which corresponds to the time dependent magnetic field that is applied orthogonal to the external magnetic field and consists of time dependent B and E fields. The RF pulse oscillates at the spectrometer reference frequency, that tilts the nuclear polarization by a certain angle (usually 90°) away from the direction of B_0. This field can be split into two components, one rotating in the same sense as the spin precession and the second in the opposite direction. The first one is called the resonant component, $B_1^{res}(t)$, and the second one the non-resonant component $B_1^{non-res}(t)$ of the RF field. This can be expressed in the following form:

$$B_1(t) = B_1^{res}(t) + B_1^{non-res}(t)$$
[2.3.8]

The oscillation of the RF field is given with:

$$B_1(t) = A\cos(\omega_{ref}t + \varphi)$$
[2.3.9]

Where φ describes the initial phase of the field. Therefore, the two components of the radio frequency field, perpendicular to B_0 can be described with:

$$B_1^{res}(t) = \frac{1}{2}A\{\cos(\omega_{ref}t + \varphi)\,e_x + \sin(\omega_{ref}t + \varphi)e_y\}$$
[2.3.10]

$$B_1^{non-res}(t) = \frac{1}{2}A\{\cos(\omega_{ref}t + \varphi)\,e_x - \sin(\omega_{ref}t + \varphi)e_y\}$$
[2.3.11]

This results in the following Hamilton operator:

$$\widehat{H^1}(t) = \omega_{nut}\{\cos(\omega_{ref}t + \varphi)\,\hat{I}_x + \sin(\omega_{ref}t + \varphi)\hat{I}_y\}$$
[2.3.12]

Where ω_{nut} describes the nutation frequency, which is dependent on the amplitude of the RF field and the gyromagnetic ratio:

$$\omega_{nut} = \left|\frac{1}{2}A\gamma\right|$$
[2.3.13]

The nutation frequency gives a rough approximation about the strength of the interaction between nuclear spins and the RF field. It is usually between three and four orders of magnitude smaller than the radio frequency.

If a radio frequency pulse is applied along the x-axis in the transverse plane, then the magnetization of the nuclear spins in the system after the pulse is given by:

$$\hat{I}_z \xrightarrow{\omega_p t_p \hat{I}_x} cos(\omega_p t_p)\hat{I}_z - sin(\omega_p t_p)\hat{I}_y \qquad [2.3.14]$$

where ω_p and t_p describe frequency and time of the pulse. If the product $\omega_p t_p$=90°, the z-component of the magnetization $\hat{I}_z$ vanishes entirely, and all spins can be found polarized along the –y-axis. This way of simplifying a pulse in NMR is known as the product-operator-formalism and makes the description of sequences with a large number of different pulses way easier.

Due to the fact, that the spins relax to their thermal equilibrium, thus aligning parallel to B_0, the time evolution of the coherent non-equilibrium states can be observed.. This effect is known as the free induction decay (FID), which can be converted into an NMR spectrum by applying a Fourier transformation (FT). Nowadays, FT-NMR spectrometers have become the standard instruments in more or less every laboratory and have repressed the previously used continuous wave NMR-spectrometers.[17,18]

2.3.3 Chemical shift

Electrons in molecular systems cause the local magnetic fields to vary. Therefore, sites in a molecule can experience different magnetic fields, if the electronic environment also differs. As an example, the carbon atoms of a CH_3 group in an acetone molecule experiences a totally different magnetic field compared to the carbon atom of the carbonyl group in the same molecule. This effect is known as the chemical shift and one of the most important parameters, that can be determined by NMR spectroscopy. This parameter does not only depend on the binding partners (as discussed for acetone) but is also influenced by the natural electron density surrounding the particular nucleus. For example, tin has a higher electron density as its light homologue carbon and therefore a higher chemical shift range. Lead on the other hand shows a higher chemical shift range than tin, which is even more pronounced by the contraction of the electrons towards the nucleus, caused by the inert pair effect. The chemical shift is predominantly an intramolecular interaction, but has also an intermolecular component. That means, that chemical shift values can differ slightly in different solvents and aggregation states. Chemical shifts can also be different in a crystal, if the asymmetric unit of the crystal structure contains more than one molecule.
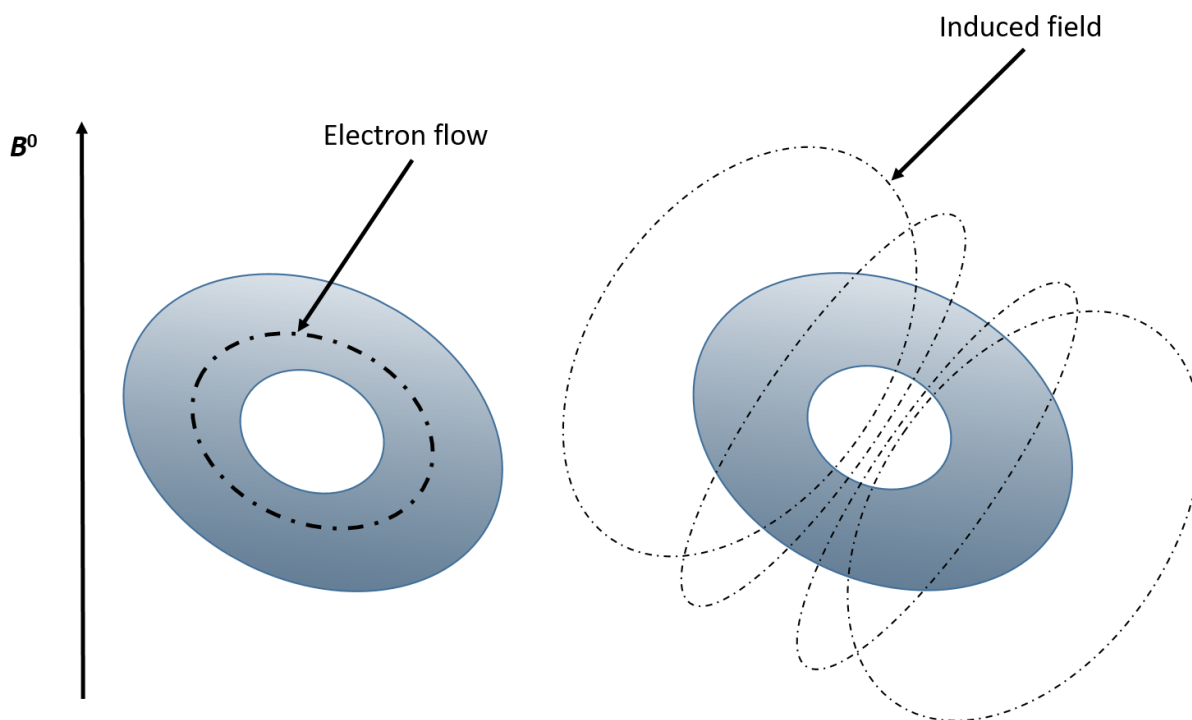
Figure 4 Schemtic mechanism of the chemical shift. The electron flow which is generated in the electron clouds of molecules induce a field that responds to the external magnetic field.

There are two major steps when it comes to the mechanism of the chemical shift. In the first one, the magnetic field B^0 induces currents in the electron clouds of the molecules. These currents in turn generate a magnetic field, which is directed opposite to the external magnetic field and often called $B^{induced}$. Although this induced magnetic field is several orders of magnitude lower than the external field, the nuclei sense the sum of both fields:

$$B^{local} = B^0 + B^{induced}$$
[2.3.15]

In other words, the strength of the locally induced magnetic field is directly proportional to the applied magnetic field.

There are two contributions to the induced currents that have been identified: the diamagnetic and the paramagnetic term. The diamagnetic term is characterized by the field-induced circulation of electrons in the ground state. The paramagnetic term, on the other hand, describes the electron circulation of the excited electronic states.

Since the induced field scales in good approximation linearly with the applied magnetic field it can also be written as:

$$B^{induced} = \delta \cdot B^0$$
[2.3.16]

Where δ describes the so called chemical shift tensor, which is a 3x3 matrix.

$$\begin{pmatrix} B_x^{induced} \\ B_y^{induced} \\ B_z^{induced} \end{pmatrix} = \begin{pmatrix} \delta_{xx} & \delta_{xy} & \delta_{xz} \\ \delta_{yx} & \delta_{yy} & \delta_{yz} \\ \delta_{zx} & \delta_{zy} & \delta_{zz} \end{pmatrix} \cdot \begin{pmatrix} 0 \\ 0 \\ B^0 \end{pmatrix} \qquad [2.3.17]$$

$$\begin{pmatrix} B_x^{induced} \\ B_y^{induced} \\ B_z^{induced} \end{pmatrix} = \begin{pmatrix} \delta_{xz} B^0 \\ \delta_{yz} B^0 \\ \delta_{zz} B^0 \end{pmatrix} \qquad [2.3.18]$$

The chemical shift tensor implies, that the induced magnetic field is usually in a different direction than the applied magnetic field. The direction of the induced field is not strictly parallel to B^0, which can be explained by the fact, that the field lines form closed loops. Since those loops go around the molecules, they must change their direction. Additionally, all molecules have a three-dimensional shape, which can make it easier for the electrons to circulate around a certain axis. Considering an aromatic system like benzene, the electrons are most likely circulating above and below the molecular plane in the doughnut-shaped p-orbitals of the molecules. Figure 4 displays such a doughnut shaped arrangement, which shows that the induced field runs through the centre of the circulating electrons. Therefore, the orientation of the molecules relative to the external magnetic field plays a crucial role for the magnitude and direction of the induced field. Another example for the orientation dependence can be illustrated using an acetone molecule.
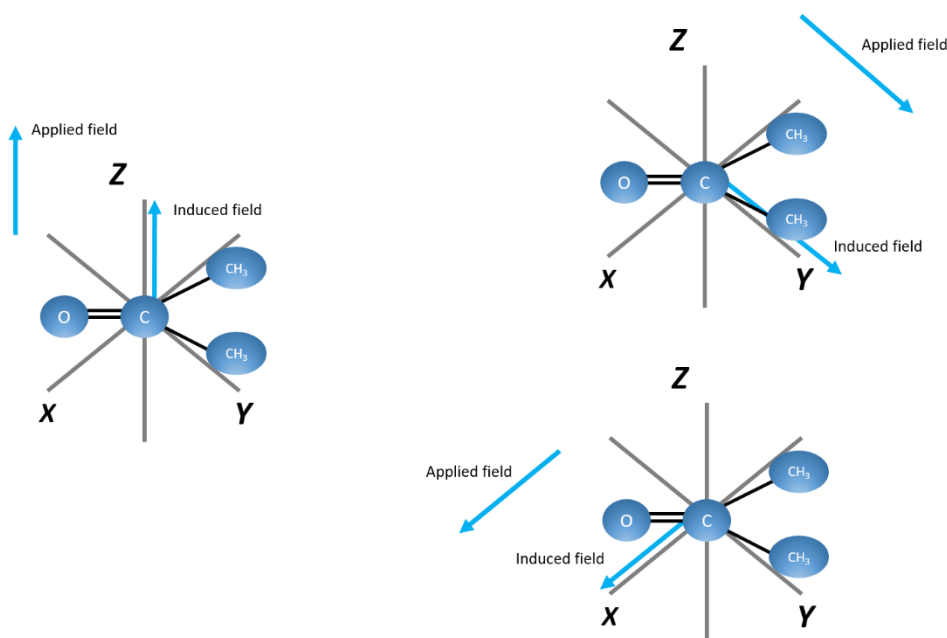

Figure 5 Orientation dependence between the external magnetic field and the induced field in the molecule acetone.

From Figure 5 it can be clearly seen, that the influence of the induced field on the different molecular sites depends on the orientation of the molecules relative to the external magnetic field. In the liquid or gas phase, the molecular movement causes an averaging of the induced magnetic fields in the

sample. The resulting chemical shift tensor in such a system is called isotropic δ^{iso} and can be calculated by forming the mean of the three values along the principal axes.

$$\delta^{iso} = \frac{1}{3}(\delta_{ZZ} + \delta_{YY} + \delta_{XX}) \hspace{4cm} \text{[2.3.19]}$$

The value of δ^{iso} determines the position of the resonances in isotropic liquids. This makes especially solution NMR an extremely powerful technique when it comes to molecular structure elucidation. Nowadays, the chemical shift values are given in units of ppm. This makes it way easier to compare NMR spectra measured at different fields, since the ppm scale is normalized while the Larmor frequencies differ, depending on the field strengths.

However, for solid samples it is more likely that the molecules do not behave as an isotropic ensemble. Therefore, the anisotropy of the chemical shift will be discussed in the next section

2.3.4 Chemical shift anisotropy (CSA)

If two or more values for the principle axes of the chemical shift tensor are inequivalent, the chemical shift tensor is called anisotropic. The most commonly used convention to assign the principal values for the anisotropic chemical shift tensor is described by:

$$\left|\delta_{ZZ} - \delta^{iso}\right| \geq \left|\delta_{XX} - \delta^{iso}\right| \geq \left|\delta_{YY} - \delta^{iso}\right| \hspace{3cm} \text{[2.3.20]}$$

The chemical shift anisotropy, δ^{aniso} is defined as the largest deviation in chemical shift from the isotropic value.

$$\delta^{aniso} = \delta_{ZZ} - \delta^{iso} \hspace{4cm} \text{[2.3.21]}$$

The asymmetry parameter η quantifies the difference between the other two principal values and is given with:

$$\eta = \frac{\delta_{YY} - \delta_{XX}}{\delta^{aniso}} \hspace{4cm} \text{[2.3.22]}$$

For the case, $\delta_{YY} = \delta_{XX}$, the asymmetry parameter becomes zero. If $\delta^{aniso} \neq 0$, the chemical shift tensor is said to be uniaxial. On the other hand, $\delta_{YY} \neq \delta_{XX}$ and $\delta^{aniso} \neq 0$ leads to a biaxial chemical shift tensor.
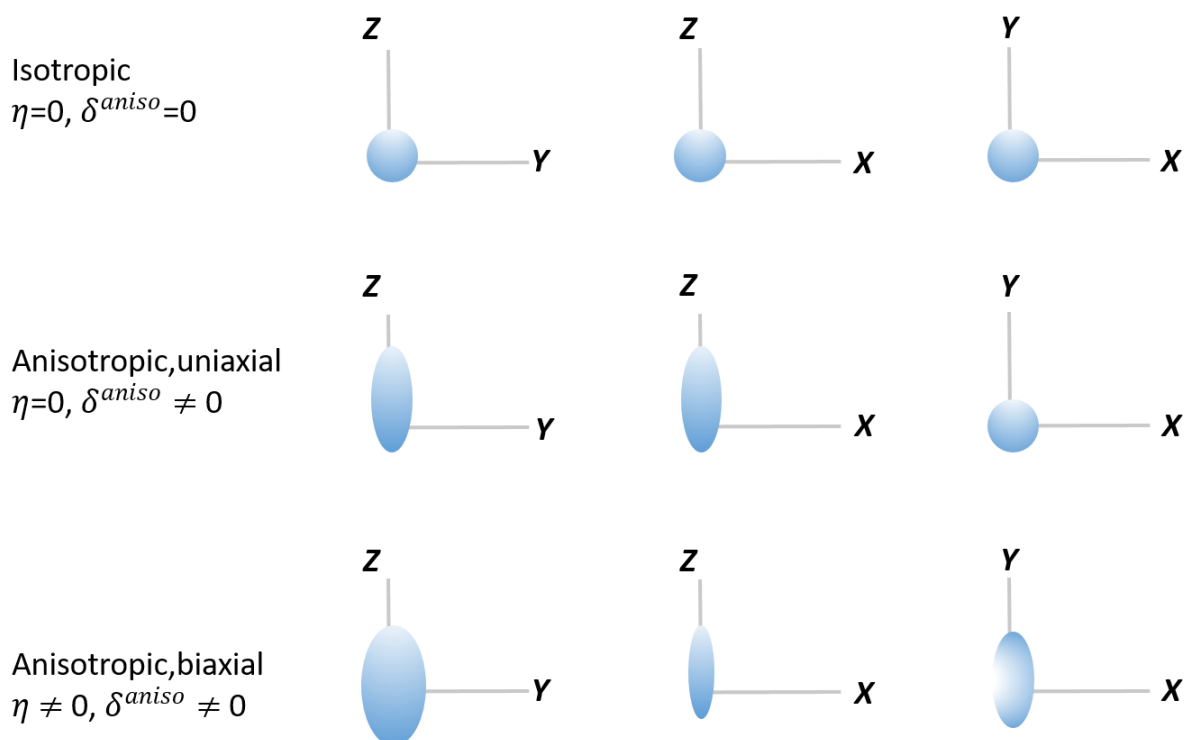
Figure 6 Visual representation of the electron distribution in molecules and the resulting isotropy or anisotropy effects.

2.3.5 Neighbouring group interactions

Neighbouring groups can contribute to the chemical shift by inducing currents in spatially close atoms. Considering a H-X group (where X can be any heteronucleus) in which the external magnetic field creates currents in the electron clouds of X that are inducing a magnetic moment which is proportional to the field. The proportionality is called the magnetic susceptibility χ, formed by two components $\chi_\parallel$ and $\chi_\perp$ (parallel and perpendicular to the symmetry axis). The value of Θ describes the angle between the B_0 axis and the vector between H and X. Therefore, the parameter of neighbouring group contribution is given with:

$$\sigma_{neighbour} \propto (\chi_\parallel - \chi_\perp) \left(\frac{1 - 3\cos^2(\Theta)}{r^3} \right)$$

[2.3.23]

Where *r* is the distance between the investigated nuclei. An example for the influence of neighbouring group contributions and thus the shielding effect of the electron density, are rigid molecules with a well defined three-dimensional structure such as crystalline solids. This is the case in materials, where the magnetic susceptibility of aromatic ring systems show a strong anisotropy, which leads to different local electronic environments and thus different chemical shifts for nuclei of the same kind. The electrons in the π-orbitals interact with the external magnetic field and a ring current is induced (circulation of electrons above and below the molecular plane). Nuclei, which are located in the plane

of the ring are shifted to the lower field (deshielded), while on the other hand, nuclei that are located above and below the plane are shifted to the higher field (shielded). This is most commonly found in solid samples do to the spatial proximity of the respective groups. However, in solution NMR experiments, the solvent molecules can cause the same effects on the chemical shifts. It is possible to determine the nuclear independent chemical shift values (NICS) to visualize such shielding and deshielding effets.

2.3.6 Dipole-dipole couplings

The through space interaction of spin ½ nuclei is in an important feature which can be detected and quantified by NMR spectroscopic methods. In terms of classical physics, two spins I and S acquire a magnetic energy of each other:

$$E = \frac{\mu_0}{4}\left(\frac{\mu_I\mu_S}{r^3} - 3\frac{(\mu_I r)(\mu_S r)}{r^5}\right)$$ [2.3.24]

The operator of the magnetic moment can be described quantum mechanically in the following way:

$$\hat{\mu} = \gamma\hbar\hat{I}$$ [2.3.25]

By using this quantum mechanical operator in [2.3.25], it is possible to obtain the Hamiltonian of the dipolar coupling between the two spins I and S:

$$\hat{H}_D = \left(\frac{\mu_0}{4\pi}\right)\gamma_I\gamma_S\hbar\left(\frac{\hat{I}_I\hat{I}_S}{r^3} - 3\frac{(\hat{I}_I r)(\hat{I}_S r)}{r^5}\right)$$ [2.3.26]

This Hamiltonian can be transformed into an expression which contains spatial and spin terms, using polar coordinates:

$$\hat{H}_D^{IS} = -D_{IS}\frac{1}{2}(3\cos^2\theta_{IS} - 1)\left[2\hat{I}_{I,z}\hat{I}_{S,z} - (\hat{I}_{I+}\hat{I}_{S-} + \hat{I}_{I-}\hat{I}_{S+})\right]$$ [2.3.27]

$$\hat{H}_D^{IS} = -D_{IS}\frac{1}{2}(3\cos^2\theta_{IS} - 1)\left[2\hat{I}_{I,z}\hat{I}_{S,z} - \hat{I}_{I,x}\hat{I}_{S,x} - \hat{I}_{I,y}\hat{I}_{S,y}\right]$$ [2.3.28]

$$\hat{H}_D^{IS} = -D_{IS}\frac{1}{2}(3\cos^2\theta_{IS} - 1)\left[3\hat{I}_{I,z}\hat{I}_{S,z} - \hat{I}_I\hat{I}_S\right]$$ [2.3.29]

The parameter θ_{IS} describes the angle between the external magnetic field and the vector that connects the two nuclei. D_{IS} is the dipolar coupling constant and has the following relation:

$$D_{IS} = \frac{\mu_0}{4\pi}\frac{\gamma_I\gamma_S\hbar}{r_{IS}^3}$$ [2.3.30]

This Hamiltonian describes the case of a homonuclear dipolar coupling. For both, homo- and heteronuclear interaction, the splitting for the chemical shift depends on the kind of nuclei and the angle θ :

$$\nu_{\text{hom}} = \nu_0 \pm \frac{3D_{II}}{4}(3\cos^2\theta_{II} - 1) \qquad\qquad [2.3.31]$$

$$\nu_{\text{het}} = \nu_0 \pm \frac{3D_{IS}}{2}(3\cos^2\theta_{IS} - 1) \qquad\qquad [2.3.32]$$

2.4 Magic angle spinning

As stated out previously, all of the nuclear magnetic interactions are in general anisotropic. This means, that the energy levels and frequencies hardly depend on the orientation of the spins in the sample to the external magnetic field. The orientational dependencies of the magnetic interactions between the nuclear spins were presented in the previous section given with:

$$\hat{H}_{CS} = \omega_0 \delta^{iso} + \frac{\omega_0 \delta^{aniso}}{2}[3\cos^2(\theta - 1) - \eta\sin^2(\theta)\cos(2\phi)]\hat{I}_z \qquad\qquad [2.4.1]$$

$$\hat{H}_{D,homo} = \frac{\mu_0 \gamma_I \gamma_S \hbar}{4\pi r_{IS}^3} \frac{3\cos^2(\theta-1)}{2}\left[3\hat{I}_{IZ}\hat{I}_{SZ} - (\hat{I}_I\hat{I}_S)\right], \text{ if } I = S \qquad\qquad [2.4.2]$$

$$\hat{H}_{D,hetero} = \frac{\mu_0 \gamma_I \gamma_S \hbar}{4\pi r_{IS}^3} \frac{3\cos^2(\theta-1)}{2}2\hat{I}_{IZ}\hat{I}_{SZ}, \text{ if } I \neq S \qquad\qquad [2.4.3]$$

The three equations describe the orientation dependence of the chemical shift, the homo- and heteronuclear dipolar coupling respectively. Note, that there is in general also an anisotropic behaviour of the quadrupolar coupling, which is however not considered in this work and therefore not discussed.

In solution NMR experiments, the rapid motions of the molecules leads to an efficient averaging of the orientational nuclear magnetic dependencies, thus leaving only the isotropic component of the chemical shift detectable. However, in solid samples, the molecules do not undergo such rapid motions, which results in broad lines, reflecting the orientational distributions of spins in the sample by their frequency and intensity profiles. These broad lines are called powder patterns and can give rise to the local environment of the molecules studied. On the other hand, such powder patterns show a distribution of the spectral intensity over a broad frequency range. This results in a loss of the resolution and severely reduced intensity. This orientation dependence of the anisotropic interactions

in a solid sample, however, can be eliminated by using the method of magic angle spinning (MAS) in which the sample is rotated around an axis of 54.7° with respect to the external magnetic field. This rotation averages the anisotropic nuclear interactions either partially or completely, if the MAS frequency exceeds the magnitude of the interaction. A partially averaging leads to the occurrence of spinning sidebands in the recorded spectrum. Those sidebands depend on the principal components of the interaction tensor and the spinning frequency. The narrowing of the lines by using the MAS method comes along with a loss of information about structure and dynamics. Specific pulse sequences, however, are capable to selectively recouple this information, which will be discussed later on.

2.5 Crosspolarization

The cross polarization (CP) technique is a double-resonance experiment, which is widely used in modern solid state NMR spectroscopy. This method overcomes two problems, coming along by measuring solid state NMR spectra of low natural abundance nuclei as ^{13}C, ^{15}N or ^{29}Si. If such spectra are recorded with a basic single pulse experiment, the low sensitivity combined with a low gyromagnetic ratio, lead to a poor signal intensity. With a cross polarization experiment, it is possible to enhance those intensity. The second problem results from the fact, that the diluted nuclei with a spin of ½ are usually characterized by long transverse relaxation times. This is mainly caused by the absence of strong homonuclear dipolar couplings which can stimulate the relaxation transitions. In the case of diluted nuclei only the weaker heteronuclear couplings remain, thus resulting in the need of long recycle delays in between subsequent scans. For the majority of solids, dilute nuclei are in spatial proximity to those with a high natural abundance and therefore coupled via the magnetic dipolar interactions.
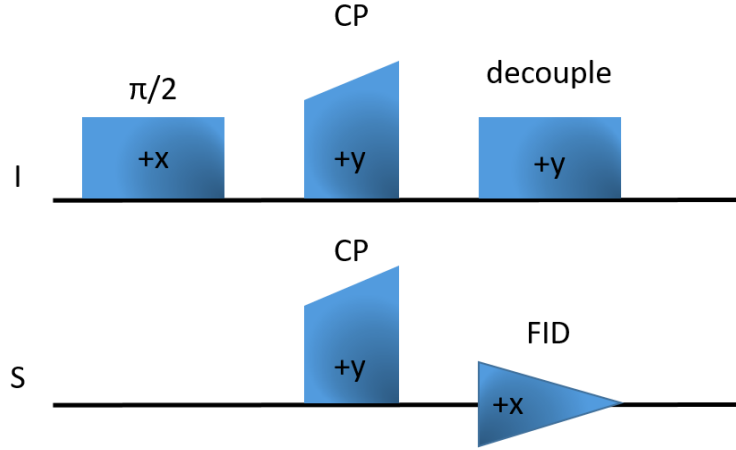
Figure 7 Pulse sequence of a CP experiment. Transverse magnetization is generated by a π/2 pulse on spin I before the cross polarization is applied. The data is then recorded for spin S while decoupling is applied to the spin I channel.

To illustrate the kinetics of a cross polarization experiment two spins I and S with a nuclear spin of ½ are considered. In terms of thermodynamics, such a system consists of a lattice with a huge heat capacity and two subsystems, namely I and S, with one of the subsystems having a way larger heat capacity than the other one. In this chapter the spin I is chosen to be that respective system. It is assumed, that the spin state I experiences a spin lock along the B_{1I} field. This can be achieved by choosing the B_{1I} to be larger than every local dipolar field. During the spin lock pulse, the magnetization of I is "hold" in the transverse plane, which corresponds to a very low spin temperature. Right before the cross polarization contact, the magnetization on spin S in the transverse plane is zero which is equal to an infinitely high spin temperature. To bring the two subsystems in thermic contact, the Hartmann-Hahn condition has to be fulfilled:

$$\gamma_I B_{1I} = \gamma_S B_{1S} \qquad\qquad [2.5.1]$$

Which allows the flow of energy from one system to the other. If the system reaches thermodynamic equilibrium, the spin temperatures equilibrate as well. In other words, the infinitely hot spin system S is cooled down by transferring its thermal energy to the cold system I. Both spins are also in contact with the lattice, linked by the longitudinal relaxation time in the rotating frame $T_{1\rho}$. The overall process of cross polarization during a contact time *t* is given by the following differential equations:

$$\frac{d}{dt}\beta_S = -\frac{(\beta_S - \beta_I)}{T_{IS}} - \frac{\beta_S}{T_{1\rho}^S} \qquad\qquad [2.5.2]$$

$$\frac{d}{dt}\beta_I = -\epsilon\alpha^2\frac{(\beta_I - \beta_S)}{T_{IS}} - \frac{\beta_I}{T_{1\rho}^I} \qquad\qquad [2.5.3]$$

The parameters β describe the inverse spin temperature of the respective state, $\frac{1}{T_{IS}}$ is the CP rate constant, ϵ is the spin population ratio and α the Hartmann-Hahn matching coefficient. For a dilute-abundant spin system ϵ has a very small value and $\alpha=1$. By solving the differential equations with the

consideration that the inverse spin temperature is proportional to the respective magnetization and in turn also proportional to the peak intensities, the following expression is obtained:

$$I(t) = I_0 \left(1 - e^{-\frac{t}{T_{IS}}} \right)$$

[2.5.4]

This equation is valid for the simplest case of CP kinetic, in which $\epsilon \alpha^2 = 0$, $\frac{T_{IS}}{T_{1\rho}^I} = 0$ and $\frac{T_{IS}}{T_{1\rho}^S} = 0$.

2.6 Basics of 2D NMR spectroscopy

The development of two dimensional NMR spectroscopy made the elucidation of molecular structures much easier and has greatly increased the complexity of the problems which can be handled. In this section, the basic principles of two dimensional experiments will be described. Nowadays, there are a huge number of pulse sequences which can be applied and are tailored for the needs of the specific experiments.

A general scheme for a pulse sequence, which is valid for all two dimensional experiments is given in Figure 8. Such a scheme is structured in a preparation, evolution and mixing segment, followed by the detection of the magnetization.
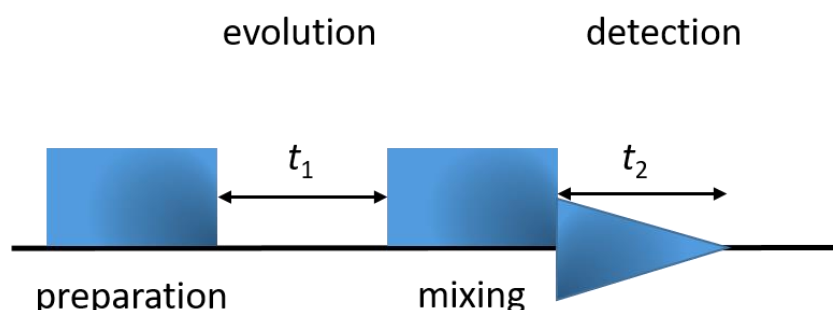
Figure 8 Basic pulse sequence of a two dimensional NMR experiment. During the preparation time, transverse magnetization is generated, which evolves during t_1. The mixing period transforms unobservable multiple quantum coherences into observable once that can be detected during t_2.

In the preparation period, something simple as a $\pi/2$ pulse is applied to the sample. This generates transverse magnetization and leads to the occurrence of single quantum coherences. However, dependent on the pulse sequence, this can be more complicated than just a single pulse, e.g. sequences that generate double quantum coherences. The evolution period is an incrementation, rather than a fixed time in a series of separate experiments. In this segment of the pulse sequence, no detections are made. Therefore, the coherences that are generated during the evolution period, do not have to be observed and thus can also be multiple quantum coherences. The ability to follow non-observable coherences is an important feature of two dimensional NMR experiments. The mixing

period manipulates the coherences to become a detectable signal which can be recorded during the detection period t_2. During the mixing time it is also possible for magnetization to be transferred from one spin to another due to scalar couplings. In the end, the mixing period is responsible for the information content of the spectrum.

The COSY (COrrelation SpectroscopY) pulse sequence is an often used in terms of NMR measurements and will be considered now to illustrate the basics of a homonuclear 2D NMR experiment. This experiment is considered as one of the most fundamental 2D NMR experiments and is used (among other methods in this work) to assign the respective ^{1}H resonances in solution experiments. After the initial π/2 pulse along the x-axis, the magnetization evolves during t_1 under the offset of spin one and the J-coupling between both spins:

$$-\hat{I}_{1y} \xrightarrow{\Omega_1 t_1 \hat{I}_{1z}} -\cos(\Omega_1 t_1)\,\hat{I}_{1y} + \sin(\Omega_1 t_1)\hat{I}_{1z} \tag{2.6.1}$$

$$-\cos(\Omega_1 t_1)\,\hat{I}_{1y} \xrightarrow{2\pi J_{12} t_1 \hat{I}_{1z}\hat{I}_{2z}} -\cos(\pi J_{12} t_1)\cos(\Omega_1 t_1)\hat{I}_{1y} + \sin(\pi J_{12} t_1)\cos(\Omega_1 t_1)2\hat{I}_{1x}\hat{I}_{2z} \tag{2.6.2}$$

$$\sin(\Omega_1 t_1)\,\hat{I}_{1x} \xrightarrow{2\pi J_{12} t_1 \hat{I}_{1z}\hat{I}_{2z}} \cos(\pi J_{12} t_1)\sin(\Omega_1 t_1)\hat{I}_{1x} + \sin(\pi J_{12} t_1)\sin(\Omega_1 t_1)2\hat{I}_{1y}\hat{I}_{2z} \tag{2.6.3}$$

The first line describes the evolution of the magnetization in the transverse plane. The second and third lines describe the time evolution of the two transverse components under the scalar coupling. The final π/2 pulse rotates every of the terms:

$$-\cos(\pi J_{12} t_1)\cos(\Omega_1 t_1)\hat{I}_{1y} \xrightarrow{(\pi/2)(\hat{I}_{1x}+\hat{I}_{2x})} -\cos(\pi J_{12} t_1)\cos(\Omega_1 t_1)\hat{I}_{1z} \tag{2.6.4}$$

$$\sin(\pi J_{12} t_1)\cos(\Omega_1 t_1)2\hat{I}_{1x}\hat{I}_{2z} \xrightarrow{(\pi/2)(\hat{I}_{1x}+\hat{I}_{2x})} -\sin(\pi J_{12} t_1)\cos(\Omega_1 t_1)2\hat{I}_{1x}\hat{I}_{2y} \tag{2.6.5}$$

$$\cos(\pi J_{12} t_1)\sin(\Omega_1 t_1)\hat{I}_{1x} \xrightarrow{(\pi/2)(\hat{I}_{1x}+\hat{I}_{2x})} \cos(\pi J_{12} t_1)\sin(\Omega_1 t_1)\hat{I}_{1x} \tag{2.6.6}$$

$$\sin(\pi J_{12} t_1)\sin(\Omega_1 t_1)2\hat{I}_{1y}\hat{I}_{2z} \xrightarrow{(\pi/2)(\hat{I}_{1x}+\hat{I}_{2x})} -\sin(\pi J_{12} t_1)\sin(\Omega_1 t_1)2\hat{I}_{1z}\hat{I}_{2y} \tag{2.6.7}$$

The first two expressions can be neglected, since the first one describes the z-Magnetization and the second one the double-quantum coherence, which are both not detectable. The operator [2.6.6] in the third line $\hat{I}_{1x}$ gives rise to a doublet of spin one in the dimension ω_2, which is modulated in t_1 with an offset Ω_1. This peak is called a diagonal peak and its location in the spectrum can be seen in Figure 9. In contrast to that, the operator $2\hat{I}_{1z}\hat{I}_{2y}$ in the last line, gives rise to an antiphase doublet, centered at the shift of the second spin in the dimension ω_2. This term is modulated in t_1, equal to term three, which is according to $\sin(\Omega_1 t_1)$. All in all, the fourth term gives rise to a crosspeak centred at Ω_1 in ω_1 and Ω_2 in ω_2. The second spin of course, experiences the same pulses as spin one. This results in a

diagonal peak with an offset of Ω_2 and a crosspeak centered at Ω_2 in ω_1 and Ω_1 in ω_2. As can be seen from Figure 9, the obtained COSY spectrum for a system of two spins is symmetric, consisting two diagonal- and two cross peaks.
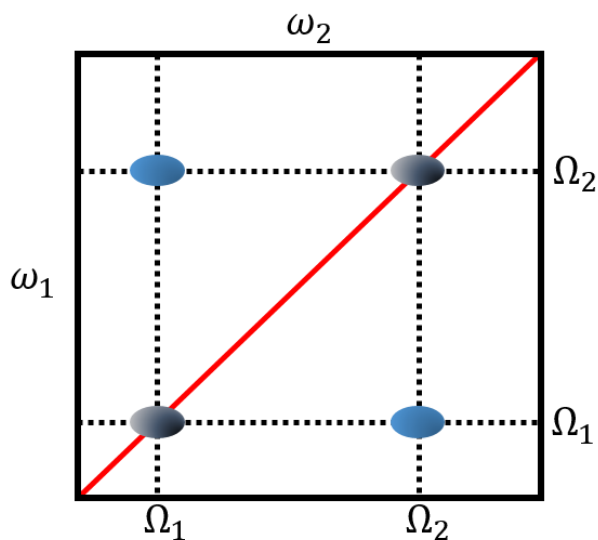
Figure 9 Schematic representation of a COSY NMR experiment. The black ellipsoids display the diagonal peaks and the blue ones the cross peaks.

As stated before, double-quantum coherences can not be detected directly. However, since no detections are made during t_1, it is possible to follow the time evolution of such unobservable coherences. The pulse sequence shall be discussed in detail hereafter. A simple pulse sequence for a double quantum experiment is given in Figure 10.
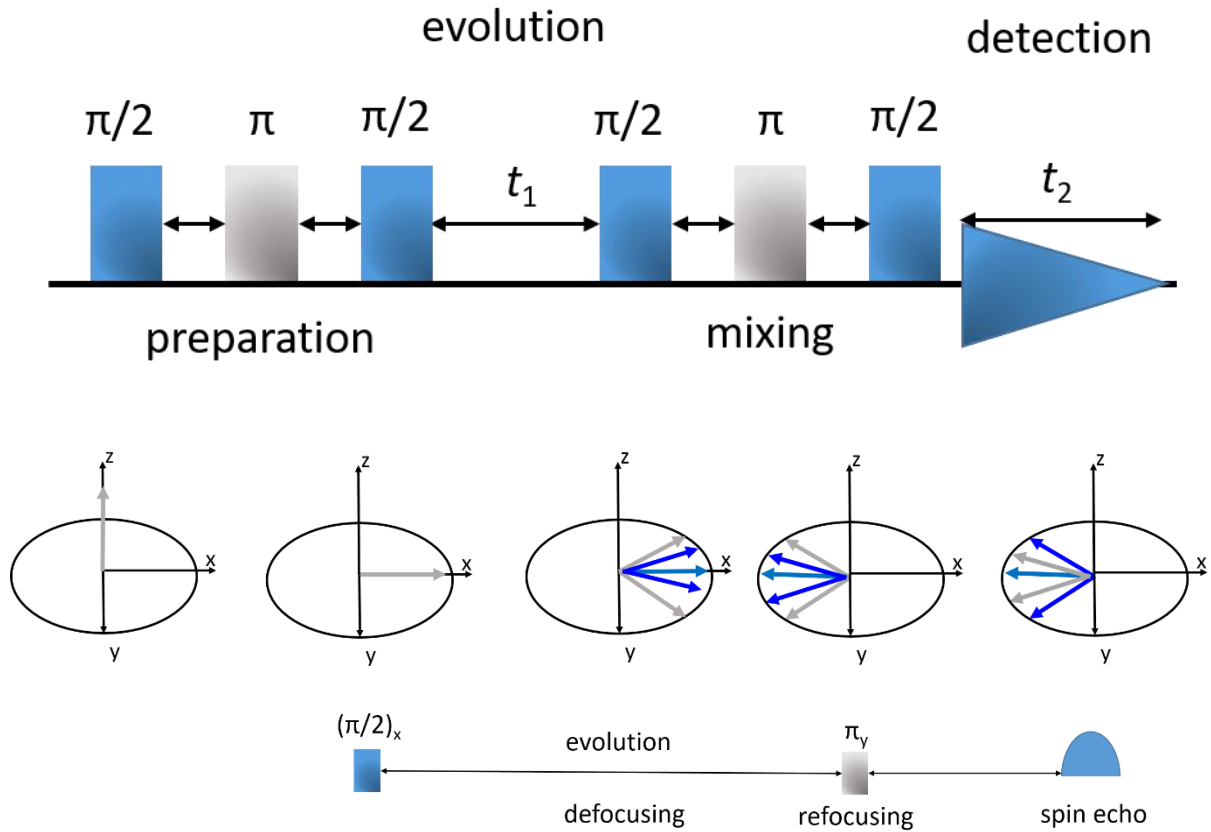
Figure 10 Pulse sequence for a double quantum NMR experiment. Double quantum coherences are generated after a spin echo period by a π/2 pulse. These coherences are then transformed into observable coherences during the mixing period. A schematic representation of the spin echo effect is given in the lower section of the figure.

The first π/2 pulse generates transverse magnetization which is followed by a spin echo period which results in some anti-phase magnetization, the amount depending on the delay τ and the strength of the coupling. Note that in DQ experiments, the π-pulse is not necessarily needed and depends on the applied pulse sequence. The second π/2 pulse converts the magnetization into a multiple quantum coherence that evolves during t_1. The final π/2 pulse transfers the multiple quantum coherence into observable magnetization, which can be detected during t_2.

At the start of the experiment, the equilibrium magnetization for a two spin system is $\hat{I}_{1z} + \hat{I}_{2z}$. Considering the $\hat{I}_{1z}$ term, which is rotated by the first pulse to $-\hat{I}_{1y}$, which is followed by the spin echo period. The spin echo refocuses the offset, while the coupling evolves for 2τ. This means, that the magnetization at the end of the spin echo period is:

$$\cos(2\pi J_{12}\tau)\,\hat{I}_{1y} - \sin(2\pi J_{12}\tau)\,2\hat{I}_{1x}\hat{I}_{2z} \qquad [2.6.8]$$

And the π/2 pulse rotates the magnetization to give:

$$\cos(2\pi J_{12}\tau)\,\hat{I}_{1z} + \sin(2\pi J_{12}\tau)\,2\hat{I}_{1x}\hat{I}_{2y} \qquad [2.6.9]$$

The double quantum part $\widehat{DQ}_y$ of the operator $2\hat{I}_{1x}\hat{I}_{2y}$ has the following relationship:

$$\frac{1}{2}\widehat{DQ}_y = \frac{1}{2}\left(2\hat{I}_{1x}\hat{I}_{2y} + 2\hat{I}_{1y}\hat{I}_{2x}\right) \tag{2.6.10}$$

Which means, that the second part of [2.6.9] has the following form at the start of t_1:

$$\frac{1}{2}\sin(2\pi J_{12}\tau)\,\widehat{DQ}_y \tag{2.6.11}$$

The double quantum term evolves during t_1:

$$\widehat{DQ}_y \xrightarrow{\text{evolution during } t_1} \cos([\Omega_1 + \Omega_2]t_1)\,\widehat{DQ}_y - \sin([\Omega_1 + \Omega_2]t_1)\,\widehat{DQ}_x \tag{2.6.12}$$

Here, the sum of the offsets $\Omega_1 + \Omega_2$ of the two spins envolved determines the time evolution of the double quantum coherence. The magnetization by the end of t_1 is given by:

$$\frac{1}{2}\sin(2\pi J_{12}\tau)\left[\cos([\Omega_1 + \Omega_2]t_1)\,\widehat{DQ}_y - \sin([\Omega_1 + \Omega_2]t_1)\,\widehat{DQ}_x\right] \tag{2.6.13}$$

The final $\pi/2$ pulse affects the double quantum operators $\widehat{DQ}_x$ and $\widehat{DQ}_y$ differently.

$$\widehat{DQ}_x = \left(2\hat{I}_{1x}\hat{I}_{2x} - 2\hat{I}_{1y}\hat{I}_{2y}\right) \xrightarrow{(\pi/2)*(\hat{I}_{1x}+\hat{I}_{2x})} \left(2\hat{I}_{1x}\hat{I}_{2x} - 2\hat{I}_{1z}\hat{I}_{2z}\right) \tag{2.6.14}$$

$$\widehat{DQ}_y = \left(2\hat{I}_{1x}\hat{I}_{2y} + 2\hat{I}_{1y}\hat{I}_{2x}\right) \xrightarrow{(\pi/2)*(\hat{I}_{1x}+\hat{I}_{2x})} \left(2\hat{I}_{1x}\hat{I}_{2z} - 2\hat{I}_{1z}\hat{I}_{2x}\right) \tag{2.6.15}$$

It can be seen, that the double quantum operator $\widehat{DQ}_x$ does not lead to any observable magnetization. The operator $\widehat{DQ}_y$, on the other hand, leads to two observable terms, one on each spin. At the start of the detection t_2 the observable magnetization is:

$$\frac{1}{2}\sin(2\pi J_{12}\tau)\cos([\Omega_1 + \Omega_2]t_1)\left(2\hat{I}_{1x}\hat{I}_{2z} - 2\hat{I}_{1z}\hat{I}_{2x}\right) \tag{2.6.16}$$

In the dimension ω_2 there is one signal generated for spin one and a similar signal for spin two. The double quantum frequency $\Omega_1 + \Omega_2$ is the only modulating frequency in t_1. (Note, that the pulses also act upon the equilibrium magnetization of the second spin $\hat{I}_{2z}$, which is not shown in this work). A schematic DQ spectrum which can be generated for a system that contains two spins is shown in Figure 11.
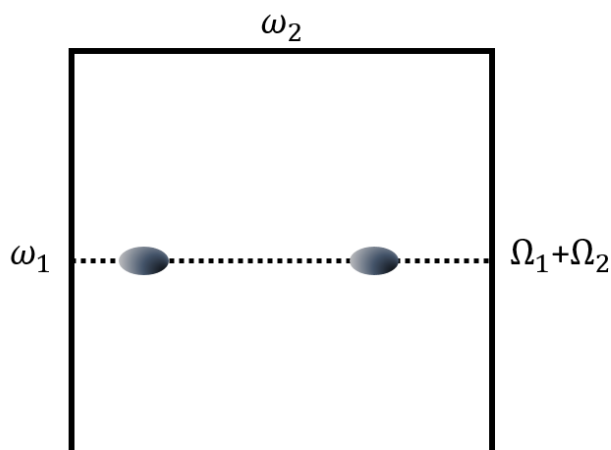
Figure 11 Schematic representation of a two dimensional double quantum NMR spectrum. The signals are observed at the sum of the values of the single quantum resonances $\Omega_1 + \Omega_2$ in the indirect dimension.

It can be seen in the scheme that both signals resonate at the same ω_1 frequency. The intensity of the generated signals depends on e.g. the factor $\sin(2\pi J_{12}\tau)$. This factor determines the overall amount of double quantum coherences, which can be created. The largest amount of double quantum coherences is found for the condition $\tau = \frac{1}{4J_{12}}$ and thus the peaks are strongest at this condition. If two spins interact through a coupling, they must share the same double quantum frequency, which makes this experiment extremely powerful for the elucidation of molecular structures. Such double quantum excitations are also valid for dipole-dipole couplings and are about three orders of magnitude larger than J-couplings and are influenced by molecular motion. In solid-state NMR experiments, the J-coupling is obscured by dipole-dipole interactions, making it way less relevant compared to solution NMR.

2.7 Relaxation

If the spins in a sample are allowed to be undisturbed after an excitation pulse they will return to thermal equilibrium. This implies, that coherences are absent and that the populations of eigenstates are described by the Boltzmann distribution at the temperature of the system under study. A radiofrequency pulse, however, disturbs this thermal equilibrium, resulting in an observable time dependence of coherent non-equilibrium states. This excitation leads to a deviation in the population states if compared to the thermal equilibrium and in most of the cases, coherences are created. For example, a π pulse inverts the magnetisation, whereas a $\pi/2$ pulse leads to an equal population of the spin state and generates coherences. The process that describes the pathway of the spins in the excited state back to the thermal equilibrium is called relaxation and the time it takes to reach such an equilibrium is named relaxation time. The following presentation of the relaxation times is based on the theory given by Levitt[13] and Keeler[14], which is only one out of some possible ways to describe this phenomenon.

There are two major relaxation processes that are of high interest in terms of NMR experiments:

1. The spin-lattice or longitudinal relaxation, which describes the return of the spins back to their Boltzmann distribution value in thermal equilibrium. The respective relaxation time, which describes this process is called T_1 relaxation time.

2. The spin-spin or transverse relaxation, which describes the phase decay of coherences. The respective relaxation time, which describes this process is called T_2 relaxation time.

An ensemble of isolated spin pairs with a quantum number of ½ can be described by these two time constants. If there are more coupled spins in the system, one needs a lot more of time constants to describe those subtle and varied phenomena.

In an NMR experiment, the fluctuation of the transverse field induces transitions between the energy eigenstates of the spins $|\alpha\rangle$ and $|\beta\rangle$. If a spin is in the energy state $|\alpha\rangle$ at a time t, this state will be different after a time $t + \tau$ and will be called $|\alpha'\rangle$ for further considerations, caused by the influences of the B_1 field. The state $|\alpha'\rangle$ can be seen as a superposition of the two eigenstates $|\alpha\rangle$ and $|\beta\rangle$. This means, that a measurement can result into a value which is appropriate to the state $|\beta\rangle$. The transition probability W between the two energy states, for small values of τ is given by:

$$W_- = \tau^{-1}\overline{|\langle\beta|\alpha'\rangle|^2} \qquad\qquad [2.7.1]$$

$\overline{|\langle\beta|\alpha'\rangle|^2}$ describes an ensemble average and the – in W_- indicates, that the spin angular momentum along the B_0 field decreases for the transition $|\alpha\rangle \rightarrow |\beta\rangle$.

Similar to this, a process which increases the spin angular momentum along the B_0 field for a transition $|\alpha\rangle \rightarrow |\beta\rangle$ can be denoted with:

$$W_+ = \tau^{-1}\overline{|\langle\alpha|\beta'\rangle|^2} \qquad\qquad [2.7.2]$$

Those transitions can be illustrated in an energy diagram as follows:
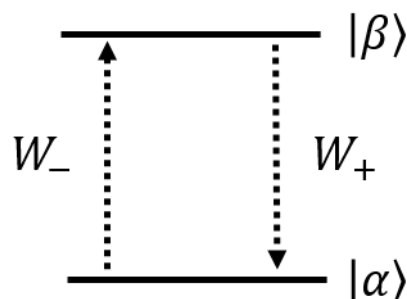
Figure 12 Energy diagramm for the transition rates between spin states $|\alpha\rangle$ and $|\beta\rangle$.

The transition probabilities in a random field model can be derived and their values are predicted to be equal and proportional to the spectral density of the random field with the Larmor frequency ω^0:

$$W_- = W_+ = \frac{1}{2}\gamma^2 \langle B_x^2 \rangle \mathfrak{J}(\omega^0) \qquad [2.7.3]$$

With the description of the transition possibilities, one can examine the changes in the spin populations under these processes. The change in the spin population of the state $|\alpha\rangle$ over the course of time can be described as:

$$\frac{d}{dt}\rho_\alpha = -W_-\rho_\alpha + W_+\rho_\beta \qquad [2.7.4]$$

Similarly, the time dependent change for the spin state $|\beta\rangle$ is given with:

$$\frac{d}{dt}\rho_\beta = W_-\rho_\alpha - W_+\rho_\beta \qquad [2.7.5]$$

Here, the first term on the right side describes the flow from the $|\alpha\rangle$ state to the $|\beta\rangle$ state and the second term the flow from the $|\beta\rangle$ to the $|\alpha\rangle$ state. The spin magnetization vector along the z-axis is proportional to the difference of the spin populations:

$$M_z = 2\mathbb{B}^{-1}(\rho_\alpha - \rho_\beta) \qquad [2.7.6]$$

The deviation of this equation leads to:

$$\frac{d}{dt}M_z = 2\mathbb{B}^{-1}\left(\frac{d}{dt}\rho_\alpha - \frac{d}{dt}\rho_\beta\right) \qquad [2.7.7]$$

$$\frac{d}{dt}M_z = 4\mathbb{B}^{-1}\left(-W_-\rho_\alpha + W_+\rho_\beta\right) \qquad [2.7.8]$$

$$\frac{d}{dt}M_z = -2W(M_z - 1) \qquad [2.7.9]$$

Followed by integration:

$$M_z(\tau) = (M_z(0) - 1)e^{-2W\tau} + 1 \qquad [2.7.10]$$

The term 2W is proportional to T_1^{-1} and is equal to twice the mean transition probability between the different states. For the model of a random fluctuating field the relation that describes T_1^{-1} is:

$$T_1^{-1} = \gamma^2 \langle B_x^2 \rangle \mathfrak{J}(\omega^0) = \gamma^2 \langle B_x^2 \rangle \frac{\tau_c}{1+(\omega^0\tau_c)} \qquad [2.7.11]$$

Where τ_c describes the correlation time of the random fields. The fluctuation of the magnetic field as well as the correlation time are temperature dependent, which results in a temperature dependence of the T_1 relaxation time as well.

In a sample with lots of spin ½ nuclei, the most important pathway of relaxation comes from through space dipole-dipole interactions. The magnetic fields in liquids are modulated by random molecular tumbling and the correlation times of the random field correspond to the molecular rotational correlation time, which gives a value for the time a molecule takes to rotate by 1 rad. In general, this means, that small molecules in solution or liquids are characterized by short rotational correlation times, whereas large molecules or solids have longer rotational correlation times.

For a coupled spinpair I_1 and I_2, there are 12 different transition probabilities between the eigenstates of the respective spins as already described above.
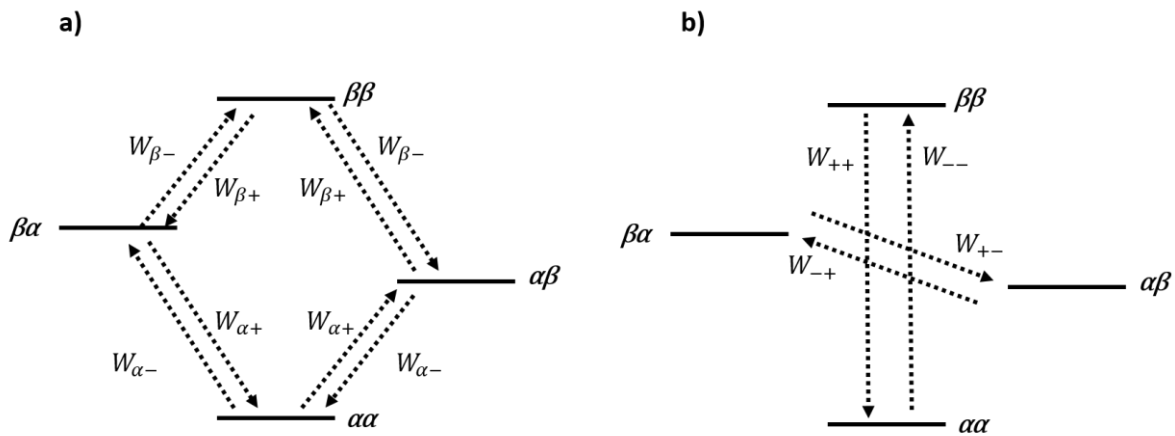
Figure 13 Transition rates for an inequivalent 1/2 spin pair. (a) single quantum transitions and (b) zero- and double quantum transitions.

Allthough this looks similar to the energy diagram which is given for coherences, those do not involve transitions, but spin-lattice relaxation processes do. In a hypothetic molecule which contains only two spins of the same type and are only interacting by dipole-dipole coupling, the following relations describe the transition probabilities:

$$W_{+\alpha} = W_{+\beta} = W_{\alpha+} = W_{\beta+} = W_1\left(1 + \frac{1}{2}\mathbb{B}\right) \qquad [2.7.12]$$

$$W_{-\alpha} = W_{-\beta} = W_{\alpha-} = W_{\beta-} = W_1\left(1 - \frac{1}{2}\mathbb{B}\right) \qquad [2.7.13]$$

$$W_{++} = W_2(1 + \mathbb{B}) \qquad [2.7.14]$$

$$W_{--} = W_2(1 - \mathbb{B}) \qquad [2.7.15]$$

$$W_{--} = W_{++} = W_0 \qquad [2.7.16]$$

The factors W_0, W_1 and W_2 are the zero, single and double quantum transition probabilities. Their values are:

$$W_0 = \frac{1}{10}b^2\mathfrak{J}(0) \qquad [2.7.17]$$

$$W_1 = \frac{3}{20} b^2 \Im(\omega^0) \tag{2.7.18}$$

$$W_2 = \frac{3}{5} b^2 \Im(2\omega^0) \tag{2.7.19}$$

With the dipole-dipole coupling constant b, which excludes the influence of vibrational motions:

$$b = \frac{\mu_0 \hbar \gamma^2}{4\pi r^3} \tag{2.7.20}$$

And the spectral density $\Im(\omega)$ at the given frequency. The reason for the occurrence of the term $2\omega^0$ in the double quantum transition probability results from the geometry of the dipolar local field.

Since all of the transition probabilities depend on the square of the dipole-dipole coupling constant, they also depend on the inverse sixth power of the distance between the interacting nuclei in the sample. For short rotational correlation times, the relationship between the transition probabilities is:

$$W_2 > W_1 > W_0 \tag{2.7.21}$$

With the spectral density function $\Im(\omega)$ being almost independent of ω^0. On the other hand, the relationship for the transition probabilities for long rotational correlation times is:

$$W_0 > W_1 > W_2 \tag{2.7.22}$$

Here, the spectral density function $\Im(\omega)$ with its peak at around $\omega = 0$ governs the magnitude of the transition probabilities. It is possible to derive an equation of motion by taking into account the transition probabilities into other states. The population of the state $|\alpha\alpha\rangle$, as an example, can deplete into three different states: $|\alpha\beta\rangle$, $|\beta\alpha\rangle$ and $|\beta\beta\rangle$, but also gets increased at the same time. The time dependent change for the population of state $|\alpha\alpha\rangle$ can be written as:

$$\frac{d}{dt}\rho_{\alpha\alpha} = -W_{-\alpha}\rho_{\alpha\alpha} - W_{--}\rho_{\alpha\alpha} - W_{\alpha-}\rho_{\alpha\alpha} + W_{+\alpha}\rho_{\beta\alpha} + W_{++}\rho_{\beta\beta} + W_{-\alpha}\rho_{\alpha\beta} \tag{2.7.23}$$

For convenience, this equation can be transformed in terms of the Solomon equations:

$$\frac{dy}{dx}\begin{pmatrix} \langle \hat{I}_{1z} \rangle \\ \langle \hat{I}_{2z} \rangle \end{pmatrix} = \begin{pmatrix} -R_{auto} & R_{cross} \\ R_{cross} & -R_{auto} \end{pmatrix} \begin{pmatrix} \langle \hat{I}_{1z} \rangle - \langle \hat{I}_{1z} \rangle^{eq} \\ \langle \hat{I}_{2z} \rangle - \langle \hat{I}_{2z} \rangle^{eq} \end{pmatrix} \tag{2.7.24}$$

The terms $\langle \hat{I}_{1z} \rangle^{eq}$ and $\langle \hat{I}_{2z} \rangle^{eq}$ describe the expectation values for the angular momentum operator of spin I$_1$ and I$_2$ at the thermal equilibrium.

R_{auto} is called the auto-relaxation rate constant and is a sum of the different transition rates:

$$R_{auto} = W_0 + 2W_1 + W_2 \tag{2.7.25}$$

On the other hand, R_{cross} is called the cross relaxation rate and has the following relationship:

$$R_{cross} = W_0 - W_2 \tag{2.7.26}$$

This rate constant is negative for short correlation times and positive for long correlation times. It vanishes at the critical rotational correlation time:

$$\tau_c^{crit} = \left| \frac{\sqrt{5}}{2\omega^0} \right|$$

[2.7.27]

For small and medium sized molecules the rotational correlation time is often close to this condition. It is possible, to derive mathematical descriptions for the longitudinal and transverse relaxation times from the Solomon equations, which will not be done in detail. However, these expressions are given with the following formular:

$$T_1^{-1} = \frac{3}{10} b^2 \left\{ \mathfrak{J}(\omega^0) + 4\mathfrak{J}(2\omega^0) \right\}$$

[2.7.28]

$$T_2^{-1} = \frac{3}{20} b^2 \left\{ \mathfrak{J}(0) + 5\mathfrak{J}(\omega^0) + 2\mathfrak{J}(2\omega^0) \right\}$$

[2.7.29]

For molecules of small size, the T_1 and T_2 relaxation times are more or less equal, which is called the extreme narrowing limit. Increasing the size of the molecules and thus the rotational correlation time, leads to a decrease for the respective relaxation times. However, in the case of T_1 relaxation, the curve passes through a minimum and then increases again. In other words this means, that the measurement time becomes long for small molecules and densely packed solids.
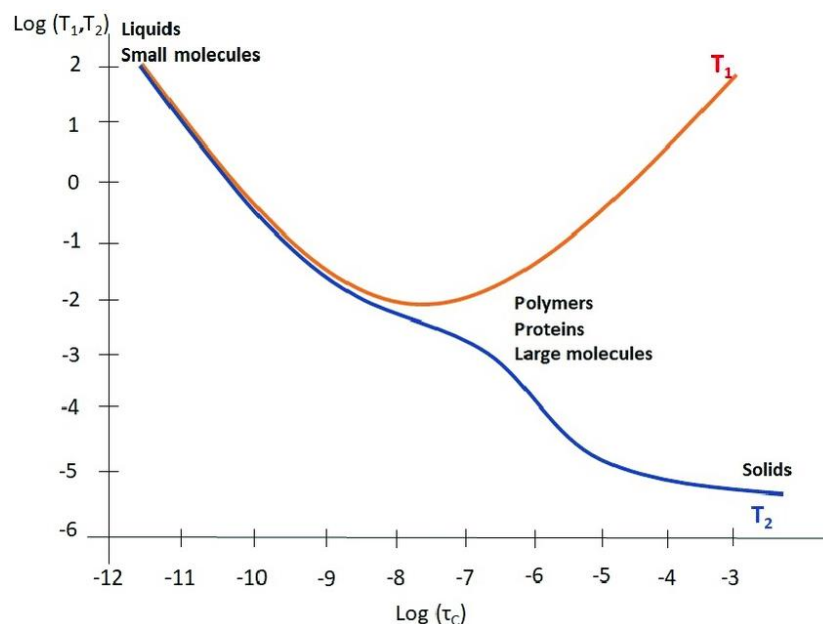
Figure 14 T_1 and T_2 relaxation times as a function of the rotational correlation time τ_c. [19]

2.7.1 Paramagnetic relaxation

Besides the temperature dependence of a relaxation process, the presence of unpaired electrons (e.g. paramagnetic species) usually has a high influence on the relaxation times. In MRI the application of so-called contrast agents is widely used to shorten ^{1}H relaxation times in tissue. Of course this

phenomenon is not only restricted to MRI and is observed in NMR experiments too. The addition of a paramagnetic species, that can either be organic radicals, metal ions or gases like oxygen, cause an increase in both, transverse and longitudinal relaxation rates:

$$\left(\frac{1}{T_i}\right)_{obs} = \left(\frac{1}{T_i}\right)_{dia} + \left(\frac{1}{T_i}\right)_{para} \tag{2.7.30}$$

Here, the first term on the right side of the equation describes the diamagnetic relaxation rate which is obtained in the absence of unpaired electrons, whereas the second one describes the paramagnetic relaxation rate. The fluctuating field in the vicinity of a paramagnetic centre provides an additional relaxation pathway. These fields fall off rapidly with increasing distance, which means that coordinating or chemically bond species show a higher contribution to the relaxation rate as those that diffuse freely within the sample. It is likely to classify two different types of interactions: the inner-sphere and outer-sphere mechanism. In the inner-sphere mechanism, the investigated nucleus is directly interacting with the paramagnetic centre, which usually leads to the highest contribution to the paramagnetic relaxation rate. In the outer-sphere mechanism, the investigated nucleus is bound to a ligand of the paramagnetic centre, which results in a larger distance compared to the one found for the inner-sphere mechanism. However, it is possible that the ligand serves as a sort of pathway for electron delocalization so that the outer-sphere mechanism can show a strong contribution to the paramagnetic relaxation. A relation for the paramagnetic relaxation rate with respect to these two interactions is given by:

$$\left(\frac{1}{T_i}\right)_{para} = \left(\frac{1}{T_i}\right)_{outer} + \left(\frac{1}{T_i}\right)_{inner} \tag{2.7.31}$$

The contribution to the longitudinal relaxation rate in an inner sphere mechanism is based on the exchange of a coordinated molecule to the paramagnetic centre with molecules in the bulk:

$$\left(\frac{1}{T_1}\right)_{inner} = \frac{P_p q}{T_{1p} + \tau_p} \tag{2.7.32}$$

Here, P_p is the molar fraction of the paramagnetic species in the sample, q is the number of molecules bound to the paramagnetic centre, T_{1p} is the relaxation time of the bound molecules and τ_p is the residence lifetime of the bound molecule. T_{1p} is described by the Solomon-Bloembergen equation and contains the relation of dipolar and scalar contributions:

$$\frac{1}{T_{1p}} = \frac{2}{15}\frac{\gamma_I^2 g^2 S(S+1)\beta^2}{r^6}\left[\frac{7\tau_c}{(1+\omega_s^2\tau_c^2)} + \frac{3\tau_c}{(1+\omega_I^2\tau_c^2)}\right] + \frac{2}{3}S(S+1)\left(\frac{A}{\hbar}\right)^2\left[\frac{\tau_e}{1+\omega_s^2\tau_c^2}\right] \tag{2.7.33}$$

In this equation, γ_I describes the gyromagnetic ratio of the investigated nucleus, g is the electronic g-factor, S is the total electron spin of the paramagnetic compound, β is the Bohr-magneton, r is the distance between the investigated nucleus and the paramagnetic centre, ω_s and ω_I are the Larmor

frequencies of the electron and the investigated nucleus and the term $\frac{A}{\hbar}$ is the electron-nuclear hyper-fine coupling constant. The dipolar and scalar relaxation mechanisms are modulated through the correlation times τ_c and τ_e.

The outer-sphere mechanism attracted less attention in the early days of paramagnetic relaxation research, since first generation contrast agents in MRI followed the structural motive of having free coordination sites for water molecules. However, with the design of polydentate ligands and an occupation of the binding sites, more interest to this mechanism emerged. It is also from high importance in NMR spectroscopy, since in many cases of mixtures between dia- and paramagnetic species there is no direct coordination or bond formation between the interacting compounds. The contribution of the outer-sphere mechanism to the overall paramagnetic relaxation rate is given with:

$$\left(\frac{1}{T_1}\right)_{outer} = \frac{C\pi N_S \gamma_I^2 \gamma_S^2 \hbar^2 S(S+1)}{d^3 \tau_D} \left[7I(\omega_S \tau_D T_{1e}) + 3I(\omega_I \tau_D T_{1e})\right] \qquad [2.7.34]$$

The parameter C describes a numerical constant, N_S is the number of paramagnetic species per volume unit, d is the closest distance between paramagnetic centre and investigated nucleus and τ_D is the relative translational diffusion time, which is described by the following relation:

$$\tau_D = \frac{d^2}{3(D_I + D_S)} \qquad [2.7.35]$$

The parameters D_I and D_S are the diffusion coefficients of the interacting species in the sample and the general expression for the diffusion coefficient is:

$$D = \frac{kT}{6\pi a \eta} \qquad [2.7.36]$$

With the Boltzmann constant k, the hydrodynamic radius of the investigated species a and the viscosity of the medium η. For a detailed description of the paramagnetic contribution to the relaxation time it is therefore crucial to determine a variety of parameters that are linked to the phenomenon as described by the above given formulars.

2.7.2 Detection of relaxation times

In practice it is possible to determine values for both, T_1 and T_2 relaxation times, by the application of different pulse sequences. For a detection of the T_1 relaxation time the saturation recovery and inversion recovery experiments are the most frequently used pulse programs. Since this relaxation occurs along the axis of the B_0 field at which no detection of the magnetization is possible, one has to use a two dimensional experiment.
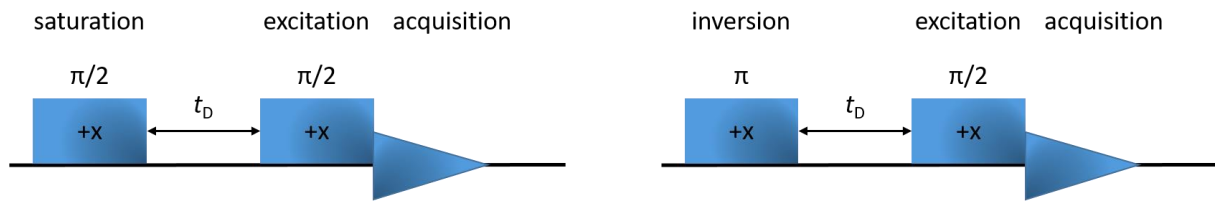
Figure 15 Pulse sequences of the saturation recovery (a) and inversion recovery experiment (b).

In a saturation recovery experiment, the magnetization is flipped entirely into the transverse plane by using saturation pulses. Thoses pulses consist of multiple $\pi/2$ pulses at relatively short repetition times. Application of a $\pi/2$ pulse immediately after a saturation will elicit no signal. A few moments later, after some T_1 recovery the system is called to be partially saturated. If the spin magnetization aligns entirely along B_0, the system is called to be unsaturated. On the other hand inversion recovery, as the name already indicates, inverts the magnetization by application of a π pulse. Both of these methods need a several number of FIDs to be recorded. The difference in those spectra is a delay, which is applied in between the saturation sequence or inversion pulse and the second $\pi/2$ pulse. For short delays, the magnetization will not have went back to thermal equilibrium. For saturation recovery, the signal intensity is close to zero for short delay times, whereas inversion recovery shows negative values for a short delay. The exponential build up for the inversion recovery pulse sequence is given by:

$$I(t_\mathrm{D}) = I_0 \left(1 - 2e^{\frac{-t_\mathrm{D}}{T_1}} \right)$$

[2.7.37]

Nowadays, it is quiet common to use an automation program, which runs consecutive experiments so that the different spectra do not have to be measured separately. The T_2 relaxation time can be determined by the spin echo pulse sequence. However, the T_2 relaxation time is not from particular interest for this work and therefore it will not be discussed in this section.

3. Recoupling techniques in solid state NMR

A wavefunction that describes a spin can be separated into a spatial and a spin part. The MAS influences the spatial part of this wavefunction and thus the anisotropic contributions, whereas the spin part interacts with the radio frequency pulses applied to the sample. By using special pulse sequences, it is possible to reintroduce the anisotropic interactions. Such procedure is called recoupling technique or recoupling pulse sequence in MAS NMR.

3.1 The principle of recoupling

Spectral resolution is a feature that is highly desired when measuring NMR experiments. However, as previously mentioned, this comes along with the loss of information about anisotropic interactions. Therefore, the development of pulse sequences that are capable to selectively reintroduce such information lead to new possibilities in terms of investigating parameters such as CSA and dipole-dipole couplings, which are highly useful for structure elucidation. Initially, the approaches to overcome those problem, were based on a fine tuning of the balance between the spinning speed and spectral resolution or a mis-setting of the magic angle. The firstly mentioned approach sacrifices some spectral resolution in trade for preserving the anisotropic information. It also benefits from the high quantity of material that is being measured, as the slow spinning speed allows the usage of rotors with diameters of 4-7 mm. At these conditions, the isotropic chemical shift is flanked by spinning sidebands, which can be analysed in terms of their intensity and contain information about the CSA tensor and the heteronuclear dipolar coupling constant. The second approach is based on a fast spinning speed at an angle, which differs slightly from the magic angle, which allows a downscaling of the anisotropic part of the interaction.

The principal of recoupling was introduced by Gullion and developed further by Levitt. For such pulse-sequences used in recoupling experiments, the applied RF pulse induces a rotation in the spin part that is contrary to the rotation of the space part. The applied length of the RF pulses allows a classification into two different recoupling types. The first one is the so called laboratory frame pulse sequence. This sequence uses short rotor-synchronized high power pulses. The second type of pulse sequences is called tilted rotating frame pulse sequence in which the B_1 field leads to a precession of the spins at a frequency that is multiples of the MAS frequency.

A general recoupling sequence is structured into five sections. The first one is the preparation period, in which magnetization for the investigated heteronucleus is generated. This can, based on the pulse sequence, either be directly (REDOR, REPT-HDOR) or via cross polarization (REREDOR), with the latter one generating transverse magnetization in the indirect dimension during the preparation segment. The preparation is then followed by an excitation sequence after which an evolution period is applied. In REPT-HDOR experiments, the transverse component of the coherence states is now brought to the indirect dimension, e.g. the heteronuclear spin. The reconversion period transforms the coherences into detectable magnetization which can then be detected during t_2.
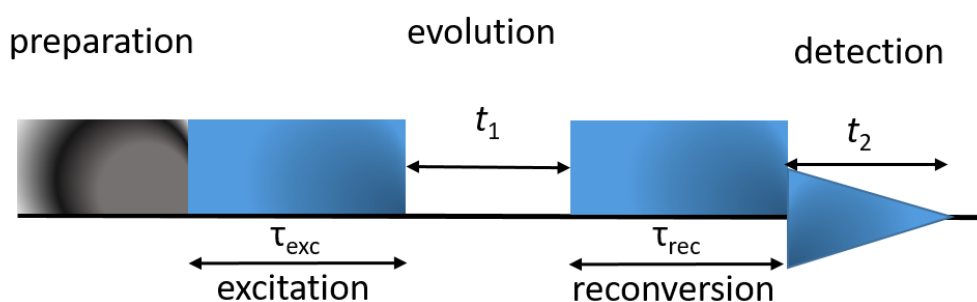
Figure 16 General pulse sequence of a recoupling NMR experiment.

The REDOR experiment (rotational echo double resonance) is the basic recoupling pulse sequence and was developed by Schaeffer and Gullion in 1989. It is a typical laboratory frame recoupling techniques. This experiment uses pulse trains of pi pulses, which are spaced by half of the rotor period τ_r. This results in a recoupling of the heteronuclear dipolar couplings. The average Hamiltonian that describes the anisotropic interactions λ, which are observed in the REDOR pulse sequence may be written as:

$$\overline{\overline{H_\lambda}} = \hat{T}_{00}\hat{A}_{00}^{\lambda,\text{lab}} + \hat{T}_{20}\frac{1}{t}\sqrt{\frac{3}{2}}\phi_\lambda \qquad [3.1.1]$$

The first term on the right side of the equation describes the isotropic contributions, whereas the second describes the anisotropic part of the Hamiltonian. The rotation of the sample at the magic angle is modulated by the second term in which ϕ_λ describes the acquired phase. Over a full rotor period ϕ_λ is equal to zero and therefore all anisotropic contributions vanish. A recoupling is effectively achieved by the application of a π pulse every second $\tau_r/2$ interval and thus the spin part $\hat{T}_{20}$ is counterrotated relative to the MAS rotation. As an effect, the contibutions from the $\tau_r/2$ intervals sum up and lead to a recoupling of the anisotropic effects.
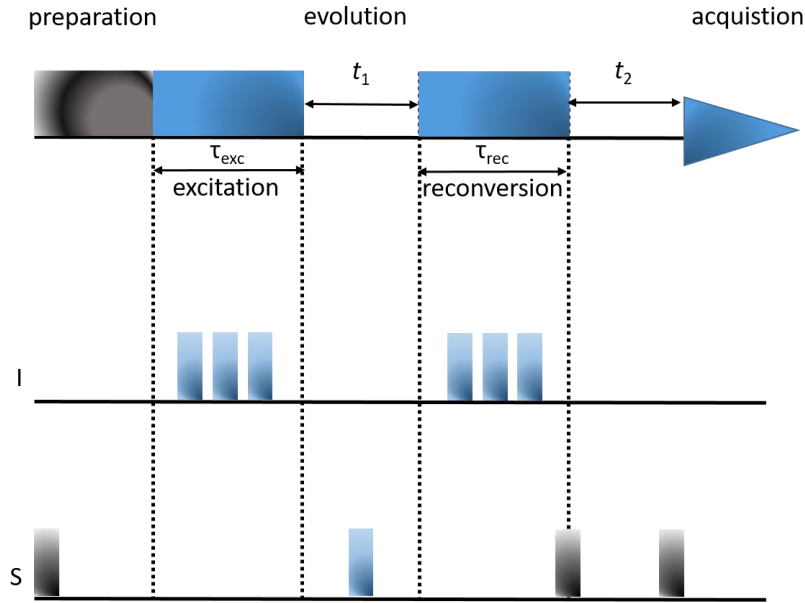
Figure 17 The REDOR pulse sequence.

For CSA and heteronuclear dipole-dipole interactions, which are linear, an inversion by a π pulse is possible. In the case of homo nuclear dipole-dipole couplings the interactions are bilinear and therefore π/2 pulses have to be used for effective excitation and reconversion (e.g. the BaBa pulse sequence).

3.2 Heteronuclear dipolar recoupling (REPT-HDOR pulse sequence)

The REPT-HDOR experiment (**RE**coupled **P**olarization **T**ransfer **H**eteronuclear **D**ipolar **O**rder **R**otor encoding) is based on the generation of a state of longitudinal dipolar order $\hat{I}_z\hat{S}_z$ during the evolution period. During the preparation time, a pulse train generates a saturated transverse magnetization for the spin S, followed by a build up of the antiphase coherence $\hat{I}_x\hat{S}_z$ during the excitation time. Now, a π/2 pulse, which is applied on the I spin right before the evolution converts the antiphase coherence into a state of longitudinal dipolar order, which does not evolve during t_1. After this segment, a π/2 pulse on the S channel converts the state back into an antiphase coherence $\hat{I}_z\hat{S}_y$. During the reconversion period, this term is transformed into a detectable single quantum coherence. The detected signal for a simple SI pair on the S channel is a sum of the magnetization of the x and y components:

$$\hat{I}_{s,x} = \langle \sin(N_{\mathrm{exc}}\overline{\phi_0}) \sin(N_{\mathrm{rec}}\overline{\phi_{t_1}}) \cos(\omega_{CS,I} t_1) \rangle \qquad [3.2.1]$$

$$\hat{I}_{s,y} = \langle \sin(N_{\mathrm{exc}}\overline{\phi_0}) \sin(N_{\mathrm{rec}}\overline{\phi_{t_1}}) \sin(\omega_{CS,I} t_1) \rangle \qquad [3.2.2]$$

Here, only the isotropic chemical shift evolution (CS) is considered. For that reason sine and cosine functions are introduced, which modulated the x- and y- components of the signal as a function of $\omega_{CS,I}$. An incrementation of the evolution period results in spinning sideband patterns which are odd-ordered and are centred at the frequency with an offset of $\Omega = 0$. During t_1 there is no chemical shift evolution for the spin I and thus, recording a second dataset of sine functions is not needed. Instead, a second dataset with cosine functions is recorded for a second rotor period of t_1 evolution.
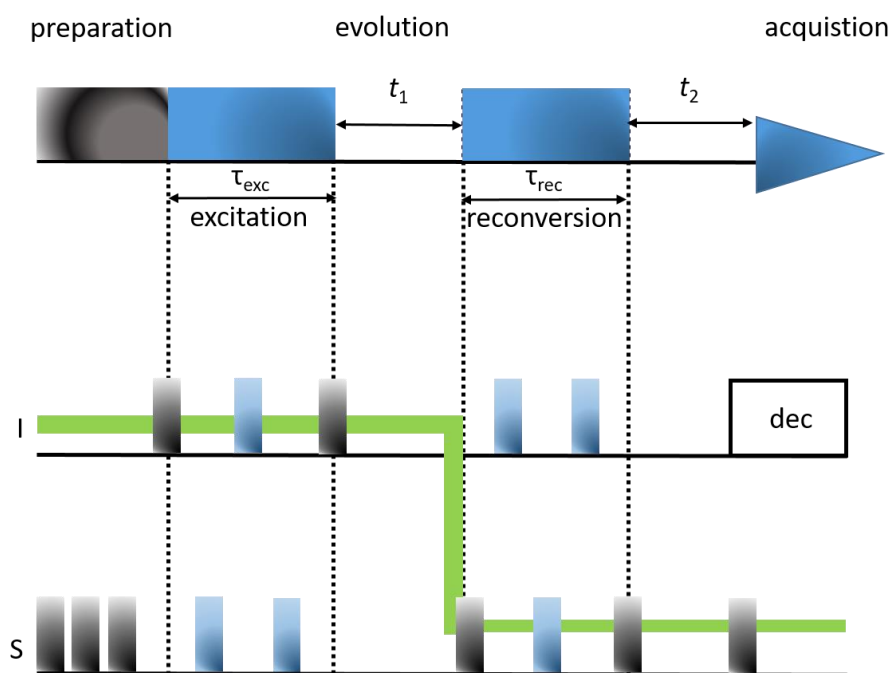
Figure 18 The REPT-HDOR pulse sequence. The green line indicates the pathway of the coherence transfer.

An advantage that comes along with the recoupling is that no signal decay is observed due to a possibly long relaxation time of the heteronucleus as those relaxation times are longer than the recoupling procedure itself. Similar to any other recoupling experiment, the number of the spinning sidebands can be adjusted by the length of the recoupling time. Since the recoupling time is a function of the spinning frequency, the recoupling time can be chosen so that $D_{IS}\tau_{rec} = 1.6$. In completely rigid solids, however, this is difficult to achieve since a fast spinning speed is needed to gain better decoupling of the homonuclear proton dipole-dipole coupling. The REPT-HDOR experiment comes along with the limitation that it is not possible to detect quantitative information of rigid CH_2 groups. For such problems the REREDOR method is advantageous. However, since rigid CH_2 groups are not from particular interest in this work, this pulse sequence will not be discussed.

3.3 Homonuclear dipolar recoupling (BaBa Pulse sequence)

The Back-to-Back (BaBa) pulse sequence is a multiple quantum technique, which was developed by Feike et al. in 1996[20] and is based on recoupling of the homonuclear dipole-dipole couplings under fast MAS. This sequence is nowadays routinely used for structure elucidation of molecules in solid samples and more precisely the determination of ^{1}H-^{1}H internuclear distances or to evaluate molecular mobility.
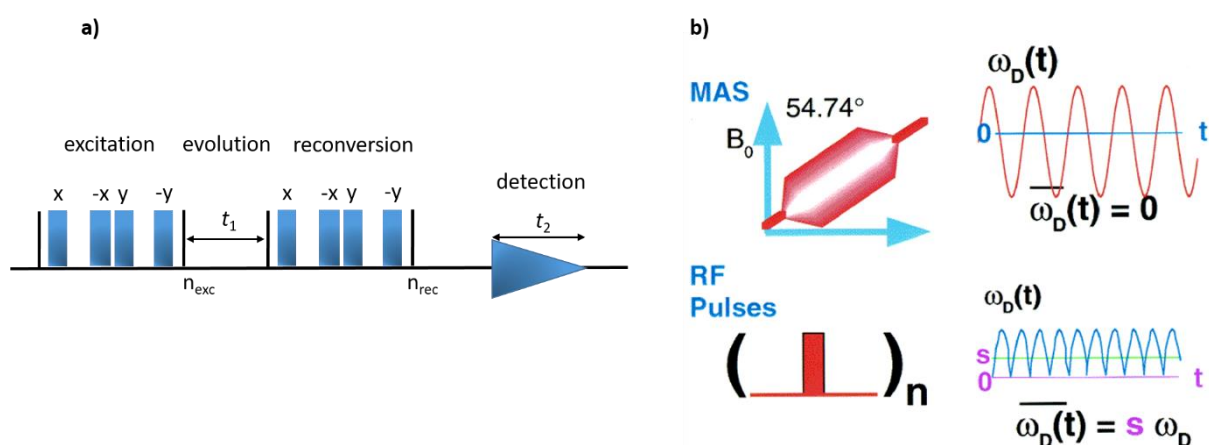
Figure 19 The general BaBa pulse sequence (a). In during the excitation and reconversion period, n pulse trains with π/2 pulses are applied (displayed in the brackets). (b) principle of rotor synchronization in a recoupling experiment.[21]

As can be seen from Figure 19, the laboratory-frame pulse sequence is built from π/2 radiofrequency pulses:

$$\left[\left(90°_x - \frac{\tau_r}{2} - 90°_x \right) \left(90°_y - \frac{\tau_r}{2} - 90°_y \right) \right]$$

Here, the second and third pulse in the sequence are placed back-to-back. The timing of the back-to-back sequence is crucial to achieve a synchronization with the sample rotation and thus for generating a pure double-quantum Hamiltonian. The spin Hamiltonian for a spin system under MAS can be written as:

$$\widehat{H}(t) = -\Delta\omega \hat{I}_z + \widehat{H}_{CS}(t) + \widehat{H}_D(t) \tag{3.2.3}$$

in which $\Delta\omega$ describes the off-resonance frequency. The second term on the right represents the chemical shielding interaction, whereas the third term describes the dipolar interaction. Their spatial part is modulated by the spinning of the sample and thus it is time dependent. The spin system responds to the pulse sequence, which can be described by the density operator formalism which is, however, not shown here, since it needs an extended approximation. For that reason, the dipolar

Hamiltonian operator $\widehat{H}_{DQ}$, e.g. the result of the approximation, will be directly shown and has the form:

$$\widehat{H}_{DQ} = \left(\frac{3}{\pi\sqrt{2}}\right)\sum_{i>j} D^{ij} \sin\left(2\beta^{ij}\right) \sin\left(\gamma^{ij}\right)\left\{T_{2,2}^{ij} + T_{2,-2}^{ij}\right\} \qquad [3.2.4]$$

The parameter D^{ij} describes the dipole-dipole coupling constant. The angles β^{ij} and γ^{ij} relate the the principal axes of the dipolar coupling tensor to the rotor frame which is used as reference. T^{ij} are called the irreduceable tensor operators. If the BaBa pulse sequence acts upon a spin pair in thermal equilibrium, a DQ coherence is generated and its amplitude is modulated with $\sin\left(\Omega_{exc}^{ij}\right)$. This modulation is similar during the reconversion process. The signal intensity which is obtained after a BaBa experiment with N rotor periods is given by:

$$S_{DQ}^{ij}(t_1) \propto \langle \sin N\Omega_{\text{exc}}^{ij} \sin N\Omega_{\text{rec}}^{ij} \rangle_{\beta,\gamma} \qquad [3.2.5]$$

This expression also describes the need of orientational averaging for powdered samples. Since the signal depends on the time t_1, an one dimensional BaBa experiment ($t_1 = 0$) acts as a double-quantum filter. On the other hand, if a spectrum is recorded in two dimensions, it is possible to obtain either a correlation spectrum or spinning sideband patterns, dependent on the incrementation of t_1.

A rotor-synchronized signal acquisition for two dimensional BaBa spectra can be recorded by incrementing t_1 in integer multiples. As result, the evolution of the double quantum coherence can be recorded during the period t_1 and is correlated with the observed single quantum signal, which is detected during t_2. Both the chemical shift and the dipole-dipole couplings influence this double quantum evolution. Here, the modulation of the chemical shift is given by the expression:

$$\Omega_{\text{CS}} = e^{i\left(\omega_{CS}^i + \omega_{CS}^j\right)t_1} \qquad [3.2.6]$$

This is valid, if no dipole-dipole interactions occur during t_1. A spin which is located a bit further away from the observed spin but still coupled, can be involved in the coherence and might give rise to the double quantum coherence since such contribution are not refocused during the reconversion of the BaBa pulse sequence. The signal position in the indirect dimension (double quantum dimension) is the sum of the isotropic chemical shifts of the single quantum dimension for the spins involved in the respective coherence.

Figure 20 shows two schematic 2D BaBa spectra for samples containing two spins in different local environments, A and B. In Figure 20 a) the two spins are located in phases which are spatially separated. This results in no dipole-dipole interactions between the different spins. However, spin A is only surrounded by spins of the same kind, which results in a signal, exactly on the diagonal of the spectrum. The same behaviour is valid for spin B. If the spins are getting mixed (Figure 20 b) and A and

B are located close to each other, two additional correlations are found at the sum of the single quantum chemical shift of A and B – situated symmetrically on both sides of the diagonal. Usually these two signals show equal intensity as this corresponds to the number of the involved spins.
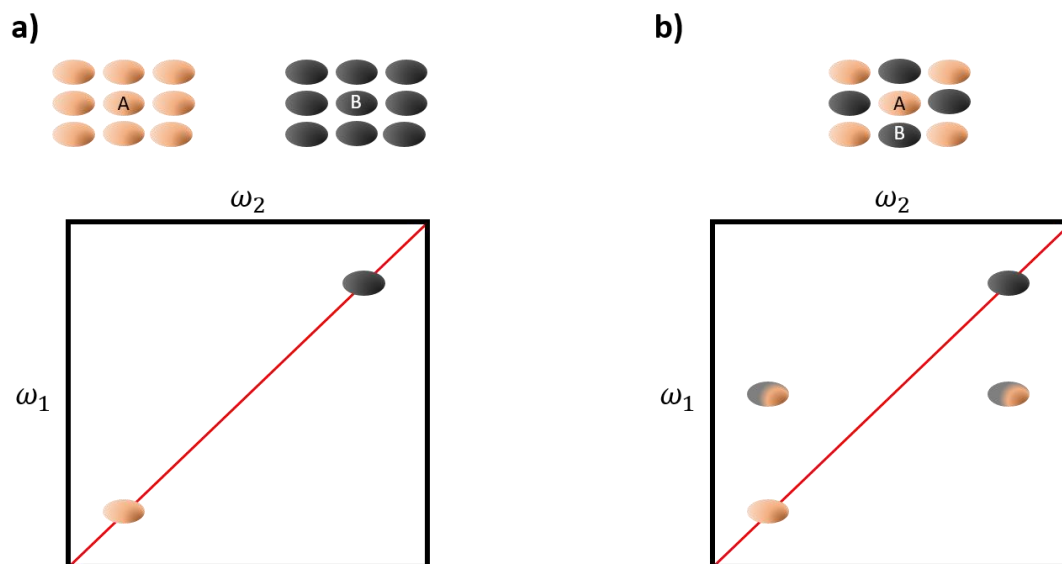
Figure 20 Schematic two dimensional representation of BaBa spectra. If the nuclei are spatially separated, only self peaks between spins in the same environment are observed along the diagonal (a). For a mixed system A-B, in which the nuclei with different local environments are close to each other, cross peaks are generated at the sum of the single quantum resonances in the indirect dimension (b)

Allthough the homonuclear dipole-dipole coupling does not contribute to the rotor synchronized modulation of the amplitude (in terms of t_1), it still governs the overall intensity of a peak in a 2D BaBa spectrum. To detect the peak of a specific coherence, a recoupling time has to be chosen in a proper way with respect to the rotor period.

4. Solid state NMR spectroscopy of organic semiconductors

Synthesis, characterization and properties of organic semiconductors is nowadays a well established research field and the basis for the development of emerging technologies.[22,23] Even though organic light emitting diodes are commercially available, the improvement of the device performance and discovery of new materials with specific photophysical properties (e.g. thermally activated delayed fluorescence) are highly desirable.[24–26] One central aspect of the functionality of organic semiconductors is their structural organization in the solid state, which has a huge influence on parameters like, absorbance, luminescence, charge transport and band gaps, as well as the thermal and mechanical stability. The mobility of charge carriers is highly impacted by the electronic coupling between neighbouring molecules which is determined by their solid state structure.[27–29] On the other hand, the spatial arrangement of molecules in the solid state is mainly caused by their molecular design and the type of processing. Interactions such as π-π stacking, Van-der-Waals forces and hydrogen bonds play a crucial role and have to be taken into account, when approaching the development of novel materials.[30,31] There are various techniques required to characterize organic semiconductors on different length scales. XRD scattering methods are typically used to determine the long range, periodical order of a material with π-π and lamellar stacking motifs.[32] However, scattering methods are often limited when it comes to the analysis of amorphous phases or semi crystalline regions.[33,34] Electron microscopy can resolve materials at atomic-scale resolution, however, this method suffers also when it comes to the analysis of partially disordered and non-robust samples, since the irradiation often causes a degradation of the sample.[35–37] To overcome those problems, solids state NMR spectroscopy is a powerful tool to fill the lack of information about disordered materials of the previously described analytical methods, since it is sensitive to short range order interactions in crystalline, semi-crystalline and amorphous phases.[38–43] Theoretical approaches as density functional theory and molecular dynamics approaches are used to bridge complementary methods, such as NMR and XRD, to obtain a good understanding of structure-property relation.[44,45] The combination of the results from the different methods leads to a deep understanding of the three dimensional structure of the investigated materials.[46–52] Opto-electronical processes are often studied by a wide range of opto-analytical methods which are not capable (except a few assumptions) of detecting structural information.[53,54]

The application of solid-state NMR spectroscopy provides important information on the local environment for every atom with a nuclear spin ≥1/2. Parameters such as the chemical shift and the dipole-dipole couplings have a high sensitivity towards small differences in bonding and conformational environment, as well as inter and intramolecular interactions. Spin-diffusion experiments allow the determination of domain sizes on a scale between a few to tenth of

nanometers. PFG NMR experiments allow the determination of the diffusivity of ions or small molecular structures in porous materials.[55] EPR methods can also provide information about paramagnetic interactions and thus, the distance between a centre that contains unpaired electrons and its periphery. Those information can be used to link results from solid state NMR spectroscopy with long-range order techniques.[56–58] It is often of particular interest to identify short-range order, which allows the relation between different morphologies and charge-carrier transport. While the isotropic chemical shift is sensitive to the bonding environments of the chemical shift, other parameters as the CSA, dipole-dipole couplings and quadrupolar interactions can arise from the orientation of different chemical moieties. The distribution of isotropic chemical shifts often cause sever broadening of the signals and thus complicate the analysis of heterogeneously packed materials.[59] Several MAS NMR experiments can be applied nowadays to overcome a lots of the problems, which come along with heterogeneous packing of organic semiconducting materials. The application of two dimensional NMR methods, that can either reveal homo or heteronuclear through space interactions, are commonly used experiments when it comes to 3D structure elucidation. Recording such spectra also benefits from the applicability of polarization transfer experiments that enhance the signal of dilute nuclei.[60] MAS and decoupling techniques average the dipole-dipole coupling which is then reintroduced by recoupling techniques.[61,62]

To gain a better understanding between the solid state structure and opto electronic properties, OLEDs made from structurally similar molecules have been studied by several research groups by using NMR spectroscopic measurements to identify intermolecular distances.[63–67] The combination of solid state NMR, XRD and DFT methods opened a ways of determining the domain sizes in bulk heterojunctions with compositions made of polymer:fullerene blends for OPV applications. Here, 2D NMR techniques are used to identify the coupling between the nuclei in the material to generate a molecular packing model. This method was used to indentify the 3D structure of polycrystalline P3HT.[68] A similar approach was used to determine the structure of the binary blend PBTTT-C_{14}:C_{71}. XRD experiments were used to determine the unit cell which was filled afterwards by the structural data obtained from NMR experiments, namely H-H couplings, followed by a molecular dynamics simulation to minimize the energy, which resulted in a 3D model of the investigated composition.[69] ^{1}H spin diffusion experiments were used to reveal the domain sizes in P3HT:$PC_{61}BM$ blends. From the CP or spin diffusion intensity it is possible to determine the spin diffusion coefficient and thus the average domain size.[70–72] Additionally, solid state NMR is capable of providing insight into intermolecular interactions of doped materials.[73–75] For example, solid state NMR measurements have been used to identify the interaction of the dopant F_4TCNQ with the respective polymer matrices. Here, the analysis of a mixture of F_4TCNQ and PBTTT-C_{14} revealed insight into a co-facial arrangement with which the high charge transfer efficiency could be explained.[76–79] It is likely, that molecular motions such as local fluctuations,

ring flips of aromatic groups or hydrogen transfer reactions occur in thin films of organic semiconducting materials. These motions can be probed by measuring dynamic sensitive parameters, such as relaxation times and dipole-dipole couplings as a function of variable temperatures. The sidechain dynamics in poly-alkylthiophenes, for example, was determined by detecting the T_1 relaxation times with increasing temperature with which the activation energies were calculated.[80]

These showcased experiments are just some examples of the applicability of solid-state NMR techniques to solve problems that come across with the organization of OSC materials in solid materials. This work emphasizes on the solid-state structure elucidation of small molecules with TADF (thermally activated delayed fluorescence, see next section) properties that shall be linked to their porperties in terms of conductivity. Another material that will be studied is the blend of $F_4TCNQ:P3HT$ in terms of stability after thermal annealing.

5. Solid State NMR spectroscopy of microcrystalline and amorphous TADF emitters

5.1 Introduction

Organic light emitting diodes (OLEDs) based on thermally activated delayed fluorescence (TADF) emitters are considered being the next-generation of noble-metal free devices.[81–83] The electroluminescent process in TADF emitters is characterized by the formation of singlet and triplet excitons, that are generated by the combination of holes and electrons which are held together by an electrostatic potential.[25] Possible pathways for singlet excitons to decay can be radiatively (fluorescence), non-radiatively or by an intersystem crossing (ISC) process, which results in the formation of a triplet state. On the other hand, low energy triplet excitons can decay non-radiatively or undergo an endothermic reverse intersystem crossing process (RISC). This RISC process results in a singlet state which can decay radiatively to the ground state, leading to the so-called delayed fluorescence. The advantage of such molecular arrangements is that both, singlet and triplet states, can be harvested. This results into a theoretical internal quantum efficiency (IQE) of 100%, whereas conventional fluorescent OLED devices suffer from low IQE of around 25-30%.[84–86]
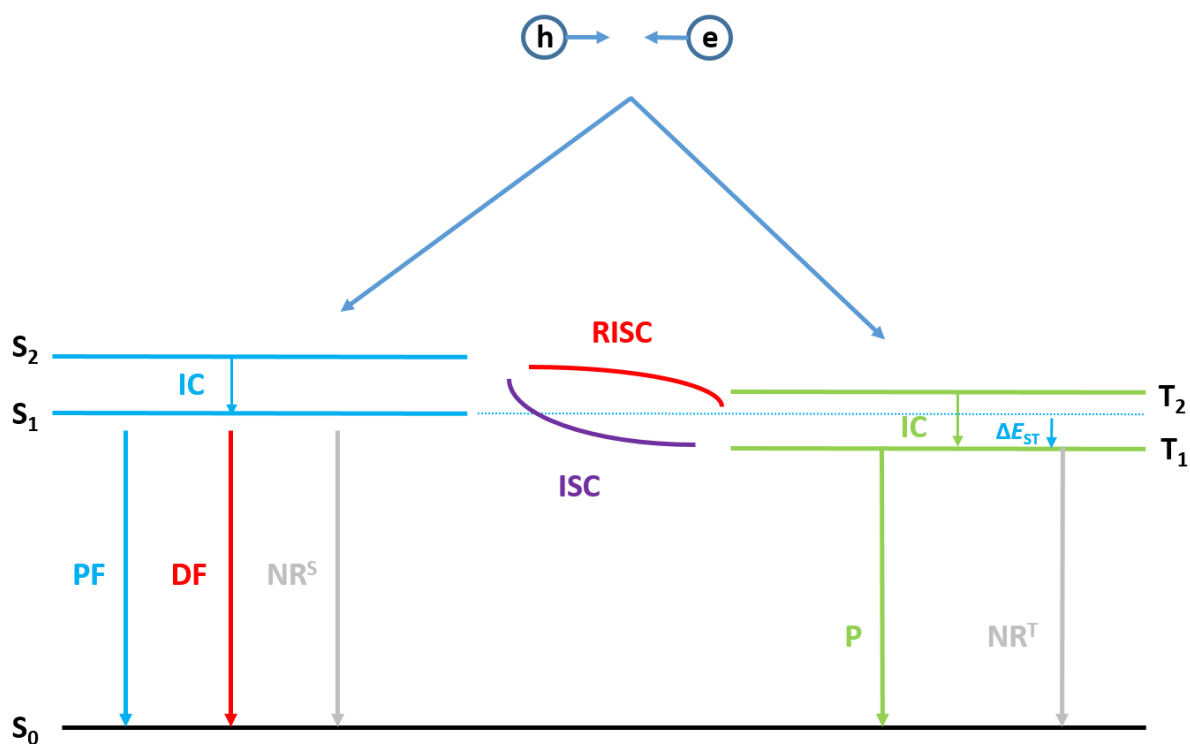
Figure 21 Schematic representation of the TADF effect. Holes and electrons can generate either singlet or triplet excitons. The singlet excitons can decay with prompt fluorescence (PF) or non-radiative (NR^S) to the ground state. Intersystem crossing (ISC) allows a transition from the singlet to triplet state. The triplet state itself can decay by the phosphorescence (P) or the non-radiative (NR^T) pathway.

Nowadays, three major classes of TADF emitters are in the focus of scientific research: monomeric, dendritic and polymeric structures. This work focuses only on the structure elucidation of the monomeric TADF emitters.

When it comes to molecular design of TADF emitters, there are some conditions, which have to be realized to increase the photo electric efficiency. Such an increase is hardly dependent on the energy gap between the singlet and triplet state ΔE_{ST}. A small value of ΔE_{ST} is the most important criterion for a high RISC transition rate. To achieve a high RISC transition rate, the electron-electron repulsion of the triplet state has to be minimized. This can be achieved by a twisted, non-planar structure, which lowers the exchange integral of the HOMO and the LUMO levels. An additional way to separate the HOMO und LUMO level is the introduction of phenyl linker between the donor and acceptor part of the TADF emitter molecule. Those requirements result in a need of relatively rigid molecular arrangements.[87] Flexible units in the structure of TADF molecules can result in different conformations, which are not favourable for an efficient RISC process.[88] Therefore, a detailed analysis of the solid-state structure of such TADF emitters is a key step to understand photo physical and electric properties of the materials.

Besides the intramolecular direct bond interaction of HOMO and LUMO levels in the TADF emitters, intermolecular through space interactions are known to play a crucial role in terms of conductivity and TADF efficiency. An interaction of the π systems of the aromatic moieties can lower or raise the HOMO and LUMO levels and has to be taken into account when discussing the photo-electric properties of the TADF emitters.[89–94]

5.2 Charge carrier trapping in organic semiconductors

The performance of organic semiconducting materials heavily depends on the efficiency with which charge carriers are able to move within the π-systems of the respective molecules. According to theory, both types of charge carriers, holes and electrons, should show a similar mobility in an organic semiconductor.[28] In praxis, however, such a behaviour is rarely the case. Here, the amount of free charge carriers changes that contribute to the charge transport within a material. For example, in most solution processed semiconducting polymers, the electron trapping was found to be the limiting factor for the electron mobility, whereas the bulk hole transport is the dominant process.[95] The depth of the traps can be reduced by increasing the electron affinity of the material. As experimental data indicate, materials with an electron affinity of >3.6 eV show a trap free electron transport, which suggests that there is a general impurity with an EA of 3.6 eV. On the other hand, the hole transport in materials is related with the ionization energy IE. Materials with an IE that is larger than 6.0 eV are limited by hole

trapping. These conditions detract the amount of materials, either small molecules or polymers that are suitable for usage in devices made of organic semiconductors. Several molecules have been studied in terms of trap free charge carrier mobility as can be seen from the trap free window.[11,96]
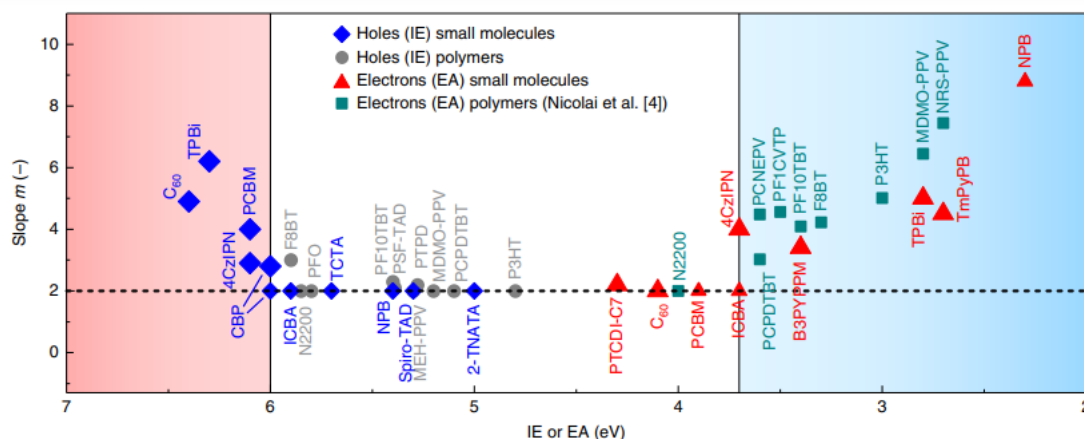
Figure 22 The trap free window of a selection of semiconducting polymers and small molecules.[11]

As a general rule for the design of novel, trap free materials, the EA and IE levels have to be chosen to fit in the trap free window between 3.6 and 6.0 eV. Since the electron trapping process is mainly addressed to a general impurity that offers an EA of around 3.6 eV, there should be possibilities to eliminate such factors. A promising approach is the design of materials that exhibit a self organization in which the conducting parts of the molecules are surrounded by protective groups. The main focus of the following chapter of this work is to identify the solid state structure of TADF materials with promising opto-electronical properties and to relate those structures to their trapping behaviour in evaporated thin films.

5.3 Solid state NMR studies of 9,9'-(5-(4,6-bis-*tert*-butyl-1,3,5-triazin-2-yl)-1,3-phenylene)biscarbazole derivatives with different degree of carbazole fluorination

Throughout this chapter, three series of TADF emitter molecules will be investigated in terms of their molecular organization in the solid state after vapour deposition. For this purpose, the crude materials were placed into a flask after synthesis. On top of the flask, an apparatus equipped with a water-cooled quartz glass was installed. After applying reduced pressure (10^{-3} mbar) the temperature was increased to 443 K. Once the sublimation procedure was finished, the sublimation apparatus was opened and the materials were collected. Those materials were then filled in 2.5 mm zirconia rotors and used for NMR measurements. For solution experiments the samples were dissolved in TCE (tetrachloethan if not differently mentioned) and transferred into standard borosilicate NMR tubes.

All molecular structures investigated in this study are designed with a triazine unit as electron acceptor part and a variable amount of carbazole units (1-3) as electron donor part. Acceptor and donor parts

are linked by a phenyl ring, which will be called the centre phenyl ring. In the case of 9,9'-(5-(4,6-bis-*tert*-butyl-1,3,5-triazin-2-yl)-1,3-phenylene)biscarbazole derivatives, the triazine rings of the different molecules are all substituted with two *tert*-butyl groups in *meta*-position relative to the centre phenyl ring. The centre phenyl ring itself is substituted with two carbazole units in *meta*-position relative to the triazine ring. The molecular variation in this series is achieved by a different number of fluorine substituents at the carbazole units (structures are given in Figure 23). In the case of the compound **1a**, no further substituents are attached to the carbazole units, whereas in the case of compound **1c** the carbazole units are symmetrically substituted with fluorine atoms in *para*-position relative to the carbazole nitrogen atom. The compound **1b** in comparison shows an asymmetric substitution pattern of the carbazole units. There, only one fluorine atom is attached in *para*-position relative to the carbazole nitrogen atom.
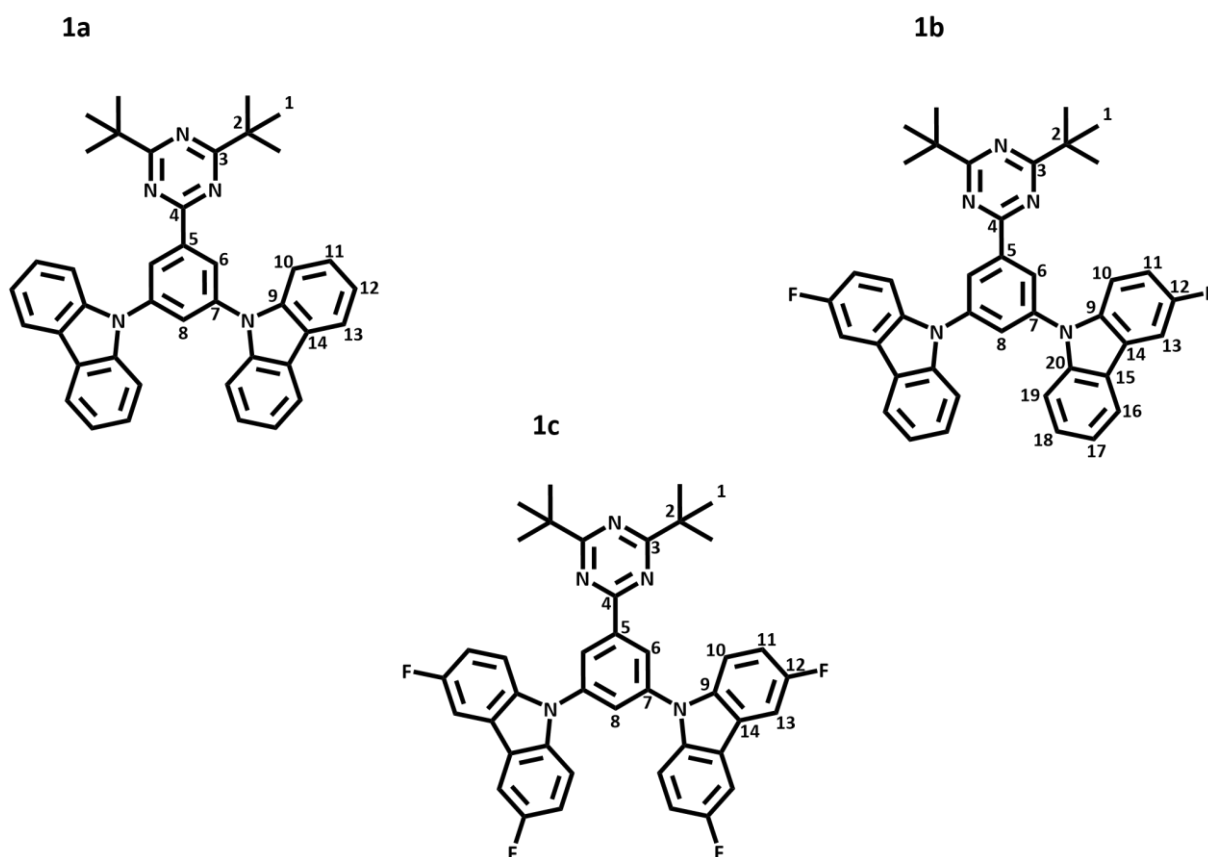
Figure 23 Two-dimensional molecular structure of the compounds **1a**, **1b** and **1c**.

The presence of hydrogen, carbon and fluorine in the investigated structures facilitates NMR spectroscopic studies. Besides crystalline domains, solid state NMR spectroscopy can detect and study also amorphous morphologies of small molecules and polymers. This feature allows us to identify short range order and stacking motifs in disordered materials by the usage of two-dimensional homo- and heteronuclear correlation spectra.

5.3.1 One dimensional NMR spectra

For a detailed NMR based structure elucidation, it is crucial to assign every atom of the investigated molecule to its respective chemical shift value. The easiest way to achieve this goal, is the usage of solution NMR experiments, where all intermolecular packing influences are removed. Moreover, the T_2 time constants of dissolved molecules are several orders of magnitude higher than their counterparts in the solid state. Such a long T_2 time constants lead to narrower lines and makes the assignment of the chemical shift values way more convenient. On the other hand, the molecules in solution are the average over all possible confirmations and accessible dihedral angles, which is not possible in the solid state. In this work, ^1H, ^{13}C and ^{19}F are the nuclei of interest. The assignment of the resp. solution NMR spectra was done with a general set of one- and two-dimensional solution NMR experiments (COSY, HMBC, HSQC, NOESY). The spectra are presented in the appendix. A detailed knowledge about the solution NMR chemical shifts is useful to identify different stacking arrangements in amorphous and crystalline samples as in the solid state the chemical shift values of NMR signals are affected additionally by the electronic surroundings.
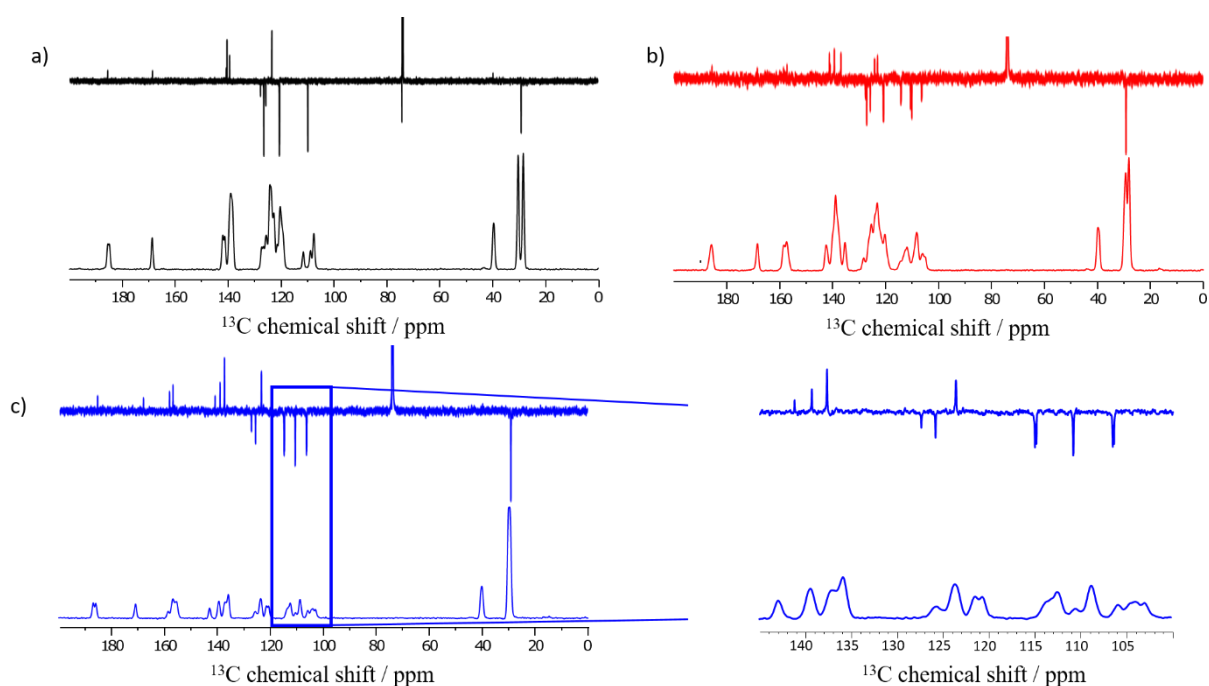
Figure 24 {^{1}H}^{13}C CP spectra recorded at 25 kHz MAS of **1a** (a), **1b** (b) and **1c** (c) presented on bottom with the j-mod spectra (measured in 1,1,2,2 tetrachloroethane at ambient temperature) displayed on top.

Figure 24a shows the ^{1}H-^{13}C CP MAS spectrum of the compound 1a (bottom) as well as the j-mod (scalar coupling polarization transfer) spectrum in TCE (top) for comparison. The negative signals in a j-mod spectrum arise from an odd number of protons attached to the respective carbon atom. In the

case of aromatic protons, it is clear that those signals correspond to CH groups. As shown in Figure 24a, the carbon signals in the chemical shift range from 100-130 ppm can be assigned to the aromatic CH carbon atoms of the carbazole and centre phenyl ring, with exception of the carbon atom at position C-14 (123.9 ppm). The second quaternary carbon atom of the carbazole unit (C-9, 140.5 ppm) as well as the quaternary carbon atoms of the centre phenyl ring (C-5/C-7, 140.8/139.6 ppm) show a clear downfield shift, relative to the protonated species.

The *tert*-butyl groups attached to the triazine ring are detected as two different signals in the aliphatic region with chemical shift values of 28.9 ppm for the methyl groups and 39.9 ppm for the quaternary carbon atom. All solution NMR ^{13}C chemical shift values for the compounds **1a**-**1c** are listed in Table 1 and will be used later in this chapter to interpret correlation and dynamics measurements acquired in the solid state.

Table 1 ^{13}C chemical shift assignment of the compounds **1a**-**1c**. The data were obtained from solution NMR experiments in TCE at ambient temperature and 700 MHz magnetic field.

Atom	1a	1b	1c
1	28.9	29.7	29.1
2	39.9	39.9	39.7
3	185.7	186.1	186.4
4	169.6	169.2	168.3
5	140.8	141.0	141.8
6	125.8	125.8	125.8
7	139.6	139.6	139.4
8	127.7	127.6	127.4
9	140.5	137.1	137.8
10	110.0	110.7	110.9
11	126.7	114.2	115.0
12	120.7	158.0	157.9
13	120.5	106.4	106.2
14	123.6	123.2	123.8
15	-	124.2	-
16	-	120.9	-
17	-	120.7	-
18	-	127.2	-
19	-	110.1	-
20	-	141.5	-

The analysis of the ^{13}C NMR spectra of organic molecules benefits from the large chemical shift range of ^{13}C. However, the low natural abundance of ^{13}C in natural samples results in long measuring times.

Moreover, crystalline and densely packed samples are characterized by long T_1 relaxation times which further increases the time needed to record a spectrum with good signal-to-noise ratio. ^{1}H and ^{19}F are the other two nuclei that will be used to study the structure of TADF emitter molecules in the solid state. Both nuclei have 100% natural abundance and faster relaxation compared to ^{13}C and thus can be measured faster. However, samples with low molecular mobility suffer from long T_1 times. A major

disadvantage of ^{1}H solid state NMR spectra is the narrow chemical shift range combined with short T_2 relaxation times, which results in broad signals that are hardly resolved and difficult to assign. The chemical shift values can give insight into the arrangement of the aromatic molecular units provided signal separation can be achieved. A spatial proximity leads to a change in the chemical shifts due to the ring current effects of the neighbouring aromatic systems. The chemical shift of a nucleus located in the plane with an aromatic system usually experiences a low-field shift, whereas a nucleus located above or below an aromatic ring experiences a high-field shift. Figure 25 shows the ^{1}H NMR spectra of compounds **1a**-**1c**. In the case of **1a** and **1b**, two aromatic signals as well as two aliphatic signals are observed. The two spectra are very similar. By measuring ^{1}H-^{13}C CP HETCOR spectra with short CP time (0.1-0.3 ms), it is possible to assign the resonances of the corresponding protons to their molecular positions (as indicated in Figure 23). The spectra measured for this purpose are shown in Appendix 1 ff. and the chemical shift values are listed in Table 2. The aforementioned line broadening, leads to the fact that it is almost impossible to precisely assign all proton resonances to a chemical shift. However, a clear difference can be seen between the ^{1}H spectra of **1a** and **1c**. While the proton signals of H-11,12,13, for compound **1a** are found in the range between 7-9 ppm, the signals H-11,13 showing a lower chemical shift value , resonating at about 5 ppm. Such a strong high-field shift is observed for aromatic protons when there is a face-to-face spatial proximity with the ring currents of neighbouring aromatics. A similar behaviour is observed for compound **1b**, but surprisingly the resolution is improved if compared to compound **1a**. It is assumed, that the better resolution results from longer T_2 times and thereby narrower lines However, for compound **1b**, as for compound **1a**, it can be assumed that there is no face-to-face stacking between the carbazoles, but rather face-to-edge stacking.

As already mentioned, ^{19}F is also a nucleus with 100% natural abundance. In contrast to ^{1}H, however, the range of the chemical shifts is significantly larger. Although the ^{19}F solution NMR spectrum shows only one signal for compounds **1b** (-122.6 ppm) and **1c** (-122.3 ppm), multiple signals can be observed in the solid state.
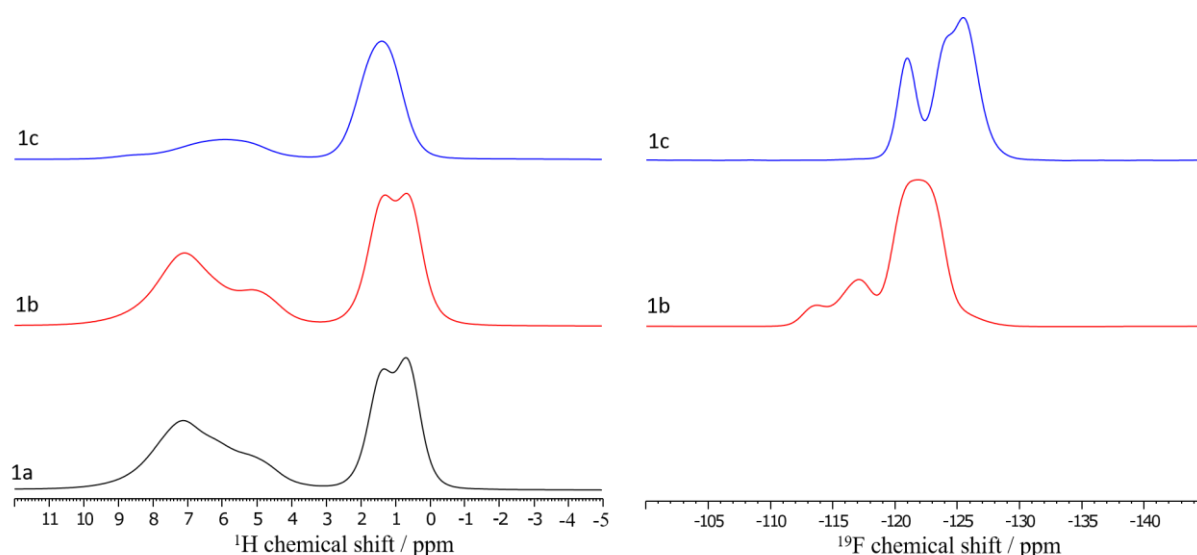
Figure 25 ^{1}H NMR spectra of the compounds **1a**, **1b** and **1c** and ^{19}F NMR spectra of the compounds **1b** and **1c** recorded at 25 kHz MAS.

In the case of compound **1c**, three fluorine signals are observed, as shown in Figure 25. In this compound, the ^{19}F chemical shifts have values of -121.9, -124.3 and -125.4 ppm with an intensity ratio of 1:1:2 respectively. The intensity ratios are determined by integration with the DMfit software.[97] Such an intensity distribution suggests that there are three different local environments of the fluorine atoms in the solid state. However, fluorine atoms of the other TADF carbazole ring appears to be characterised by a different local environment.

Table 2 ^{1}H chemical shift values for the compounds **1a**-**1c** detected at a field of 700 MHz and a MAS spinning speed of 25 kHz.

	1a		**1b**		**1c**	
	0.73	Al1	0.72	Al1	-	
	1.37	Al2	1.30	Al2	1.43	Al1
	4.40	H-10	5.15	H-10	4.97	H-11,13
	7.48	H-6,8,11	7.32	H-6,8,18,19	6.41	H-10
	8.66	H-12,13				

Compound **1b** also shows three ^{19}F signals as can be seen in Figure 25. Compared to compound **1c**, other chemical shifts were observed with values of -113.6, -117.0 and -121.9 ppm. It was also determined that the fluorine species with a chemical shift of -121.9 ppm has a significantly higher intensity than the other two signals and shows a very broad, featureless line. The maximum of the signal is not sharp but rather forms a plateau, which suggests that there are a number of superimposed signals. A deconvolution fit of the broad signal yields a number of at least three different species with relative intensities of: 31:31:38.
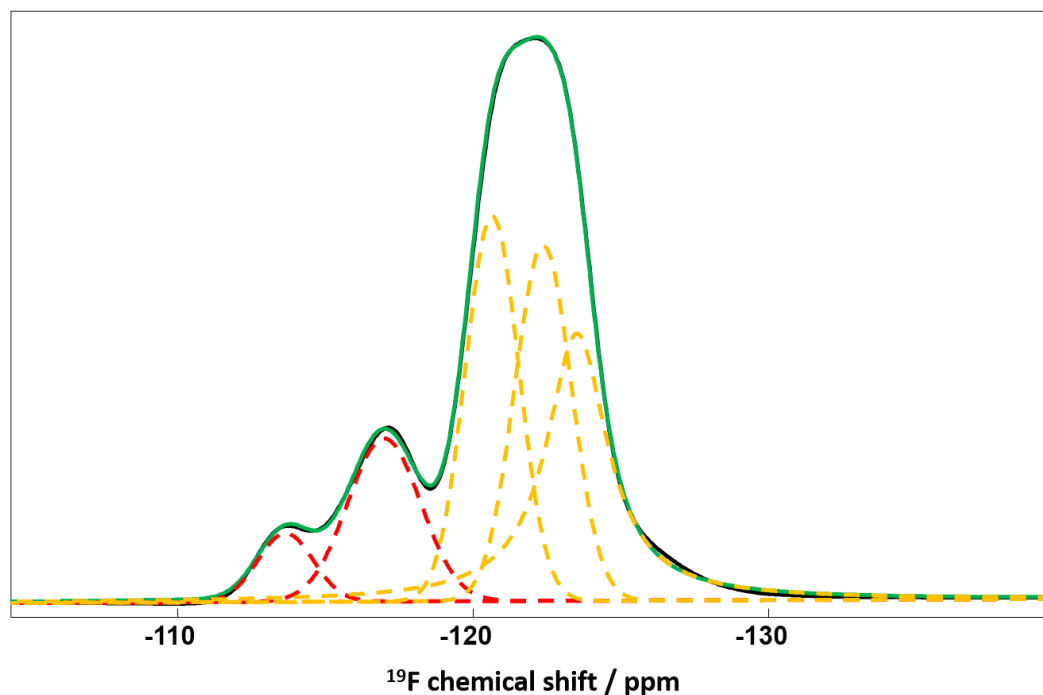
Figure 26 Deonvoluted ^{19}F MAS spectrum of compound **1b**. The peaks obtained by deconvolution are displayed as dotted lines. Red indicates the resonances belonging to the crystalline portion, whereas orange dotted lines describing the amorphous portions, merging together as one signal.

In the case of TADF molecule **1b**, the signals could originate from different ^{19}F local environments in the solid that are caused by the formation of different phases present in the sample. This would be discussed in detail below.

Table 3 ^{19}F chemical shift extracted from ^{19}F MAS NMR spectra, acquired at a field of 500 MHz and a spinning speed of 25 kHz.

1b	1c
-113.6	-121.0
-117.0	-124.2
-121.9	-125.4
Deconvolution:	
-120.6	
-122.4	
-123.5	

5.3.2 Homo- and heteronuclear correlation spectra

The chemical shift assignments allow evaluating the two-dimensional correlation spectra used to investigate through space interactions. Such spectra are measured to probe spatial proximities, using the homonuclear (e.g. ^{19}F-^{19}F, ^{1}H-^{1}H) and the heteronuclear (e.g. ^{1}H-^{13}C, ^{1}H-^{19}F) interactions.

NMR spectroscopy allows obtaining local structural information in both amorphous and crystalline phases in the solid state. In addition, information about interfaces and the presence of different polymorphs is accessible.[98–100] For this amorphous samples, short range interactions can be used to identify the arrangement of molecules without periodic order.
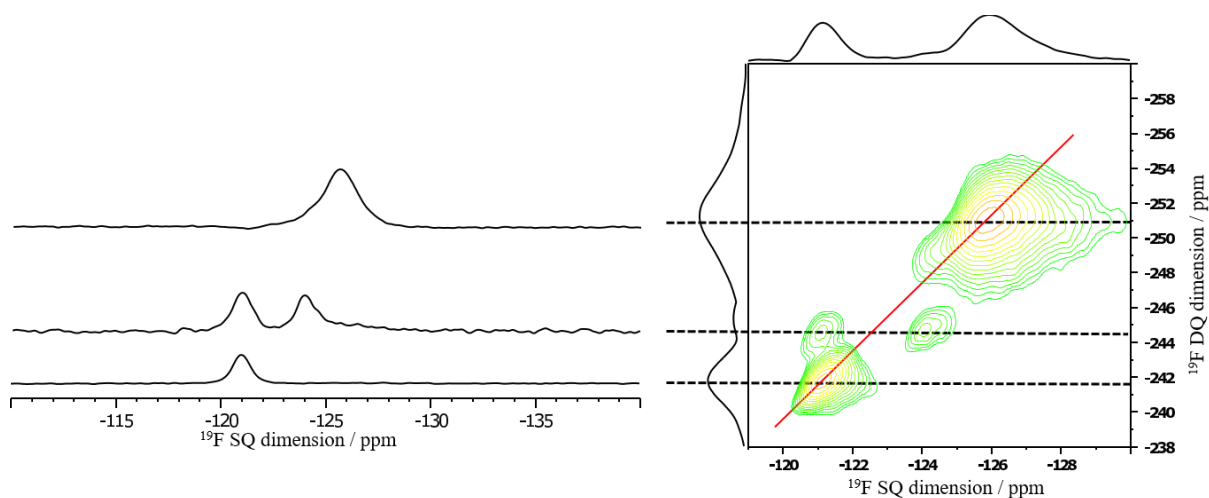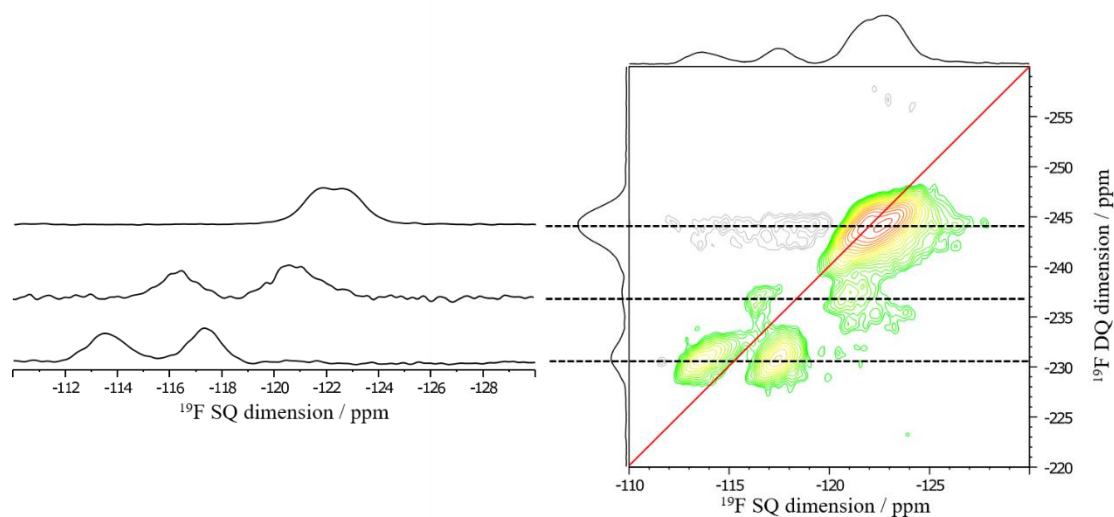

Figure 27 ^{19}F-^{19}F DQ BaBa NMR spectrum of compound **1c** measured at a spectrometer frequency of 500 MHz and a spinning speed of 25 kHz MAS with an excitation time of 160 μs.

The spectrum presented in Figure 27 reveals the self-correlation signals which appear on the diagonal of the spectrum (-121.0 and -125.4 ppm) of two ^{19}F nuclei with the same chemical shift. In addition, the spectrum shows a correlation between the signals resonating at -121.0 and -124.2 ppm. The information that can be extracted from the ^{19}F-^{19}F DQ-SQ correlation spectrum is consistent with the assumptions made about the different local environment of the fluorine sites in the molecules. The strong self-correlation of the signal at a chemical shift of -125.4 ppm indicates that the fluorine atom attached to the carbazole ring with a symmetric local environment interacts with another fluorine of the same kind.

The ^{19}F signal resonating at -121.0 ppm in the second carbazole ring of a TADF molecule shows also a self-correlation. However, since the signal at -124.2 ppm does not show any self-correlations, it can be assumed that the fluorine atom attached to second carbazole ring does not have a sufficiently strong dipole-dipole coupling with its nearest neighbour to excite a detectable intensity of the DQ coherence. This carbazole unit is likely to be rotated by 180° at the axis orthogonal to the bond between carbazole

and centre phenyl ring. Both translational and rotational motions are most likely strongly limited by the presence of the bulky *tert*-butyl groups, attached to the triazine ring and the resulting self-assembly behavior after vacuum sublimation. The distance between the fluorine atoms, attached to the carabzole units of the same TADF molecule ranges from 7.9-13.9 Å (depending on the investigated fluorine site) and is therefore too large to realize a double quantum excitation.

The CP HETCOR NMR technique relies on the heteronuclear dipole-dipole couplings and is also used to obtain spatial information about the arrangement of small molecules in the solid state.
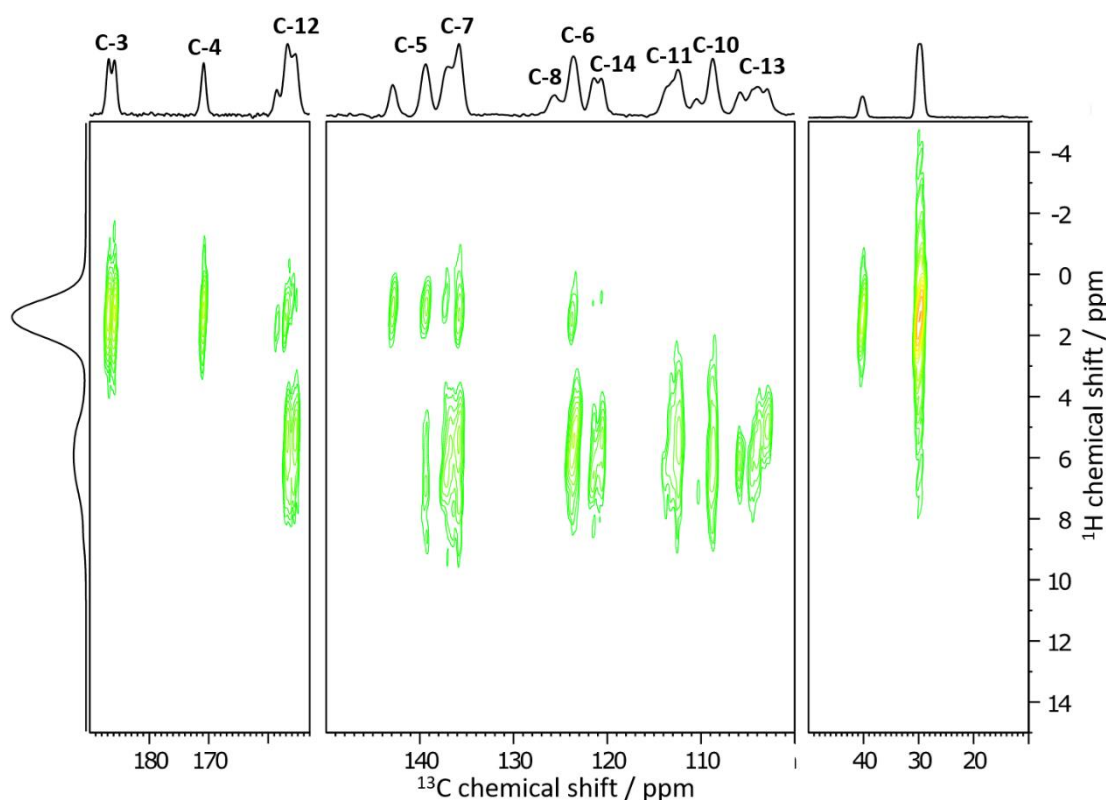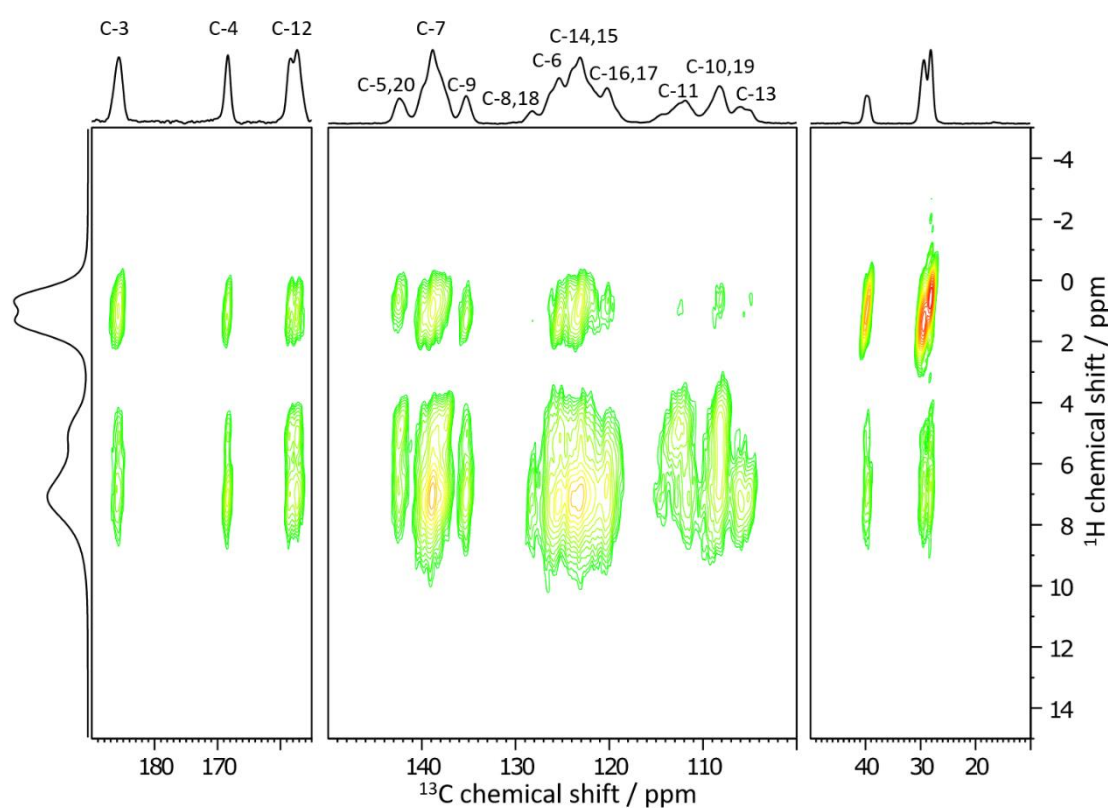

Figure 28 ¹H-¹³C HETCOR NMR spectrum of compound **1c** measured at a field of 700 MHz and a rotation frequency of 25 kHz. The CP time was 3 ms and the recycle delay 5 s.

The aromatic region of the ¹H-¹³C HETCOR NMR spectrum of compound **1c** measured with a CP time of 3 ms and recycle delay of 5 s is shown in Figure 28. The aliphatic carbon signals show only a correlation with the respective aliphatic protons. In the aromatic region of the carbon spectrum, the signal of carbon atom C-13 is split into three signals with chemical shifts of 102.9, 104.1 and 105.9 ppm. These signals show no spatial connectivity with the aliphatic protons. However, correlations between the aromatic proton signals can be observed. Here, the signal with a chemical shift of 102.9 ppm is in spatial proximity to the aromatic protons with a chemical shift of 5.1 ppm. The signal with a chemical shift of 104.1 ppm has a spatial connectivity with the aromatic protons at 5.9 ppm. The third signal with a chemical shift of 105.9 ppm shows a correlation to protons with a chemical shift of 6.2

ppm. This means in fact, that the protons are affected in the same way as the carbon atoms, which leads to a signal distribution for the ^{1}H nuclei at the same molecular site but in different local environments. The carbon atoms C-10 and C-11 are only spatially close to the aromatic protons. In addition, it can be observed that there is an inhomogeneous broadening for the signals of the named carbon atoms, which also show a high-field shift when compared with the solution NMR data (an analogous change in the chemical shift towards the high field can also be observed for the proton species). Such a high-field shift could indicate a sandwich-like stacking, since it was observed for both proton and carbon species. The carbon atoms C-6 and C-14 show no correlation with the aliphatic protons, but are also high field shifted. In contrast, the carbon atom C-8 of the central phenyl ring shows a correlation to the aliphatic signals. All other carbon atoms of the carbazole units and the central phenyl ring in compound **1c** form correlations with both the aromatic and aliphatic protons, with the exception of the carbon atom C-5 of the central phenyl ring. For the fluorinated carbon atom C-12 (158 ppm), a splitting pattern into three signals can be observed, which shows a similarity to the observed splitting of the fluorine signals in the 19F spectrum. The carbon signals of the triazine ring show only correlations to the aliphatic protons. The signal of the carbon atom C-3 is split into two peaks, while the signal of C-2 does not show any splitting.

Next, the correlation spectra of compound **1b** will be discussed. Already from the drawn 2D structure of compound **1b**, the asymmetric substitution pattern can be recognized. The molecule contains no steric information about a preferred orientation of the fluorinated part of the carbazole ring. Accordingly, many different stacking geometries are conceivable in the case of compound **1b**.

Figure 29 ^{19}F-^{19}F DQ BaBa NMR spectrum of compound **1b** measured at a spectrometer frequency of 500 MHz and a spinning speed of 25 kHz MAS with an excitation time of 160 µs.

First, the [19]F-^{19}F DQ BaBa spectrum shown in Figure 29 shall be considered. The ^{19}F signals with chemical shifts of -113.6 and -117.0 ppm do not show any correlation with spins with equal chemical shift, but correlations between each other. In the double quantum dimension, an additional signal can be observed at -237.0 ppm. This signal shows only very weak correlations. The intense fluor signal at -121.9 ppm can be identified in the DQ spectrum as a superposition of two correlating signals. Here, the signal with the chemical shift of -121.9 ppm exhibits a self-correlation. The signal at a chemical shift of -122.8 ppm correlates with the signal at -121.9 ppm.

It is assumed that the signals at -113.6 and -117.0 ppm belong to a crystalline phase, while the signals at -121.9 and -122.8 ppm originate from amorphous portions of the sample, which is based on the analysis of the relaxation time that will be discussed in a later section of the chapter. The signal at -237.0 ppm in the double quantum dimension probably originates from an interface between crystalline and amorphous domains, causing amorphous and crystalline ^{19}F signals to correlate with each other. The fact that signals for such an interface are observed indicates that the crystalline domains that compound **1b** forms in the solid state have a small size, which has not been determined further.

Figure 30 ^{1}H-^{13}C HETCOR NMR spectrum of compound **1b**, measured at a field of 700 MHz and a rotation frequency of 25 kHz with a CP time of 3 ms and a recycle delay of 5 s.

The ^{1}H-^{13}C HETCOR spectrum of compound **1b** is shown in Figure 30. The featureless broad signals in the aromatic range of 100-150 ppm already support the assumption that a large part of the molecules is present in an amorphous phase. In addition, the asymmetric substitution pattern of the carbazole units results in chemically non-equivalent carbon atoms, which lead to an increased signal density in this spectral region. The ^{13}C signals of the methyl groups are split into two peaks, while the quaternary aliphatic carbon signal shows only one peak with a broad plateau. This is not surprising, since packing effects will affect the *tert*-butyl groups only at the outside, thus at the methyl positions and not at the centre. All aliphatic ^{13}C signals show a correlation with the aliphatic protons. The methyl signal with a chemical shift of 28.2 ppm correlates with the proton signal at 0.72 ppm, while the signal with a chemical shift of 29.4 ppm correlates with the proton signal at 1.30 ppm. Those aliphatic signals show an intensity ratio of 1:1 and therefore it is assumed, that both resonances belong to molecules within the same phase. The quaternary carbon atom signal correlates with both aliphatic proton signals, but is only located in close proximity to the aromatic proton signal at 7.13 ppm. The two ^{13}C methyl signals are also spatially connected with the latter proton signal, while only the signal at 28.2 ppm correlates with the proton species resonating at 5.15 ppm, located at the fluorinated site of the carbazole unit. A closer look at the aromatic carbon region reveals that the carbon atoms C-10 and C-19 are represented by several signals in the solid state. The signals of these carbon atoms range from 114.7 to 105.4 ppm. For all of them, only very weak interactions with the aliphatic protons are detected. This is mainly due to truncation of the through space correlations by the strong coupling of directly bond protons in C-H pairs. The broad signal with a chemical shift of 105.4 ppm has no spatial connectivity with the proton signal at 5.15 ppm, but with that at 7.13 ppm. All of the other carbon atoms in this range are in close proximity to the aromatic proton signals. The carbon atoms C-16 and C-17 at a chemical shift of 120.3 ppm show only weak correlations with the aliphatic signals. For these, as well as all other aromatic carbon atoms of compound **1b**, the correlations to the aromatic protons are pronounced. An interesting correlation pattern can be observed for the carbon atoms C-9 and C-20. While C-9 (135.5 ppm) correlates with the aliphatic proton signal at 1.30 ppm, a correlation between C-20 and the proton signal is formed at 0.72 ppm. Therefore, it can be assumed, that the protons resonating at 1.30 ppm experience a low field shift that is caused by their spatial proximity (~3 Å) to the fluorinated site of the carbazole units. The protons with a chemical shift of 0.72 ppm on the other hand are located closely to the non-fluorinated site of the carbazole units.
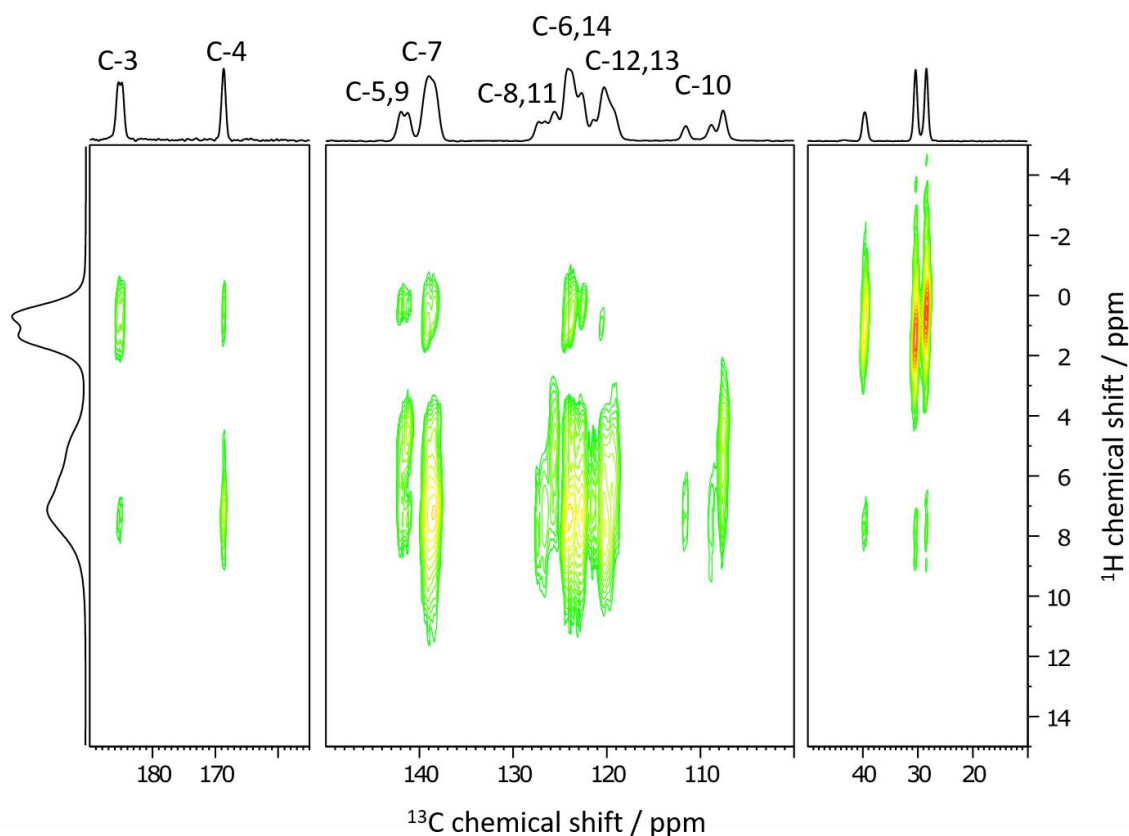
Figure 10 ¹H-¹³C HETCOR NMR spectrum of compound **1a**, measured at a field of 700 MHz with a rotation frequency of 25 kHz. The CP time was 3 ms and the recycle delay 5 s.

In contrast to compound **1b** and **1c**, compound **1a** is not fluorinated. Thus, a ¹⁹F analysis is not feasible. However, the ¹H-¹³C HETCOR spectrum can be used to obtain useful information about the local molecular packing. Due to the symmetrical line shape of the ¹³C signals, it can be assumed that compound **1a** has a significant degree of crystallinity in the solid state after vacuum sublimation. The ¹³C signal of the methyl groups splits again into two peaks in compound **1a**, of which the high field shifted one (28.3 ppm) correlates with the proton signal at 0.73 ppm and the ¹³C signal at 30.5 ppm correlates with the proton signal at 1.37 ppm. Both signals show an intensity ration of 1:1, similar to the intensity ratio that has been observed for the aliphatic proton species. The quaternary aliphatic ¹³C signal shows a broad correlation with both aliphatic proton signals. All aliphatic ¹³C signals also correlate, albeit weakly, with the aromatic proton signal at 7.14 ppm. The signal of C-10 does not correlate with aliphatic protons and is also split into three individual peaks. This splitting results from different local environments of the respective carbon atom C-10 that is mainly caused by different stacking geometries of the respective molecular sites. The signal with a chemical shift of 107.6 ppm shows correlations to both aromatic protons signals, while the other two signals correlate only with the signal at 7.14 ppm. The carbon atoms C-6 and C-8 (125.5 and 127.0 ppm) of the central phenyl ring show no correlations with the protons of the *tert*-butyl groups. The remaining carbon signals show

correlations to both aliphatics and aromatics. The carbon atoms of the triazine ring also show correlations to all proton species. The signal of C-3 is split into two signals and shows a correlation to the aliphatic and aromatic protons, whereby the latter is only formed to the signal at 7.14 ppm and is not particularly strong. C-4 shows only one signal and shows strong correlations to the aliphatic signal at 0.73 ppm and to the aromatic signal at 7.14 ppm. The correlations to the other two proton signals are not strong.

The NMR data allows to draw conclusions about the organisation of compounds **1a**, **1b** and **1c** in the solid state. The ^{19}F data allow two possible interpretations. First, it is possible that the splitting of the ^{19}F signal results from a different local environment of the respective fluorine atoms. In this case, the molecules may be present in a unit cell and form a homogeneous phase without further superstructures. The second possible explanation is that the different signals belong to different phases.

The first possibility seems to be the realistic description for compound **1c**. This is supported by the fact that an intensity ratio of 1:1:2 was found for the respective fluorine atoms. Such a distribution suggests that one carbazole unit is probably in a symmetrical environment, while the second carbazole unit experiences different local environments. In the case of compound **1b**, two phases are most likely present, with the amorphous part being assigned to the broad ^{19}F signal at -121.9 ppm. The other two signals at -113.6 and -117.0 ppm are assumed to originate from the crystalline phase. The proportion of the broad ^{19}F signal of compound **1b** can be determined by integration of the signals, which leads to an amorphous content of roughly 83%.

The ^{19}F-^{19}F BaBa spectra of compounds **1c** and **1b** provide additional information about the local environment of the respective fluorine atoms. In the case of compound **1c**, it can be assumed that two carbazole units characterized by the same chemical shift form a sandwich-like stacking structure. Due to the fact that the internuclear distance of two fluorine atoms of the same carbazole unit is 7.9 Å, the occurrence of double quantum coherence due to an interaction of the fluorine atoms in the same carbazole unit is hardly possible. Another aspect indicating a sandwich-like stacking structure of the carbazole units in compound **1c** can be seen in the ^{1}H MAS spectrum. The signal at a chemical shift of 5.95 ppm can be assigned to the protons of the carbazole units by analysis of the ^{1}H-^{13}C HETCOR spectrum and is thus, compared to compound **1a** and **1b**, clearly more shifted towards the high field. Such a shift suggests a pi-stacking arrangement involving the carbazole units. In addition, the lacking correlation signals of the ^{1}H-^{13}C HETCOR spectrum indicate that in the case of compound **1c**, the carbazole units have some degree of spatial separation from the triazine rings. Compounds **1a** and **1b**, on the other hand, show correlations between the triazine ^{13}C sites and aromatic protons of the

carbazole units. However, these aromatic protons are not shifted into the high field, so it can be assumed that stacking of the carbazole units does not occur.

5.3.3 XRD and single crystal NMR

To support the NMR spectroscopic data of the TADF molecules, the crystal structure was also determined by XRD. The compounds were dissolved in $CHCl_3$ and pentane was diffused in as an anti-solvent for crystallization. The crystal structure obtained after crystallization from solvent is not necessarily in agreement with the structure in micro-crystallites obtained by vapour deposition. The gas phase fabrication of thin layer electronics is the method of choice, since it allows a more precise adjustment of the film layer thickness. The crystallites that are obtained after sample sublimation are way too small for XRD measurements and can also contain a high amount of molecules in amorphous phases (in this study up to 83% for **2b**, see above). Solid state NMR offers an insight into the close range order of the respective material for both, vapour deposited and solvent crystallized samples and allows a comparison between the two preparation methods.

The space group of compound **1c**, which was found after solvent crystallization, is P 2_1/c, a monoclinic space group. As can be seen in Figure *31* a), two carbazole units of adjacent TADF molecules are stacked in a 180° degree offset arrangement. This stacking arrangement initially suggests that it is responsible for the observed strong self-correlation between the fluorine atoms of the carbazole rings. However, the minimum distance determined from the crystal structure of 4.6 A is does not indicate such a strong self-correlation. Due to the fact that a double quantum excitation scales with r^6 (for spin $\frac{1}{2}$ nuclei), a small distance (< 5 Å) is necessary to observe these strong DQ correlations. It can therefore be assumed that the carbazole rings, which are rotated by 180°, do not lie exactly planar on top of each other after vacuum sublimation (compare Figure 31 c). The second carbazole ring of a TADF molecules in contrast does not show a 180° offset stacking arrangement after crystallization from solution. From the crystal structure, it can be seen, that the second carbazole ring of a TADF molecule interacts with only one benzyl unit with its nearest neighbour. The second benzyl unit of the same carbazole ring is not involved in stacking. As a result, one of the fluorine atoms has another of the same type in close proximity, i.e., an average distance of 4.8 Å. The second fluorine atom, which is bonded to the carbazole ring that is not involved in the stacking, shows no self-correlation, as already discussed. However, correlations to the fluorine atoms with a chemical shift of -121.0 ppm were observed. Here, the inter-nuclear distance is 5.4 Å, which results in weaker correlations due to the weaker dipolar interactions. ^{19}F NMR spectroscopic examination of the sublimed sample suggests a very similar arrangement for these specific carbazole rings. Here, self-correlations occur which can also be

observed for the single crystals (compare Figure 31 c). The torsion angles between the centre phenyl ring and the carbazole units were determined to be 63° and 43°. The central phenyl ring and the triazine ring have a torsion angle of 153°.
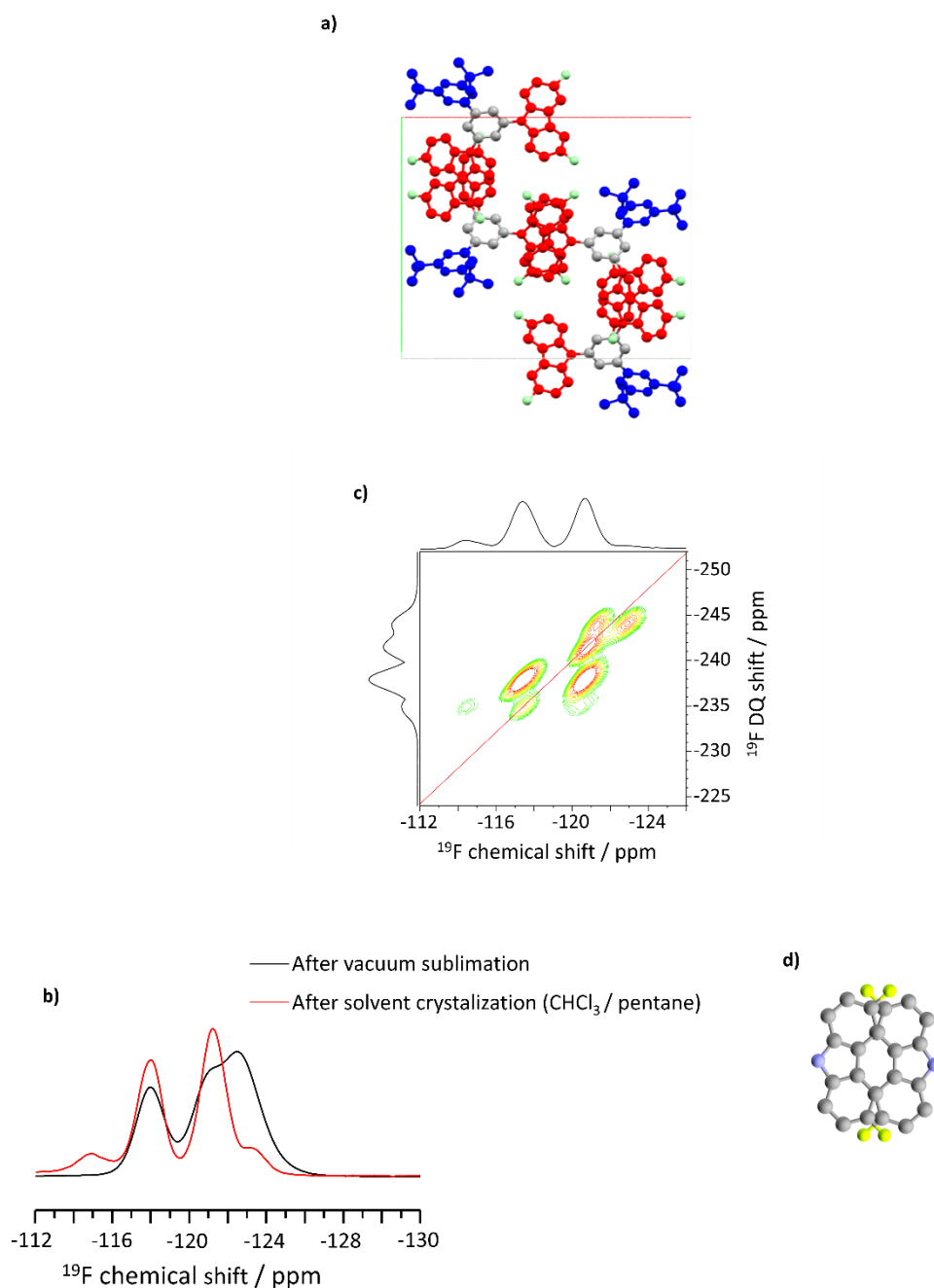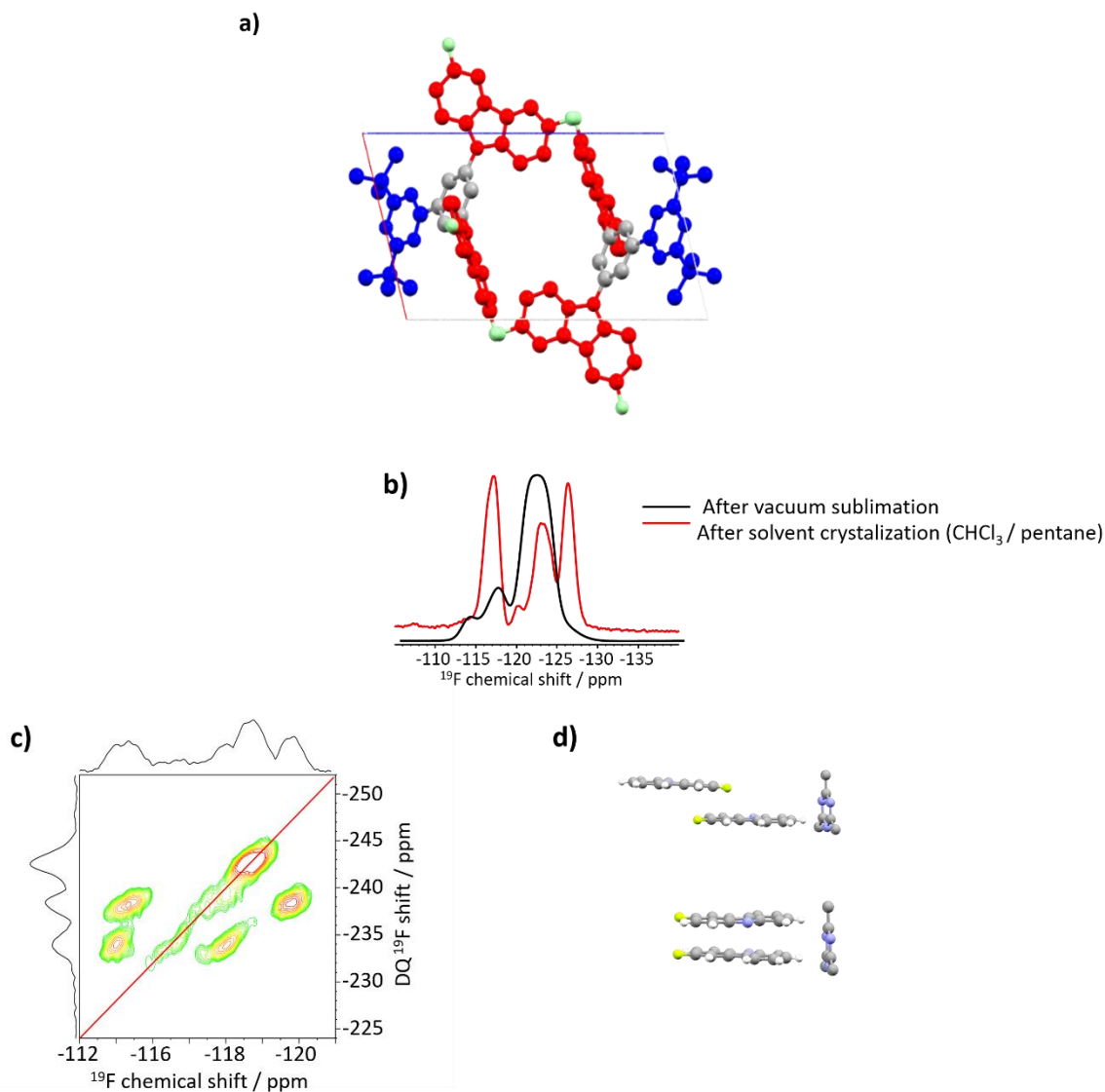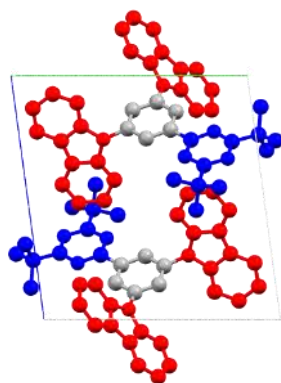

Figure 31 a) Crystalstructure of the compound **1c**, crystallized from CHCl₃/pentane. The carbazole units (donor) are colored in red and the triazine/*tert*-butyl units (acceptor) in blue. Fluorine atoms are colored in green for better visualization. b) ^{19}F MAS spectra for compund **1c** after vakuum sublimation (black) and after crystalization from CHCl₃/pentane (red) measured at a filed of 700 MHz and a rotation frequency of 50 kHz. c) 2D ^{19}F-^{19}F BaBa-spectrum of compound **1c** crystalized from CHCl₃/pentane, measured at a field of 700 MHz, a rotation frequency of of 50 kHz and a excitation time of 160 µs. d) possible allignment of the carbazole units after vacuum sublimation.

Compound **1b** crystallizes in a triclinic crystal system with space group P1 (see *Figure 31* a). The unit cell contains two molecules separated by a larger spatial distance of about 7-9 Å. A cavity can be seen in the center of the unit cell. The carbazole units are represented in the unit cell with two fluorine atoms, since the carbazole units are arranged with a 50:50 antiparallel distribution and the missing periodicity in the crystalline compound does not allow discrimination between fluorinated and non-fluorinated side of the carbazole ring by XRD measurements. The torsion angles between the central phenyl ring and carbazole units are 53° and 48°. The central phenyl ring and the triazine ring have a torsion angle of 167°.

Although the fluorine atoms are spaced by 5 Å, these correlations could be detected as shown above, suggesting that the crystalline structure shown, which was obtained after crystallization from the solvent mixture $CHCl_3$/pentane, differs from the structure formed after vacuum sublimation. Since the amorphous fraction in sample **1b** is 83%, a general comparison between NMR and XRD data is hardly possible. However, based on the information obtained from the ^1H-^{13}C HETCOR spectrum, it can be assumed that the carbazole rings are located in the amorphous phase in the vicinity of the triazine rings. The minimum distance between a carbazole proton and a carbon atom of the triazine ring is 4.9 Å in the crystal structure, which is a large distance for the detection of a strong correlation. One way of arranging the carbazole rings of adjacent molecules as they exist after vacuum sublimation is shown in Figure 32 d. On the one hand, this implies a small distance between the fluorine atoms, which leads to a dipole-dipole interaction of the nuclear spins and thus enables excitation of the double quantum coherences. On the other hand, the carbazole rings can be assumed to be in an edge-on stacking with the triazine rings of neighbouring molecules. This explains the observed low field shift of protons H-18 and H-19, as well as the heteronuclear correlations that occur between the triazine ring and the carbazole protons, observed in the ^1H-^{13}C HETCOR spectrum. In addition, a comparison of the ^{19}F MAS spectra of solution-crystallized and vacuum-sublimated samples of compound **1b** shows that the structures are different (Figure 32d). The ^{19}F-^{19}F BaBa spectrum shown in Figure 32 c) suggests that there are at least three local environments for fluorine atoms, which also supports the statement made earlier that the crystal structure only partially describes the local structure of the fluorine atoms. The strong self-correlation of the signal at -242.6 ppm results from carbazole units in which the fluorine atoms are aligned to the same side, resulting in a small distance between two identical nuclei. The other two correlations at -238.3 and -233.9 ppm show less pronounced resonances resulting from fluorine atoms in the same vicinity. These are interactions between nuclei characterized by different chemical shifts.

Figure 32 a) Crystalstructure of the compound **1b**, crystallized from CHCl₃/pentane. The carbazole units (donor) are colored in red and the triazine/tert-butyl units (acceptor) in blue. Fluorine atoms are colored in green for better visualization. b) ^{19}F MAS spectra for compund **1b** after vakuum sublimation (black) and after crystalization from CHCl₃/pentane (red) measured at a filed of 700 MHz and a rotation frequency of 50 kHz. c) 2D ^{19}F-^{19}F BaBa-spectrum of compound **1b** crystalized from CHCl₃/pentane, measured at a field of 700 MHz, a rotation frequency of of 50 kHz and a excitation time of 160 µs. d) possible allignment of the carbazole units after vacuum sublimation.

Like compound **1b**, compound **1a** crystallizes from solution in a triclinic crystal lattice with the space group P1. The unit cell also contains two molecules. As can be seen from Figure 33, there is no large cavity in the unit cell. Such a denser arrangement of the molecules can be realized by the lack of repulsive interactions of the fluorine atoms, which are present in compound **1b** but not in **1a**. Here, the carbazole units are spatially close to the triazine ring and have proton-carbon distances between 2.9 and 3.5 Å. These small distances give rise to the correlations in the ^{1}H-^{1}3C HETCOR spectrum. The torsion angles between the central phenyl ring and the carbazole moieties are 77° and 51°, respectively, and thus are slightly larger than the same angles in compounds **1c** and **1b**. The central

phenyl ring and the triazine ring have a torsion angle of 177°, which indicates an almost planar arrangement of the two building blocks. Due to the lack of fluorine atoms and the poor resolution of the ^{1}H MAS NMR spectra of compound **1a**, a comparison between solution and sublimation processed samples cannot be made. The ^{1}H-^{13}C HETCOR spectrum, however, provides data that can be reconciled with the obtained crystal structure.

Figure 33 Crystalstructure of the compound **1a**, crystallized from CHCl$_3$/pentane. The Carbazole units are colored in red and the triazine/*tert*-butyl units in blue.

5.3.4 Molecular order and dynamics

Another method that can be used to better understand the morphology of a sample in the solid state is the determination of longitudinal NMR relaxation times, called T_1 relaxation times. Crystalline, densely packed molecules result in long T_1 relaxation times, while amorphous arrangements of molecules exhibit in many cases shorter T_1 relaxation times. The ^{19}F T_1 relaxation times of the vacuum sublimated samples were measured using saturation recovery pulse sequence and are listed in table 1. As can be seen from the values, the ^{19}F relaxation time constants for the fluorine atoms in compound **1c** is significantly larger than that determined for compound **1b**, indicating a higher crystallinity of the sample.

In addition, the relaxation times of the crystalline part in compound **1b** is about 35% longer than the relaxation times of the amorphous part. In compound **1c**, the difference between the individual fluorine T_1 relaxation times is significantly less pronounced. The fluorine T_1 relaxation time constants assigned to the central carbazole rings in the 180° stacking arrangement are only about 15% higher than the T_1 relaxation time constants of the other two fluorine sites.

Table 4 ^{19}F T_1 relaxation times of the compounds **1b** and **1c** determined with the saturation recovery pulse sequence at a field of 500 MHz and a rotation frequency of 25 kHz.

1b		1c	
^{19}F CS / ppm	T_1 / s	^{19}F CS / ppm	T_1 / s
-113.6	3.9	-121.0	18.4
-117.0	3.4	-124.2	21.4
-121.9	2.4	-125.4	23.0

In addition to the ^{19}F T_1 relaxation times, the ^{1}H T_1 relaxation times were also determined. Due to the high line broadening in combination with the low chemical shift range, a detailed determination of the relaxation times is possible only to a limited extent. However, a good approximation of the values can be obtained by integrating the entire signals of the aromatic and aliphatic regions separately. It should be noted that in the case of a mixture of crystalline and amorphous components in the sample, a biexponential behaviour is expected. However, if the spin system of protons is dense, spin diffusion effects can lead to an average of the observed relaxation times. The T_1 relaxation time of the protons of the *tert*-butyl groups is not surprisingly lower for compounds **1a** and **1b** with 0.7 s than the relaxation times determined for the aromatic signals. In compound **1c**, the relaxation time of the *tert*-butyl groups is twice as high at 1.5 s, but it is only 7.6 % of the value compared to the T_1 time of the aromatic protons of this compound. This indicates as expected free rotation of the *tert*-butyl and methyl groups about the symmetry axis in the solid state. The T_1 relaxation times of the aromatic protons, however, differ slightly for compounds **1a** and **1b** with a difference of 0.4 s. Although this change is very small, the measured T_1 relaxation times support the assumption that compound **1b** has a higher amorphous content due to the very short relaxation time. Compound **1c**, on the other hand, shows a T_1 relaxation time for the aromatic protons that is an order of magnitude longer than for the aromatic protons of compounds **1a** and **1b**.

Table 5 ^{1}H T_1 relaxation times of the compounds **1a**, **1b** and **1c** determined with the saturation recovery pulse sequence at a field of 700 MHz and a rotation frequency of 25 kHz.

1a		1b		1c	
^{1}H CS / ppm	T_1 / s	^{1}H CS / ppm	T_1 / s	^{1}H CS / ppm	T_1 / s
12.4-2.9	1.8	11.5-2.8	1.4	15.1-6.5	19.7
2.9-(-3.5)	0.7	2.8-(-3.9)	0.7	6.5-0.1	1.5

In addition to the determination of T_1 relaxation time constants probing the spectral density at the Larmor frequency, other NMR methods are available for the analysis of molecular dynamics parameters different time scales. In the study of TADF molecules used in this work, the REPT-HDOR pulse sequence was used to excite the rotational sideband patterns of ^{13}C nuclei (exemplarily shown in Figure 34). Those rotational sideband patterns were analysed using a fitting script in MATLAB, to obtain the residual dipolar coupling constants of the CH pairs, which corresponds to motions on the

milli to microsecond time scale. Those coupling constants were then used to determine the order parameters and jumping angles (Table 6) in the studied molecules.
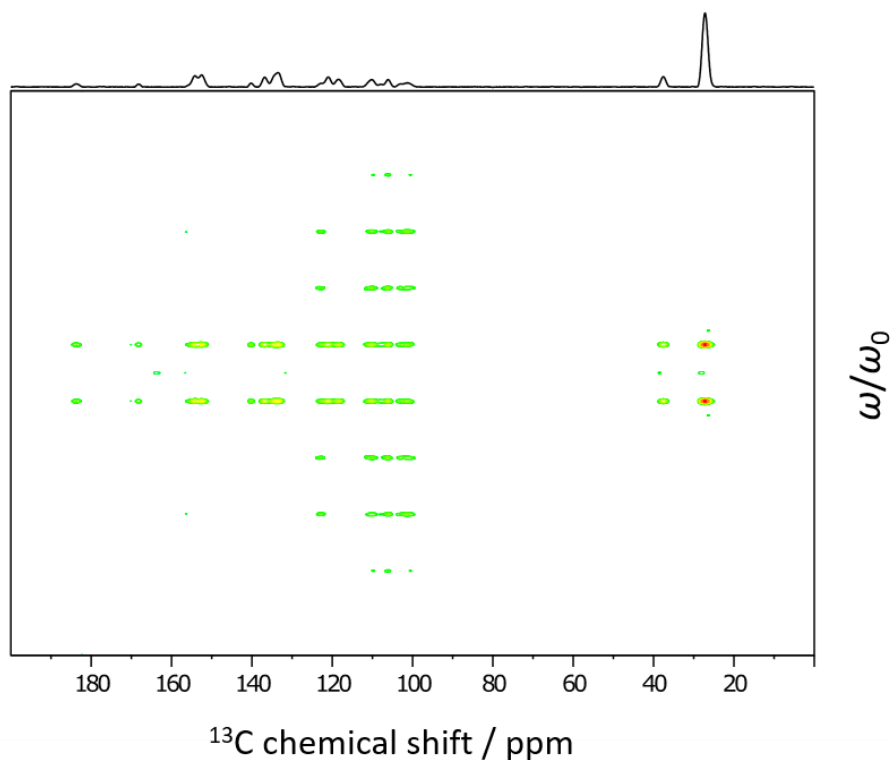
Figure 34 Exemplary ^{13}C REPT-HDOR spectrum of compound **1a**. Measured at a field of 500 MHz and a spinning speed of 25 kHz.

The experimentally determined heteronuclear coupling constants, as well as the order parameters and jumping angles calculated from them, are listed in Table 6Table 6. In the case of compound **1a**, many of the aromatic C-H bond pairs are rigid, as determined by the dynamics measurements. However, C-H pairs are also present, which have a higher mobility. In Figure 35, the molecular C-H positions are shown with the corresponding rotational sideband patterns and the heteronuclear coupling constants calculated from them for compound **1a**. It can be seen that both non-equivalent carbon atoms of the central phenyl ring (C-6 and C-8) have a coupling constant reduced by 13 and 23 %, respectively, compared to a rigid C-H pair. For the carbon atom of the carbazole ring at position C-11, a coupling constant reduced by 18% was also measured. These deviations from an order parameter $S = D/D_0$ with S=1 can be explained by the position of the C-H pairs relative to the rotation axis of the respective molecular fragment.
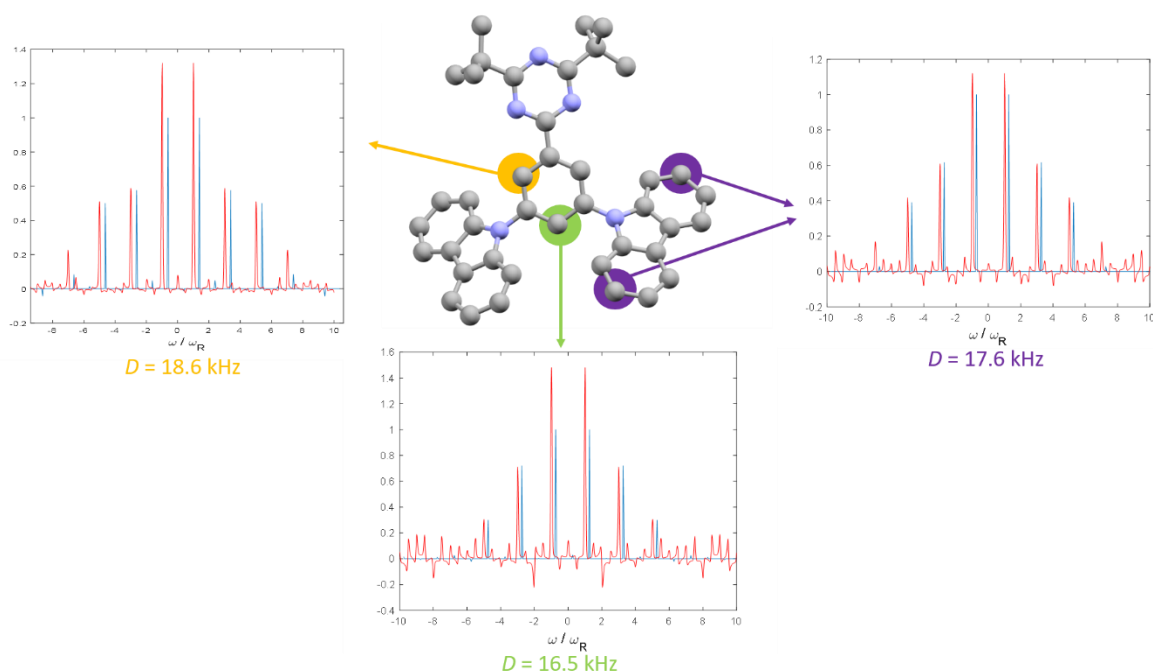
Figure 35 Rotational sideband patterns extracted from REPT-HDOR measurements of compound **1a** of selected aromatic positions.

With an alignment close to the magic angle, even small fluctuations can lead to a substantial reduction of the effective dipolar coupling In the case of compound **1a**, it can therefore be assumed that the molecules in the solid state form a densely packed arrangement, which allows only low molecular mobility and reorientation.

Comparing the results of the REPT-HDOR measurements of compound **1a** with those of **1b**, it can be seen that in the case of **1b**, lower dipolar coupling constants are determined in the solid state. This is not surprising since, as already shown by the T_1 relaxation time measurements as well as the analysis of 1D and 2D spectra, a mobile amorphous morphology is dominant for compound **1b** in the solid state. Compound **1c**, on the other hand, shows slightly reduced dipolar coupling constants despite the demonstrated crystal structure. A closer look at the molecular arrangement presented in Figure 31 a) reveals that the packing of the molecules has a certain degree of free volume. This free volume allows the activation of dynamic processes for conformational degrees of freedom of the individual molecular fragments resulting in a reduced dipolar coupling constant.

Table 6 Calculated dipolar coupling constants, order parameters and jumping angels Θ for the respective C-H pairs in compounds **1a-1c**.

1a				**1b**				**1c**			
Position	D/kHz	S/S_0	Θ	Position	D/kHz	S/S_0	Θ	Position	D/kHz	S/S_0	Θ
C-10	21.5	1	0°	C-13	20.8	0.97	20°	C-13	20.9	0.97	18°
"	21.5	1	0°	"	19.9	0.93	44°	"	20.4	0.95	33°
"	21.5	1	0°	"	19.3	0.90	52°	"	18.1	0.84	75°
C-13	21.5	1	0°	C-10,19	18.9	0.88	64°	C-10	19.0	0.88	62°
C-12	21.5	1	0°	C-16	18.9	0.88	64°	"	20.0	0.93	42°
C-14	21.1	0.98	14°	C-17	19.5	0.91	32°	C-11	18.8	0.87	19°
C-6	18.6	0.87	45	"	19.5	0.91	32°	C-6	20.6	0.96	22°
C-11	17.6	0.82	31°	C-18	18.2	0.85	26°				
C-8	16.5	0.77	45°	C-8	18.0	0.84	32°				

In summary, it can be assumed that compound **1a** is a crystalline solid after vacuum sublimation. In the case of this compound, the low T_1 relaxation time of the aromatic protons is not due to an amorphous environment of the molecules, but due to the spatial proximity of the protons of the *tert*-butyl groups to the respective carbazole protons. The rotation of the *tert*-butyl groups in close spatial proximity provides via the modulation of dipolar couplings a suitable relaxation path for the aromatic protons. The dense arrangement of the molecules does not allow fluctuations of the carbazole units around the C-N bond, which does not lead to a reduction of the effective dipolar coupling

Compound **1b** exhibits both an amorphous phase and a crystalline phase, of which the former represents the dominant fraction (83%, determined by integration as mentioned above) after vacuum sublimation. It is assumed, that the solvent crystallization leads to 100% crystalline molecules. The carbon atoms of the carbazole units in this compound exhibit reduced effective hetero-nuclear dipolar coupling, indicating fluctuations of the molecular sub-units in the solid state. The crystal structure, obtained by XRD, describes the crystalline part of the sample, which has significantly more cavities. Such a stronger spatial separation of the molecules can be caused by the electronic repulsion of the fluorine atoms.

The high proton T_1 relaxation time of 19.7 s in compound **1c** can be explained, among other things, by the absence of rotating methyl groups in the vicinity of the carbazole units. The reduced effective dipolar couplings of the carbazole sites, on the other hand, suggest some fluctuation of these sub-units. This can be explained by more free volume of the molecules within their solid state arrangement.

5.4 Solid state NMR of 9-(5-(4,6-di-*para*-fluorophenyl-1,3,5-triazin-2-yl)-phenylene)carbazole derivatives with variable, *tert*-butyl substituted carbazole units.

As the next part of this work, TADF molecules with an altered substitution pattern (compare chapter 3.2) are considered. The basic structure, consisting of a triazine ring and a tethered phenyl ring (central phenyl ring), is identical to the molecules described in chapter 3.2. The change is that the *tert*-butyl groups, which are attached to the triazine ring in the meta position to the central phenyl ring, are substituted by para-fluorinated phenyl rings. The second change is that the number of carbazole units attached to the central phenyl ring varies.
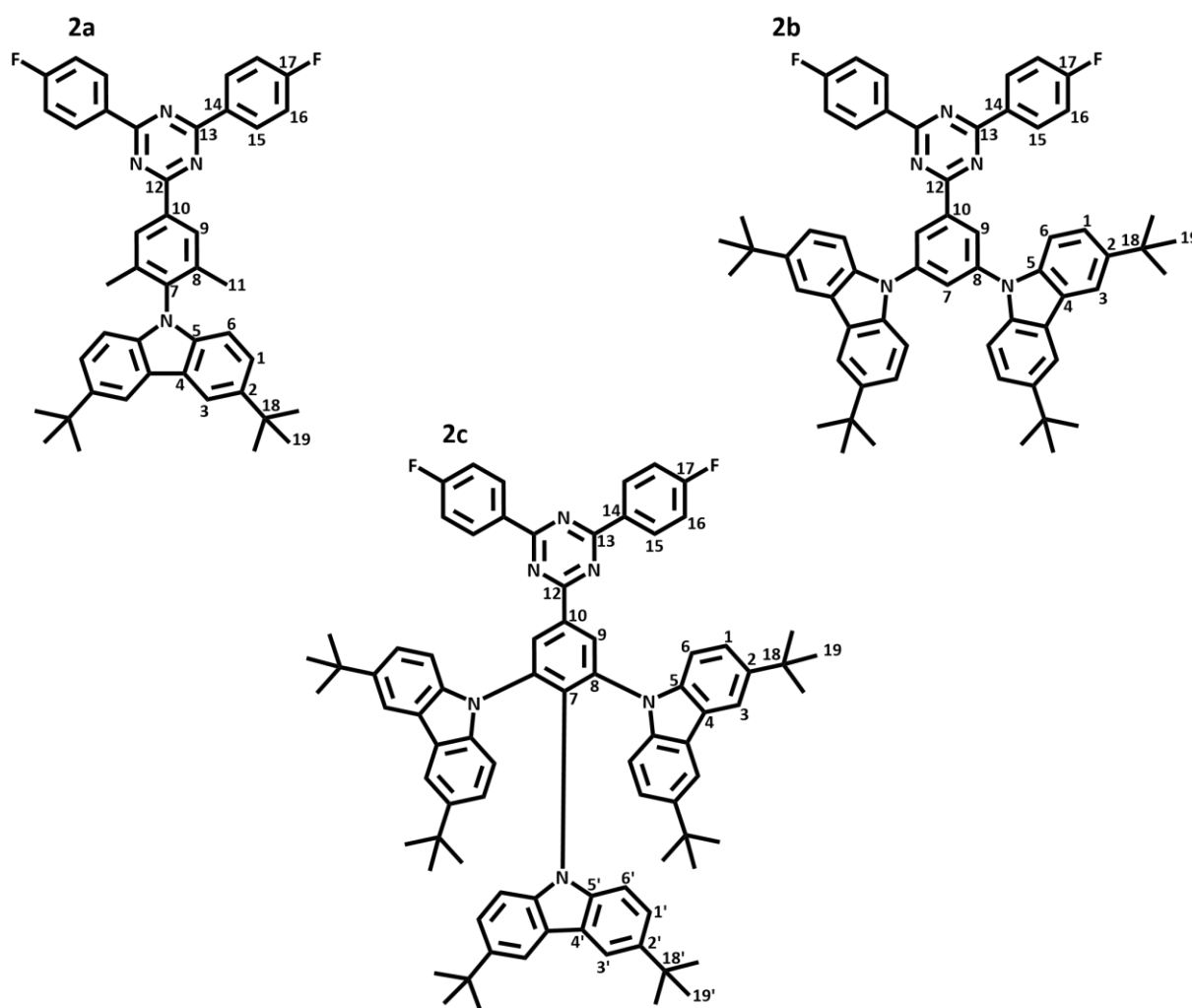
Figure 36 Two dimensional molecular structure of the TADF molecules with variable carbazole units studied in this paragraph.

Compound **2a** is substituted with only one carbazole unit, which is in the para position to the triazine ring. In addition, two methyl groups are attached to the centre phenyl ring in ortho position to the carbazole unit. Compound **2b** is characterized by the attachment of two carbazole units in the meta position. Compound **2c** is substituted on the center phenyl ring with three carbazole units, one of

which is in para and two in meta position to the triazine ring. In addition, all carbazole units of the compounds are substituted with *tert*-butyl groups in para position to the nitrogen atom.

5.4.1 One dimensional NMR spectra

First, the ^{13}C chemical shift in solution was determined for compounds **2a**-**2c** and Tetrachloroethan was used as solvent.

Table 7 ^{13}C chemical shifts of the compounds **2a**-**2c** from solution NMR experiments, measured at a field of 700 MHz. All values are given in ppm.

Atom	2a	2b	2c
1	124.1	124.4	123.5
2	142.5	143.8	143.2
3	116.3	116.8	115.7
4	122.8	123.6	123.4
5	138.4	139.0	138.8
6	109.2	109.5	109.7
1'	-		122.6
2'	-		142.9
3'	-		115.0
4'	-		124.3
5'	-		137.5
6'	-		110.3
7	135.8	128.4	137.1
8	138.9	140.2	138.0
9	129.3	125.4	130.1
10	139.4	139.4	136.8
11	18.4	-	-
12	171.5	170.7	169.9
13	170.1	171.2	171.0
14	132.4	131.9	131.8
15	131.5	131.6	131.7
16	116.0	116.1	116.0
17	165.7	166.1	165.3
18	34.8	34.8	34.6
19	32.4	32.1	32.0
18'	-	-	34.6
19'	-	-	31.8

T

It should be noted that compound **2c** has an additional set of ^{13}C chemical shifts (cf. Table 7, 1'-6'). This deviation from the ^{13}C chemical shifts determined for carbon atoms 1-6 can be explained by the fact that the carbazole unit attached the phenyl ring in para position to the triazine unit is flanked by two further carbazole units. These provide additional electronic shielding or de-shielding via the ring current effect to the central carbazole unit, resulting in a change on the ^{13}C chemical shift values. An additional contribution to the change in the chemical shift is made by inductive and mesomeric effects (-I/+M)[101,102], which, however, should play a subordinate role in compound **2c**.

The ^{13}C solid-state NMR spectrum of compound **2b** shows no splitting of the signals, with the exception of the methyl ^{13}C atoms of the *tert*-butyl group. In contrast to this observation are the ^{13}C signals determined for compounds **2a** and **2c**. Compound **2a** shows a splitting of the ^{13}C signals of the methyl groups attached to the central phenyl ring. The signals of the quaternary and methyl ^{13}C atoms of the *tert*-butyl groups, on the other hand, show only a single peak. The same behaviour can be observed for the ^{13}C signals of the *tert*-butyl groups in compound **2c**. The aromatic signals of compounds **2a** and **2c** also show splittings for certain ^{13}C atoms. In the C-H aromatic region, splitting of the carbon atoms C-6 and C-16 can be observed for both compounds. In the range of the quaternary aromatic carbon atoms, position C-2 (compound **2a**) as well as positions C-2 and C-8 (compound **2c**) show a splitting of the signals. The 13C signals of the triazine rings also show a splitting of the ^{13}C signals into different peaks for all three compounds.

Since all TADF molecules have a C_2 axis, the above mentioned changes indicate a reduction of symmetry in the solid state by the molecular packing of the TADF molecules. A detailed description follows later in this chapter with the help of correlation spectra.
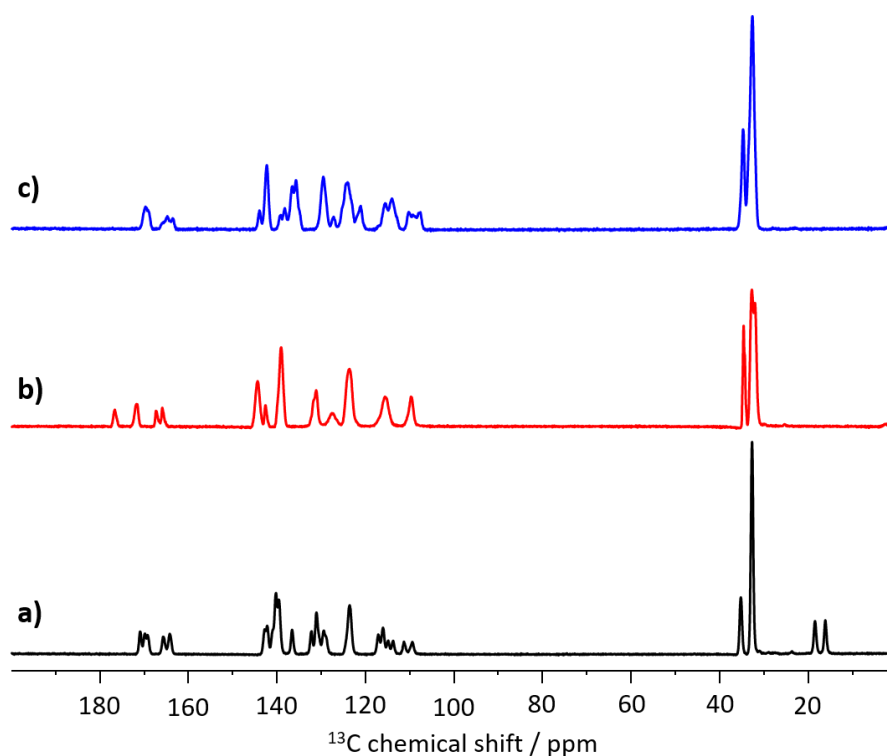
Figure 37 ^{13}C CP MAS spectra for compound **2a** (a), **2b** (b) and **2c** (c), measured at a field of 700 MHz and a rotation frequency of 25 kHz. The crosspolarization time was 3 ms.

The ^{19}F MAS NMR spectra of the three TADF molecules studied are characterized by a different number of signals , as shown in Figure 38. The spectrum of compound **2a** is characterized by two signals with a chemical shift of -102.6 and -107.3 ppm, where the high field shifted signal has a higher linewidth (615 Hz) than the low field shifted one (416 Hz). The spectrum of compound **2b** shows only one broad, featureless signal at -106.4 ppm with an asymmetric line shape and a width of 1212 Hz. Five signals can be observed in the spectrum of compound **2c**. These signals extend over a spectral range from -100.8 to -107.4 ppm. The determined chemical shifts are summarized in table Table 8.

Table 8 ^{19}F chemical shift values for the TADF compounds **2a**-**2c**. Measurements were performed at a field of 500 MHz and a rotation frequency of 25 kHz.

2a		2b		2c	
Position	CS / ppm	Position	CS / ppm	Position	CS / ppm
F-1	-102.6	F-1	-106.4	F-1	-100.6
F-2	-107.3			F-2	-103.0
				F-3	-105.2
				F-4	-106.3
				F-5	-107.3

The ^{1}H MAS spectra of compounds **2a**-**2c** are shown in Figure 38 (a-c). Again, ^{1}H-^{13}C HETCOR spectra with a CP time of 0.1 ms were used to identify the direct correlations. Compound **2a** shows an aromatic pattern with two signals resonating at 8.3 (H-15) and 6.0 ppm (H-1, H-4). Both signals show a shoulder with a high field shift at chemical shift values of around 7.60 and 5.30 ppm (H-16, H-6). In addition, the

spectrum shows a signal for the aliphatic protons resonating at a chemical shift of 1.2 ppm. The ^{1}H MAS spectrum of compound **2b** shows four signals in the aromatic region of the spectrum. The signal shifted furthest to low field with a chemical shift value of 7.9 ppm exhibits the highest intensity. According to the assignment of the CP experiments this signal arises from a superposition of the protons H-7, H-9, H-15 and H-16. At 6.5 ppm, the ^{1}H spectrum shows a broad signal with a low-field shifted shoulder. These signals are assigned to the protons H-3 and H-6. Furthermore, two signals with chemical shifts of 5.6 and 5.2 ppm (H-1, H-4) can be observed. The aliphatic 1H signal for compound **2b** has a chemical shift value of 0.6 ppm. Compound **2c** shows three signals for the aromatic protons in the ^{1}H MAS spectrum. The chemical shift values of these signals was determined to be 7.4 (H-3, H-16), 6.3 (H-1) and 5.9 ppm (H-9). The signal with the lowest chemical shift value is significantly broader than the other two aromatic signals, superimposing with the signal resonating at 6.3 ppm. The aliphatic signal at 1.4 ppm has a broader line width than the aliphatic signal of compounds **2a** and **2b** with a value of 607 Hz.
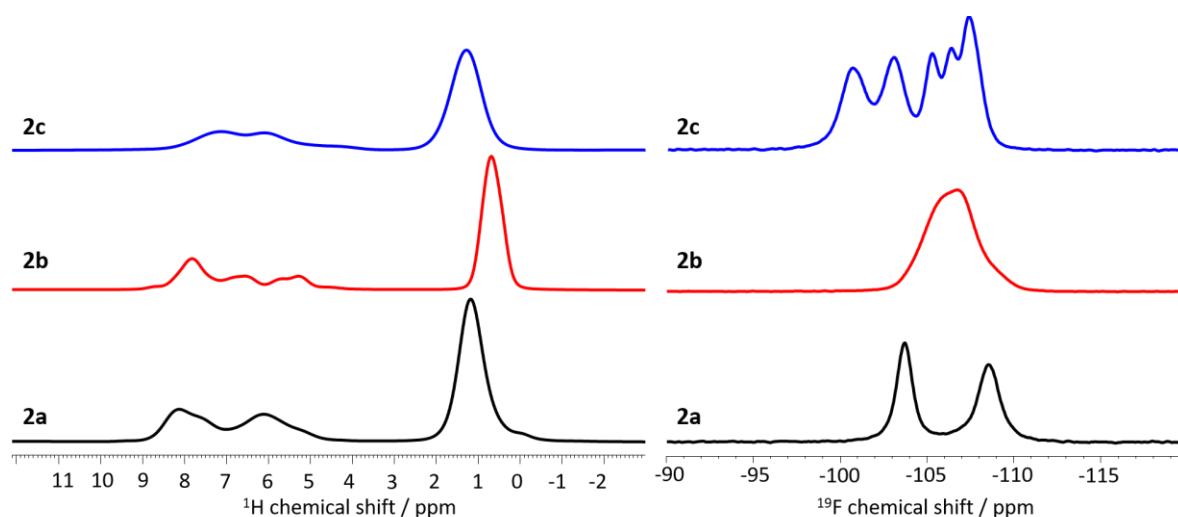
Figure 38 ^{1}H MAS spectra of compund **2a, 2b** and **2c** measured at a field of 700 MHz and a rotation frequency of 25 kHz. [19]F MAS spectra of the compounds **2a**, **2b** and **2c** measured at a field of 500 MHz and a rotation frequency of 25 kHz.

All determined ^{1}H chemical shift values with their respective assignment are listed in Table 9. The values determined in this way will be used in the following chapter to ensure a better assignment of the correlation spectra.

Table 9 ^{1}H chemical shift assignment of compounds **2a**-**2c** after vacuum sublimation.

2a		2b		2c	
Position	CS / ppm	Position	CS / ppm	Position	CS / ppm
Al	1.2	Al	0.6	Al	1.4
H-1, H-4	6.0	H-3, H-6	6.1	H-16	4.5
H-6	5.3	H-16	8.0	H-3	7.5
H-16	7.6	H-1	5.2	H-1	6.4
H-15, H-9	8.3	H-7, H-9, H-15	8.2	H-9	5.9
		H-4	5.6	H-15	7.6

5.4.2 Homo- and heteronuclear correlation spectra

To obtain information about the local structure in the TADF compounds, both homo- and heteronuclear correlation spectra of compounds **2a**-**2c** were measured, which will be discussed below. The methods that were used are DQ-SQ correlation (BaBa), homonuclear correlation (NOESY) and heteronuclear correlation experiments (HETCOR). The NOESY spectrum was recorded to identify correlations, which can not be detected by DQ-SQ experiments, due to a high molecular mobility.

First, the correlation spectra recorded for compound **2a** will be discussed. In Figure *39* the ^{1}H-^{13}C HETCOR spectrum of compound **2a** is shown. Hardly surprising, the aliphatic carbon atoms show correlations with the aliphatic protons. In addition, correlations with the aromatic proton signals can be observed, with the exception of the signal at a chemical shift of 18.5 ppm.
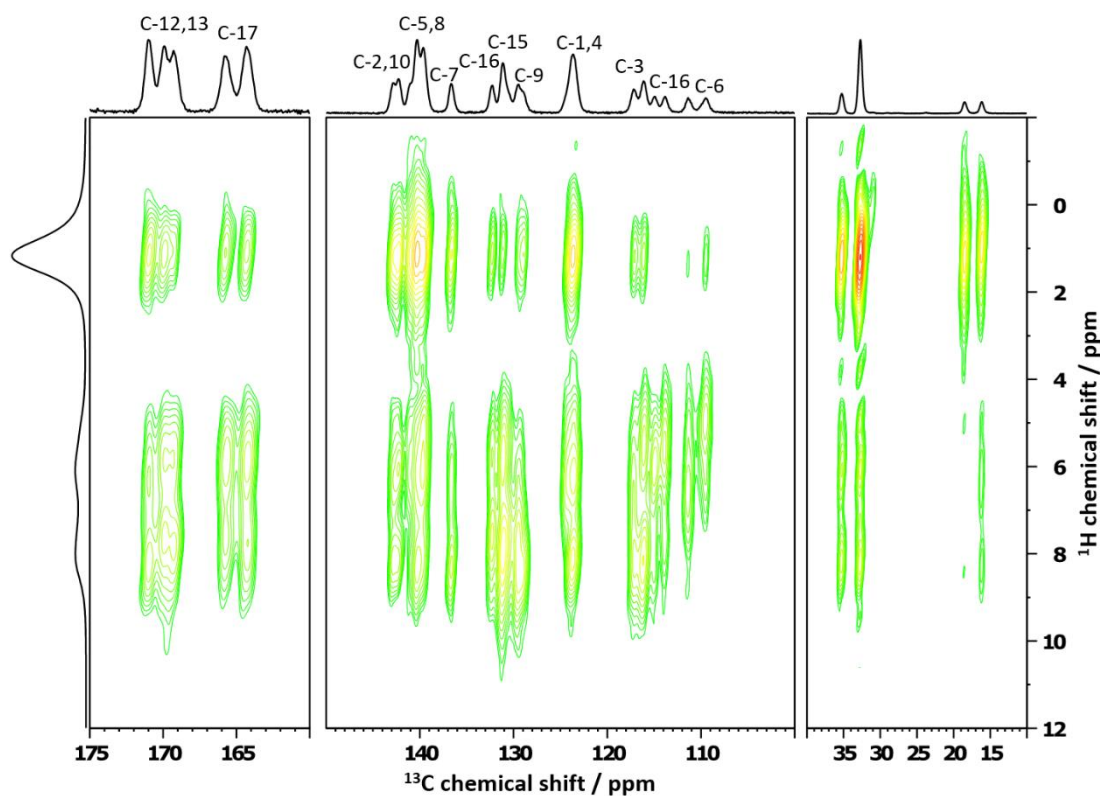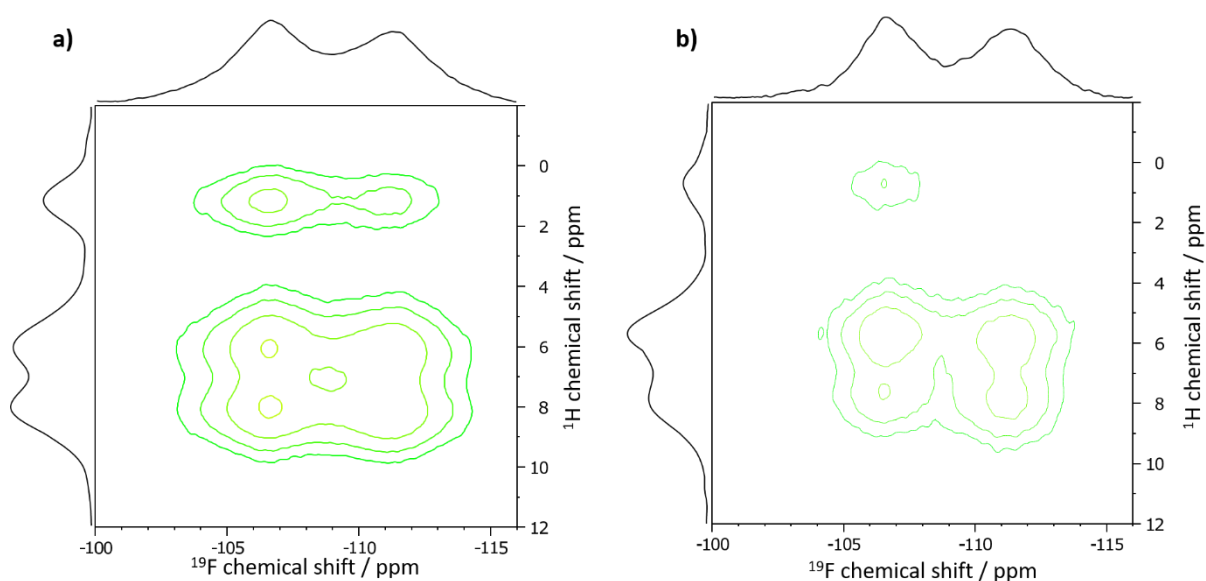

Figure 39 ^{1}H-^{13}C HETCOR spectrum of compound **2a** measured at a field of 700 MHz, a rotation frequency of 25 kHz and with a crosspolarization time of 3 ms. The spectrum is separated into three parts, one showing the triazin spectral range, another the rest of the aromatic protons and the third showing the aliphatic region.

Looking at the aromatic region in the carbon dimension, it can be seen that all carbon atoms, with the exception of two, are located in close proximity of the aliphatic protons. However, the correlations between aliphatic protons and the carbon atom C-6 (split into 109.4 and 111.4 ppm) are only weak. The signals with a chemical shift of 113.9 and 115.0 ppm deviate from the values determined by solution NMR. They show no interaction with the aliphatic proton signals. The signal with a chemical

shift of 113.9 ppm shows a correlation with the proton signal at a chemical shift of 5.3 ppm corresponding to H-16. This in fact means, that the signal experiences a change in the chemical shift by 2.1 ppm caused by changes in the local environment relative to the value which was determined for the molecules in solution. The carbon atoms with chemical shifts resonating at 116.1, 131.2 and 132.3 ppm are also in spatial proximity to this proton signal, which is hardly surprising, since all of those signals belong to carbon species located in the fluorinated phenyl ring. The resonances at 131.2 and 132.3 ppm are another indication for different local environments of the fluorinated phenyl rings, which causes a deviation compared to solution NMR data. It can be assumed that the signal at 116.1 ppm which originates from a fluorinated phenyl ring that is not involved in an interaction with another aromatic system. Therefore, the chemical shift is almost identical to that determined in solution. The second signal at 113.9 ppm, on the other hand, indicates that the second fluorinated phenyl ring has probably a face-to-face stacking geometry with another aromatic ring. Such parallel stacking is most likely to lead to a change in the chemical shift towards high field. The ^{13}C signal at a chemical shift of 115.0 ppm shows a correlation with the aromatic proton signal at 6.0 ppm. Correlations to the same proton signal were found for the carbon chemical shifts of 117.2, 123.6, 139.7, 142.3, and 142.8 ppm. The signal with a chemical shift of 117.2 ppm can be assigned to the carbon atom C-3 (see Table 7). The ^{13}C signal with a chemical shift of 115.0 ppm belongs to the same carbon atom, C-3, but is in a different chemical environment than the signal at 117.2 ppm. Relative to the solution experiments, the signals are shifted by about 1 ppm, both into high-field and low-field. The carbon nuclei C-1, C-2, C-4 and C-5 are located in close proximity to the aromatic proton signal at a chemical shift of 8.4 ppm (H-9). Due to the special separation of proton H-9 and the above-mentioned carbon atoms, the observed correlation arises most likely from an interaction of neighbouring molecules. All carbon atoms on the central phenyl ring (C7-C10) show an interaction with the proton signal resonating at a chemical shift of 8.1 ppm. In addition, C-7, C-8, and C-10 are located close to a proton with a chemical shift of 6.0 ppm. For C-7 and C-8 such an interaction can be expected even in the isolated molecules. C-10 on the other hand is located too far away from the carbazole protons H-1 and H-3 to result in an intramolecular correlation. Here it is again more likely, that the observed cross-peaks result from interaction between neighbouring molecules. The ^{13}C signal of the fluorinated carbon atom C-17 shows a splitting into two signals with resonating at a chemical shift of 164.3 and 165.8 ppm, the former showing a slightly stronger correlation to the aliphatic protons. In addition, C-17 was found to be in spatial proximity to the aromatic protons at 6.0 ppm (H-1 and H-3) and 8.3 ppm (H-15), again with a stronger interaction of the signal at 164.3 ppm. C-12, which is located in the triazine ring, shows only one signal, while the carbon atoms C-13, to which the fluorinated phenyl rings are attached, are split again into two signals with values of 169.3 and 170.0 ppm. The signal with the larger high-field shift shows only a very weak spatial interaction with the aliphatic protons. The correlations with the

aromatic protons at 6.0 and 8.3 ppm are equally strong for both resonances, again indicating an interaction between neighbouring molecules, since the intramolecular distance between interacting nuclear pairs is clearly too large for an NMR spectroscopic observation.

The ^{1}H-^{1}H DQ-SQ correlation spectrum is shown in *Figure 40*. As expected, the aliphatic signals show a strong self-correlation. The aliphatic signals show cross-peaks to both aromatic signals at 7.1 and 9.3 ppm in the double quantum dimension. These interactions are arising from the spatial proximity of the *tert*-butyl protons with the aromatic protons H-1 and H-4 (intramolecular) as well as from the interaction with the proton in the central phenyl ring H-9 (intermolecular). Another close proximity, which is likely to be intermolecular, was found between the protons H-1, H-4 and H-16. Additionally, H-1 and H-4 are also showing a crosspeak by the correlation with the signal of H-15, resonating in the double quantum dimension at a chemical shift value of 14.3 ppm.
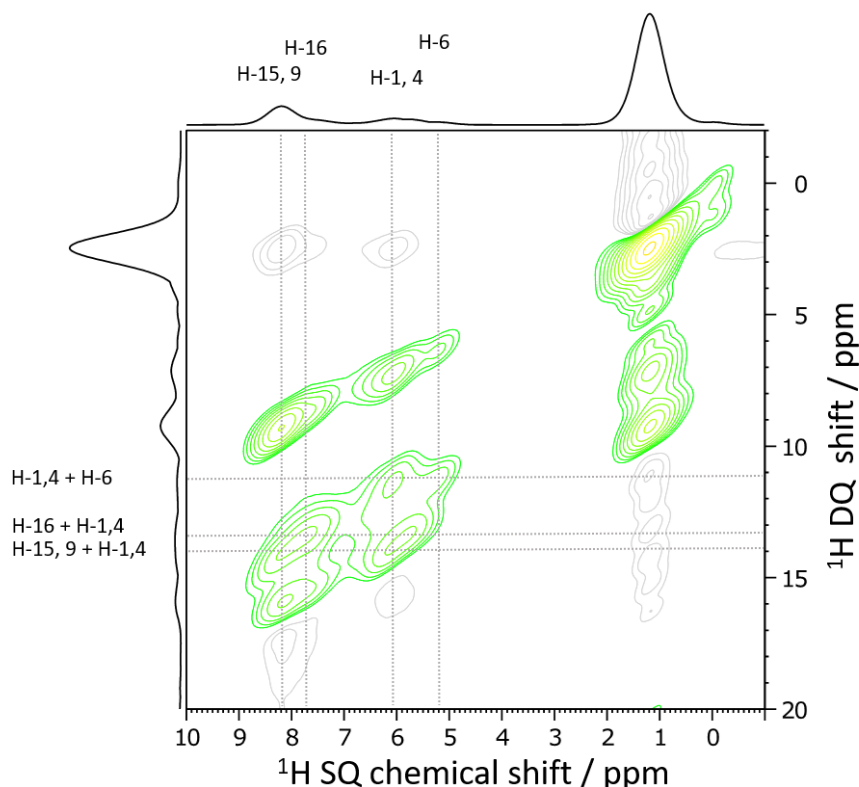
Figure 40 ^{1}H-^{1}H BaBa spectrum of compound **2a** measured at a field of 850 MHz, a MAS spinning frequency of 50 kHz and a recoupling time of 160 µs.

The two-dimensional ^{19}F-^{19}F BaBa spectrum of compound **2a** (Figure 41) shows two strong cross-peaks for each of the two fluorine signals, resonating at a double quantum chemical shift of -210.8 ppm. In addition, two weak self-peaks are detected for each of the fluorine atom. These self-peaks are way less pronounced than the cross-peaks, indicating that the distance between molecules with the same local environment is further than between two molecules with different local environments.
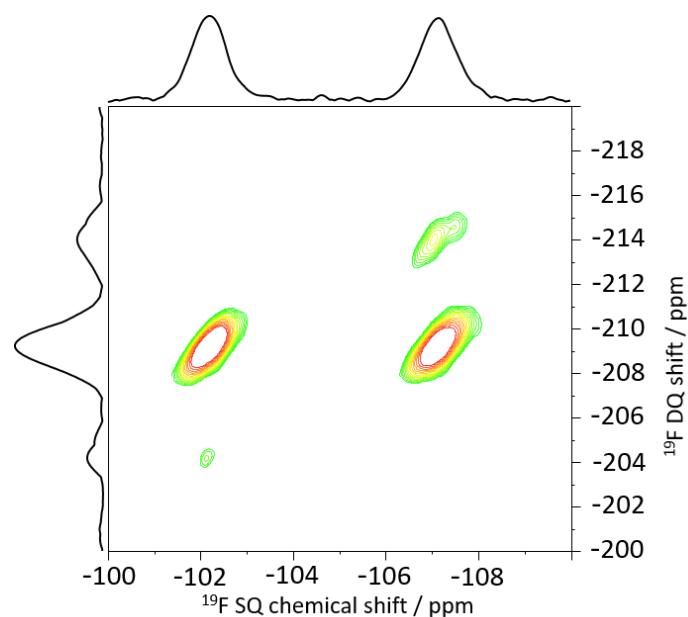
Figure 41 ¹⁹F-¹⁹F BaBa spectrum of compound **2a** measured at a field of 700 MHz, a MAS spinning frequency of 50 kHz and a recoupling time of 160 µs.

Next, the heteronuclear ¹H-¹⁹F HETCOR spectra of compound **2a**, shown in Figure 42, is considered. It can be seen that in the case of a long CP time of 3 ms, both ¹⁹F signals show correlations with both the aliphatic and aromatic signals. However, due to the respective proton signal intensity, the selectivity of the polarization transfer is lost. This results in a low amount of information content. While the correlations between ¹⁹F and the aromatic protons persist when the CP time is reduced to 0.3 ms, the correlations between fluorine and the protons of the methyl groups decrease. The correlation between the fluorine atom with a chemical shift of -107.3 ppm and the aliphatic protons disappears completely, , which leads to the assumption that the two named sites are not located close to each other.

Figure 42 ¹H-¹⁹F HETCOR spectrum of compound **2a** measured at a field of 500 MHz, a spinning frequency of 25 kHz and a crosspolarization time of 3 ms (a) and 0.3 ms (b).
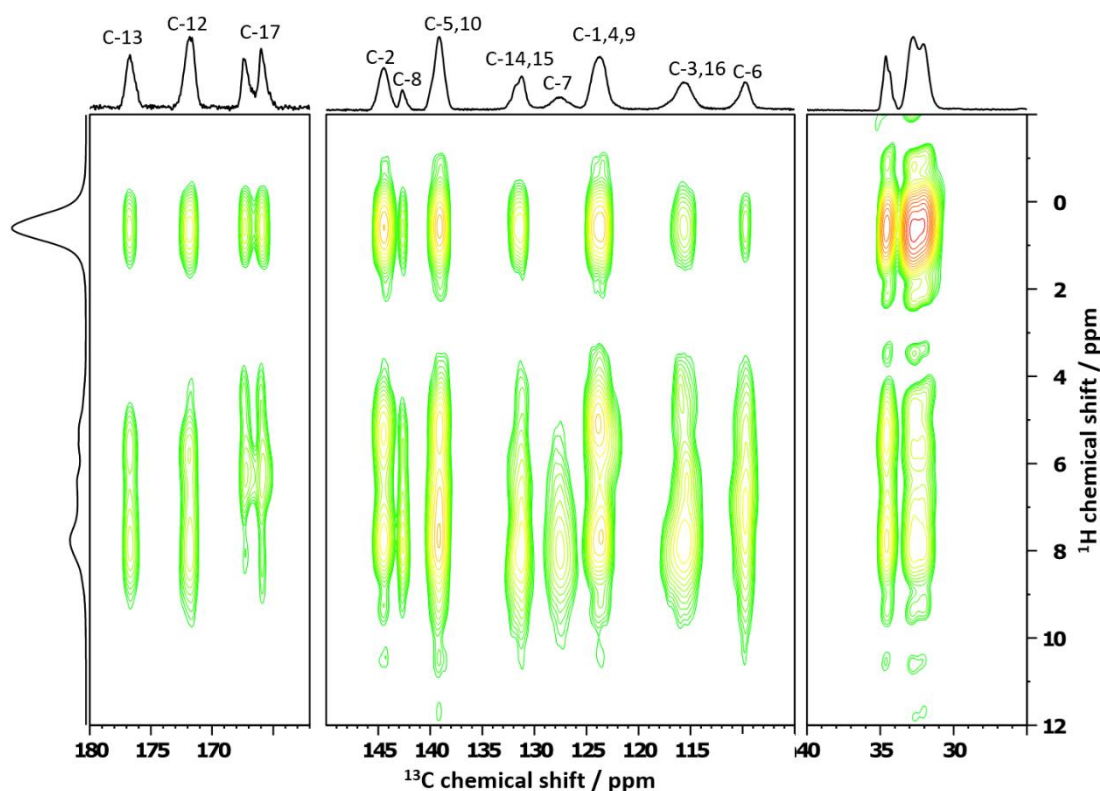
*Figure 43 ^{1}H-^{13}C HETCOR spectrum of compound **2b**, measured at a field of 700 MHz and a spinning frequency of 25 kHz. The crosspolarization time was 3 ms.*

The structure elucidation of compound **2b** follows the same scheme as it was done for compound **2a** above. First, the ^{1}H-^{13}C HETCOR spectrum is considered. Due to absence of signal splitting in the vacuum sublimated compound **2b**, the interpretation of this correlation spectrum is relatively straightforward. The aliphatic carbon atoms were found to be in close proximity to all proton species present in the molecule, thus resulting in strong correlations with the aliphatic and aromatic protons. Only one of the carbon atoms, C-9, does not show any interaction with the aliphatic protons. Although this particular position was found to be not in a close proximity with the aromatic protons H-1 and H-3. Only one clear correlation between C-9 and H-9 was detected. However, it can't be entirely excluded, that C-9 does interact with H-7 and H-15, since the proton signal at 8.0 ppm is a superposition of three species (see Table 9). The carbon atom C-6 is also showing only one correlation with its directly attached proton H-6. C-15 and C-16 are also showing cross-peaks with the protons of their direct bond partner. The quarternary carbon atoms C-10, C-8 and C-2, are showing less obvious correlations with different proton species. C-10 can be considered to be located in spatial proximity to the carbazol protons H-1 and H-3 and to the protons merged together in the superimposed signal (H-7, H-9 and H-15). C-2 shows the exact same cross-peak pattern like C-10, even being located far away from C-10 by only considering the two dimensional structure of the molecule. The correlation pattern for C-8 on the other hand is slightly different. While no interactions between this carbon atom and the carbazole

protons H-1 and H-3 were found, a clear spatial proximity between H-6 and again the protons in the superimposed signal is present. C-17, which is the signal corresponding to the carbon atom with fluorine as a direct bond partner, shows interestingly a strong interaction with H-6. Weak correlations between C-17 and H-1 and H-3 were also found. The spatial proximity of H-16 results in an interaction with C-16, which is less surprising than the once mentioned before. Lastly, the protons which are located close to the triazine rings are considered. Here, correlations between the protons of the superimposed signal and with the proton H-6 are found. The observation that were made in this correlation spectrum are pointing towards a solid-state structure in which the molecules of **2b** are aligned on top of each other displaced by a degree of 180°.

The ^{19}F-^{19}F BaBa spectrum of compound **2b** shows only a self-correlation of the broad signal, which has no special spectral features and is not useful to gain structural information about this particular TADF molecule in the solid state.
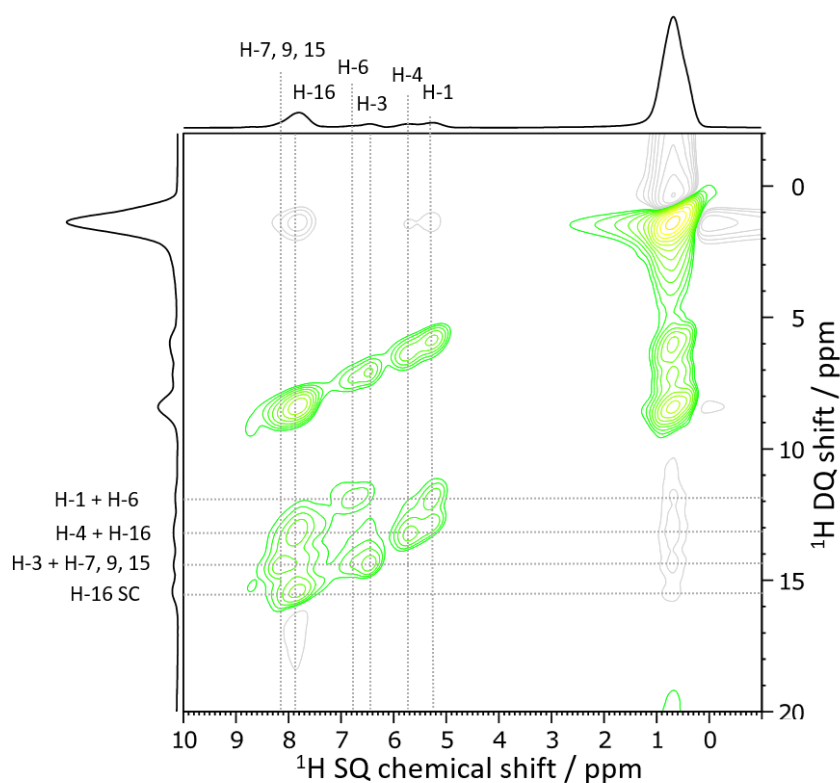
Figure 44 ^1H-^1H DQ-SQ correlation spectrum of compound **2b** measured at a field of 850 MHz, a MAS spinning frequency of 50 kHz and a BaBa-xy16 recoupling time of 160 µs.

The ^1H-^1H BaBa spectrum of compound **2b**, on the other hand, reveals the correlations between the respective protons. Again, a very obvious self-peak between the protons in the *tert*-butyl groups was detected. On top of that, the aliphatic signal interacts with all of the aromatic signals found in the proton spectrum of compound **2b**. H-1 and H-6 are in close intramolecular proximity resulting in a

double quantum signal resonating at 11.7 ppm. H-1 and H-3 are also in spatial proximity to the protons with a chemical shift of 8.0 ppm. H-6 forms a correlation with the proton signal H-16, underlining the statement about the molecular arrangement that was made on the discussion of the ^{1}H-^{13}C HETCOR spectrum. Lastly, the signal at 8.2 ppm (superposition of H-7, H-9 and H-15) shows a self-correlation. It is likely, that this self-correlation results from the close spatial proximity of the position H-9, if at least two of the molecules are stacked on top of each other, rotated by 180°.

The ^{1}H-^{19}F HETCOR spectra of compound **2b** are shown in Figure 45. As described for compound **2a**, the HETCOR spectra were recorded with variable CP times of 1 and 0.1 ms. The spectrum with the longer CP time shows correlations of the ^{19}F signal with the aliphatic proton signals and the aromatic proton signals at 8.0, 6.1 and 4.9 ppm. Reducing the CP time to 0.1 ms leads to a strong reduction of the signal intensity describing the correlation between the ^{19}F signal and the signals at 8.0 and 4.9 ppm, while the other two correlations (aliphatic and 6.1) are preserved. Such a strong interaction between H-16 and the ^{19}F nucleus of the fluorinated phenyl rings underlines the suggestions made about the solid-state arrangement of compound **2b** furthermore.
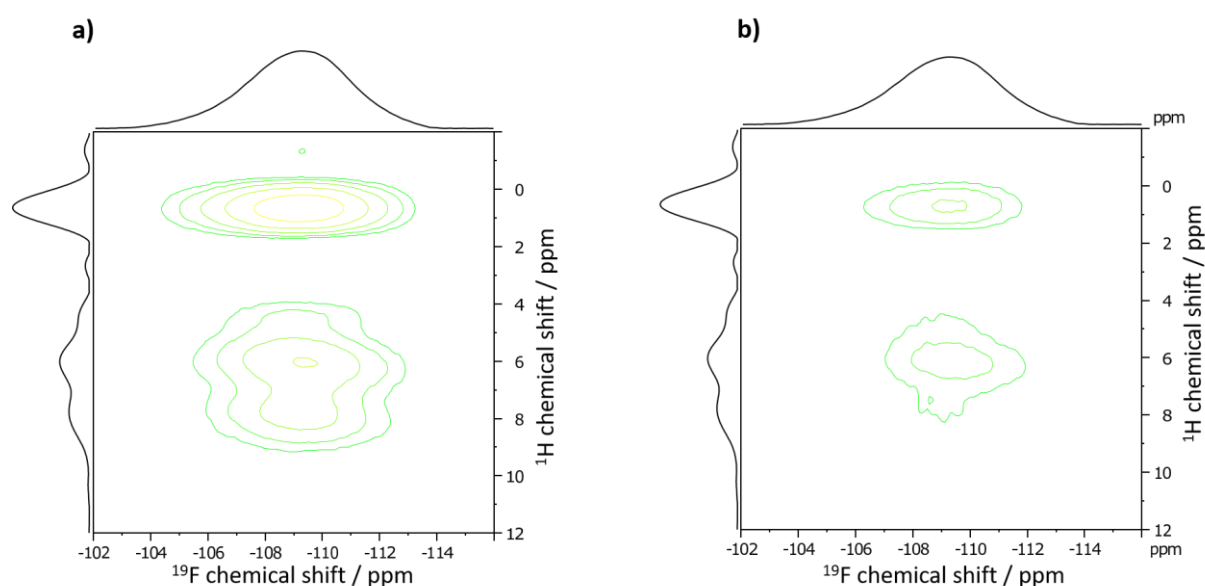
Figure 45 ^{1}H-^{19}F HETCOR spectrum of compound **2b** measured at a field of 500 MHz, a spinning frequency of 25 kHz and a crosspolarization time of 1 ms (a) and 0.1 ms (b).
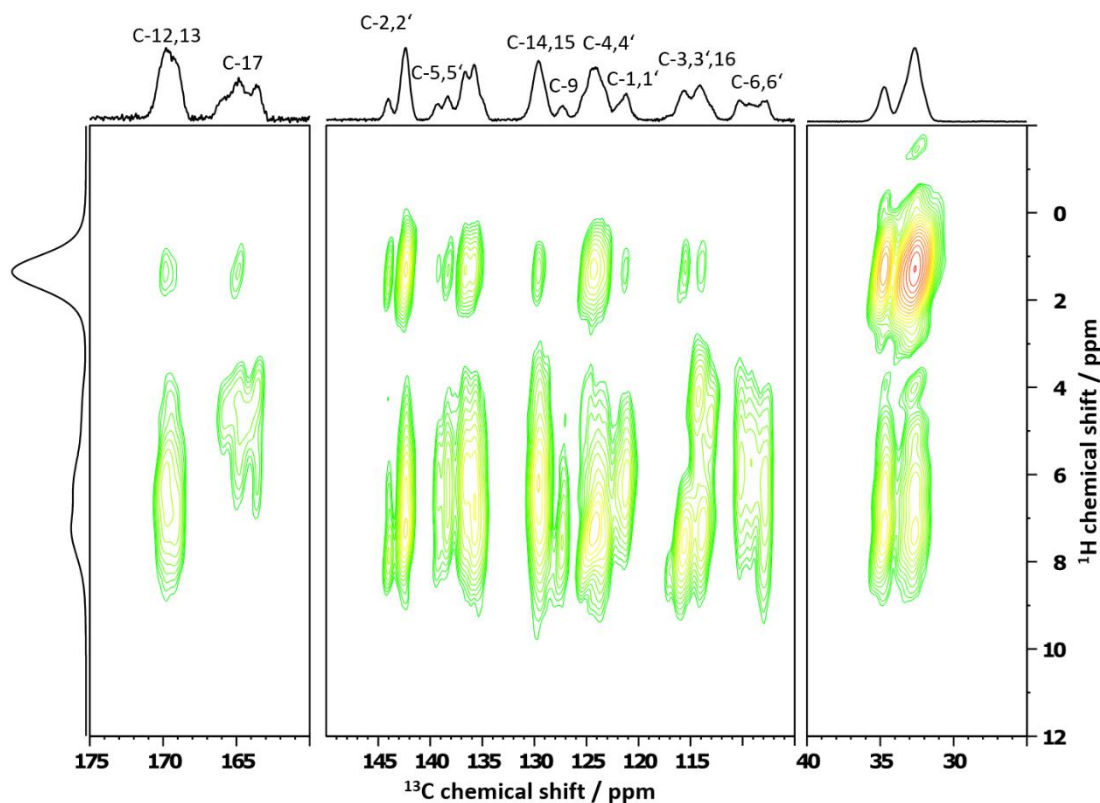
Figure 46 ^{1}H-^{13}C HETCOR spectrum of compound **2c**, measured at a field of 700 MHz and a spinning frequency of 25 kHz. The cross-polarization time was 3 ms.

As described in the single pulse spectra section, compound **2c** is likely to form more than one phase after vacuum sublimation. Therefore, it can already be assumed, that a detailed assignment of the solid-state structure is hard to achieve. A possible way to get insight into detailed structural information is the measurement of ^{19}F-^{13}C HETCOR spectra. However, such an experiment is not easy to carry out without the usage of ^{13}C-enriched samples. The strong CSA of ^{19}F at an intermediate MAS spinning speed of 25 kHz leads to an encoding of both, distance and orientation information and are therefore not suitable for the sample under investigation.[103] Here, faster MAS spinning speeds are required since the impact of the CSA tensor orientation is minimized. Nevertheless, an investigation of the ^{1}H-^{13}C HETCOR spectra was done to identify at least some structural information about a possible molecular arrangement of **2c** in the solid state.

The aliphatic carbon atoms show correlations to the aliphatic protons and all aromatic protons. On the other hand, all aliphatic protons are located in spatial proximity to all aromatic carbon atoms with the exception of C-9 and the signals resonating at 110.1, 109.3 and 107.9 ppm. Due to their chemical shift values, the latter mentioned resonances are arising most likely from the carbon atom C-6 and C-6', whereas at least one is located in different local environments in the solid state. In the case of aromatic proton-carbon interactions, these three signals correlate with the protons H-1 and H-9, which can be

achieved by the intramolecular proximity. The carbon atoms C-3 and C-3' are only showing an interaction with their directly bond protons H-3 (H-3'). C-16, resonating at 115.6 ppm, is interestingly close to the aliphatic protons. The large spatial separation in a single TADF molecule makes this observation most likely to arise from neighbouring molecules. The carbon atoms C-1 and C-1' again show only interactions with their directly bond protons. C-4 and C-4' on the other hand are as expected located close to H-3, which also counts for C-2 and C-2'. The central phenyl-ring carbon atoms C-7, C-8 and C-10 show correlations with H-9 and H-1, which are most likely all intramolecular. C-17 which is directly bond to the fluorine atom showing resonances at 165.8 and 163.5 ppm and correlations to H-16 and H-1, the latter one coming again with high probability from a neighbouring molecule. Lastly, the triazine carbon atoms are close to H-9, H-1 and H-3, whereas the latter two are again located not in the same molecule.

The ^{1}H-^{13}C HETCOR analysis does not provide any detailed insight into the possible formation of different phases after vacuum sublimation. However, homonuclear ^{19}F-^{19}F experiments (DQ-SQ correlation and NOESY), allow to identify the local environment of the fluorine nuclei and thereby making guesses about the number of phases that are formed by **2c** in the solid state.

The ^{19}F-^{19}F DQ-SQ correlation spectrum, which is shown in Figure 47, is characterized by double quantum coherences formed only by the signals at -105.2, -106.3 and -107.3 ppm. The signals at -100.6 and -103.0 ppm vanish upon DQ filtration, and no correlations were found in the DQ-SQ correlation spectrum, indicating that either the nuclei are too far away from each other to result in detectable double quantum coherences or the molecules are mobile and DQ coherences cannot be excited with fluctuating dipolar couplings. NOESY experiments, however, which are based on single quantum transitions (mixing time = 200ms), allow to detect correlations between the fluorine atoms resonating at -100.6 and -103.0 ppm. With these observations, it is possible to state, that compound **2c** forms two phases after vacuum sublimation. While one has a crystalline structure in which four different local environments for the fluorine atoms were found. The second phase is much more mobile and the fluorine nuclei have two different environments. The latter mentioned phase is thereby more likely in an amorphous arrangement, allowing the molecules to have a certain degree of molecular motion due to a less dense packing.
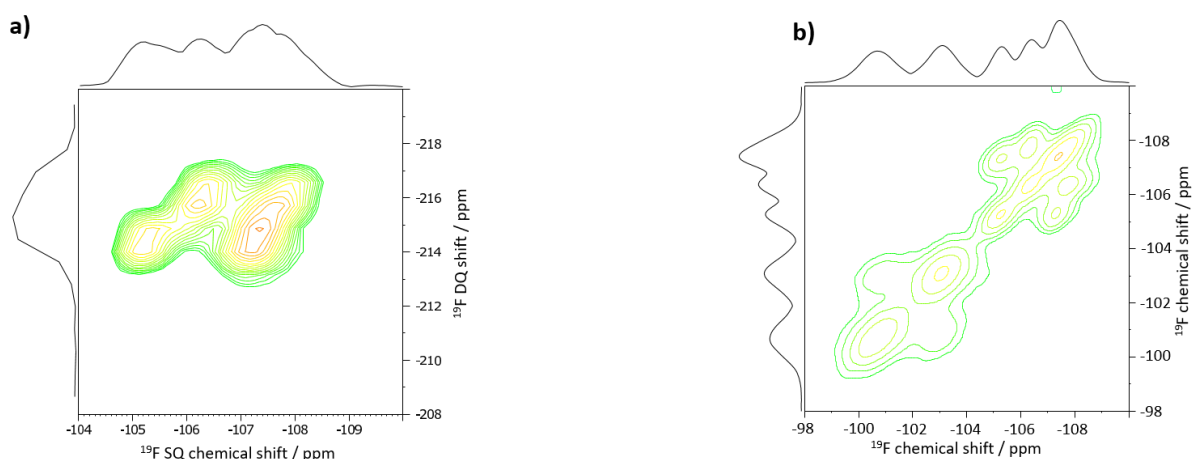
Figure 47 ^{19}F-^{19}F BaBa spectrum of compound **2c** measured at a field of 500 MHz, a MAS spinning frequency of 25 kHz and a recoupling time of 80 μs (a). ^{19}F-^{19}F NOESY spectrum of compound **2c** measured at a field of 500 MHz, a MAS spinning frequency of 25 kHz and a mixing time of 200 ms.

5.4.3 XRD and single crystal NMR

As in the previous chapter, crystal structures for compounds **2a**-**2c** were determined after solvent crystallization. For compounds **2a** and **2b**, the procedure was analogous to **1a**-**1c** and CHCl3/pentane was selected as solvent. However, the volatility of the above mentioned solvent mixture did not lead to crystallization in the case of **2c**. Therefore, in this case, single crystals were grown from EtAc.

Compound **2a** crystallizes in a monoclinic space group P 2_1/c. The unit cell parameters were determined to be a = 26.27 Å, b = 11.47 Å and c = 11.71 Å. The angles between the individual axes are a = 90°, b = 93.1° and c = 90° and a unit cell contains four different molecules. The molecules of compound **2a** are arranged in the unit cell in pairs with an offset of 180°. Thereby, the acceptors of two molecules point to each other. The torsion angle between the fluorinated phenyl rings and the triazine ring of 174° can be regarded as almost planar. The same applies to the angle between the triazine ring and the central phenyl ring (172°). The carbazole unit is almost completely orthogonal to the central phenyl ring, which is stabilized, among other things, by the two methyl groups in the ortho position. In compound **2a**, π-π stacking occurs when one fluorinated phenyl ring overlaps with a triazine ring of a neighbouring molecule. The distance between the planes is 3.5 Å. For compound **2a**, no co-crystallizing solvent molecules were found in the unit cell.
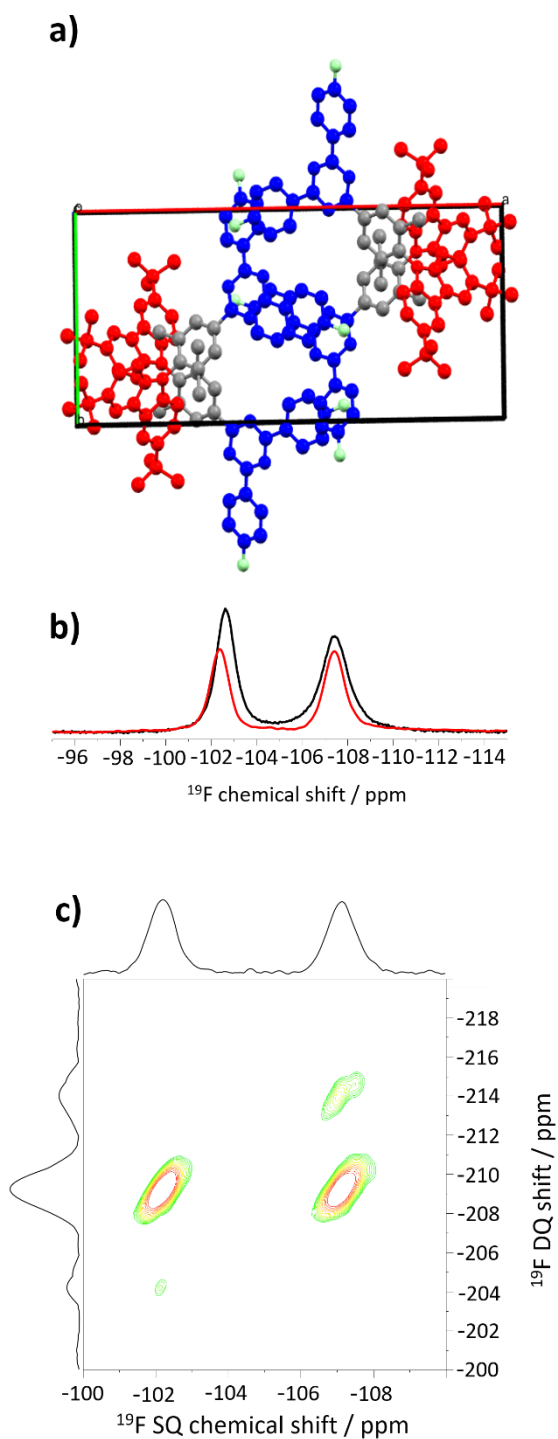
Figure 48 Crystal structure of compound **2a** after crystalization from CHCl$_3$/pentane mixture, viewed along the b-axis of the unit cell (a). ^{19}F MAS spectra of compound **2a** (b) after vacuum sublimation (black) and crystalization from CHCl$_3$/pentane (red).

Compound **2b** crystallizes in the triclinic space group P1, with two molecules per unit cell. The lattice constants were determined to be a=11.9 Å, b=13.0 Å and c=19.5 Å. The angles between the axis of the unit cell are a=94.5°, b=102.6° and c=98.3°. As in compound **2a**, there are always two molecules in a unit cell, which are arranged as pairs with a 180° offset. However, there are also two chloroform

molecules in the centre of the unit cell of compound **2b**. The acceptor unit of the TADF molecule shows a planar structure for the two fluorinated phenyl rings and the triazine ring. The central phenyl ring as well as the acceptor unit show a slight drilling of 25.1°. Although the absence of steric hindrance groups on the central phenyl ring favours a planar arrangement of the carbazole units, an angle of 56.4° was found between these two molecular sites. Even though the presence of the chloroform molecules results in a large distance between the two TADF molecules within a unit cell, the acceptor units of two molecules from adjacent unit cells are 3.5 Å away from each other.
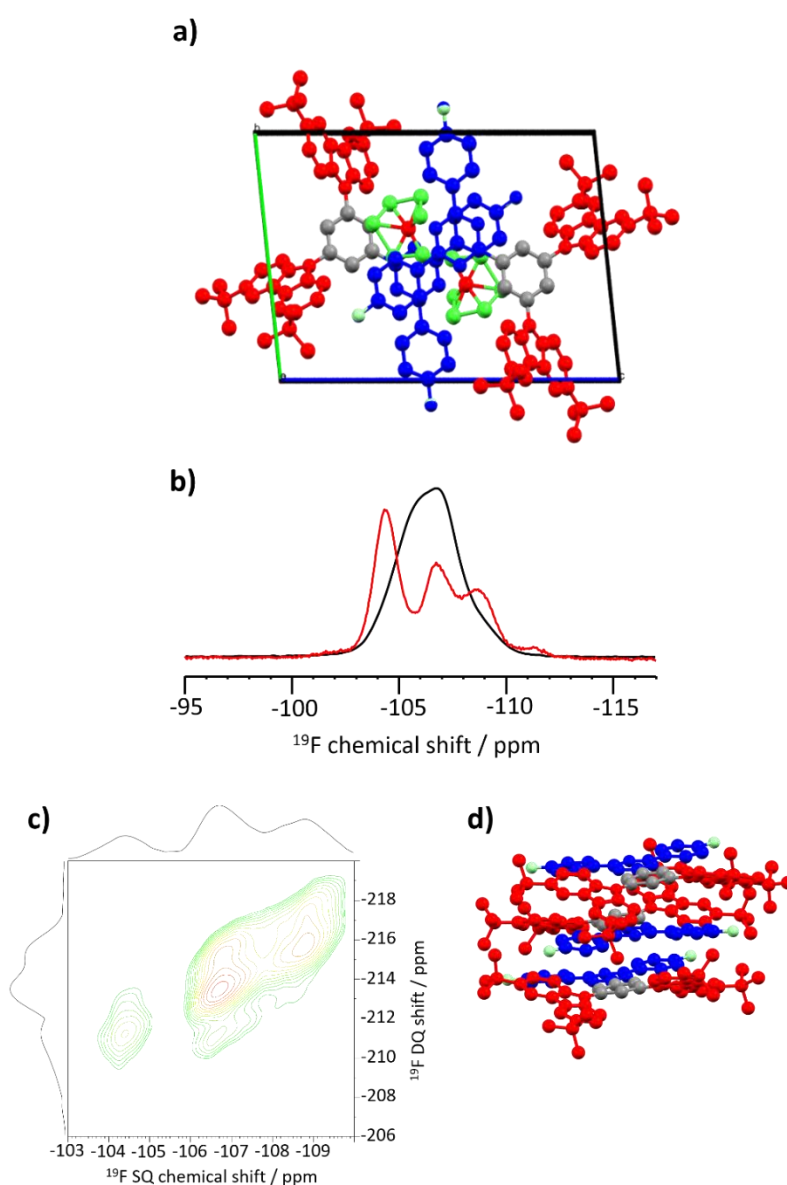
Figure 49 Crystal structure of compound **2b** after crystallization from CHCl$_3$/pentane mixture, viewed along the a-axis of the unit cell (a). ^{19}F MAS spectra of compound **2a** (b) after vacuum sublimation (black) and crystallization from CHCl$_3$/pentane (red). ^{19}F-^{19}F DQ-SQ correlation spectrum of compound **2b** after solvent crystallization measured at a field of 700 MHz, a MAS spinning frequency of 50 kHz and a recoupling time of 160 µs (c). Vacuum optimized structure (MMFF94) for three molecules of **2b** (d).

The presence of the chloroform molecules suggests that the crystal structure of compound **2b** determined by XRD is very different from the structure after vacuum sublimation. This can also be seen from the measured ^{19}F NMR spectra. While only one broad, featureless signal was observed for compound **2b** after vacuum sublimation, the ^{19}F spectrum of the single crystals shows three individual signals. This is most likely due to different fluorine environments in the crystal lattice. Looking at the DQ-SQ correlation (*Figure 44*) and HETCOR spectra (*Figure 45*) measured for the sublimed samples, it can be assumed that the molecules are stacked on top of each other, shifted by 180°. In this case, however, stacking between the acceptor units is not to be expected as for the TADF molecules in the single crystal, but rather a superposition of the carbazole units and the fluorinated phenyl rings.

Compound **2c** also crystallizes in the triclinic space group P1. The lattice constants of the unit cell for this compound are a=17.9 Å, b=20.0 Å and c=23 Å, where the angles between the cell axes are a=85.6°, b=68.4° and c=65.4°. A unit cell contains four TADF molecules and four ethyl acetate solvent molecules. As for compounds **2a** and **2b**, a planar arrangement of the acceptor unit was found. Also, the central phenyl ring and the triazine ring are nearly planar (9.4° twist). The carbazole units do not exhibit complete orthogonality to the central phenyl ring, but are slightly tilted with an angle of 50.9°.
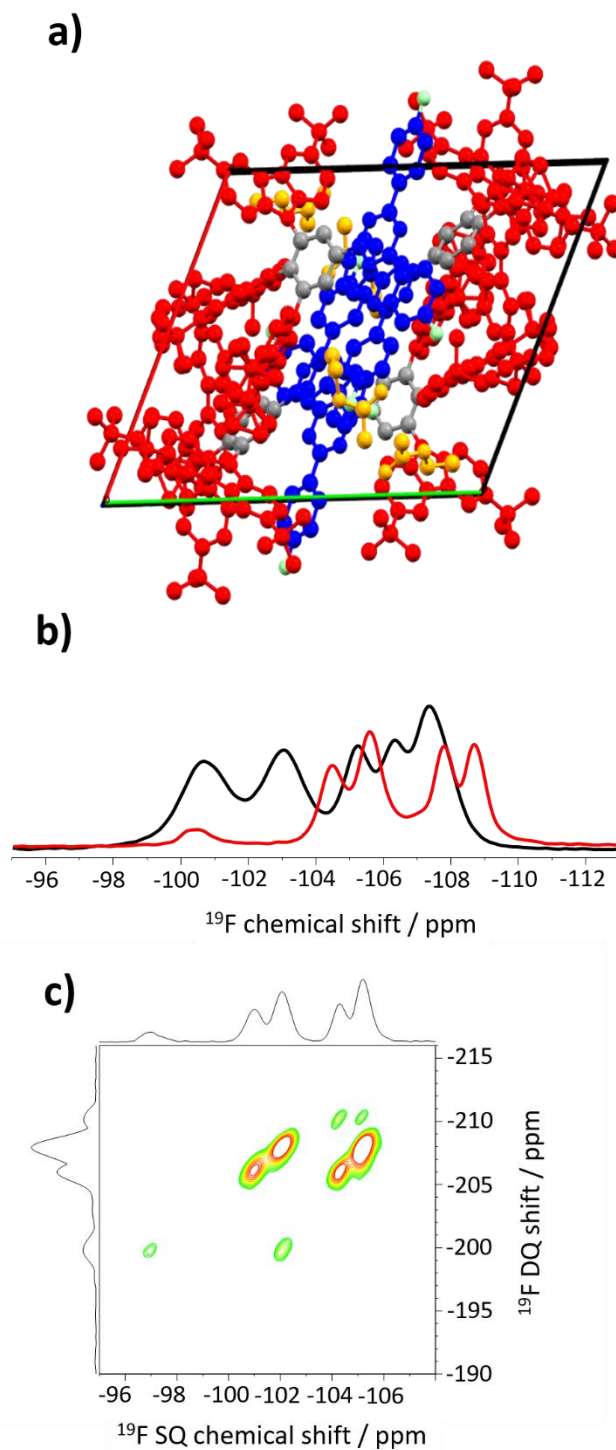
Figure 50 Crystal structure of compound **2c** after crystallization from ethylacetate, viewed along the c-axis of the unit cell (a). [19]F MAS spectra of compound **2c** (b) after vacuum sublimation (black) and crystallization from ethylacetate (red). [19]F-^{19}F DQ-SQ correlation spectrum of compound **2c** after solvent crystallization measured at a field of 700 MHz, a MAS spinning frequency of 50 kHz and a BaBa-xy16 recoupling time of 160 µs (c).

As expected, the crystallization of compound **2c** from a solvent also leads to a different structure compared to that found after vacuum sublimation. The ^{19}F spectrum shows four sharp signals at -104.5, -105.6, -107.8 and -108.7 ppm for the single crystal measurement. In addition, a signal with a lower

intensity can be observed at -100.3 ppm. While the four sharp signals can clearly be assigned to the crystalline phase, the signal resonating at -100.3 ppm can be assumed to be either molecules that did not participate in the crystallization after removal of the solvent or fluorine species located at the interface of the crystallites. Since a correlation, albeit weak, was found between the signals at -100.3 and -105.6 ppm, the latter assumption is the more likely with respect to the interface.

5.4.4 Dynamics

In order to characterize the vacuum sublimated TADF molecules studied also in terms of their dynamics, ^{19}F T1 relaxation times were determined, which are listed in Table 10.

Table 10 ^{19}F T_1 relaxation times of compounds **2a**-**2c** for the respective fluorine resonances. (T_1^* describes the second relaxation value that was obtained due to a biexponential behaviour of the ^{19}F relaxation time).

2a		2b		2c		
^{19}F CS / ppm	T_1 / s	^{19}F CS / ppm	T_1 / s	^{19}F CS / ppm	T_1 / s	T_1^* / s
-102.6	80.8	-106.4	4.3	-101.5	2.5	-
-107.3	57.3			-104.0	2.8	-
				-106.2	1.8	0.5
				-107.3	2.1	0.6
				-108.4	2.0	0.7

First of all, the ^{19}F T_1 relaxation time of compound **2a** is one to two orders of magnitude higher than that of compounds **2b** and **2c**. This indicates a high crystallinity of compound **2a** after vacuum sublimation and is consistent with the results discussed in the previous section. From the similarities observed in the ^{19}F single pulse and ^{19}F-^{19}F DQ-SQ correlation spectra as well as the fact that no solvent molecules are included during solution crystallization, it can be concluded that compound **2a** shows a very high similarity in structure after crystallization from solution and after vacuum sublimation.

Compounds **2b** and **2c**, on the other hand, exhibit significantly shorter relaxation times. In the case of **2b**, as already discussed, only one signal was found. This signal has a low relaxation time of 4.3 s and indicates an amorphous arrangement of the TADF molecules in the solid. The lack of splitting in ^{19}F and ^{13}C spectra supports this statement.

Compound **2c** is present in two different phases after vacuum sublimation. It would be expected that the phase with the higher mobility has a shorter T_1 relaxation time. However, the opposite is the case. One possible explanation for this could be the arrangement in the crystalline phase. *Tert*-butyl groups, which can be arranged in spatial vicinity of the fluorine atoms, open up a further relaxation pathway via modulation of heteronuclear dipolar couplings due the methyl and the tert-butyl rotation. In the case of this compound a biexponential relaxation behaviour was observed, which is driven by strong

heteronuclear interactions between ^1H-^{19}F pairs in which one species undergoes a dynamic process around a C_3 axis (axis through the centre of the methyl and/or *tert*-butyl groups).[104] Due to the absence of a biexponetial behaviour of the ^{19}F relaxation times in compound **2b**, it is assumed that the fast relaxation is mainly driven by the amorphous morphology of the samples and that the heteronuclear dipolar couplings of the rotating aliphatic groups does not influence the T_1 time.

To further characterize the dynamics in the samples, the dipolar coupling constants were determined using REPT-HDOR spectra. These are listed in Table 11 together with the order parameters and jumping angles calculated from them.

Table 11 Dipolar coupling constants, order parameter and jumping angles for C-H pairs in the compounds **2a-2c**. Different jumping angles for the same heteronuclear dipolar coupling constants result from different orientations of the respective C-H bond relative to the rotation axis of the molecular fragment.

2a				**2b**				**2c**			
Position	D/kHz	S	Θ	Position	D/kHz	S	Θ	Position	D/kHz	S	Θ
C-6	21.5	1	0°	C-6	21.5	1	0°	C-6	21.5	1	0°
"	17.8	0.83	48°	C-16	18.8	0.88	29°	C-6',10	21.5	1	0°
C-16	21.5	1	0°	C-1	19.8	0.92	31°	C-16	21.5	1	0°
"	21.5	1	0°	C-9	21.3	0.99	10°	C-1,1'	17.8	0.83	29°
C-1	18.8	0.88	20°	C-7	16.3	0.76	59°	"	18.4	0.85	22°
C-9	18.5	0.86	40°					"	18.6	0.87	22°
"	18.5	0.86	40°								

It can be seen for all carbon atoms of the three samples, that if there is a reduction in the effective dipolar coupling at all, it is only a minor reduction. Many of the CH sites show a rather rigid arrangement. In compound **2a**, the C-H pair of C-6 has the largest deviation from a rigid dipolar coupling constant at 17.8 kHz. In contrast, the C-H pair with a chemical shift of 107 ppm has a completely rigid coupling constant of 21.5 kHz. This results from two different local environments which slightly influence both the chemical shift and the dynamics of the carbazole rings. A reduction of the dipolar coupling of the C-H pair of C-9 is also observed, which is due to small angle fluctuations of the bond angle between the central phenyl ring and the acceptor unit.

In compound **2b**, this behaviour is even more evident. For the C-H pair of C-7, a dipolar coupling constant of 16.3 kHz was determined, resulting in a rotational fluctuation of 59° on the milli- to microsecond timescale. The calculations are based on the NMR-WEBLAB by Macho et al.[105] Such a dynamic process contributes to the short relaxation time discussed above, but also underlines the mobility of the molecules in an amorphous solid.

Compound **2c** shows a rather rigid behaviour for the fluorinated phenyl rings. The other C-H pairs for which the effective dipolar couplings were determined also show only a rather small reduction in their

value. The rotational fluctuation between the central phenyl ring and the acceptor unit is much smaller compared to compound **2b**.

5.5 Solid state NMR studies of (5-(4,6-di-*para*-fluorophenyl-1,3,5-triazin-2-yl)-phenylene)carbazole derivatives with variable carbazole units.

The molecules used in the last study of the three TADF molecule series are similar to the ones shown in the previous chapter, with the exception of the missing *tert*-butyl groups at the carbazole rings. The lack of aliphatic chains leads to longer T_1 relaxation times which results in long measuring times of the particular samples.
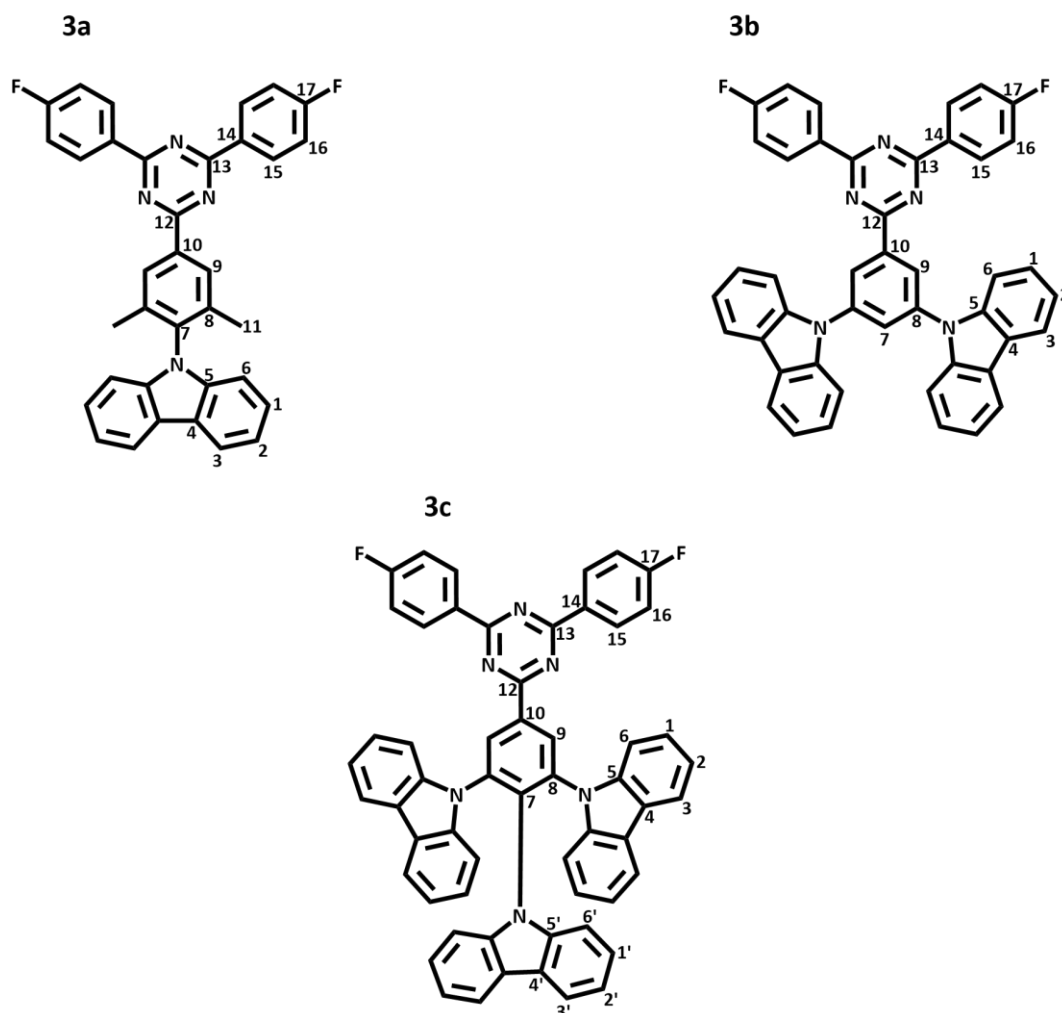
Figure 51 Two dimensional structure of the compounds **3a**-**3c**.

On the other hand, the short T_2 relaxation times result in signal broadening which affects the resolution of the spectra. Especially ^{1}H spectra are likely to not show any spectral features but rather result in one signal with a large linewidth, making one and two dimensional spectra not very suited for structural elucidation. The long T_1 relaxation times as well as the low natural abundance are making ^{13}C

experiments even less useful for identifying the solid state arrangements of the TADF molecules. Therefore, ^{19}F seems the best nucleus to get at least some information about the local order and structure of the compounds **3a**-**3c**. However, ^{13}C and ^{1}H spectra will be shown to visualize the problems mentioned before.

5.5.1 One Dimensional NMR Spectra

The ^{13}C chemical shifts, determined by solution NMR are listed in Table 12. As solvent tetrachloroethane was chosen with exception of compound **3b**. Here, ortho-dichlorbenzene was used and the sample was heated to a temperature of 353 K to achieve better solubility of the sample.

Table 12 ^{13}C chemical shift assignment of the compounds **3a**-**3c**. The data were obtained from solution NMR experiments in TCE at ambient temperature and 700 MHz magnetic field. Spectra given in Appendix 31 ff.

Atom	3a	3b	3c
1	126.4	126.7	125.7
2	119.8	120.7	120.4
3	120.7	120.4	119.9
4	123.1	123.8	123.4
5	140.2	140.9	139.9
6	109.5	109.7	110.0
1'	-	-	124.9
2'	-	-	120.6
3'	-	-	119.3
4'	-	-	123.7
5'	-	-	138.0
6'	-	-	110.2
7	138.8	129.2	138.1
8	138.9	140.5	137.7
9	129.1	126.4	130.2
10	136.2	140.2	135.7
11	18.1	-	-
12	171.4	170.6	171.0
13	170.8	171.6	170.0
14	132.1	132.1	
15	131.7	131.6	131.7
16	115.9	115.9	116.0
17	165.9	165.7	165.9

Figure 52 shows the ^{13}C CP MAS NMR spectra, measured at a field of 850 MHz and a rotation frequency of 25 kHz. The spectrum of compound **3a** splits into three different spectral areas: aliphatic, aromatic and the resonances of the triazine signals. The material **3b**, as well as **3c**, shows not surprisingly only signals for the aromatic region and the triazine rings. As previously mentioned, the resolution of the spectra is poor, mainly due to broad, overlapping signals.
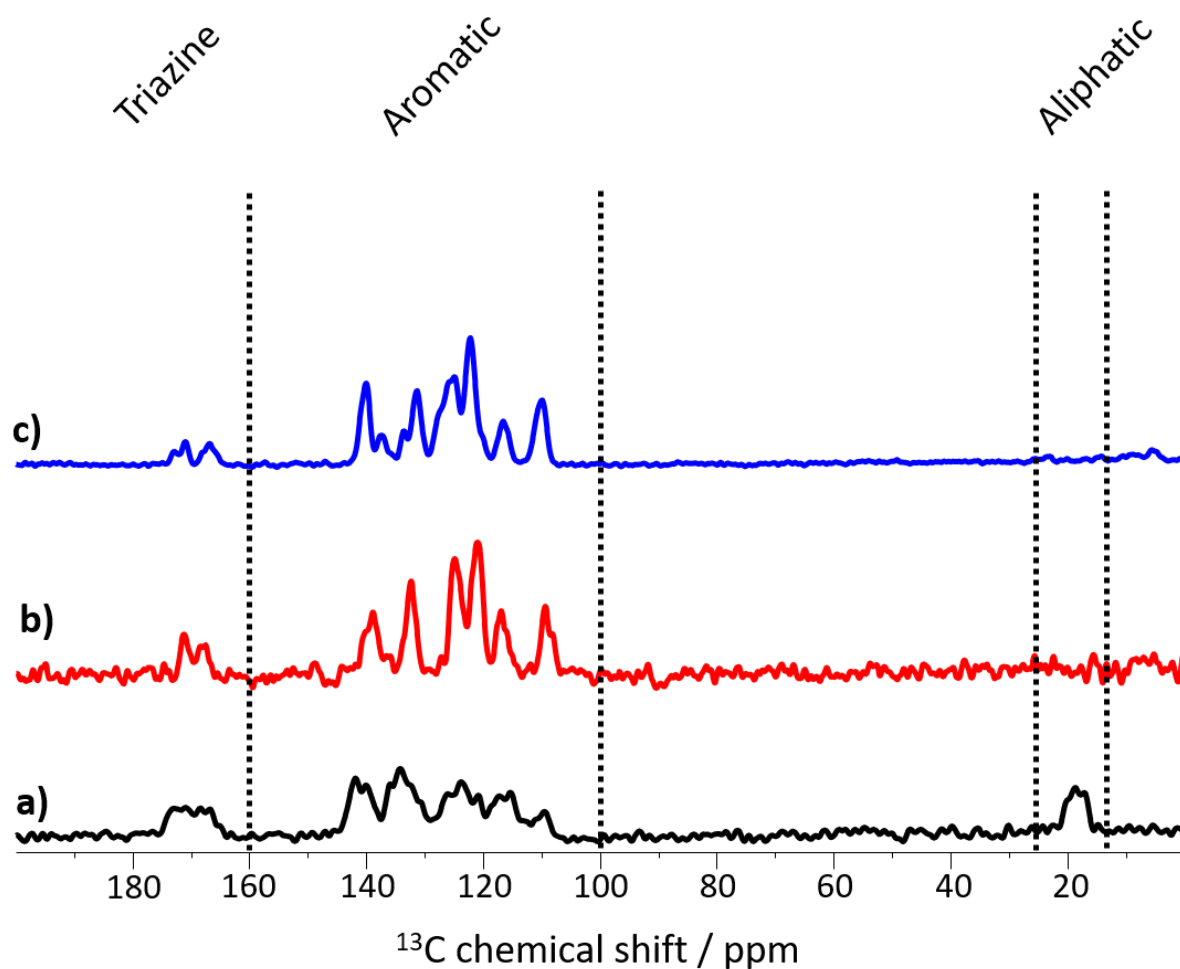
Figure 52 ^{13}C CP MAS spectra for the compounds **3a** (a), **3b** (b) and **3c** (c) measured at a field of 850 MHz, a rotation frequency of 25 kHz and a CP time of 3 ms.

The ^{1}H MAS NMR spectra, shown in Figure 53 a-c, suffer from the same resolution problem as the carbon spectra. Compound **3b** and **3c** show only one broad signal, arising from the superposition of all aromatic protons. The molecules of **3a** on the other hand show a pattern containing one aliphatic signal from the methyl groups and at least two aromatic signals. Due to the better resolution in the case of **3a**, homonuclear correlation experiments are suited to obtain structural information about the sample and will be discussed in the next chapter.
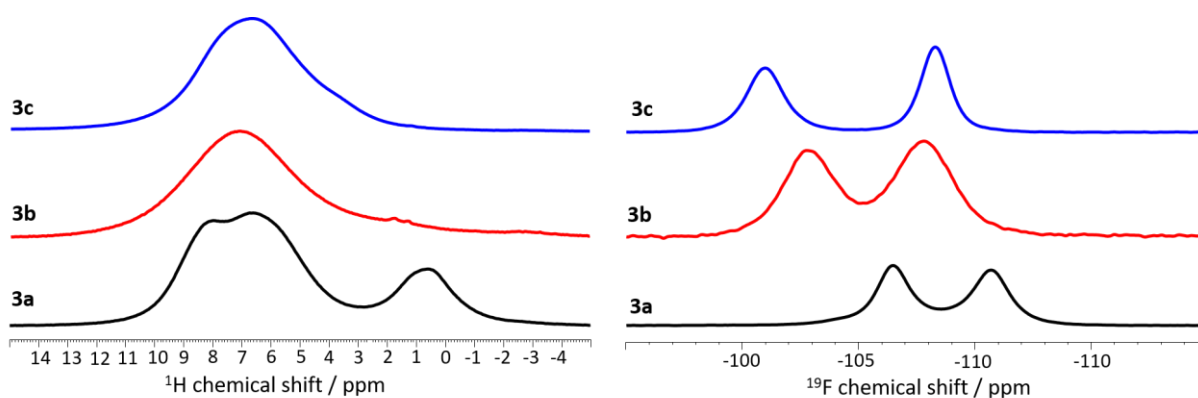
Figure 53 ¹H MAS spectra of **3a**, **3b** and **3c** measured at a field of 700 MHz and a rotation frequency of 25 kHz. ¹⁹F spectra of **3a**, **3b** and **3c** recorded at a field of 500 MHz 1H Larmor frequency and a MAS rotation frequency of 25 kHz.

Figure 53 d-f shows the ¹⁹F MAS spectra of the materials **3a**-**3c**. All compounds show two fluorine signals at different chemical shift values. The signals in compound **3a** resonate at -106.5 and -110.6 ppm, in compound **3b** at -102.8 and -107.7 ppm and in compound **3c** at -101.0 and -108.3 ppm. Another spectral feature that is different for all three materials are the linewidths of the different signals. Especially compound **3b** shows way more broadened lines in comparison to **3a** and **3c**, which is in agreement with the observation about the bad solubility. Here it can be suggested, that this specific material shows a very dense packing with low degrees of freedom when it comes to mobility of different units in the molecules. Compound **3a** and **3c** on the other hand show way less broadened signals with linewidths between 600-800 Hz. In the dynamic section, these observations will be discussed more detailed with the usage of T_1 relaxation times.

5.5.2 Correlation experiments

Since both, ¹H-¹⁹F and ¹H-¹³C HETCOR spectra, were not measured due to slow relaxation and bad proton resolution in case of **3b** and **3c**, this section will only deal with the analysis of ¹H and ¹⁹F BaBa spectra. Figure 54 shows the ¹H-¹H BaBa spectrum of compound **3a** at a field of 850 MHz and a rotation frequency of 50 kHz. The higher field and higher spinning speed (compare **1a-1c** and **2a-2c**) was chosen for better resolution. It can be seen, that the aliphatic proton signal is split into two resonances at 1.3 and 0.6 ppm, with the latter one showing a slightly weaker selfcorrelation. The spectrum also indicates that the aliphatic protons are in spatial proximity to the aromatics. However, those interactions are rather weak compared to the correlations detected for the aromatic protons among each other. Here, the aromatic protons H-15 have a strong self-peak and also a strong interaction with their neighbouring protons H-16. The self-correlation arises most likely from an intermolecular spatial proximity where the fluorinated phenylrings are located close to each other. Besides that H-15 also shows an interaction

with H-9 of the centre phenyl ring. The protons of the carbazole ring on the other hand show no interaction with the fluorinated phenyl rings.
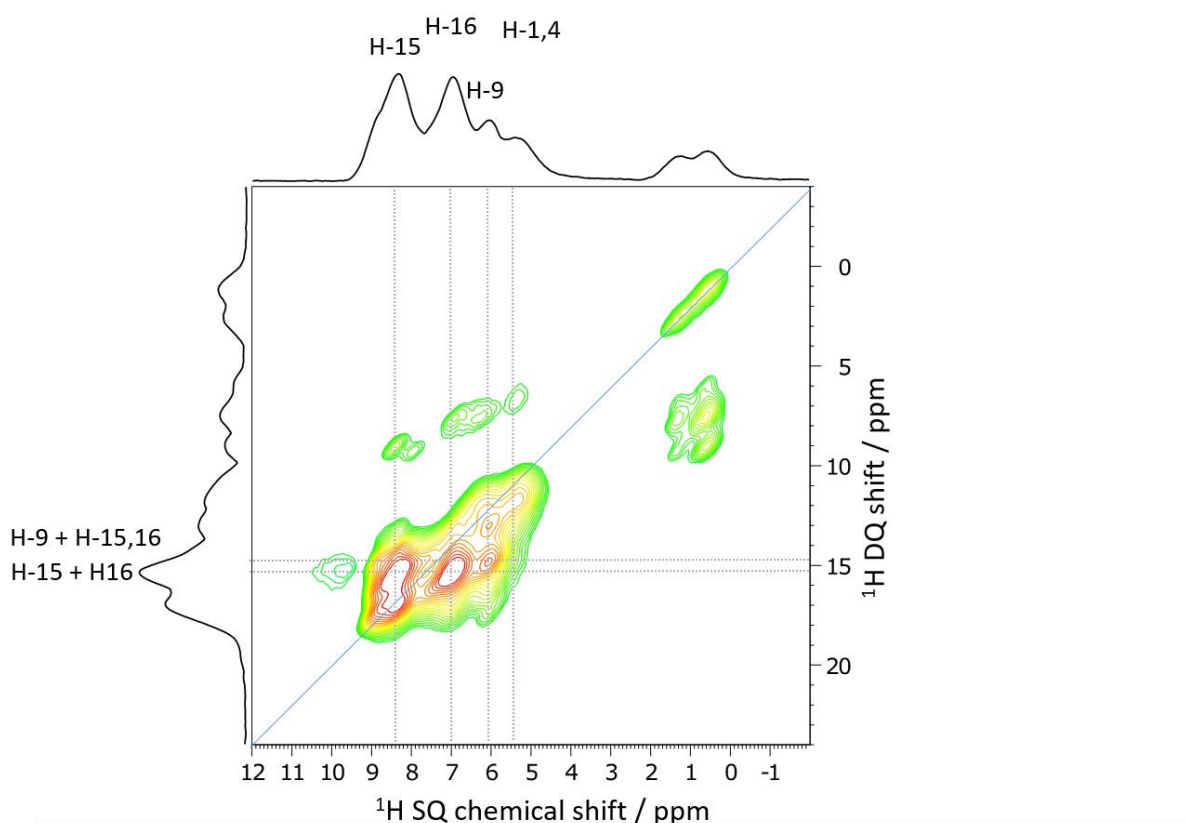
Figure 54 ^{1}H-^{1}H DQ-SQ BaBa correlation spectrum of compound **3a** measured at a field of 850 MHz, a MAS spinning frequency of 50 kHz and a BaBa-xy16 recoupling time of 160 µs.

The ^{19}F-^{19}F DQ-SQ correlation spectrum, Figure 55, displays strong self peaks for both fluorine species in the sample **3a**. Additionally, the distinct ^{19}F site interact with each other but with a larger spatial separation between the fluorine sites with different chemical shift, compared to the distance between those with the same chemical shifts. Combined with the observations made in the ^{1}H-^{1}H DQ-SQ correlation spectrum, two structural arrangements can be considered. In the first one, it is assumed that the molecules are stacked pairwise on top of each other rotated by 180°, similar to compound **2a**. The second possibility is an arrangement, in which the triazine ring acts as the only pi system involved in the stacking with the molecules rotated by 60° degrees. Since the ^{19}F-^{19}F DQ self-correlations for compound **3a** are strong, the latter mentioned molecular arrangement is the more likely. This shall be discussed more detailed in the next paragraph with the usage of the obtained XRD data.
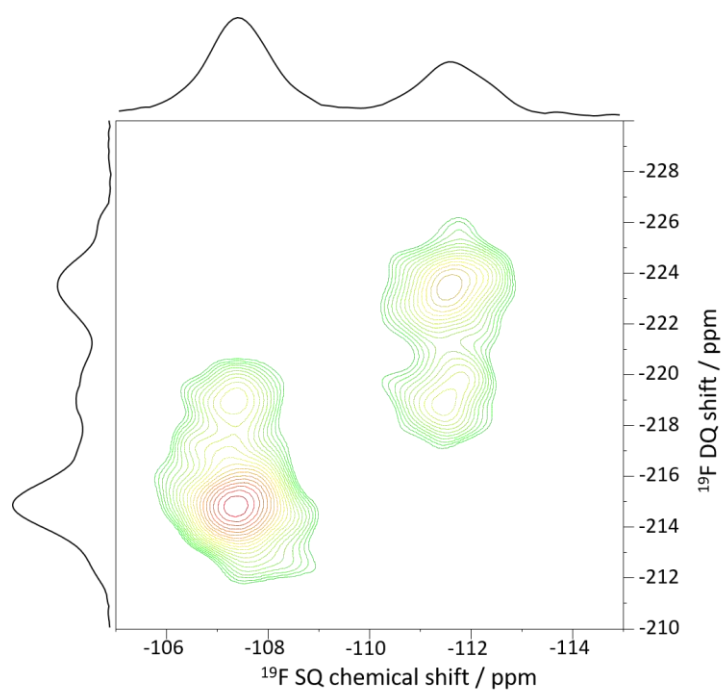
Figure 55 ^{19}F-^{19}F BaBa spectrum of compound **3a** measured at a field of 500 MHz, a MAS spinning frequency of 25 kHz and a recoupling time of 160 µs.

Due to the unfavourable T_1 relaxation times and missing aliphatic groups in **3b**, no ^{19}F-^{19}F DQ-SQ correlation spectrum was only recorded for this compound. The ^{19}F-^{19}F DQ-SQ Baba spectrum of **3c** is shown in Figure 56. This shows a self-correlation for the signal resonating at -108.3 ppm. The second signal at -101.0 ppm lacks the self-correlation. However, both signals show a correlation with each other at a double quantum shift of -208.8 ppm.
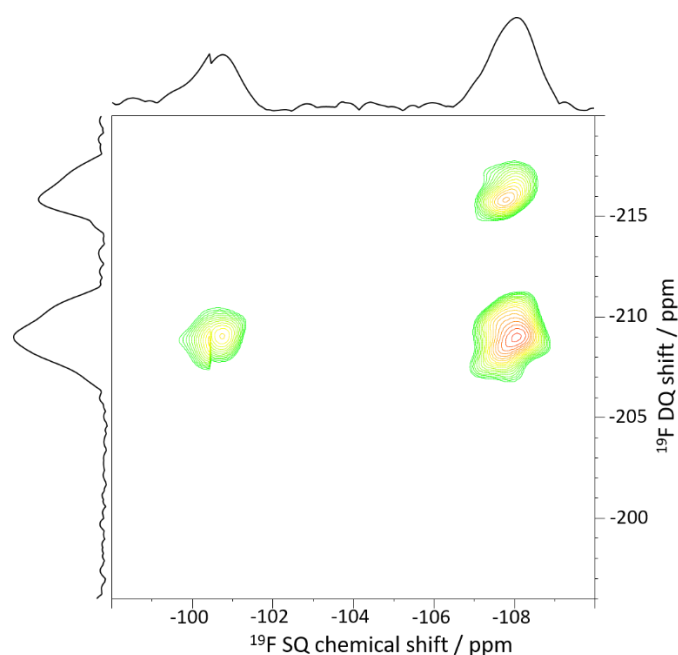
Figure 56 ^{19}F-^{19}F BaBa spectrum of compound **3c** measured at a field of 500 MHz, a MAS spinning frequency of 25 kHz and a recoupling time of 160 µs.

Although the information that can be obtained from the NMR measurements, especially for the samples **3b** and **3c**, are limited there are ways to link those spectroscopic findings to the crystal structure. In the next paragraph it shall be shown, that in some cases the crystal- structure which was determined for the molecules after solution treatment are in a good agreement with the NMR spectroscopic results.

5.5.3 XRD and single crystal NMR

All three materials were crystallized from CHCl$_3$/pentane. Compound **3a** crystalizes from CHCl$_3$/pentane in the monoclinic spacegroup P 2$_1$/c with cell constants of a=25.2 Å, b=12.0 Å and c=8.6 Å. The angles between the cell axis are a=c=90° and b=93.4°. The unit cell contains four TADF molecules without incorporation of solvent molecules. The acceptor unit, consisting of the two fluorinated phenyl rings and the triazine ring, is flat without any distortions. Same counts for the acceptor unit and the central phenyl ring. The carbazole unit shows a nearly orthogonal arrangement with a binding angle of 92.6°. Two molecules, interacting through the triazine ring, form a dimeric stack, in which the molecules are rotated by 58.7° and separated by pi stacking distance of 4.2 Å. Two of these stacks are point symmetrically distributed in the unit cell. First, the ^{19}F NMR spectra of the solvent crystallized and the vacuum sublimated sample show identical chemical shifts, which already indicate high similarity between the solid state structure of **3a** after solvent crystallization and vacuum sublimation. This similarity is underlined by the results of the homonuclear correlation spectra. The fluorine atoms, which are pointing towards the centre of the unit cell are separated by 4.2 Å. This distance can directly

be extracted from the XRD data. The self-correlation of the fluorine atoms in the different local environment arises also from neighbouring molecules, stacking periodically along the b-axis.
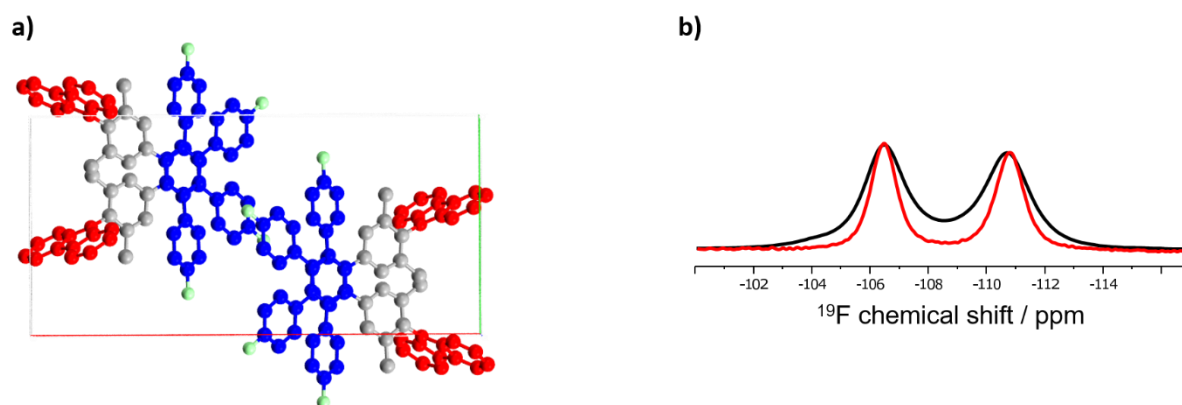
Figure 57 Crystal structure of **3a** after crystalization from CHCl$_3$/pentane along the c-axis (a). ^{19}F MAS spectra of **3a** after vacuum sublimation measured at a field of 500 MHz and a rotation frequency of 25 kHz (black) and after solvent crystallization from CHCl$_3$/pentane measured at a field of 700 MHz and a rotation frequency of 50 kHz (red).

The material **3b** is an exception from all other TADF materials studied in this work. Due to its bad solubility, it was not possible to grow crystals that were suitable for XRD measurements. However, the vacuum sublimation of this material resulted in very fine needles with crystalline characteristics. Those needles are too small for a usage in XRD studies, but can be studied via transmission electron microscopy (TEM) to obtain 3-dimensional structures of the molecules in the material. The advantage of this method is, that the sample doesn't need any further treatment, which makes the comparison between TEM and NMR a lot easier than the comparison between XRD and NMR. The results of the TEM measurement is shown in Figure 58. **3b** crystalizes in the orthorhombic space group Pna2$_1$ with unit cell constants of a=29.8 Å, b=28.9 Å and c=4.1 Å. The angles between the cell axis are a=b=c=90°. The unit cell contains four molecules. Those molecules form stacks with their neighbours in the next unit cell. Contrary to the observations made for all other materials, no offset of the stacking partners was observed. All aromatic systems are aligned parallel on top of each other with a spacing of 4 Å. It can be assumed that due to the strong pi-pi interactions, the molecules are insoluble in a large variety of solvents. Additionally, such an arrangement in the solid state hinders out of plane fluctuations of

the aromatic sub-units, which will lead to long T_1 relaxation times being discussed in the next paragraph.
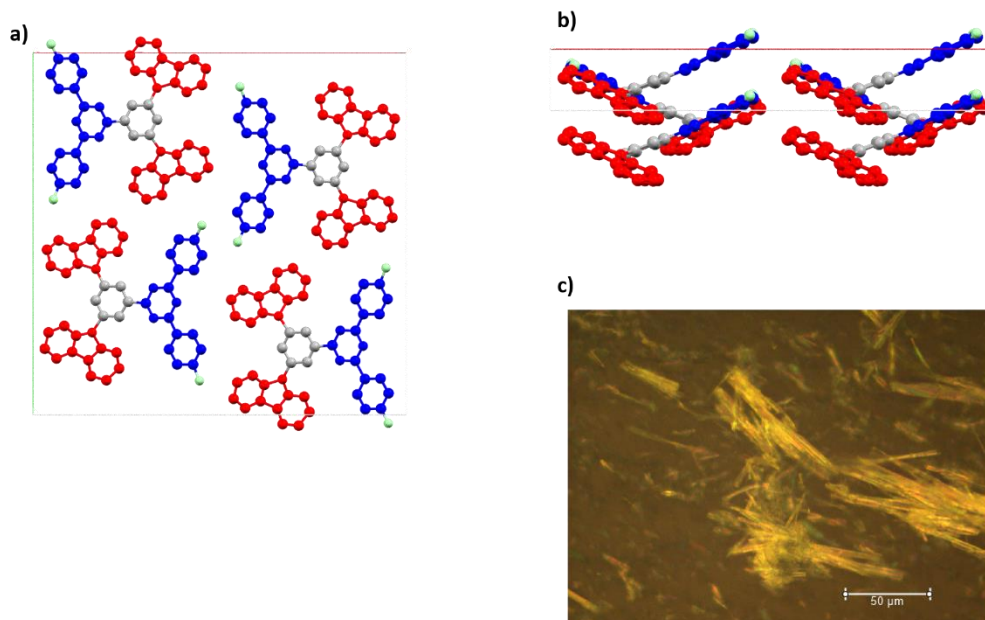
Figure 58 Crystal structure of compound **3b** viewed along the c (a) and b (b) axis. Light microscope image of the needle morphology of compound **3b** after vacuum sublimation.

Compound **3c** was again crystallized from CHCl$_3$/pentane by antisolvent diffusion. The material crystalizes in the triclinic spacegroup P 1 with cell parameters of a=13.7 Å, b=16.5 Å and c=21.1 Å. The angles between the axis are α=80.4°, β=78.8° and γ=70.4°. The unit cell contains four TADF and two chloroform molecules. The TADF molecules are arranged in point symmetric dimeric stacks. Here, the acceptor parts are not perfectly aligned parallel and not perfectly on top of each other, separated by a distance of 3.5 Å. The acceptor unit and central phenyl ring do not show any degree of distortion. The carbazole units are tilted by 53° relative to the central phenyl ring. As the ^{19}F MAS NMR spectra indicate, the structure of the crystallized sample is different from the one obtained after vacuum sublimation. This is hardly surprising, since the additional solvent molecules lead of course to a different packing of the molecules.
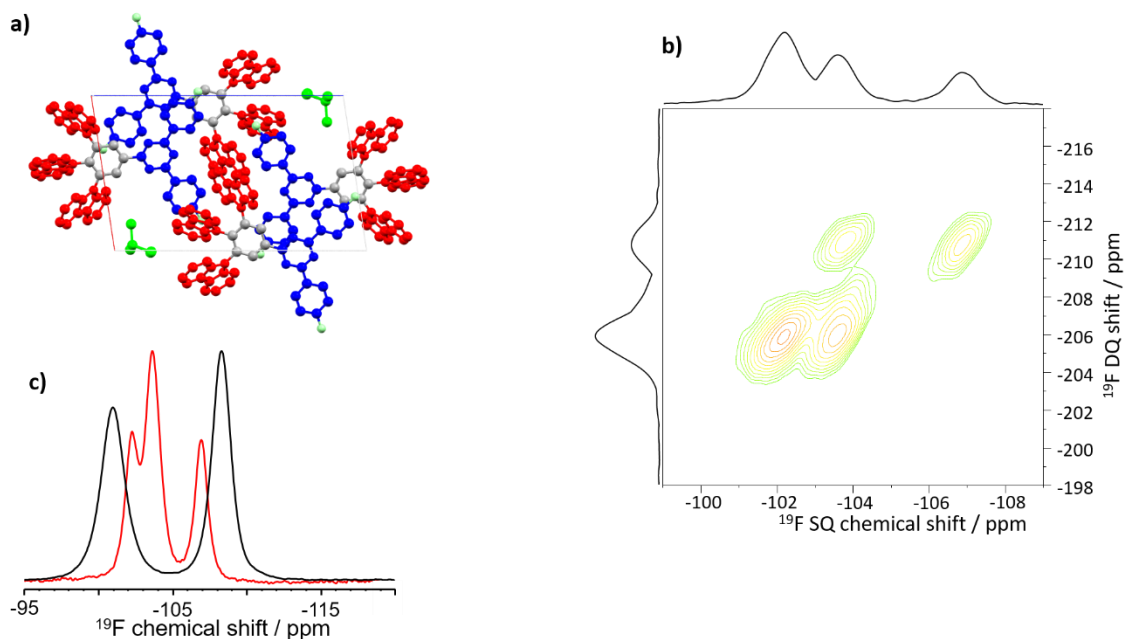
Figure 59 Crystal structure of compound **3c** after crystallization from CHCl$_3$/pentane viewed along the b axis (a). ^{19}F-^{19}F DQ-SQ correlation spectrum of the solution crystalized sample measured at a field of 700 MHz, a rotation frequency of 50 kHz and a BaBa-xy16 recoupling time of 160 µs (b). ^{19}F MAS spectra (c) of **3c** crystalized from CHCl$_3$/pentane (red) and after vacuum sublimation (black).

5.4.4 Dynamics

The ^{19}F relaxation times were determined with the saturation recovery pulse sequence and are listed in Table 13. Compound **3c** shows the shortest T$_1$ relaxation time, which is addressed to the low content of crystalline phase in the solid after vapour deposition. In contrast to that, the fluorine sites in compound **3b** show the highest T_1 relaxation time with over 200s. This behaviour is based on the dense stacking of the molecules in the solid material. The lack of any molecular motion leads to such a high value for the particular relaxation time. The ^{19}F T1 relaxation times of the fluorine nuclei in compound **3a** are in the same order of magnitude like those in compound **3c,** but with slightly higher values. Here, the main relaxation pathway is attributed to the unhindered rotation of the methyl groups, which are in spatial proximity to the fluorine atoms.

Table 13 ^{19}F T_1 Relaxation time for the different fluorine resonances in the compounds **3a**-**3c**.

3a		3b		3c	
^{19}F CS / ppm	T_1 / s	^{19}F CS / ppm	T_1 / s	^{19}F CS / ppm	T_1 / s
-107.4	26.9	-103.6	239.7	-100.6	17.6
-111.6	27.3	-108.6	212.9	-107.7	18.6

Table 14 ^{1}H T_1 relaxation times for the compounds **3a** and **3c**. *(**3b** was not determined due to long relaxation time).

3a		**3b**		**3c**	
^{1}H CS / ppm	T_1 / s	^{1}H CS / ppm	T_1 / s	^{1}H CS / ppm	T_1 / s
Aliphatic	9.6	*		Aliphatic	-
Aromatic	14.7			Aromatic	3.6

The ^{1}H T_1 relaxation times show a similar trend, where the aromatic protons of compound **3c** show a significantly lower value than the aromatics in **3a**. This behaviour is addressed to the increased rotational fluctuations of the carbazole units in **3c**.

5.5.5 Structure optimization by NICS

Co-crystallization of solvent molecules does very often lead to a change of the molecular order in solids. Therefore, it can be quite helpful to support the NMR results, which are obtained for the vacuum sublimated films, by computational simulations. Determining the so called NICS (nuclear independent chemical shift) values leads to information about the ring current of aromatic units at a given distance to the respective molecule. For the following investigation, it is considered that the distance between the acceptor units is 3.5 Å (obtained from XRD data) and that the changes in the chemical shifts of the fluorine atoms is only caused by the ring current of the closest acceptor part. To determine the NICS values, a lattice of equidistant helium atoms was created and the isotropic shielding was calculated for every helium atom in the lattice, with and without the TADF acceptor unit, using the B3LYP/6-31G* functional. The lattice has an expansion of 11x11 Å, with 1 Å distance between the helium atoms. The difference between two points at the same location of the two lattices (with and without the acceptor unit) yields the respective isotropic shielding parameters of the NICS. Helium was used as a probe atom for the reason of having a closed shell electron configuration and a low number of electrons in total, making the time required for the simulations way shorter. To calculate the chemical shift, it is necessary to generate a calibration curve by plotting the simulated isotropic shielding values of a variety of ^{19}F standards vs their measured chemical shift values. In this specific study, the material **3c** was chosen as a model system, using the ^{19}F chemical shift values obtained from solution NMR experiments together with the simulated isotropic shielding parameters.
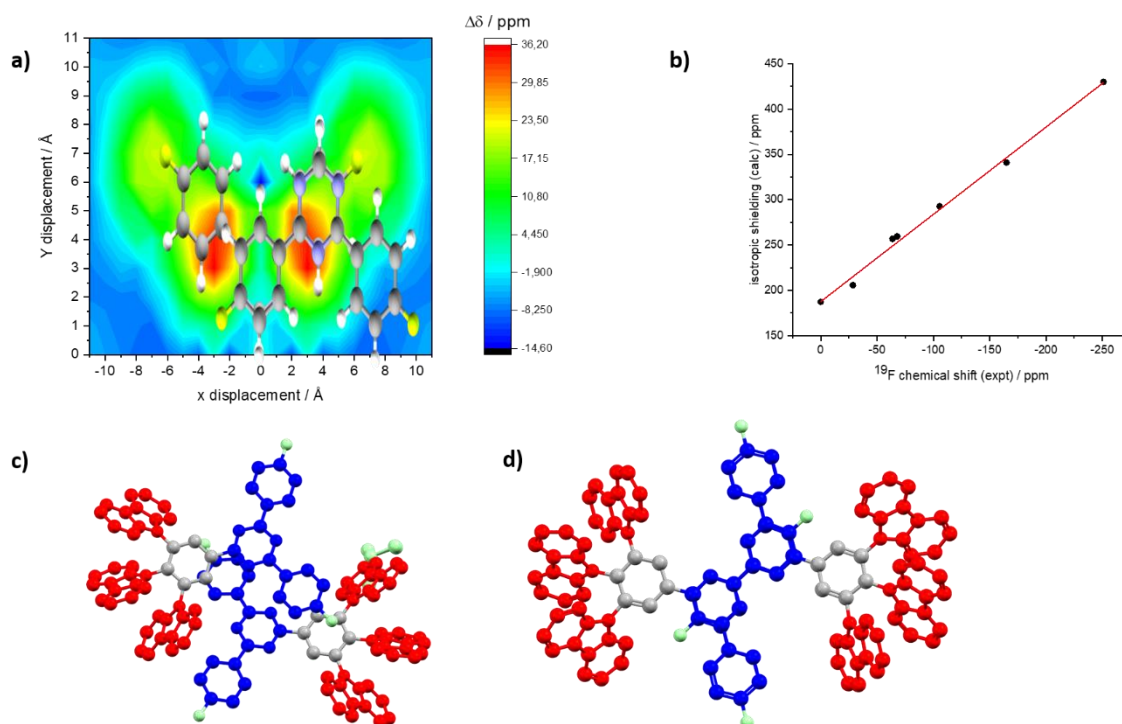
Figure 60 Ring current mapping based on the NICS simulation 3.5 Å above the acceptor plane (a). Calibration curve for calculated isotropic shielding and chemical shift values (b). Dimeric stacks of **3c** extracted from the crystalstructure (c) and simulated (d).

The chemical shift values that were simulated based on the helium lattice are displayed as a colorflow map in Figure 60. By scaling the acceptor unit of the TADF it is possible to probe the changes in the chemical shift for different conformations. One conformation was found to be in a good agreement with the data obtained from solid state NMR measurements. A detailed overview of the measured and calculated values is listed in Table 15.

Table 15 Experimental ^{19}F chemical shifts and simulated NICS.

	F1	F2
Solution / ppm	-105.5	-105.5
Solid state / ppm	-101.0	-108.3
NICS value / ppm	-6.1	3.4
Simulated chemical shift / ppm	-99.4±3.6	-108.9±3.9
Deviation	1.6 %	0.6 %

Although this optimization plays a minor role in terms of triazine shielding, since in both cases the acceptor units are surrounded by a total of six carabzole rings, it can be used to gain more precise understanding of other physical properties of the particular material.

5.6 Summary of structural data

The following section summarizes the structural findings of all TADF emitter molecules studied in this work. Here, the main focus is on the sterically shielding of the acceptor parts (substituted triazine rings) of the molecules, since they are the units which react the most sensitive to external impurities as e.g. oxygen and water. In Table 16, a summary of the main outcome of the structure elucidation is given. The first series, containing the materials **1a**-**1c**, is characterized by an acceptor unit with *tert*-butyl groups, directly attached to the triazine ring. These *tert*-butyl groups do directly lead to a sterical shielding in the plane of the nitrogen containing aromatic triazine ring system. However, the two-dimensional structure of the molecules does not display the shielding of the acceptor along the z-axis. For this purpose, the results from the NMR and XRD experiments are crucial to reveal the arrangements of molecular units which are capable of keeping impurities away from the triazine rings. In the case of material **1a**, the [1]H-^{13}C HETCOR experiment indicates, that the carbazole units and the triazine rings are in spatial proximity, which is most likely to be intermolecular. Since the bulky *tert*-butyl groups do not allow a face-to-face stacking of carbazole and triazine, a face-to-edge stacking is more likely, which is indicated by the low-field ^{1}H chemical shift of the respective protons. Compound **1b**, shows a similar carbazole-triazine interaction, when it comes to proton-carbon correlations and also a low field ^{1}H chemical shift of the carbazole protons. However, the ^{19}F NMR experiments show, that the solid-state structure of this material has a 83% amorphous morphology. It is very likely, that the z-axis of the triazine units is only shielded by the non-fluorinated site of the carbazole heterocycles, which are causing the observable correlations in the [1]H-^{13}C HETCOR experiment. This is a logic consequence of the repulsive interactions between fluorine and the electron-rich pi system of a triazine ring. The third compound of this series **1c** shows an entirely different behaviour. For this material, the ^{1}H resonances of the carbazole rings are shifted strongly to high-field, indicating a face-to-face stacking of the aromatic moieties. Correlations between triazine carbon atoms and carbazole protons were not found for this sample. It is assumed, that the double fluorinated carbazole rings do not allow any face-to-edge interaction with the triazine rings, due to the previously mentioned repulsion, so that the acceptor unit of compound **1c** does not experience any z-axis protection against impurities. For this series the trend for the shielding of the triazine rings is **1a>1b>1c**.

Table 16 Structural summary of the TADF compounds **1a**-**1c**, **2a**-**2c** and **3a**-**3c** with emphasize on their acceptor unit shielding. The method NMR always refers to the measurement of the sublimated samples, whereas XRD are the data obtained from the single crystal samples.

Compound	Methods	Structural Similarity	Optimization	Comment	Sterically shielding
1a	NMR/XRD	Yes	-		Face-to-edge Tz-Cz
1b	NMR/XRD	No	No	Guesses about close range order possible, high amorphous content after vac. sub.	Face-to-edge Tz-Cz Lower quantity as **1a**, due to repulsive interactions
1c	NMR/XRD	No	No	Data indicating comparable stacking of Cz rings in vac. sub. and solv. cryst. samples	Face-to-Face Cz-Cz Trz acceptor not shielded in z direction
2a	NMR/XRD	Yes	-		Acceptor stacking Trz-FPh Acceptor not well protected vs impurities due to low number of Cz
2b	NMR/XRD	No	Yes	Optimization by minimization of steric energy (close range)	
2c	NMR/XRD	No	No	Compound forms two phases after vacuum sublimation, distinguishable via ^{19}F NMR	
3a	NMR/XRD	Yes	-		Acceptor stacking Tz-Tz Acceptor not well protected vs impurities due to low number of Cz
3b	NMR/TEM	Yes	-		
3c	NMR/XRD	No	Yes	Optimization by NICS (close range)	

In the second series, **2a**-**2c**, the acceptor part differs from the one in the first series. Here, two para-fluorinated phenyl rings are attached to the triazine rings instead of *tert*-butyl groups. Therefore, different molecular interactions can be expected. For compound **2a**, a stacking between the acceptor parts of two TADF emitter molecules was observed. The data obtained from NMR and XRD were in a good agreement, showing that the interaction between the molecules occurs via Tz-FPh overlapping. However, due to the low amount of carbazole heterocycles, the acceptor unit is poorly protected against external impurities. The material **2c** is likely to have a similar stacking mechanism as compound **2a**. Although the solid state structures after vacuum sublimation and solvent crystallization differ significantly, an overlapping of the acceptor units is expected after both processing steps. This is basically due to the fact, that the bulky *tert*-butylated carbazole units do not allow any other arrangement of the molecules, than forming dimers with the acceptors as anchoring point of the stacking. Material **2b** is considered to show a different behaviour when it comes to the molecular arrangement in the solid state. Here, no indications for acceptor-acceptor overlapping were found. The crystal structure after solvent processing does not show any similarities with the data for the vacuum deposited material. However, removing the solvent molecules from the crystal structure, resulting in an overall sample which is close to the sublimated molecules and minimizing the steric energy of the molecules lead to an arrangement in which the acceptor units are aligned on top of the carbazole rings. Here, it can be expected, that the acceptor is not well shielded against impurities
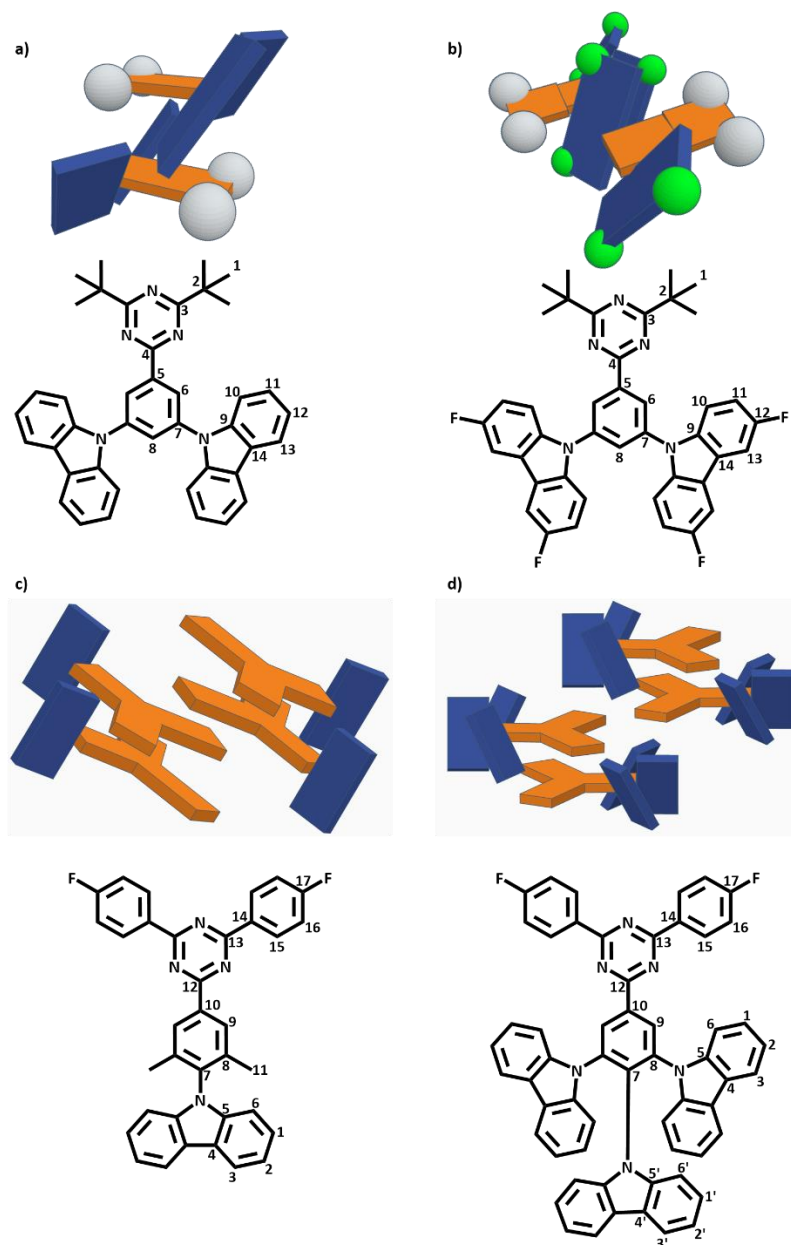
Figure 61 Schematic representation of the stacking pattern in the solid state for compounds **1a** (a), **1c** (b), **3a** (c) and **3c** (d). Grey balls display the *tert*-butyl groups and green balls the fluorine atoms for **1a** and **1c**. In all compounds the orange bricks display the acceptor unit and central phenyl ring, whereas the blue bricks represent the carbazole units.

The third series contains the molecules **3a**-**3c**. For **3a** and **3b** the crystal structure matches the NMR observations made for the vacuum sublimated samples pretty well. In the material **3a**, stacking occurs through two triazine rings of neighbouring molecules. The carbazole units align orthogonal to the central phenyl ring. In a dimeric stack, the carbazole heterocycles point into one direction with a tilt of 58°. This means, that the opposite side of the TADF emitters is not shielded and open for contamination with parasitic impurities. The molecules of material **3b** show a dense packing with full parallel stacking between aromatic ring systems of the same kind. The acceptor units are not specifically shielded but it is possible, that the dense structure does not allow any impurities to enter. Lastly, compound **3c** is discussed. For this material, the crystal and vacuum sublimation results show differences in their NMR

spectra. In case of the crystallization, solvent molecules were found in the unit cell. The molecules do form dimeric stacks, in which the acceptors overlap and the carbazole rings act as a shield against impurities. With the determination of the NICS, a guess about the short range order of the molecules can be made. It is assumed simulated dimers also have the carbazole units forming a barrier against external impurities. The structure optimization by using the NICS method leads to an improved overlap model of the acceptor part.

5.7 Structure property relation

5.7.1 Current density-Voltage characteristics and electron trapping.

As it was stated, the main goal of this study is to link the solid-state structure of the TADF materials to their property of shielding their acceptor part by the organization in the solid state. In the previous section the structural findings for all investigated molecules were summarized with emphasis on the respective acceptor protection. It is assumed, that impurities such as oxygen are responsible to cause electron trapping in organic semiconductor devices. Therefore, a closer look to the conductivity data is necessary to understand the influence of the structure on the respective physical properties. The current density voltage characteristics of all materials are displayed in Figure 62. Electron-only devices used for the electrical characterization were fabricated on glass substrates. The substrates were cleaned with detergent solution and were ultrasonicated in acetone and isopropanol. The substrates were heated at 140 °C for 10 min and subsequently treated with O_3-plasma for 20 min. The substrates were transferred into a nitrogen-filled glove box and 30 nm of Al was thermally evaporated, followed by the organic layer (~100 nm) and a 4 nm TPBi layer. For completion a 5 nm Ba and 100 nm Al layer was evaporated on top. Electrical characterization was carried out under a N_2 atmosphere with a Keithley 2400 source meter.
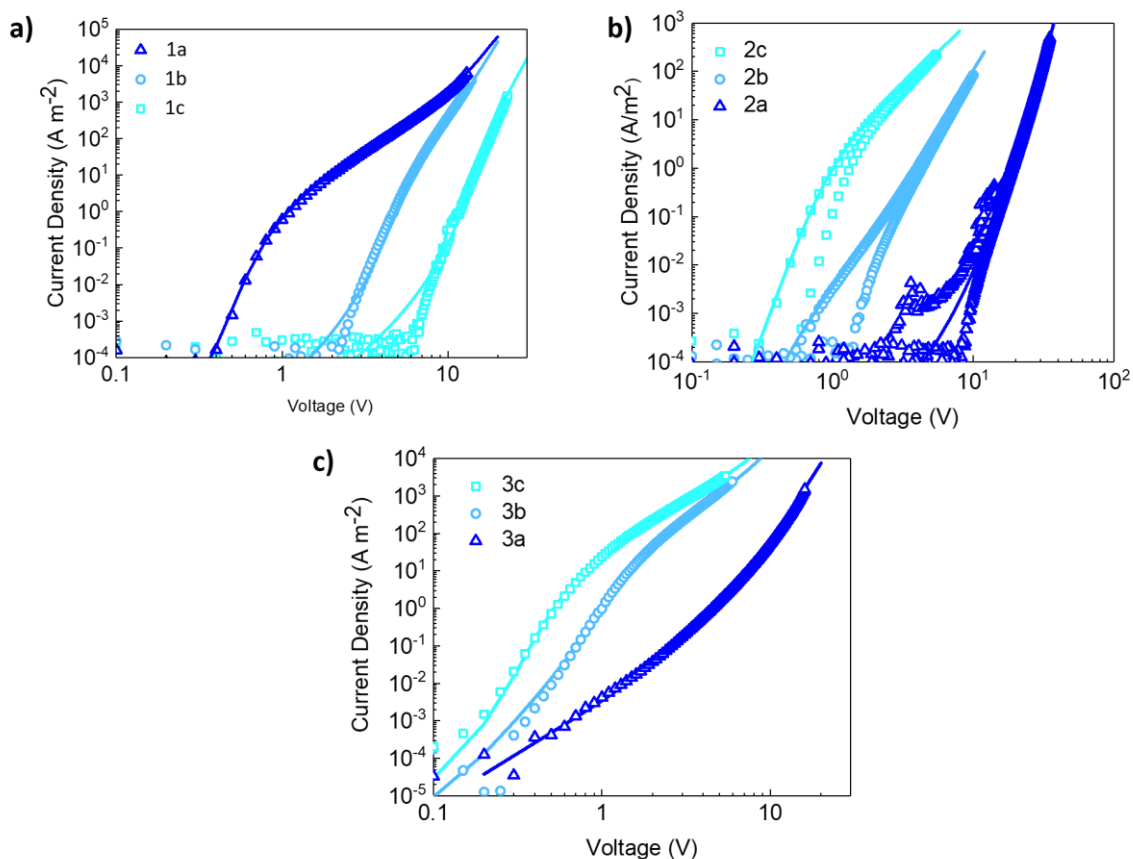
Figure 62 J-V characteristics for the series **1a**-**1c** (a), **2a**-**2c** (b) and **3a-3c** (c). (J-V data, as well as trap density simulations were provided by Oskar Sachnik and Xiao Tan, Department of molecular electronics, MPIP Mainz.)

A clear trend can be seen for all series under investigation. As can be extracted from literature, the slope of the J-V curves on a log-log plot correlate with the presence of traps in a semiconducting material.[106] In the first series, compound **1c** shows lowest current, indicating more severe trapping that can be the result of either a higher amount of traps or traps that are deeper in energy. Additionally, the J-V characteristics show a higher voltage that is needed to generate a current flow with increasing number of fluorine atoms. For compound **1a** and **1b** this shielding is way more pronounced reducing the number of traps by face-to-edge stacking between triazine and carbazole rings. In the case of **1b**, the number of traps is higher than in compound **1a**, which is due to the less shielded-axis of the acceptor caused by the repulsive interactions of the fluorine atoms.

Table 17 Trap density for all TADF materials simulated from the C-V characteristics. Trap densities were extracted from the experimental currentdensity-voltage data, shown in Figure 62 and are calculated based on the procedure described by Michels et al.[106]

Compound	Trap density, N_t gauss (x 10^{22} m^{-3})
1a	1
1b	30
1c	80
2a	190
2b	50
2c	4
3a	100
3b	6
3c	1

For the TADF emitters of the series **2a**-**2c**, the highest trap density was found for compound **2a** that is characterized by the attachment of only one carbazole unit to the centre phenyl ring, which results from an unprotected triazine unit do to the 180° displaced stacking. The trap density is reduced by one order of magnitude for each carbazole attached, resulting in calculated density of 50 x 10^{22} m^{-3} for compound **2b** and 4 x 10^{22} m^{-3} for compound **2c**.

In the series **3a**-**3c**, the compound with the lowest number of carbazole shows the highest trapping, which is due to the more open structure of the dimers formed in the solid state. Material **3b** on the other hand has a very dense packing in the solid state. The overlap of all aromatic rings leads to a hindered diffusion of impurities within the material. The molecules of compound **3c** form dimeric stacks after vacuum sublimation. Here, the surrounding carbazole groups protect the acceptor unit. This leads to a trap density which is by two orders of magnitude lower than the one determined for material **3a**.

To understand the trapping behavior of the molecules in more detail on the molecular scale, theoretical simulations are required. Therefore the DOS of the crystalline phases was simulated, using the structural data obtained from XRD for **3a** and **3c**. The main reason for this simulation is to link the HOMO and LUMO (ionization energy IE and electron affinity EA) energy levels of the materials to the respective energy levels of oxygen. The calculations were based on the OPLS-AA forcefield[107,108] and the non-bonded parameters, atomic partial charges as well as the Lennard-Jones potentials were derived following the procedure proposed by Cole et al.[109] The dihedral fragments, here the *tert*-butyl groups, are usually not implemented and are calculated using the ωB97X-D3/def2-TZVP functional.[110–

[112]. Note, that the simulations which are discussed in the following section are performed by the group of Denis Andrienko, Department of theory of polymers, MPIP Mainz.

As Figure 63 indicates, the *EA* distributions of oxygen are quite similar in crystalline and amorphous **3c**. In contrast, for **3a** the *EA* distribution of oxygen is much lower in the crystalline phase than in the amorphous phase. This change in the *EA* distribution in the crystalline state is largely attributed to a change in the electrostatic contribution to the *EA*. Considering the fact that there are regions in organic thin films with molecular packing resembling the crystalline state, the deep O_2 traps in crystalline **3a** result in a higher overall trap density as compared to **3c.** As a result, the molecular packing governs the electron trapping by oxygen in two ways: First, it affects the energy distribution of the traps by electrostatic interactions, leading in case of **3a** to enhanced trapping. However, as shown in Figure 63 energetic considerations alone cannot account for the trap-free transport observed in **3c**. This clearly suggests that the molecular packing is also an essential ingredient to obtain a trap-free current due to shielding of the electron transporting core from impurities by the stacking geometry. To further elucidate the effectiveness of the O_2 traps in the **3a** and **3c** compounds we have evaluated the electronic transfer integrals representing the coupling between close lying oxygen and CzTrz-F pairs. It is demonstrated that the total coupling strength, represented by the area under the histogram, is largest in the **3a** crystalline phase, thereby stabilizing the oxygen and resulting in oxygen becoming a deeper and more effective trap in the crystalline **3a.**
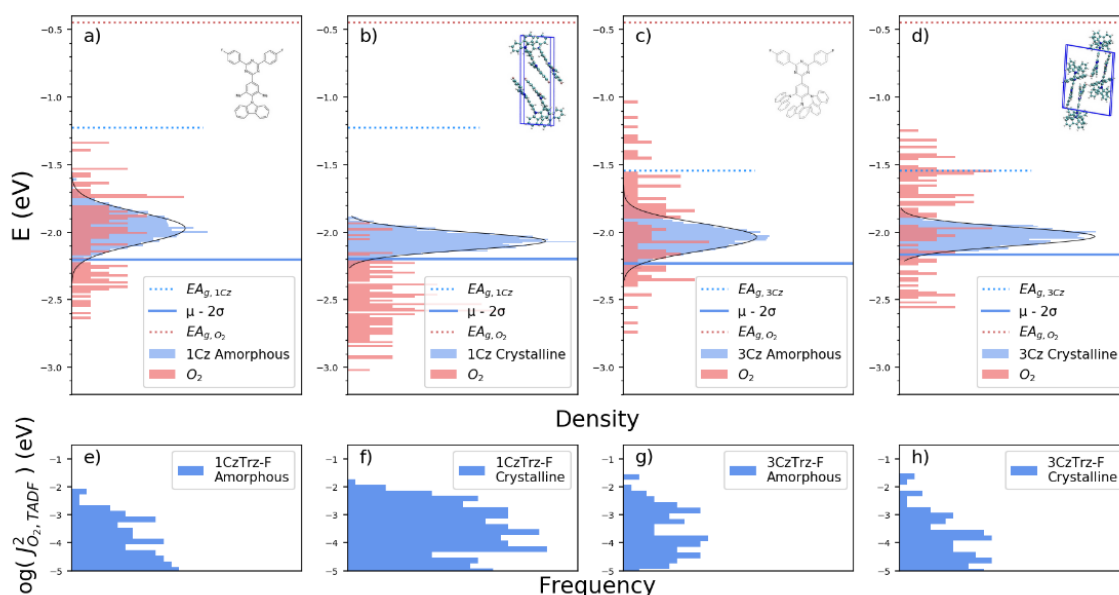
Figure 63 Calculated density-of-states distributions. a,b,c,d, The density of states of electron affinity of (a) amorphous **3a**, (b) crystalline **3a**, (c) amorphous **3c**, and (d) crystalline **3c**. e,f,g,h, Magnitude of electronic transfer integral vs. occurrence frequency in (e) amorphous **3a**, (f) crystalline **3a**, (g) amorphous **3c**, and (h) crystalline **3c**, respectively. The amorphous simulation is based on the TADF molecules by varying the bond angles within the respective molecules in vacuum.

For the series **1a**-**1c**, it is expected that the addition of electronegative fluorine atoms will enhance both the IE and *EA* of the molecules. This is indeed observed experimentally from C-V measurements, where the *EA* is enhanced from 2.6 eV (**1a**, no fluorine) to 2.8 eV (**1c**, 4 fluorine atoms). For similar oxygen levels strongest electron trapping is therefore expected for the non-fluorinated compound **1a**. However, experimentally the opposite behaviour is observed, as shown in Figure 62. To obtain further insight the DOS of both amorphous and crystalline phases of these three compounds was simulated, shown in Figure 64. According to the amorphous phase simulations similar trapping behavior would be expected for all compounds, clearly in disagreement with experiment. Similar to the compound **3a** the *EA* distribution of oxygen is significantly lowered in the crystalline phase of **1c**, leading to enhanced trapping. Thus, also for this compound the enhanced trapping in the crystalline phase is a result of a change in the energetics. However, similar to **3c**, the occurrence of a trap-free current in **1a** cannot be explained by the simulations alone. In both amorphous and crystalline phase severe trapping is predicted. This again strongly suggests that another packing related mechanism plays an important role, which is in the case of **1a** realized by the shielding of the z-axis of the acceptor unit.
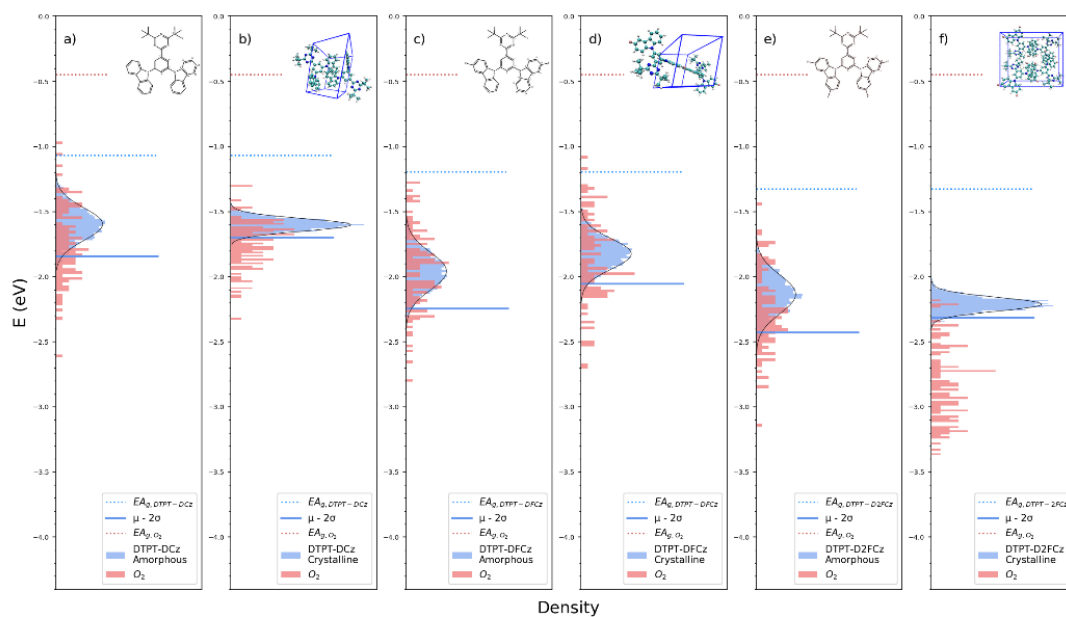
Figure 64 Calculated density-of-states distributions. a,b,c,d,e,f The density of states of electron affinity of (a) amorphous **1a**, (b) crystalline **1a**, (c) amorphous **1b**, (d) crystalline **1b**, (e) amorphous **1c** and (f) crystalline **1c**, respectively.

Summarizing, the fact that electron transport in **3c** and **1a** is almost trap-free despite their low electron affinity demonstrates that charge trapping by extrinsic impurities can be prevented by molecular design.

5.7.2 Relaxometric oxygen detection

There are two different ways to detect oxygen in samples by NMR spectroscopy. The nucleus ^{17}O can be used for direct measurement. However, its low natural abundance of 0.038% makes the usage of enriched ^{17}O gas necessary to avoid extremely long measuring times. On the other hand, ^{17}O is a quadrupolar isotope with a nuclear spin of 5/2 which can lead to broad lines dependent on the local environment of the respective molecules. The cheaper and faster method to detect the presence of oxygen by NMR experiments is the indirect detection based on the paramagnetic nature of O_2. It is expectable, that nuclei in spatial proximity to molecular oxygen (e.g. ^{13}C or ^1H) experience a change in their T_1 relaxation times due to the polarization transfer between electron and nuclear spins.

To demonstrate the interaction of TADF molecules with molecular oxygen, compound **2b** was used as a model system. The sample was put into a roundflask and dissolved in tetrachloroethan, put on a magnetic stirrer. Oxygen gas was then introduced over a duration of 1h while stirring. The sample was sealed with a Teflon cap in an inert gas NMR tube. After the T_1 inversion recovery experiment, the sample was frozen in liquid nitrogen and the oxygen was removed under reduced pressure. After each step, the sample was purged with nitrogen and the procedure was repeated three times to ensure the best possible removal of oxygen gas.

A comparison of the relaxation behaviour for oxygen saturated and degassed samples gives rise to the possible interaction between O_2 and the nuclei in the TADF molecule. The relaxation data indicate a close proximity of oxygen and the acceptor unit of the molecule. Here, the ^{13}C T_1 relaxation times are reduced for the carbon sites of the triazine ring to about 50-70% of the degassed sample values. The ^1H relaxation times for the protons attached to the fluorinated phenyl ring are also lowered by 50%. Another reduction of T_1 by was found for H-9 at the centre phenyl ring as well as for H-6, H-2 and their attached carbon atoms. Here the T_1 relaxation time reduction was less pronounced with a value of 80% of the value of the degassed sample. The summary of those findings allow a guess about the localization of the oxygen molecules at the TADF emitter of material **2b**. An energy minimized structure of **2b** in vacuum with four oxygen molecules is shown in Figure 65.
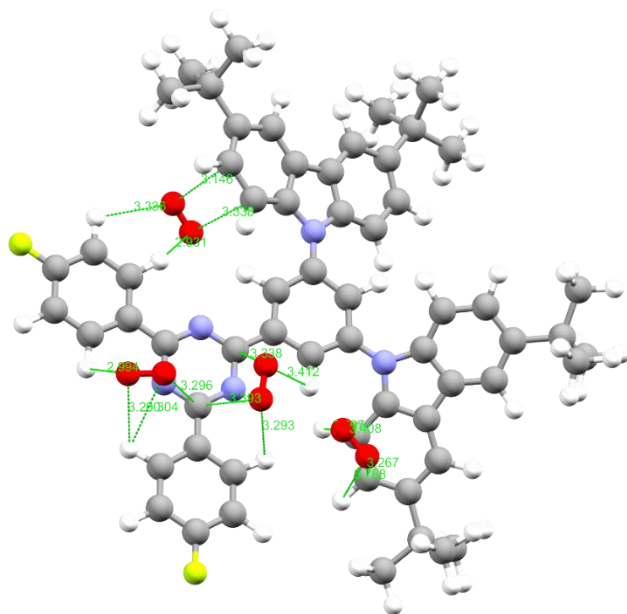
Figure 65 Vacuum simulated struture for the spatial interaction between the TADF molecule **2b** and molecular oxygen.

The distribution of the oxygen molecules is in an agreement with the observed changes in the T_1 relaxation times. However, a determination of the relaxation times in the solid state would be more convenient since it displays the real situation in thin films obviously more precise than the dissolved molecules in solution. Such solid state experiments are very time-consuming, since the saturation with oxygen can take several weeks. The solution experiments should give a rough overview about possible sites in the TADF molecules which are sensitive for oxygen interaction.

5.7.3 TADF-Polystyrene blends

In this next paragraph, the TADF materials **2c** and **3c** were blended into a polystyrene matrix. The samples were prepared by mixing polystyrene and the respective TADF material in the given ratios, dissolved in toluene. The substrates for spin coating were cleaned with acetone and isopropanol and afterwards treated with O_3-plasma for 20 min. The compounds **2c** and **3c** and there blends were characterized in terms of their photoluminescence behaviour at film thicknesses of 100 nm. (PL spectra and additional data are given in Appendix 47 f.) Here it was observed, that the *tert*-butylation and even more the blending of TADF emitters into polystyrene matrices has a large impact on the photoluminescence quantum yield. The simulation of the obtained PL data were done according to literature and the results are summarized in Table 18. Note, that the PL data were recorded and simulated by K. Thakur and B. van der Zee based on the method developed in an earlier publication (see for further details).[113]

Table 18 PLQY and initial singlet density for the compounds **3c**, **2c** and **2c** on the host polysytrene in 1:3 dilution. The value of PLQY is determined experimentally by measuring the PL emission in ambient and nitorgen environment.

	3c	**2c**	1 : 3 **2c**:PS
PLQY [%]	46	80	100
$[S_0]$ [m^{-3}]	3.3x10^{23}	2.6x10^{23}	7.0x10^{22}

Furthermore, it can be shown, that the non-radiative decay rate of triplet states decreases by the introduction of *tert*-butyl groups to the TADF molecules. To gain a better understanding of the process that reduces the non-radiative decay rate upon introducing *tert*-butyl groups to the TADF system, it is essential to take a closer look at the organization and dynamics of the TADF molecules in the solid state. Here the MAS NMR spectroscopic results that are presented in the previous sections of this thesis can provide detailed information about dynamic processes of the corresponding compounds in the pure sublimated sample as well as in a binary mixture with polystyrene. Common methods used here are the determination of ^{19}F T_1 relaxation times by saturation recovery experiments probing spectral density at the Larmor frequency and the determination of dipolar coupling constants of C-H pairs with the REPT-HDOR pulse sequence probing molecular motion with correlation times in the kHz – MHz range.

The determined ^{19}F T_1 relaxation times of compounds **2c** and **3c** and their mixtures with polystyrene are shown in Table 19. It is worth noting that the molecular symmetry, where the two fluorine sites in the molecules are equivalent, is typically broken for molecules in the solid state due to different local environments of the fluorine atoms (e.g. molecules in an amorphous matrix), which is seen as distinct chemical shifts in the ^{19}F MAS NMR spectrum. (compare previous sections.)

Table 19 ^{19}F T_1 relaxation times for **2c** and **3c** and their respective mixtures with polystyrene.

pure TADF material					TADF material in polystyrene			
2c			3c		2c		3c	
δ^{19}F [ppm]	T_1 time [s]	I_0	δ^{19}F [ppm]	T_1 time [s]	δ^{19}F [ppm]	T_1 time [s]	δ^{19}F [ppm]	T_1 time [s]
-101.5	2.5		-101.0	25	-105.0	13.3	-100.8	25
-104.0	2.8		-108.3	28			-102.7	32
-106.2	0.5 / 1.8	(1.3±0.3)·10^8 / (1.6±0.3)·10^8					-104.3	15 / 90
-107.3	0.6 / 2.1	(5.9±3.0)·10^7 / (2.6±0.3)·10^8					-107.6	29
-108.4	0.7 / 2.0	(1.7±0.5)·10^8 (2.4±0.5)·10^8					-110.1	18

The neat sample 3tCzTrz shows five different ^{19}F signals. These signals can be assigned to two different phases, which was done using single pulse as well as double quantum filtered ^{19}F correlation spectra.
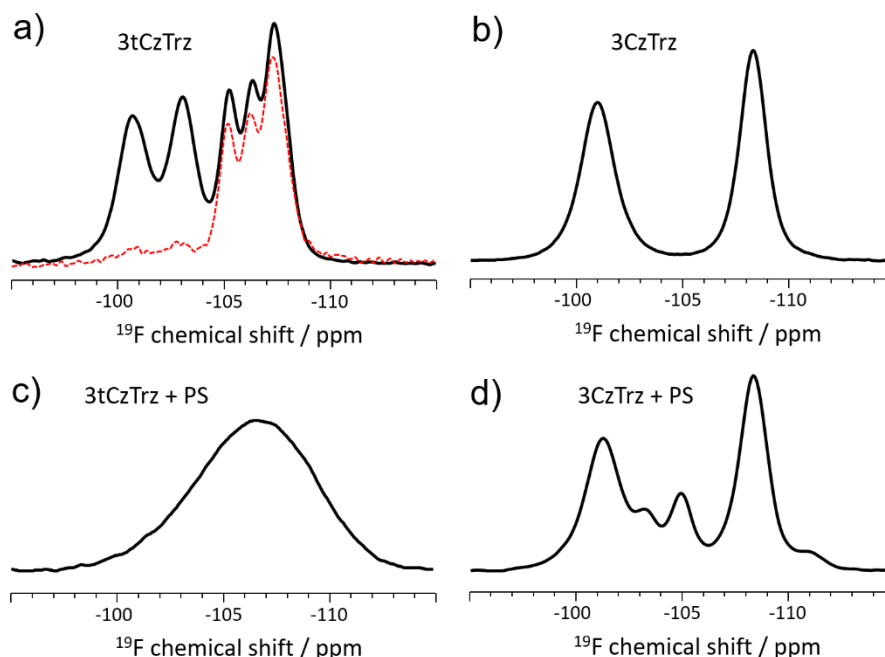
Figure 66 ^{19}F MAS spectrum (a) and ^{19}F BaBa DQ spectrum of the compound **2c**. ^{19}F MAS spectrum of compound **3c** (b), compound **2c** in a PS matrix with a mixing ratio of 1:3 (c) and compound **3c** in a PS matrix with a mixing ratio of 1:3 (d) measured at a field of 500 MHz and a MAS spinning speed of 25 kHz.

For the two broader signals at lower field the ^{19}F T_1 relaxation times of about 2.6 s are significantly longer that the relaxation times the other three sharper signals. However, their T_1 relaxation times of 2.5 and 2.8 seconds, respectively, are in a range in which amorphous or nanocrystalline materials with a high internal mobility of the individual molecular fragments are observed. The extinction of these two signals after the use of a double quantum filter indicates that the fluorine atoms are not in close spatial proximity (< 0.5nm). However, the other three signals show double-quantum coherences, suggesting that this phase has much denser packing of the molecules, which results from the fact that both translational and rotational motion can be strongly limited by the steric demand of the *tert*-butyl groups in the crystal lattice.

The signals of the fluorine atoms in the crystalline phase, spanning from -105.2 to -107.4 ppm, show a biexponential T_1 relaxation behaviour. Here, the shorter relaxation time was determined to be in the range of hundreds of milliseconds while the slower relaxing component shows a behaviour comparable to the relaxation processes determined for the non-crystalline phase. Usually T_1 relaxation times in rigid crystalline morphologies are significantly longer, compared to those in non-crystalline regions. In this special case, however, dynamic processes of the *tert*-butyl groups located in close spatial proximity to the fluorine atoms, which is ensured by the crystalline packing, lead to their very short T_1 relaxation time. The biexponential time dependence of the T_1 relaxation for both ^{1}H and ^{19}F NMR signals in the

115

crystalline environment is in full agreement with the common relaxation theory and known from literature for cases where the T_1 relaxation is driven by strong $^1H - ^{19}F$ heteronuclear dipolar couplings and one of the spin species shows a dynamic process around a local C_3 symmetry axis.

In contrast, **3c** without *tert*-butyl groups shows only two signals in the ^{19}F MAS spectrum. The ^{19}F T_1 relaxation times are almost an order of magnitude higher than those of the compound **2c**, which we attribute to the lacking perturbation by the rotation processes of the aliphatic units in the materials.

Mixing the two compounds with polystyrene leads to changes in chemical shifts, number of signals and T_1 relaxation times. For the compound **2c**, only one broad, featureless ^{19}F NMR signal was detected. For this signal, a single T_1 relaxation time of 13.3 seconds was determined. This can be explained by the good miscibility of the TADF molecules with polystyrene, a process that is mainly driven by a large gain in entropy. Thermodynamically spoken, the necessary condition for two compounds to mix is that the Gibbs free energy of the blend system is lower than the sum of the Gibss free energy of the separate components. The dispersion of the TADF molecules in PS removes the ordering of the molecules in the crystalline phase, indicated by the loss of the five different resonances and resulting in a spatial separation between ^{19}F sites and *tert*-butyl groups. The absence of the rotating aliphatic group in close proximity to the fluorine atoms leads to a longer T_1 relaxation time.

After mixing with polystyrene, **3c** shows five signals in the ^{19}F MAS NMR spectrum, whereby the two signals observed in the pure sample are retained. A quantitative analysis of the spectrum by fitting shows that the proportion of the initial morphology is approximately 80%.

The two of the three new signals, at -102.7 and at -110.1 ppm, show a T_1 relaxation behaviour similar to the crystalline fraction suggesting that these signals originate from the interface between the TADF crystallites and the polystyrene. The third new ^{19}F signal shows a bi-exponential relaxation behaviour, which may reflect the dynamic heterogeneity in the sample.

In order to monitor molecular dynamics on micro to milli second times scales, the C-H heteronuclear dipolar coupling for the pure compounds (see previous chapter) and the mixtures with polystyrene have been determined and will be compared. The data for this procedure were extracted from REPT-HDOR experiments[9], with which dipolar rotational sideband patterns for the particular carbon atoms can be identified. Here, the primary carbon atoms of the carbazole units, which are oriented towards the central phenyl ring will be considered. Assuming a Gaussian distribution of thermal molecular fluctuations, fitting of the residual dipolar couplings D_{exp} yields the width 2σ of the distribution of the molecular fluctuations. Comparing the determined dipolar coupling constants D_{exp} with the rigid case D_0, depending exclusively on the distance between the ^{13}C and the ^1H nuclear spin, provides the dynamic order parameter is described by $S = \frac{D_{exp}}{D_0}$.[42,105] An order parameter S=1 indicates the fully

rigid case, while the amplitude of molecular fluctuations increases with decreasing values of S. A values of S = 0 corresponds to fully isotropic molecular fluctuations. It should be pointed out, that the dynamic order parameter S describes the time averaged behaviour of a molecular orientation, and therefore deviates from the ensemble averaged order parameter known from liquid crystalline systems in non-ergodic systems. The determined dipolar coupling constants D, the resulting dynamic order parameter S and the width 2σ of Gaussian molecular fluctuations are summarized in Table 20.

Table 20 Dipolar C-H coupling constants, order parameters and fluctuation angels for the carbazole units of **2c** and **3c** and their respective mixtures with polystyrene. A schematic representation of the molecular fragment that is considered is shown below the table. The angle Θ describes the cone angle between the C-H pair and the rotation axis and the angle φ is the jumping angle. 2σ is the width of Gaussian molecular fluctuations.

pure TADF material						TADF material in polystyrene					
3c			2c			3c			2c		
D [kHz]	S	2σ	D [kHz]	S	2σ	D [kHz]	S	2σ	D [kHz]	S	2σ
21.5	1.0	0°	21.5	1.0	0°	21.0	0.98	15°	17.2	0.8	47°
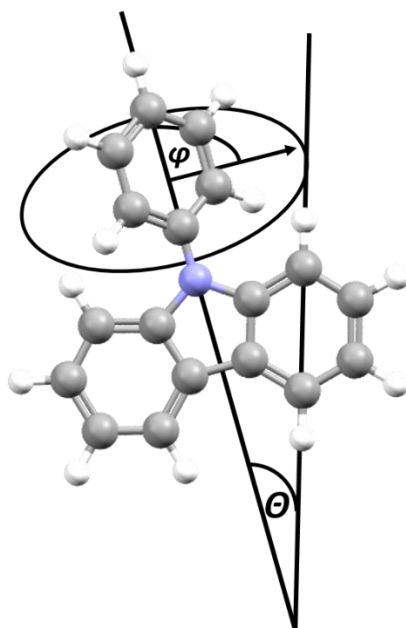
In the crystalline environment of the neat TADF materials, no molecular fluctuations of the carbazole units are observed. When the TADF molecules are incorporated into a polystyrene matrix, the mobility of the donor fragments clearly changes. Here, **2c** is most affected with larger angle molecular fluctuations of $2\sigma = 47°$ width. In the case of **3c**, this width of the distribution increases to only 15°.

This value has to be taken with care, as the REPT-HDOR method cannot distinguish between molecules in the crystalline environment and those dispersed in the polymer matrix.

The NMR observations clearly indicate a good miscibility for the *tert*-butylated TADF material with polystyrene, while for the non *tert*-butylated material a formation of phase separated crystals occurs. For the neat **2c** material, two phases were observed after vapour deposition, which are addressed to a non-crystalline and a crystalline morphology. Here, the non-crystalline phase shows a high mobility of the molecules or an irregular packing of the fluorine sites, so that no double-quantum resonances were found. The crystalline material shows shorter relaxation times than the non-crystalline phase, mainly caused by the spatial proximity of the *tert*-butyl groups and fluorine sites due to a regular dense packing. However, the aliphatic groups should lead to an enlarged spacing between the TADF molecules, thus reducing the possibility of electronic couplings between neighbouring molecules which results in an improved photoluminescence behaviour compared to **3c**. The mixing of the TADF molecules with polystyrene leads to even larger spatial separation between the molecules. However, only **2c** blends homogeneously into the polymer matrix, while **3c** retains with 80% in its pure crystalline state. Therefore, it is not surprising, that the blend of **2c** shows an increase in the PL efficiency if compared to the neat compound, while **3c** does not show any difference in the behaviour upon blending.

6. Thermal annealing and thermally induced degradation of P3HT:F$_4$TCNQ blends

6.1 Introduction

A key element for high-performance devices based on organic semiconductors is molecular doping to increase the low intrinsic carrier density. Despite intense ongoing research activities in this area for more than a decade,no clear picture of the fundamental mechanisms of molecular doping has been achieved. This is partly due to the significantly broader variation of microstructures of organic materials compared to silicon-based devices and the resulting challenge to control these microstructures. This makes both the operation and study of molecularly doped organic systems a challenging task. A better understanding of the governing processes is crucial for successful device operation through proper selection of materials and parameters for processing and treatment.

The current understanding of molecular doping in blends consisting 2,3,5,6-tetrafluoro-7,7,8,8-tetracyanoquinodimethane (F$_4$TCNQ) as a p –type dopant and poly(3-hexylthiophene-2,5-diyl) (P3HT) (molecular structures shown in Figure 67), an organic semiconducting donor polymer, distinguishes between two possible mechanisms of charge donation to the polymer-host: either integer charge transfer (ICT) or partial charge transfer through the formation of charge transfer complexes (CTC).[114,115]
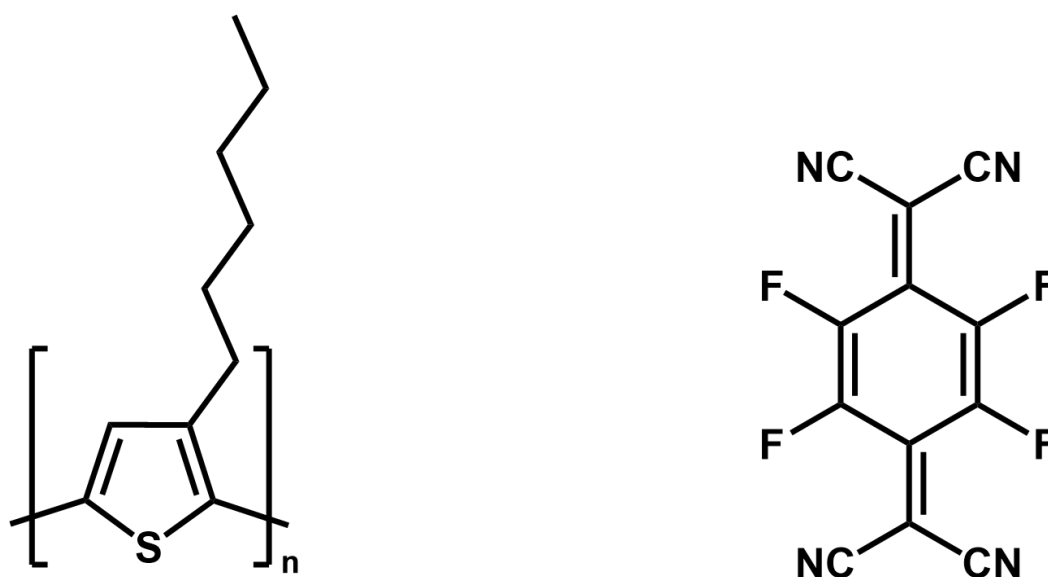
Figure 67 Molecular structure of P3HT (left) and F$_4$TCNQ (right)

ICT has been mainly reported in the literature for the P3HT:F$_4$TCNQ system, but CTC has also been found in polymorphs.[116] In this case, polymorphism describes the capability of a solid substance to exist in different crystal forms that can vary in terms of their unit cell parameters, density and melting/sublimation points. Most studies assume that alternating π-π stacking of the F$_4$TCNQ

molecules and the P3HT backbones as a microstructure enables an efficient doping process, which implies a full transfer of electrons (ICT) from the OSC to the dopant molecule.[117] Recently, the presence of F_4TCNQ molecules between the side chains of P3HT has also been discussed in literature as a prerequisite for efficient doping in this system.[118,119] Fourier transform infrared spectroscopy (FTIR) has become the standard method for determining the ionization state of F_4TCNQ, using a C≡N vibrational strain mode frequency as a linear indicator of the molecular charge,[115,120,121] although it has been pointed out that this method may suffer from bias challenges in the solid state.[120,122]

Here, solid-state NMR spectroscopy is applied to elucidate the behavior of the P3HT:F_4TCNQ model system. This organic doping system has been extensively studied in the past[93,114–116,118,119,123–137] and is therefore an ideal model system for solid-state NMR studies of the doping mechanism, which have not been performed previously, most likely due to the low concentrations of the dopant molecules leading to very weak NMR signals, resulting in time consuming, long NMR measurements. However, a NMR study of the F_4TCNQ doping in P3HT has the advantage of involving two of the most sensitive NMR nuclei, ^1H and ^{19}F. Moreover, they are exclusively bound to one of the two chemical entities involved, which opens the possibility to perform very sensitive studies on both chemical structures to obtain a better understanding of the doping process at the molecular level. Compared to other spectroscopic methods applied to the reported system so far, well-resolved NMR spectra provide direct information about molecular structures and electronic as well as chemical reactions of the involved molecules. As mentioned before, ICT and CTC are the two mainly discussed doping mechanisms described by other groups.[117,138] The major challenge for NMR measurements in the doped model system is the transfer reaction of an electron from the polymer to the dopant, which results in radical formation on either the F_4TCNQ molecule or the P3HT polymer. In NMR spectroscopy, such radicals can lead to line broadening up to such an extent causing the NMR signals to vanish. In this work it will be shown, however, that for F_4TCNQ specific ^{19}F but also ^{13}C sites of the radical anion, which is formed upon high temperature annealing, can be monitored by solid state NMR. In literature the ICT state the radical anion $F_4TCNQ^{·-}$ was found to be located between the aliphatic sidechains of the P3HT and while in the case of the CTC state this molecular species organizes at the P3HT backbone.[117]

The fact that both molecular structures, F_4TCNQ and P3HT, are redox active species is discussed in the literature[139,140] and the redox potentials of both compounds indicate that an electron transfer reaction may occur upon blending.[141] The doubly reduced form of F_4TCNQ is a carbanion bearing negative charges on the carbon atoms flanked by two cyano groups. Since the two-electron reduction does not proceed as a concerted reaction, it is possible to isolate the monoanionic radical state. The significant basicity of F_4TCNQ in the reduced form leads to a high affinity for protonation, giving rise to the formation of neutral H_2F_4TCNQ.[142]

On the other hand, the sensitivity of P3HT to oxidation has been studied in the past. There are two possible reaction sites per repeat unit: oxidation can occur at the backbone and at the alpha position of the aliphatic side chain.[140,143,144] In the case of the side chain reaction, hydrogen atoms are abstracted and the subsequently formed radical can recombine with other radicals of similar origin, leading to crosslinking of the polymer matrix, a recombination of radicals on the polymer chain or the attachment of a small molecule such as oxygen or F4TCNQ.

6.2 Structure elucidation and qualitative analysis

P3HT is a widely used semiconducting organic polymer that has already been studied in great detail by NMR methods.[80,145–147] However, there are known batch-to-batch variations in regio-regularity in this polymer, which also cause significant variations in the device performance as well as in the NMR spectra of P3HT samples from different batches. In order to characterize the P3HT material used in this study, ^{1}H and ^{13}C{^{1}H} CP MAS NMR measurements were performed on the pure polymer. The results are shown in Figure 68 a) and b). Both, the ^{1}H as well as the ^{13}C NMR spectra are split into two distinct regions, which is expected for a polymer containing aromatic and aliphatic moieties. In the proton spectrum, the peak for the thiophene protons has a value of 6.2 ppm, while the chemical shift for the aliphatic moieties is 1.2 ppm. It is noteworthy that both peaks have a symmetrical shape with no visible shoulder. That means in fact, that the polymer shows a certain degree of order in the solid state.

The ^{13}C{^{1}H} CP MAS spectrum shows four resonances for the four chemically distinct aromatic carbon sites without overlap. They can be assigned by the following values: 136.3 ppm (c), 132.9 ppm (a), 130.8 ppm (d), and 126.0 ppm (b). The signal for carbon atom (c) shows a shoulder, which originates mainly from amorphous domains with varying dihedral angels to the α-carbon site of the 0attached sidechain in the polymeric material. The aliphatic region of the spectrum from 32.9-14.9 ppm shows the resonances of the carbon sites along the aliphatic side chain. The δ carbon atom has a chemical shift value of 32.9 ppm, while the peaks for the α-γ carbon atoms overlap, resulting in an intense signal at 30.7 ppm. The outer CH_2 and CH_3 groups have chemical shift values of 23.6 ppm and 14.8 ppm, respectively. All signals of aliphatic carbon sites are narrow compared to those signals of carbon sites along the polymer backbone due to the high local mobility of the aliphatic side chains.

In addition to NMR measurements of the P3HT polymer, the dopant molecule F_4TCNQ in its pure form was analyzed. For characterization, ^{19}F and ^{13}C{^{19}F} CP MAS spectra were recorded, shown in Figure 68 c) and d), and ^{19}F-^{19}F SQ-DQ correlation NMR spectra (Figure 68 e) and f)). Note that the signal of Teflon at -122.7 ppm was used as an internal standard for the calibration of ^{19}F chemical shifts. The ^{19}F MAS spectrum of pure F_4TCNQ shows a double peak with chemical shift values of -129.1 and -132.3 ppm. This double peak results from the reduction of molecular symmetry in the asymmetric unit cell in

crystalline F_4TCNQ. The dipole-dipole interaction of the magnetically in-equivalent fluorine atoms can be revealed by 2D ^{19}F DQ-SQ correlation NMR experiments, which are discussed in the following section. In addition to the chemical shift values, the spin-lattice relaxation time T_1 for fluorine was determined by inversion recovery experiments. As expected, the relaxation times are in the range of several minutes (485 s), which is quite common for crystalline small molecules.

The local packing of F_4TCNQ molecules in crystalline environments and in films processed from solution can be analyzed qualitatively by simple ^{19}F MAS NMR studies. F_4TCNQ molecules in regions without periodic long-range order, like F_4TCNQ molecules in non-crystalline regions, are seen as a broad featureless signal, while F_4TCNQ molecules in crystalline environments lead to sharp peaks in the ^{19}F MAS NMR spectrum due to the well-defined isotropic chemical shift in their periodic regular environment. In addition to the molecular packing, the local electronic state of the molecule, whether it is in an ionized, a charge transfer or a neutral state, also affects the chemical shift of the ^{19}F signal.

Figure 68 c) shows the ^{19}F-MAS NMR spectrum of crystalline F_4TCNQ and illustrates the chemical shift pattern of crystalline F_4TCNQ. The ^{19}F-DQ correlation spectra in parts e) and f) of the figure help to elucidate the two ^{19}F NMR signals in the crystalline state. In spin ½-systems such as ^{19}F, double quantum (DQ) coherences can be excited only if there are two ^{19}F sites in close spatial proximity, such that the dipolar coupling between these sites is strong enough to allow for DQ excitation. For short DQ excitation times, the DQ excitation efficiency is proportional to the sixth power of the inverse distance between the ^{19}F sites, which opens the possibility of distinguishing small distance differences. Since DQ coherences are observed at the sum of the chemical shifts of the two spins involved, coherences between nuclear spins with the same chemical shifts are observed on the red dashed diagonal, while coherences between spins with different chemical shifts are observed as split signals of equal intensity symmetric to this diagonal. Thus, the pattern in Figure 68 e) indicates that neighbouring ^{19}F sites at the central ring of F_4TCNQ, which are definitely the closest ^{19}F sites in crystalline F_4TCNQ, have different chemical shifts. The difference in the chemical shift of the two neighbouring sites can be easily understood by taking a closer look at the herringbone structure of the F_4TCNQ molecules in the crystal lattice. One of these two ^{19}F sites coordinates to the π-system of the neighbouring molecule, while the adjacent ^{19}F site coordinates to the nitrogen of a cyano group, as shown in literature.[148] For a double quantum excitation time of 4 rotor periods corresponding to 134.4 μs (see Figure 68 f)), coherences are observed between spins with the same chemical shifts resulting from spatial contacts along the diagonal of the central ring of the F_4TCNQ molecule and to other neighbouring molecules.
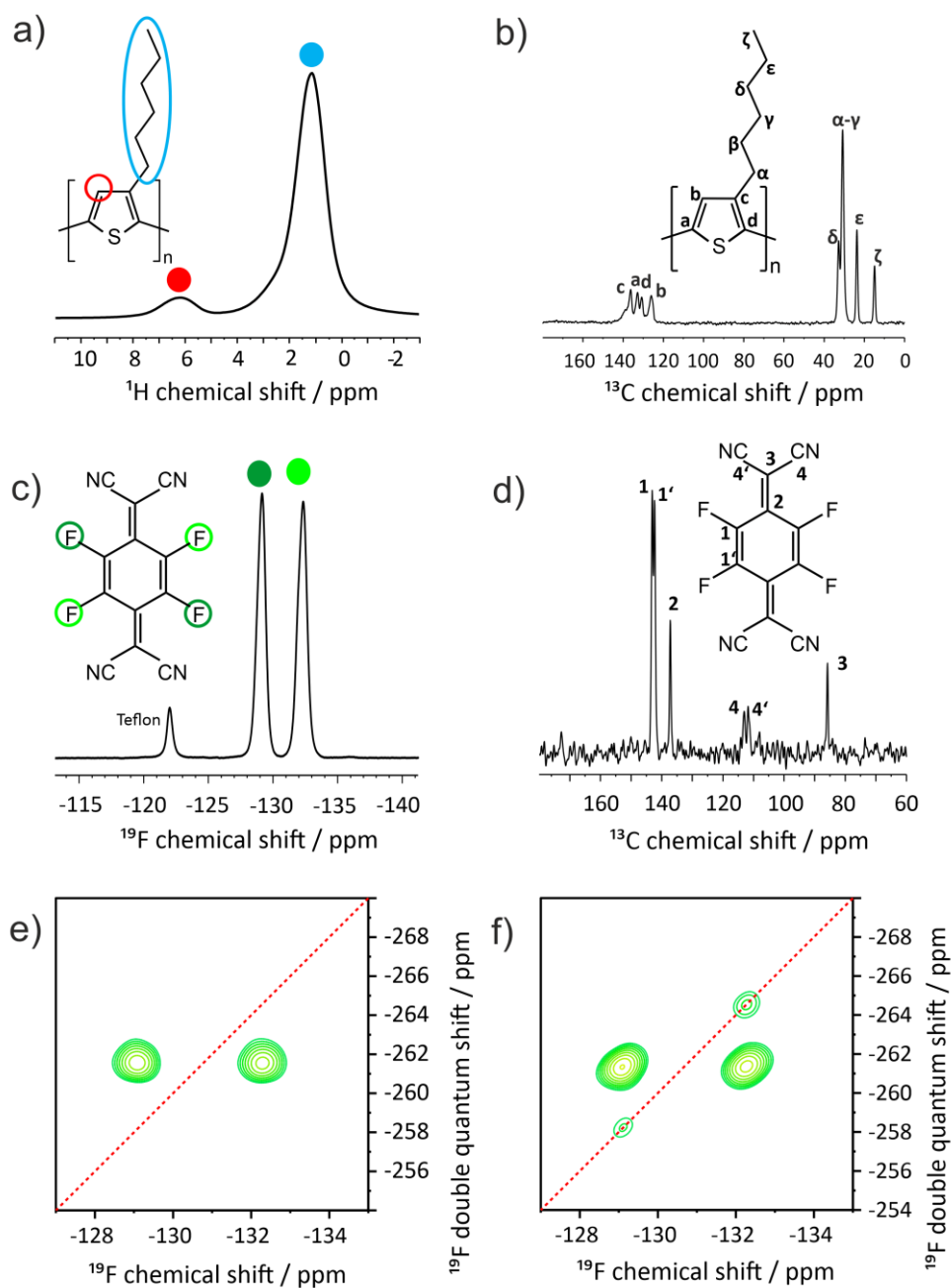
Figure 68: MAS spectrum of neat P3HT (a), ^{13}C-{^{1}H} CP MAS spectrum of neat P3HT (b), ^{19}F MAS spectrum of neat F$_4$TCNQ with a Teflon signal as internal reference (c), ^{13}C-{^{19}F} CP MAS spectrum of neat F$_4$TCNQ (d), ^{19}F-^{19}F DQ-SQ NMR spectra of neat F$_4$TCNQ with a recoupling time of 2τ (e) and 4τ (f).

In order to capture the chemical shifts of the carbon atoms in the pure F$_4$TCNQ for later comparison with blend samples, a ^{13}C-{^{19}F} CP MAS spectrum has been recorded (Figure 68 d). Two carbon signals are split into a double peak, namely C-4 (143.1 and 142.4 ppm) and C-1 (113.2 and 111.8 ppm), while carbon atoms C-2 and C-3 show only a single signal at 85.9 and 137.2 ppm, respectively. Please note,

that pure F_4TCNQ in the solid state exhibits diamagnetic behavior, which does not affect the linewidth of the NMR signals, since there are no unpaired electrons in this redox state. In solution, however, F_4TCNQ behaves like a paramagnetic species with extremely short T_2 relaxation times, broadening the NMR lines to such an extent that the ^{19}F signals can hardly be detected. This in fact is a result of solvent interactions with the F_4TCNQ that are capable of stabilizing the radical state. The corresponding ^{19}F solution NMR spectrum of F_4TCNQ dissolved in *ortho*-dichlorobenzene is given in the appendix (Appendix 54 ff).

With the chemical shift assignment of the pure compounds, it is possible to look more closely at the changes that occur during blending and annealing.

For this study, thin films were prepared by mixing stock solutions of the polymer and the dopant, dissolved in DCB at 343K. The mixtures were stirred for 1h, then applied to a pre heated glass plate and bar coated manually. The concentrations were ranging from 1:16 to a 1:1 F_4TCNQ:P3HT molar ratio. For each concentration and each annealing temperature, ^{1}H, ^{19}F, and [13]C{[1]H} CP MAS spectra were recorded at a rotation frequency of 25 kHz. Since the probehead that was used in this study had no high temperature function, the annealing steps had to be performed separately outside of the magnet. Therefore the rotorcaps of the zirconia rotors were removed, and the samples were annealed in a nitrogen environment for 120 min to prevent interactions between the sample and atmospheric moisture. This procedure was performed for every temperature step with a heating rate of 10 K/min. The cooling of the samples to room temperature took roughly 60 minutes and was achieved by switching of the heating unit resulting in temperature equilibration with the environment.

In all directly (after processing) measured, solution-processed P3HT-F_4TCNQ films with F_4TCNQ concentration higher than a F_4TCNQ:P3HT molar ratio of 1:16, the ^{19}F MAS NMR spectra show sharp signals at -129 and -132 ppm increasing with increasing F_4TCNQ concentration. These signals indicate the presence of phase-separated crystalline pure F_4TCNQ in the dyed film, despite the significant color change of the processing solution upon the mixing of the two solute components, indicating complexation of P3HT and F_4TCNQ in solution.

Upon annealing at elevated temperature, the signals of the crystalline, pure F_4TCNQ decrease in intensity and disappear, while the broad ^{19}F NMR signal of the F_4TCNQ molecules in the P3HT film becomes slightly narrower. Annealing for 2h at 423 K causes the complete removal of the signals originating from crystalline F_4TCNQ (mixing ratio 1:16-1:4) from the ^{19}F MAS NMR spectrum or leads to a drastic decrease in their intensity in F_4TCNQ rich samples (mixing ratio 1:2 & 1:1). Instead, a new crystalline species has evolved that shows similar patterns in the DQ correlation spectra, suggesting herring bone stacking similar to F_4TCNQ in the crystalline state. However, the significant difference in chemical shift compared to regular crystalline F_4TCNQ shows a substantial redistribution of electron

density in the molecule, indicating chemical modification or an ionic state of the F$_4$TCNQ molecules in these newly formed crystals.
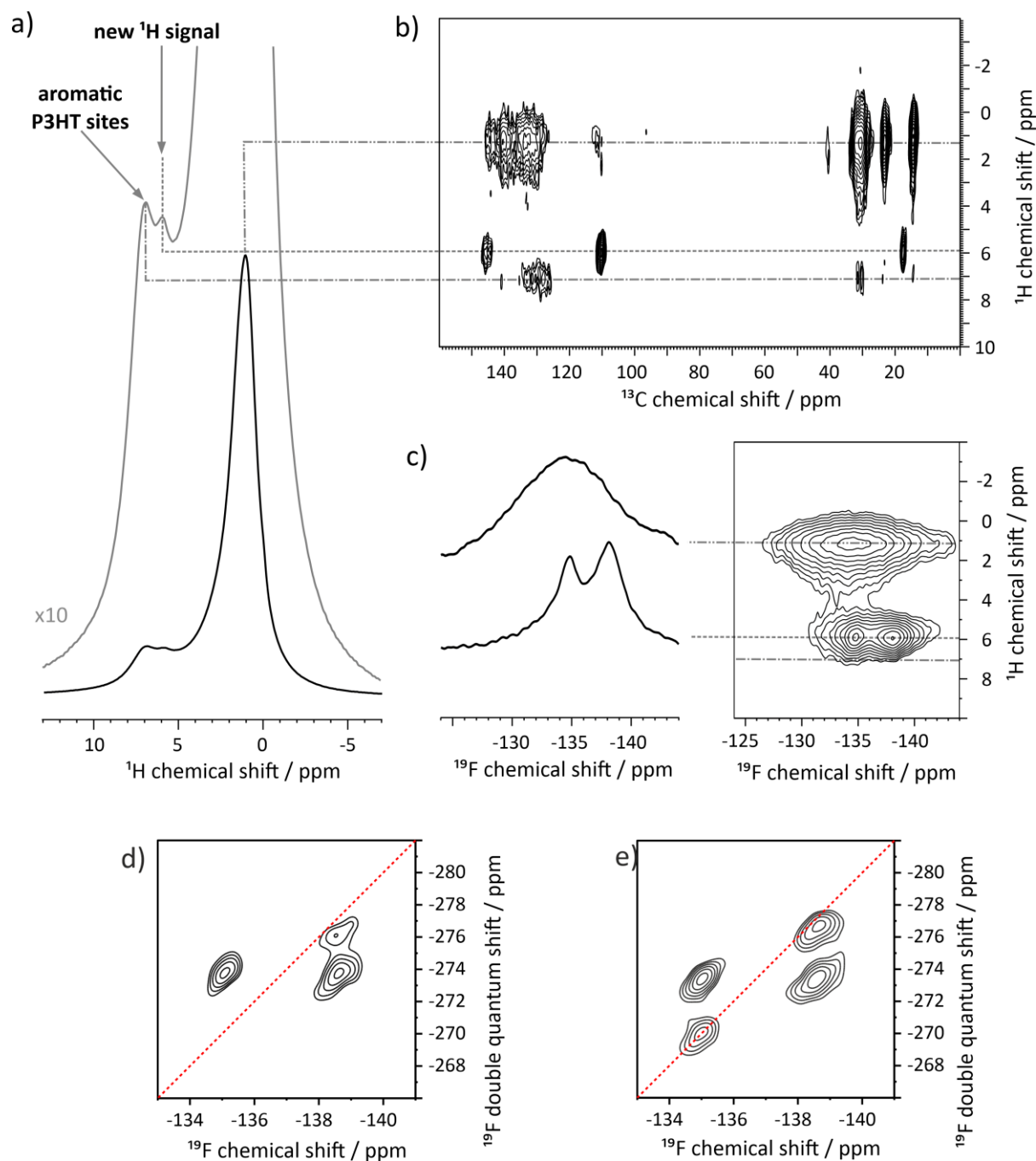
Figure 69 ^{1}H MAS spectrum of a 1:4 molar ratio F$_4$TCNQ:P3HT blend annealed at 393K (a), ^{1}H-^{13}C HETCOR spectrum of the same blend (b),^{19}F MAS and ^{1}H-^{19}F HETCOR spectra of the same blend (c), ^{19}F-^{19}F DQ-SQ correlation NMR spectra of the same blend with a recoupling time of 2τ (d) and 4τ (e).

In addition to the changes observed in the ^{19}F spectra, the ^{1}H resonances show significant changes. At an annealing temperature of 363 K, a line broadening of the aromatic signal was observed in the proton spectra, while the aliphatic region remained unchanged. This broadening can be explained by the fact that the polymer has a low degree of order immediately after solution processing and subsequent

annealing at low temperatures. Increasing the annealing temperature to 393 K (120 min), however resulted in the formation of a new proton signal at 5.9 ppm (Figure 69 a, exemplified for a 1:4 F_4TCNQ:P3HT blend). In order to identify the origin of this signal, $^{13}C\{^1H\}$ and $^{19}F\{^1H\}$ HETCOR NMR spectra were recorded (Figure 69 b & c). The new proton signal shows no correlation with aromatic or aliphatic carbon sites of P3HT, whereas correlations with carbon signals assigned to F_4TCNQ were observed in these correlation experiments. Another change initiated by the annealing of the blend is the formation of a new carbon signal in the aliphatic region at 17.5 ppm, which occurs in parallel to the changes in the ^1H spectra. The changes observed in the carbon spectrum will be discussed later in the text.

Further inspection of the ^1H-^{19}F-HETCOR NMR spectrum shows no correlation between aromatic protons and fluorine atoms. This indicates that F_4TCNQ molecules do not form stable stacks with the thiophene units of the P3HT backbone. The correlation signal between the proton sites of the aliphatic side chains and a broad signal in the ^{19}F dimension, gives some insight into the distribution of the F_4TCNQ molecules in the polymer. The significant line width of the ^{19}F signals suggests a heterogeneous distribution of F_4TCNQ molecules between the side chains. (Figure 69 c)

Remarkably, the ^1H-^{19}F-HETCOR NMR spectrum shows that a fluorinated species with a sharp double peak has a strong correlation with the new proton signal at 5.9 ppm. The double peak, shown in Figure 69, has chemical shifts (-134.7 and -138.2 ppm) that are different from those found in pure F_4TCNQ. It is suggested that this change is due to electron transfer from P3HT (donor) to F_4TCNQ (acceptor). The addition of electron density to the F_4TCNQ molecules will increase electronic shielding of the fluorine atoms, causing a shift of the NMR signals towards higher field. Looking more closely to the molecular processes, the reduction of pure F_4TCNQ can be described as a two-step reaction. In the first step, F_4TCNQ is reduced by electron transfer from P3HT to the radical anion $F_4TCNQ^{\cdot-}$, leading to the formation of the charge transfer complex [P3HT][F_4TCNQ]. The second step involves the abstraction of a hydrogen atom from P3HT, which is then transferred to the C-3 position of the F_4TCNQ molecule. The resulting species HF_4TCNQ^- serves as a strong base and can accept a proton from acidic sites in the polymer to form the neutral molecule H_2F_4TCNQ. The increased molecular mobility at high annealing temperatures then leads to segregation of P3HT and H_2F_4TCNQ, resulting in a new crystalline phase that is observed in the ^{19}F MAS NMR spectrum as a double peak with different chemical shifts compared to pure F_4TCNQ. Indeed, similar properties for the crystalline phases of pure F_4TCNQ and H_2F_4TCNQ were found by SQ-DQ NMR experiments. Based on the solid-state NMR results, the following scheme (see Figure 70) has been derived to illustrate various possible electron and proton transfer reactions involving F_4TCNQ.
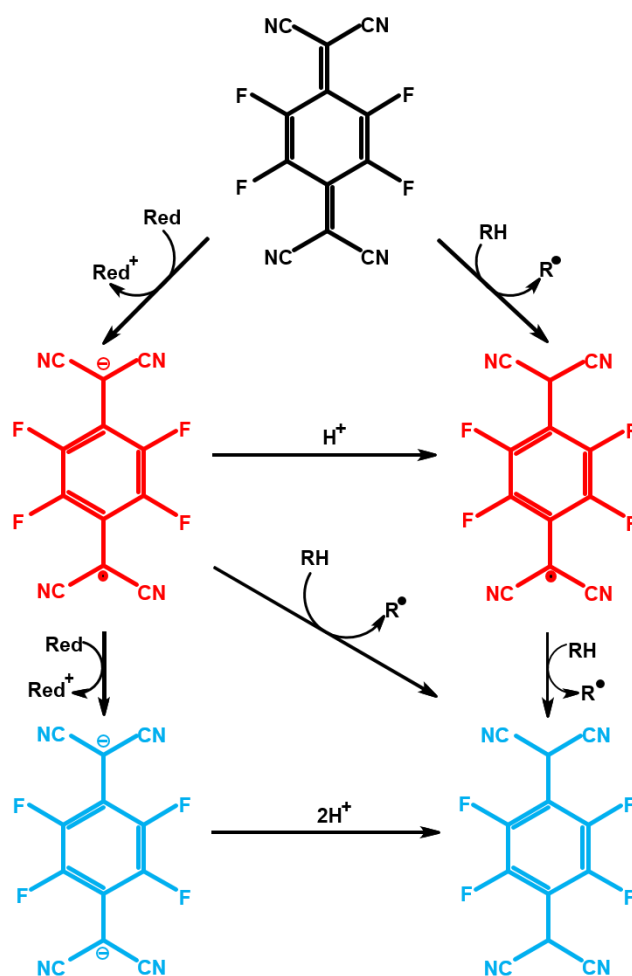
Figure 70; Protonation and reduction steps for F_4TCNQ. Neat F_4TCNQ is displayed in black, single reduced derivatives are given in red and double reduced derivatives in blue. RH represents a CH_2 group at the α-position of the P3HT side chain.

Although the changes found in ^{19}F and ^1H NMR experiments provide good insight into the chemical transformations taking place in P3HT:F_4TCNQ blends upon annealing, thermally induced changes in the ^{13}C NMR spectra may help to elucidate the underlying chemical processes in the doped P3HT films. For all P3HT blends with F_4TCNQ ratios higher than 1:16, a new species is formed with a ^{13}C chemical shift value of 41 ppm. This signal is also observed in the ^1H-^{13}C-HETCOR NMR spectrum shown in Figure 69b. The correlation of this signal with the aliphatic protons, suggests a distribution of these species along the side chains. Upon annealing at higher temperatures above 453 K, the signal disappears from the ^{13}C NMR spectrum. From this observation it can be concluded, that this signal has to be assigned to a reaction intermediate of the redox processes between P3HT and F_4TCNQ formed at elevated temperatures, which is, however, not stable at high temperatures. This kind of molecular arrangement is assigned to the ICT state and thus the molecular species $F_4TCNQ^{\cdot-}$. Indeed, our DFT calculations (see *Table 21*) for different oxidation and protonation states of F_4TCNQ show that the radical anion $F_4TCNQ^{\cdot-}$, has a chemical shift value of 41.2 ppm for the carbon atom C-3, comparable to the new species observed in our measurements. The strong correlation signal of this site with proton sites of the

aliphatic side chains indicates that the formation of H_2F_4TCNQ occurs mainly via a hydrogen transfer reaction from the P3HT side chain to the radical anion F_4TCNQ^- supporting our earlier considerations.
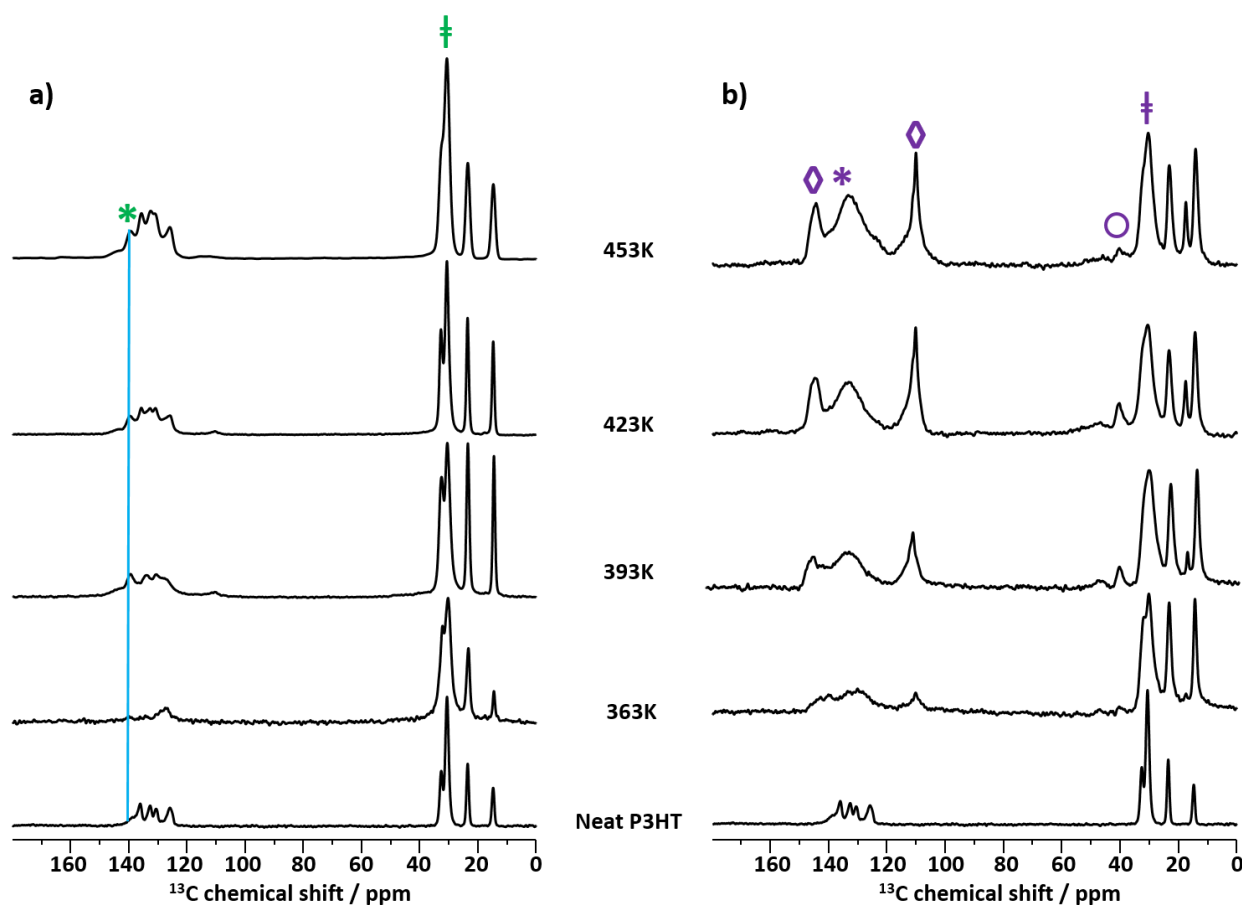
Figure 71: ^{13}C-{^1H} CP MAS spectra of 1:16 molar ratio (a) (blue line indicates the new formed signal) and 1:1 molar ratio (b) F_4TCNQ:P3HT blends. Neat P3HT is displayed at the bottom, stacked spectra with increasing temperature on top. The heatingrate of the annealing was 10K/min and the target temperature was hold for 120 min. Cooling down to room temperature took 60 min.

The chemical shifts calculated for the radical anion fit our experimental data quite well, except for the shift for the C-3 site in the protonated form H_2F_4TCNQ. Here the calculated value differs significantly from the results of the ^{13}C measurements. One reason for this difference might be that the chemical shifts were calculated for the optimized geometry in vacuum. For the C-3 site, however, different rotational orientations of the -CH(CN)$_2$ groups relative to the plane of the aromatic ring lead to different local electronic interactions between the substituents and thus change the chemical shift of this position, keeping in mind that the substituents may rotate to optimize the local molecular packing in bulk material. As can be seen from Table 21, the carbon atoms 1 and 1` of the aromatic ring have slightly different chemical shift values as indicated by the DFT calculations. The *cis* conformation shows a spacing of 2.56 Å and a chemical shift value of 148.7 ppm, while the *trans* conformation shows an interatomic spacing of 3.41 Å and a chemical shift value of 150 ppm.

Table 21 Calculated values of ^{13}C chemical shifts for different F_4TCNQ redox and protonation states. For calculations, the DFT functional B3LYP, 6-31G+ (d,p) was used.[149–152]

Carbon Atom	F_4TCNQ	$F_4TCNQ^{\cdot-}$	F_4TCNQ^{2-}	H_2F_4TCNQ
1	128.9 ppm	128.0 ppm	146.9 ppm	150.0 ppm
1`	128.9 ppm	128.0 ppm	146.9 ppm	148.7 ppm
2	123.9 ppm	108.6 ppm	128.7 ppm	117.9 ppm
4,4`	92.2 ppm	100.3 ppm	119.0 ppm	109.0 ppm
3	76.7 ppm	41.2 ppm	20.0 ppm	23.1 ppm
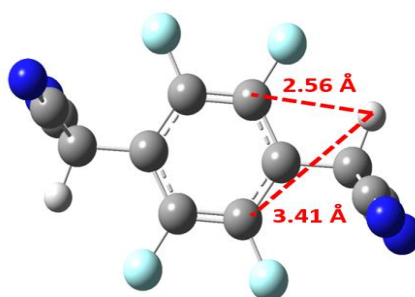
In addition to the structural changes found for the dopant F_4TCNQ, the changes of P3HT were analyzed by ^{13}C-$\{^1H\}$ CP MAS. Although changes in macromolecular systems are much more complicated to analyze compared to small molecules such as F_4TCNQ, a few comments can be made about chemical transformations of the P3HT polymer. In Figure 71 the NMR spectra obtained for 1:16 and 1:1 molar mixing ratios and the respective annealing temperatures of 363-453K are shown. Annealing temperature dependent spectra for all other doping rations are given in the supporting information. ^{13}C NMR spectra obtained immediately after processing are not shown, because they showed only very broad and obscure signals due the high degree molecular disorder in the freshly solution processed films, which do not allow for detailed analysis. Another aspect which may lead to line broadening is the formation of the CTC state that forms directly after processing.[117] Thus, after low temperature annealing, a large amount of the F_4TCNQ molecules is distributed in different local packing arrangements along the polymer backbone. Since the CTC can be considered to be a radical state, the unpaired electrons may contribute to the observed line broadening as well. This line broadening effect is still visible after low temperature annealing at T = 363 K. Here, only small undefined signals are observed in the aromatic region and the signals for the aliphatic side chains show broadening.

Annealing the samples at higher temperature establishes better molecular order, so that the aromatic NMR signals are better resolved and the aliphatic signals undergo a narrowing of the NMR lines. Note that this line narrowing is no relaxation based effect, but is caused by fewer local environments of the particular nuclei resulting in less resonances contributing to the observed signal. Apparently, the CTC complex becomes unstable at higher temperatures, resulting in a spatial separation of the doping partners and thus to the formation of the ICT state. As can be seen from Figure 71, the ICT state starts to vanish at annealing temperatures higher than 423 K, as soon as the radical species begin to recombine under the formation of HF_4TCNQ^-. A feature that is observed in the ^{13}C-$\{^1H\}$ CP MAS spectra for all mixing ratios is a broadening of the aromatic signals compared to pure P3HT. This broadening may be caused by free charge carriers formed at the backbone of the polymer during oxidation.

Another feature that becomes visible already at low doping ratios like 1:16 is the formation of a new signal in the aromatic region (marked with green *,Figure 71). Since this signal does not originate from F_4TCNQ, it is conceivable that the formation is caused by a positive charge located at the thiophene units of P3HT. The lower electron density then leads to a deshielding compared to the unoxidized sites in the polymer. It is supposed that this new signal can be assigned to a localized polaron state formed at the P3HT backbone.

In addition to the changes observed in the aromatic region, a broadening of the signal at 32.0 ppm can be seen. After annealing at 453K, the resolution is gone, which might be due to crosslinking of the side chains. The relative intensity, however, between the central and the end segments of the sidechain indicates, that the stoichiometric ratio fits the expected values and no radicals (or only a very low percentage of radicals) is prevailed through the annealing process. In contrast, after low temperature annealing, the signals of the chain center are significantly weaker than the expected stoichiometric ratio, which may originate from the presence of an unpaired electron state at the α-position of the side chain.

The ^{13}C-$\{^1H\}$ CP MAS NMR spectra of the 1:1 blends exhibit remarkably a different pattern, especially for the aromatic region (purple *). After low temperature annealing, the signal is broad and featureless. With further thermal treatment at higher temperature, the signals become better defined. Here, the aromatic region shows only a broad signal flanked by the two aromatic signals originating from H_2F_4TCNQ (purple ◊, Figure 71). The observed broadening results from the numerous degradation products formed during the reaction of the P3HT, especially with the radical anion. The spectra also show the annealing temperature-dependent formation of the radical anion at 41 ppm mentioned earlier (purple ○). The aliphatic region shows a strong broadening especially for the signal corresponding to the α-γ and δ carbon atoms (purple ǂ). In pure P3HT and a lower mixing ratio of 1:16,

these signals are sharp and remain well defined upon thermal treatment. In the sample with 1:1 concentration, these signals can no longer be distinguished.

6.3 Quantitative analysis

With the assignment of the ^{19}F signals to the different redox and protonation states of F_4TCNQ, it is possible to estimate the amount of different redox states of the dopant, depending on the mixing ratio and the applied annealing temperature. In contrast to ^{13}C-{^{1}H} CP-MAS spectra, the fluorine MAS NMR measurements provide well-defined signals in freshly prepared samples without further thermal treatment. ^{19}F-MAS spectra were recorded for all mixing ratios and annealing temperatures. Please note, that a distinction between CTC and ICT state cannot be made via chemical shift resolution by solid state NMR techniques, since both states are considered to be radicals and therefore are summarized here as anion. The spectra recorded directly after solution processing of the doped P3HT films are shown in Figure 72 a. At the lowest molar mixing ratio of 1:16, no signals from F_4TCNQ crystallites were observed and two broad signals at lower ppm values compared to the two sharp peaks of crystalline F_4TCNQ dominate the NMR spectrum. This decrease in the chemical shift value indicates an electron transfer from P3HT to F_4TCNQ, leading to stronger electronic shielding of the fluorine sites. In Figure 72 a, the red line depicts the fluorine signal for the singly reduced species F_4TCNQ$^{\cdot-}$, while the blue line marks the peak associated with the doubly reduced species F_4TCNQ^{2-}. Note that the dianion signal also has a weak shoulder at -148.9 ppm. This shoulder may result from different rotational orientations of the substituents attached to the aromatic core (see also Table 21, DFT calculation).

With an increase in dopant concentration, the double peak of crystalline F_4TCNQ becomes visible in the ^{19}F-MAS spectra, marked by the black lines in Figure 72 a. Since ^{19}F-MAS NMR is quantitative, unlike ^{13}C-CP-MAS NMR, integration of these signals provides insight into the relative distribution of the different F_4TCNQ species in the doped blends. At low doping concentrations, all F_4TCNQ molecules are expected to be dissolved in the P3HT polymer matrix and are thus observed in a reduced oxidation state. At higher concentrations, thermal energy is required to trigger complete electron transfer from the polymer to the dopant. Another aspect that has a major impact on the chemical transformation is that at high doping ratios, most of the F_4TCNQ is in a phase-separated crystalline state. Here, increasing the temperature leads to better mixing of F_4TCNQ and P3HT, allowing for charge transfer between these two molecules and thus to chemical reactions. This is the reason, why with increasing doping ratios only a small percentage of the mixed F_4TCNQ is reduced (Figure 72 b). Annealing to temperatures of 423 K and higher leads to the observed formation of the H_2F_4TCNQ species.
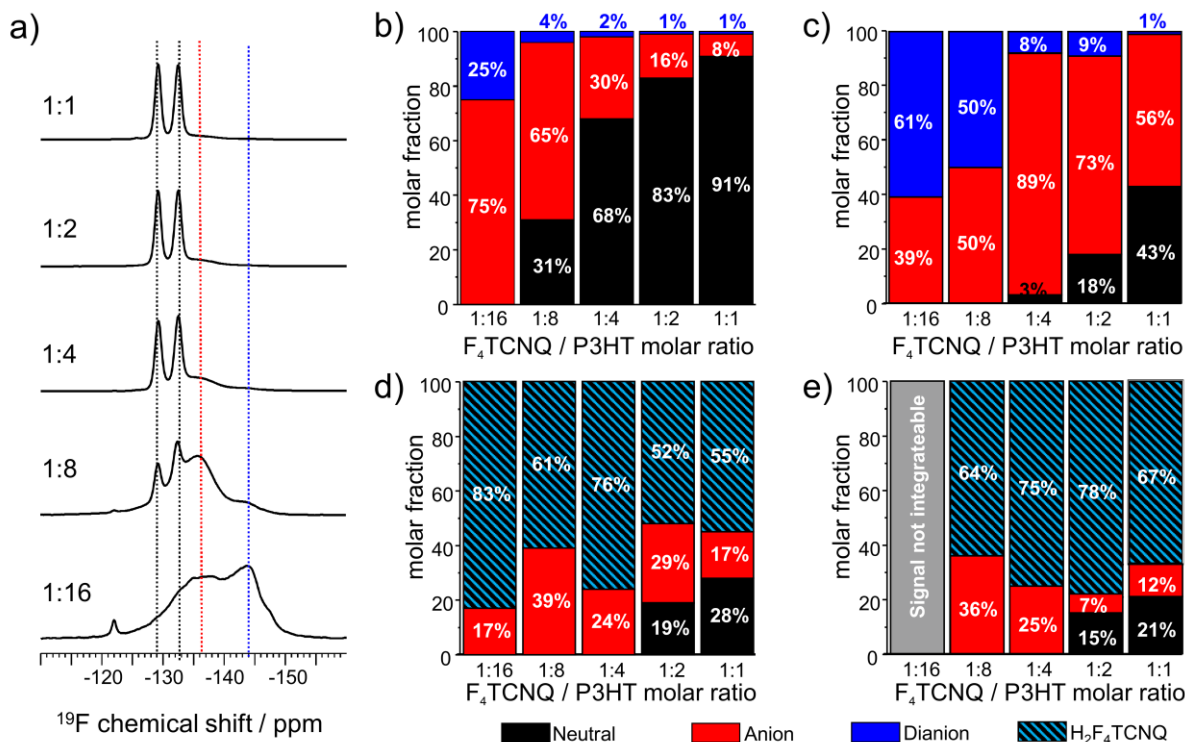
Figure 72 ^{19}F MAS spectra of F$_4$TCNQ:P3HT blends ranging from 1:16 to 1:1, measured after bar coating on SiO$_2$ surface (a). Distribution of different F$_4$TCNQ redox states after processing (b) and distribution of different F$_4$TCNQ redox states after annealing at 393 K (c), 423 K (d) and 453 K (e). Annealing was performed under nitrogen atmosphere. Note that at higher temperatures the F$_4$TCNQ was fully dissolved in the polymer matrix for blending ratios of 1:16, which leads to a featureless, non-integrable signal.

In Figure 72 c, the doubly reduced species was determined by integrating the signal obtained for H$_2$F$_4$TCNQ. Here, the amount of H$_2$F$_4$TCNQ increases up to a concentration of 1:2. At 1:1, the doubly reduced species is formed with a relative amount of only 67%, which is 11% lower than the value that was found for the 1:2 mixing ratio. The reason for this observation is that the high density of positive charges on the polymer is an unfavourable condition that leads to polymer degradation, as mentioned earlier. This results not only into oxidation, but leads also to degradation of the polymer chain into smaller chain fragments via multiple possible reaction channels.

6.4 Solution NMR experiments

To prove this conjecture, the mixed and thermally treated pellets from the MAS rotor after the solid-state NMR measurements were redissolved in d_5-bromobenzene, which was chosen because pure P3HT has a high solubility in this solvent. In order to achieve water and oxygen free conditions, inert gas NMR tubes with sealing Teflon caps were used. While the pellets with low F4TCNQ doping ratios (1:16 and 1:8) showed a strong swelling and colored the solvent orange, the color of the solvent in solutions of the highly doped polymer films with molar ratios of 1:4 and 1:2 remained almost unchanged. The pellet with highest F4TCNQ concentration in molar ratio 1:1 resulted in bromobenzene in a brownish colored solution with dark dispersed particles inside. A photo of the different pellets dissolved in d5-bromobenzene is included in the supporting information.

Diffusion ordered spectroscopy (DOSY) NMR measurements have been used to determine the diffusion coefficients D of the molecules and dissolved molecular fragments from the annealed film pellets of our previous solid-state NMR studies. In the case of the 1:16 F_4TCNQ doped P3HT film sample, the observed diffusion parameters were $D = 1.18 \cdot 10^{-10}$ m^2 s^{-1} expected for the neat dissolved P3HT polymer. The presence of unreacted P3HT polymer chains in solution suggest that not all of the P3HT chains have been involved in covalent cross-linking reactions during the annealing procedure or are kept by strong coulombic interactions in the crosslinked pellet. The DOSY spectrum of the redissolved 1:8 mixture pellet shows the same pattern and diffusion coefficient $D = 1.17 \cdot 10^{-10}$ m^2 s^{-1} expected for a large polymeric molecules. The overall signals intensity, however, was substantially weaker, indicating that much less polymer chains can be dissolved from the annealed pellet. From the annealed P3HT pellets with higher F_4TCNQ concentrations, i.e. molar mixing ratios of 1:4, 1:2, and 1:1, no slow diffusing component (compare 1:16 and 1:8 mixing ratio results) could be extracted and for all extracted components significantly higher diffusion coefficient values comparable to those of the solvent were observed. The diffusion coefficients were found to be $D = 1.3 \cdot 10^{-9}$ m^2 s^{-1} for a mixing ratio of 1:4, $D = 1.59 \cdot 10^{-9}$ m^2 s^{-1} for a mixing ratio of 1:2, and $D = 1.31 \cdot 10^{-9}$ m^2 s^{-1} for a mixing ratio of 1:1. Moreover, the observed small molecular fragments indicate, that chain scission processes has occurred during the annealing procedure. The chain fragments show diffusion coefficients that are about an order of magnitude higher than the diffusion coefficients of the pure polymer. The corresponding DOSY spectra are shown in the supporting information.

In addition to the discussed diffusion parameters obtained for the re-dissolved P3HT polymer and its fragments, a species with a chemical shift value of 4.86 ppm and a diffusion coefficient of $D = 7.16 \cdot 10^{-9}$ m^2 s^{-1} was observed. This species is present in all spectra from a mixing ratio of 1:8 and higher. The obtained ^{1}H-^{19}F-HMBC spectra indicate that this species originates from a fluorinated molecule. This signal was assigned to the dissolved H_2F_4TCNQ species. Note that the chemical shift value obtained

from the ^{1}H solution spectra is significantly lower (about 1 ppm) than that observed in the solid state. This change may result from the free rotation of the substituent groups, leading to an in average more "shielded environment" than in the crystalline phase observed in solid-state NMR experiments.

Another finding from solution NMR experiments was that more than one fluorinated species is present in the re-dissolved annealed pellets from our solid state NMR study. The ^{1}H-^{19}F HMBC spectra mentioned earlier indicate at least two species that can be monitored by proton-fluorine correlation. The 1D-^{19}F solution spectra, however, reveal more fluorinated species formed by the reaction of P3HT with F$_4$TCNQ. The ^{19}F spectra of the re-dissolved 1:16 and 1:1 F4TCNQ/P3HT samples are shown in Figure 73.
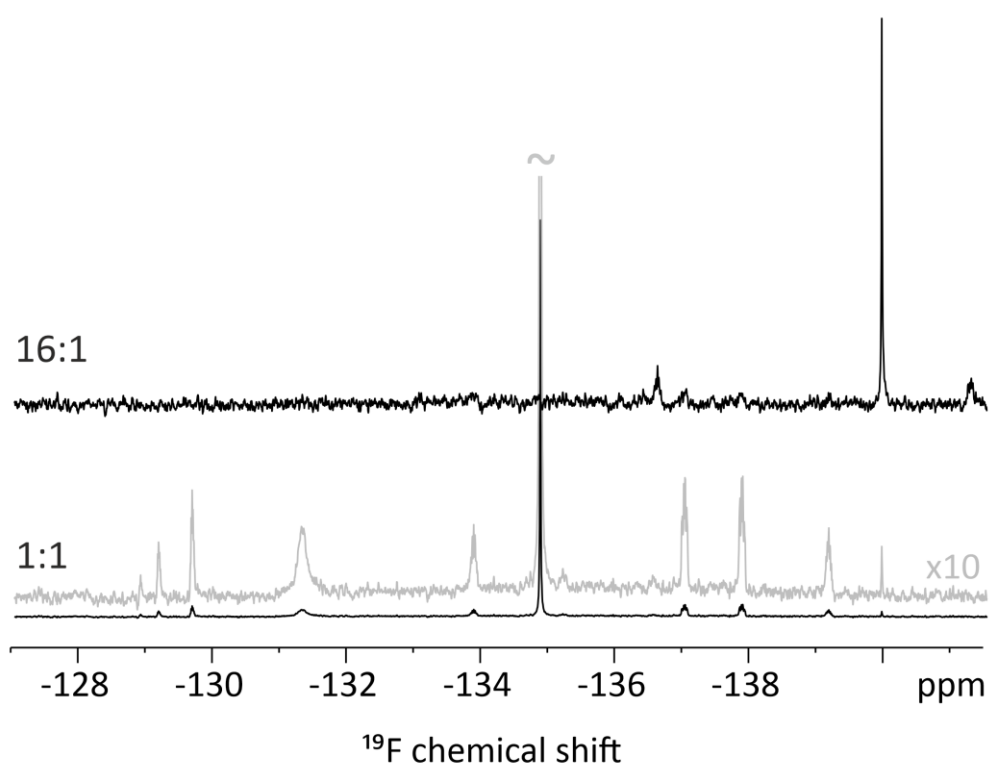
Figure 73 ^{19}F solution NMR spectra obtained from the annealed rotor pellets for 1:16 (top) and 1:1 (bottom) dissolved in bromo-benzene.

These results suggest that the F$_4$TCNQ molecules not only take up hydrogen from the P3HT, but are also capable of forming other reaction products, leading to a widespread distribution of different molecular arrangements and products. The structural elucidation, however, of all these degradation fragments would go far beyond the scope of the study performed in this work. The ^{19}F NMR spectra were presented to provide a brief insight into the wide variety of reaction products that F$_4$TCNQ can form upon annealing with an oxidation-sensitive polymer such as P3HT even under fully inert conditions.

6.5 Conclusions

In section of the thesis, it was shown that thermal annealing of P3HT:F_4TCNQ blends leads to chemical degradation, even under fully inert conditions. It has been observed that predominantly formed species is the protonated form of the dopant, H_2F_4TCNQ. The formation of this neutral species leads to an immediate segregation of the blends and a phase-separated crystallization of this species after cooling to room temperature. It has been shown that this protonation occurs not only under ambient conditions in a humid atmosphere but as well under controlled inert conditions, which is a good indication of radical hydrogen transfer from the polymer side chains to F_4TCNQ molecules. It is assumed that only small amounts of residual water in the films contribute to the protonation reaction. The results presented in this section of the thesis are also in good agreement with IR spectroscopic results obtained by other groups.[153] Their study focused mainly on the formation of the electronically still active HF_4TCNQ$^-$ species, which can be detected by IR spectroscopy. The formation of a crystalline phase, however, has not been detected in the IR study. From the here presented data, it can concluded that both, the radical hydrogen transfer reaction as well as the deprotonation of the P3HT sidechain by HF_4TCNQ$^-$ lead as a sum to the formation of H_2F_4TCNQ. The following mechanism is considered: i) Formation of a CTC complex at processing temperature. ii) Unmixing of F_4TCNQ/P3HT backbone arrangement at high annealing temperatures and thereby formation of the ICT state (F_4TCNQ$^{\cdot-}$ located at the sidechains) and a localized polaron at the P3HT backbone. iii) Hydrogen transfer from the sidechain to F_4TCNQ$^{\cdot-}$ under the formation of HF_4TCNQ$^-$. iv) Transfer of acidic protons from the P3HT to the HF_4TCNQ$^-$ under the formation of H_2F_4TCNQ.

The radical anion state, which has been observed in the investigated samples at ambient temperature, is related to the ICT state. The CTC state was not observed, since no correlations between the fluorine atoms of the F_4TCNQ and the aromatic protons in the P3HT were found. Since the NMR measurements were performed at ambient conditions after each annealing step, however, it cannot be excluded, that the CTC state is formed during the radical formation process upon annealing. The CTC state might be essential at the initial stages of the doping process to provide a partial electron transfer from the thiophene backbone of P3HT to F_4TCNQ molecules. Returning after annealing back to ambient temperatures, the F_4TCNQ$^{\cdot-}$ forms the ICT state, which can then be located via NMR correlation methods between P3HT sidechains. Extending the annealing procedure to even higher temperatures leads then to the chemical reaction which is responsible for the previously mentioned formation of HF_4TCNQ$^-$ (not detected in this work) and H_2F_4TCNQ.

The distribution of the different redox states of F_4TCNQ and it's derivatives after annealing was determined by integration of the ^{19}F MAS NMR spectra for different annealing temperatures and

mixing ratios. This has, according to the current state of knowledge, not reported elsewhere in literature by now.

It has been shown that high doping ratios of F_4TCNQ in P3HT lead to chain scission as a result of an over-oxidation of the polymer. Here it should be emphasized that chain scission is likely to occur even in materials with non-reactive side chains during annealing procedures. In particular, if doping induced formation of too many positive charges in close spatial proximity, the polymer backbone can be destabilized significantly.

The results that are provided with this study narrow down the possible mixing partners for F_4TCNQ for a successful doping application in organic electronic devices. It is also conceivable that other quinoid systems may act as oxidants and thus hydrogen acceptors, leading to a rapid degradation and thus poorly performing organic electronic devices.

7.List of figures

8. List of tables

9. Literature

1. Purcell, E. M., Torrey, H. C. & Pound, R. V. Resonance Absorption by Nuclear Magnetic Moments in a Solid. *Phys. Rev.* **69**, 37–38 (1946).

2. Bloch, F., Hansen, W. W. & Packard, M. The Nuclear Induction Experiment. *Phys. Rev.* **70**, 474–485 (1946).

3. Lauterburg, P. Image formation by induced local interactions. Examples employing nuclear magnetic resonance. 1973 - PubMed. https://pubmed.ncbi.nlm.nih.gov/2663289/.

4. Mansfield, P. & Grannell, P. K. NMR 'diffraction' in solids? *J. Phys. C Solid State Phys.* **6**, L422 (1973).

5. Hennel, J. W. & Klinowski, J. Magic-Angle Spinning: a Historical Perspective. 1–14 (2005) doi:10.1007/B98646.

6. Andrew, E. R., Bradbury, A. & Eades, R. G. Nuclear Magnetic Resonance Spectra from a Crystal rotated at High Speed. *Nat. 1958 1824650* **182**, 1659–1659 (1958).

7. Lowe, I. J. Free Induction Decays of Rotating Solids. *Phys. Rev. Lett.* **2**, 285 (1959).

8. Gullion, T. & Schaefer, J. Rotational-echo double-resonance NMR. *J. Magn. Reson.* **81**, 196–200 (1989).

9. Saalwächter, K. & Schnell, I. REDOR-Based Heteronuclear Dipolar Correlation Experiments in Multi-Spin Systems: Rotor-Encoding, Directing, and Multiple Distance and Angle Determination. *Solid State Nucl. Magn. Reson.* **22**, 154–187 (2002).

10. Gullion, T. & Schaefer, J. Detection of Weak Heteronuclear Dipolar Coupling by Rotational-Echo Double-Resonance Nuclear Magnetic Resonance. *Adv. Magn. Opt. Reson.* **13**, 57–83 (1989).

11. Kotadiya, N. B., Mondal, A., Blom, P. W. M., Andrienko, D. & Wetzelaer, G. J. A. H. A window to trap-free charge transport in organic semiconducting thin films. *Nat. Mater. 2019 1811* **18**, 1182–1186 (2019).

12. Zuo, G., Linares, M., Upreti, T. & Kemerink, M. General rule for the energy of water-induced traps in organic semiconductors. *Nat. Mater.* **18**, 588–593 (2019).

13. Levitt, M. H. Spin Dynamics: Basics of Nuclear Magnetic Resonance. *Wiley* 1–752 (2015).

14. Keeler, J. *Understanding NMR spectroscopy*. (John Wiley and Sons, 2010).

15. Bildsøe, H., Jacobsen, J. P. & Schaumburg, K. Application of density matrix formalism in NMR spectroscopy. I. Development of a calculation scheme and some simple examples. *J. Magn. Reson.* **23**, 137–151 (1976).

16. Jacobsen, J. P., Bildsøe, H. K. & Schaumburg, K. Application of density matrix formalism in NMR spectroscopy. II. The one-spin-1 case in anisotropic phase. *J. Magn. Reson.* **23**, 153–164 (1976).

17. Esvan, Y. J. & Zeinyeh, W. Basics of Fourier Transform Applied to NMR Spectroscopy: An Interactive Open-Source Web Application. *J. Chem. Educ.* **97**, 263–264 (2020).

18. Blunt, J. W. Principles of Fourier-transform nuclear magnetic resonance. *J. Chem. Educ.* **60**,

97–98 (1983).

19. Besghini, D., Mauri, M. & Simonutti, R. Time Domain NMR in Polymer Science: From the Laboratory to the Industry. *Appl. Sci. 2019, Vol. 9, Page 1801* **9**, 1801 (2019).

20. Feike, M. *et al.* Broadband Multiple-Quantum NMR Spectroscopy. *J. Magn. Reson. Ser. A* **122**, 214–221 (1996).

21. Griffin, R. G. Dipolar recoupling in MAS spectra of biological solids. *Nat. Struct. Biol.* **5**, 508–512 (1998).

22. Da Como, E. & von Hauff, E. The WSPC Reference on Organic Electronics: Organic Semiconductors. Materials and Energy Series. Band 1: Basic Concepts, Band 2: Fundamental Aspects of Materials and Applications. Herausgegeben von Jean-Luc Brédas und Seth R. Marder. *Angew. Chemie* **129**, 4995–4996 (2017).

23. Stallinga, P. Low Molecular Weight Organic Semiconductors Electrical Characterization of Organic Electronic Materials and Devices Physical and Chemical Aspects of Organic Electronics From Fundamentals to Functioning Devices Flexible Solar Cells Organic Molecular Solids. (2006).

24. Hamze, R. *et al.* Eliminating nonradiative decay in Cu(I) emitters: >99% quantum efficiency and microsecond lifetime. *Science (80-.).* **363**, 601–606 (2019).

25. Liu, Y., Li, C., Ren, Z., Yan, S. & Bryce, M. R. All-organic thermally activated delayed fluorescence materials for organic light-emitting diodes. *Nat. Rev. Mater. 2018 34* **3**, 1–20 (2018).

26. Di, D. *et al.* High-performance light-emitting diodes based on carbene-metal-amides. *Science (80-.).* **356**, 159–163 (2017).

27. Brédas, J. L., Calbert, J. P., Da Silva Filho, D. A. & Cornil, J. Organic semiconductors: A theoretical characterization of the basic parameters governing charge transport. *Proc. Natl. Acad. Sci. U. S. A.* **99**, 5804–5809 (2002).

28. Coropceanu, V. *et al.* Charge transport in organic semiconductors. *Chem. Rev.* **107**, 926–952 (2007).

29. Mas-Torrent, M. & Rovira, C. Role of molecular order and solid-state structure in organic field-effect transistors. *Chem. Rev.* **111**, 4833–4856 (2011).

30. Martinez, C. R. & Iverson, B. L. Rethinking the term "pi-stacking". *Chem. Sci.* **3**, 2191 (2012).

31. Wang, C., Dong, H., Jiang, L. & Hu, W. Organic semiconductor crystals. *Chem. Soc. Rev.* **47**, 422–500 (2018).

32. Delongchamp, D. M., Kline, R. J., Fischer, D. A., Richter, L. J. & Toney, M. F. Molecular Characterization of Organic Electronic Films. *Adv. Mater.* **23**, 319–337 (2011).

33. Rivnay, J., Mannsfeld, S. C. B., Miller, C. E., Salleo, A. & Toney, M. F. Quantitative determination of organic semiconductor microstructure from the molecular to device scale. *Chem. Rev.* **112**, 5488–5519 (2012).

34. Rivnay, J., Noriega, R., Kline, R. J., Salleo, A. & Toney, M. F. Quantitative analysis of lattice disorder and crystallite size in organic semiconductor thin films. *Phys. Rev. B - Condens. Matter Mater. Phys.* **84**, 045203 (2011).

35. Urban, K. W. Studying atomic structures by aberration-corrected transmission electron microscopy. *Science (80-.).* **321**, 506–510 (2008).

36. Panova, O. *et al.* Diffraction imaging of nanocrystalline structures in organic semiconductor molecular thin films. *Nat. Mater.* **18**, 860–865 (2019).

37. Takacs, C. J., Brady, M. A., Treat, N. D., Kramer, E. J. & Chabinyc, M. L. Quadrites and crossed-chain crystal structures in polymer semiconductors. *Nano Lett.* **14**, 3096–3101 (2014).

38. Brown, S. P. & Spiess, H. W. Advanced solid-state NMR methods for the elucidation of structure and dynamics of molecular, macromolecular, and supramolecular systems. *Chem. Rev.* **101**, 4125–4155 (2001).

39. Hansen, M. R., Graf, R. & Spiess, H. W. Interplay of Structure and Dynamics in Functional Macromolecular and Supramolecular Systems As Revealed by Magnetic Resonance Spectroscopy. (2015) doi:10.1021/acs.chemrev.5b00258.

40. Hansen, M. R., Graf, R. & Spiess, H. W. Interplay of Structure and Dynamics in Functional Macromolecular and Supramolecular Systems As Revealed by Magnetic Resonance Spectroscopy. *Chem. Rev.* **116**, 1272–1308 (2016).

41. Spiess, H. W. 50th Anniversary Perspective: The Importance of NMR Spectroscopy to Macromolecular Science. *Macromolecules* **50**, 1761–1777 (2017).

42. Hansen, M. R., Graf, R. & Spiess, H. W. Solid-state NMR in macromolecular systems: Insights on how molecular entities move. *Acc. Chem. Res.* **46**, 1996–2007 (2013).

43. Selter, P. & Hansen, M. R. Chapter 16:Molecular Chain Packing and Conformation in π-Conjugated Polymers from Solid-state NMR. *New Dev. NMR* **2019**-**January**, 363–386 (2019).

44. Oganov, A. R., Pickard, C. J., Zhu, Q. & Needs, R. J. Structure prediction drives materials discovery. *Nat. Rev. Mater. 2019 45* **4**, 331–348 (2019).

45. Brouwer, D. H. *et al.* A general protocol for determining the structures of molecularly ordered but noncrystalline silicate frameworks. *J. Am. Chem. Soc.* **135**, 5641–5655 (2013).

46. Dudenko, D. *et al.* A strategy for revealing the packing in semicrystalline π-conjugated polymers: Crystal structure of bulk poly-3-hexyl-thiophene (P3HT). *Angew. Chemie - Int. Ed.* **51**, 11068–11072 (2012).

47. Bryce, D. L. NMR crystallography: structure and properties of materials from solid-state nuclear magnetic resonance observables. *IUCrJ* **4**, 350–359 (2017).

48. Pickard, C. J., Salager, E., Pintacuda, G., Elena, B. & Emsley, L. Resolving structures from powders by NMR crystallography using combined proton spin diffusion and plane wave DFT calculations. *J. Am. Chem. Soc.* **129**, 8932–8933 (2007).

49. Chaudhari, S. R. *et al.* Donor–acceptor stacking arrangements in bulk and thin-film high-mobility conjugated polymers characterized using molecular modelling and MAS and surface-enhanced solid-state NMR spectroscopy. *Chem. Sci.* **8**, 3126–3136 (2017).

50. Olivier, Y. *et al.* 25th Anniversary Article: High-Mobility Hole and Electron Transport Conjugated Polymers: How Structure Defines Function. *Adv. Mater.* **26**, 2119–2136 (2014).

51. Suzuki, F., Fukushima, T., Fukuchi, M. & Kaji, H. Refined structure determination of blue-emitting tris(8-hydroxyquinoline) aluminum(III) (Alq3) by the combined use of cross-polarization/magic- angle spinning 13C solid-state NMR and first-principles calculation. *J. Phys. Chem. C* **117**, 18809–18817 (2013).

52. Brus, J. *et al.* Efficient Strategy for Determining the Atomic-Resolution Structure of Micro- and Nanocrystalline Solids within Polymeric Microbeads: Domain-Edited NMR Crystallography. *Macromolecules* **51**, 5364–5374 (2018).

53. Gélinas, S. *et al.* Ultrafast long-range charge separation in organic semiconductor photovoltaic diodes. *Science (80-.).* **343**, 512–516 (2014).

54. Bredas, J. L. When Electrons Leave Holes in Organic Solar Cells. *Science (80-.).* **343**, 492–493 (2014).

55. Schmidt-Rohr, K. & Spiess, H. W. Multidimensional solid-state NMR and polymers.

56. Drescher, M. & Jeschke, G. EPR spectroscopy : applications in chemistry and biology.

57. Niklas, J. & Poluektov, O. G. Charge Transfer Processes in OPV Materials as Revealed by EPR Spectroscopy. *Adv. Energy Mater.* **7**, 1602226 (2017).

58. Biskup, T. Structure-function relationship of organic semiconductors: Detailed insights from time-resolved EPR spectroscopy. *Front. Chem.* **7**, 10 (2019).

59. Liu, Y. *et al.* Application of anisotropic NMR parameters to the confirmation of molecular structure. *Nat. Protoc.* **14**, 217–247 (2019).

60. Kolodziejski, W. & Klinowski, J. Kinetics of cross-polarization in solid-state NMR: A guide for chemists. *Chem. Rev.* **102**, 613–628 (2002).

61. Wu, C. H., Ramamoorthy, A. & Opella, S. J. High-Resolution Heteronuclear Dipolar Solid-State NMR Spectroscopy. *J. Magn. Reson. Ser. A* **109**, 270–272 (1994).

62. De Paëpe, G. *et al.* Transverse Dephasing Optimized Solid-State NMR Spectroscopy. *J. Am. Chem. Soc.* **125**, 13938–13939 (2003).

63. Brinkmann, M. *et al.* Correlation between molecular packing and optical properties in different crystalline polymorphs and amorphous thin films of mer-tris(8-hydroxyquinoline)aluminum(III). *J. Am. Chem. Soc.* **122**, 5147–5157 (2000).

64. Amati, M. & Lelj, F. Luminescent compounds fac- and mer-aluminum tris(quinolin-8-olate). A pure and hybrid density functional theory and time-dependent density functional theory investigation of their electronic and spectroscopic properties. *J. Phys. Chem. A* **107**, 2560–2569 (2003).

65. Kaji, H., Kusaka, Y., Onoyama, G. & Horii, F. CP/MAS 13C NMR characterization of the isomeric states and intermolecular packing in tris(8-hydroxyquinoline) aluminum(III) (Alq 3). *J. Am. Chem. Soc.* **128**, 4292–4297 (2006).

66. Curioni, A. & Andreoni, W. Metal-Alq3 complexes: The nature of the chemical bonding. *J. Am. Chem. Soc.* **121**, 8216–8220 (1999).

67. Tsuboi, T. & Torii, Y. Photoluminescence characteristics of green and blue emitting Alq 3 organic molecules in crystals and thin films. *J. Non. Cryst. Solids* **356**, 2066–2069 (2010).

68. Bohle, A. *et al.* A Generalized Packing Model for Bulk Crystalline Regioregular Poly(3-alkylthiophenes) with Extended Side Chains. *Macromol. Chem. Phys.* **219**, 1700266 (2018).

69. Miller, N. C. *et al.* Use of X-Ray Diffraction, Molecular Simulations, and Spectroscopy to Determine the Molecular Packing in a Polymer-Fullerene Bimolecular Crystal. *Adv. Mater.* **24**, 6071–6079 (2012).

70. Clauss, J., Schmidt-Rohr, K. & Spiess, H. W. Determination of domain sizes in heterogeneous polymers by solid-state NMR. *Acta Polym.* **44**, 1–17 (1993).

71. Schlagnitweit, J. *et al.* A solid-state NMR method to determine domain sizes in multi-component polymer formulations. *J. Magn. Reson.* **261**, 43–48 (2015).

72. Nieuwendaal, R. C. *et al.* Measuring the extent of phase separation in poly-3-hexylthiophene/phenyl- C61-butyric acid methyl ester photovoltaic blends with 1H spin diffusion NMR spectroscopy. *Chem. Mater.* **22**, 2930–2936 (2010).

73. Abate, A. *et al.* Lithium salts as "redox active" p-type dopants for organic semiconductors and their impact in solid-state dye-sensitized solar cells. *Phys. Chem. Chem. Phys.* **15**, 2572–2579 (2013).

74. Cochran, J. E. *et al.* Molecular interactions and ordering in electrically doped polymers: Blends of PBTTT and F4TCNQ. *Macromolecules* **47**, 6836–6846 (2014).

75. Yurash, B. *et al.* Atomic-Level Insight into the Postsynthesis Band Gap Engineering of a Lewis Base Polymer Using Lewis Acid Tris(pentafluorophenyl)borane. *Chem. Mater.* **31**, 6715–6725 (2019).

76. McCulloch, I. *et al.* Liquid-crystalline semiconducting polymers with high charge-carrier mobility. *Nat. Mater. 2006 54* **5**, 328–333 (2006).

77. Schuettfort, T. *et al.* Microstructure of polycrystalline PBTTT films: domain mapping and structure formation. *ACS Nano* **6**, 1849–1864 (2012).

78. Lim, E., Peterson, K. A., Su, G. M. & Chabinyc, M. L. Thermoelectric Properties of Poly(3-hexylthiophene) (P3HT) Doped with 2,3,5,6-Tetrafluoro-7,7,8,8-tetracyanoquinodimethane (F $_4$ TCNQ) by Vapor-Phase Infiltration. *Chem. Mater.* **30**, 998–1010 (2018).

79. Cho, E. *et al.* Three-dimensional packing structure and electronic properties of biaxially oriented poly(2,5-bis(3-alkylthiophene-2-yl)thieno[3,2- b]thiophene) films. *J. Am. Chem. Soc.* **134**, 6177–6190 (2012).

80. Martini, F. *et al.* P3HT/PCBM photoactive materials for solar cells: Morphology and dynamics by means of solid-state NMR. *J. Phys. Chem. C* **117**, 131–139 (2013).

81. Zhang, Q. *et al.* Design of efficient thermally activated delayed fluorescence materials for pure blue organic light emitting diodes. *J. Am. Chem. Soc.* **134**, 14706–14709 (2012).

82. Uoyama, H., Goushi, K., Shizu, K., Nomura, H. & Adachi, C. Highly efficient organic light-emitting diodes from delayed fluorescence. *Nat. 2012 4927428* **492**, 234–238 (2012).

83. Goushi, K., Yoshida, K., Sato, K. & Adachi, C. Organic light-emitting diodes employing efficient reverse intersystem crossing for triplet-to-singlet state conversion. *Nat. Photonics 2012 64* **6**, 253–258 (2012).

84. Baldo, M. A. *et al.* Highly efficient phosphorescent emission from organic electroluminescent devices. *Nat. 1998 3956698* **395**, 151–154 (1998).

85. Adachi, C., Baldo, M. A., Thompson, M. E. & Forrest, S. R. Nearly 100% internal phosphorescence efficiency in an organic light-emitting device. *J. Appl. Phys.* **90**, 5048 (2001).

86. Lee, C. W. & Lee, J. Y. Above 30% External Quantum Efficiency in Blue Phosphorescent Organic Light-Emitting Diodes Using Pyrido[2,3-b]indole Derivatives as Host Materials. *Adv. Mater.* **25**, 5450–5454 (2013).

87. Im, Y. *et al.* Molecular Design Strategy of Organic Thermally Activated Delayed Fluorescence Emitters. *Chem. Mater.* **29**, 1946–1963 (2017).

88. Aizenshtat, Z., Klein, E., Weiler-Feilchenfeld, H. & Bergmann, E. D. Conformational Studies on Xanthene, Thioxanthene and Acridan. *Isr. J. Chem.* **10**, 753–763 (1972).

89. Li, Z. Z., Liao, L. S. & Wang, X. D. Controllable Synthesis of Organic Microcrystals with Tunable Emission Color and Morphology Based on Molecular Packing Mode. *Small* **14**, 1702952 (2018).

90.   Wu, J. J. *et al.* Tunable Emission Color and Morphology of Organic Microcrystals by a "Cocrystal" Approach. *Adv. Opt. Mater.* **6**, (2018).

91.   Han, M. *et al.* 1.42-Fold Enhancement of Blue OLED Device Performance by Simply Changing Alkyl Groups on the Acridine Ring. *Cell Reports Phys. Sci.* **1**, 100252 (2020).

92.   Li, Q. & Li, Z. Molecular Packing: Another Key Point for the Performance of Organic and Polymeric Optoelectronic Materials. *Acc. Chem. Res.* **53**, 962–973 (2020).

93.   Pingel, P. *et al.* Charge-transfer localization in molecularly doped thiophene-based donor polymers. *J. Phys. Chem. Lett.* **1**, 2037–2041 (2010).

94.   Zhang, X. *et al.* Thermally Activated Delayed Fluorescence of Aggregates Induced by Strong π–π Interactions and Reversible Dual-Responsive Luminescence Switching. *CCS Chem.* **4**, 625–637 (2022).

95.   Nicolai, H. T. *et al.* Unification of trap-limited electron transport in semiconducting polymers. *Nat. Mater. 2012 1110* **11**, 882–887 (2012).

96.   Kotadiya, N. B. *et al.* Universal strategy for Ohmic hole injection into organic semiconductors with high ionization energies. *Nat. Mater. 2018 174* **17**, 329–334 (2018).

97.   Massiot, D. *et al.* Modelling one- and two-dimensional solid-state NMR spectra. *Magn. Reson. Chem.* **40**, 70–76 (2002).

98.   Fiat, D., Reuben, J. & Folman, M. NMR Relaxation Mechanisms at Solid—Gas Interfaces. CH3OH, CD3OH, and CH3OD Adsorbed on Porous Glass. *J. Chem. Phys.* **46**, 4453–4456 (1967).

99.   Haber, S. & Leskes, M. What Can We Learn from Solid State NMR on the Electrode–Electrolyte Interface? *Adv. Mater.* **30**, 1706496 (2018).

100.   Marchetti, A. *et al.* Understanding Surface and Interfacial Chemistry in Functional Nanomaterials via Solid-State NMR. *Adv. Mater.* **29**, 1605895 (2017).

101.   Yaghmaeiyan, N., Mirzaei, M. & Bamoniri, A. The study of stereoselectivity and mesomeric effect of N-nitrosamines via 1H NMR spectroscopy. *Struct. Chem.* 1–8 (2023) doi:10.1007/S11224-022-02109-5/METRICS.

102.   Lee, G. S. H., Taylor, R. C., Dawson, M., Kannangara, G. S. K. & Wilson, M. A. High-resolution solid state 13C nuclear magnetic resonance spectra of 3,4-methylenedioxyamphetamine hydrochloride and related compounds and their mixtures with lactose. *Solid State Nucl. Magn. Reson.* **16**, 225–237 (2000).

103.   Roos, M., Mandala, V. S. & Hong, M. Determination of Long-Range Distances by Fast Magic-Angle-Spinning Radiofrequency-Driven 19F-19F Dipolar Recoupling NMR. *J. Phys. Chem. B* **122**, 9302 (2018).

104.   Horsewill, A. J. & Tomsah, I. B. I. Bi-exponential nuclear spin-lattice relaxation in solid hexafluoroacetylacetone. *Solid State Nucl. Magn. Reson.* **2**, 61–72 (1993).

105.   Macho, V., Brombacher, L. & Spiess, H. W. The NMR-WEBLAB: An internet approach to NMR lineshape analysis. *Appl. Magn. Reson.* **20**, 405–432 (2001).

106.   Pasveer, W. F. *et al.* Unified description of charge-carrier mobilities in disordered semiconducting polymers. *Phys. Rev. Lett.* **94**, 206601 (2005).

107.   Jorgensen, W. L. & Tirado-Rives, J. The OPLS Potential Functions for Proteins. Energy Minimizations for Crystals of Cyclic Peptides and Crambin. *J. Am. Chem. Soc.* **110**, 1657–1666 (1988).

108. Jorgensen, W. L., Maxwell, D. S. & Tirado-Rives, J. Development and testing of the OPLS all-atom force field on conformational energetics and properties of organic liquids. *J. Am. Chem. Soc.* **118**, 11225–11236 (1996).

109. Stanzione, F., Giangreco, I. & Cole, J. C. Use of molecular docking computational tools in drug discovery. *Prog. Med. Chem.* **60**, 273–343 (2021).

110. Zhang, K. *et al.* Solid-State Effect Induced Thermally Activated Delayed Fluorescence with Tunable Emission: A Multiscale Study. *J. Phys. Chem. A* **124**, 8540–8550 (2020).

111. Řezáč, J. Non-Covalent Interactions Atlas Benchmark Data Sets 2: Hydrogen Bonding in an Extended Chemical Space. *J. Chem. Theory Comput.* **16**, 6305–6316 (2020).

112. Sirohiwal, A., Berraud-Pache, R., Neese, F., Izsák, R. & Pantazis, D. A. Accurate Computation of the Absorption Spectrum of Chlorophyll a with Pair Natural Orbital Coupled Cluster Methods. *J. Phys. Chem. B* **124**, 8761–8771 (2020).

113. Thakur, K. *et al.* Quantifying Exciton Annihilation Effects in Thermally Activated Delayed Fluorescence Materials. (2021) doi:10.1002/adom.202101784.

114. Salzmann, I., Heimel, G., Oehzelt, M., Winkler, S. & Koch, N. Molecular Electrical Doping of Organic Semiconductors: Fundamental Mechanisms and Emerging Dopant Design Rules. *Accounts of Chemical Research* vol. 49 370–378 (2016).

115. Jacobs, I. E. & Moulé, A. J. Controlling Molecular Doping in Organic Semiconductors. *Advanced Materials* vol. 29 (2017).

116. Jacobs, I. E. *et al.* Polymorphism controls the degree of charge transfer in a molecularly doped semiconducting polymer. *Mater. Horizons* **5**, 655–660 (2018).

117. Stanfield, D. A., Wu, Y., Tolbert, S. H. & Schwartz, B. J. Controlling the Formation of Charge Transfer Complexes in Chemically Doped Semiconducting Polymers. *Chem. Mater.* **33**, 2343–2356 (2021).

118. Hamidi-Sakr, A. *et al.* A Versatile Method to Fabricate Highly In-Plane Aligned Conducting Polymer Films with Anisotropic Charge Transport and Thermoelectric Properties: The Key Role of Alkyl Side Chain Layers on the Doping Mechanism. *Adv. Funct. Mater.* **27**, 1700173 (2017).

119. Scholes, D. T. *et al.* The Effects of Crystallinity on Charge Transport and the Structure of Sequentially Processed F4TCNQ-Doped Conjugated Polymer Films. *Adv. Funct. Mater.* **27**, (2017).

120. Meneghettim, M. & Pecile, C. Charge-transfer organic crystals: Molecular vibrations and spectroscopic effects of electron-molecular vibration coupling of the strong electron acceptor TCNQF4. *J. Chem. Phys.* **84**, 4149–4162 (1986).

121. Kampar, E. & Neilands, O. Degree of Charge Transfer in Donor–Acceptor Systems of the π–π Type. *Russ. Chem. Rev.* **55**, 334–342 (1986).

122. Haworth, N. L. *et al.* Diagnosis of the Redox Levels of TCNQF $_4$ Compounds Using Vibrational Spectroscopy. *Chempluschem* **79**, 962–972 (2014).

123. Gao, J. *et al.* The effect of 2,3,5,6-tetrafluoro-7,7,8,8-tetracyanoquinodimethane charge transfer dopants on the conformation and aggregation of poly(3-hexylthiophene). *J. Mater. Chem. C* **1**, 5638–5646 (2013).

124. Salzmann, I. & Heimel, G. Toward a comprehensive understanding of molecular doping organic semiconductors (review). *J. Electron Spectros. Relat. Phenomena* **204**, 208–222 (2015).

125. Méndez, H. *et al.* Charge-transfer crystallites as molecular electrical dopants. *Nat. Commun.* **6**,

1–11 (2015).

126. Jacobs, I. E. *et al.* Comparison of solution-mixed and sequentially processed P3HT:F4TCNQ films: effect of doping-induced aggregation on film morphology. *J. Mater. Chem. C* **4**, 3454–3466 (2016).

127. Hynynen, J. *et al.* Enhanced Electrical Conductivity of Molecularly p-Doped Poly(3-hexylthiophene) through Understanding the Correlation with Solid-State Order. *Macromolecules* **50**, 8140–8148 (2017).

128. Neelamraju, B., Watts, K. E., Pemberton, J. E. & Ratcliff, E. L. Correlation of Coexistent Charge Transfer States in F 4 TCNQ-Doped P3HT with Microstructure. *J. Phys. Chem. Lett.* **9**, 6871–6877 (2018).

129. Watts, K. E., Neelamraju, B., Ratcliff, E. L. & Pemberton, J. E. Stability of Charge Transfer States in F4TCNQ-Doped P3HT. *Chem. Mater.* **31**, 6986–6994 (2019).

130. Yee, P. Y., Scholes, D. T., Schwartz, B. J. & Tolbert, S. H. Dopant-Induced Ordering of Amorphous Regions in Regiorandom P3HT. *J. Phys. Chem. Lett.* **10**, 4929–4934 (2019).

131. Chappell, J. S. *et al.* Degree of Charge Transfer in Organic Conductors by Infrared Absorption Spectroscopy. *J. Am. Chem. Soc.* **103**, 2442–2443 (1981).

132. Aziz, E. F. *et al.* Localized charge transfer in a molecularly doped conducting polymer. *Adv. Mater.* **19**, 3257–3260 (2007).

133. Gao, J., Niles, E. T. & Grey, J. K. Aggregates promote efficient charge transfer doping of Poly(3-hexylthiophene). *J. Phys. Chem. Lett.* **4**, 2953–2957 (2013).

134. Duong, D. T., Wang, C., Antono, E., Toney, M. F. & Salleo, A. The chemical and structural origin of efficient p-type doping in P3HT. *Org. Electron.* **14**, 1330–1336 (2013).

135. Pingel, P. & Neher, D. Comprehensive picture of p-type doping of P3HT with the molecular acceptor F4TCNQ. *Phys. Rev. B - Condens. Matter Mater. Phys.* **87**, 115209 (2013).

136. Lu, G. *et al.* Moderate doping leads to high performance of semiconductor/insulator polymer blend transistors. *Nat. Commun.* **4**, 1–8 (2013).

137. Méndez, H. *et al.* Doping of organic semiconductors: Impact of dopant strength and electronic coupling. *Angew. Chemie - Int. Ed.* **52**, 7751–7755 (2013).

138. Watts, K. E., Neelamraju, B., Ratcliff, E. L. & Pemberton, J. E. Stability of Charge Transfer States in F 4 TCNQ-Doped P3HT. *Chem. Mater.* **31**, 6986–6994 (2019).

139. Aoyama, Y. *et al.* Initial photooxidation mechanism leading to reactive radical formation of polythiophene derivatives. *Polym. J.* **47**, 26–30 (2015).

140. Woo, T. G. *et al.* Unveiling the Complexity of the Degradation Mechanism of Semiconducting Organic Polymers: Visible-Light-Induced Oxidation of P3HT Films on ZnO/ITO under Atmospheric Conditions. *J. Phys. Chem. C* **121**, 18692–18701 (2017).

141. Lei, X., Zhang, F., Song, T. & Sun, B. P-type doping effect on the performance of organic-inorganic hybrid solar cells. *Appl. Phys. Lett.* **99**, 233305 (2011).

142. Watts, K. E., Clary, K. E., Lichtenberger, D. L. & Pemberton, J. E. FTIR Spectroelectrochemistry of F4TCNQ Reduction Products and Their Protonated Forms. *Anal. Chem.* **92**, 7154–7161 (2020).

143. Sai, N., Leung, K., Zádor, J. & Henkelman, G. First principles study of photo-oxidation degradation mechanisms in P3HT for organic solar cells. *Phys. Chem. Chem. Phys.* **16**, 8092–

8099 (2014).

144. Rodrigues, A. *et al.* Thermal stability of P3HT and P3HT:PCBM blends in the molten state. *Polym. Test.* **32**, 1192–1201 (2013).

145. Nieuwendaal, R. C., Snyder, C. R. & Delongchamp, D. M. Measuring order in regioregular poly(3-hexylthiophene) with solid-state 13C CPMAS NMR. *ACS Macro Lett.* **3**, 130–135 (2014).

146. Nieuwendaal, R. C. How to measure absolute P3HT crystallinity via ^{13} C CPMAS NMR. *Magn. Reson. Chem.* **54**, 740–747 (2016).

147. Chen, L. *et al.* Fine-tuning the solid-state ordering and thermoelectric performance of regioregular P3HT analogues by sequential oxygen-substitution of carbon atoms along the alkyl side chains. *J. Mater. Chem. C* **7**, 2333–2344 (2019).

148. Ji, L. F., Fan, J. X., Zhang, S. F. & Ren, A. M. Theoretical study on the charge transport in single crystals of TCNQ, F2-TCNQ and F4-TCNQ. *Phys. Chem. Chem. Phys.* **20**, 3784–3794 (2018).

149. Becke, A. D. Density-functional thermochemistry. III. The role of exact exchange. *J. Chem. Phys.* **98**, 5648–5652 (1993).

150. Lee, C., Yang, W. & Parr, R. G. Development of the Colle-Salvetti correlation-energy formula into a functional of the electron density. *Phys. Rev. B* **37**, 785–789 (1988).

151. Vosko, S. H., Wilk, L. & Nusair, M. Accurate spin-dependent electron liquid correlation energies for local spin density calculations: a critical analysis. *Can. J. Phys.* **58**, 1200–1211 (1980).

152. Stephens, P. J., Devlin, F. J., Ashvar, C. S., Chabalowski, C. F. & Frisch, M. J. Theoretical calculation of vibrational circular dichroism spectra. *Faraday Discuss.* **99**, 103–119 (1994).

153. Watts, K. E. *et al.* Thermally Induced Formation of HF4TCNQ-in F4TCNQ-Doped Regioregular P3HT. *J. Phys. Chem. Lett.* **11**, 6586–6592 (2020).

9. Appendix

NMR Spectrometers and standards

500 MHz Wide Bore System

The 500 MHz NMR system is controled by a Bruker Avance III console with four high power RF channels. In this work, a 2.5 mm MAS ^{1}H-^{19}F-X probehead was mainly used to study the respective systems and to record ^{19}-F MAS and ^{19}F-^{1}H correlation spectra as well as T_1 relaxation times and REPT-HDOR experiments.

700 MHz Standard Bore System

The 700 MHz spectrometer is controled by a Bruker Avance III console configured for double resonance experiments under fast MAS and HR-MAS NMR experiments with 2H lock. In this thesis a 1.3 mm MAS ^{1}H-X, a wide and a low range 2.5 mm MAS ^{1}H-X were used mainly to record ^{1}H-^{13}C HETCOR spectra and ^{19}F-MAS spectra of single crystals. Solution experiments were performed at the same system equipped with a QXI probehead.

850 MHz Standard Bore System

The 850 MHz system is equipped with 4 channels plus 2H lock channel. This NMR spectrometer can be used for high resolution NMR studies with a Bruker SX40 sample changer or for solid state NMR measurements with a Bruker MAS3 unit. Variable temperature measurements can be performed in the temperature range from 200 - 400 K with a BCUII cooling unit controled by a BSVT temperature unit. . In this thesis a 1.3 mm MAS ^{1}H-X and a 2.5 mm MAS ^{1}H-X probehead were used to record ^{1}H and ^{13}C MAS experiments.

NMR standards

Solution NMR experiments were referenced with the following standards (Bruker standard samples):

^{1}H: Tetramethylsilane

^{13}C: Tetramethylsilane

^{19}F: Hexafluorobenze

Solid state NMR experiments were referenced with the following standards:

^{1}H: ^{13}C*-L-Alanine

^{13}C: ^{13}C*-L-Alanine

^{19}F: Teflon

Chemicals

The TADF samples used in this thesis were synthesized and purified by Oskar Sachnik, Department of molecular electronics, MPIP, Mainz.

P3HT and F_4TCNQ were obtained from the company Ossila and used without further purification.

NMR solvents for solution experiments were purchased from the company Deutero.

Solvents for crystal growth were obtained from the company Sigma Aldrich.
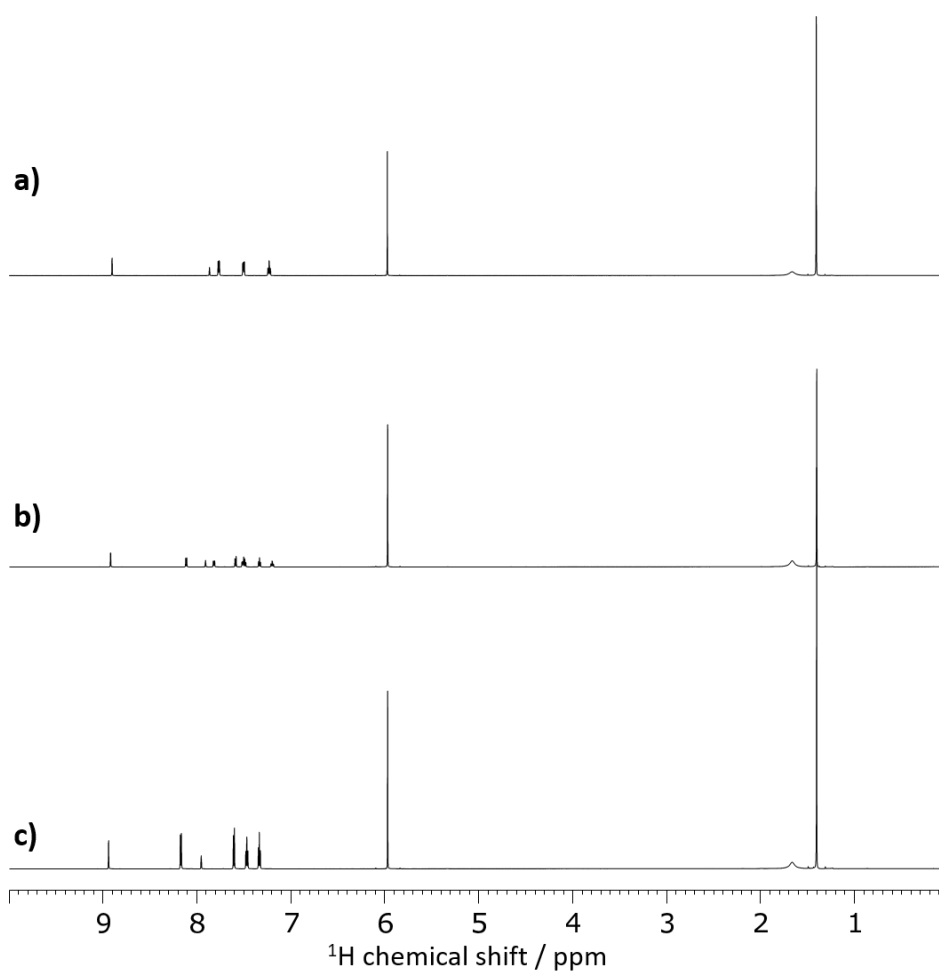
Appendix 1 ^{1}H spectra of the compounds 1a (c), 1b (b) and 1c (a) measured in TCE and RT at a field of 700 MHz.
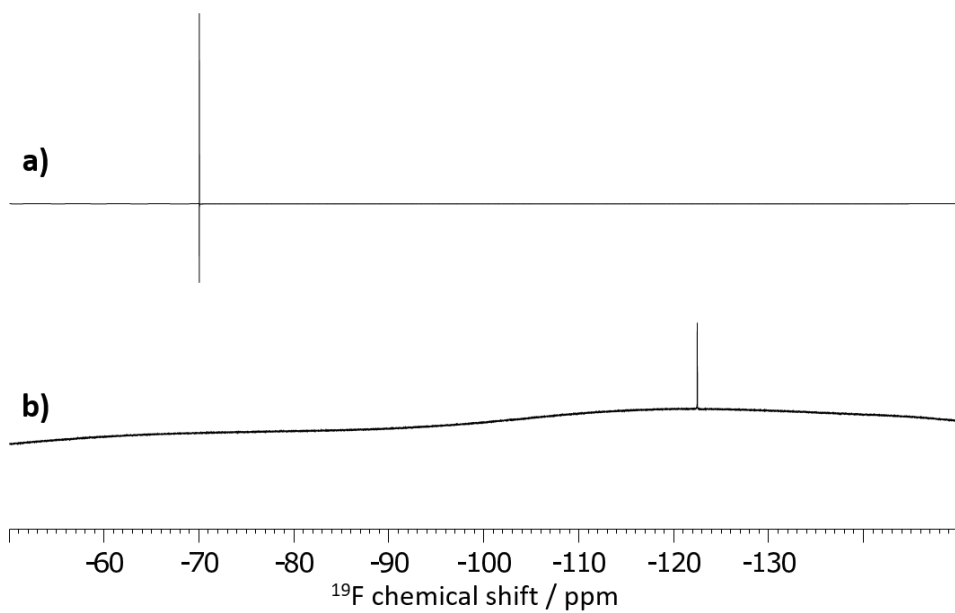
Appendix 2 ^{19}F spectra of the compounds 1a (b) and 1b (a) measured in TCE and RT at a field of 700 MHz.
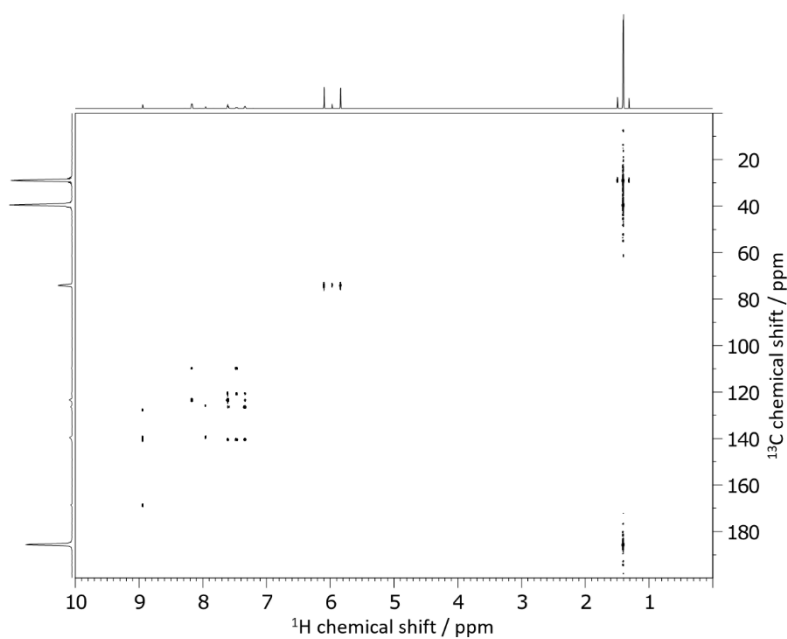
Appendix 3 ^{1}H-^{13}C HMBC spectrum of the compound 1a measured in TCE and RT at a field of 700 MHz.
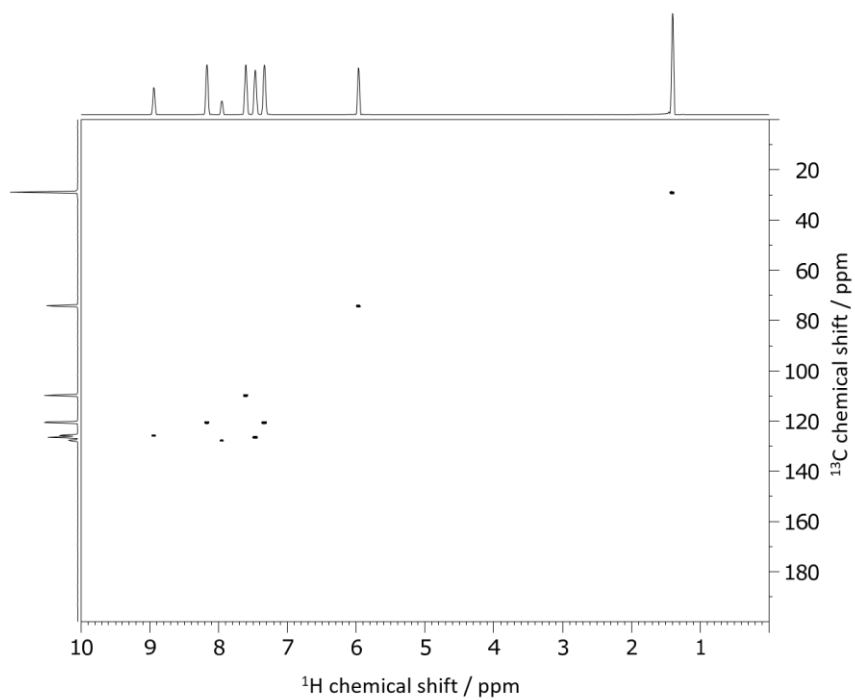
Appendix 4 ^{1}H-^{13}C HMBC spectrum of the compound 1a measured in TCE and RT at a field of 700 MHz.
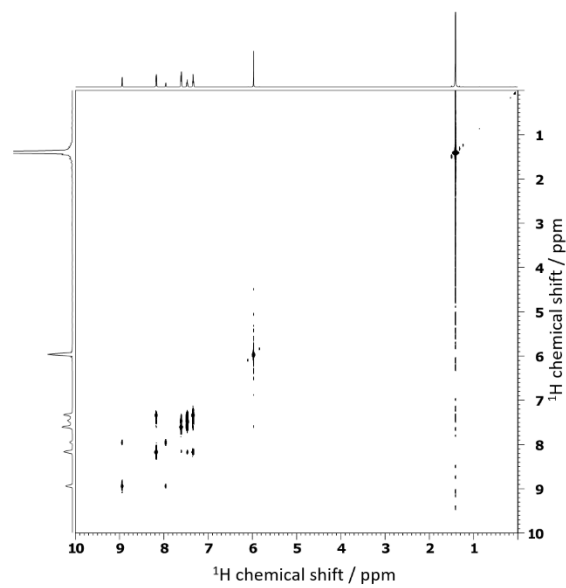
Appendix 5 ^{1}H-^{1}H COSY spectrum of the compound 1a measured in TCE and RT at a field of 700 MHz.

Appendix 6 ^{1}H-^{1}H NOESY spectrum of the compound 1a measured in TCE and RT at a field of 700 MHz.

Appendix 7 ^{1}H-^{13}C HMBC spectrum of the compound 1b measured in TCE and RT at a field of 700 MHz.
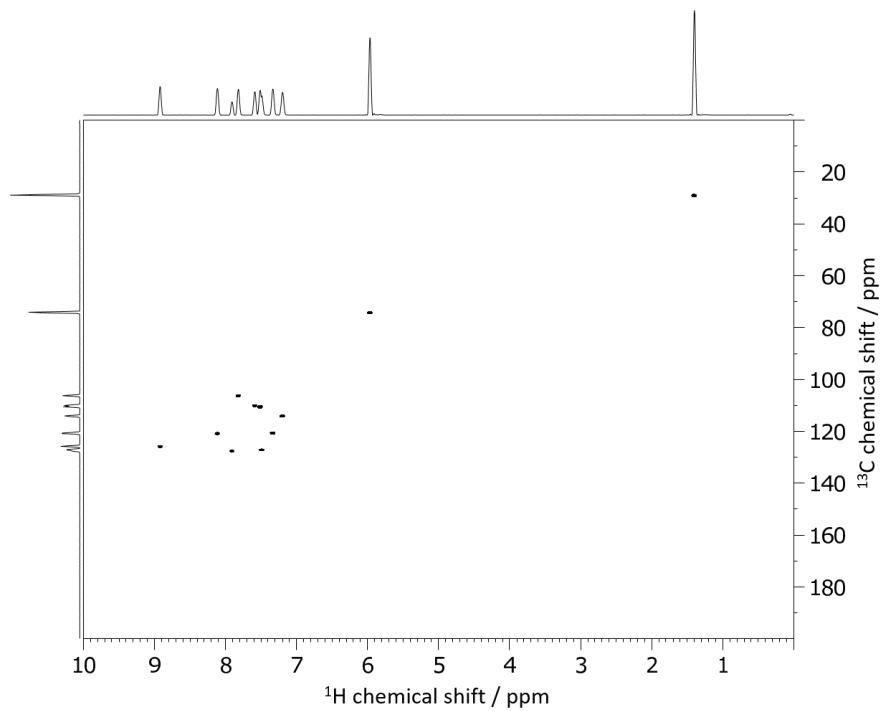
Appendix 8 ^{1}H-^{13}C HSQC spectrum of the compound 1b measured in TCE and RT at a field of 700 MHz.
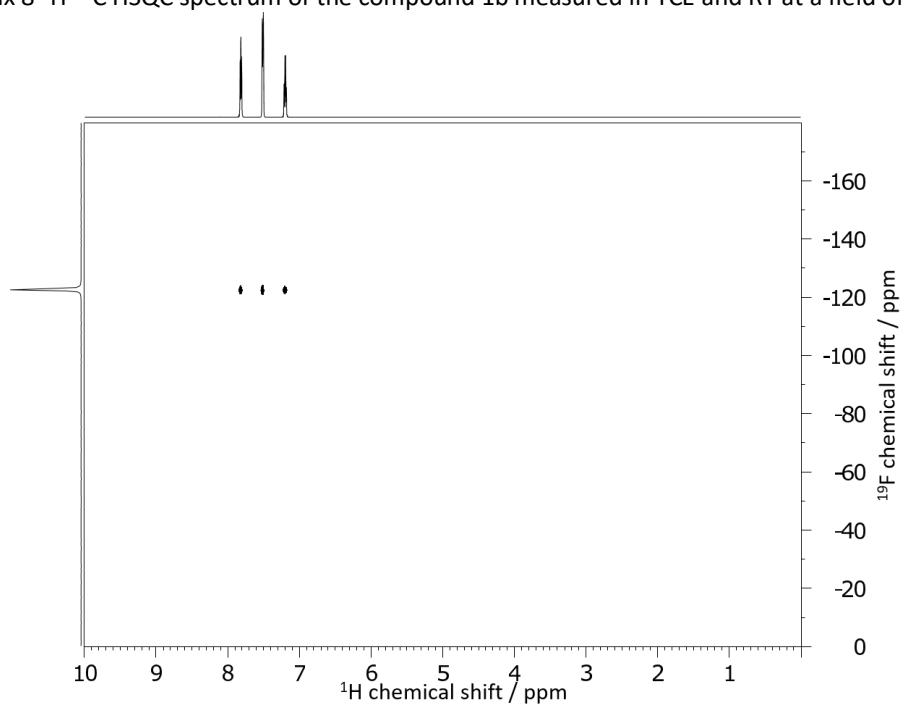
Appendix 9 ^{1}H-^{19}F HMBC spectrum of the compound 1b measured in TCE and RT at a field of 700 MHz.
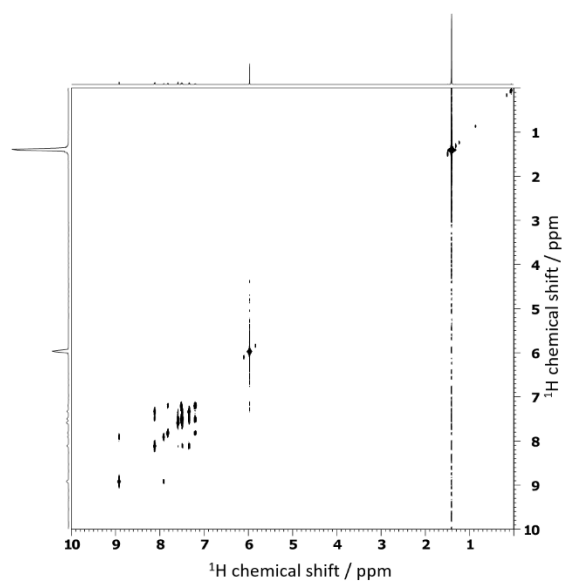
Appendix 10 ¹H-¹H COSY spectrum of the compound 1b measured in TCE and RT at a field of 700 MHz.
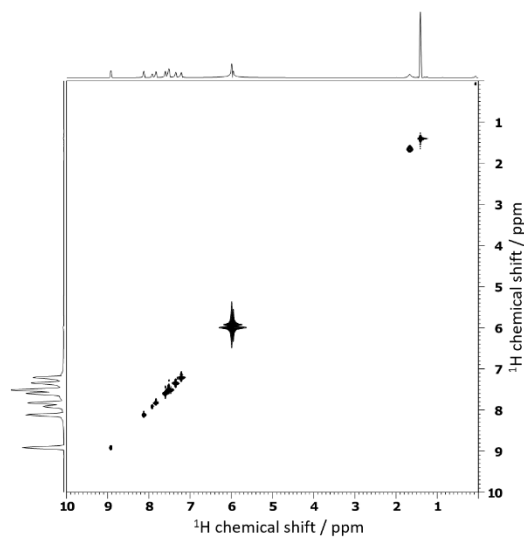
Appendix 11¹H-¹³C HMBC spectrum of the compound 1b measured in TCE and RT at a field of 700 MHz.
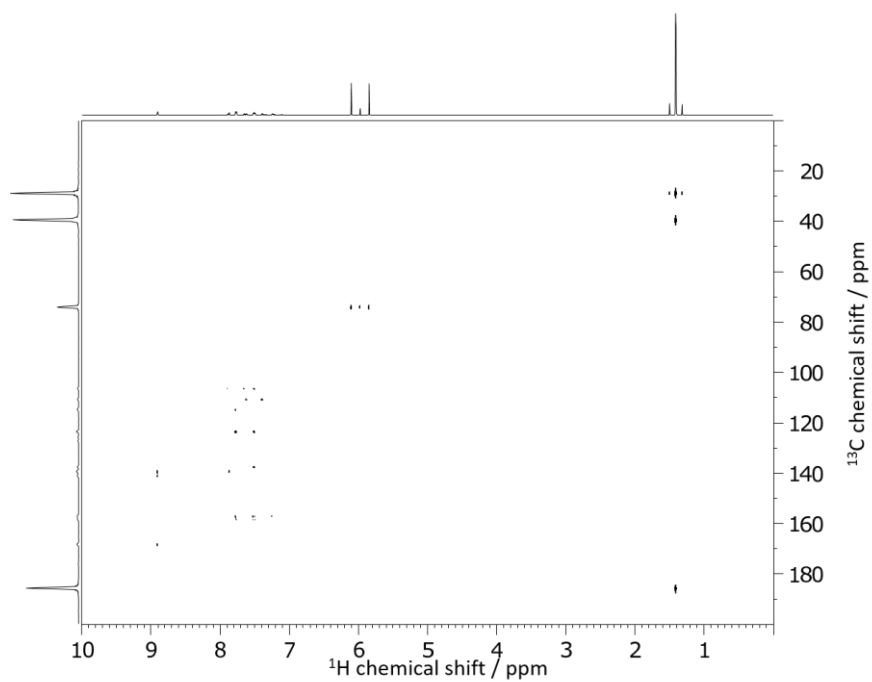
Appendix 12 ^{1}H-^{13}C HMBC spectrum of the compound 1c measured in TCE and RT at a field of 700 MHz.
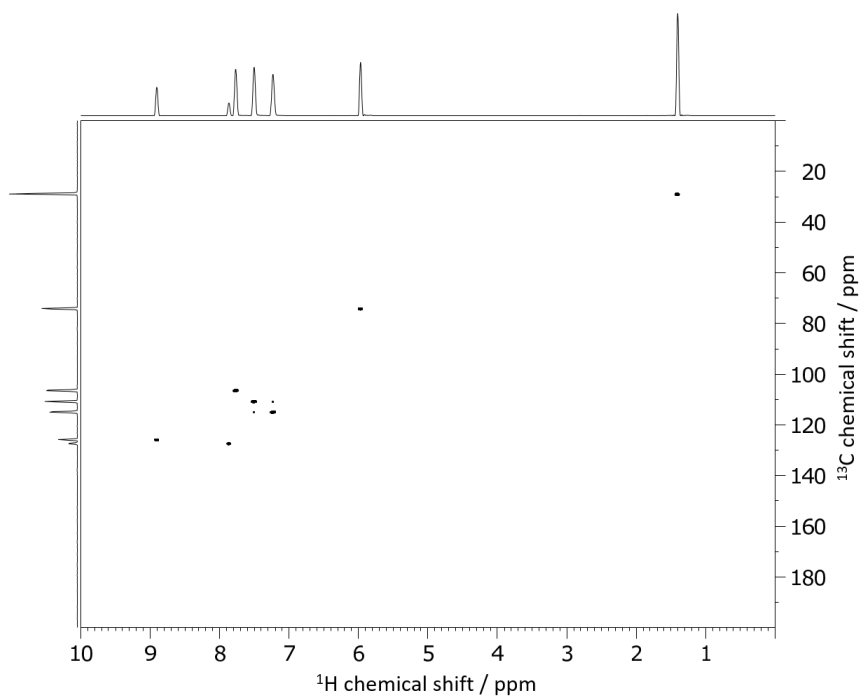
Appendix 13 ^{1}H-^{13}C HSQC spectrum of the compound 1c measured in TCE and RT at a field of 700 MHz.
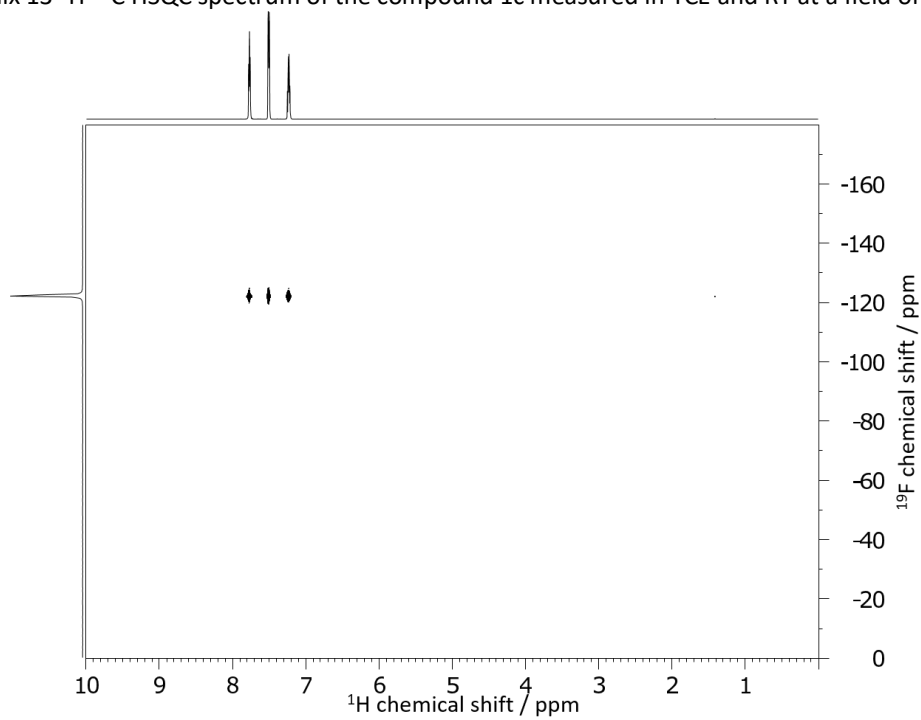
Appendix 14 ^{1}H-^{19}F HMBC spectrum of the compound 1c measured in TCE and RT at a field of 700 MHz.
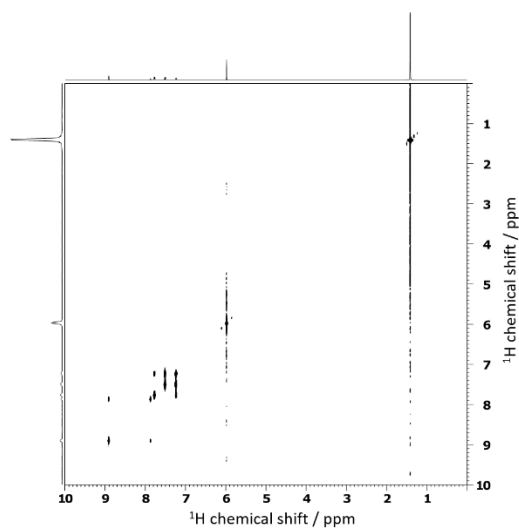
Appendix 15 ^{1}H-^{1}H COSY spectrum of the compound 1c measured in TCE and RT at a field of 700 MHz.
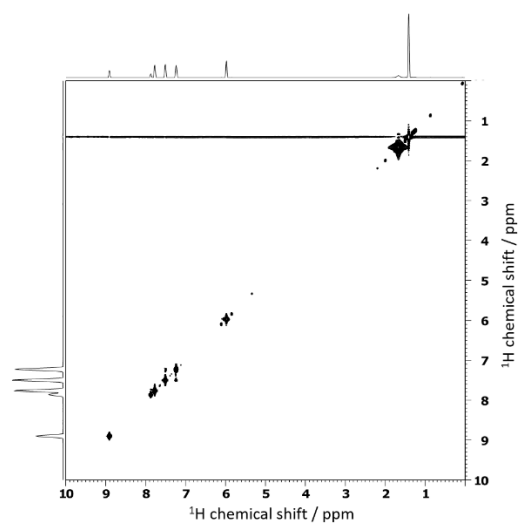
Appendix 16 ^{1}H-^{1}H HSQC spectrum of the compound 1c measured in TCE and RT at a field of 700 MHz.
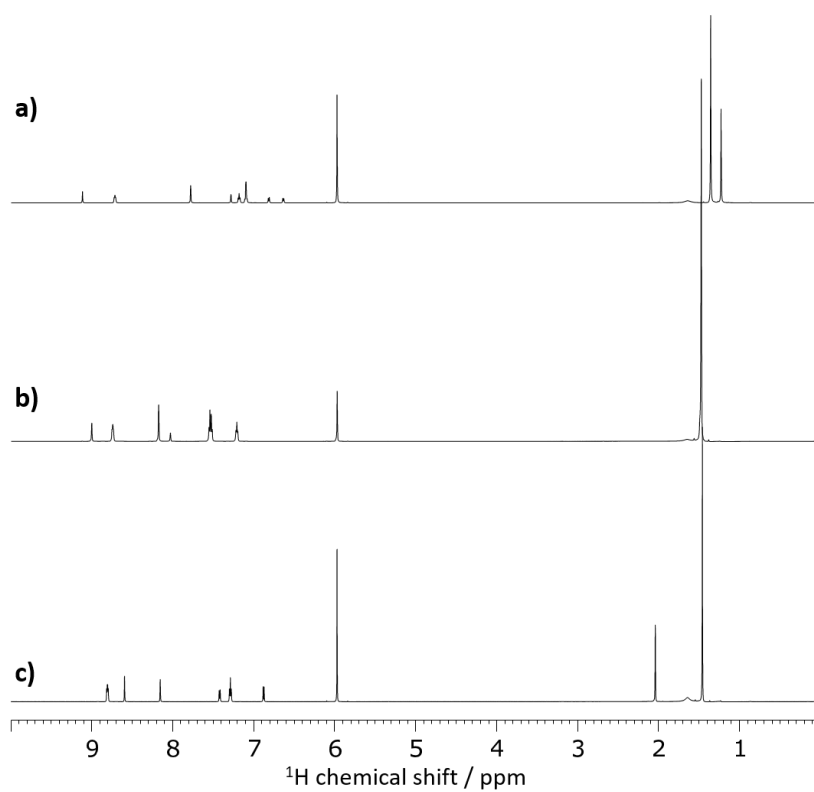
Appendix 17 ^{1}H spectra of the compounds 2a (c), 2b (b) and 2c (a) measured in TCE and RT at a field of 700 MHz.
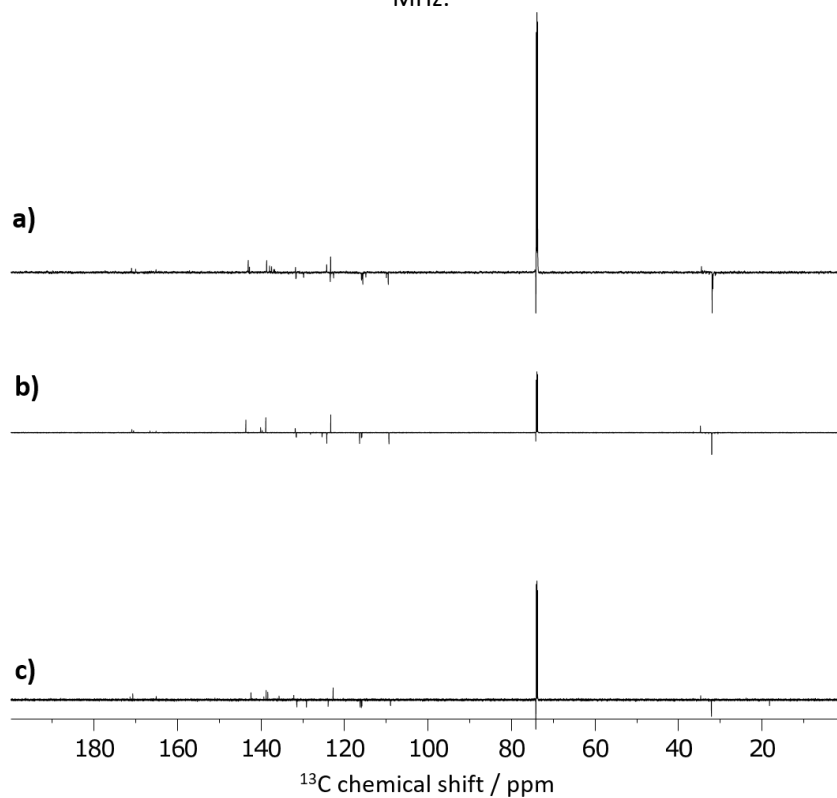
Appendix 18 ^{13}C spectra of the compounds 2a (c), 2b (b) and 2c (a) measured in TCE and RT at a field of 700 MHz.
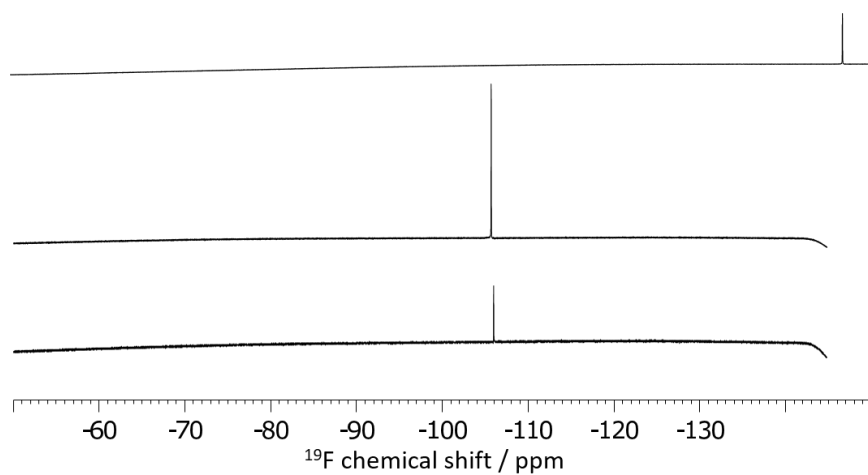
Appendix 19- ^{19}F spectra of the compounds 2a (c), 2b (b) and 2c (a) measured in TCE and RT at a field of 700 MHz.
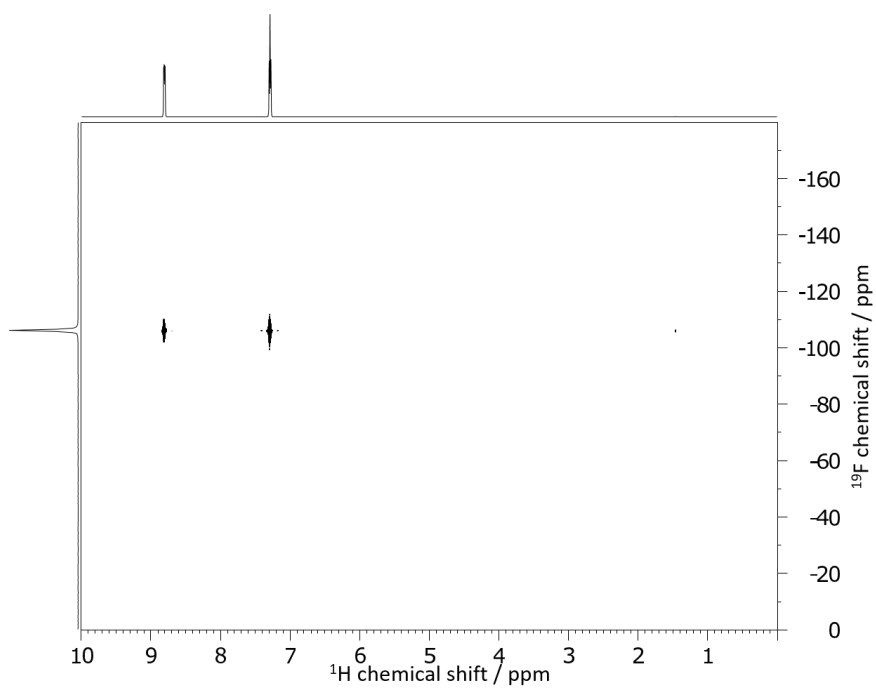
Appendix 20 ^{1}H-^{19}F HMBC spectrum of the compound 2a measured in TCE and RT at a field of 700 MHz.
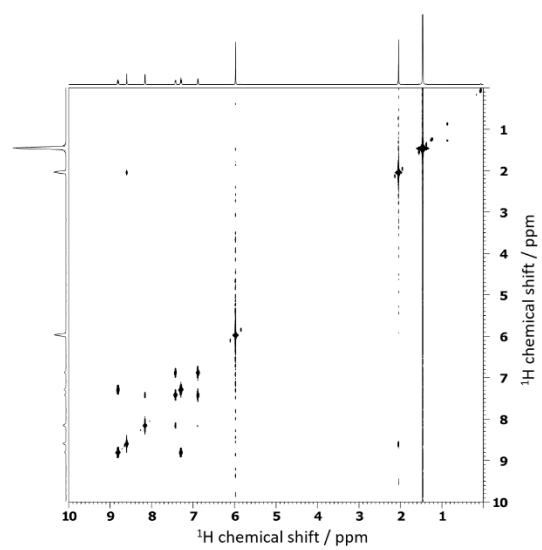
Appendix 21 ^{1}H-^{1}H COSY spectrum of the compound 2a measured in TCE and RT at a field of 700 MHz.
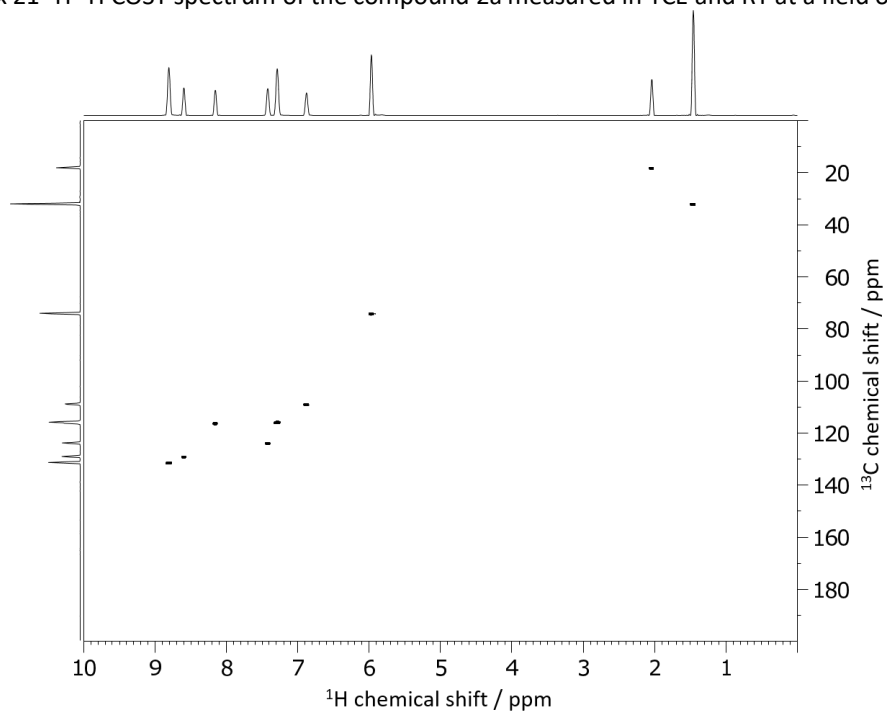
Appendix 22 ^{1}H-^{13}C HSQC spectrum of the compound 2a measured in TCE and RT at a field of 700 MHz.
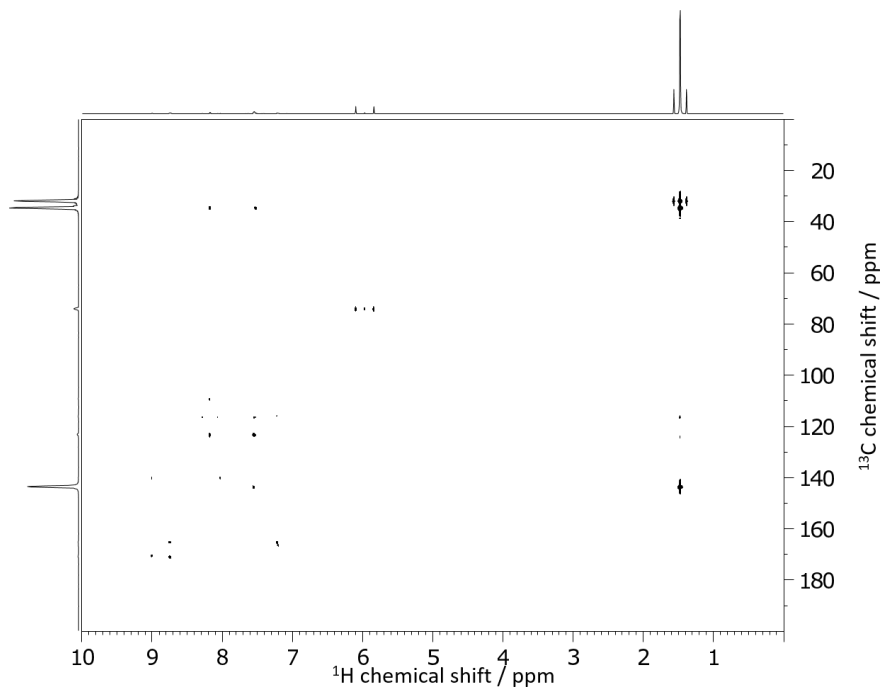
Appendix 23 ^{1}H-^{13}C HMBC spectrum of the compound 2b measured in TCE and RT at a field of 700 MHz.
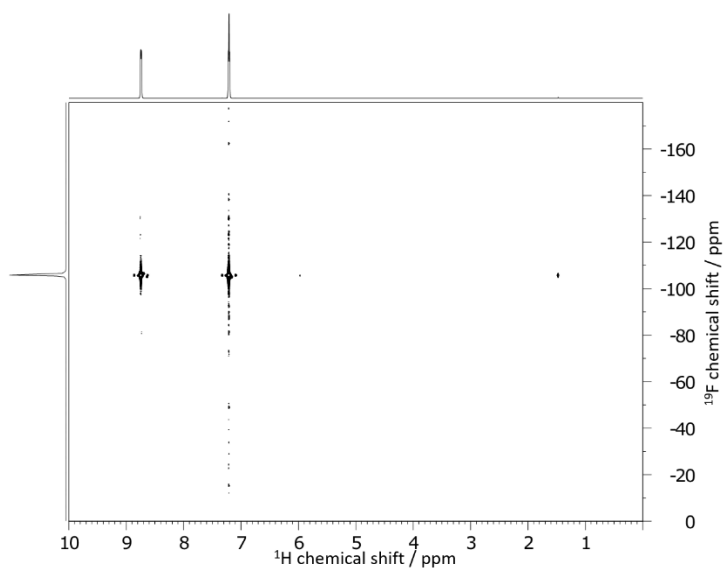
Appendix 24 ^{1}H-^{19}F HSQC spectrum of the compound 2b measured in TCE and RT at a field of 700 MHz.
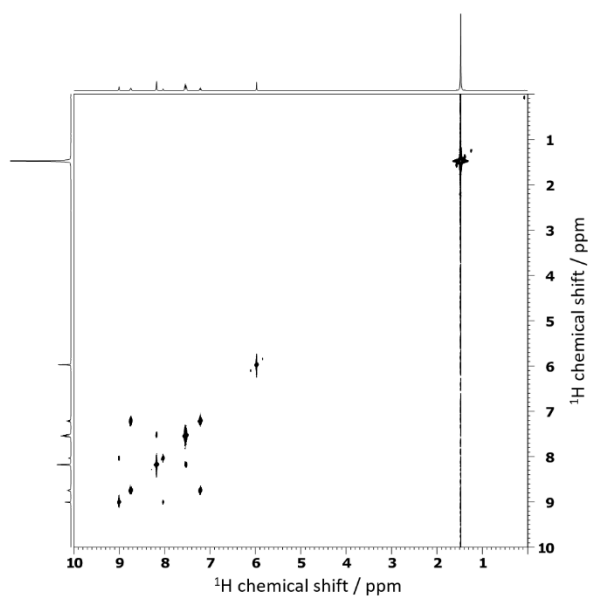
Appendix 25 ^{1}H-^{1}H COSY spectrum of the compound 2b measured in TCE and RT at a field of 700 MHz.
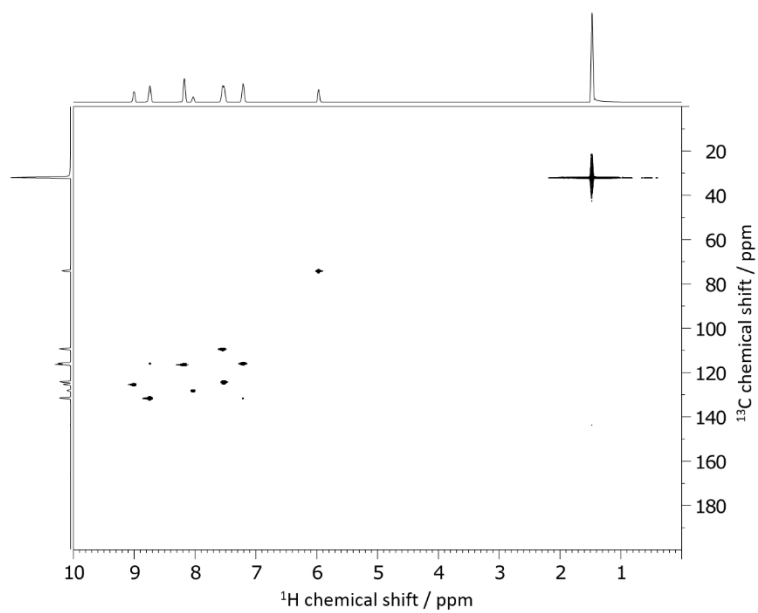
Appendix 26 ^{1}H-^{13}C HSQC spectrum of the compound 2b measured in TCE and RT at a field of 700 MHz.
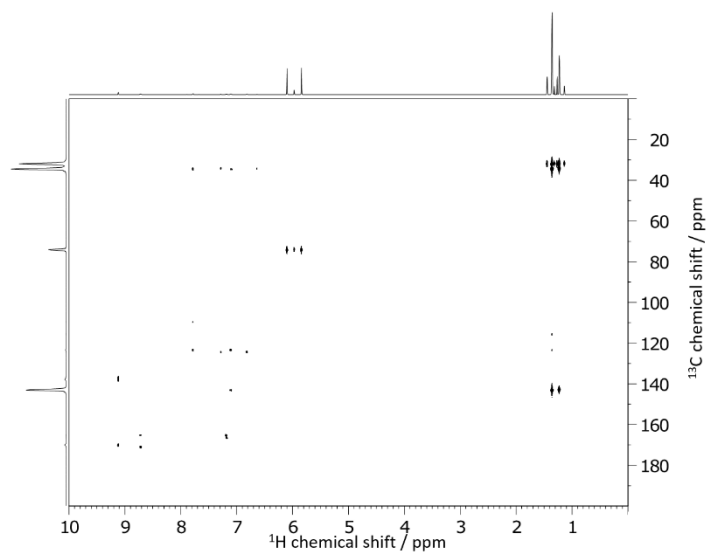
Appendix 27 ¹H-¹³C HMBC spectrum of the compound 2c measured in TCE and RT at a field of 700 MHz.
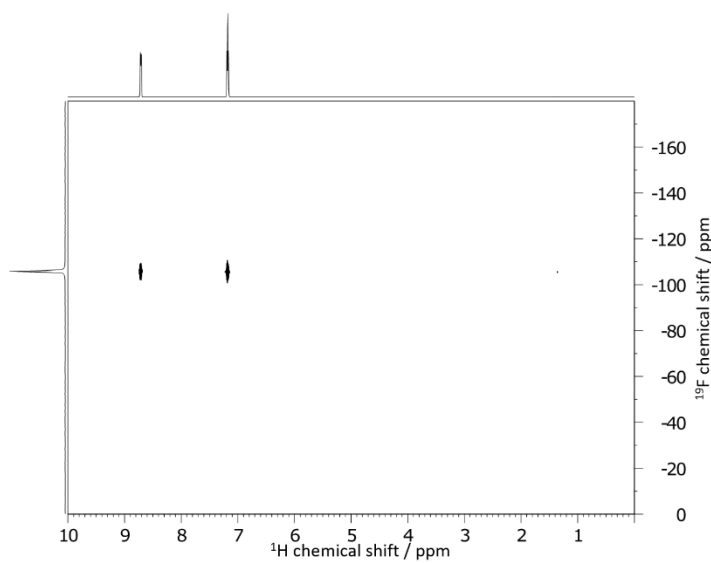
Appendix 28 ¹H-¹⁹F HMBC spectrum of the compound 2c measured in TCE and RT at a field of 700 MHz.
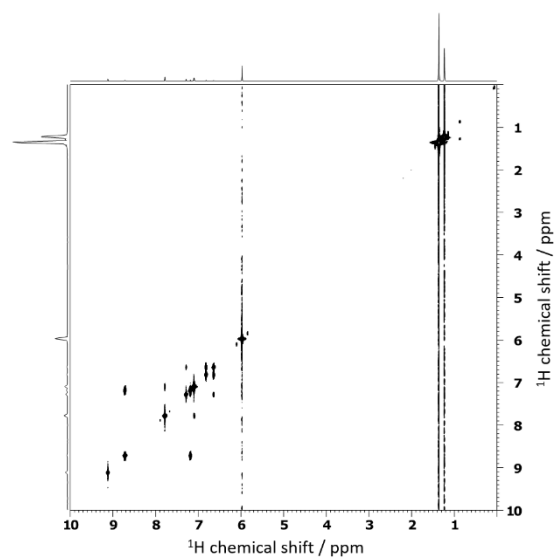
Appendix 29 ^{1}H-^{1}H COSY spectrum of the compound 2c measured in TCE and RT at a field of 700 MHz.
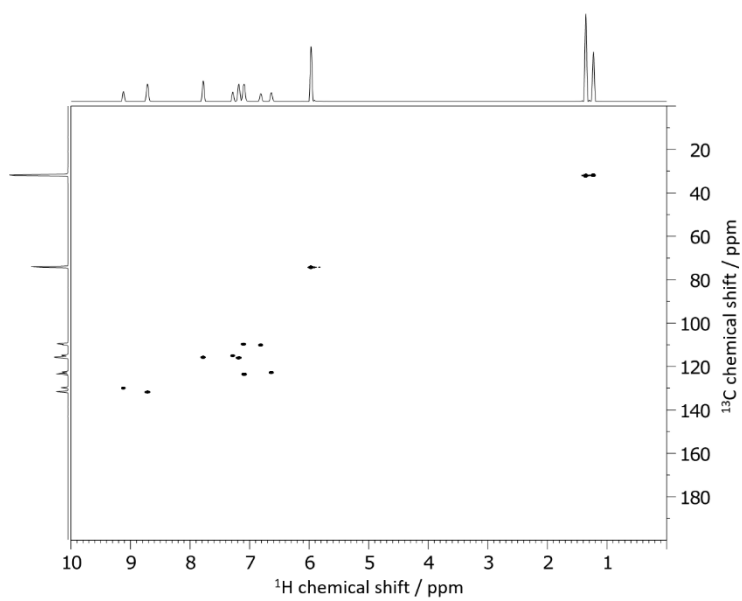
Appendix 30 ^{1}H-^{13}C HSQC spectrum of the compound 2c measured in TCE and RT at a field of 700 MHz.
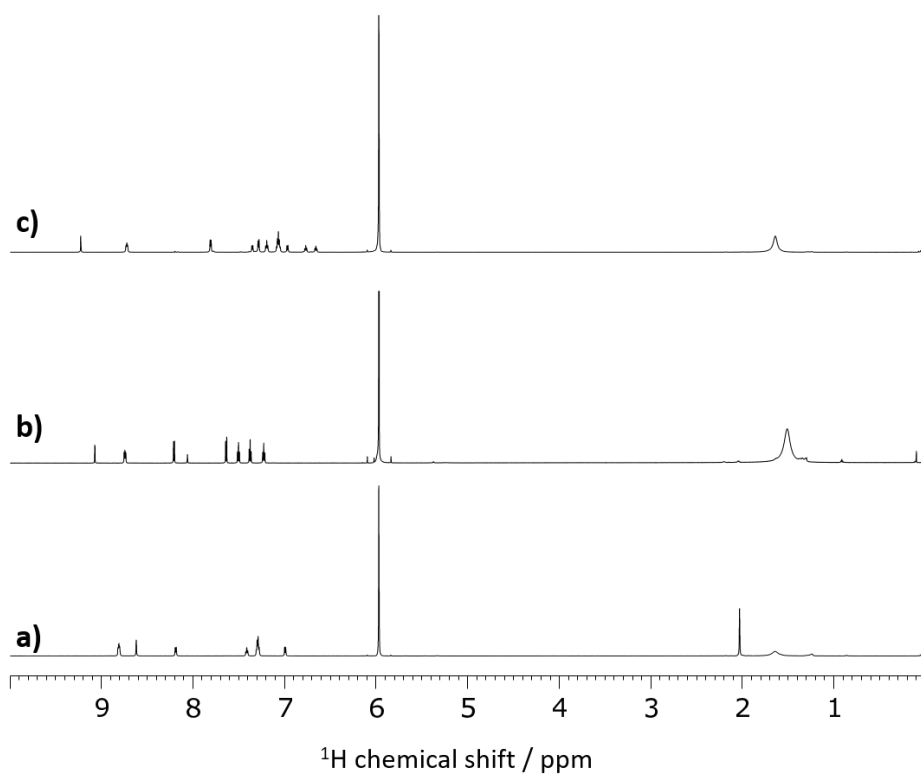
Appendix 31 ¹H spectra of the compounds 3a (a) (RT), 3b (b) (353 K) and 3c (c) (RT) measured in TCE at a field of 700 MHz.
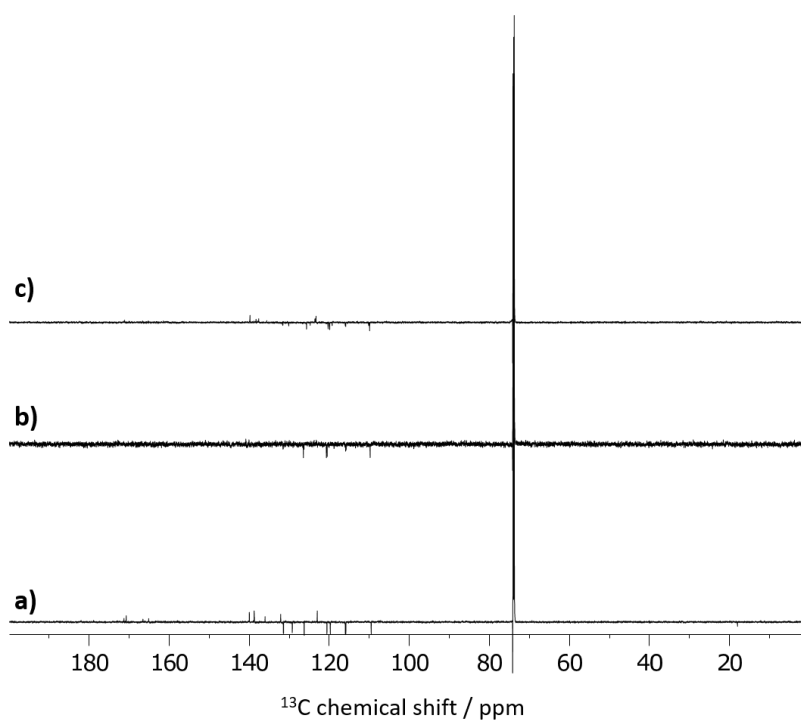
Appendix 32 ¹³C spectra of the compounds 3a (a) (RT), 3b (b) (353 K) and 3c (c) (RT) measured in TCE at a field of 700 MHz.
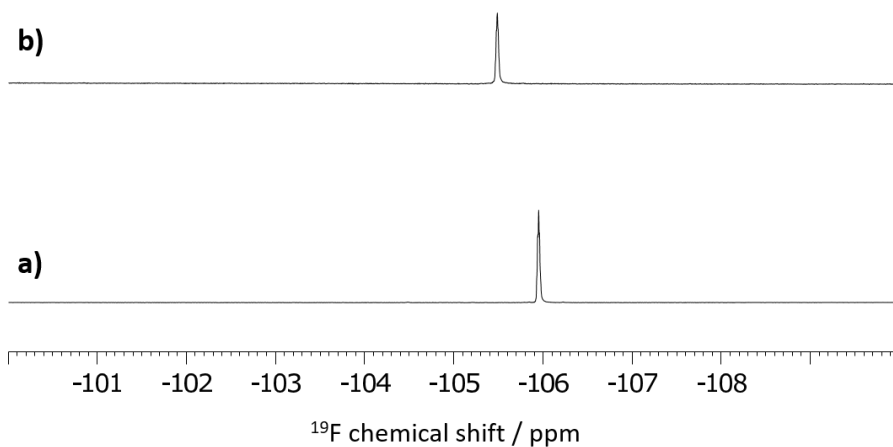
Appendix 33 ¹⁹H spectra of the compounds 3a (a) (RT), 3c (c) (RT) measured in TCE at a field of 700 MHz.
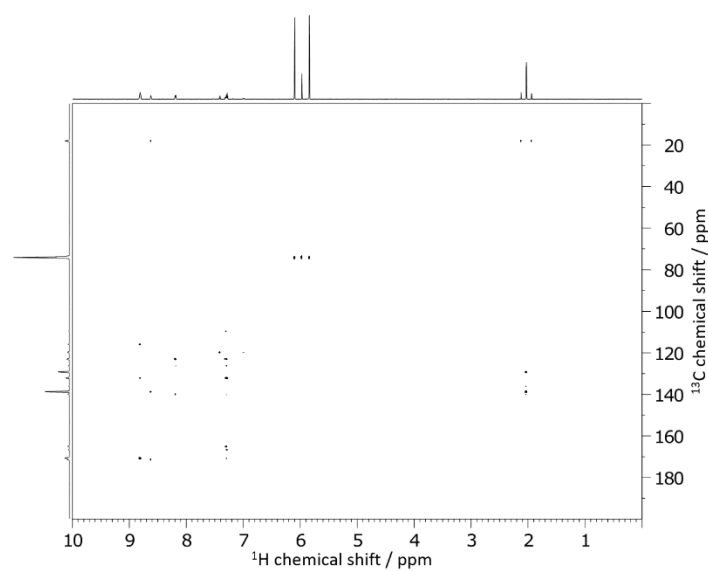
Appendix 34 ¹H-¹³C HMBC spectrum of the compound 3a measured in TCE and RT at a field of 700 MHz.
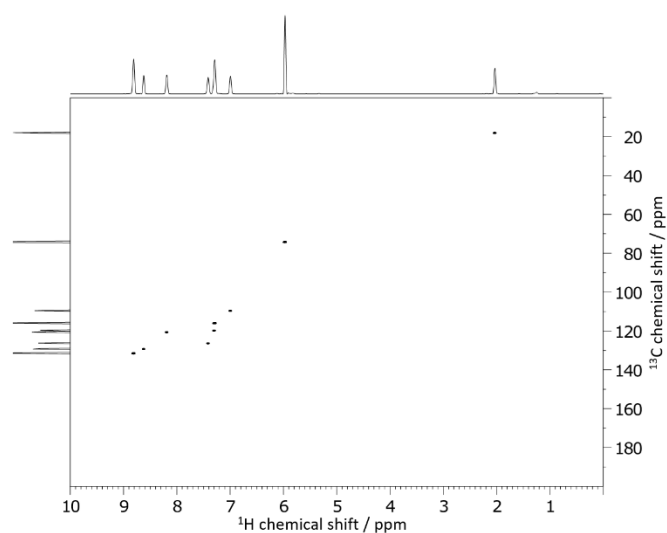
Appendix 35 ¹H-¹³C HSQC spectrum of the compound 3a measured in TCE and RT at a field of 700 MHz.
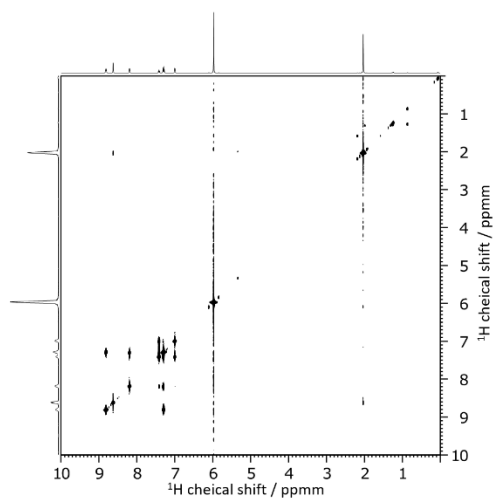
Appendix 36 ^{1}H-^{1}H COSY spectrum of the compound 3a measured in TCE and RT at a field of 700 MHz.
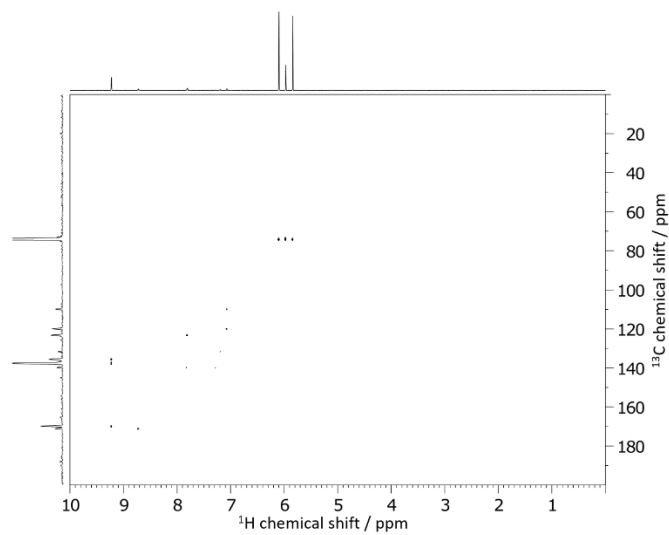
Appendix 37 ^{1}H-^{13}C HMBC spectrum of the compound 3c measured in TCE and RT at a field of 700 MHz.
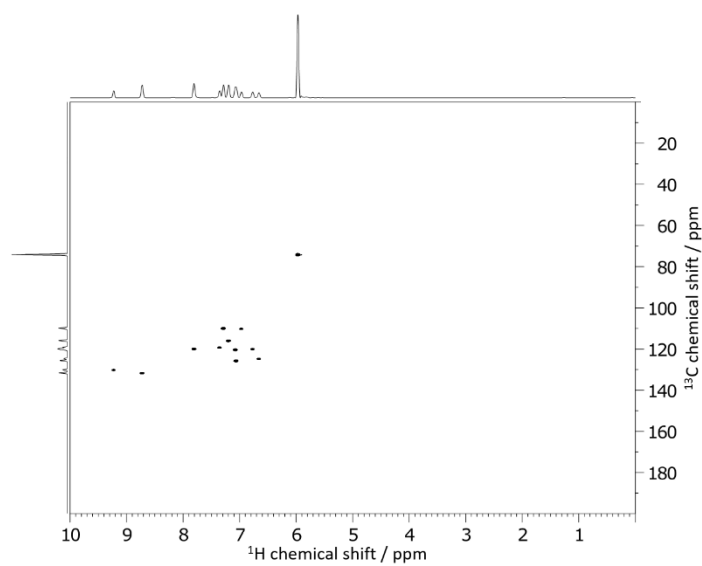
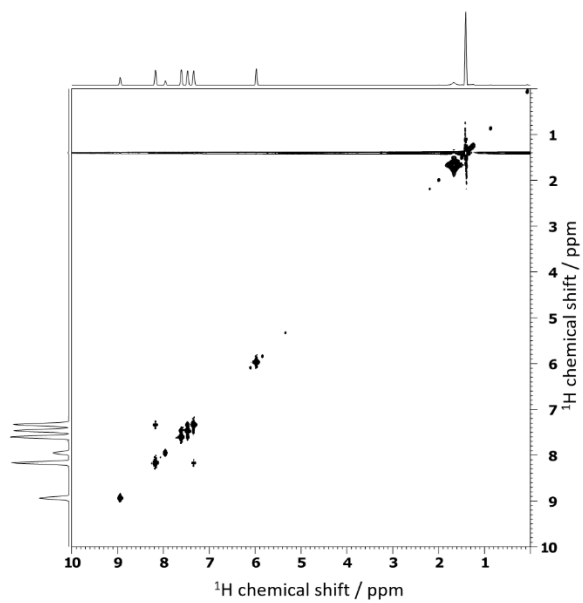Appendix 38 ^{1}H-^{13}C HSQC spectrum of the compound 3c measured in TCE and RT at a field of 700 MHz.
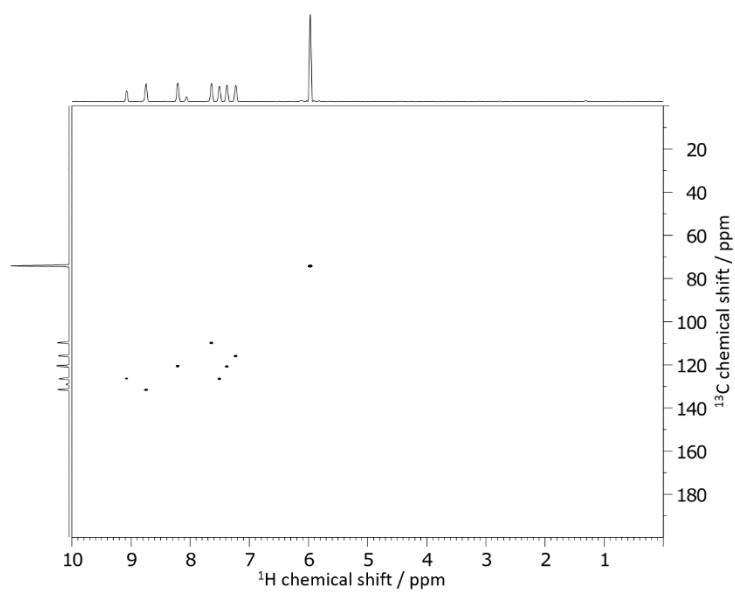
Appendix 39 ^{1}H-^{13}C HMBC spectrum of the compound 3b measured in TCE and 353K at a field of 700 MHz.
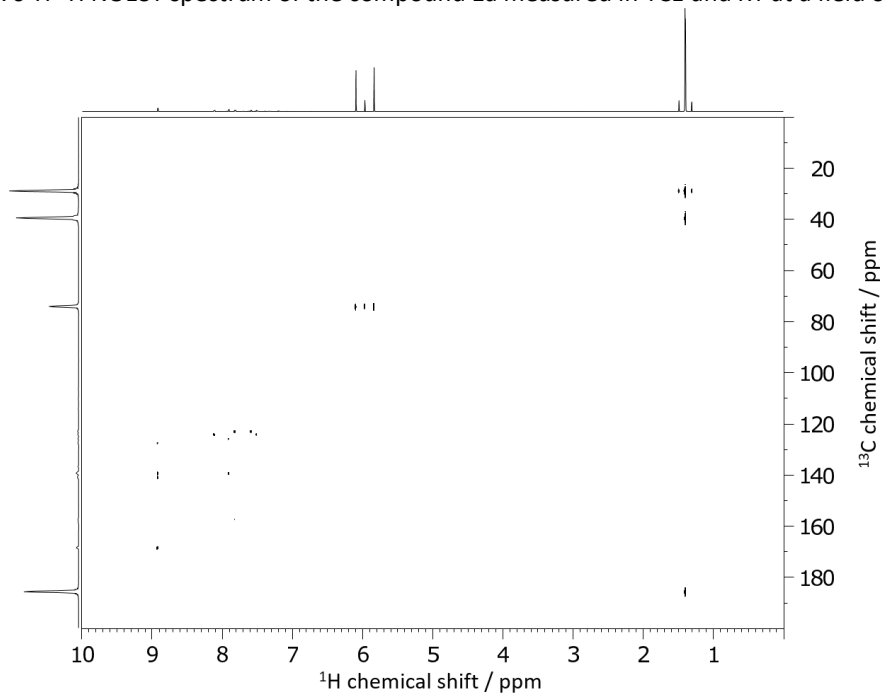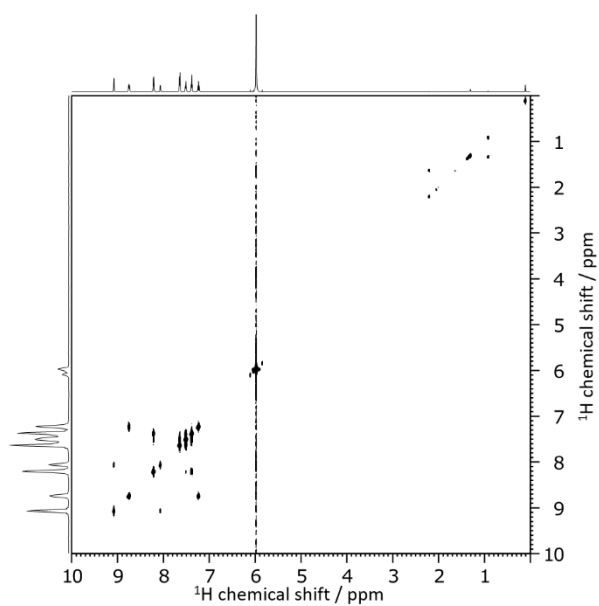
Appendix 40 ^{1}H-^{1}H COSY spectrum of the compound 3b measured in TCE and 353K at a field of 700 MHz.
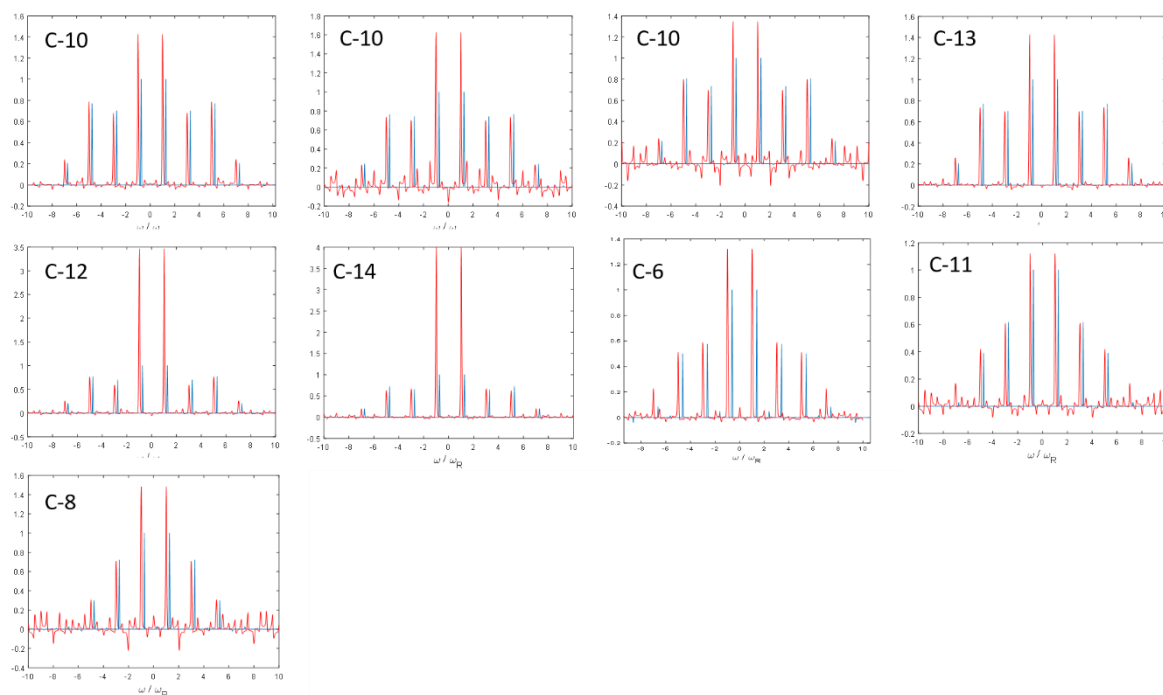

Appendix 41 Rotational sideband patterns for the C-H pairs of compound 1a, extracted from REPT-HDOR spectra, measured at a field of 500 MHz and a rotation frequency of 50 kHz.
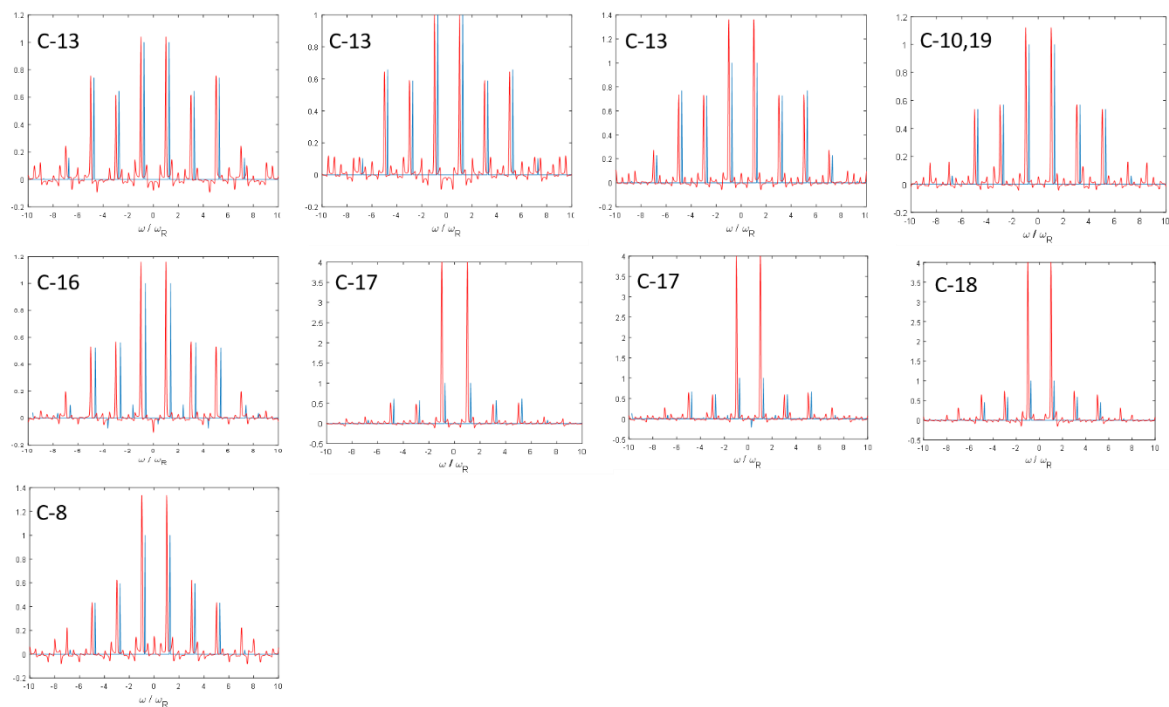
Appendix 42 Rotational sideband patterns for the C-H pairs of compound 1b, extracted from REPT-HDOR spectra, measured at a field of 500 MHz and a rotation frequency of 50 kHz.
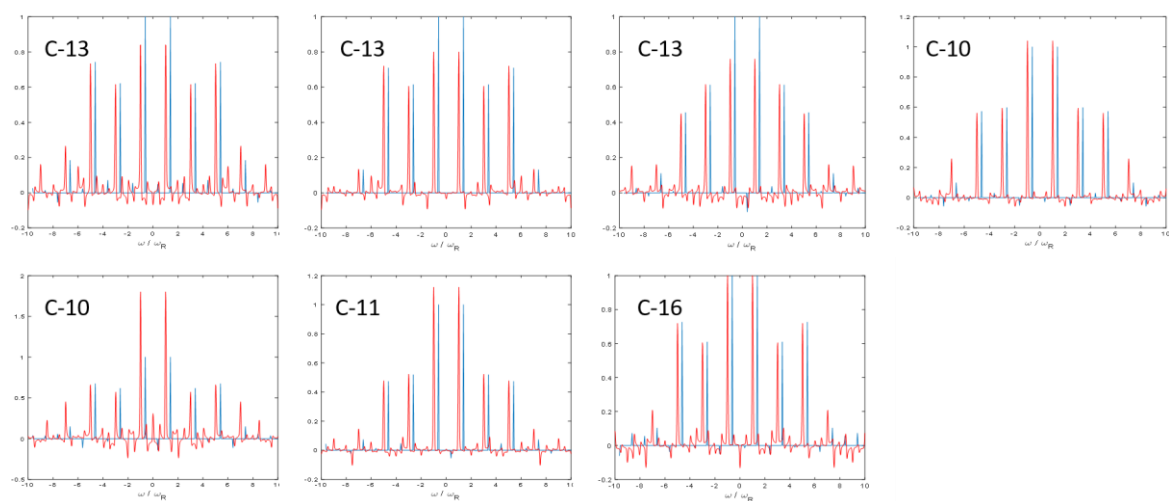
Appendix 43 Rotational sideband patterns for the C-H pairs of compound 1c, extracted from REPT-HDOR spectra, measured at a field of 500 MHz and a rotation frequency of 50 kHz.
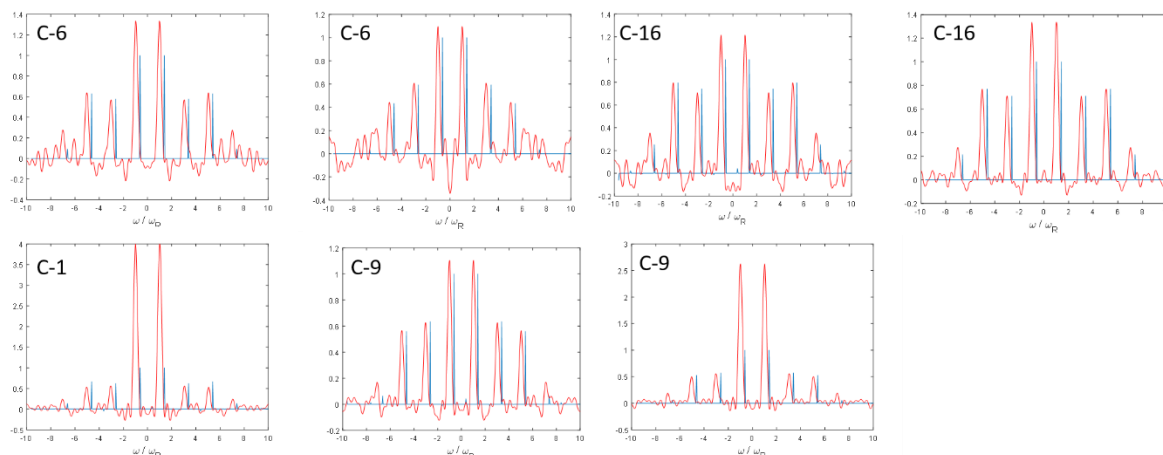
Appendix 44 Rotational sideband patterns for the C-H pairs of compound 2a, extracted from REPT-HDOR spectra, measured at a field of 500 MHz and a rotation frequency of 50 kHz.
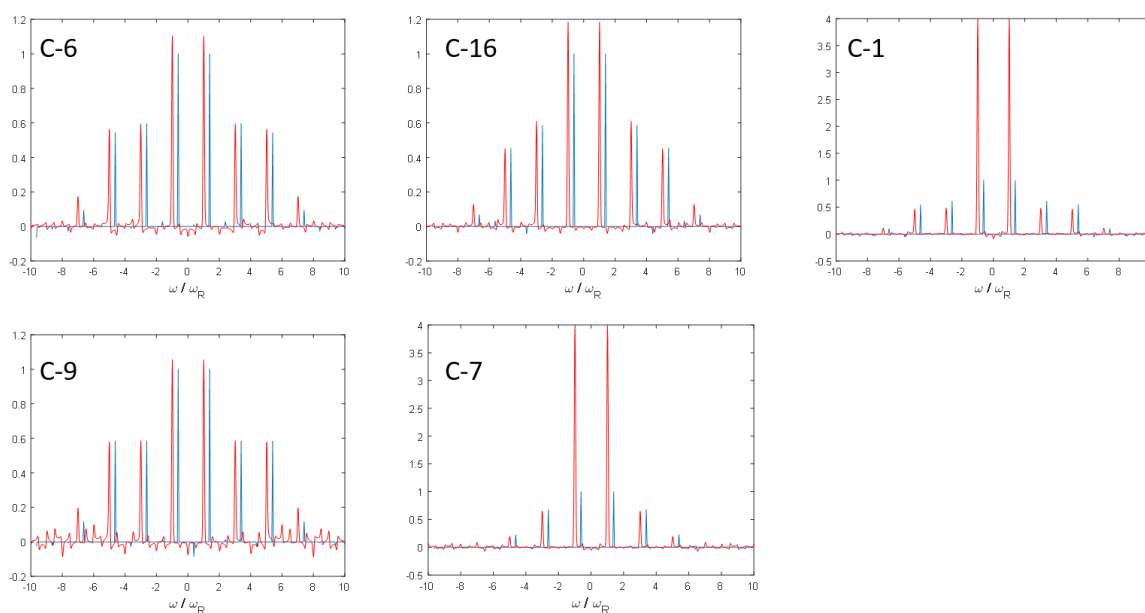
Appendix 45 Rotational sideband patterns for the C-H pairs of compound 2b, extracted from REPT-HDOR spectra, measured at a field of 500 MHz and a rotation frequency of 50 kHz.
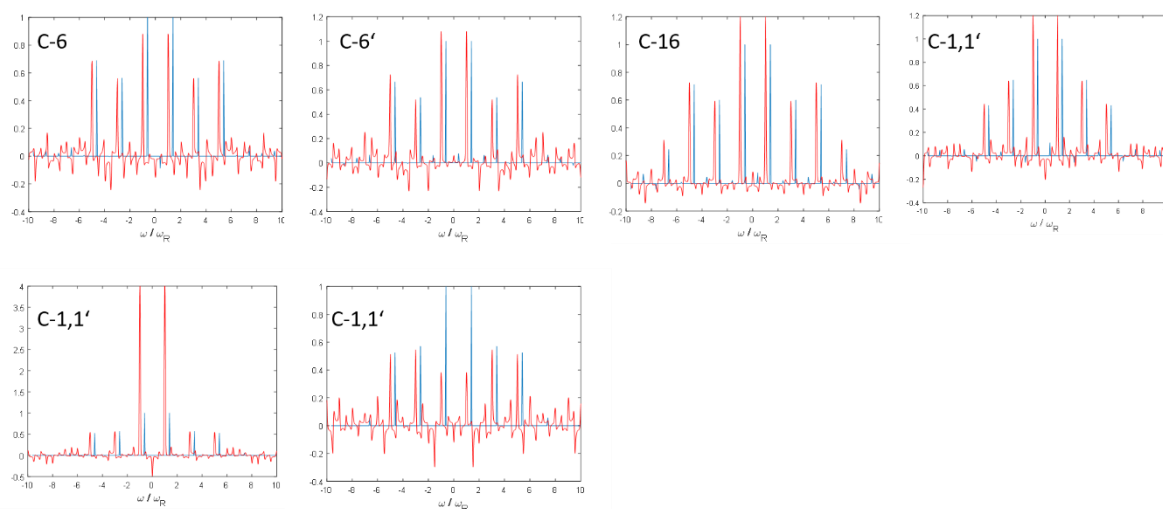
Appendix 46 Rotational sideband patterns for the C-H pairs of compound 1a, extracted from REPT-HDOR spectra, measured at a field of 500 MHz and a rotation frequency of 50 kHz.

REPT Simulation Input

Input parameter

spin: 1

coupling δ_0:   21.50 kHz

anisotropy Δ_0:   32.25 kHz

asymmetry η_0:   0.00

cone angle θ: 78.00

jump angle ϕ: 31.00

euler angle α: 0.00

type of motion: fast   2-site

site pos/deg   pop

 1 -15.50   0.500

 2   15.50   0.500

jump angle distribution gaussian

full width 2σ: 30.00 deg

lorentzian line broadening

linewidth: 3.00

plot from: -150.0 kHz to: 150.0 kHz

number of points: 256

points per line: 2

Results

Tensor in PAS System

	x	y	z
x	-10.75	0.00	-0.00

y   0.00 -10.75   0.00

z -0.00   0.00   21.50

Averaged Tensor in cone frame

	x	y	z
x	16.21	0.00	6.11
y	0.00	-6.85	0.00
z	6.11	0.00	-9.36

Eigenvalues

$\langle X \rangle$: -10.74 kHz

$\langle Y \rangle$:   -6.85 kHz

$\langle Z \rangle$:   17.59 kHz

Eigenvectors

	$e_{\langle X \rangle}$	$e_{\langle Y \rangle}$	$e_{\langle Z \rangle}$	
x	0.2210	-0.0000	0.9753	α: -90.00
y	-0.0000	1.0000	-0.0000	β: 77.23
z	-0.9753	-0.0000	0.2210	γ: 180.00

Θ 12.769 90.000 77.231

Φ 0.000 90.000 0.000

Averaged coupling and asymmetry

$\langle \delta \rangle$:   17.59 kHz

$\langle \delta/\delta_0 \rangle$: 0.818

$\langle \eta \rangle$:   0.221

Input parameter

spin: 1

coupling δ_0:   21.50 kHz

anisotropy Δ_0:   32.25 kHz

asymmetry η_0:   0.00

cone angle θ: 42.00

jump angle ϕ: 45.00

euler angle α: 0.00

type of motion: fast   2-site

site pos/deg   pop

 1 -22.50   0.500

 2   22.50   0.500

jump angle distribution gaussian

full width 2σ: 30.00 deg

lorentzian line broadening

linewidth: 3.00

plot from: -150.0 kHz to: 150.0 kHz

number of points: 256

points per line: 2

Results

Tensor in PAS System

```
      x      y      z
 x  -10.75    0.00   -0.00
 y    0.00  -10.75    0.00
 z   -0.00    0.00   21.50
```

Averaged Tensor in cone frame

```
      x      y      z
 x    0.92    0.00   14.32
 y    0.00   -7.98    0.00
 z   14.32    0.00    7.06
```

Eigenvalues

$\langle X \rangle$: -10.65 kHz

$\langle Y \rangle$:   -7.98 kHz

$\langle Z \rangle$:   18.63 kHz

Eigenvectors

```
   e<X>    e<Y>    e<Z>
x  0.7777 -0.0000  0.6286   α:  -90.00
y -0.0000  1.0000  0.0000   β:   38.95
z -0.6286 -0.0000  0.7777   γ:  180.00
```

Θ 51.051 90.000 38.949

Φ   0.000 90.000   0.000

Averaged coupling and asymmetry

<δ>:   18.63 kHz

<δ/δ$_0$>: 0.867

<η>:   0.143

Input parameter

spin: 1

coupling δ$_0$:   21.50 kHz

anisotropy Δ$_0$:   32.25 kHz

asymmetry η$_0$:   0.00

cone angle θ: 65.00

jump angle φ: 45.00

euler angle α: 0.00

type of motion: fast   2-site

site pos/deg   pop

 1 -22.50   0.500

 2   22.50   0.500

jump angle distribution gaussian

full width 2σ: 30.00 deg

lorentzian line broadening

linewidth: 3.00

plot from: -150.0 kHz to: 150.0 kHz

number of points: 256

points per line: 2

Results

Tensor in PAS System

	x	y	z
x	-10.75	0.00	-0.00
y	0.00	-10.75	0.00
z	-0.00	0.00	21.50

Averaged Tensor in cone frame

	x	y	z
x	10.66	0.00	11.03
y	0.00	-5.67	0.00
z	11.03	0.00	-4.99

Eigenvalues

<X> : -10.69 kHz

<Y> : -5.67 kHz

<Z> : 16.36 kHz

Eigenvectors

$e_{<X>}$ $e_{<Y>}$ $e_{<Z>}$

x 0.4590 -0.0000 0.8885 α: -90.00

y -0.0000 1.0000 -0.0000 β: 62.68

z -0.8885 -0.0000 0.4590 γ: 180.00

Θ 27.320 90.000 62.680

Φ 0.000 90.000   0.000

Averaged coupling and asymmetry

$\langle\delta\rangle$:   16.36 kHz

$\langle\delta/\delta_0\rangle$: 0.761

$\langle\eta\rangle$:   0.307
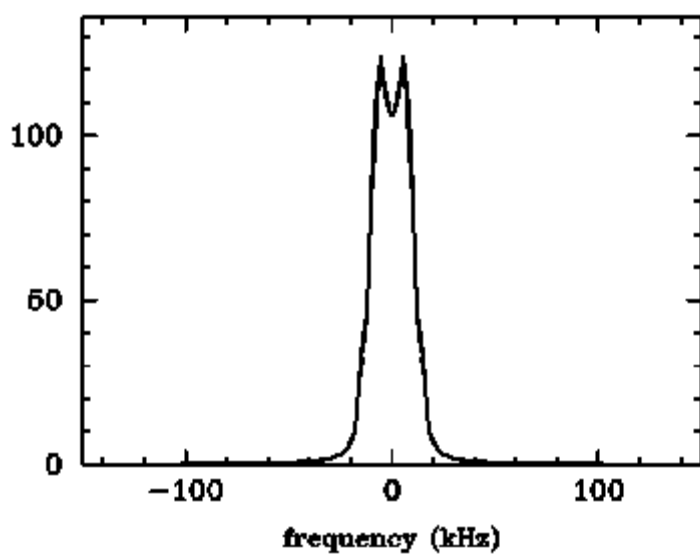
coupling δ_0:   21.50 kHz

anisotropy Δ_0:   32.25 kHz

asymmetry η_0:   0.00

cone angle θ: 17.00

jump angle φ: 0.00

euler angle α: 0.00

type of motion: fast   2-site

site pos/deg   pop

 1   0.00   0.500

 2   0.00   0.500

lorentzian line broadening

linewidth: 3.00

plot from: -150.0 kHz to: 150.0 kHz

number of points: 256

points per line: 2

Results

Tensor in PAS System

     x   y   z

 x -10.75   0.00   -0.00

 y   0.00 -10.75   0.00

 z -0.00   0.00   21.50

Averaged Tensor in cone frame

     x   y   z

 x -7.99   0.00   9.02

 y   0.00 -10.75   0.00

 z   9.02   0.00   18.74

Eigenvalues

<X> : -10.75 kHz

<Y> : -10.75 kHz

<Z> :   21.50 kHz

Eigenvectors

   $e_{<X>}$ $e_{<Y>}$ $e_{<Z>}$

x 0.9563 -0.0000 0.2924   α: -90.00

y -0.0000 1.0000 0.0000   β: 17.00

z -0.2924 -0.0000 0.9563   γ: 180.00

Θ 73.000 90.000 17.000

Φ   0.000 90.000   0.000

Averaged coupling and asymmetry

<δ>:   21.50 kHz

<δ/δ$_0$>: 1.000

<η>:   0.000

Input parameter

spin: 1

coupling δ_0:   21.50 kHz

anisotropy Δ_0:   32.25 kHz

asymmetry η_0:   0.00

cone angle θ: 65.00

jump angle φ: 32.00

euler angle α: 0.00

type of motion: fast   2-site

site pos/deg   pop

 1 -16.00   0.500

 2   16.00   0.500

jump angle distribution gaussian

full width 2σ: 30.00 deg

lorentzian line broadening

linewidth: 3.00

plot from: -150.0 kHz to: 150.0 kHz

number of points: 256

points per line: 2

Results

Tensor in PAS System

	x	y	z
x	-10.75	0.00	-0.00
y	0.00	-10.75	0.00
z	-0.00	0.00	21.50

Averaged Tensor in cone frame

	x	y	z

x   12.29   0.00   11.47

y   0.00   -7.30   0.00

z   11.47   0.00   -4.99

Eigenvalues

<X> :   -10.71 kHz

<Y> :   -7.30 kHz

<Z> :   18.01 kHz

Eigenvectors

   e$_{<X>}$ e$_{<Y>}$ e$_{<Z>}$

x 0.4464 -0.0000 0.8948   α: -90.00

y -0.0000 1.0000 -0.0000   β: 63.49

z -0.8948 -0.0000 0.4464   γ: 180.00

Θ 26.511 90.000 63.489

Φ 0.000 90.000 0.000

Averaged coupling and asymmetry

<δ>:   18.01 kHz

<δ/δ$_0$>:   0.838

<η>:   0.190
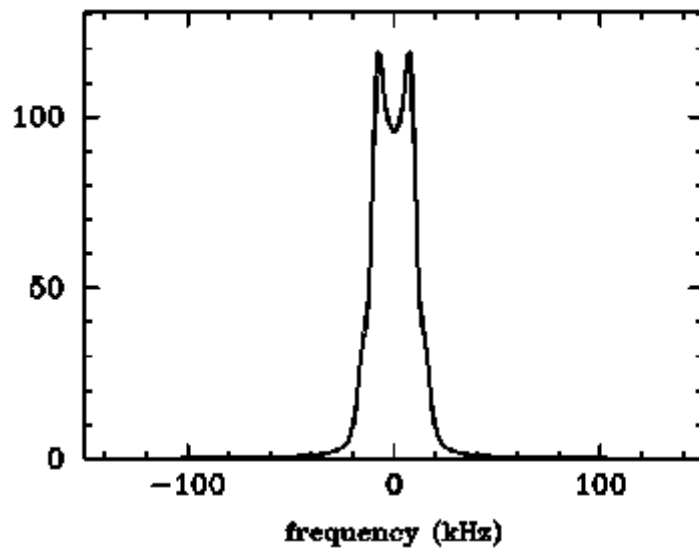
Input parameter

spin: 1

coupling δ_0:   21.50 kHz

anisotropy Δ_0:   32.25 kHz

asymmetry η_0:   0.00

cone angle θ: 78.00

jump angle ϕ: 28.00

euler angle α: 0.00

type of motion: fast   2-site

site pos/deg   pop

 1 -14.00   0.500

 2   14.00   0.500

jump angle distribution gaussian

full width 2σ: 30.00 deg

lorentzian line broadening

linewidth: 3.00

plot from: -150.0 kHz to: 150.0 kHz

number of points: 256

points per line: 2

Results

Tensor in PAS System

```
     x      y     z
x  -10.75    0.00   -0.00
y    0.00  -10.75    0.00
z   -0.00    0.00   21.50
```

Averaged Tensor in cone frame

```
     x      y     z
x   16.12    0.00    7.10
y    0.00   -7.26    0.00
z    7.10    0.00   -8.86
```

Eigenvalues

$\langle X \rangle$: -10.74 kHz

$\langle Y \rangle$: -7.26 kHz

$\langle Z \rangle$: 17.99 kHz

Eigenvectors

```
   e<X>    e<Y>    e<Z>
x  0.2555 -0.0000  0.9668   α: -90.00
y -0.0000  1.0000 -0.0000   β:  75.20
z -0.9668 -0.0000  0.2555   γ: 180.00
```

Θ 14.804 90.000 75.196

Φ 0.000 90.000 0.000

Averaged coupling and asymmetry

$\langle\delta\rangle$:   17.99 kHz

$\langle\delta/\delta_0\rangle$: 0.837

$\langle\eta\rangle$:   0.194

Input parameter

spin: 1

coupling δ_0:   21.50 kHz

anisotropy Δ_0:   32.25 kHz

asymmetry η_0:   0.00

cone angle θ: 42.00

jump angle ϕ: 32.00

euler angle α: 0.00

type of motion: fast   2-site

site pos/deg   pop

 1 -16.00   0.500

 2 16.00   0.500

jump angle distribution gaussian

full width 2σ: 30.00 deg

lorentzian line broadening

linewidth: 3.00

plot from: -150.0 kHz to: 150.0 kHz

number of points: 256

points per line: 2

Results

Tensor in PAS System

	x	y	z
x	-10.75	0.00	-0.00
y	0.00	-10.75	0.00
z	-0.00	0.00	21.50

Averaged Tensor in cone frame

	x	y	z
x	1.81	0.00	14.90
y	0.00	-8.87	0.00
z	14.90	0.00	7.06

Eigenvalues

<X> : -10.69 kHz

<Y> : -8.87 kHz

<Z> :   19.56 kHz

Eigenvectors

   $e_{<X>}$ $e_{<Y>}$ $e_{<Z>}$

x 0.7660 -0.0000 0.6428 α: -90.00

y -0.0000 1.0000 0.0000 β: 40.00

z -0.6428 -0.0000 0.7660 γ: 180.00

Θ 49.999 90.000 40.001

Φ 0.000 90.000   0.000

Averaged coupling and asymmetry

$<\delta>$:   19.56 kHz

$<\delta/\delta_0>$: 0.910

$<\eta>$:   0.093
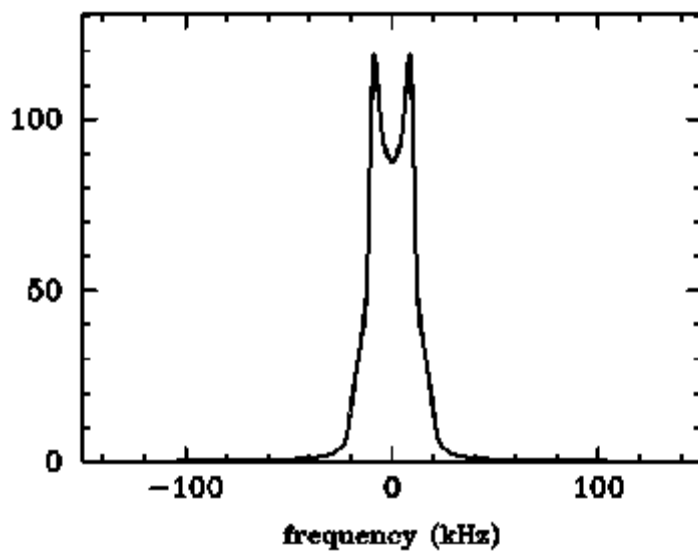
Input parameter

spin: 1

coupling δ_0:   21.50 kHz

anisotropy Δ_0:   32.25 kHz

asymmetry η_0:   0.00

cone angle θ: 30.00

jump angle ϕ: 44.00

euler angle α: 0.00

type of motion: fast   2-site

site pos/deg   pop

 1 -22.00   0.500

 2   22.00   0.500

jump angle distribution gaussian

full width 2σ: 30.00 deg

lorentzian line broadening

linewidth: 0.00

plot from: -150.0 kHz to: 150.0 kHz

number of points: 256

points per line: 0

Results

Tensor in PAS System

	x	y	z
x	-10.75	0.00	-0.00
y	0.00	-10.75	0.00
z	-0.00	0.00	21.50

Averaged Tensor in cone frame

	x	y	z
x	-4.19	0.00	12.51

y   0.00   -9.25   0.00

z   12.51   0.00   13.44

Eigenvalues

<X> : -10.68 kHz

<Y> :   -9.25 kHz

<Z> :   19.93 kHz

Eigenvectors

    $e_{<X>}$ $e_{<Y>}$ $e_{<Z>}$

x 0.8877 -0.0000 0.4605   α: -90.00

y -0.0000 1.0000 0.0000   β: 27.42

z -0.4605 -0.0000 0.8877   γ: 180.00

Θ 62.582 90.000 27.418

Φ   0.000 90.000   0.000

Averaged coupling and asymmetry

<δ>:   19.93 kHz

<δ/δ$_0$>: 0.927

<η>:   0.072
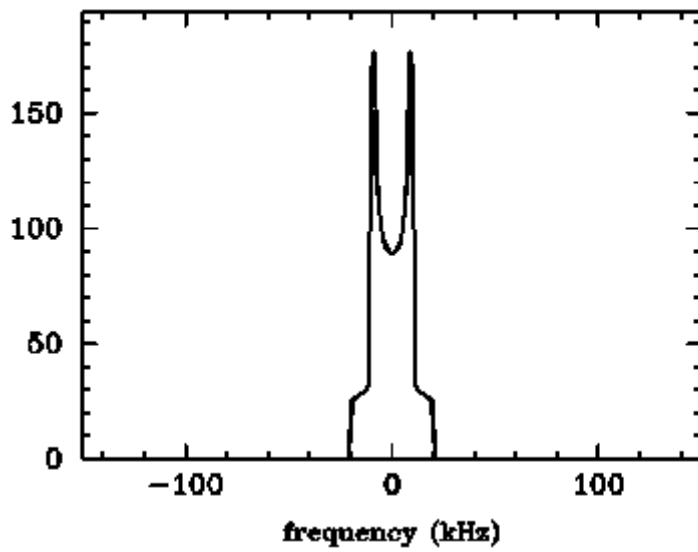
Input parameter

spin: 1

coupling δ_0:   21.50 kHz

anisotropy Δ_0:   32.25 kHz

asymmetry η_0:   0.00

cone angle θ: 30.00

jump angle φ: 55.00

euler angle α: 0.00

type of motion: fast   2-site

site pos/deg pop

 1 -27.50   0.500

 2   27.50   0.500

jump angle distribution gaussian

full width 2σ: 30.00 deg

lorentzian line broadening

linewidth: 0.00

plot from: -150.0 kHz to: 150.0 kHz

number of points: 256

points per line: 0

Results

Tensor in PAS System

```
     x      y      z
x  -10.75    0.00   -0.00
y    0.00  -10.75    0.00
z   -0.00    0.00   21.50
```

Averaged Tensor in cone frame

```
     x      y      z
x   -4.70    0.00   11.97
y    0.00   -8.73    0.00
z   11.97    0.00   13.44
```

Eigenvalues

<X> : -10.65 kHz

<Y> :   -8.73 kHz

<Z> :   19.39 kHz

Eigenvectors

```
    e<X>    e<Y>    e<Z>
x  0.8955 -0.0000  0.4450   α:  -90.00
y -0.0000  1.0000  0.0000   β:   26.42
z -0.4450 -0.0000  0.8955   γ:  180.00
```

Θ 63.577 90.000 26.423

Φ 0.000 90.000   0.000

Averaged coupling and asymmetry

$\langle\delta\rangle$:   19.39 kHz

$\langle\delta/\delta_0\rangle$: 0.902

$\langle\eta\rangle$:   0.099
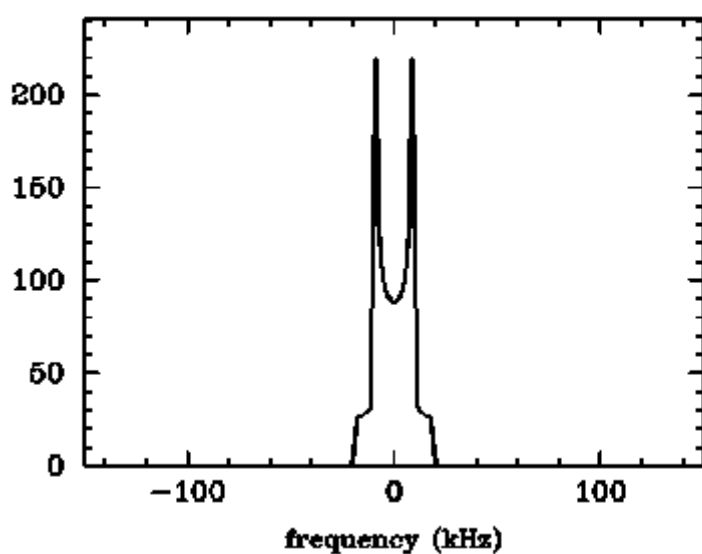
Input parameter

spin: 1

coupling δ_0:   21.50 kHz

anisotropy Δ_0:   32.25 kHz

asymmetry η_0:   0.00

cone angle θ: 30.00

jump angle ϕ: 64.00

euler angle α: 0.00

type of motion: fast   2-site

site pos/deg   pop

 1 -32.00   0.500

 2 32.00   0.500

jump angle distribution gaussian

full width 2σ: 30.00 deg

lorentzian line broadening

linewidth: 0.00

plot from: -150.0 kHz to: 150.0 kHz

number of points: 256

points per line: 0

Results

Tensor in PAS System

```
      x      y      z
 x  -10.75    0.00   -0.00
 y    0.00  -10.75    0.00
 z   -0.00    0.00   21.50
```


Averaged Tensor in cone frame

```
      x      y      z
 x   -5.18    0.00   11.44
 y    0.00   -8.26    0.00
 z   11.44    0.00   13.44
```


Eigenvalues

<X> : -10.62 kHz

<Y> :   -8.26 kHz

<Z> :   18.88 kHz

Eigenvectors

```
      e<X>     e<Y>     e<Z>
x  0.9030 -0.0000  0.4295   α:  -90.00
y -0.0000  1.0000  0.0000   β:   25.44
z -0.4295 -0.0000  0.9030   γ:  180.00


Θ  64.562  90.000  25.438
Φ   0.000  90.000   0.000
```
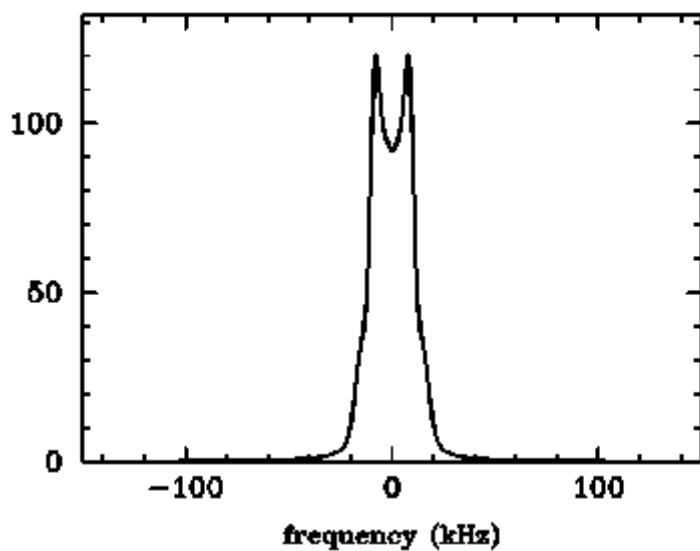
Averaged coupling and asymmetry

$\langle\delta\rangle$:   18.88 kHz

$\langle\delta/\delta_0\rangle$: 0.878

$\langle\eta\rangle$:   0.125
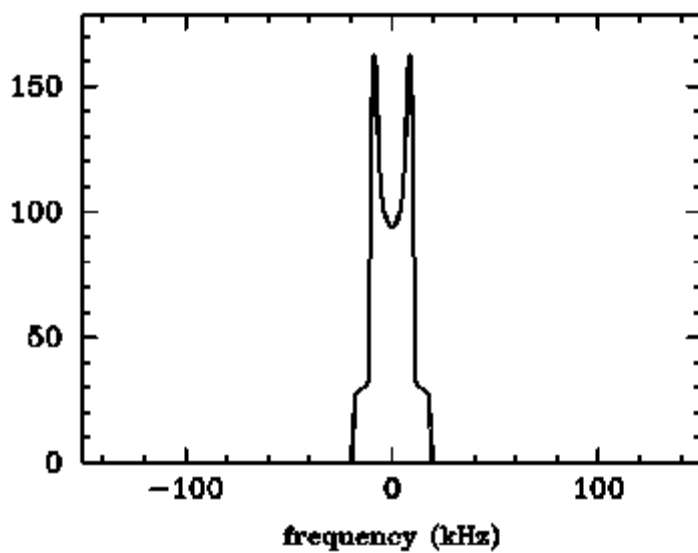
Input parameter

spin: 1

coupling δ_0:   21.50 kHz

anisotropy Δ_0:   32.25 kHz

asymmetry η₀: 0.00

cone angle θ: 30.00

jump angle φ: 42.00

euler angle α: 0.00

type of motion: fast   2-site

site pos/deg   pop

 1 -21.00   0.500

 2   21.00   0.500

jump angle distribution gaussian

full width 2σ: 30.00 deg

lorentzian line broadening

linewidth: 0.00

plot from: -150.0 kHz to: 150.0 kHz

number of points: 256

points per line: 0

Results

Tensor in PAS System

	x	y	z
x	-10.75	0.00	-0.00
y	0.00	-10.75	0.00
z	-0.00	0.00	21.50

Averaged Tensor in cone frame

	x	y	z
x	-4.11	0.00	12.60
y	0.00	-9.33	0.00

z   12.60   0.00   13.44

Eigenvalues

<X> : -10.69 kHz

<Y> :   -9.33 kHz

<Z> :   20.02 kHz

Eigenvectors

    $e_{<X>}$ $e_{<Y>}$ $e_{<Z>}$

x 0.8864 -0.0000 0.4629   α: -90.00

y -0.0000 1.0000 0.0000   β: 27.58

z -0.4629 -0.0000 0.8864   γ: 180.00

Θ 62.425 90.000 27.575

Φ   0.000 90.000   0.000

Averaged coupling and asymmetry

<δ>:   20.02 kHz

<δ/δ$_0$>: 0.931

<η>:   0.068
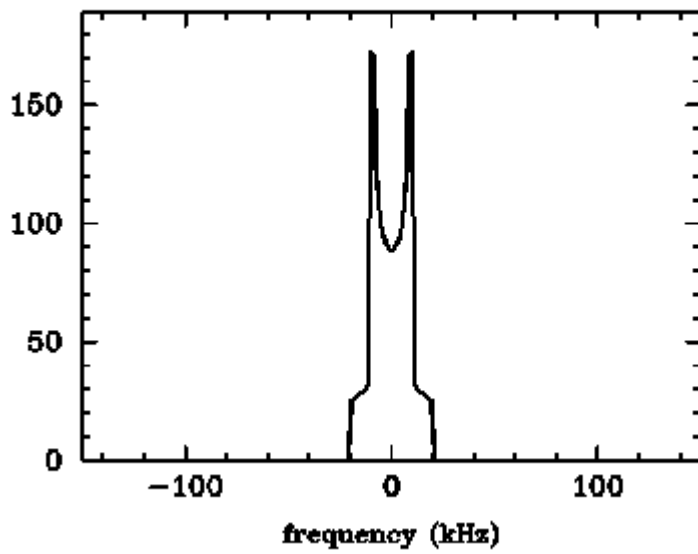
Input parameter

spin: 1

coupling δ_0:   21.50 kHz

anisotropy Δ_0:   32.25 kHz

asymmetry η_0:   0.00

cone angle θ: 78.00

jump angle φ: 19.00

euler angle α: 0.00

type of motion: fast   2-site

site pos/deg pop

 1 -9.50   0.500

 2   9.50   0.500

jump angle distribution gaussian

full width 2σ: 30.00 deg

lorentzian line broadening

linewidth: 0.00

plot from: -150.0 kHz to: 150.0 kHz

number of points: 256

points per line: 0

Results

Tensor in PAS System

```
     x      y      z
x  -10.75    0.00   -0.00
y    0.00  -10.75    0.00
z   -0.00    0.00   21.50
```

Averaged Tensor in cone frame

```
     x      y      z
x   17.40    0.00    6.25
y    0.00   -8.04    0.00
z    6.25    0.00   -9.36
```

Eigenvalues

<X> :   -10.74 kHz

<Y> :   -8.04 kHz

<Z> :   18.79 kHz

Eigenvectors

```
   e<X>    e<Y>    e<Z>
x  0.2168 -0.0000  0.9762   α:  -90.00
y -0.0000  1.0000 -0.0000   β:   77.48
z -0.9762 -0.0000  0.2168   γ:  180.00
```

Θ 12.523 90.000 77.477

Φ 0.000 90.000   0.000

Averaged coupling and asymmetry

<δ>:   18.79 kHz

<δ/δ$_0$>:   0.874

<η>:   0.144
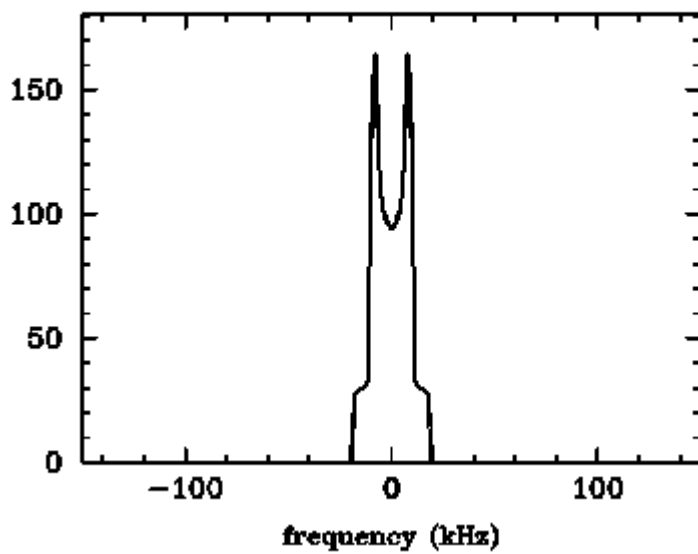
2a

Input parameter

spin: 1

coupling   δ$_0$:   21.50 kHz

anisotropy Δ$_0$:   32.25 kHz

asymmetry η$_0$:   0.00

cone angle θ: 78.00

jump angle φ: 20.00

euler angle α: 0.00

type of motion: fast   2-site

site pos/deg   pop
 1 -10.00   0.500
 2   10.00   0.500

jump angle distribution gaussian
full width 2σ: 30.00 deg

lorentzian line broadening
linewidth: 0.00
plot from: -150.0 kHz to: 150.0 kHz
number of points: 256
points per line: 0

Results

Tensor in PAS System

	x	y	z
x	-10.75	0.00	-0.00
y	0.00	-10.75	0.00
z	-0.00	0.00	21.50

Averaged Tensor in cone frame

	x	y	z
x	17.32	0.00	6.24
y	0.00	-7.96	0.00
z	6.24	0.00	-9.36

Eigenvalues

$<X>$: -10.74 kHz

$<Y>$: -7.96 kHz

\<Z\> :   18.71 kHz

Eigenvectors

   $e_{<X>}$ $e_{<Y>}$ $e_{<Z>}$

x 0.2171 -0.0000 0.9761   α: -90.00

y -0.0000 1.0000 -0.0000   β: 77.46

z -0.9761 -0.0000 0.2171   γ: 180.00

Θ 12.539 90.000 77.461

Φ   0.000 90.000   0.000

Averaged coupling and asymmetry

\<δ\>:   18.71 kHz

\<δ/δ$_0$\>: 0.870

\<η\>:   0.149
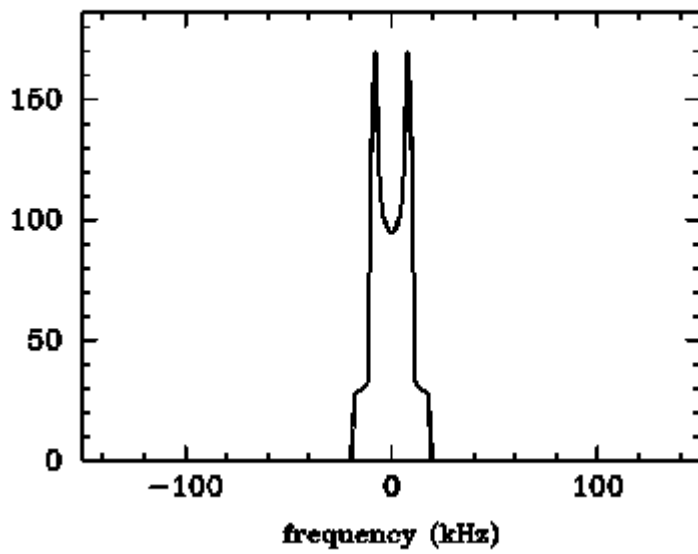
Input parameter

spin: 1

coupling δ_0:   21.50 kHz

anisotropy Δ_0:   32.25 kHz

asymmetry η_0:   0.00

cone angle θ: 46.00

jump angle φ: 40.00

euler angle α: 0.00

type of motion: fast   2-site

site pos/deg   pop

 1 -20.00   0.500

 2   20.00   0.500

jump angle distribution gaussian

full width 2σ: 30.00 deg

lorentzian line broadening

linewidth: 0.00

plot from: -150.0 kHz to: 150.0 kHz

number of points: 256

points per line: 0

Results

Tensor in PAS System

```
     x       y      z
x  -10.75    0.00   -0.00
y    0.00  -10.75    0.00
z   -0.00    0.00   21.50
```

Averaged Tensor in cone frame

```
     x       y      z
x    3.17    0.00   14.63
y    0.00   -7.98    0.00
z   14.63    0.00    4.81
```

Eigenvalues

<X> :   -10.67 kHz

<Y> :   -7.98 kHz

<Z> :   18.65 kHz

Eigenvectors

```
   e<X>    e<Y>    e<Z>
x  0.7267 -0.0000  0.6870   α:  -90.00
y -0.0000  1.0000  0.0000   β:   43.39
z -0.6870 -0.0000  0.7267   γ:  180.00
```
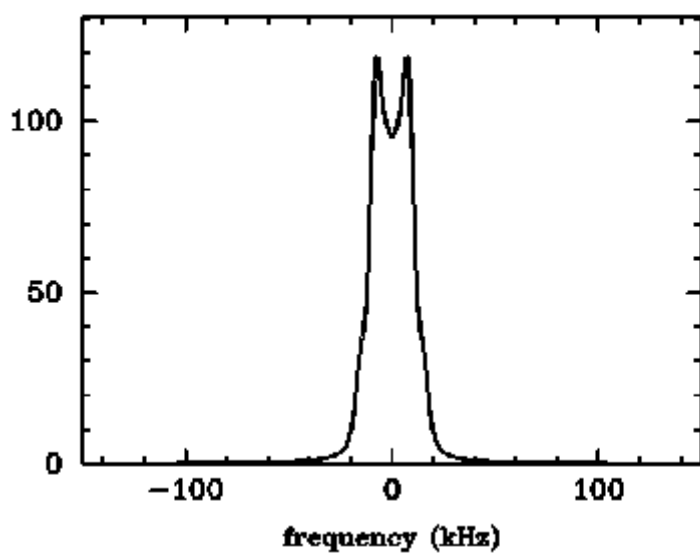
Θ 46.609 90.000 43.391

Φ 0.000 90.000   0.000

Averaged coupling and asymmetry

$\langle\delta\rangle$:   18.65 kHz

$\langle\delta/\delta_0\rangle$:   0.867

$\langle\eta\rangle$:   0.144

Input parameter

spin: 1

coupling δ_0:   21.50 kHz

anisotropy Δ_0:   32.25 kHz

asymmetry η_0:   0.00

cone angle θ: 56.00

jump angle ϕ: 29.00

euler angle α: 0.00

type of motion: fast   2-site

site pos/deg   pop

 1 -14.50   0.500

 2   14.50   0.500

jump angle distribution gaussian

full width 2σ: 30.00 deg

lorentzian line broadening

linewidth: 3.00

plot from: -150.0 kHz to: 150.0 kHz

number of points: 256

points per line: 2

Results

Tensor in PAS System

```
      x       y       z
x  -10.75    0.00   -0.00
y    0.00  -10.75    0.00
z   -0.00    0.00   21.50
```

Averaged Tensor in cone frame

```
      x       y       z
x    8.78    0.00   13.99
y    0.00   -8.12    0.00
z   13.99    0.00   -0.67
```

Eigenvalues

<X> : -10.70 kHz

<Y> : -8.12 kHz

<Z> : 18.82 kHz

Eigenvectors

```
   e<X>    e<Y>    e<Z>
x  0.5831 -0.0000  0.8124   α:  -90.00
y -0.0000  1.0000 -0.0000   β:   54.33
z -0.8124 -0.0000  0.5831   γ:  180.00
```

Θ 35.667 90.000 54.333

Φ   0.000 90.000   0.000

Averaged coupling and asymmetry

⟨δ⟩:   18.82 kHz

⟨δ/δ₀⟩: 0.875

⟨η⟩:   0.137

Input parameter

spin: 1

coupling δ_0:   21.50 kHz

anisotropy Δ_0:   32.25 kHz

asymmetry η_0:   0.00

cone angle θ: 78.00

jump angle φ: 29.00

euler angle α: 0.00

type of motion: fast   2-site

site pos/deg   pop

 1 -14.50   0.500

 2   14.50   0.500

jump angle distribution gaussian

full width 2σ: 30.00 deg

lorentzian line broadening

linewidth: 3.00

plot from: -150.0 kHz to: 150.0 kHz

number of points: 256

points per line: 2

Results

Tensor in PAS System

	x	y	z
x	-10.75	0.00	-0.00
y	0.00	-10.75	0.00
z	-0.00	0.00	21.50

Averaged Tensor in cone frame

	x	y	z
x	16.44	0.00	6.14
y	0.00	-7.09	0.00
z	6.14	0.00	-9.36

Eigenvalues

<X> :   -10.74 kHz

<Y> :   -7.09 kHz

<Z> :   17.83 kHz

Eigenvectors

	$e_{<X>}$	$e_{<Y>}$	$e_{<Z>}$		
x	0.2202	-0.0000	0.9755	α:	-90.00
y	-0.0000	1.0000	-0.0000	β:	77.28
z	-0.9755	-0.0000	0.2202	γ:	180.00

Θ 12.719 90.000 77.281

Φ 0.000 90.000 0.000

Averaged coupling and asymmetry

<δ>:   17.83 kHz

<δ/δ$_0$>: 0.829

<η>:   0.205
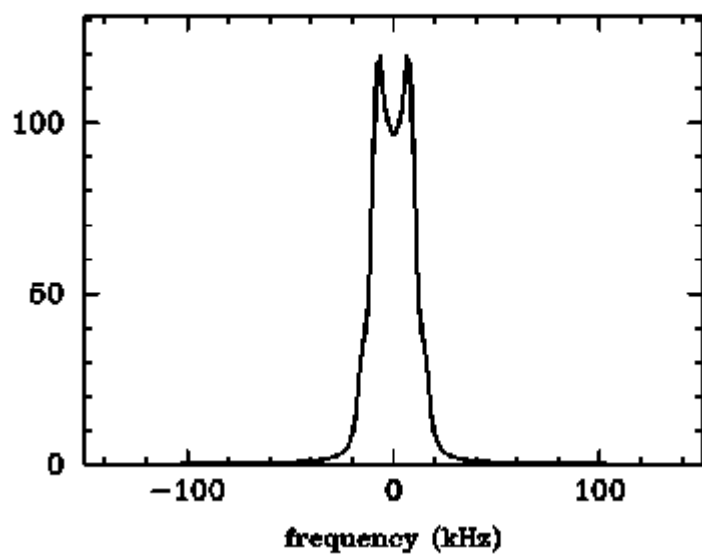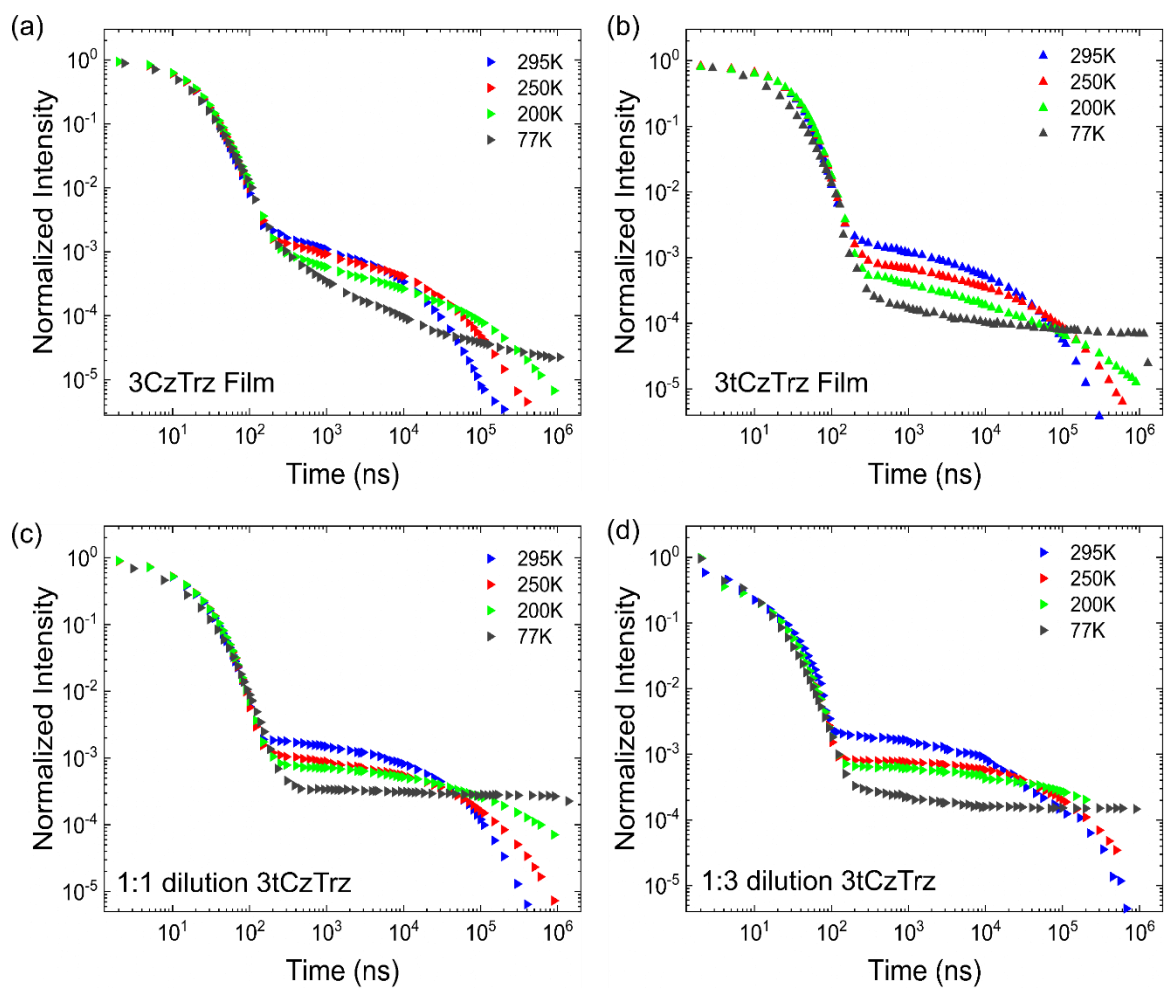
Appendix 47 Temperature scan of transient photoluminescence spetra of (a)-(d) the neat film of 3c and 2c and (c)-(d) diluted film of 2c in polysytrene host.
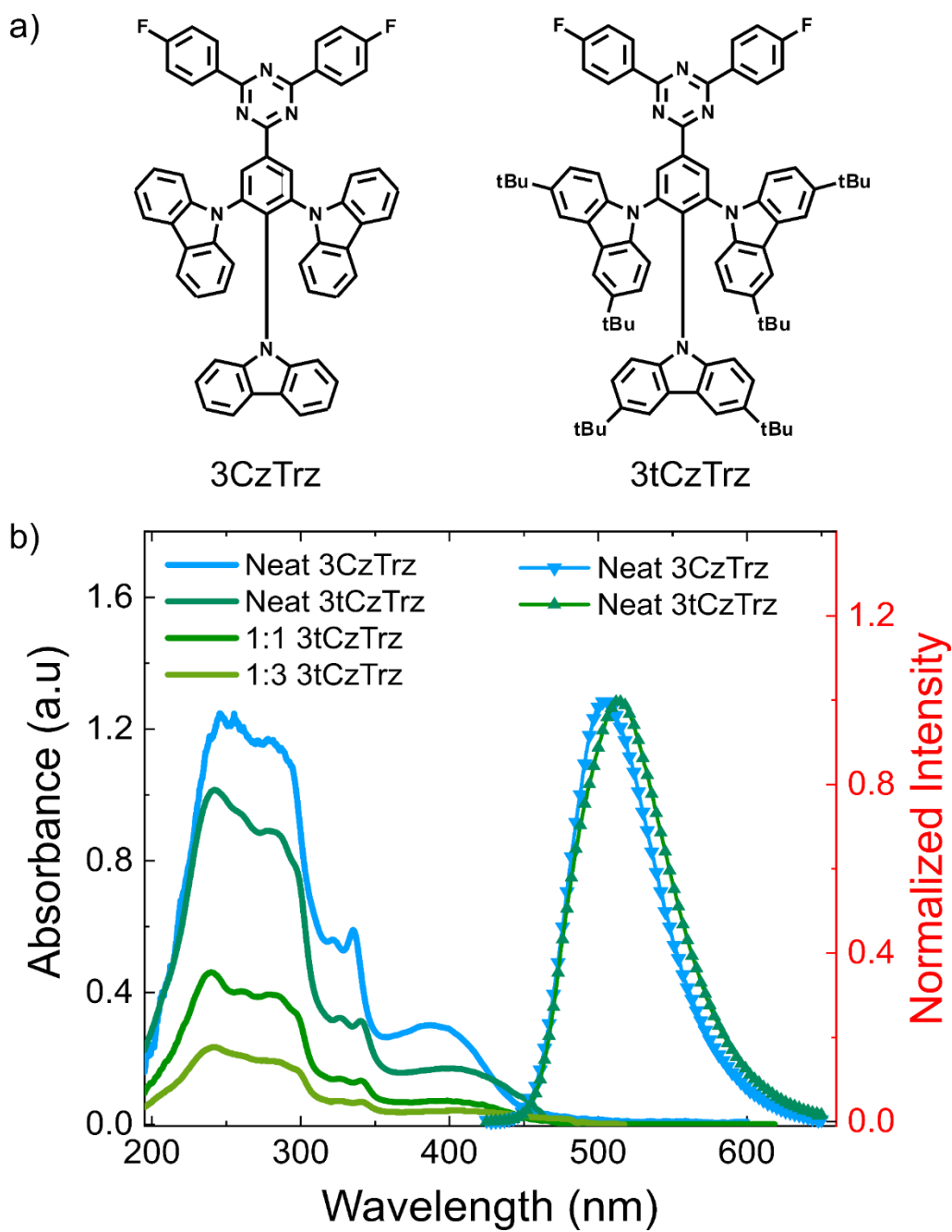
*Appendix 48: (a) Chemical structure of **3c** and tert-butyl substituted **2c**. (b) Absorption spectrum of solution processed neat film of **3c** and **2c** in blue and green respectively; and 1:1 and 1:3 dilution of **2c** in polystyrene (PS) in the gradient of green color respectively. The sprectra in the downward facing(in blue) and upward facing (in green) triangles represent the steady-tate emission of neat film **3c** and **2c** respectively.*
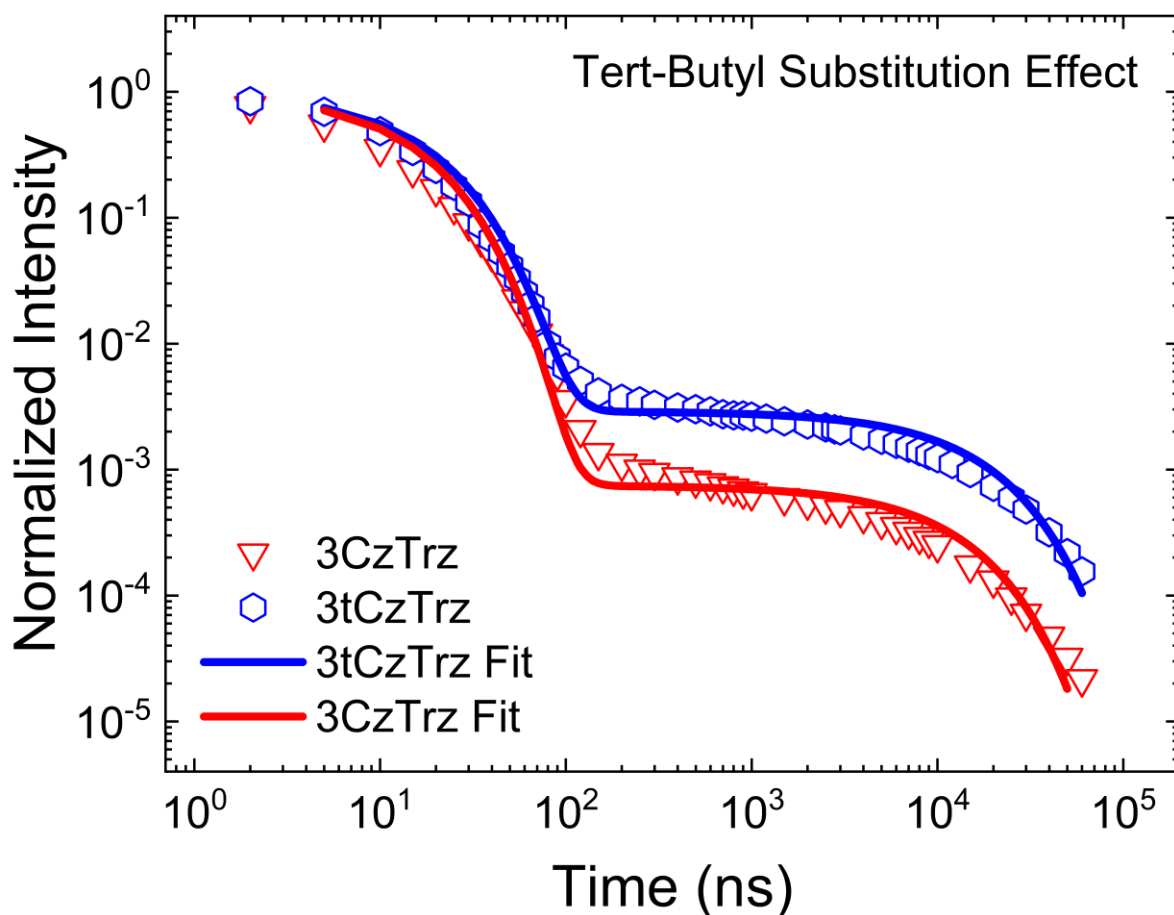
*Appendix 49 Transient PL curves of neat **3CzTrz** and **3tCzTrz** films at the excitation density of 8 mW cm^{-2} shown in circle symbol in red and blue respectively. The line in red and blue represents the fit obtained from the kinetic modelling of the PL curves.*

*Appendix 50 Summary of photophysical paramneters determined from the kinetic fitting of the transient kinetic curves of **3CzTrz** and **3tCzTrz** measured at the power 8 mW cm^{-2}.*

TertButyl Effect	3CzTrz	3tCzTrz
$[S_0]$ [m^{-3}]	3.3×10^{23}	2.6×10^{23}
τ_s [ns]	80	90
k_{nrT} [s^{-1}]	6.3×10^{4}	1.4×10^{4}
PLQY [%]	37	80
k_{ISC} [s^{-1}]	4.2×10^{7}	4.0×10^{7}
k_{rISC} [s^{-1}]	6.0×10^{4}	1.9×10^{5}

	1CzTrz-F	2CzTrz-F	3CzTrz-F
HOMO (eV)	5.87	5.85	5.85
LUMO (eV)	2.73	2.91	2.94
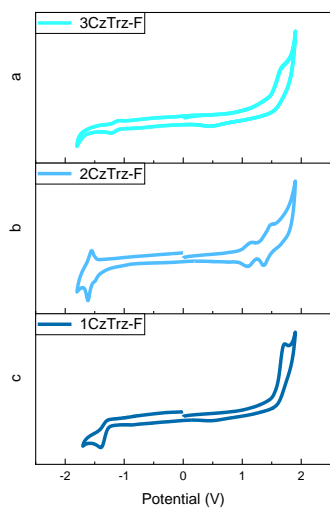
*Appendix 51 CV data for compounds **3a-3c***

Sample	E_{ox}(V)	E_{red}(V)	HOMO(eV)	LUMO (eV)	E_g(eV)
1a	0.69	-2.19	-5.49	-2.61	2.88
1b	0.94	-2.03	-5.74	-2.77	2.97
1c	1.02	-1.99	-5.82	-2.81	3.01
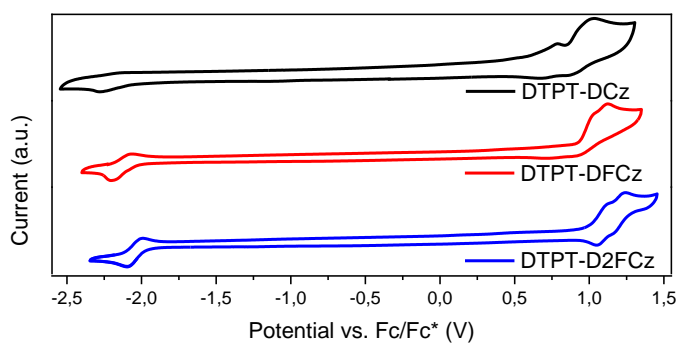
*Appendix 52 CV data for compounds **1a-1c***

Drift-diffusion modeling parameters for electron-only devices of 3a-3c.

	3a	3b	3c
Trap density, N_t gauss ($\times 10^{22}$ m^{-3})	100	6.0	0.9
Trap depth, E_t (eV)	0.48	0.63	0.70
Width of Gaussian trap distribution, σ_t (eV)	0.10	0.10	0.10
Lattice constant EGDM, a ($\times 10^{-9}$ m)	1.60	1.40	1.80
DOS variance EGDM, σ (eV)	0.10	0.11	0.09
Mobility at 295 K, μ ($\times 10^{-10}$ m²/Vs)	8.12	4.15	27.92
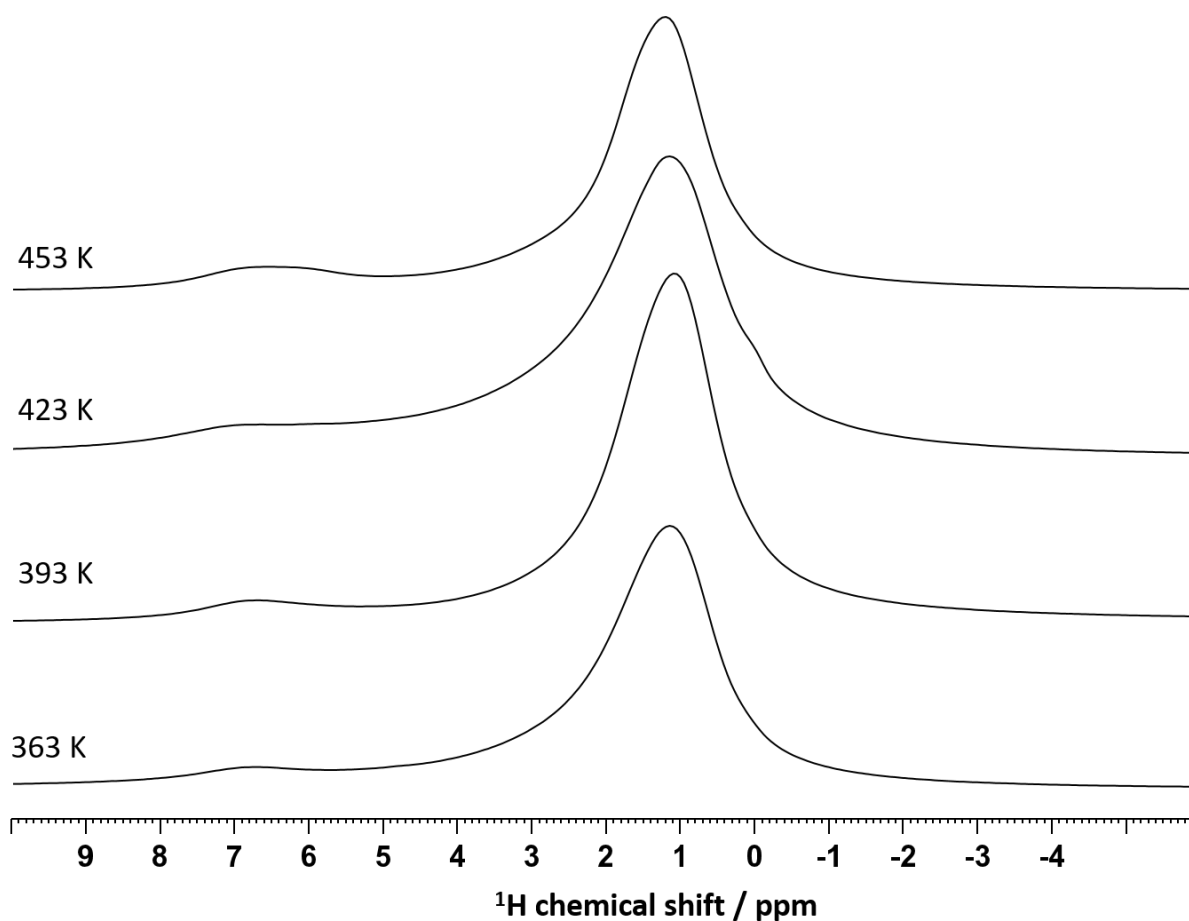
Appendix 54 ^{1}H MAS spectra of 1:16 molar ratio F$_4$TCNQ doped P3HT films recorded at 25 kHz MAS and ambient conditions after annealing for 2h at different temperatures.
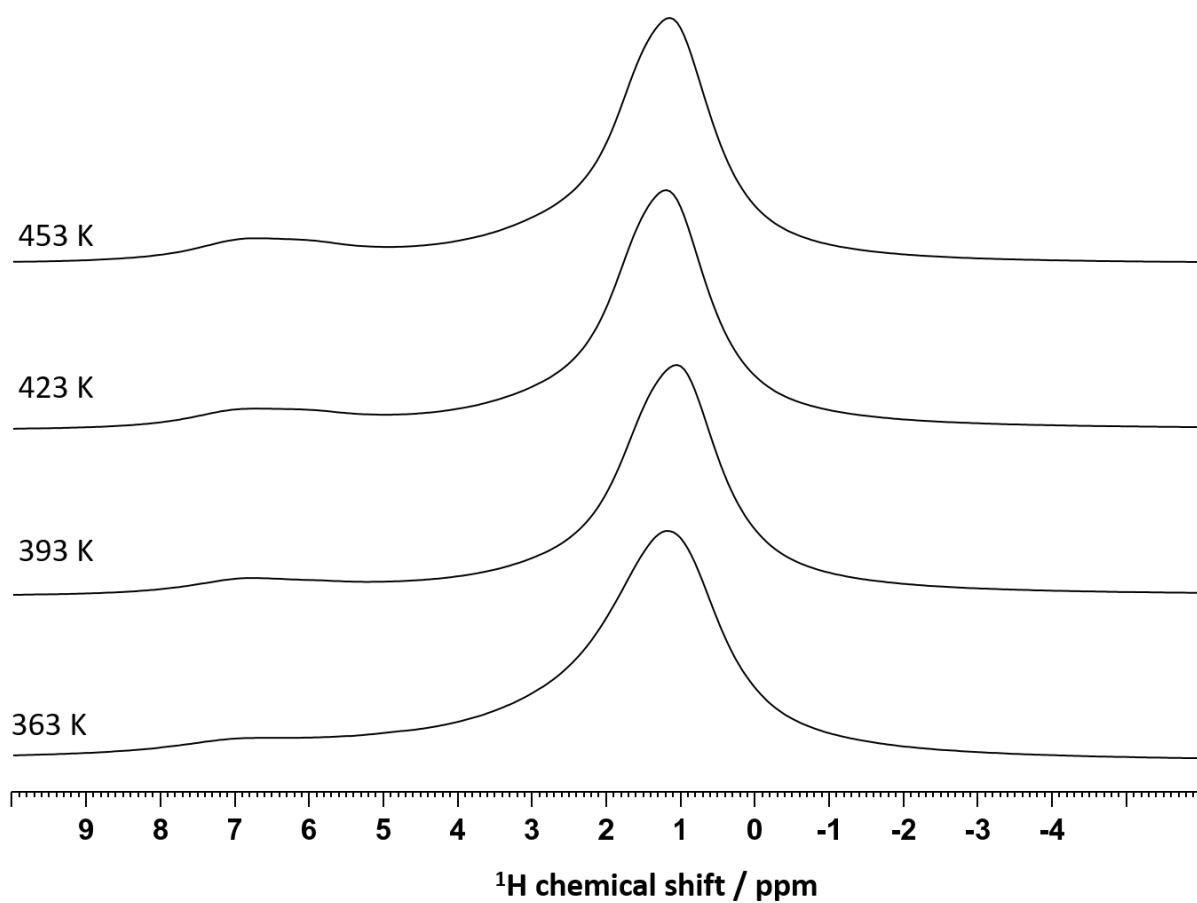
Appendix 55 *^{1}H MAS spectra of 1:8 molar ratio F$_4$TCNQ doped P3HT films recorded at 25 kHz MAS and ambient conditions after annealing for 2h at different temperatures.*
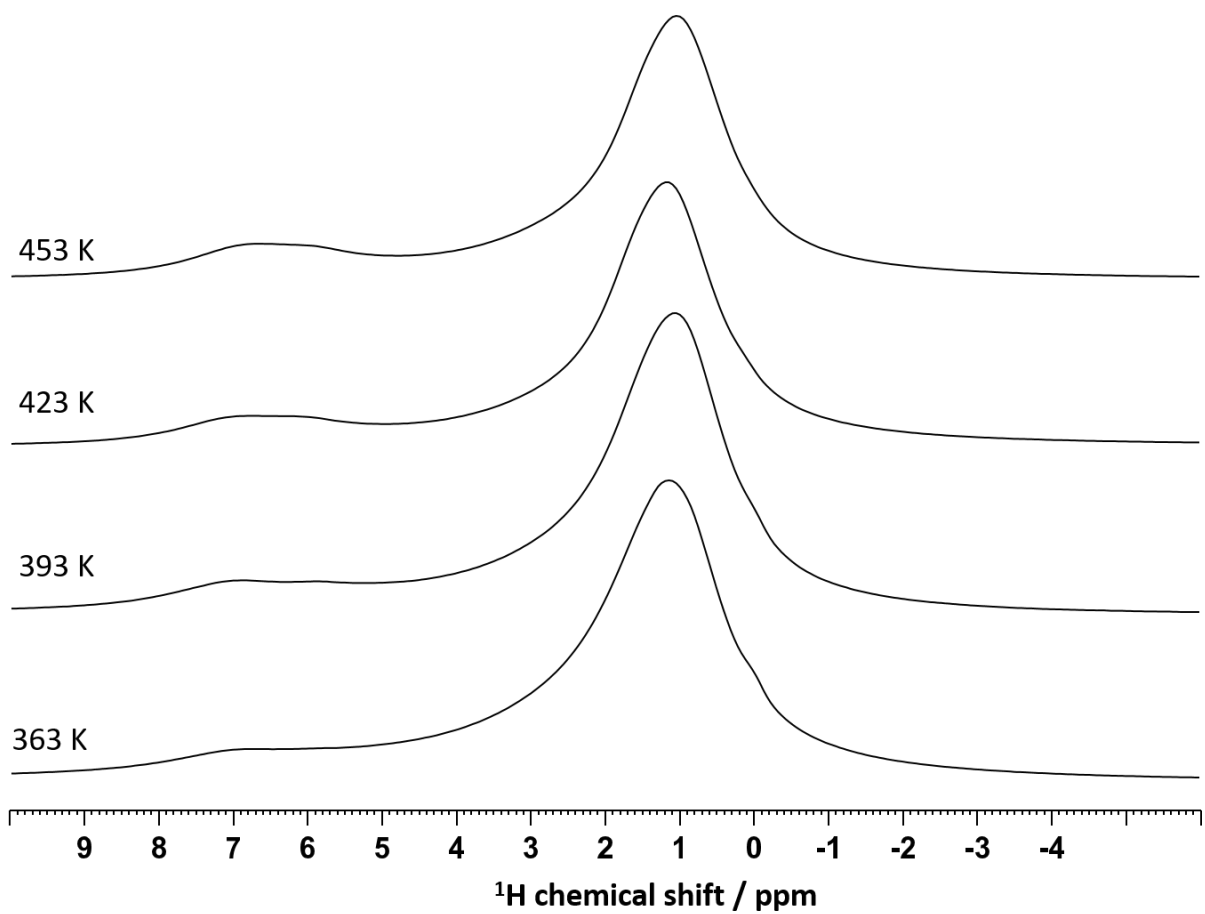
Appendix 56 ^{1}H MAS spectra of 1:4 molar ratio F$_4$TCNQ doped P3HT films recorded at 25 kHz MAS and ambient conditions after annealing for 2h at different temperatures.
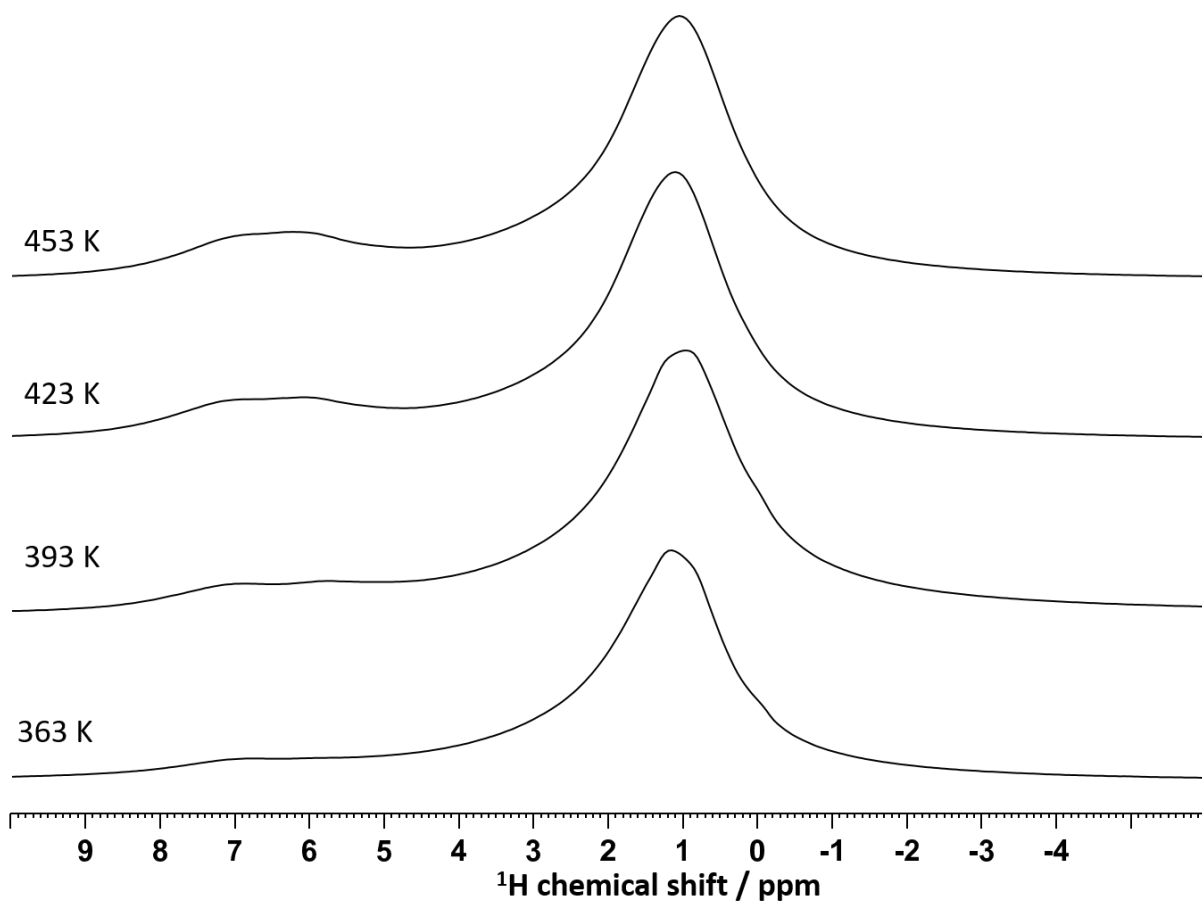
Appendix 57 ^{1}H MAS spectra of 1:2 molar ratio F4TCNQ doped P3HT films recorded at 25 kHz MAS and ambient conditions after annealing for 2h at different temperatures.

453 K

423 K

393 K

363 K

9 8 7 6 5 4 3 2 1 0 -1 -2 -3 -4

^{1}H chemical shift / ppm
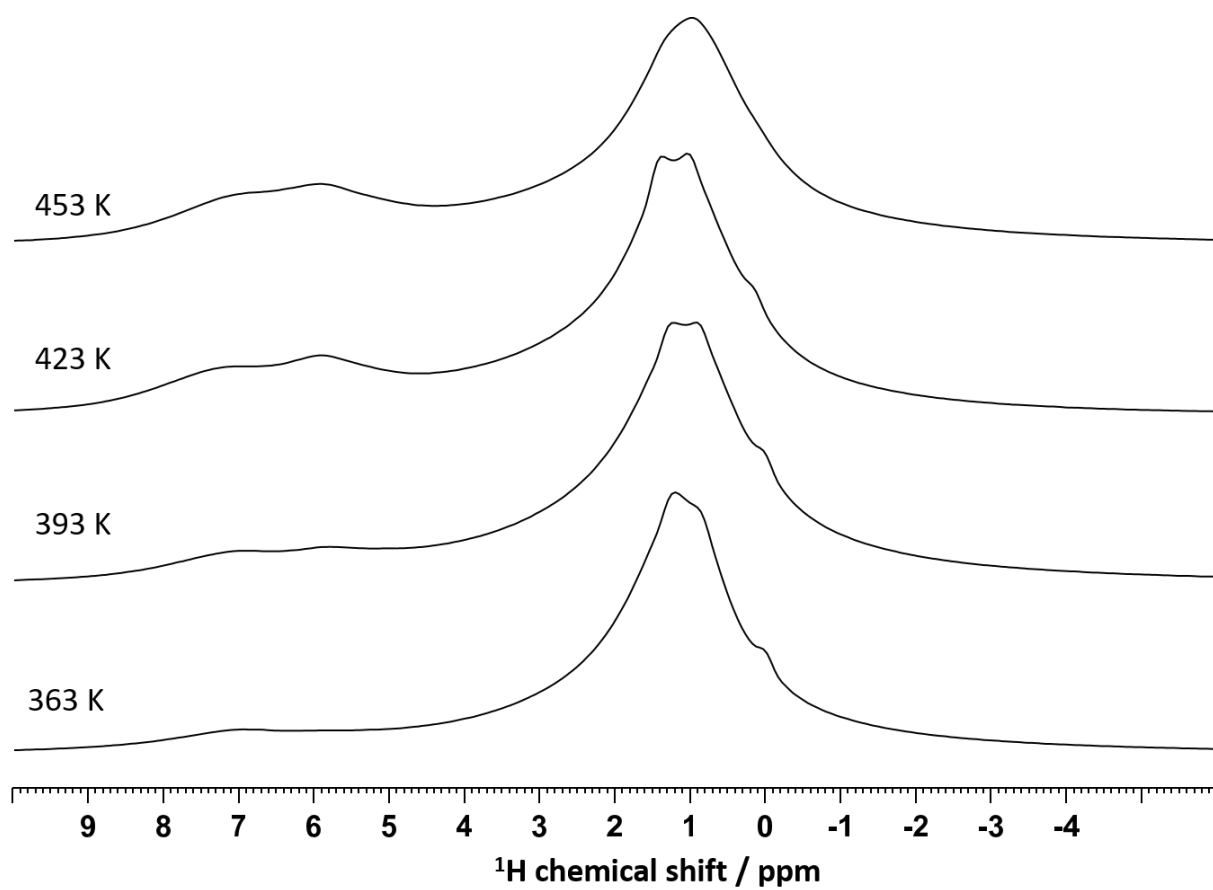
Appendix 58 ^{1}H MAS spectra of 1:1 molar ratio F4TCNQ doped P3HT films recorded at 25 kHz MAS and ambient conditions after annealing for 2h at different temperatures.

453 K

423 K

393 K

363 K

160   140   120   100   80   60   40   20

^{13}C chemical shift / ppm
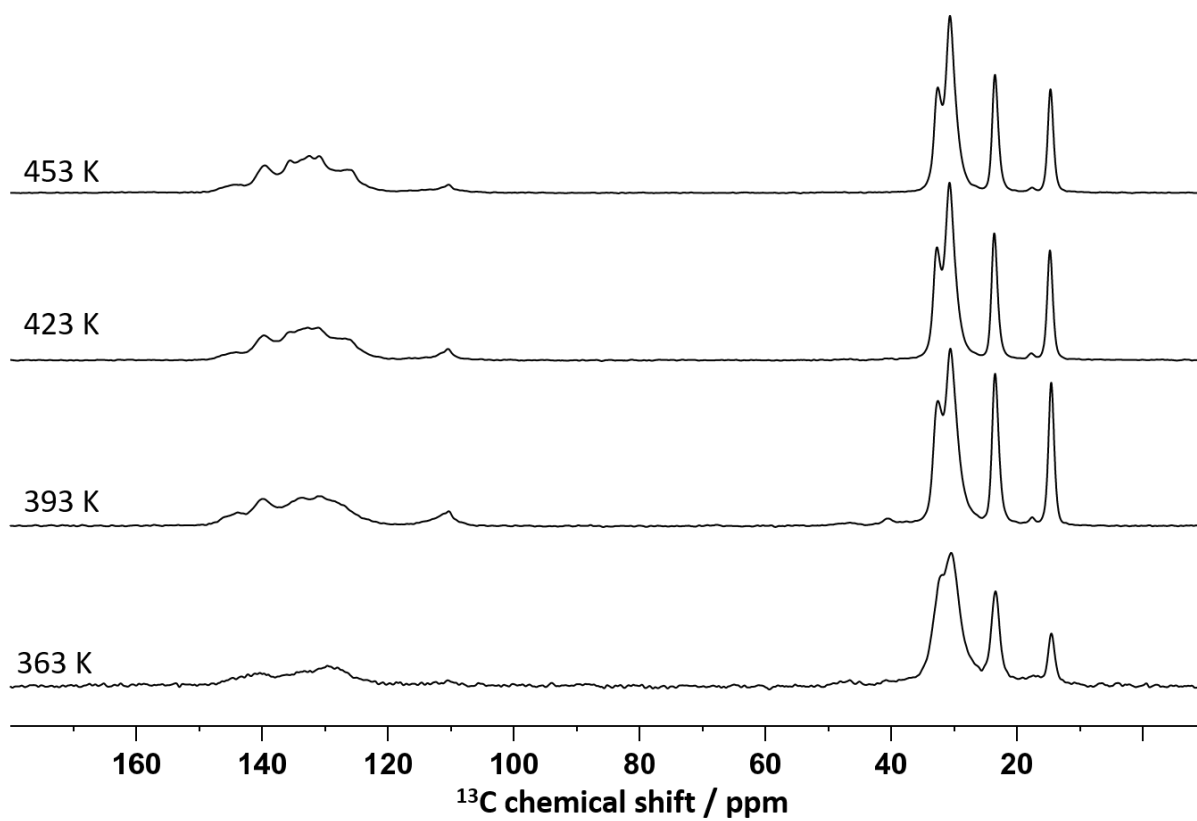
Appendix 59 {^{1}H}-^{13}C CP MAS spectra of 1:8 molar ratio F4TCNQ doped P3HT films recorded at 25 kHz MAS and ambient conditions after annealing for 2h at different temperatures.
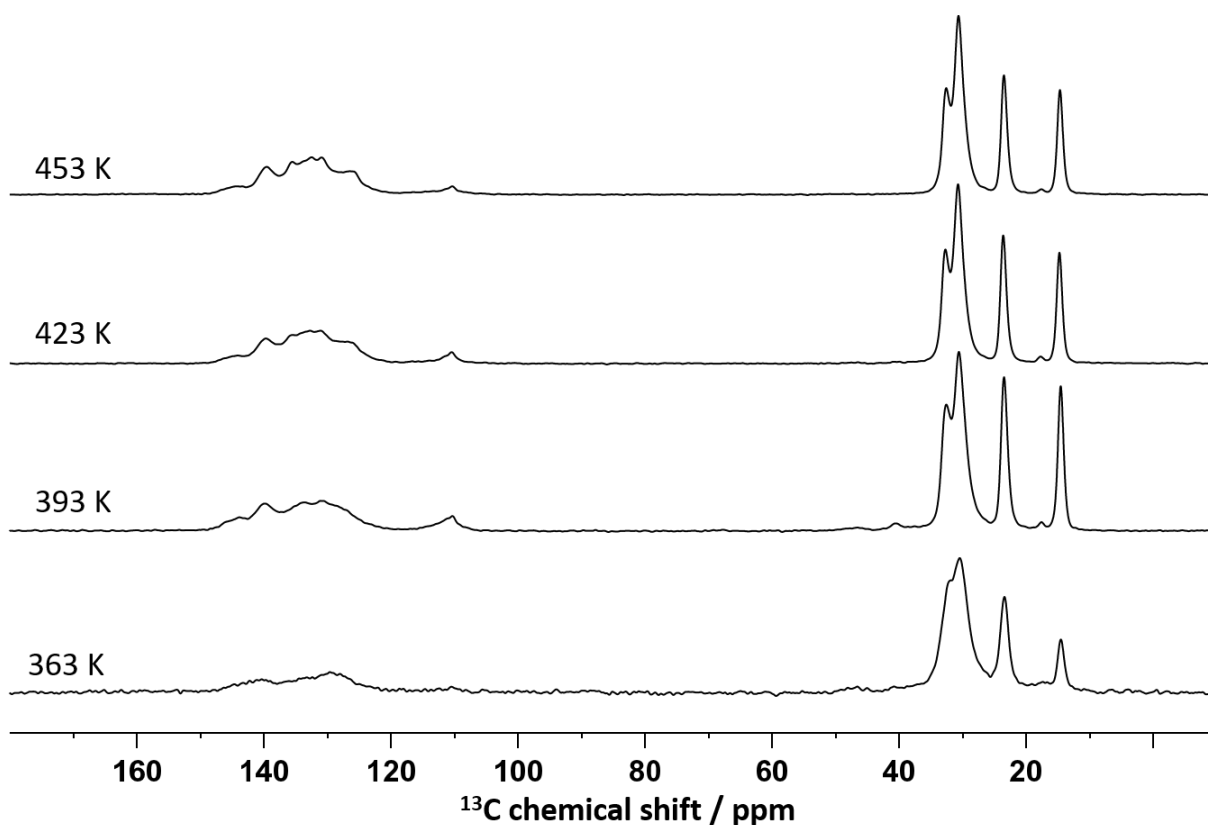
Appendix 60 {^{1}H}-^{13}C CP MAS spectra of 1:4 molar ratio F4TCNQ doped P3HT films recorded at 25 kHz MAS and ambient conditions after annealing for 2h at different temperatures.
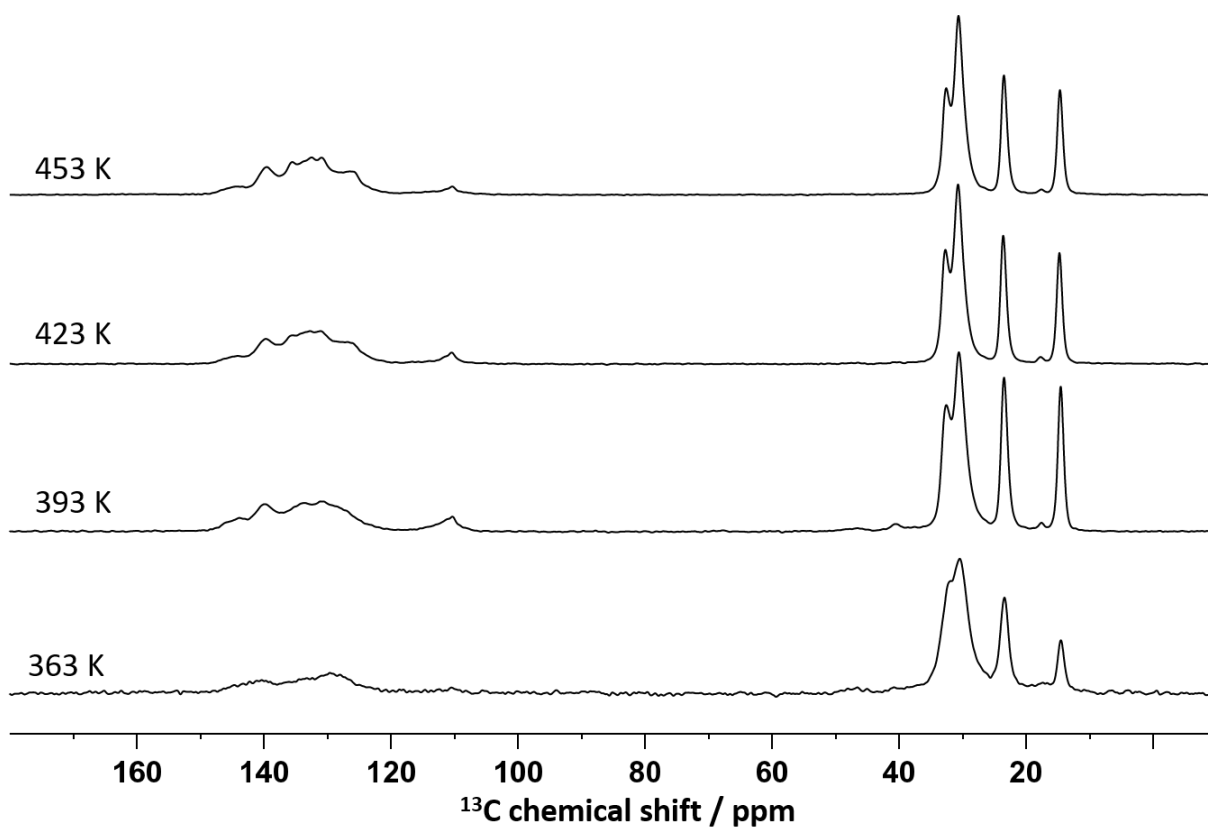
Appendix 61 {^{1}H}-^{13}C CP MAS spectra of 1:2 molar ratio F4TCNQ doped P3HT films recorded at 25 kHz MAS and ambient conditions after annealing for 2h at different temperatures.
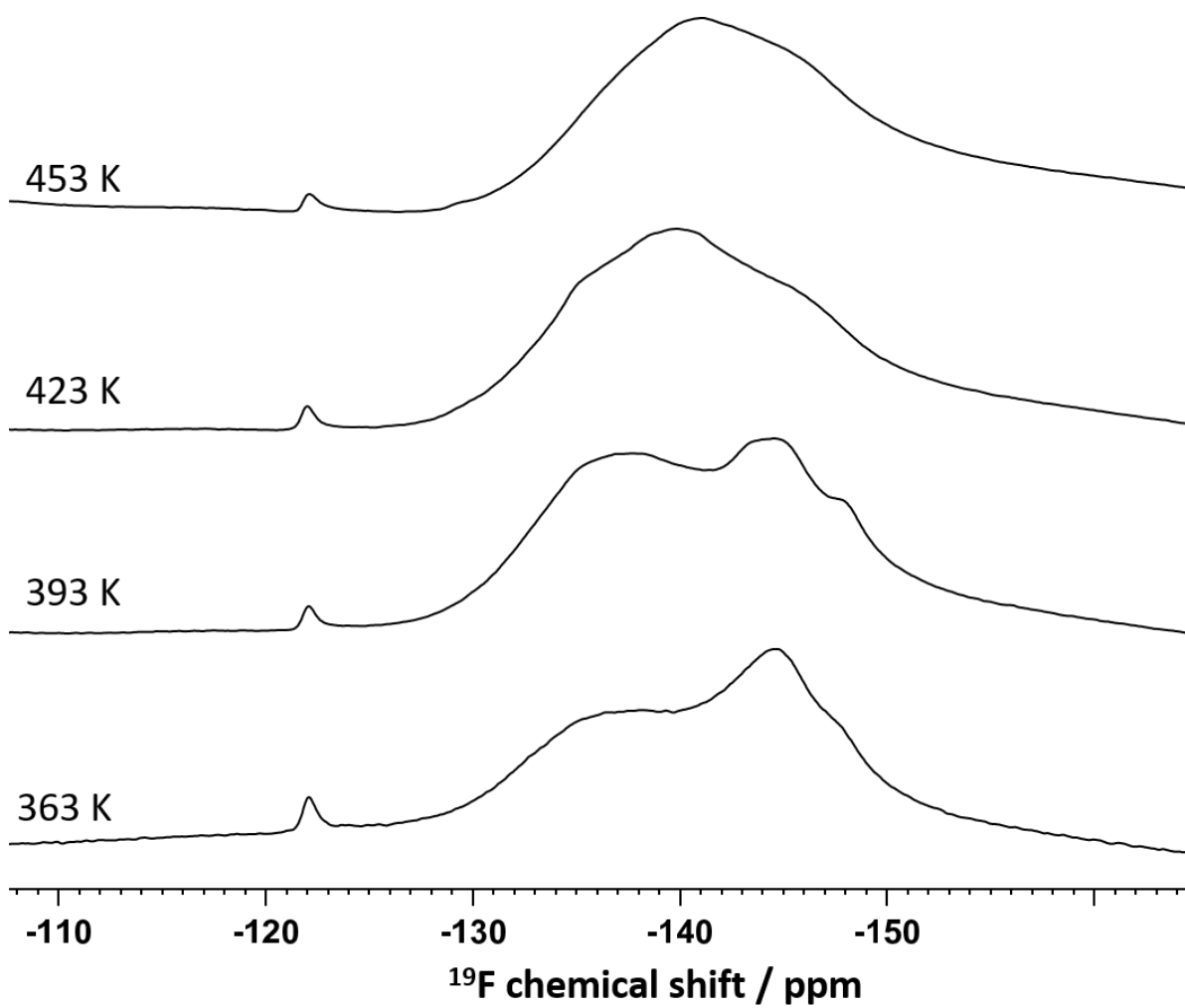
Appendix 62 ^{19}F MAS spectra of 1:16 molar ratio F4TCNQ doped P3HT films recorded at 25 kHz MAS and ambient conditions after annealing for 2h at different temperatures.
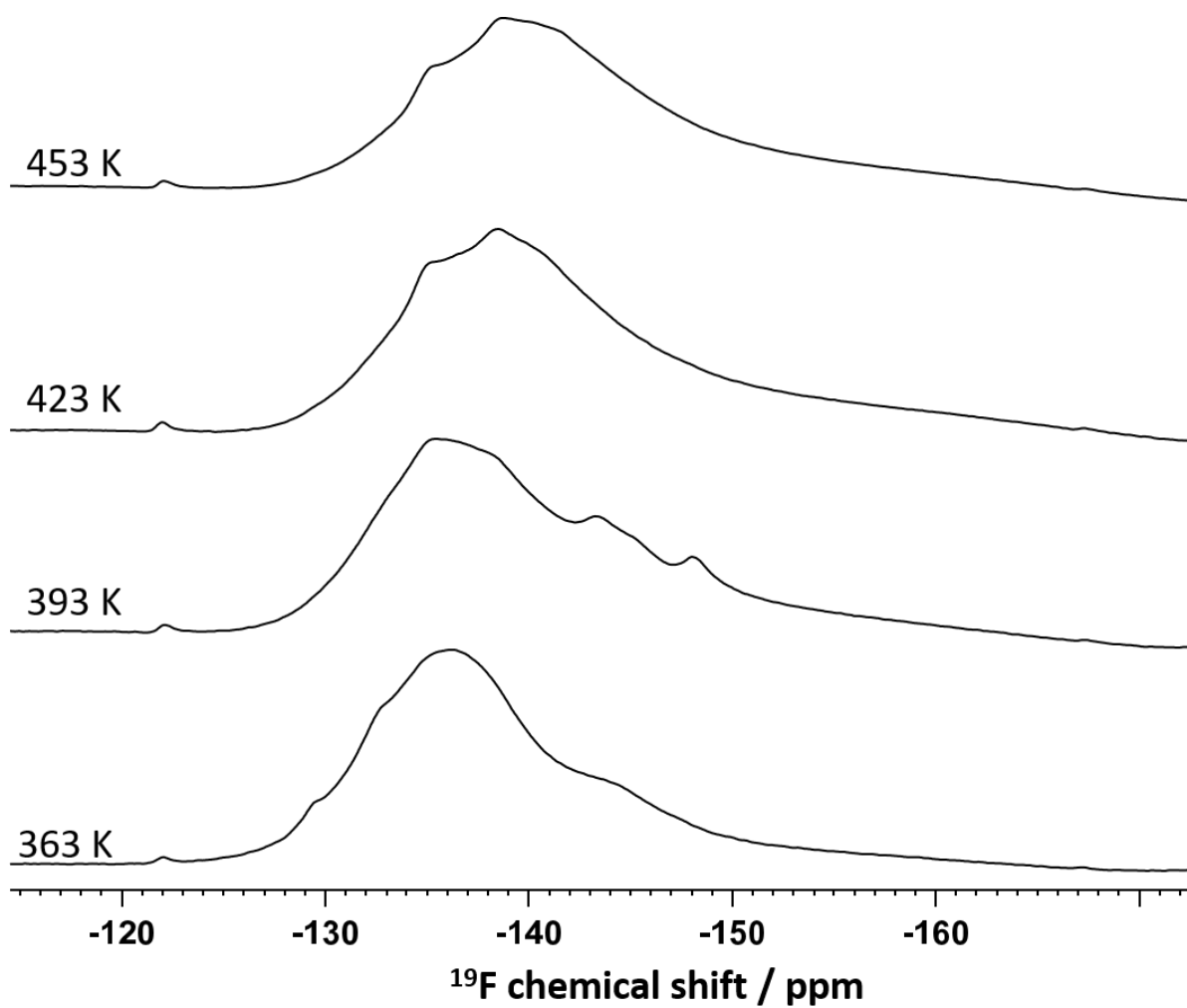
Appendix 63 ^{19}F MAS spectra of 1:8 molar ratio F4TCNQ doped P3HT films recorded at 25 kHz MAS and ambient conditions after annealing for 2h at different temperatures.
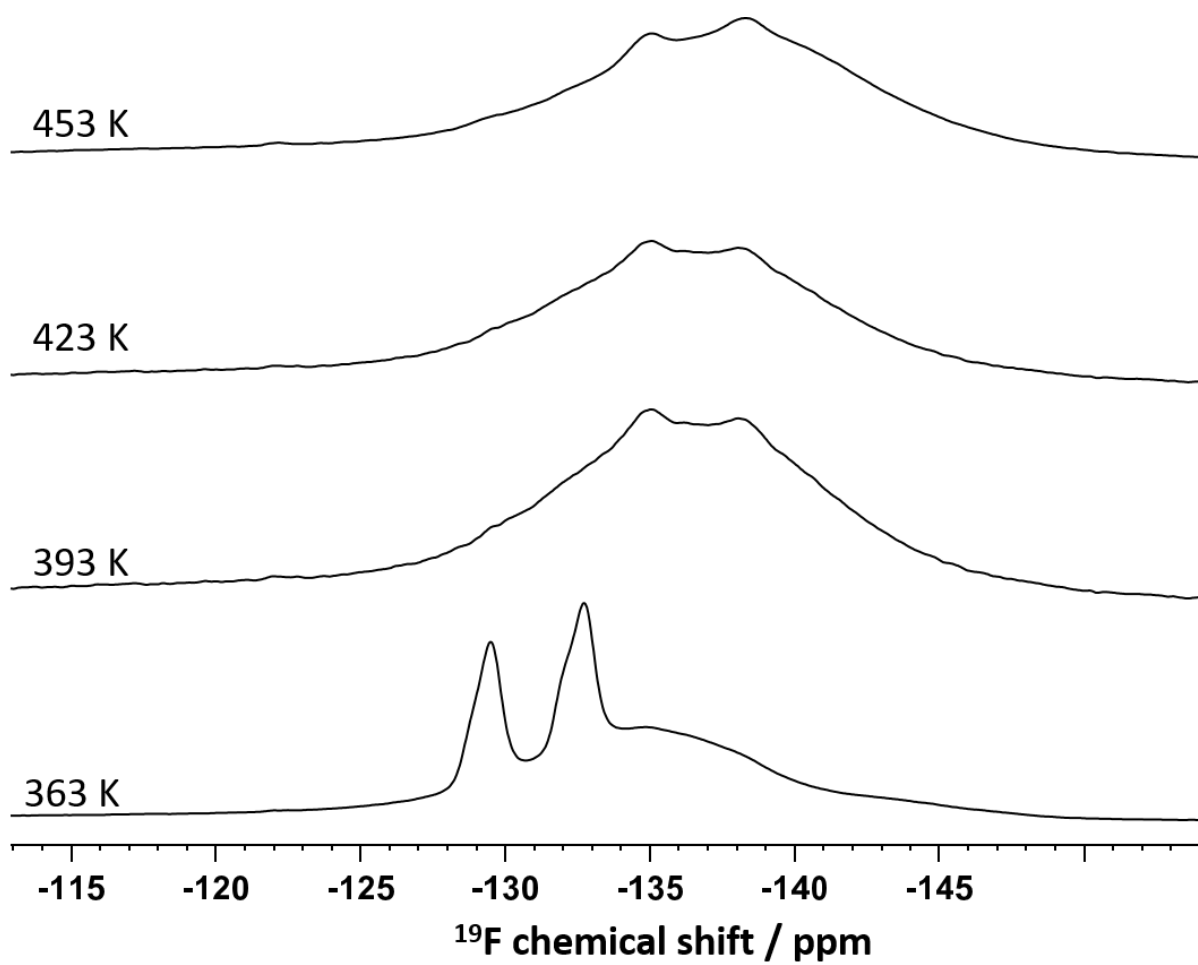
Appendix 64 ^{19}F MAS spectra of 1:4 molar ratio F4TCNQ doped P3HT films recorded at 25 kHz MAS and ambient conditions after annealing for 2h at different temperatures.
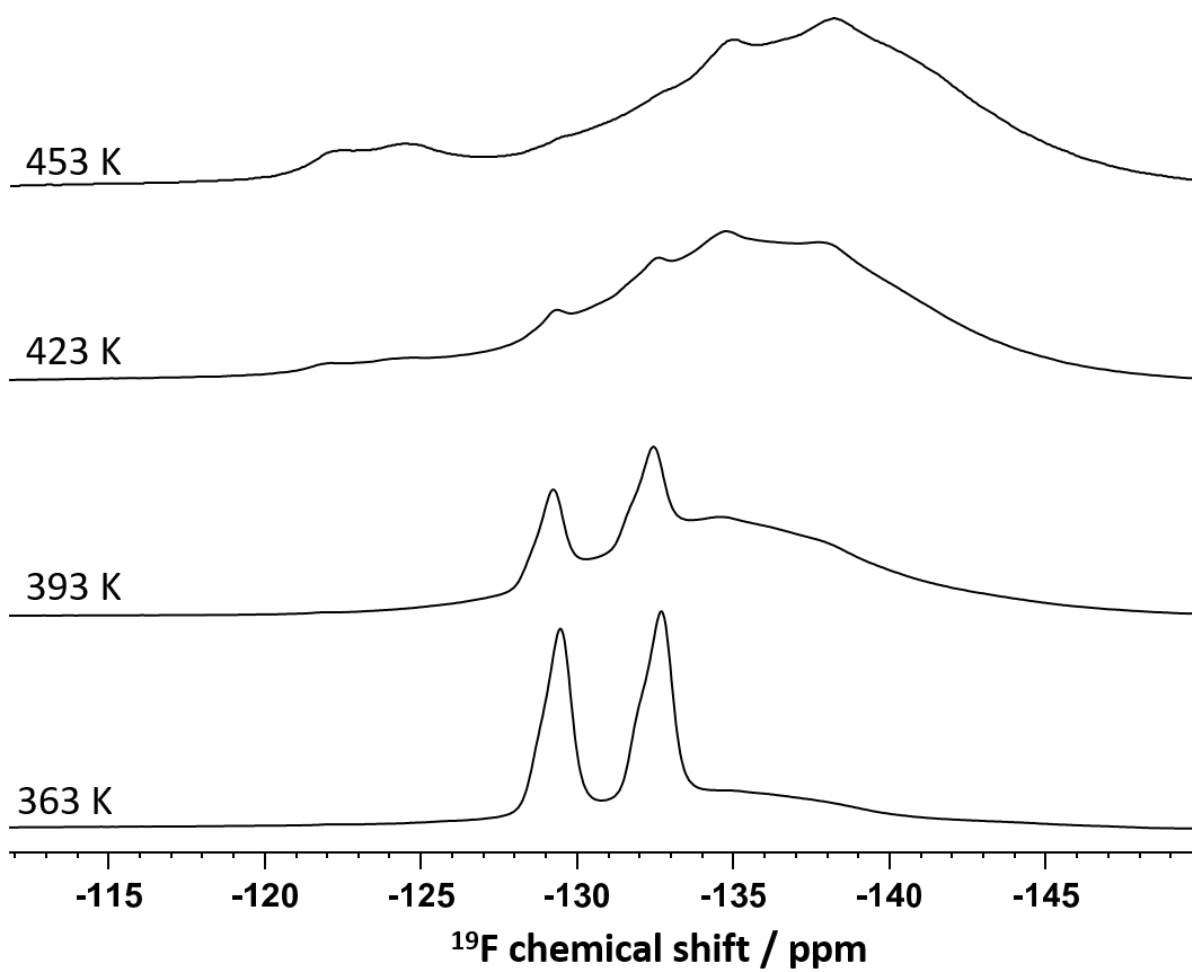
Appendix 65 ^{19}F MAS spectra of 1:2 molar ratio F4TCNQ doped P3HT films recorded at 25 kHz MAS and ambient conditions after annealing for 2h at different temperatures.
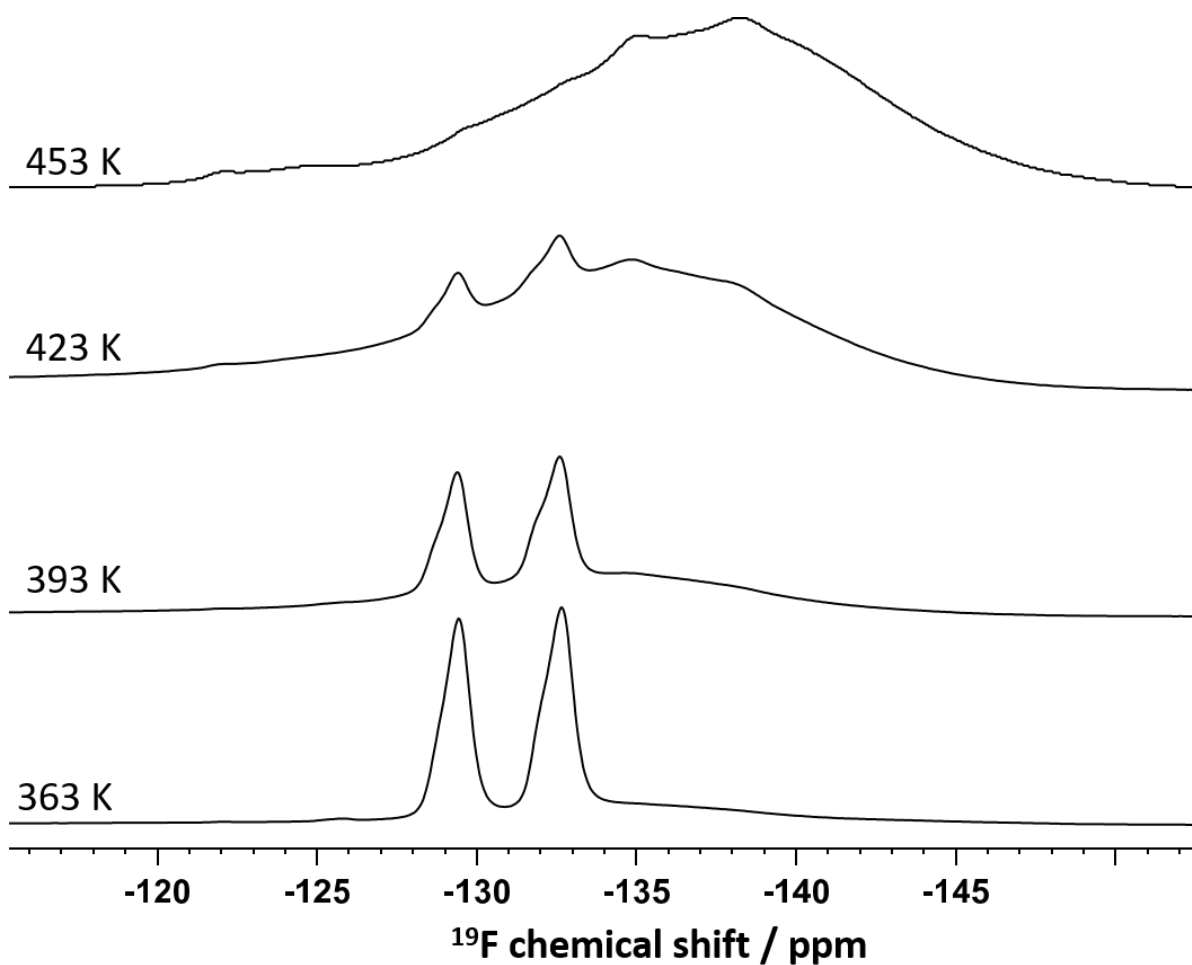
Appendix 66 ^{19}F MAS spectra of 1:1 molar ratio F4TCNQ doped P3HT films recorded at 25 kHz MAS and ambient conditions after annealing for 2h at different temperatures.
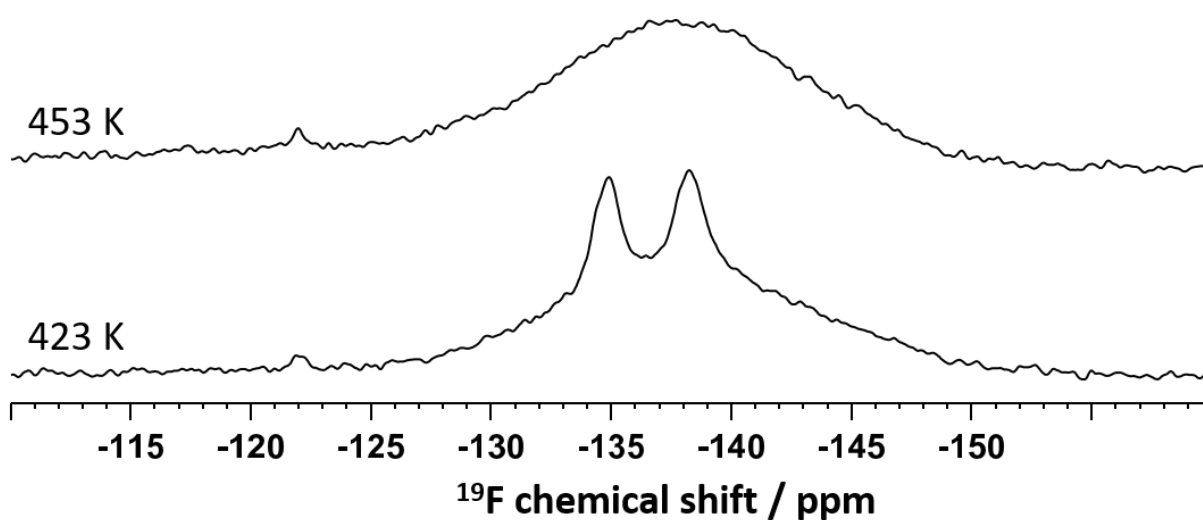
Appendix 67 ^{19}F MAS spectra of 1:16 molar ratio F4TCNQ doped P3HT films recorded at 25 kHz MAS and ambient conditions with long d1 (1000s) after annealing for 2h at different temperatures.
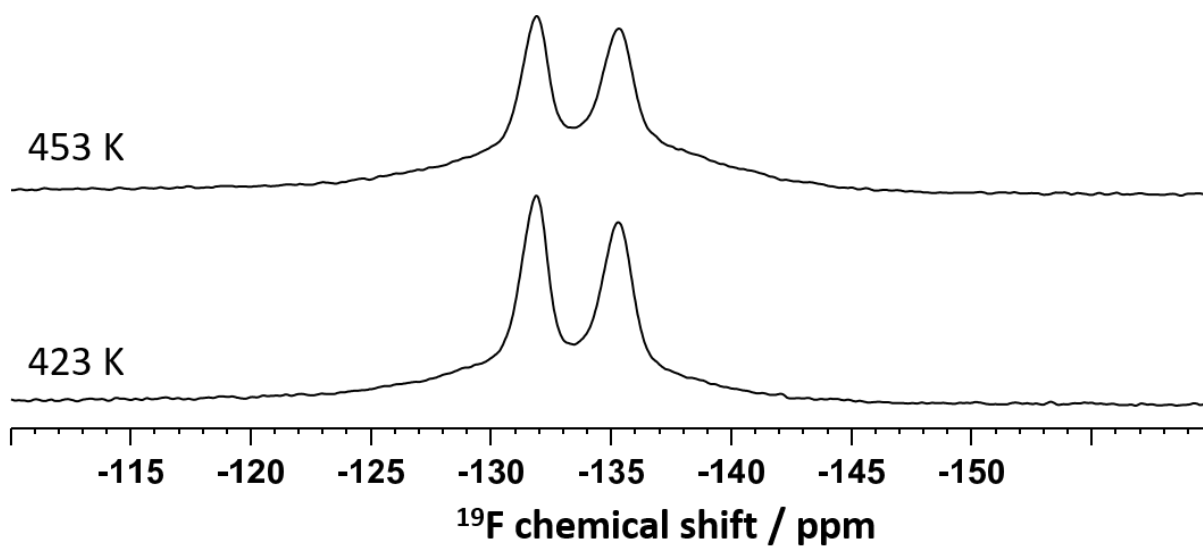
Appendix 68 ^{19}F MAS spectra of 1:8 molar ratio F4TCNQ doped P3HT films recorded at 25 kHz MAS and ambient conditions with long d1 (1000s) after annealing for 2h at different temperatures.
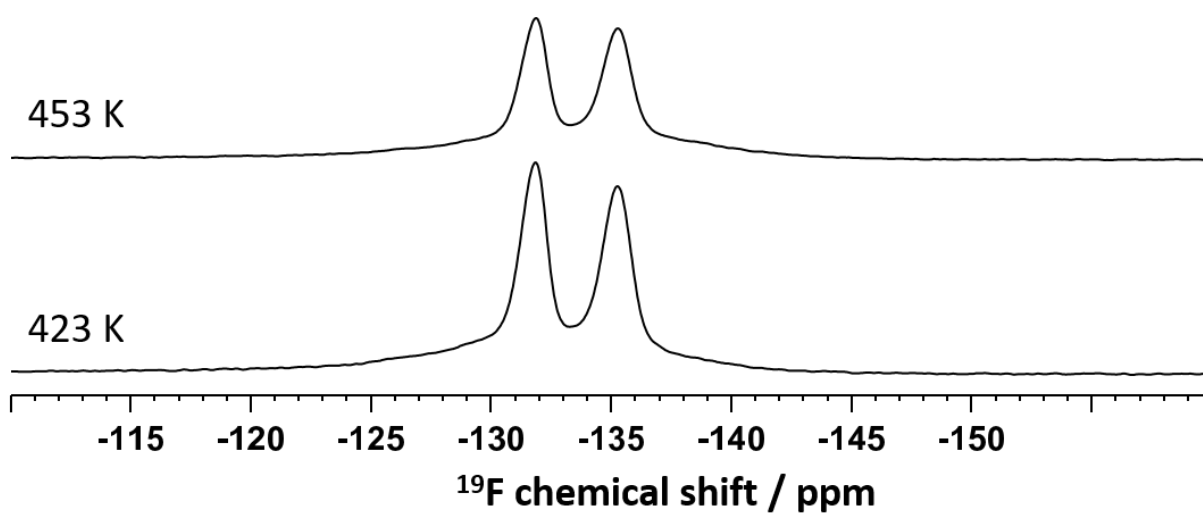
Appendix 69 ^{19}F MAS spectra of 1:4 molar ratio F4TCNQ doped P3HT films recorded at 25 kHz MAS and ambient conditions with long d1 (1000s) after annealing for 2h at different temperatures.
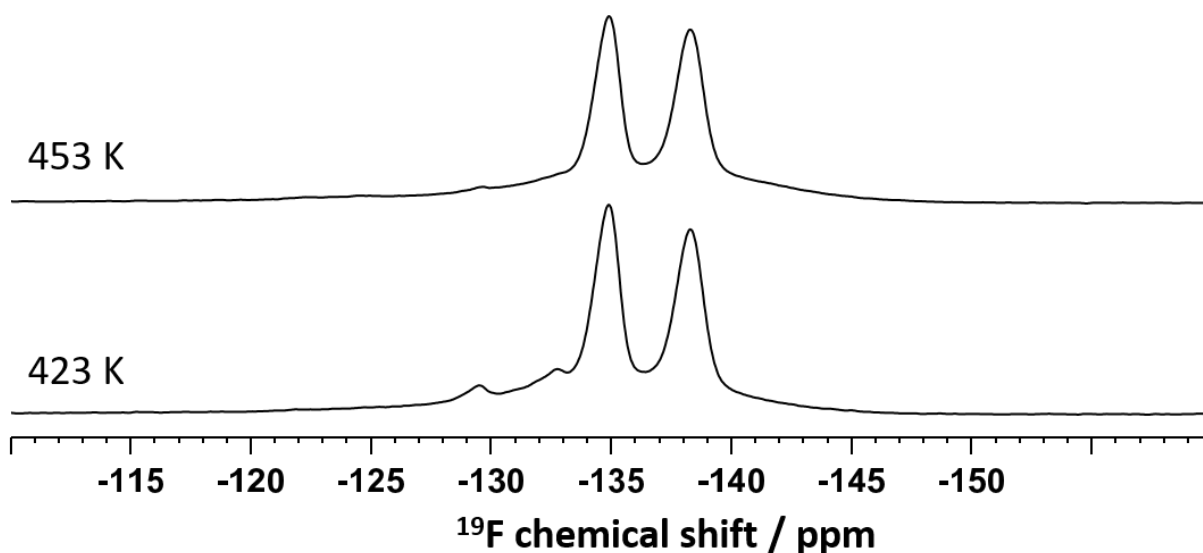
Appendix 70 ^{19}F MAS spectra of 1:2 molar ratio F4TCNQ doped P3HT films recorded at 25 kHz MAS and ambient conditions with long d1 (1000s) after annealing for 2h at different temperatures.
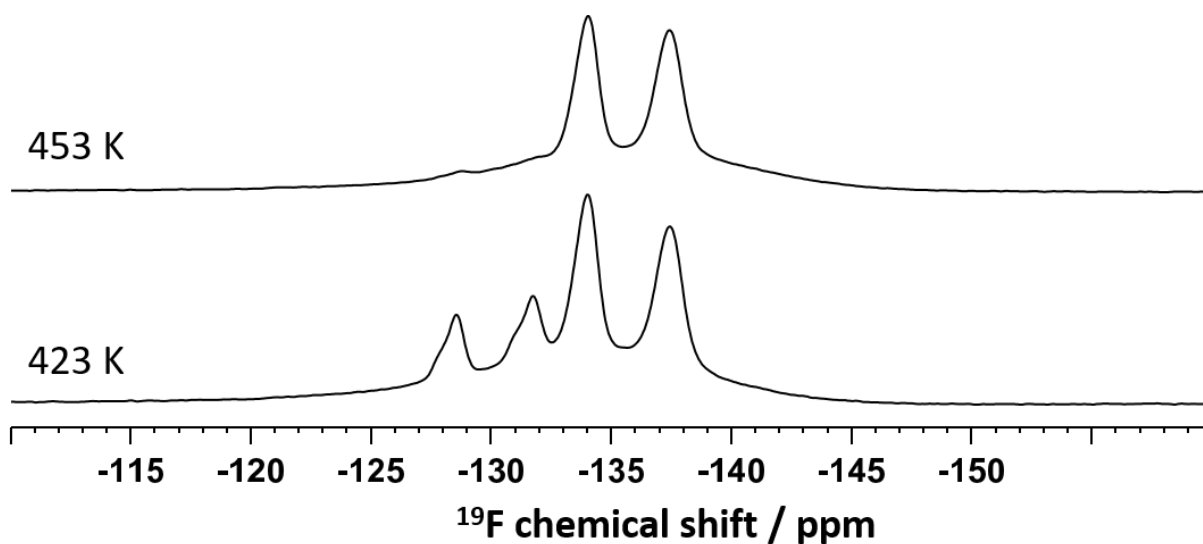
Appendix 71 ^{19}F MAS spectra of 1:1 molar ratio F4TCNQ doped P3HT films recorded at 25 kHz MAS and ambient conditions with long d1 (1000s) after annealing for 2h at different temperatures.
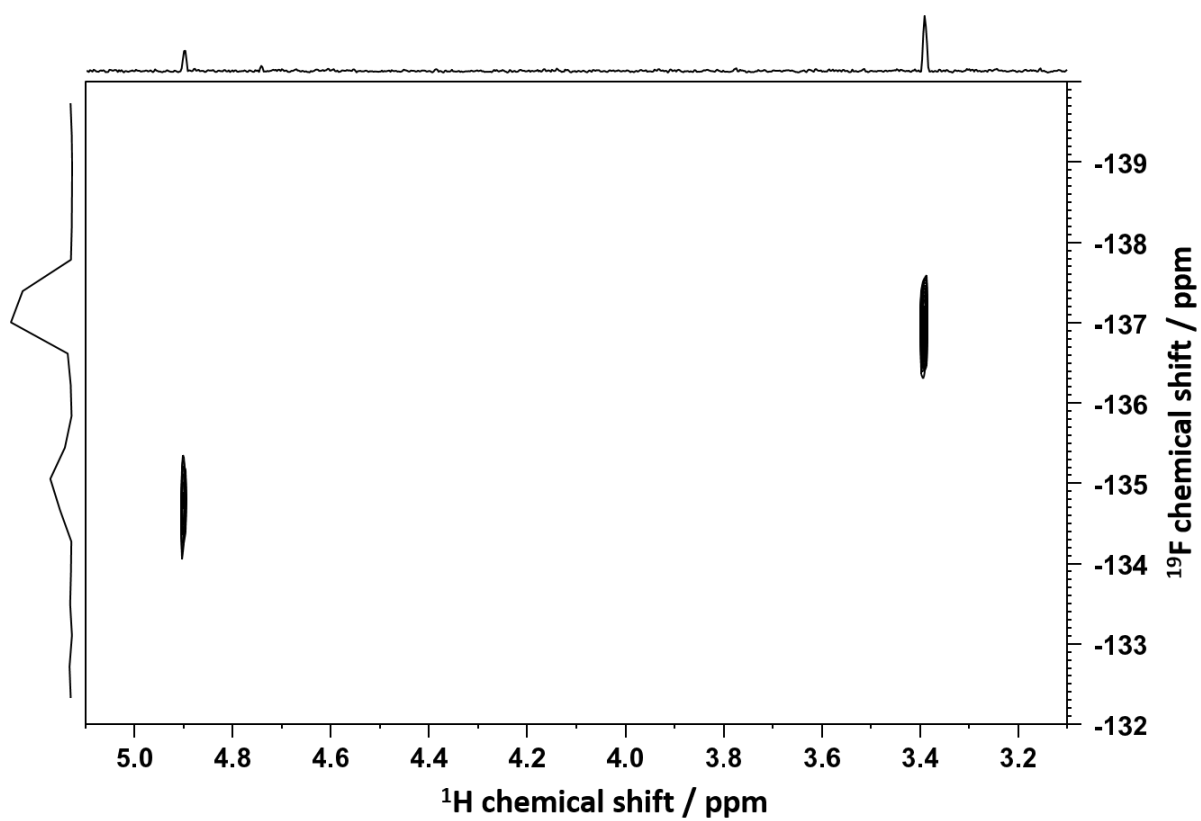
Appendix 72 ^{1}H-^{19}F HMBC spectrum of a 1:1 molar ratio F$_4$TCNQ:P3HT pellet after annealing at 453 K dissolved in bromobenzene.
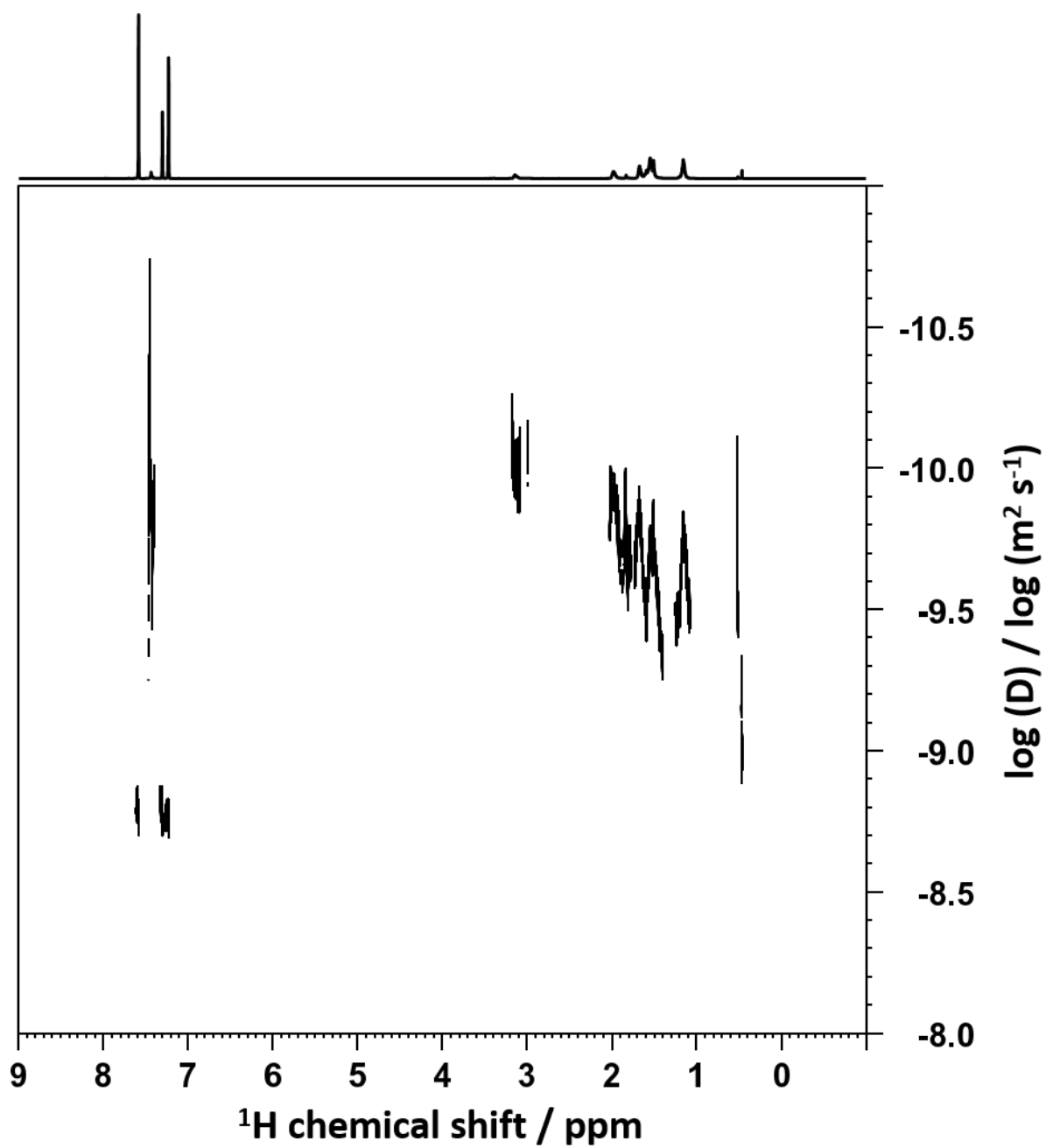
Appendix 73 ^{1}H DOSY spectrum of a 1:16 molar ratio F$_4$TCNQ:P3HT pellet after annealing at 453 K dissolved in bromobenzene.
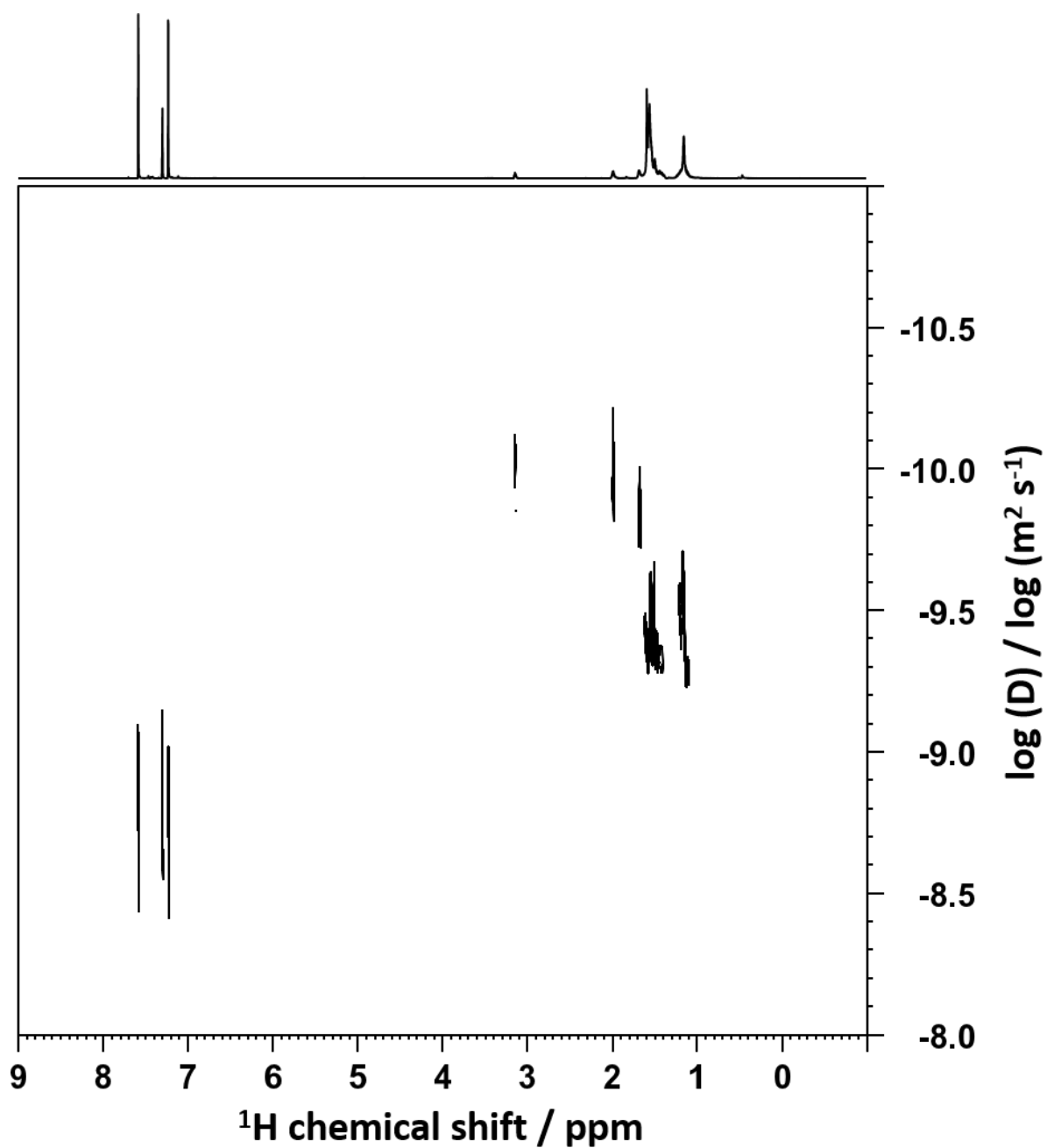
Appendix 74 ^{1}H DOSY spectrum of a 1:8 molar ratio F$_4$TCNQ:P3HT pellet after annealing at 453 K dissolved in bromobenzene.
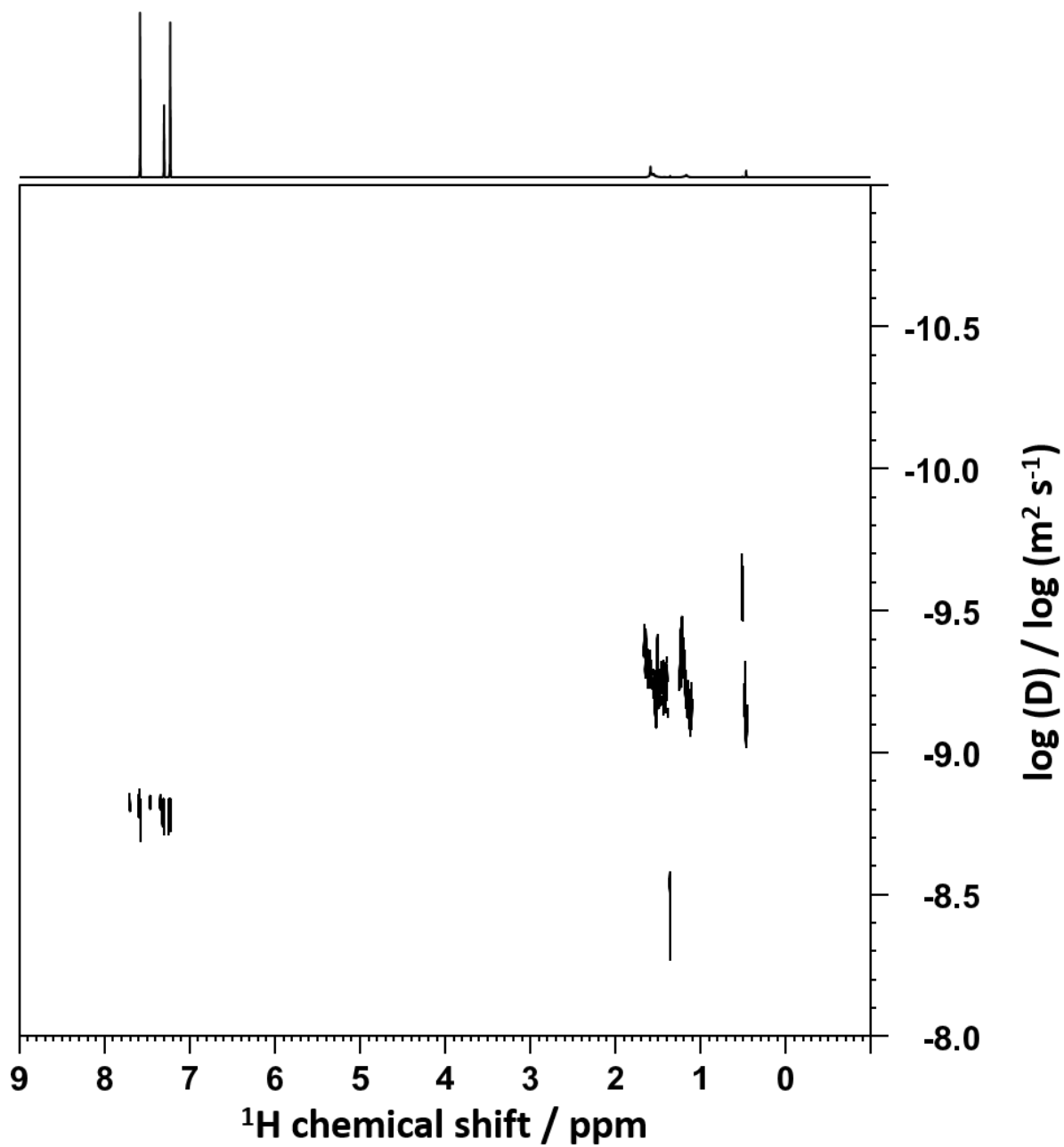
Appendix 75 ^{1}H DOSY spectrum of a 1:4 molar ratio F$_4$TCNQ:P3HT pellet after annealing at 453 K dissolved in bromobenzene.
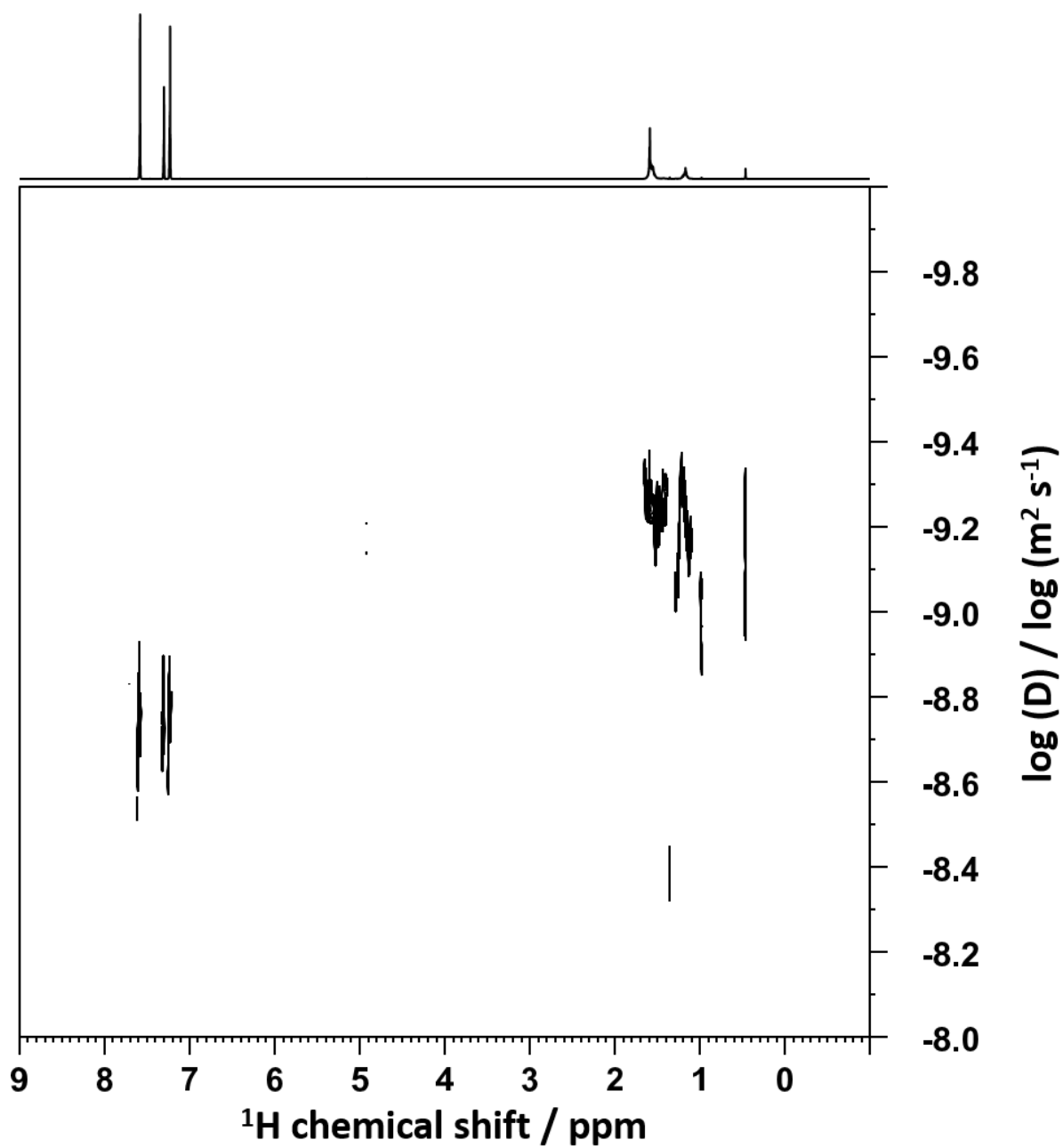
Appendix 76 ^{1}H DOSY spectrum of a 1:2 molar ratio F$_4$TCNQ:P3HT pellet after annealing at 453 K dissolved in bromobenzene.
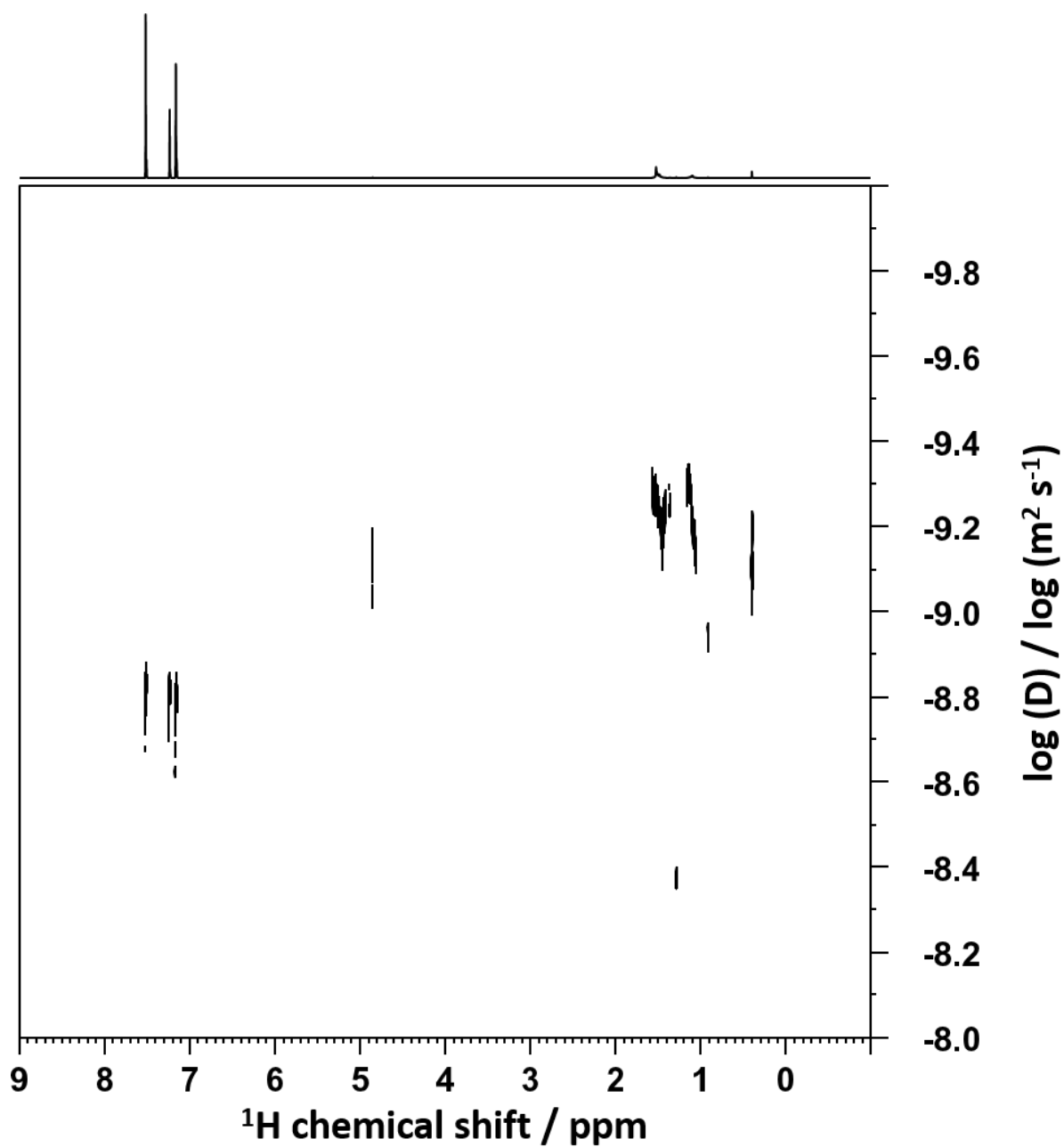
Appendix 77 ^{1}H DOSY spectrum of a 1:1 molar ratio F$_4$TCNQ:P3HT pellet after annealing at 453 K dissolved in bromobenzene.
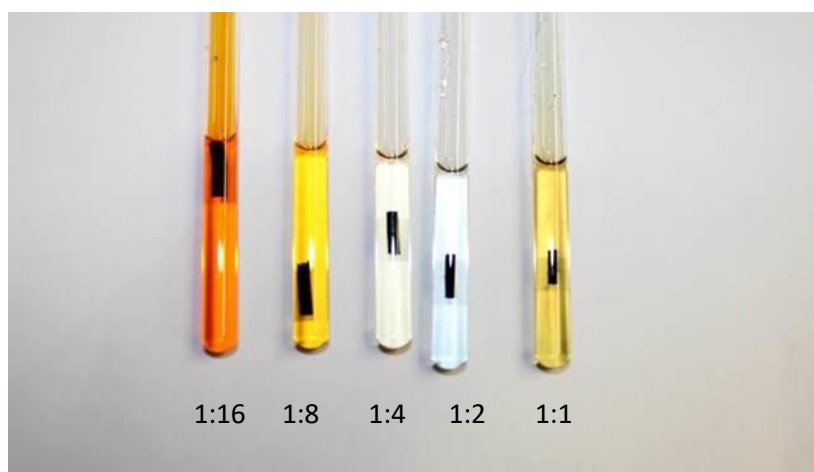
Appendix 78 F$_4$TCNQ:P3HT film pellets (with Increasing F$_4$TCNQ concentration from left to right) after annealing at 453 K dissolved in bromobenzene.

10. Curriculum Vitae and additional scientific contributions

Daniel Pinkal für die gute Vorarbeit während seiner Zeit als mein Vorgänger am MPIP.

Ernst Artes, Daniel Kodura, Fabian Durben, Tung Nguyen, Florian Kreuter, Jens-Georg Becker, Can Özbek, Zaneta Papadopolou, Sophia Burger und *Evokaktus* für die häufig anstrengende, aber dennoch witzige Studienzeit. Ohne euch hätte es sicherlich deutlich länger gedauert.

Zum Schluss danke ich selbstverständlich *meinen Eltern* und *Großeltern* für die physische als auch psychische Unterstützung sowohl während des Studiums als auch während der Anfertigung meiner Dr. Arbeit.

Lebenslauf

✉ chaese4792@gmail.com ☎ 015142452918 📍 Heidesheimer Straße 60, 55218 Ingelheim

Berufserfahrung

Wissenschaftliche Hilfskraft März 2013 - Apr. 2018
Bioscientia, Ingelheim
- RIA und ELISA Analytik
- Erstellen Mikrobiologischer Proben

Wissenschaftliche Hilfskraft am Institut für Anorganische und Analytische Chemie Okt. 2014 - Aug. 2019
Johannes-Gutenberg-Universität, Mainz
- 04/2018 – 04/2019 Arbeit in der Zentralanalytik
- 10/2014 – 10/2018 Leitung Tutorium Anorganische Chemie 1 u. 2
- 04/2016 – 10/2018 Betreuung Praktikum Chemie für Biologen

Praktika

Sept. 2012 - Okt. 2012

Koblenzer Brauerei, Koblenz
Praktikum im chemisch technischen und mikrobiologischen Labor Koblenzer Brauerei

Jan. 2013 - März 2013

Bioscientia, Ingelheim
Bioscientia Institut für Medizinische Diagnostik GmbH, Ingelheim

Ausbildung

Promotion, analytische Chemie Aug. 2019 - Aug. 2023
Max-Planck-Institut für Polymerforschung, 55122 Mainz
Abschlussarbeit: "Solid state NMR studies of organic semiconductors for molecular electronics"

Master-Studium der Chemie Aug. 2017 - Juli 2019
Johannes-Gutenberg-Universität, 55122 Mainz
Abschluss: Master of Science (1,8)
Abschlussarbeit: "Interplay between structure and supramolecular organisation investigated by solution NMR Spectroscopy"

Bachelor-Studium der Chemie Okt. 2013 - Aug. 2017
Johannes-Gutenberg-Universität, 55122 Mainz
Abschluss: Bachelor of Science (2,4)
Abschlussarbeit: "Synthese und Charakterisierung von Dithiomolybdänkomplexen als Enzym-Mimetika"

Bachelor-Studium der Biotechnologie Okt. 2012 - Okt. 2013
Technische Hochschule, 55411 Bingen

Abitur Okt. 2003 - März 2012
Wilhelm-Hofmann-Gymnasium, 56346 St. Goarshausen

Persönliche Daten

Name
Constantin Haese

Geburtsdatum
4. Juli 1992

Geburtsort
Boppard

Führerschein
Klasse B

Staatsangehörigkeit
Deutsch

Familienstand
ledig

Sprachen

Deutsch

Englisch

Grundschule   Sept. 1999 - Juli 2003
Rheinfels-Schule, 56329 St. Goar

Publikationen

[1] Haese C., Boecker M., Vasilev A., Mondeshki M., Stability and Self-Association of styryl hemicyanine dyes in water studied by 1H NMR spectroscopy, *Journal of Molecular Liquids* (2022)

[2] Sachnik O., Tan X., Haese C., Kinaret N., Lin K.-H., Andrienko D., Graf R., Wetzelaer G.-J. A. H., Michels J. J., Blom P. W. M, Elimination of Charge-Carrier Trapping by Molecular Design, *Nat. Mater.* (2023)

[3] Krevert, C.S., Gunkel, L., Haese, C. et al. Ion-specific binding of cations to the carboxylate and of anions to the amide of alanylalanine. *Commun Chem* (2022)

[4] S. Wang, K. Bidinakis, C. Haese, F.H. Hasenburg, O. Yildiz, Z. Ling, S. Frisch, M. Kivala, R. Graf, P. W. M. Blom, S. A. L. Weber, W. Pisula, T. Marszalek, Modification of Two-Dimensional Tin-Based Perovskites by Pentanoic Acid for Improved Performance of Field-Effect Transistors, *Small* (2023)

[5] J. Sutter, C. Haese, R. Graf, and J. Hunger, Charge transport in protic ionic liquids: Effect of protonation state in 1-methylimidazolium – acetate/trifluoroacetate mixtures, *Journal of Molecular Liquids*, (2023)

[6] C.-C. Meyer*, E. Artes, M. Bender, J. Brötz, C. E. Düllmann, C. Haese, E. Jäger, B. Kindler, B. Lommel, M. Major, M. Rapps, D. Renisch, C. Trautmann, and A. Yakushev, Fabrication, swift heavy ion irradiation,and damage analysis of lanthanide targets, *Radiochimica Acta* (2023), submitted

[7] C. Haese, D. Pinkal, P. Blom, R. Graf, Thermal annealing and thermally induced degradation of P3HT:F4TCNQ blends: A comprehensive NMR study, in preparation

[8] K. Thakur, B. van der Zee, O. Sachnik, C. Haese, R. Graf, J. Michels, G.-J. A.H. Wetzelaer, C. Ramanan, and P.W.M Blom, Effect of tert-butyl group on the photophysics of solution processable thermally activated delayed fluorescence emitters, in preparation

ARTICLE

Check for updates

Ion-specific binding of cations to the carboxylate and of anions to the amide of alanylalanine

Carola Sophie Krevert [1], Lucas Gunkel [1], Constantin Haese[2] & Johannes Hunger [1✉]

Studies of ion-specific effects on oligopeptides have aided our understanding of Hofmeister effects on proteins, yet the use of different model peptides and different experimental sensitivities have led to conflicting conclusions. To resolve these controversies, we study a small model peptide, L-Alanyl-L-alanine (2Ala), carrying all fundamental chemical protein motifs: C-terminus, amide bond, and N-terminus. We elucidate the effect of GdmCl, LiCl, KCl, KI, and KSCN by combining dielectric relaxation, nuclear magnetic resonance (^{1}H-NMR), and (two-dimensional) infrared spectroscopy. Our dielectric results show that all ions reduce the rotational mobility of 2Ala, yet the magnitude of the reduction is larger for denaturing cations than for anions. The NMR chemical shifts of the amide group are particularly sensitive to denaturing anions, indicative of anion-amide interactions. Infrared experiments reveal that LiCl alters the spectral homogeneity and dynamics of the carboxylate, but not the amide group. Interaction of LiCl with the negatively charged pole of 2Ala, the COO^- group, can explain the marked cationic effect on dipolar rotation, while interaction of anions between the poles, at the amide, only weakly perturbs dipolar dynamics. As such, our results provide a unifying view on ions' preferential interaction sites at 2Ala and help rationalize Hofmeister effects on proteins.

[1] Department of Molecular Spectroscopy, Max Planck Institute for Polymer Research, Ackermannweg 10, 55128 Mainz, Germany. [2] Department of Molecular Electronics, Max Planck Institute for Polymer Research, Ackermannweg 10, 55128 Mainz, Germany. ✉email: hunger@mpip-mainz.mpg.de

Since the discovery by Hofmeister that salts can specifically (de-)stabilize proteins in solution[1], and thereby alter protein functions[2–5], specific ion effects have been intensively studied[6–16]. In recent years, there has been increasing evidence for such specific ion effects originating from direct ion–protein interactions[17–20]. Yet, the manifold of potential protein interaction sites—including charged residues, hydrophobic fragments, and the amide backbone—make it difficult to resolve the site-specificity of Hofmeister effects. Moreover, not only the chemical nature of the protein sites but also their hydration—intimately connected to the protein structure—affects interaction with ions[21]. Together, this complexity makes it difficult to rationalize specific ion effects on a molecular level[11,20,22,23].

Model systems, like amide-rich polymers, have tremendously helped understanding the underlying principles of specific ion effects on proteins[24–26], as the effect of salts on the phase transition of the polymers resembles the effect on proteins. Ion-specific macroscopically observable phase transitions have been traced back to microscopic interactions of ions with the amide backbone: spectroscopic studies and molecular dynamics simulations have confirmed direct ion-amide interactions[13,27–31]. In addition, the hydration of the macromolecule can affect ion binding[21], and interactions between anions and cations in bulk compete with ion-amide binding[25,32,33]. Yet, considering only the interaction of ions with amide groups is insufficient to explain the salts' impact on protein stabilities[13,23]. Clearly, interaction sites beyond the amide backbone have to be taken into account[18,23]. Indeed, the charged termini have been shown to markedly affect the solubility of model peptides[34] and interactions with charged residues have been suggested to be critical, particularly for the strongly denaturing guanidinium cation[16,18,35]. As such, to fully understand specific ion effects on proteins, peptides, and polymer model systems necessitates going beyond model system containing an individual site (e.g., amide) and considering multiple binding sites and competitive interactions[18].

The above conclusions have been drawn using a variety of model compounds, including simple molecules like N-methyl-acetamide[13,36–38], short oligopeptides[16,39,40], and polymers[21,24,38,41,42]. Comparison of the results using small molecules to those obtained with macromolecules[21,38] has suggested that small model systems cannot account for all details of ion-specific effects on proteins and the length of the macromolecule largely impacts the interaction with ions. This different behavior has been explained by the different hydration structures of small molecules and macromolecules[21]. Conversely, using large, conformationally flexible molecules makes it more challenging to isolate ion interactions: an ion-induced change of an experimental observable may stem from direct interaction of an ion with the model system or from an indirect, ion-induced change in the conformation[16]. For instance, hydration of salt may lead to dehydration and conformational variation of a macromolecule[43].

In addition to the complexity due to the use of different molecular models with different conformational degrees of freedom, also the use of different experimental approaches with different sensitivities adds an experimental complexity. So far, different experimental techniques have been used to elucidate ions' interactions with protein sites. With dielectric relaxation (DR) spectroscopy, the reduction of the dipolar rotational degree of freedom of model peptides can be readily detected[14,15,44]. As this reduction is considered to stem from coupling of the ions' translation to the peptides' dipolar rotation, the proximity of both, cations and anions to the peptide can be detected with equal sensitivity, but site-specific information cannot be obtained[13–16]. Site-specific information can be readily obtained from nuclear magnetic resonance (NMR) experiments. The salt-induced

variation of the chemical shift of peptide nuclei has been demonstrated to sensitively report on the site-specific interaction of ions (predominantly anions) with the peptides' protons[18,31,34,39]. Information on the interaction with cations is more challenging to extract from NMR experiments[37,45]. In turn, vibrational spectroscopies, like infrared absorption (IR) spectroscopy, can detect (cat)ion-induced changes in the environment of the amide carbonyl group or of carboxylate groups[46,47]. Yet, monovalent cations hardly affect these vibrations[27] and marked shifts in the vibrational frequencies are only observed for bivalent cations[27,48]. As such, orthogonal conclusions have been obtained with either cations[13,29,49] or anions[11,31,38] interacting more strongly with the model peptides.

These seemingly contradicting conclusions may be partly explained by different experimental sensitivities: linear vibrational spectroscopies such as infrared absorption spectroscopy or Raman spectroscopy show little sensitivity to interactions with monovalent cations[50]. However, the sensitivity can be enhanced by using nonlinear vibrational spectroscopies, as not only the shift of the resonance frequency can be detected, but also the dynamics with which the oscillators adapt their frequency as a response to fluctuations in their direct environment[46]. Using these fluctuations, salt-induced changes to the dynamic environment of the vibrational probes can be uncovered. Thus, combining nonlinear spectroscopies with previously used spectroscopies (DR, NMR, and IR) on the very same peptide has the potential to experimentally elucidate the salt-specific distribution of ions around model peptides in solution.

Here, we combine these experiments to study specific interactions of different ions around zwitterionic alanyl-alanine (2Ala) in solution. 2Ala carries all functional groups discussed above—both termini and an amide bond. Although 2Ala contains only one amide bond, and thus cannot fully represent the amide backbone of proteins, 2Ala has a rather rigid conformation[51], which limits changes in the spectroscopic observables due to conformational changes and thus allows isolating ionic interactions spectroscopically. To study specific ion effects on 2Ala, we chose two prominent cationic denaturants (GmdCl, LiCl), two salts with denaturing anions (KI, KSCN), and KCl as a reference. Our dielectric data show that the denaturing anions only moderately reduce the rotational mobility of 2Ala, and the NMR results suggest that these anions predominantly bind to the amide N–H group. GdmCl and LiCl have a much stronger effect on the rotation of 2Ala in solution. While none of the salts alters the infrared absorption spectra for the carboxylate and the amide CO groups significantly, 2D-IR experiments show that spectral dynamics of the COO^- group are slowed down in the presence of LiCl, indicative of Li^+ interacting with the C-terminus. Together, this site-specific information and the deduced competitive binding provide a geometric rationale for apparently contradicting previous observations for ion-specific effects on model peptides.

Results and discussion

To provide a consistent view on ion-specific effects on a small model peptide, we herein use a combination of experimental approaches on solutions of the same dipeptide, alanlylalanine, which probe different properties of 2Ala: salt-induced changes to the dynamics of its electrical dipole, site-specific changes to the chemical environment of individual protons, and ion-induced changes to the carbonyl/carboxylate vibrational structure and dynamics (Fig. 1). In the following, we will first discuss these experiments individually.

Rotational mobility of 2Ala probed by dielectric spectroscopy. To study the effect of ions on the rotational mobility of 2Ala we

use DR spectroscopy[16], which probes the polarization of a sample in an externally applied oscillating electric field with field frequency v. The polarization is typically expressed in terms of the complex permittivity spectrum ($\hat{\varepsilon} = \varepsilon'(v) - i\varepsilon''(v)$), with the real permittivity, ε', corresponding to the in-phase polarization and the dielectric loss, ε'', representing the out-of-phase (absorptive) polarization. For liquids at Gigahertz frequencies, polarization typically stems from the rotation of dipolar molecules. Thus, besides dipolar water, the reorientation of highly dipolar, zwitterionic peptides gives rise to marked polarization contributions[52,53]. The orientational relaxation of each dipolar species is characterized by dispersion in ε' and a loss peak at the rotational frequency of the dipolar species[54].

Before studying the effect of Hofmeister salts, we first characterize the polarization dynamics of aqueous 2Ala solutions. The dielectric spectrum of a 0.25 M 2Ala solution in water (Fig. 2a) exhibits two well-separated dispersions in $\varepsilon'(v)$ and two peaks in $\varepsilon''(v)$ at ~20 GHz and ~1 GHz, respectively, evidencing two disparate relaxations. The higher-frequency relaxation is due to the orientational relaxation of water's hydrogen-bonded network at ~20 GHz[55]. The lower-frequency relaxation can be ascribed to the rotational relaxation of zwitterionic 2Ala—similar to earlier findings for other oligopeptides or amino acids[15,16,56]. Consistent with this notion, the relaxation strength (loss peak amplitude) at ~1 GHz increases with increasing 2Ala concentration (Fig. 2b).

To exclude marked 2Ala–2Ala interactions (i.e., dipole–dipole correlations) contributing to the observed 2Ala relaxation, we quantify the contribution of both relaxations to the experimental spectra. In line with our earlier studies[13,14,16], we model the experimental spectra using a Debye mode[57] for the 2Ala

Fig. 1 Schematic illustration of the combined experimental approach to study ion-specific effects on 2Ala. Dielectric relaxation spectroscopy probes the dynamics of 2Ala's electrical dipole (gray arrow), ^{1}H-NMR spectroscopy the chemical environment of 2Ala's protons (marked green), and 2D-IR detects the vibrational dynamics of the CO and anti-symmetric COO$^-$ stretching vibrations of 2Ala (marked brown).

contribution and a Cole–Cole[58,59] mode for the water relaxation:

$$\hat{\varepsilon}(v) = \frac{S_{2Ala}}{1 + (2\pi i v \tau_{2Ala})} + \frac{S_{H2O}}{1 + (2\pi i v \tau_{H2O})^{1-\alpha}} + \varepsilon_\infty + \frac{\kappa}{2\pi i v \varepsilon_0} \quad (1)$$

with the relaxation amplitude S_j, and the relaxation time τ_j. The Cole–Cole parameter α accounts for the symmetrical broadening of the water relaxation as compared to a Debye relaxation. ε_∞ accounts for all polarizations occurring at frequencies higher than covered in our experiment (e.g., electronic, vibrational contributions). The last term of Eq. (1) accounts for losses due to the finite conductivity of the samples, where we assume the conductivity κ to be real and frequency-independent. ε_0 is the permittivity of free space.

The model in Eq. (1) describes the experimental spectra very well (Fig. 2a, b), and the obtained parameters are shown in the supporting information (see Supplementary Fig. 1 and Supplementary Discussion 1). Most importantly, the peptide's amplitude S_{2Ala} increases linearly with increasing peptide concentration. For uncorrelated rotation of 2Ala, S_{2Ala} is related to the 2Ala concentration and the squared effective dipole moment $\mu_{eff}(2Ala)$[16]. We find this dipole moment as calculated from S_{2Ala} according to ref. [16] (see Supplementary Eq. (1)) to be constant $\mu_{eff}(2Ala) \approx 30$ D (Fig. 2c). The insensitivity of $\mu_{eff}(2Ala)$ to concentration demonstrates that 2Ala zwitterions do not exhibit preferred parallel or antiparallel dipolar correlations and do not undergo marked conformational changes at concentrations up to 250 mM. As such, salt-induced changes of S_{2Ala} due to ion-induced changes in the conformation or screened dipolar correlations are rendered unlikely.

After having established that 2Ala's contribution to the dielectric response is due to uncorrelated rotational motion of the peptides' zwitterions, we now focus on how different salts affect 2Ala in solution. As can exemplarily be seen in Fig. 3a, the addition of LiCl to a $c_{2Ala} = 0.25$ M solution results in a marked depolarization—a reduction of the dielectric permittivity and loss—with increasing salt concentration (for other salts, see Supplementary Fig. 2). This depolarization stems in part from the dilution of water due to the salt, as the volume concentration of water decreases with increasing salt concentration[14]. In addition, kinetic depolarization[60,61] upon adding salt reduces the dipolar response: The dipolar molecules tend to align according to the local electric field of a translating ion, rather than to the externally applied electric field, which reduces the dipolar relaxation amplitude. As kinetic depolarization only relies on the coupling between the translation of ions and rotation of dipoles in an external electric field, the dipolar response of both, water and 2Ala, is subject to kinetic depolarization. Indeed, zooming into

Fig. 2 Dielectric spectra of aqueous 2Ala solutions are consistent with uncorrelated dipolar rotation of 2Ala. Complex permittivity spectrum of (**a**) 0.25 M aqueous 2Ala solution and **b** aqueous 2Ala solutions with increasing concentration of 2Ala. Solid circles and crosses show the experimental dielectric permittivity (ε') and dielectric loss spectra (ε''), respectively. Solid lines show fits of Eq. (1) to the experimental data. The contribution of the 2Ala and the water relaxations to the dielectric loss are shown as shaded areas in (**a**). Conductivity contributions (last term of Eq. (1)) have been subtracted for visual clarity in (**a**, **b**). **c** Shows the constant effective dipole moment of 2Ala $\mu_{eff}(2Ala)$ as calculated from the 2Ala relaxation amplitude as a function of 2Ala concentration. Error bars are based on the standard deviation within eight independent measurements.
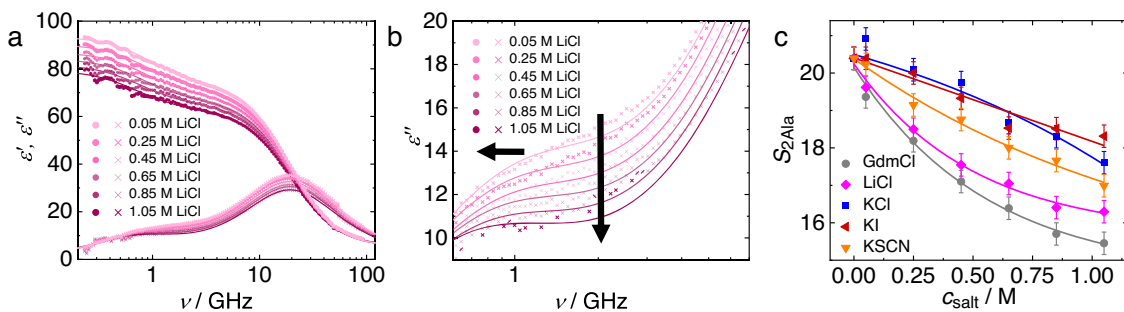
Fig. 3 Decrease in 2Ala's relaxation amplitude is salt-specific. a Complex permittivity spectra of aqueous 2Ala solutions (0.25 M) with increasing concentration of LiCl. **b** Zoom into lower-frequency loss spectra, which are dominated by the 2Ala relaxation, with arrows indicating the trend with increasing concentration. Solid circles and crosses show the experimental dielectric permittivity (ε') and dielectric loss spectra (ε''), respectively. Solid lines show fits of Eq. (1) to the experimental data. Note that the conductivity contribution (last term of Eq. (1)) has been subtracted for visual clarity. **c** 2Ala relaxation strength, S_{2Ala}, (Eq. (1)) as a function of c_{salt} for different salts. Error bars correspond to twice the standard deviation from the parameters obtained from eight independent experiments. Lines are guides to the eye.
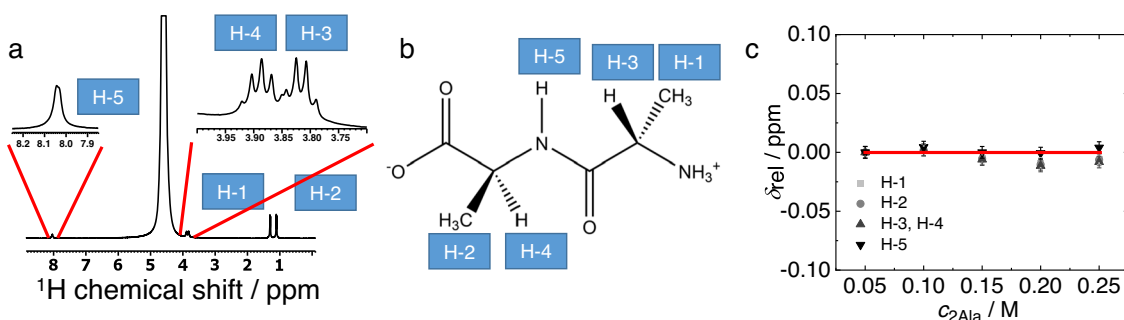
Fig. 4 ^{1}H-NMR chemical shifts are independent of 2Ala concentration. a ^{1}H-NMR spectrum of 0.25 M 2Ala (in H$_2$O (DMSO-d5h1 capillary included). Proton signals are assigned to 2Ala's protons as indicated in the structure shown in (**b**). The variation of the chemical shifts $\delta_{rel} = \delta(c_{2Ala}) - \delta(c_{2Ala} = 50\,mM)$ as function of 2Ala concentrations is shown in (**c**). The solid red-line in (**c**) corresponds to $\delta_{rel} = 0$. Error bars show the typical experimental reproducibility of ±0.005 ppm (see the text).

the dielectric loss spectra at frequencies where the 2Ala relaxation dominates (Fig. 3b) shows that also 2Ala's contribution to the experimental spectra decreases with increasing LiCl concentration. Upon the addition of other salts (GdmCl, KCl, KI, KSCN), we find qualitatively similar trends. Yet, the depolarization of the peptide mode can be quantitatively different depending on the nature of the ions[13–16]: Kinetic depolarization of the peptide relaxation requires spatial proximity of the ions to the peptide and, as such, stronger interactions (on average closer proximity) result in a more pronounced reduction of the relaxation strength.

To quantify the ion-specific depolarization of the 2Ala relaxation, we also model the ternary samples with Eq. (1). The parameters obtained from these fits (see Supplementary Fig. 3) show that the 2Ala relaxation slows down with increasing salt concentration (increase in τ_{2Ala} with increasing salt concentration), which can be related[13,16] to the increasing viscosity with increasing salt concentration[62,63]. For all investigated salts, we find a reduction of the relaxation amplitude S_{2Ala} (Fig. 3c), indicative of the presence of ions in the coordination sphere of 2Ala. We find the effect of the different salts on S_{2Ala} to be ion-specific: KCl and KI reduce the relaxation strength only by ~10% for the highest salt concentration (1.05 M), while for KSCN, we find a reduction by almost 20% (Fig. 3c). As such, the studied denaturing anions moderately reduce the rotational degree of freedom of the model peptide. For the salts with a denaturing cation, LiCl and GdmCl, we find the strongest reduction of S_{2Ala} by up to ~25%. These findings are in broad agreement with what we have concluded for the rotational mobility of N-methylacetamide and triglycine[13–16] in aqueous solution: salts with increasing denaturation tendency

on proteins affect the rotational mobility of model peptides more profoundly, with a more pronounced effect for denaturing cations as compared to denaturing anions. Based on the kinetic depolarization mechanism described above, our findings imply (on average) closer proximity of Hofmeister cations to 2Ala, as compared to Hofmeister anions when approximating 2Ala as a point dipole. Yet, the effect of the finite size of 2Ala, which makes ion-dipole interactions location-specific, is not considered. Therefore, site-specific molecular-level details cannot be pinpointed.

Chemical environment of 2Ala's protons probed by ^{1}H-NMR spectroscopy. To obtain insights into site-specific interactions of ions with 2Ala we probe the chemical environment of 2Ala's protons using ^{1}H-NMR spectroscopy[31,34]. First, we assign all NMR signals detected in the ^{1}H-NMR spectra (see Supplementary Figs. 4 and 5) of solutions of 2Ala in H$_2$O (DMSO-d5-h1 capillary included): Based on ^{13}C-NMR spectra (see Supplementary Fig. 6), ^{1}H-^{13}C-HSQC, and ^{1}H-^{13}C-HMBC (see Supplementary Figs. 7 and 8 and Supplementary Discussion 2) we ascribe the NMR peaks at 1.29 ppm and 1.10 ppm to the β protons (CH$_3$ groups) at the N-terminus (H-1) and the C-terminus (H-2), respectively (Fig. 4a, b). The peptide's α-protons at the N-terminal Ala unit (H-3) and at the C-terminal (H-4) alanine group give rise to signals at 3.82 and 3.88 ppm, respectively. We detect the amide proton (H-5) at 8.04 ppm (Fig. 4a, b). As can be seen from the concentration-dependent relative chemical shifts ($\delta_{rel} = \delta(c_{2Ala}) - \delta(c_{2Ala} = 50\,mM)$, Fig. 4c), all these chemical shift values are insensitive to the concentration of 2Ala within the experimental uncertainties
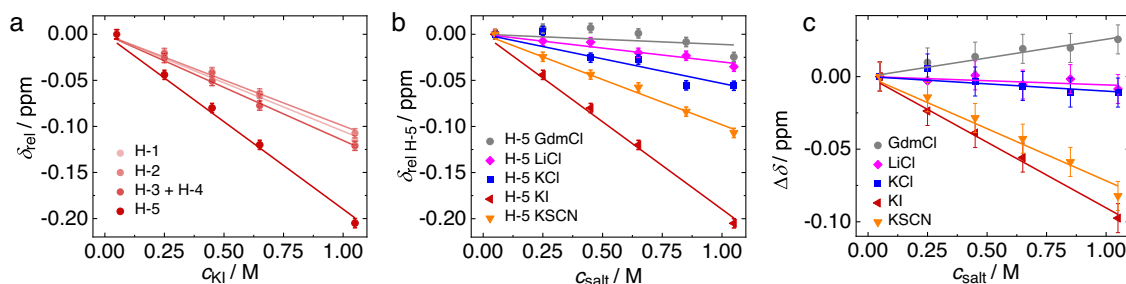
Fig. 5 Salt-induced changes of the chemical shifts of the amide proton (H-5) differ from aliphatic protons H-1–H-4. a Concentration-dependent relative chemical shift, $\delta_{rel} = \delta(c_{salt}) - \delta(c_{salt} = 0.05\,M)$ for aqueous solutions of 250 mM 2Ala with increasing concentration of KI. **b** Concentration and salt-dependent relative shift of the NH proton H-5, $\delta_{rel\,H-5} = \delta_{H-5}(c_{salt}) - \delta_{H-5}(c_{salt} = 0.05\,M)$. **c** Differential chemical shift $\triangle\delta = \delta_{rel\,H-5} - \delta_{rel\,H-1}$. Symbols show experimental data and error bars are based on the typical experimental reproducibility. Solid lines show linear fits.

(±0.005 ppm), which is largely due to inaccuracies in referencing the signals to the dimethylsulfoxide included in the capillary (see experimental section). As such, the data in Fig. 4c confirm that 2Ala aggregation can be neglected[64], as already concluded from the dielectric data (Fig. 2c).

Conversely, the chemical shifts vary markedly upon adding salt: as exemplarily shown for KI in Fig. 5a (representative ^{1}H-NMR spectra are shown in Supplementary Fig. 9), increasing concentration of salt results in an up-field shift of all five detected proton signals.

In general, such variation of the chemical shift can be due to a change of the solvent properties upon replacing the solvent H_2O for an aqueous salt solution (medium effect)[39,65] or due to specific binding of ions to the peptide[39]. Yet, for weak, specific binding both contributions are challenging to discriminate based on the concentration-dependent shift values as they lead to an approximately linear variation in the chemical shift[66]. In the case of KI, we find the protons H-1–H-4 to exhibit a similar variation of the chemical shifts with increasing salt concentration: The shaded red traces in Fig. 5a showing $\delta_{rel} = \delta(c_{salt}) - \delta(c_{salt} = 0.05\,M)$ for H-1–H-4 nearly overlap. The same applies to the other salts used in the present study (see Supplementary Fig. 10), with an ion-specific slope for the $\delta_{rel}(c_{salt})$ curves. The similar salt-induced shift for H-1–H-4 suggests that the aliphatic protons H-1–H-4 predominantly sense medium effects due to the variation of the solvents electronic properties with increasing c_{salt}. Accordingly, the salt specificity of the slopes of δ_{rel} can be ascribed to the different (electronic) properties of the aqueous salt solutions. In contrast to the protons H-1–H-4, the amide proton H-5 undergoes different changes in the chemical environment and δ_{rel} of H-5 decreases more steeply for KI, as compared to H-1–H-4. This different sensitivity of H-5 to added KI points towards enrichment or closer proximity of iodide to the amide proton, as compared to the aliphatic protons. We note that we detect virtually the same changes for solutions containing 50 mM 2Ala, suggesting that also in the presence of KI aggregation induced changes to the chemical shift of 2Ala can be neglected (see Supplementary Fig. 11 and Supplementary Discussion 2).

Similar to the findings for KI, we also find for KSCN a marked decrease of the chemical shift of H-5 with increasing concentration (Fig. 5b), while for KCl and LiCl the decrease is only moderate—in line with negligible interaction of these salts with the amide group[24]. For the denaturant GdmCl, we find a weak down-field shift at low-salt concentrations, and a moderate up-field shift at higher salt content. To isolate the salt-specific changes of the amide proton's chemical shift from medium effects[65], we assume the variation of δ_{rel} of H-1 to be solely due to medium effects. Based on this assumption, the concentration-dependent variation of the difference in the chemical shifts of H-5

and H-1 report on specific effects of the salts on the amide proton: As can be seen in Fig. 5c, this differential chemical shift value $\triangle\delta = \delta_{rel\,H-5} - \delta_{rel\,H-1}$ varies linearly with increasing salt concentration for all studied salts. Due to its differential nature, the shift difference can also account for nonlinear medium effects[21] and reduces the scatter of the data, which originate from inaccuracies in referencing the spectra with the external capillary (see "Methods").

The data in Fig. 5c suggest that—within experimental error—KCl and LiCl do not affect the differential shift, consistent with the notion that the observed variation can be solely ascribed to medium effects[65]. For KI and KSCN, the marked shift of the H-5 signals to lower ppm values with increasing salt concentration is indicative of the interaction of the anions with the amide group: Given the weak hydrogen-bond acceptor strengths of these anions compared to the chloride salts[67], increasing substitution of water molecules by I^- or SCN^- anions is expected to result in enhanced shielding of the NH proton due to the anions themselves and due to weakening of the N–H hydrogen-bond[68]. Interestingly, for GdmCl, the shift difference increases with increasing GdmCl concentration (Fig. 5c). Hence, despite the guanidinium cation being a moderately strong hydrogen-bond donor[69], it apparently can affect the H-bond donating N–H group of 2Ala. This observation may be explained by the interaction of Gdm^+ with the amides CO group via bidentate binding to both, the amide and the carboxylate group[16]. Hence, hydrogen bonding of Gdm^+ to 2Ala's CO group may also affect the charge distribution at the N–H group such that the N–H proton is de-shielded. Altogether, our NMR results suggest that denaturing anions preferentially accept hydrogen bonds from the amide N–H group. The almost perfect linear variation of the data in Fig. 5c suggests that this binding is weak, and a fourfold excess of salt with respect to 2Ala is not sufficiently high to make the chemical shift values plateau at the value of 2Ala-ion complexes.

The environment of 2Ala's C–O groups probed by linear infrared and 2D-IR spectroscopy. To probe salt-induced changes in the vicinity of the carbonyl or carboxylate groups of 2Ala, we use infrared (IR) spectroscopy, which is particularly sensitive to molecular vibrations with a high transition dipole moment[70]. Here, we focus on two vibrational modes, the amide I vibration (CO stretch vibration) at ~1660 cm^{-1} (see ref. [28]) and the anti-symmetric COO^- stretching vibration at ~1590 cm^{-1} (see ref. [71]), which are common vibrational probes for the structure and dynamics of peptides and proteins[27,28,72–77]. These two vibrational modes are well-separated for a 250 mM solution of 2Ala in D_2O (Fig. 6a), with the carboxylate mode being somewhat narrower than the amide I vibration. At the highest salt concentration used for the NMR and DRS experiments (~1 M), the salts hardly affect
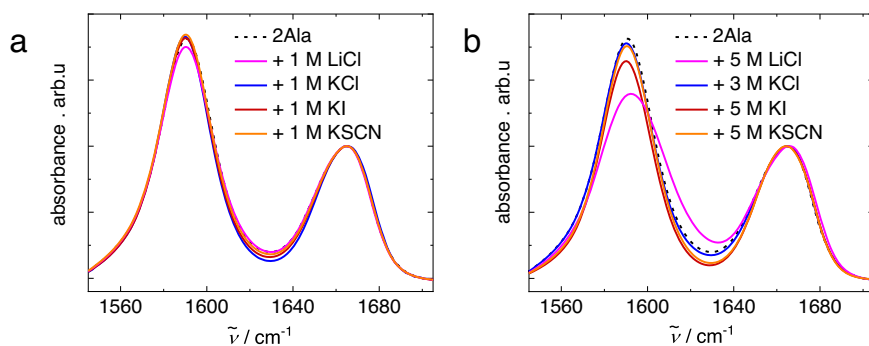
Fig. 6 Salts hardly affect the IR bands of the amide I and anti-symmetric carboxylate stretching mode. Infrared absorption spectra in the absence of salt: 250 mM 2Ala in D_2O (dashed black line) and in the presence of (**a**) 1 M and (**b**) 5 M (3 M for KCl) salt. Spectra were corrected for a linear background and normalized to the CO peak at ~1660 cm^{-1}.

these vibrational modes: the addition of 1 M LiCl, KCl, KI, or KSCN does not affect the lineshape of both vibrations, and results in only minor changes in the amplitude of the anti-symmetric carboxylate stretching band relative to the amide I mode. We note that the presence of the anti-symmetric CN stretching mode of Gdm^+ at ~1610 cm^{-1} (see ref. [78]) prevents us from isolating the carbonyl and carboxylate bands for solutions containing GdmCl (see Supplementary Fig. 12 and Supplementary Discussion 3). Nevertheless, the amide I band appears as a shoulder of the C–N band and coincides with the amide I band in solutions with other salts, suggesting that also GdmCl does not affect the amide I mode of 2Ala significantly. The insensitivity of both vibrational bands in the presence of 1 M salt (Fig. 6a) is consistent with earlier studies[27,28,77], that found salt-induced changes to the vibrational modes only at elevated concentrations. Changes to the IR spectra are hardly detectable for the presently studied salts, also at elevated salt concentrations (5 M for LiCl, KI, and KSCN; 3 M for less soluble KCl, Fig. 6b), except for LiCl, for which the carboxylate band slightly broadens (see Supplementary Fig. S13 and Supplementary Discussion 3). This broadening is also observed for samples containing 50 mM 2Ala, which suggests that it is not related to 2Ala self-aggregation, but can be related to peptide-salt interactions (see Supplementary Fig. 14).

The lineshape of the linear infrared bands can typically be traced to distribution of molecular oscillators in different microenvironments (inhomogeneous broadening). While this distribution is largely unaffected by the salts for the present samples, the dynamics with which these microenvironments interconvert can be altered by salts. These dynamics remain hidden in the linear spectra, but nonlinear infrared spectroscopies can uncover these dynamical aspects. Here, we perform two-dimensional infrared (2D-IR) spectroscopy[70], where a specific vibration is "tagged" via vibrational excitation. For the time-domain experiments used herein, the excitation is generated using two laser pulses, and the excitation frequency is resolved in the time domain. The response of the excited vibrations is probed by a probe pulse, which is detected in the frequency domain. In a typical 2D-IR experiment, the (probe) frequency-dependent response is mapped as a function of the excitation frequency.

Figure 7a shows the 2D-IR spectra of a 0.25 M solution of 2Ala in D_2O right after the excitation (waiting time $T_2 = 0$ fs). For both, the amide I and the carboxylate band, we detect a pair of signals: a negative (shaded blue) signal at the diagonal, at which the excitation frequency equals the detection frequency, due to the population depletion of the vibrational ground state/stimulated emission from the excited state and a positive signal (shaded red, induced absorption) due to the anharmonically red-shifted excited state absorption.

With increasing waiting time, the intensities of these signals decrease due to relaxation to the vibrational ground state. This decrease is more pronounced for the carboxylate band than for the amide I mode, demonstrating faster vibrational relaxation of the COO^- mode (see, e.g., Fig. 7b). To quantify vibrational relaxation dynamics, we extract the peak volumes for both modes as a function of delay times (see Supplementary Fig. 15 and Supplementary Discussion 4). These volumes decay with a characteristic vibrational relaxation time τ_{VER} of ~0.4 ps for the anti-symmetric COO^- stretching band and ~ 0.7 ps for the amide I mode. The latter is about twofold faster than what has been reported for 2Ala or 3Ala at low pH, at which the carboxylate group is protonated[79]. The faster relaxation observed here is presumably related to the altered vibrational and electronic structure of 2Ala upon deprotonation[80], but also coupling between the carboxylate and amide I mode can constitute a relaxation channel[81]. In fact, we detect low-intensity cross-peaks for both modes (see Fig. 7b), peaking at ~200 fs waiting time, consistent with vibrational energy transfer (see Supplementary Fig. 16). As such, coupling with the COO^- group appears to provide a relaxation path from the excited state of the amide I mode. Yet, within experimental accuracy, we find no indications for ion-specific effects on the vibrational relaxation dynamics (see Supplementary Fig. 17) or the cross-peaks dynamics/intensities (see Supplementary Fig. 16), which indicates that the addition of ions negligibly influences the coupling of the vibrations to the environment (Supplementary Discussion 4).

The spectral shape of the detected signals, however, depends on both the waiting time and the added salt. In general, the frequency response of the sample is correlated to the excitation frequency for an inhomogeneously broadened band, which results in an elongation of the 2D-IR signals along the diagonal[70]. For 2Ala in the absence of salt, the signals due to the CO stretch vibration (at 1660 cm^{-1}) are markedly elongated along the diagonal, indicative of inhomogeneous broadening, while the anti-symmetric COO^- stretching mode (at 1590 cm^{-1}) appears more parallel to the pump axis. With increasing waiting time, as shown exemplarily for 2Ala at 500 fs in Fig. 7b (for other concentrations and waiting times, see Supplementary Figs. 18–29), the correlation between excitation and probing frequencies is reduced due to spectral diffusion, as evident from the increased vertical elongation of the detected signals[70].

The addition of salt can alter these correlations and their decay dynamics: In the presence of 5 M LiCl, the COO^- signal is markedly elongated along the diagonal (Fig. 7c), and the correlations partly persist up to a waiting time of 500 fs (Fig. 7d). In contrast to the observations for LiCl, the 2D-IR spectra of 2Ala in the presence of 3 M KCl (Fig. 7e, f), 5 M KI (Fig. 7g, h), and
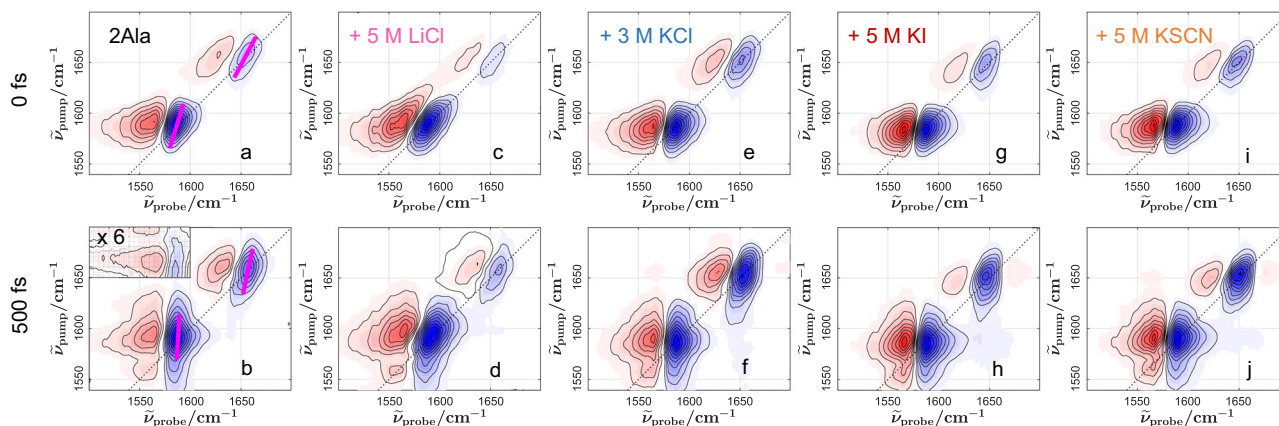
Fig. 7 2D-IR spectra of 2Ala + salt to reveal the ion-specific vibrational structure and spectral dynamics. 2D-IR spectra of 0.25 M 2Ala in D_2O (**a**, **b**) in the absence of salt, with 5 M LiCl (**c**, **d**), with 3 M KCl (**e**, **f**), with 5 M KI (**g**, **h**) and 5 M KSCN (**i**, **j**). Top panels show spectra at 0 fs waiting time. With increasing waiting time, vibrational relaxation results in a decay of the signals, leading to a variation of the relative intensities of both diagonal peaks at a waiting time of 500 fs (bottom panels). The dotted black lines indicate the diagonal line. The inset in (**b**) shows a zoom into the region where the cross-peak is detected. Pink lines in (**a**, **b**) represent the center line slope used to quantify frequency–frequency correlations.
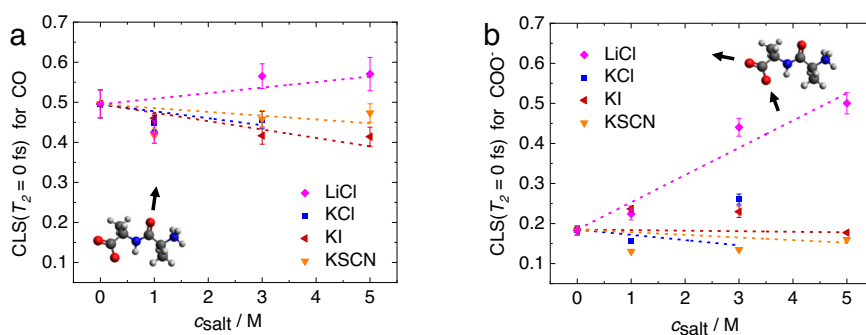
Fig. 8 Spectral heterogeneity is salt-specific for the COO^- mode but not for the amide CO. Center line slope at 0 fs waiting time for **a** the amide CO and **b** the anti-symmetric COO^- stretching mode. Symbols show experimental data, dashed lines are a visual aid. Error bars correspond to the standard deviation of the CLS of the bleaching signal determined from five different scans.

5 M KSCN (Fig. 7i, j) qualitatively resemble the spectra for 2Ala in the absence of salt (Fig. 7a, b).

To quantify the heterogeneity of the detected signals and the decay dynamics of the correlations (spectral diffusion), we determine the waiting-time-dependent center line slopes (CLS, see Supplementary Discussion 4) and fit an exponential decay $(CLS(T_2) = CLS_0 \exp(-k_j T_2))$ to the data (see Supplementary Figs. 30–33)[82]. The instantaneous ($T_2 = 0$ fs) center line slope of the amide I mode in the absence of salt is determined to ~0.5 (Fig. 8a), which agrees well with the value reported for protonated 2Ala[79]. From single exponential fits to the waiting-time-dependent CLS, we also find the decay time of ~1.1 ps (see Supplementary Fig. 31b) for the amide I mode to be comparable to protonated 2Ala[79,83]. This similarity suggests that the exchange of microenvironments of the amide CO, which stems from the hydrogen-bond dynamics of the hydrating water molecules, is hardly affected by protonation at the C-terminus.

We find that the presence of salts hardly affects the instantaneous heterogeneity of the CO mode (Fig. 8a): addition of all potassium salts results in a (<10%) decrease of the $CLS(T_2 = 0)$, which may be explained by salts altering the hydration structure of the amide group due to the altered osmolality. Upon addition of LiCl, we find a minor increase in $CLS(T_2 = 0)$. Overall, the salt-induced variations in the spectral heterogeneity are very modest, and none of the presently studied salts significantly alters the associated spectral diffusion dynamics (see Supplementary Fig. 31b). As such, our results imply that the

environment of the CO groups in the aqueous salt solutions is comparable to its environment in aqueous 2Ala solutions. This notion is broadly consistent with the earlier finding that cations interact only weakly with amide groups[38].

In turn, the CLS at 0 fs for the anti-symmetric carboxylate stretching vibration is markedly altered in a salt-specific manner (Fig. 8b): While we find the detected instantaneous heterogeneity is nearly unchanged even at $c_{salt} = 5$ M KI, KSCN, and 3 M KCl, the $CLS(T_2 = 0)$ increases by a factor of ~2.5 upon addition of 5 M LiCl. As such, the modest changes to the infrared bands (Fig. 6) originate from a marked change in the environment of the COO^- group in the presence of LiCl. These profound changes upon addition of LiCl presumably stem from a slow-down of the fast (within our experimental time resolution) spectral diffusion dynamics, which also affect the magnitude of $CLS(T_2 = 0)$. Indeed, within experimental error, KCl, KSCN, and KCl do not affect the detected CLS decay dynamics (see Supplementary Fig. 31a), but the CLS (~300 fs decay time in the absence of salt) decays markedly slower (~1.3 ps decay time) in the presence of 5 M LiCl (see Supplementary Figs. 31 and 34). Together, these observations suggest that LiCl markedly alters the microenvironments and their dynamics for the COO^- group: Li^+ cations interact with the negatively charged carboxylate group. The enhanced tendency of Li^+ to interact with 2Ala's carboxylate group is in line with the general tendency of alkali cations to bind to carboxylates[84]. In this context, it is interesting to note that for the interaction of Li^+ with carboxylates direct ion contacts have been suggested to play only a

minor role, rather solvent-separated contacts prevail[84]. Our observation that LiCl can efficiently alter the vibrational structure of 2Ala's carboxylate group may thus only partially stem from direct contacts. Yet, also long-lived contacts with hydrated ions could alter 2Ala's vibrational dynamics, as water in ionic hydration shells is less dynamic than in bulk water.

Conclusion. In summary, we studied the effect of salts on the environment and dynamics of alanyl-alanine in water. Our DRS results suggest that salts with increasing protein denaturation tendency can increasingly restrict the diffusive rotational motion of the dipolar 2Ala zwitterion. We find denaturing cations, like Gdm^+ and Li^+ to be most efficient in reducing the rotational relaxation of 2Ala, indicative of closer proximity of these cations to 2Ala in solution. Denaturing anions, like I^- and SCN^-, also affect 2Ala's diffusive rotation, however, to a lesser extent. ^{1}H-NMR chemical shift experiments evidence that salts induce a change in the chemical environment of all protons of 2Ala. This change can, however, largely be explained by a bare medium effect, except for 2Ala's amide proton: the chemical shift of the amide proton is very sensitive to the presence of KI and KSCN. This increased sensitivity suggests that the denaturing I^- and SCN^- anions interact with the amide N–H group. Conversely, for GdmCl, the shift variation is reversed, which— in contrast to Li^+ and K^+—points toward the binding of Gdm^+ to the amide CO. Our 2D-IR results show that both the infrared absorption spectra at amide I and anti-symmetric carboxylate stretching frequencies and the spectral dynamics of the amide I band are rather insensitive to the presence of salts, and the salt-induced changes to the vibrational structure and dynamics are similar for all salts, irrespective of their denaturation tendency. Conversely, we find the salt-induced changes to the vibrational structure and dynamics of the COO^- group to be salt-specific: we find the strongest effect for LiCl, for which the spectral heterogeneity and its associated spectral diffusion dynamics are markedly slowed down. Although previous reports have indicated that ions like Li^+ can bind to the amide group[18,31], and that for an isolated amide group in N-methylacetamide cations can perturb the amide more efficiently than anions[13], our results show that in the presence of an amide group and a C-terminal COO^- group, the carboxylate group is the prevailing interaction site for Li^+.

Based on our findings for 2Ala, our results thus provide a unifying view of ion model-peptide interactions, for which previous experiments based on different experimental techniques have led to partially inconsistent conclusions, in particular related to the interaction strengths of anions compared to cations. We find that anions preferably interact with the N–H group of 2Ala. This interaction site can explain why—despite their high denaturation efficiency towards proteins[18]—anions are less efficient in reducing the rotational mobility of small model peptides as detected with DRS. The N–H group is located close to the geometric center (i.e., rotational axis) of the 2Ala dipole, but more distant from the ionic sites—the poles of the dipole. At this location, ion-dipole interactions are weaker as compared to ions in the proximity of the charged sites. The opposite argument holds for cations: interaction of the cation with the charged carboxylate group is consistent with stronger ion-dipole interactions. Our infrared experiments confirm that cation–carboxylate interactions prevail over amide CO—cation interactions. This interaction with the carboxylate presumably has only limited effect on the backbone of a real protein, but may be relevant to the interactions of charged residues that stabilize proteins[85]. Also for the self-assembly of short peptides charged sites can play a key role[86], and our results suggest that LiCl can efficiently distort such interactions. More general, the herein-found preference of anions to the amide group and the

preference for cations to the carboxylate groups may help rationalize why denaturing anions are often more efficient denaturants than cations: amide groups are typically much more abundant in a protein than carboxylate groups.

Methods

Sample preparation. Guanidinium chloride (GdmCl), LiCl, KCl, KSCN, KI, and ʟ-alanyl-ʟ-alanine (2Ala) were used without further purification. Solutions for DRS and NMR experiments were prepared using H_2O with a specific resistivity >18 MΩcm^{-1} from a Millipore MILLI-Q purification unit or using D_2O for infrared experiments. All samples were prepared by weighing the appropriate amount of salt and peptide into a 1 mL volumetric flask using an analytical balance. The peptide concentration was kept constant at 250 mM for all samples, while the salt concentration was varied from 0.05 M to 1.05 M for DRS and NMR experiments. For infrared experiments, we used salts concentrations of 1.05, 3, and 5 M.

For DRS experiments, 1 mL of each sample was brought in contact with the coaxial probes. For NMR experiments, 0.5 mL of the samples were placed in an NMR tube together with a capillary filled with DMSO-d6 for referencing. For all infrared experiments, solutions were contained between two CaF_2 windows (2 mm thickness, 2.54 cm diameter) separated by a 25 μm Teflon spacer. The infrared absorption spectra were measured right before collecting the 2D-IR data.

DRS measurements. Dielectric permittivity spectra were measured using an Anritsu MS4647A vector network analyzer in the frequency range 0.25–125 GHz. To cover the frequency range at 0.25–54 GHz, a frequency domain reflectometer based on 1.85 mm coaxial connectors and an open-ended probe head was used[87,88]. For the frequency range 54–125 GHz, an external frequency converter (Anritsu 3744 A mmW module) connected to a 1 mm open-ended probe was used. To calibrate the instrument for directivity, source match, and frequency response errors, three different references were measured on the same day as the samples: open (air), short (conductive silver paint), and load (pure water). The sample temperature was controlled to 25 ± 1 °C using a Julabo F12-ED thermostat. All measurements at both probe heads were performed eight times per sample.

NMR measurements. All NMR spectra were recorded using a Bruker DRX 400 MHz Spectrometer equipped with a commercial Bruker 5-mm 2-channel inverse probe head with z-gradients. ^{1}H and ^{13}C spectra were obtained at room temperature with the standard pulse sequences and parameters. The number of scans ranged from 8 to 128, depending on the concentration of the samples. All spectra were referenced using the residual DMSO-d$_5$h$_1$ signal at 2.5 ppm[89]. The absolute chemical shifts of 2Ala were extracted using Topspin 3.6.1.

Gradient-enhanced two-dimensional (2D) ^{1}H–^{13}C HSQC experiments were performed using the hsqcetgp pulse program with the following acquisition parameters: F2 and F1 spectral widths of 20.61 ppm and 179.99 ppm and a F2 and F1 resolution of 8.06 Hz/pt and 70.78 Hz/pt, respectively. In total, 256 FIDs were recorded, each consisting of 32 scans and 2048 data points. The relaxation delay was set to 2 s. Gradient-enhanced 2D ^{1}H–^{13}C HMBC experiments were based on the hmbcgpndqf pulse program with the following acquisition parameters: F2 and F1 spectral widths of 20.61 ppm and 239.99 ppm and F2 and F1 resolution of 4.03 Hz/pt and 94.38 Hz/pt, respectively. In total, 256 FIDs were recorded, each consisting of 16 scans and 2048 data points. The relaxation delay was set to 2 s.

FT IR measurements. Linear infrared absorption (IR) spectra were measured using a Bruker Vertex 70 spectrometer in transmission geometry. The spectra were recorded with a resolution of 4 cm^{-1} at frequencies ranging from 400 to 4000 cm^{-1}. The sample compartment was purged with nitrogen during the measurement.

2D-IR measurements. The two-dimensional infrared setup is based on 800 nm laser pulses (7 W, 35 fs, 1 kHz) from a regenerative amplifier laser system (Coherent, Astrella). In all, 2.7 W of the 800 nm pulses were used to pump an optical parametric amplifier Topas Prime (Coherent) to generate signal and idler pulses. Signal and idler pulses were used to generate infrared pules at ~6000 nm (18 μJ, 400 cm^{-1} FWHM) using non-collinear difference frequency generation (NDFG) Topas (Coherent). The IR beams are guided into a commercial 2D infrared spectrometer 2D Quick IR (Phasetech, Inc.).

In the spectrometer, a weak reflection[90,91] from a wedged ZnSe window is used as probe beam. The transmitted IR light is guided to a pulse shaper, where it is diffracted from a grating (150 l/mm), collimated using a parabolic mirror, and guided to a Germanium-based acousto-optic modulator (AOM). The IR light is diffracted at the AOM and focused onto a second grating (150 l/mm). The shaped beam is reflected from a retroreflector on a translational stage to control the waiting time (T_2) between the pump and the probe beams. After setting the polarization of the pump beam to 45° relative to the probe beam polarization, the pump and the probe beams are focused into the sample using an off-axis parabolic mirror. After the sample, the probe beam is re-collimated and split into polarization components, parallel and perpendicular relative to the pump beam with a polarizer. Both probe components are focused into an imaging spectrograph

(SP2156 spectrograph, Princeton Instruments, 30 l/mm grating) and detected using a 128×128 pixel mercury cadmium telluride (MCT) array detector.

Frequency resolution on the pump axis is obtained in time domain, using the pulse shaper to generate two pump pulses delayed by 0 to 2555 fs at increments of 35 fs. To reduce data acquisition time we used a rotating frame at $1400 \, cm^{-1}$. Pump pulses were corrected for group-velocity dispersion, and the dispersion parameters were optimized using the transient signal generated from multi-photon absorption in a 0.5 mm thick Ge plate. Before transforming the thus determined free induction decays into the frequency domain, the time-domain data were zero-padded to 128 data points and filtered with a Hamming window.

Data availability

The datasets generated during the current study are available from the corresponding author upon reasonable request.

References

1. Hofmeister, F. Arbeiten aus dem pharmakologisehen Institut der deutschen Universität zu Prag. 12. Zur Lehre von der Wirkung der Salze. Dritte Mittheilung. *Arch. Exp. Pathol. Pharmakol.* **25**, 1–30 (1888).
2. Gaigeot, M. P. Infrared spectroscopy of the alanine dipeptide analog in liquid water with DFT-MD. Direct evidence for PII/β conformations. *Phys. Chem. Chem. Phys.* **12**, 10198–10209 (2010).
3. Gaigeot, M. P. Unravelling the conformational dynamics of the aqueous alanine dipeptide with first-principle molecular dynamics. *J. Phys. Chem. B* **113**, 10059–10062 (2009).
4. Goodman, M., Naider, F. & Rupp, R. Conformations of alanine oligopeptides in solution. *Bioorg. Chem.* **328**, 310–328 (1971).
5. Ghaouar, N., Elmissaoui, S., Aschi, A. & Gharbi, A. Concentration regimes and denaturation effects on the conformational changes of α-chymotrypsin by viscosity and dynamic light scattering measurements. *Int. J. Biol. Macromol.* **47**, 425–430 (2010).
6. Neurath, H., Greenstein, J. P., Putnam, F. W. & Erickson, J. O. The chemistry of protein denaturation. *Chem. Rev.* **34**, 157–265 (1944).
7. Collins, K. D. & Washabaugh, M. W. The Hofmeister effect and the behaviour of water at interfaces. *Q. Rev. Biophys.* **18**, 323–422 (1985).
8. Pinna, M. C. et al. Hofmeister effects in biology: effect of choline addition on the salt-induced super activity of horseradish peroxidase and its implication for salt resistance of plants. *J. Phys. Chem. B* **109**, 16511–16514 (2005).
9. Kunz, W., Lo Nostro, P. & Ninham, B. W. The present state of affairs with Hofmeister effects. *Curr. Opin. Colloid Interface Sci.* **9**, 1–18 (2004).
10. Jungwirth, P. & Winter, B. Ions at aqueous interfaces: from water surface to hydrated proteins. *Annu. Rev. Phys. Chem.* **59**, 343–366 (2008).
11. Jungwirth, P. & Cremer, P. S. Beyond hofmeister. *Nat. Chem.* **6**, 261–263 (2014).
12. Kastelic, M., Kalyuzhnyi, Y. V., Hribar-Lee, B., Dil, K. A. & Vlachy, V. Protein aggregation in salt solutions. *Proc. Natl Acad. Sci. USA* **112**, 6766–6770 (2015).
13. Balos, V., Kim, H., Bonn, M. & Hunger, J. Dissecting Hofmeister effects: direct anion–amide interactions are weaker than cation–amide binding. *Angew. Chem. Int. Ed.* **55**, 8125–8128 (2016).
14. Balos, V., Bonn, M. & Hunger, J. Quantifying transient interactions between amide groups and the guanidinium cation. *Phys. Chem. Chem. Phys.* **17**, 28539–28543 (2015).
15. Balos, V., Bonn, M. & Hunger, J. Anionic and cationic Hofmeister effects are non-additive for guanidinium salts. *Phys. Chem. Chem. Phys.* **19**, 9724–9728 (2017).
16. Balos, V. et al. Specific ion effects on an oligopeptide: bidentate binding matters for the guanidinium cation. *Angew. Chem. - Int. Ed.* **58**, 332–337 (2019).
17. Zhang, Y. & Cremer, P. S. Chemistry of hofmeister anions and osmolytes. *Annu. Rev. Phys. Chem.* **61**, 63–83 (2010).
18. Okur, H. I. et al. Beyond the Hofmeister series: ion-specific effects on proteins and their biological functions. *J. Phys. Chem. B* **121**, 1997–2014 (2017).
19. Xie, W. J. & Gao, Y. Q. A simple theory for the hofmeister series. *J. Phys. Chem. Lett.* **4**, 4247–4252 (2013).
20. Cremer, P. S., Flood, A. H., Gibb, B. C. & Mobley, D. L. Collaborative routes to clarifying the murky waters of aqueous supramolecular chemistry. *Nat. Chem.* **10**, 8–16 (2018).
21. Rogers, B. A. et al. Weakly hydrated anions bind to polymers but not monomers in aqueous solutions. *Nat. Chem.* **14**, 40–45 (2022).
22. Salis, A. & Ninham, B. W. Models and mechanisms of Hofmeister effects in electrolyte solutions, and colloid and protein systems revisited. *Chem. Soc. Rev.* **43**, 7358–7377 (2014).
23. Rembert, K. B., Okur, H. I., Hilty, C. & Cremer, P. S. An NH moiety is not required for anion binding to amides in aqueous solution. *Langmuir* **31**, 3459–3464 (2015).
24. Zhang, Y., Furyk, S., Bergbreiter, D. E. & Cremer, P. S. Specific ion effects on the water solubility of macromolecules: PNIPAM and the Hofmeister series. *J. Am. Chem. Soc.* **127**, 14505–14510 (2005).
25. Bruce, E. E. et al. Molecular mechanism for the interactions of Hofmeister cations with macromolecules in aqueous solution. *J. Am. Chem. Soc.* **142**, 19094–19100 (2020).
26. Pastoor, K. J. & Rice, C. V. Cation effects on the phase transition of N-isopropylacrylamide hydrogels. *Macromol. Chem. Phys.* **216**, 1024–1032 (2015).
27. Okur, H. I., Kherb, J. & Cremer, P. S. Cations bind only weakly to amides in aqueous solutions. *J. Am. Chem. Soc.* **135**, 5062–5067 (2013).
28. Cracchiolo, O. M., Geremia, D. K., Corcelli, S. A. & Serrano, A. L. Hydrogen bond exchange and Ca2+binding of aqueous N-methylacetamide revealed by 2DIR spectroscopy. *J. Phys. Chem. B* **124**, 6947–6954 (2020).
29. Heyda, J., Vincent, J. C., Tobias, D. J., Dzubiella, J. & Jungwirth, P. Ion specificity at the peptide bond: molecular dynamics simulations of N-methylacetamide in aqueous salt solutions. *J. Phys. Chem. B* **114**, 1213–1220 (2010).
30. Harding, M. M. The architecture of metal coordination groups in proteins. *Acta Crystallogr. Sect. D. Biol. Crystallogr.* **60**, 849–859 (2004).
31. Rembert, K. B. et al. Molecular mechanisms of ion-specific effects on proteins. *J. Am. Chem. Soc.* **134**, 10039–10046 (2012).
32. Bruce, E. E., Bui, P. T., Rogers, B. A., Cremer, P. S. & van der Vegt, N. F. A. Nonadditive ion effects drive both collapse and swelling of thermoresponsive polymers in water. *J. Am. Chem. Soc.* **141**, 6609–6616 (2019).
33. Bruce, E. E., Bui, P. T., Cao, M., Cremer, P. S. & van der Vegt, N. F. A. Contact ion pairs in the bulk affect anion interactions with poly(N-isopropylacrylamide). *J. Phys. Chem. B* **125**, 680–688 (2021).
34. Hladílková, J. et al. Effects of end-group termination on salting-out constants for triglycine. *J. Phys. Chem. Lett.* **4**, 4069–4073 (2013).
35. O'Brien, E. P., Dima, R. I., Brooks, B. & Thirumalai, D. Interactions between hydrophobic and ionic solutes in aqueous guanidinium chloride and urea solutions: Lessons for protein denaturation mechanism. *J. Am. Chem. Soc.* **129**, 7346–7353 (2007).
36. Yan, C. & Mu, T. Molecular understanding of ion specificity at the peptide bond. *Phys. Chem. Chem. Phys.* **17**, 3241–3249 (2015).
37. Rao, C. P., Balaram, P. & Rao, C. N. R. 13C nuclear magnetic resonance studies of the binding of alkali and alkaline earth metal salts to amides. *J. Chem. Soc. Faraday Trans. 1 Phys. Chem. Condens. Phases* **76**, 1008–1013 (1980).
38. Algaer, E. A. & Van Der Vegt, N. F. A. Hofmeister ion interactions with model amide compounds. *J. Phys. Chem. B* **115**, 13781–13787 (2011).
39. Paterová, J. et al. Reversal of the Hofmeister series: specific ion effects on peptides. *J. Phys. Chem. B* **117**, 8150–8158 (2013).
40. Zhao, J., Dong, T., Yu, P. & Wang, J. Conformation and metal cation binding of zwitterionic alanine tripeptide in saline solutions by infrared vibrational spectroscopy and molecular dynamics simulations. *J. Phys. Chem. B* **126**, 161–173 (2022).
41. Pérez-Fuentes, L., Bastos-González, D., Faraudo, J. & Drummond, C. Effect of organic and inorganic ions on the lower critical solution transition and aggregation of PNIPAM. *Soft Matter* **14**, 7818–7828 (2018).
42. Zajforoushan Moghaddam, S. & Thormann, E. Hofmeister effect on PNIPAM in bulk and at an interface: surface partitioning of weakly hydrated anions. *Langmuir* **33**, 4806–4815 (2017).
43. Moghaddam, S. Z. & Thormann, E. The Hofmeister series: specific ion effects in aqueous polymer solutions. *J. Colloid Interface Sci.* **555**, 615–635 (2019).
44. Rodríguez-Arteche, I., Cerveny, S., Alegría, Á. & Colmenero, J. Dielectric spectroscopy in the GHz region on fully hydrated zwitterionic amino acids. *Phys. Chem. Chem. Phys.* **14**, 11352–11362 (2012).
45. Adams, M. J., Baddiel, C. B., Jones, R. G. & Matheson, A. J. Interaction of lithium salts with amides. Part 1. - ultrasonic relaxation. *J. Chem. Soc. Faraday Trans. 2 Mol. Chem. Phys.* **70**, 1114–1120 (1974).
46. Kim, H. & Cho, M. Infrared probes for studying the structure and dynamics of biomolecules. *Chem. Rev.* **113**, 5817–5847 (2013).
47. Drexler, C. I. et al. Local electric fields in aqueous electrolytes. *J. Phys. Chem. B* **125**, 8484–8493 (2021).
48. Vazquez de Vasquez, M. G., Wellen Rudd, B. A., Baer, M. D., Beasley, E. E. & Allen, H. C. Role of hydration in magnesium versus calcium ion pairing with carboxylate: solution and the aqueous interface. *J. Phys. Chem. B* **125**, 11308–11319 (2021).
49. Du, H., Wickramasinghe, R. & Qian, X. Effects of salt on the lower critical solution temperature of poly (N-isopropylacrylamide). *J. Phys. Chem. B* **114**, 16594–16604 (2010).
50. Kim, H., Lee, H., Lee, G., Kim, H. & Cho, M. Hofmeister anionic effects on hydration electric fields around water and peptide. *J. Chem. Phys.* **136**, 03B612 (2012).

51. Bhate, M. P., Woodard, J. C. & Mehta, M. A. Solvation and hydrogen bonding in alanine- and glycine-containing dipeptides probed using solution- and solid-state NMR spectroscopy. *J. Am. Chem. Soc.* **131**, 9579–9589 (2009).

52. Barthel, J. et al. Dielectric relaxation spectroscopy of electrolyte solutions. Recent developments and prospects. *J. Mol. Liq.* **78**, 83–109 (1998).

53. Buchner, R. What can be learnt from dielectric relaxation spectroscopy about ion solvation and association? *Pure Appl. Chem.* **80**, 1239–1252 (2008).

54. Kremer, F. & Schönhals, A. *Broadband Dielectric Spectroscopy* (Springer-Verlag Berlin Heidelberg GmbH, 2003).

55. Fukasawa, T. et al. Relation between dielectric and low-frequency Raman spectra of hydrogen-bond liquids. *Phys. Rev. Lett.* **95**, 197802-1–4 (2005).

56. Sato, T., Buchner, R., Fernandez, Š., Chiba, A. & Kunz, W. Dielectric relaxation spectroscopy of aqueous amino acid solutions: dynamics and interactions in aqueous glycine. *J. Mol. Liq.* **117**, 93–98 (2005).

57. Debye, P. *Polar Molecules* (Dover Publications, 1930).

58. Cole, K. S. & Cole, R. H. Dispersion and absorption in dielectrics: I. alternating current characteristics. *J. Chem. Phys.* **9**, 341 (1941).

59. Cole, K. S. Dispersion and absorption in dielectrics II. Direct current characteristics. *J. Chem. Phys.* **10**, 98 (1942).

60. Hubbard, J. B., Onsager, L., van Beek, W. M. & Mandel, M. Kinetic polarization deficiency in electrolyte solutions. *Proc. Natl Acad. Sci. USA* **74**, 401–404 (1977).

61. Sega, M., Kantorovich, S. & Arnold, A. Kinetic dielectric decrement revisited: phenomenology of finite ion concentrations. *Phys. Chem. Chem. Phys.* **17**, 130–133 (2015).

62. Kumar, A. Aqueous guanidinium salts. Part II. Isopiestic osmotic coefficients of guanidinium sulphate and viscosity and surface tension of guanidinium chloride, bromide, acetate, perchlorate and sulphate solutions at 298.15 K. *Fluid Phase Equilib.* **180**, 195–204 (2001).

63. Abdulagatov, I. M., Zeinalova, A. B. & Azizov, N. D. Experimental viscosity B-coefficients of aqueous LiCl solutions. *J. Mol. Liq.* **126**, 75–88 (2006).

64. Mandal, A. B. & Jayakumar, R. Aggregation, hydrogen bonding and thermodynamic studies on tetrapeptide micelles. *J. Chem. Soc. Faraday Trans.* **90**, 161 (1994).

65. Creekmore, R. W. & Reilley, C. N. Nuclear magnetic resonance determination of hydration numbers of electrolytes in concentrated aqueous solutions. *J. Phys. Chem.* **73**, 1563–1568 (1969).

66. Fielding, L. NMR methods for the determination of protein–ligand dissociation constants. *Prog. Nucl. Magn. Reson. Spectrosc.* **51**, 219–242 (2007).

67. Pike, S. J., Hutchinson, J. J. & Hunter, C. A. H-bond acceptor parameters for anions. *J. Am. Chem. Soc.* **139**, 6700–6706 (2017).

68. Zarycz, M. N. C. & Fonseca Guerra, C. NMR 1 H-shielding constants of hydrogen-bond donor reflect manifestation of the Pauli principle. *J. Phys. Chem. Lett.* **9**, 3720–3724 (2018).

69. Pike, S. J., Lavagnini, E., Varley, L. M., Cook, J. L. & Hunter, C. A. H-Bond donor parameters for cations. *Chem. Sci.* **10**, 5943–5951 (2019).

70. Hamm, P. & Zanni, M. *Concepts and Methods of 2D Infrared Spectroscopy* (Cambridge University Press, 2011).

71. Pearson, J. F. & Slifkin, M. A. The infrared spectra of amino acids and dipeptides. *Spectrochim. Acta Part A Mol. Spectrosc.* **28**, 2403–2417 (1972).

72. Feng, Y. et al. Structure of penta-alanine investigated by two-dimensional infrared spectroscopy and molecular dynamics simulation. *J. Phys. Chem. B* **120**, 5325–5339 (2016).

73. Kim, Y. S. & Hochstrasser, R. M. Dynamics of amide-I modes of the alanine dipeptide in D 2O. *J. Phys. Chem. B* **109**, 6884–6891 (2005).

74. Fang, C. et al. Two-dimensional infrared spectroscopy of isotopomers of an alanine rich α-helix. *J. Phys. Chem. B* **108**, 10415–10427 (2004).

75. Deflores, L. P., Ganim, Z., Nicodemus, R. A. & Tokmakoff, A. Amide I′-II′ 2D IR spectroscopy provides enhanced protein secondary structural sensitivity. *J. Am. Chem. Soc.* **131**, 3385–3391 (2009).

76. DeCamp, M. F. et al. Amide I vibrational dynamics of N-methylacetamide in polar solvents: the role of electrostatic interactions. *J. Phys. Chem. B* **109**, 11016–11026 (2005).

77. Huerta-Viga, A. & Woutersen, S. Protein denaturation with guanidinium: a 2D-IR study. *J. Phys. Chem. Lett.* **4**, 3397–3401 (2013).

78. Drozd, M. Molecular structure and infrared spectra of guanidinium cation. A combined theoretical and spectroscopic study. *Mater. Sci. Eng. B Solid-State Mater. Adv. Technol.* **136**, 20–28 (2007).

79. Feng, C. J. & Tokmakoff, A. The dynamics of peptide-water interactions in dialanine: an ultrafast amide i 2D IR and computational spectroscopy study. *J. Chem. Phys.* **147**, 1–11 (2017).

80. Khalil, M., Demirdöven, N. & Tokmakoff, A. Vibrational coherence transfer characterized with Fourier-transform 2D IR spectroscopy. *J. Chem. Phys.* **121**, 362–373 (2004).

81. Ghosh, A., Tucker, M. J. & Hochstrasser, R. M. Identification of arginine residues in peptides by 2D-IR echo spectroscopy. *J. Phys. Chem. A* **115**, 9731–9738 (2011).

82. Fenn, E. E. & Fayer, M. D. Extracting 2D IR frequency-frequency correlation functions from two component systems. *J. Chem. Phys.* **135**, 074502 (2011).

83. Hamm, P., Lim, M. & Hochstrasser, R. M. Structure of the amide I band of peptides measured by femtosecond nonlinear-infrared spectroscopy. *J. Phys. Chem. B* **102**, 6123–6138 (1998).

84. Van der Vegt, N. F. A. et al. Water-mediated ion pairing: occurrence and relevance. *Chem. Rev.* **116**, 7626–7641 (2016).

85. Donald, J. E., Kulp, D. W. & DeGrado, W. F. Salt bridges: geometrically specific, designable interactions. *Proteins Struct. Funct. Bioinforma.* **79**, 898–915 (2010).

86. Chen, P. Self-assembly of ionic-complementary peptides: a physicochemical viewpoint. *Colloids Surf. A Physicochem. Eng. Asp.* **261**, 3–24 (2005).

87. Blackham, D. V. & Pollard, R. D. An improved technique for permittivity measurements using a coaxial probe. *IEEE Trans. Instrum. Meas.* **46**, 1093–1099 (1997).

88. Ensing, W., Hunger, J., Ottosson, N. & Bakker, H. J. On the orientational mobility of water molecules in proton and sodium terminated Nafion membranes. *J. Phys. Chem. C.* **117**, 12930–12935 (2013).

89. Hoffman, R. E. Standardization of chemical shifts of TMS and solvent signals in NMR solvents. *Magn. Reson. Chem.* **44**, 606–616 (2006).

90. Middleton, C. T., Woys, A. M., Mukherjee, S. S. & Zanni, M. T. Residue-specific structural kinetics of proteins through the union of isotope labeling, mid-IR pulse shaping, and coherent 2D IR spectroscopy. *Methods* **52**, 12–22 (2010).

91. Strasfeld, D. B., Middleton, C. T. & Zanni, M. T. Mode selectivity with polarization shaping in the mid-IR. *N. J. Phys.* **11**, 105046 (2009).

Acknowledgements

Author contributions

C.K. and J.H. designed the experiments and the research project. C.K. prepared the samples and performed the DRS measurements. C.H. and C.K. performed the NMR measurements. L.G. and C.K. performed the IR measurements. All authors discussed the results. C.K. and J.H. wrote the manuscript.

Funding

Competing interests

The authors declare no competing interests.

Additional information

Supplementary information The online version contains supplementary material available at https://doi.org/10.1038/s42004-022-00789-y.

Correspondence and requests for materials should be addressed to Johannes Hunger.

Peer review information *Communications Chemistry* thanks the anonymous reviewers for their contribution to the peer review of this work. Primary Handling Editors: Dr. Huijuan Guo and Dr. Teresa Ortner. Peer reviewer reports are available.

Reprints and permission information is available at http://www.nature.com/reprints

Publisher's note Springer Nature remains neutral with regard to jurisdictional claims in published maps and institutional affiliations.

Modification of Two-Dimensional Tin-Based Perovskites by Pentanoic Acid for Improved Performance of Field-Effect Transistors

Shuanglong Wang, Konstantinos Bidinakis, Constantin Haese, Franziska H. Hasenburg, Okan Yildiz, Zhitian Ling, Sabine Frisch, Milan Kivala, Robert Graf, Paul W. M. Blom, Stefan A. L. Weber, Wojciech Pisula,* and Tomasz Marszalek*

Understanding and controlling the nucleation and crystallization in solution-processed perovskite thin films are critical to achieving high in-plane charge carrier transport in field-effect transistors (FETs). This work demonstrates a simple and effective additive engineering strategy using pentanoic acid (PA). Here, PA is introduced to both modulate the crystallization process and improve the charge carrier transport in 2D 2-thiopheneethylammonium tin iodide ((TEA)$_2$SnI$_4$) perovskite FETs. It is revealed that the carboxylic group of PA is strongly coordinated to the spacer cation TEAI and [SnI$_6$]$^{4-}$ framework in the perovskite precursor solution, inducing heterogeneous nucleation and lowering undesired oxidation of Sn^{2+} during the film formation. These factors contribute to a reduced defect density and improved film morphology, including lower surface roughness and larger grain size, resulting in overall enhanced transistor performance. The reduced defect density and decreased ion migration lead to a higher p-channel charge carrier mobility of 0.7 cm^2 V^{-1} s^{-1}, which is more than a threefold increase compared with the control device. Temperature-dependent charge transport studies demonstrate a mobility of 2.3 cm^2 V^{-1} s^{-1} at 100 K due to the diminished ion mobility at low temperatures. This result illustrates that the additive strategy bears great potential to realize high-performance Sn-based perovskite FETs.

1. Introduction

Organic–inorganic halide perovskites have attracted extensive interest in solar cells and light-emitting diodes over the last decade due to their favorable optoelectronic properties and facile processability.[1,2] However, the application of perovskites in field-effect transistors (FETs) has received less attention and has remained challenging because of ion migration under operational conditions at room temperature due to the low formation energy of mobile ions or ionic defects in these ionic materials.[3,4] Mobile ions in perovskite FETs screen the applied gate field and reduce the gate modulation of the current yielding low field-effect mobility and large hysteresis.[5] In contrast, 2D Sn-based perovskites reveal favorable properties due to the insulating property of bulky organic ligands. The advantages of dielectric confinement in 2D layered structures are expected to significantly suppress ion movement in the device.[6] More importantly, the device performance can be tuned by tailoring the chemical structure of the spacer cations.[7]

2D Sn-based perovskites are promising semiconductors for high-performance FETs.[8,9] The Sn-based perovskites typically show high charge carrier mobility due to the smaller in-plane effective mass and longer carrier lifetime compared with their Pb analogs.[10] Nevertheless, there are several drawbacks to 2D Sn-based perovskite FETs. First, easy oxidation of Sn^{2+} to its tetravalent state Sn^{4+}, especially during solution processing, gives rise to ionic defects and leads to p-type self-doping.[11] Second, the fast

S. Wang, K. Bidinakis, C. Haese, F. H. Hasenburg, O. Yildiz, Z. Ling,
R. Graf, P. W. M. Blom, S. A. L. Weber, W. Pisula, T. Marszalek
Max Planck Institute for Polymer Research
Ackermannweg 10, 55128 Mainz, Germany
E-mail: pisula@mpip-mainz.mpg.de; marszalek@mpip-mainz.mpg.de

The ORCID identification number(s) for the author(s) of this article
can be found under https://doi.org/10.1002/smll.202207426.

S. Frisch, M. Kivala
Organisch-Chemisches Institut
Ruprecht-Karls-Universität Heidelberg
Im Neuenheimer Feld 270, 69120 Heidelberg, Germany

S. A. L. Weber
Institute of Physics
Johannes Gutenberg University Mainz
Duesbergweg 10-14, 55128 Mainz, Germany

W. Pisula, T. Marszalek
Department of Molecular Physics
Faculty of Chemistry
Lodz University of Technology
Zeromskiego 116, Lodz 90-924, Poland

crystallization rate of Sn-based perovskites as compared to Pb counterparts results in poor film morphology and low surface coverage.[12] Therefore, controlling the crystallization and oxidation to reduce defects and charge traps is crucial in suppressing ion migration and maximizing the charge carrier transport in 2D Sn-perovskite films with respect to the ultimate FET performance.

To date, several approaches, involving solvent and precursor engineering,[13] 2D/3D structure,[14] and metallic iodide doping,[15] have been proposed to address the above limitations and present promising improvements in 2D Sn-based perovskite FET devices. Recently, we introduced hot-cast 2-thiopheneethylammonium tin iodide ((TEA)$_2$SnI$_4$) perovskite thin films to control the film crystallization and morphology. The increased grain size resulted in an overall enhanced FET performance with pronounced gate modulation.[16] As an alternative strategy, introducing additives into the precursor solution has been demonstrated to be an effective and facile method in modulating perovskite crystallization, passivating defects, and improving charge transport in solar cells.[17–19] Inspired by the recent breakthroughs in Sn-based perovskite solar cells through additive engineering, various additives for FET applications, including nanotubes and polymers, have been proposed to optimize the transistor performance.[20,21] However, a deep understanding of the influence of additives on the crystallization process of perovskites is still missing, which prevents the further rational design of additive molecules for perovskites FETs.

In this work, we propose a simple and effective additive engineering strategy via the incorporation of a pentanoic acid (PA) molecule with a carboxylic group into the perovskite precursor solution. The effects of PA on the passivation of defects, film formation, crystallinity, and device performance of 2D (TEA)$_2$SnI$_4$-based FETs are systematically investigated. It is demonstrated that PA interacts with TEAI and [SnI$_6$]$^{4-}$ through hydrogen and coordination bonding effectively improving crystallinity, enlarging grain size, and reducing defect density. Kelvin probe force microscopy (KPFM) measurement further confirms the additive effect and the origin of the improvement in FET performance. As a result, the p-channel (TEA)$_2$SnI$_4$ transistors exhibit increased charge carrier mobility at room temperature from 0.2 cm^2 V^{-1} s^{-1} of

the control device to 0.7 cm^2 V^{-1} s^{-1} with additive treatment. At a low temperature of 100 K, the mobility further rises to 2.3 cm^2 V^{-1} s^{-1} along with reduced dual-sweep hysteresis.

2. Results and Discussion

The chemical structures of organic spacer TEA and additive PA are shown in **Figure 1**a. Liquid-state ^{1}H and ^{119}Sn nuclear magnetic resonance (NMR) spectroscopy is performed in order to understand and identify the interaction between PA and perovskite precursors TEAI and SnI$_2$. Different contents of PA are used from 0, 0.25, 0.5, 0.75, to 1 vol% in the precursor solution. The preparation details of the precursor solution are described in the Experimental Section. First, a plain PA solution without the perovskite precursors is probed and the result is shown in Figure S1, Supporting Information. The resonance signal with a ^{1}H chemical shift at 11.9 parts per million (ppm) can be attributed to the active hydrogen in the carboxylic group of PA. Then PA is added as an additive at various volumes to the TEAI precursor deuterated dimethyl sulfoxide-d_6 (DMSO-d_6) solution. In the ^{1}H NMR spectra for the PA+TEAI mix solution, the gradual emerging of the PA signal is observed with its higher concentration indicating the formation of O=C−OH···I$^-$ hydrogen bonding with a significant exchange dynamic. In addition, ^{119}Sn NMR spectra are analyzed after the addition of PA to the SnI$_2$ solution at different concentrations (Figure S2, Supporting Information). Figure 1b shows the ^{119}Sn chemical shift as a function of the PA volume ratio. The observed down-field shift of the ^{119}Sn signal with increasing PA concentration can be explained by the electronic deshielding of the Sn^{2+} ion during its coordination bonding to the oxygen of PA in the form of HO−C=O···Sn^{2+}.[22] From these results, it can be concluded that PA undergoes hydrogen and coordination bonding by the carboxylic group with iodide and tin atoms of the precursors (Figure 1c).

To verify the influence of the PA additive on the surface morphology of the perovskite films, atomic force microscopy (AFM) measurement is employed for pristine and PA-modified (TEA)$_2$SnI$_4$ films deposited on a silicon/silicone dioxide wafer, and the corresponding results are shown in **Figure 2**a–e. The
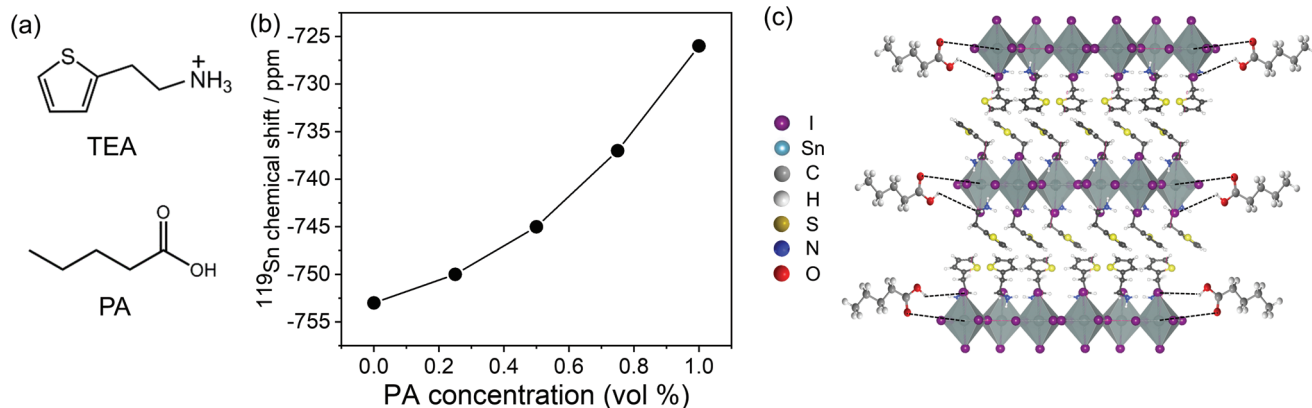
Figure 1. a) Chemical structures of organic spacer TEA and additive PA. b) ^{119}Sn chemical shift as a function of the PA volume ratio. c) Representation of hydrogen bonding (C−OH···I) and coordination bonding (C=O···Sn) between PA and (TEA)$_2$SnI$_4$.

**ADVANCED
SCIENCE NEWS**
www.advancedsciencenews.com

NANO · MICRO
small
www.small-journal.com
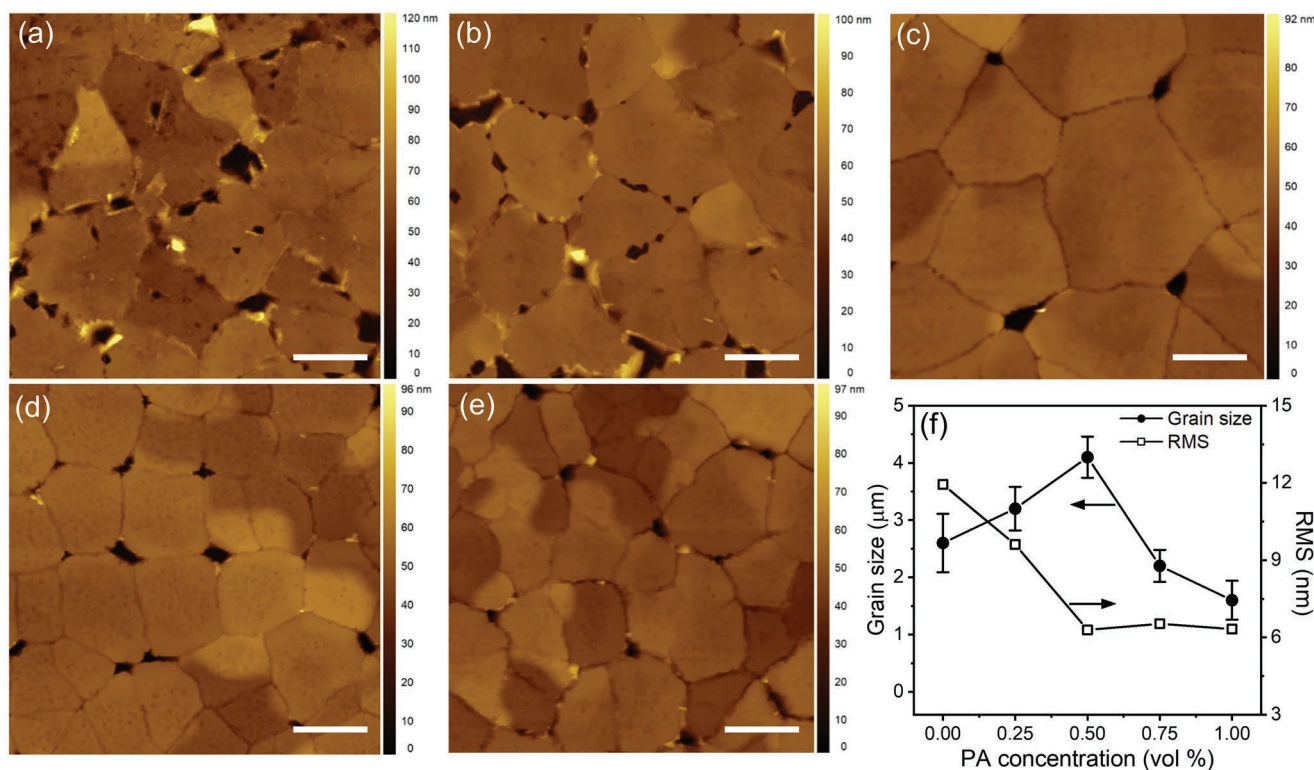
Figure 2. AFM height images of $(TEA)_2SnI_4$ films with PA at the concentration of a) 0 vol%; b) 0.25 vol%; c) 0.5 vol%; d) 0.75 vol%; and e) 1 vol%. Scale bar in all images is 2 µm. f) Grain size distribution and surface roughness of $(TEA)_2SnI_4$ films as a function of PA concentration.

control film without additives exhibits a small grain size as confirmed by the literature.[23] Inferior film morphology and poor film coverage with numerous inevitably unfavorable pinholes appear due to the fast crystallization, which is a typical drawback for tin-based perovskites.[24] Upon addition of PA to the $(TEA)_2SnI_4$ precursor solution, smoother and more homogeneous films with less pinholes are obtained. Furthermore, the grain size increases to around 4 µm at a PA concentration of 0.5 vol%. The dependence of the grain size on PA concentration is shown in Figure 2f. We postulate that the strong interaction between the PA additive and the precursors initiates heterogeneous nucleation centers inducing crystal growth preferentially at these nucleation sites, which induces the growth of perovskite grains with high surface coverage.[25] In addition, the perovskite film with 0.5 vol% PA exhibits a much smaller surface roughness with a root-mean-square (RMS) value of 6.3 nm in comparison to 11.9 nm for the pristine sample. A smoother film surface is beneficial for the contact between the electrodes and perovskite film in the FET facilitating carrier injection and extraction.[26] Indeed there are still small pinholes in the film with 0.5 vol% PA. However, their size and density are significantly reduced in comparison to the pristine $(TEA)_2SnI_4$ film and further optimization of the crystallization process will be performed in the future. The RMS values for all perovskite films are summarized in Figure 2f. At higher PA levels between 0.5 and 1 vol%, the grain size clearly decreases compared with the pristine sample, probably due to an excessive formation of heterogeneous nucleation sites in the precursor solution.[27] The results demonstrate that the PA additive effectively tunes

the crystallization process and improves film morphology, including the surface roughness and grain size, which is expected to enhance the electronic properties of the perovskite films in FET devices.

Based on the above AFM results, we choose the PA concentration of 0.5 vol% as an optimum to investigate the impact of the additive on the crystal structure and molecular organization of the $(TEA)_2SnI_4$ films by X-ray diffraction (XRD) and grazing incidence wide-angle X-ray scattering (GIWAXS) measurements. **Figure 3**a shows the XRD patterns of the corresponding two $(TEA)_2SnI_4$ films without and with 0.5 vol% PA. The two samples exhibit the typical (00l) out-of-plane organization ($l = 2$, 4, 6, 8, 10, and 12) indicating a layered structure.[28] Both films show the same position for the (002) diffraction peak at 5.68°, while the calculated interlayer spacing D_{002} is 15.6 Å. These results prove that the PA additive does not cause any disruption of the out-of-plane lattice in the layered perovskite structure. The films with 0.5 vol% PA additive exhibit substantially increased intensities of the main diffraction peaks compared with the pristine film, although the two films have the same thickness. In addition, the corresponding full width at half maximum (FWHM) values are extracted to be 0.23° and 0.21°, respectively, suggesting slightly improved out-of-plane crystallinity of the film with PA. GIWAXS measurements are further executed to understand the contribution of the PA additive on the molecular organization. The crystal coherence lengths in the (002) direction calculated from the Scherrer equation are 197 nm for pristine and 236 nm for the optimized $(TEA)_2SnI_4$ film as shown in Figure 3b,c. Higher order reflections,

**ADVANCED
SCIENCE NEWS**

www.advancedsciencenews.com

NANO · MICRO

small

www.small-journal.com
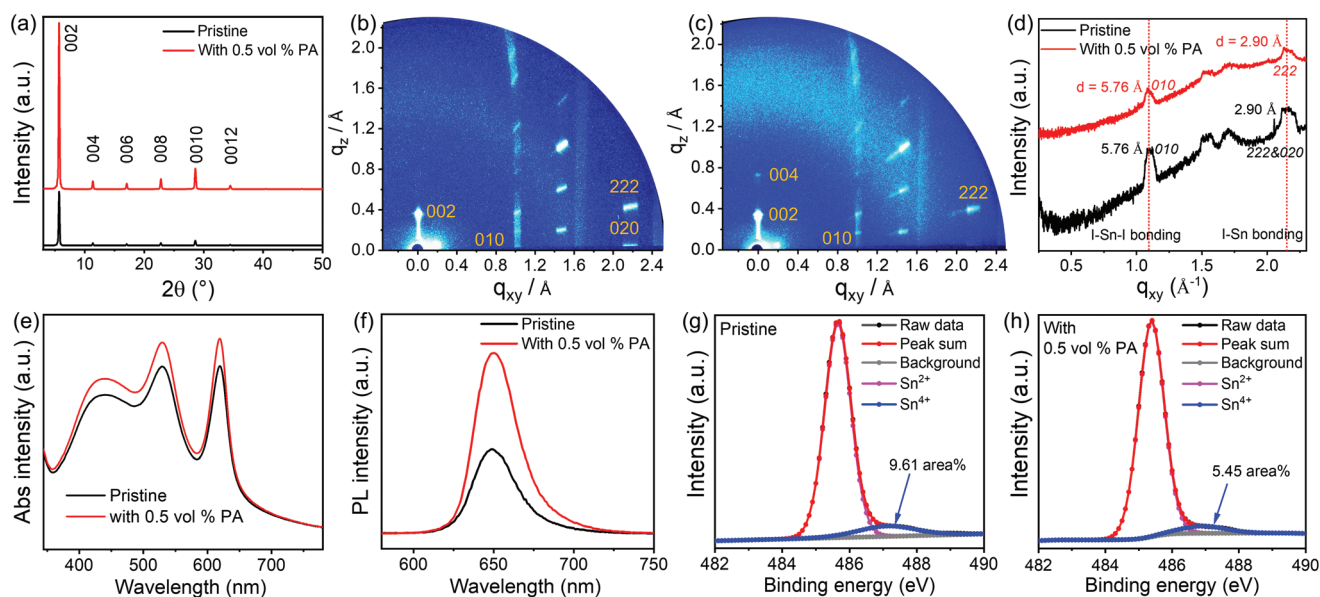
Figure 3. a) XRD and b,c) GIWAXS patterns (main reflections are assigned by Miller indices) for pristine and PA containing (TEA)$_2$SnI$_4$ films; d) in-plane profiles of both GIWAXS patterns; e) UV–vis absorption and f) photoluminescence spectra; XPS spectra of Sn 3d for (TEA)$_2$SnI$_4$ films prepared without (g) and with (h) PA. The peak fitting indicates the ratio changes of Sn^{4+} upon PA addition.

including (004), are observed in the film with PA indicating a long-range organization of crystal structures in the out-of-plane direction of the film, further confirming the XRD results. From the out-of-plane position of the (00l) reflections, it is possible to conclude that the inorganic part [SnI$_6$]$^{4-}$ is organized parallel to the substrate, which is favorable for the in-plane charge carrier transport in FETs.[29] The in-plane integration of the peak intensity for q_{xy} from 0° to 15° is shown in Figure 3d. The in-plane (010) and (020) reflections are attributed to Sn–I and I–Sn–I bonds with corresponding d-spacings of 2.9 and 5.8 Å, which agree well with the literature.[30] However, the (020) reflection is missing for the film with PA additive compared to the pristine (TEA)$_2$SnI$_4$ film, probably due to the strong interaction between PA and the inorganic [SnI$_6$]$^{4-}$ framework.

To evaluate the impact of the PA additive on the optoelectronic properties of the (TEA)$_2$SnI$_4$ films, we acquired UV–vis absorption (Abs) and steady-state photoluminescence (PL) spectra of pristine and films with 0.5 vol% PA, as shown in Figure 3e,f. In the absorption spectra, both (TEA)$_2$SnI$_4$ films without and with 0.5 vol% PA show three peaks at 440, 529, and 619 nm, where the sharp absorption peak at 619 nm can be attributed to the intrinsic exciton absorption in the crystal lattice. The film with 0.5 vol% PA exhibits slightly stronger absorption than the pristine one. Similar behavior is observed in the PL spectra. The stronger PL intensity for the film with 0.5 vol% PA in comparison to the pristine sample indicates a reduced number of defects within the optimized perovskite layer.[31] X-ray photoelectron spectra (XPS) measurements were further used to identify the existence of PA additive and Sn^{2+} oxidation for pristine and 0.5 vol% PA-based (TEA)$_2$SnI$_4$ films. The Sn 3d XPS spectra confirm that Sn from (TEA)$_2$SnI$_4$ is the active site to coordinate with the O=C–OH units in PA since the peak exhibits a shift toward lower binding energy from pristine to PA added (TEA)$_2$SnI$_4$ films (Figure 3g,h). More impor-

tantly, a reduced proportion of Sn^{4+} from 9.61 atomic% for the pristine sample to 5.45 atomic% for the PA-based (TEA)$_2$SnI$_4$ film is also observed. Since Sn^{2+} is prone to be oxidized to the Sn^{4+} ionic defect which can occur either in precursor solution and/or during film formation processing. Therefore, minimizing the Sn^{4+} valence state is desirable to reduce the trap density and prolong the carrier diffusion length in the film.[32] From the XPS results, we conclude that the PA additive can effectively passivate defects through strong retardation of Sn^{2+} oxidation. Additionally, we analyzed the XPS wide spectra in-depth for pristine and optimized PA-added (TEA)$_2$SnI$_4$ films (Figure S3a, Supporting Information). As the PA additive contains carbon and oxygen elements, we compare the XPS peaks of C 1s and O 1s for pristine and PA-based (TEA)$_2$SnI$_4$ films. From elemental analysis, we find a distinct shoulder peak for C 1s at 285.2 eV (Figure S3b, Supporting Information) and an overall increased amount of C concentration for the (TEA)$_2$SnI$_4$ film with PA additive. For O 1s, we find a dominant peak at 532 eV, which can be assigned to C–OH and C–O–C groups (Figure S3c, Supporting Information). Therefore, combined with the above analysis, we can conclude that the PA additive is successfully incorporated into the perovskite film.

To study the effect of PA on the electrical properties of the (TEA)$_2$SnI$_4$ semiconducting film and determine the optimum concentration of PA in the perovskite films regarding the device performance, FETs with a bottom-gate top-contact geometry were fabricated, as shown in **Figure 4**a. The transfer characteristics were recorded at $V_{ds} = -60$ V with V_g scanned from +60 to –60 V in pulse mode (see more details in the Experimental Section). Figure 4b,c shows the statistics of the charge carrier mobility and hysteresis (V_g difference at $|I_{ds}| = 10^{-7}$ A of both sweeping directions) in the transfer characteristics as a function of the PA concentration at 295 K. The mobility is extracted from the saturation region of the transfer curve in a forward

**ADVANCED
SCIENCE NEWS**

www.advancedsciencenews.com

NANO · MICRO

small

www.small-journal.com
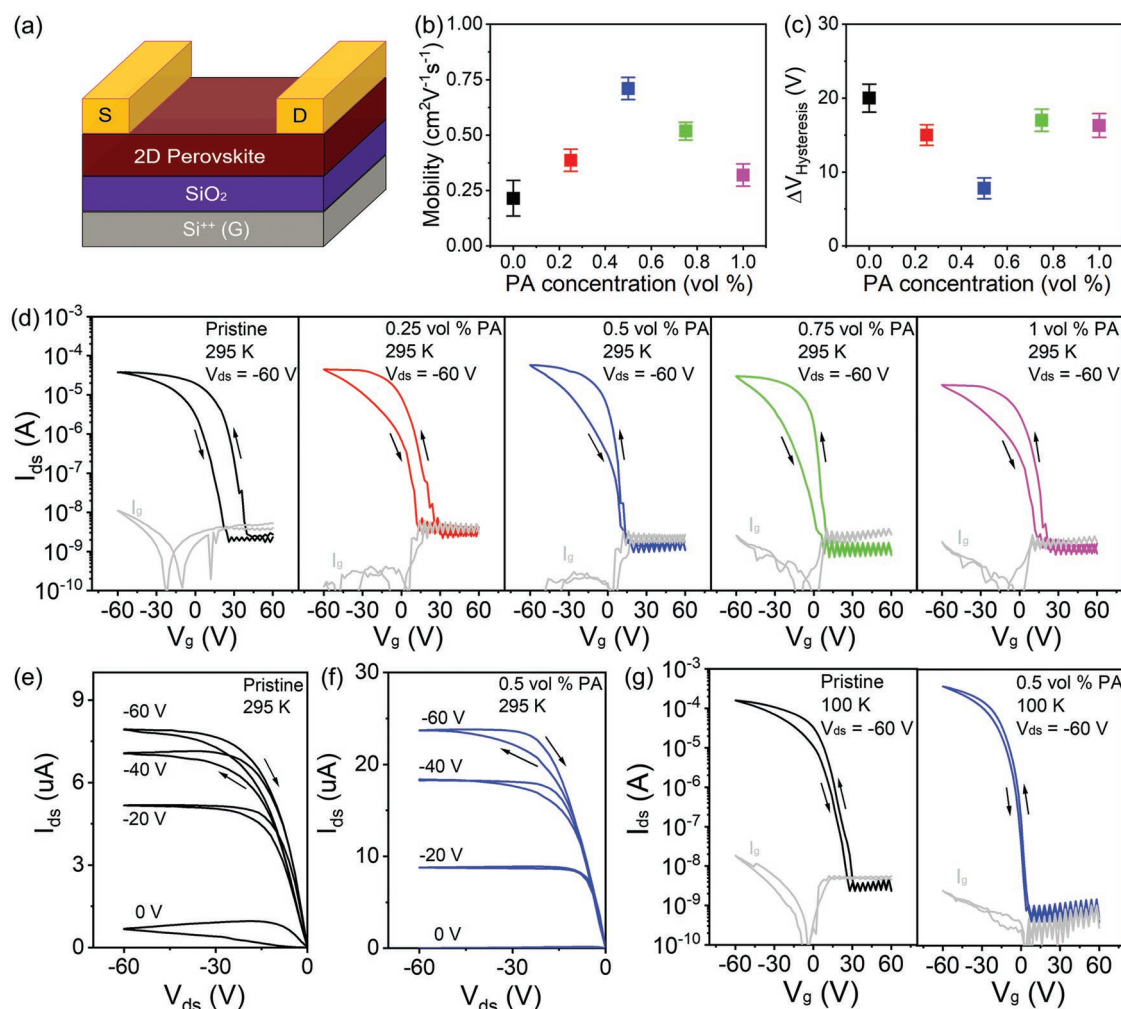
Figure 4. a) Device structure of $(TEA)_2SnI_4$ FETs. b) Charge carrier mobility and c) hysteresis width of $(TEA)_2SnI_4$ FETs with different PA concentrations. Error bars present standard deviation calculated from 12 devices per type. d) Transfer characteristics at 295 K (I_g is the gate leakage current). Corresponding output characteristics of pristine (e) and PA-based (at 0.5 vol%) devices (f) at 295 K. g) Transfer characteristics of pristine and modified devices with PA concentration of 0.5 vol% at 100 K. Arrows indicate the direction of the sweeps.

direction. The pristine $(TEA)_2SnI_4$ FET reveals p-channel FET characteristics with an average hole mobility (μ_h) of 0.2 cm^2 V^{-1} s^{-1}, a subthreshold swing (SS) of 5 V dec^{-1}, an on/off current ratio ($I_{on/off}$) of 1.5×10^4, and a threshold voltage (V_{th}) of 33 V (Figure S4, Supporting Information). The FETs based on the additive PA at various concentrations exhibit markedly improved overall performance. Notably, the device with 0.5 vol% PA demonstrates the best performance. At the optimal PA concentration of 0.5 vol%, the maximum channel current in the transfer curve corresponds to a smaller SS value of 2.9 V dec^{-1}, a charge carrier mobility of 0.7 cm^2 V^{-1} s^{-1}, an $I_{on/off}$ of 6.1×10^4, and a V_{th} of 9 V, representing a remarkable improvement in the transistor performance (Table S1, Supporting Information). In our device with PA additive, the V_{th} values are significantly reduced compared to the pristine FET demonstrating that the PA additive effectively eliminates defects. However, V_{th} increases for a higher concentration of PA possibly due to the insulating nature of the PA additive, reduced grain size, and increased number of grain boundaries. Based on the repeated

measurements of a large number of devices, the device performance is confirmed to be highly reliable and reproducible with a small standard deviation of ±0.053 cm^2 V^{-1} s^{-1}. The trap density (N_t) at the dielectric/perovskite interface with the whole channel area of 80 μm × 1000 μm is calculated using SS values as defined by the following equation[33]

$$SS = \frac{k_B T \ln 10}{q}\left[1 + \frac{q^2}{C_i} N_t\right] \tag{1}$$

with k_B the Boltzmann constant; T the absolute temperature; q the elementary charge; and C_i the areal capacitance of the dielectric layer. Accordingly, N_t decreases from 6.1×10^{12} cm^{-2} eV^{-1} for the pristine FET to 3.5×10^{12} cm^{-2} eV^{-1} for the 0.5 vol% PA-based FET, as shown in Figure S5, Supporting Information. However, when the PA concentration is further increased to 1 vol%, the trap density N_t rises again to 5.6×10^{12} cm^{-2} eV^{-1}, which can be ascribed to the decreased grain size leading to a high density of grain boundaries. These results suggest that

ADVANCED
SCIENCE NEWS
www.advancedsciencenews.com

NANO · MICRO
small
www.small-journal.com

the additive at optimal concentration improves the film quality at the perovskite/dielectric interface contributing to lower SS and reduced trap density. When the PA concentration is further increased, a declined device performance is observed. The PA concentration of 1 vol% leads to a decreased mobility of 0.3 cm^2 V^{-1} s^{-1}, as shown in Figure 4d. The above results reveal an optimum PA concentration to achieve the highest device performance. At a too-high concentration, the insulating properties of the additive and reduced grain size possibly result in poor charge transport.[34] The output characteristics of the optimal device at 295 K in Figure 4f are significantly improved compared to the pristine device in Figure 4e, which shows a weak gate modulation of the current. These observations further confirm the beneficial effect of PA on the electronic properties of (TEA)$_2$SnI$_4$ FETs and more details on the charge transport are discussed below. It is worth noting that the hysteresis directions of the output and transfer curves are opposite. Perovskite-based transistors exhibit gradually expanded hysteresis when the bias sweep rate changes in the presence of ion migration.[20] For this reason, the transfer characteristics were recorded by using pulse mode to eliminate this effect. Nevertheless, V_{DS} in the output characteristics is changed in sweep mode. The sweep range of the output curve is from 0 to −60 V and then back from −60 to 0 V. These are the typical measurement modes for perovskite transistors.[35] We assume that due to the sweeping mode, the polarization of the source and drain area occurs which results in clockwise hysteresis in the output characteristics. However, this aspect will be studied in more detail in the future. The corresponding output characteristics of the device with other PA concentrations are shown in Figure S6, Supporting Information. Photoelectron yield spectra were performed to analyze the electronic structure of pristine and optimized 0.5 vol% PA-based (TEA)$_2$SnI$_4$. As shown in Figure S7, Supporting Information, the valence-band maximum (VBM) values are determined to be 5.18 and 5.23 eV, respectively. This indicates that the PA additive has negligible impact on the charge injection barrier at Au/perovskite interface in the FET devices.[36]

In addition to higher mobilities, the FETs based on (TEA)$_2$SnI$_4$ with PA also exhibit reduced dual-sweep hysteresis. To quantitatively analyze the hysteresis for the FET devices operating at room temperature, the width of the hysteresis for V_g (ΔV) in the forward and backward direction is calculated at $|I_{ds}| = 10^{-7}$ A, which is around halfway between the on and off states.[37,38] The pristine devices demonstrate a large ΔV of 19 V, which decreases to 8 V at the optimized PA concentration of 0.5 vol%. The lowered hysteresis is attributed to the strong interaction between PA and precursors which passivates defects, increases the grain size, and inhibits ion migration in the film. We notice that the optimized device with 0.5 vol% PA additive still exhibits gate voltage-dependent hysteresis in the transfer characteristics. When positive (negative) ions drift toward (away from) the interface under a negative gate voltage, the accumulation of these mobile ions shields the applied gate field and reduces the concentration of holes in the accumulation layer of the FET. The larger negative V_g significantly increases the number of accumulated ions and strengthens the screening of the gate voltage.[20] At higher gate bias in the saturation region, we assume that all mobile ions are accumulated at the perovskite/dielectric interface. In this case, further

increasing the gate voltage has only negligible influence on the screening effect but increases the number of charge carriers, resulting in a lower hysteresis. The hysteresis in metal halide perovskite transistors is generally believed to originate from ion migration and interface traps. The hysteresis induced by mobile ions is strongly dependent on the presence of defects in the perovskite films.[14] The enlarged grain size is also beneficial for the device's performance due to the reduced grain boundaries which act as trap centers for charge carriers and pathways for ions in the perovskite film, as confirmed by our previous work.[16] Iodide vacancies are believed as main ionic defects in the solution-processed tin halide polycrystalline perovskite thin films due to their low formation energy during film processing.[39] In 2D (TEA)$_2$SnI$_4$ FETs, the spacer cation TEA is stable because of its large molecular size, so iodine anions are considered to be the dominant undesired mobile ions. The lateral mobile ions accumulate at the electrode/semiconductor interface in the channel and create a built-in electric field opposite to the externally applied V_{ds}, which seriously retards the in-plane charge carrier transport in the FET.[40] Due to the strong hydrogen and coordination bonding between PA and source materials, the density of defect-associated mobile ions is significantly suppressed accompanied by enlarged grain size, greatly improving charge transport, and reducing ion migration in the device during operation.

To further confirm the reduction of the defect density by PA treatment, we investigate the FET characteristics of pristine and PA-treated films at a low temperature of 100 K. Figure 4g shows the transfer characteristics of the pristine and optimized devices. The device with PA additive exhibits a high average μ_h of 2.3 cm^2 V^{-1} s^{-1} at 100 K. The devices with other PA concentrations (0.25, 0.75, and 1 vol% PA) expose also higher mobilities at low temperatures in comparison to 295 K (Figures S8 and S9, Supporting Information). The movement of ions is commonly significantly inhibited at low temperatures. As the temperature decreases to 100 K, all devices show a reduced hysteresis compared with 295 K. This suggests that the mobile ions significantly contribute to the FET hysteresis at 295 K since it is generally believed that ion migration is drastically inhibited at low temperatures. Nevertheless, even greatly suppressed, hysteresis can be still observed at 100 K. The residual hysteresis at 100 K can be attributed to traps at the dielectric/perovskite interface.[41] In addition, we also have calculated the interface trap densities (N_t) for devices operating at 100 K based on the SS values extracted from transfer curves in a forward direction. All devices show lower N_t values at 100 K than at 295 K, which are 5.8×10^{12}, 5.4×10^{12}, 2.7×10^{12}, 2.9×10^{12}, and 3.3×10^{12} cm^{-2} eV^{-1}, for the PA concentrations of 0, 0.25%, 0.5%, 0.75%, and 1%, respectively. The slightly increased interface trap densities (N_t) with higher PA concentration can be attributed to the moderately decreased grain size. It clearly shows that the N_t values are reduced with the PA concentration, further confirming that the strong hydrogen and coordination bonding between PA additive and precursor materials can effectively passivate the defects in the film and consequently improve the quality of the dielectric/perovskite interface. These results are in line with the drastically suppressed hysteresis in the output curves at 100 K. It should be pointed out that the output curve at 100 K shows a sublinear region at a small V_{ds},

**ADVANCED
SCIENCE NEWS**

www.advancedsciencenews.com

NANO · MICRO

small

www.small-journal.com
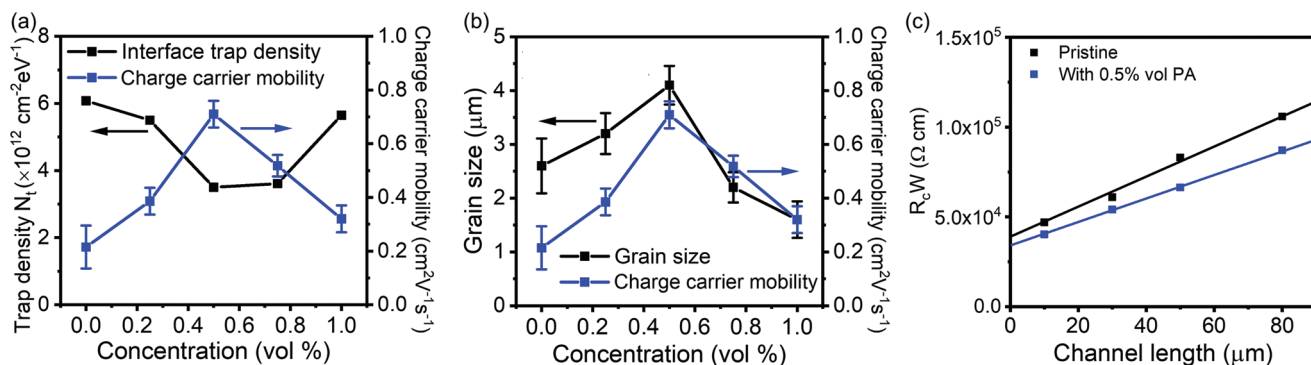
Figure 5. a) Correlation between interface trap density and charge carrier mobility and the corresponding b) correlation between grain size and charge carrier mobility for $(TEA)_2SnI_4$ FETs processed with different PA concentrations. c) Transmission-line method with R_cW as a function of channel length for pristine and optimal 0.5 vol% PA-based $(TEA)_2SnI_4$ perovskite FETs at 295 K. The contact resistance is determined from the y-axis intercept. The drain current was collected from the linear region at $V_g = -60$ V and $Vds = -6$ V.

which indicates contact resistance in the device. The effect of stationary ions cannot be neglected and they might contribute to the remaining contact resistance.[42,43] Through optimization of the contact resistance and/or the choice of optimized interlayers, some improvements in performance are expected to be achieved in the future.

We have then checked the correlation between the interface trap density and field-effect mobility for different PA concentrations at 295 K. **Figure 5**a reveals a clear correlation between trap density and mobility. The charge carrier mobility increases with lower interface trap density. On the contrary, the grain size is not closely linked to the charge carrier mobility as presented in Figure 5b, although both parameters exhibit similar trends with differences regarding the concentration of PA additive (Figure S10, Supporting Information). For example, the pristine film shows a grain size of around 2.6 µm, which is much larger than that of 1.6 µm in the film with the highest PA concentration of 1 vol%. However, the corresponding pristine device results in lower mobility. Additionally, $(TEA)_2SnI_4$ film without and 0.75 vol% PA exhibit similar grain sizes of around 2.6 and 2.2 µm, respectively. Nevertheless, the pristine $(TEA)_2SnI_4$ FET leads to a charge carrier mobility of 0.2 cm^2 V^{-1} s^{-1}. This is significantly lower than the mobility of 0.52 cm^2 V^{-1} s^{-1} for the device with 0.75 vol% PA. Therefore, the above discussion further confirms that the superior FET performance for $(TEA)_2SnI_4$ films with optimized PA concentration can be ascribed to two factors: defect passivation by suppressing Sn^{2+} oxidation and improved film morphology. Both of these effects synergistically result in improved charge carrier transport and inhibited ion migration.

We examined the influence of PA additives on contact resistance (R_CW) in the devices through the transmission line method (TLM).[16] As shown in Figure 5c, the contact resistance of 4.1×10^4 Ω cm for pristine devices is reduced to 3.5×10^4 Ω cm for the optimized 0.5 vol% PA-based FETs, which can be attributed to the decreased ionic defects by PA additive. The reduction of contact resistance is expected to improve the charge injection in FET devices. We have also investigated the bias stress stability for pristine and 0.5 vol% PA optimized $(TEA)_2SnI_4$ FETs. Figure S11, Supporting Information, shows the change in source-drain current under a constant bias of $V_g = V_{ds} = -60$ V for 500 s. The normalized source-drain cur-

rent ($I_{ds}(t)/I_{ds}(0)$) of the pristine $(TEA)_2SnI_4$ FET degrades significantly faster than the optimized device. For example, the decay time to reach 20% of the initial channel current is significantly increased from 56 to 185 s for the $(TEA)_2SnI_4$ FET with 0.5 vol% PA. The above results further confirm that the PA additive plays an efficient role in improving the device stability by effectively reducing defects and inhibiting ion migration.

The above results demonstrate the beneficial effects of additive engineering on film formation and FET operation. To further investigate the microscopic origin of the improved FET performance by the addition of PA, the film morphology and the potential distribution are examined using KPFM. KPFM correlates the nanoscale sample topography with the local surface potential. With all electrodes grounded, the contact potential difference (CPD) between the tip and sample gives rise to electrostatic forces (Figure S12a, Supporting Information).[44] Compensating these electrostatic forces by applying an external bias to the tip allows mapping the CPD variations. By establishing electrical connections for the source, drain, and gate electrode, we can put the FET into operating conditions and map the voltage distribution across the FET channel (Figure S12b, Supporting Information).[45] In order to avoid cross-talk to the KPFM signal from accentuated topographical features at the grain boundaries, heterodyne frequency-modulation KPFM is employed, which is deemed as the most reliable KPFM method.

First, the effect of the additive in terms of the localization and passivation of defects in the perovskite film is analyzed. Since the charge carrier transport occurs laterally along the channel, defects giving rise to deep trap states within the band gap would pose a hindrance to charge flow from source to drain, and therefore, negatively affecting the transistor performance. Moreover, these energy states are expected to cause band bending leading to a change in the measured CPD at the grain boundaries. In the first step, we conducted KPFM while keeping all three FET electrodes grounded in order to map the relative work functions of the gold electrodes, perovskite grain interiors, and grain boundaries. For both the pristine (Figure S13a, Supporting Information) and the 0.5 vol% PA modified device (Figure S13b, Supporting Information), a clear increase of the CPD at the grain boundaries with respect to the grain interiors

**ADVANCED
SCIENCE NEWS**

www.advancedsciencenews.com

NANO · MICRO

small

www.small-journal.com

is observed, which corresponds to energetic barriers for charge carrier movement (Figure S14, Supporting Information). A statistical analysis of ten random grain boundary CPD crests for both pictures reveals that the amount of voltage by which the CPD rises does not vary much between the two devices we measured, within experimental error (Figure S15, Supporting Information). However, we identify the superior structure in the sample treated with the PA additive in terms of a larger grain size distribution. Having larger grains along the channel path means that charge carriers migrate through less energetically unfavorable boundaries, which could explain the improved electronic characteristics of the optimized device when current flows across the channel.

To investigate the advantage of the optimized morphology with additive engineering in transistors, KPFM measurements on pristine and modified devices under operating conditions are conducted (**Figure 6**a,c). Specifically, a voltage of −9 V is applied on the drain, while keeping the source grounded, which corresponded to the output characteristics (Figure 4e,f) in the linear regime. Additionally, a voltage of −44 V is applied to the gate accordingly, which exceeded the threshold voltage from the transfer characteristics in Figure 4d and corresponded to a conductive channel. In the case of the pristine device, we notice from Figure 6a,b that the potential decreases from source to drain in a stepwise manner. The large voltage drops correspond to resistive barriers to charge carrier flow, which seem to be more pronounced on certain grain boundaries. Previous studies on perovskite solar cells and FETs have linked this behavior to a pronounced ion migration and accumulation inside the perovskite film.[46] The extent to which ionic accumulation obstructs electronic charge carrier flow can be explained through simple electrostatics. We propose that the high density of ionic defects in the pristine device leads to an accentuated ion drift due to the source-drain voltage and hence ionic accu-

mulation close to the electrode/semiconductor interfaces. This screens the applied electric field, thus inhibiting the charge flow required for device operation, as mentioned earlier. Since electrostatic fields are conservative, they relate to their corresponding electrical potential as $E = -\nabla V$, or in 1D as $E = -\dfrac{dV}{dx}$.

For the calculation of the electric field in the pristine device due to ion migration, the adjacent-averaging smoothing method is employed for the potential plot, in order to avoid artifacts in the electric field plot because of the differentiation. The resulting plot (Figure S16, Supporting Information) reveals an electric field close to the source electrode, which partially screens the source-drain voltage and lowers the field-effect mobility values for that transistor, further confirming that iodine anions are the dominant mobile ions.[42] On the other hand, the modified device exhibits a mostly continuous linear decline along the channel, implying that the current is only limited by the bulk lateral resistance of the perovskite film. These results once again confirm that the addition of 0.5 vol% PA to the perovskite precursor solution is beneficial for device operation, as the current flow is less governed by the energy barriers at the grain boundaries.

3. Conclusion

In this work, PA is incorporated as an additive into the precursor solution for the fabrication of high-performance 2D $(TEA)_2SnI_4$ FETs. We found that the PA additive effectively modifies the perovskite nucleation through the formation of hydrogen and coordination bonding. As a result, the $(TEA)_2SnI_4$ film with 0.5 vol% PA shows significantly suppressed Sn^{2+} oxidation, improved film morphology regarding the surface roughness and grain size, and increased crystallinity,
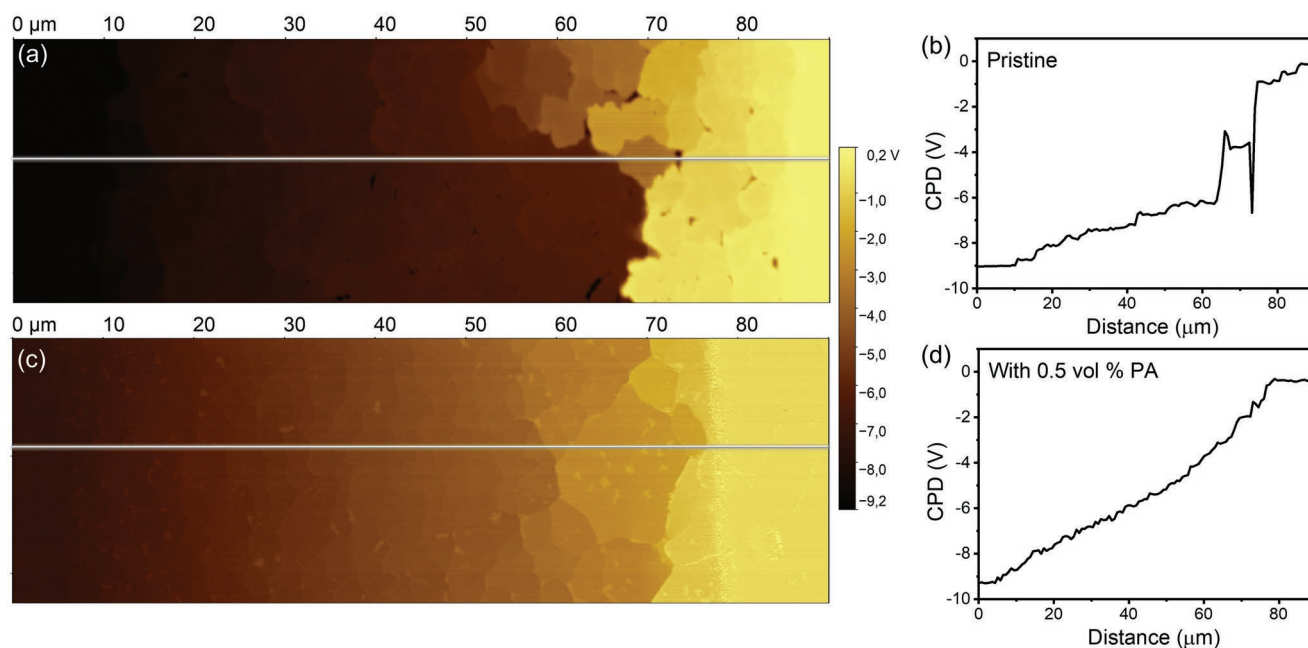
Figure 6. Potential maps and corresponding profiles of a,b) pristine and c,d) optimized FET measured with KPFM for $V_g = -44$ V and $V_{ds} = -9$ V.

**ADVANCED
SCIENCE NEWS**

www.advancedsciencenews.com

**NANO · MICRO
small**

www.small-journal.com

which synergistically augmented the FET performance with the highest mobility of 0.7 cm^2 V^{-1} s^{-1} at 295 K. This is a more than threefold enhancement compared to the control pristine device with 0.2 cm^2 V^{-1} s^{-1}. In addition, the ion-induced hysteresis in the transfer characteristics of the transistor is greatly inhibited and the corresponding mechanism is elucidated. Moreover, benefiting from the reduced defects and ion migration, the optimal device results in higher mobility of 2.3 cm^2 V^{-1} s^{-1} at 100 K. These results demonstrate the important role of additive engineering in modulating the film quality and electronic properties of 2D tin halide perovskite films. Our proposed strategy provides a facile solution for the realization of high-performance tin-based perovskite FETs.

4. Experimental Section

Materials: The organic cation TEA was synthesized according to a previously reported procedure.[16] Tin (II) iodide (99.999%), pentanoic acid solution (CAS Number: 109-52-4), and dimethylformamide (DMF) (anhydrous, 99.8%) were obtained from Sigma-Aldrich. All chemicals were used without further purification. Silicon wafers were purchased from Ossila Ltd.

Preparation of Precursor Solution: The precursor solution was obtained by mixing the precursor materials TEAI and SnI$_2$ at a molar ratio of 2:1 in DMF at 0.1 M concentration. For the PA-incorporated (TEA)$_2$SnI$_4$ precursor, 0.25, 0.5, 0.75, and 1 vol% of PA were added to the pristine (TEA)$_2$SnI$_4$ solution. The solution then was stirred overnight at 60 °C in a glovebox and cooled to room temperature before use. The as-prepared fresh precursor solution was filtered through a 0.2 µm PTFE filter before spin-coating.

Device Fabrication and Measurement: Heavily doped Si/SiO$_2$ wafers (1.5 × 2 cm) were used as the substrates and cleaned by sonicating in deionized water, acetone, and isopropyl, consecutively for 20 min each. After drying in nitrogen flow, the substrates were treated by UV/ozone for 20 min and then transferred into a glovebox for film deposition. This was followed by spin coating of the (TEA)$_2$SnI$_4$ perovskite semiconductor layer at 4000 rpm for 60 s and subsequent annealing at 100 °C for 10 min. The SiO$_2$ layer with a thickness of 300 nm was adopted as a dielectric layer. Finally, 80 nm gold source and drain electrodes were deposited by thermal evaporation through a shadow mask to construct 80 × 1000 µm (length × width) transistor channels. The device characterization was performed using a semiconductor parameter analyzer (Keithley 4200-SCS) in a vacuum (10^{-6} mbar) to avoid degradation. The transfer characteristics were recorded in pulse mode, and the output characteristics were measured in continuous mode. In the pulse mode, V_g was applied over a short impulse of 1 s. The temperature-dependent measurements were performed using a Desert Cryogenics low-temperature probe station. Mobility values of FETs were extracted with the following equation[47]

$$\mu = \frac{2L}{WC_i}\left(\frac{\partial\sqrt{I_{ds}}}{\partial V_g}\right)^2 \tag{2}$$

where L, W, and C_i are the channel length and width and the unit capacitance of the oxide dielectric, respectively.

Film Characterization: Solution NMR experiments were performed on a Bruker Avance 400 MHz spectrometer equipped with a BBI probehead with z-gradients. ^{1}H spectra were acquired using 32 scans and a recycle delay of 2 s. ^{119}Sn spectra were acquired using 256 scans and a recycle delay of 10 s. d$_6$-DMSO from the company Deutero GmbH was used as a solvent without further purification. All NMR experiments were performed under ambient conditions. The thin film morphology was characterized by a Bruker Dimension Icon FS AFM in tapping mode at room temperature. GIWAXS measurements were performed by means of a solid anode X-ray tube (Siemens Kristalloflex X-ray source, copper anode X-ray tube operated at 35 kV and 20 mA), Osmic confocal MaxFlux optics, X-ray beam with pinhole collimation, and a MAR345 image plate detector. All X-ray scattering measurements were measured under a vacuum (≈1 mbar) to reduce air scattering and prevent degradation of the sample. All data processing and analysis were performed using the software package Data squeeze. The thin film XRD patterns were recorded in the 2θ between 3° and 50°, with a step of 0.01° and a speed of 10 degrees per minute, using a Rigaku D/MAX 2600 V with Cu Kα (λ = 1.5406 Å) radiation. The interlayer distance was calculated by Bragg's law 2dsin θ = nλ, where λ is the X-ray wavelength, 1.5406 Å; θ is the Bragg angle of the diffraction peak, and n = 2, respectively. XPS measurements were conducted by using a PHI 5500 Multi-technique System with a base pressure of ≈10^{-9} torr. The X-ray radiation was Al Kα emission (1486.7 eV; take-off angle, 75°). Thin film absorption spectra were recorded on an Agilent UV–vis-NIR Cary-5000 spectrometer in transmission mode. Spectra were collected in the range of 300–800 nm. PL measurements were conducted using a high-resolution monochromator and hybrid photomultiplier detector (PMA Hybrid 40, PicoQuant GmbH). For the photoelectron yield measurements, the thin films were coated on conductive Si substrates. Then the valence band minimum was evaluated with a photoelectron spectrometer (AC-2S LC) by RIKEN KEIKI CO., LTD. The spectra were recorded for three samples to confirm the producibility of the measurement.

Kelvin Probe Force Microscopy Measurement: Mapping of the FET potential distribution was performed via KPFM, using an Asylum Research MFP3D Microscope (Oxford Instruments) together with a lock-in amplifier (HF2LI-MOD, Zurich Instruments). To avoid degradation of the perovskite film, the setup was placed in an argon-filled glovebox with an atmosphere containing less than 1 ppm O$_2$ and minimal humidity. The sample holder allowed to establish an electrical connection to the source, drain, and gate electrodes and ground them, or apply direct current voltages to them individually. Due to the limitation of the setup, the auxiliary output channels of the HF2 lock-in amplifier was used and applied a maximum source and drain voltage of −9 V. To generate the gate voltage, a −44 V battery stack was used with resonance frequency $\omega_0 \approx$ 75 Hz and spring constant ≈ 3 N m^{-1}. The scan rate of the measurements was 0.2 Hz. To obtain reliable data, frequency modulation KPFM was employed in the heterodyne configuration, whereby the cantilever was mechanically excited at its first resonance, ω_0, and electrically excited with an amplitude of 1 V at its second resonance minus the first ($\omega_1 - \omega_0$).[48] Frequency mixing between the mechanical motion and the periodic electrostatic force generated a sideband signal on the second resonance frequency, ω_1, that was used as an input signal for the KPFM feedback.

Supporting Information

Supporting Information is available from the Wiley Online Library or from the author.

Acknowledgements

Conflict of Interest

The authors declare no conflict of interest.

Author Contributions

S.A.L.W. conceived the idea and designed the experiment; T.M. and W.P. supervised the study; K.B. and F.H.H. performed KPFM measurement and analyzed the data with support from S.W.; C.H. conducted the solution NMR measurement and analyzed the data with support from R.G.; O.Y. and Z.L. carried out GIWAXS measurement and data analysis under the supervision of T.M.; S.F. synthesized the organic cations under the supervision of M.K.; P.W.M.B. coordinated the work. S.A.L.W. prepared the manuscript with support from all co-authors. All authors discussed the results and contributed to this work.

Data Availability Statement

The data that support the findings of this study are available from the corresponding author upon reasonable request.

[1] S. A. Veldhuis, P. P. Boix, N. Yantara, M. Li, T. C. Sum, N. Mathews, S. G. Mhaisalkar, *Adv. Mater.* **2016**, *28*, 6804.

[2] W. J. Yin, J. H. Yang, J. Kang, Y. Yan, S. H. Wei, *J. Mater. Chem. A* **2015**, *3*, 8926.

[3] X. Liu, D. Yu, X. Song, H. Zeng, *Small* **2018**, *14*, 1801460.

[4] Y. T. Li, L. Ding, J. Z. Li, J. Kang, D. H. Li, L. Ren, T. L. Ren, *ACS Cent. Sci.* **2019**, *5*, 1857.

[5] F. Haque, M. Mativenga, *Jpn. J. Appl. Phys.* **2020**, *59*, 081002.

[6] S. Ma, M. Cai, T. Cheng, X. Ding, X. Shi, A. Alsaedi, S. Dai, *Sci. China Mater.* **2018**, *61*, 1257.

[7] X. Li, J. M. Hoffman, M. G. Kanatzidis, *Chem. Rev.* **2021**, *121*, 2230.

[8] C. R. Kagan, D. B. Mitzi, C. D. Dimitrakopoulos, *Science* **1999**, *286*, 945.

[9] T. Matsushima, S. Hwang, A. S. Sandanayaka, C. Qin, S. Terakawa, T. Fujihara, C. Adachi, *Adv. Mater.* **2016**, *28*, 10275.

[10] C. Qin, F. Zhang, L. Qin, X. Liu, H. Ji, L. Li, Y. Hu, Z. Lou, *Adv. Electron. Mater.* **2021**, *7*, 2100384.

[11] A. Treglia, F. Ambrosio, S. Martani, G. Folpini, A. J. Barker, M. D. Albaqami, A. Petrozza, *Mater. Horiz.* **2022**, *9*, 1763.

[12] J. Wang, Z. Gao, J. Yang, M. Lv, H. Chen, D. J. Xue, S. Yang, *Adv. Energy Mater.* **2021**, *11*, 2102131.

[13] H. Zhu, A. Liu, H. Kim, J. Hong, J. Y. Go, Y. Y. Noh, *Chem. Mater.* **2020**, *33*, 1174.

[14] H. Zhu, A. Liu, K. I. Shim, J. Hong, J. W. Han, Y. Y. Noh, *Adv. Mater.* **2020**, *32*, 2002717.

[15] J. Kim, Y. S. Shiah, K. Sim, S. Iimura, K. Abe, M. Tsuji, H. Hosono, *Adv. Sci.* **2022**, *9*, 2104993.

[16] S. Wang, S. Frisch, H. Zhang, O. Yildiz, M. Mandal, N. Ugur, B. Jeong, C. Ramanan, D. Andrienko, H. I. Wang, M. Bonn, P. W. M. Blom, M. Kivala, W. Pisula, T. Marszalek, *Mater. Horiz.* **2022**, *9*, 2633.

[17] J. Y. Go, H. Zhu, Y. Reo, H. Kim, A. Liu, Y. Y. Noh, *ACS Appl. Mater. Interfaces* **2022**, *14*, 9363.

[18] Y. Reo, H. Zhu, J. Y. Go, K. In Shim, A. Liu, T. Zou, Y. Y. Noh, *Chem. Mater.* **2021**, *33*, 2498.

[19] F. Zhang, Q. Zhang, X. Liu, L. Qin, Y. Hu, Z. Lou, F. Teng, *J. Mater. Chem. A* **2021**, *9*, 22842.

[20] H. Zhu, A. Liu, H. L. Luque, H. Sun, D. Ji, Y. Y. Noh, *ACS Nano* **2019**, *13*, 3971.

[21] F. Zhang, Q. Zhang, X. Liu, Y. Hu, Z. Lou, Y. Hou, F. Teng, *ACS Appl. Mater. Interfaces* **2021**, *13*, 24272.

[22] M. A. Ruiz-Preciado, D. J. Kubicki, A. Hofstetter, L. McGovern, M. H. Futscher, A. Ummadisingu, M. Grätzel, *J. Am. Chem. Soc.* **2020**, *142*, 1645.

[23] Z. Zhu, X. Jiang, D. Yu, N. Yu, Z. Ning, Q. Mi, *ACS Energy Lett.* **2022**, *7*, 2079.

[24] D. Cui, X. Liu, T. Wu, X. Lin, X. Luo, Y. Wu, L. Han, *Adv. Funct. Mater.* **2021**, *31*, 2100931.

[25] X. Meng, Y. Li, Y. Qu, H. Chen, N. Jiang, M. Li, S. Yang, *Angew. Chem.* **2021**, *133*, 3737.

[26] M. E. Kayesh, K. Matsuishi, R. Kaneko, S. Kazaoui, J. J. Lee, T. Noda, A. Islam, *ACS Energy Lett.* **2018**, *4*, 278.

[27] M. Ulfa, P. Wang, J. Zhang, J. Liu, W. D. de Marcillac, L. Coolen, T. Pauporte, *ACS Appl. Mater. Interfaces* **2018**, *10*, 35118.

[28] F. Lédée, P. Audebert, G. Trippé-Allard, L. Galmiche, D. Garrot, J. Marrot, C. Quarti, *Mater. Horiz.* **2021**, *8*, 1547.

[29] H. Jia, H. Shi, R. Yu, H. Ma, Z. Wang, C. Zou, Z. A. Tan, *Small* **2022**, *18*, 2200036.

[30] Y. Gao, Z. Wei, P. Yoo, E. Shi, M. Zeller, C. Zhu, L. Dou, *J. Am. Chem. Soc.* **2019**, *141*, 15577.

[31] D. Hong, Y. Zhou, S. Wan, X. Hu, D. Xie, Y. Tian, *ACS Photonics* **2018**, *5*, 2034.

[32] H. Liang, F. Yuan, A. Johnston, C. Gao, H. Choubisa, Y. Gao, E. H. Sargent, *Adv. Sci.* **2020**, *7*, 1903213.

[33] F. Balestra, M. Benachir, J. Brini, G. Ghibaudo, *IEEE Trans. Electron Devices* **1990**, *37*, 2303.

[34] M. Abdel-Shakour, T. H. Chowdhury, K. Matsuishi, I. Bedja, Y. Moritomo, A. Islam, *Sol. RRL* **2021**, *5*, 2000606.

[35] S. P. Senanayak, M. Abdi-Jalebi, V. S. Kamboj, R. Carey, R. Shivanna, T. Tian, H. Sirringhaus, *Sci. Adv.* **2020**, *6*, eaaz4948.

[36] Z. Wang, F. Wang, B. Zhao, S. Qu, T. Hayat, A. Alsaedi, Z. A. Tan, *J. Phys. Chem. Lett.* **2020**, *11*, 1120.

[37] H. Zhu, A. Liu, K. I. Shim, H. Jung, T. Zou, Y. Reo, H. Kim, J. W. Han, Y. Chen, H. Y. Chu, J. H. Lim, H.-J. Kim, Y.-Y. Noh, *Nat. Commun.* **2022**, *13*, 1741.

[38] H. Wan, Y. Cao, L. W. Lo, J. Zhao, N. Sepulveda, C. Wang, *ACS Nano* **2020**, *14*, 10402.

[39] S. Zhao, L. Xiao, *Phys. Chem. Chem. Phys.* **2022**, *24*, 403.

[40] F. Jiang, J. Pothoof, F. Muckel, R. Giridharagopal, J. Wang, D. S. Ginger, *ACS Energy Lett.* **2020**, *6*, 100.

[41] I. Vladimirov, S. Müller, R. P. Baumann, T. Geßner, Z. Molla, S. Grigorian, R. T. Weitz, *Adv. Funct. Mater.* **2019**, *29*, 1807867.

[42] F. Liu, L. Wang, J. Wang, F. Wang, Y. Chen, S. Zhang, C. Jiang, *Adv. Funct. Mater.* **2021**, *31*, 2005662.

[43] X. J. She, C. Chen, G. Divitini, B. Zhao, Y. Li, J. Wang, H. Sirringhaus, *Nat. Electron.* **2020**, *3*, 694.

[44] A. Axt, I. M. Hermes, V. W. Bergmann, N. Tausendpfund, S. A. Weber, *Beilstein J. Nanotechnol.* **2018**, *9*, 1809.

[45] L. Bürgi, H. Sirringhaus, R. H. Friend, *Appl. Phys. Lett.* **2002**, *80*, 2913.

[46] S. A. Weber, I. M. Hermes, S. H. Turren-Cruz, C. Gort, V. W. Bergmann, L. Gilson, R. Berger, *Energy Environ. Sci.* **2018**, *11*, 2404.

[47] H. H. Choi, K. Cho, C. D. Frisbie, H. Sirringhaus, V. Podzorov, *Nat. Mater.* **2018**, *17*, 2.

[48] J. L. Garrett, J. N. Munday, *Nanotechnology* **2016**, *27*, 245705.
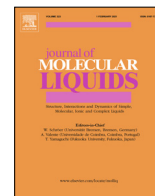
Stability and Self-Association of styryl hemicyanine dyes in water studied by ^{1}H NMR spectroscopy

Constantin Haese [a], Marcel Boecker [a], Aleksey Vasilev [b],*, Mihail Mondeshki [a],*

[a] Department Chemie, Johannes Gutenberg Universität, Duesbergweg 10-14, 55128 Mainz, Germany
[b] Department of Pharmaceutical and Applied Organic Chemistry, Faculty of Chemistry and Pharmacy, Sofia University "St. Kliment Ohridski", James Bourchier Blvd. 1, 1164 Sofia, Bulgaria

A B S T R A C T

The stability in water of five styryl hemicyanine dyes containing benzoxazole, benzothiazole, benzoselenazole and oxazolopyridne rings with different substituents at different pH values has been investigated. All compounds are stable at acidic and neutral pH, however, at basic pH the oxazole dyes undergo a ring opening reaction. The stability at basic pH is increased by substituting the benzooxazolium with oxazolopyridium function in the oxazole dyes **3a** and **3e**. ^{1}H and ^{1}H DOSY solution NMR spectroscopy prove that slight structural changes result in significant differences in the process of self-association. The association constants for dimerization have been determined by curve fitting the concentration dependent ^{1}H NMR spectra based on the isodesmic model. Van't Hoff analysis has been used to determine the thermodynamic parameters of the self-association process. The aggregation in water decreases with decreasing electronegativity and increasing the charge delocalization in the row (*E*)-2-(4-(dimethylamino)styryl)-3-methylbenzo[*d*]oxazol-3-ium iodide (**3a**), (*E*)-2-(4-(dimethylamino)styryl)-3-methylbenzo[*d*]thiazol-3-ium iodide (**3b**), (*E*)-2-(4-(dimethylamino)styryl)-3-methylbenzo[*1,3-d*]selenazol-3-ium iodide (**3d**) in the oxazole/thiazole/selenazole analogues. Introducing methyl groups in the benzothiazole ring enhances stacking effects in water due to stronger hydrophobic character. This derivative is characterized by the highest self-association constant (k_a = 299 L mol^{-1}) and the lowest Gibbs energy (ΔG = -14 kJ mol^{-1}). Substituting the phenyl with pyridyl ring in the oxazole analogue enhances significantly the solubility in water and thus decreases the self-association constant. Concentration dependent ^{1}H ROESY spectra provide information about the orientation of the molecules in the stack.

© 2022 Elsevier B.V. All rights reserved.

1. Introduction

Self-assembly of molecules, containing aromatic moieties, is often related to π-π interaction.[1,2] This non-covalent interaction has a significant contribution in supramolecular chemistry regarding the overall stability of DNA duplexes in water[3] and the biological recognition processes in the case of DNA, RNA and protein interactions[4] and labelling[5]. Other fields where π-π stacking plays an important role are host–guest complexation[6], self-assembly in aramids[7] and composite materials[8] as well as optical sensitizers in dye sensitized solar cells[9], organic light emitting diodes[10] and field effect transistors[11]. Numerous theoretical and experimental studies and reviews have been dedicated to explaining the origin, strength and orientational dependence of

the π-π interactions.[1,2,12] The model of Hunter and Sanders predicts that the interaction is mostly due to the electrostatic forces. [13] The authors postulate several rules to characterize the nature of the interaction, namely: (i) π- π repulsion dominates face-to-face π -stacked geometry, (ii) π -σ attraction dominates an edge-on geometry, (iii) π -σ attraction dominates in an offset π -stacked geometry, (iv) in case of polarized π systems, charge-charge interactions dominate.[13] These rules based on the benzene dimer model, however, do not take into account the effect of the substituents. Different studies dedicated to investigating this effect showed that both electrostatic[14] as well as dispersive forces[15,16] are involved. According to Mei et al electron-donating substituents increase binding in face-to-face π-π interaction.[17] Furthermore, increasing the difference in the electronic density of two aromatic systems (one possessing electron-donating and the other one accepting groups) favors face-to-face stacking.[18]

The polymethine (or cyanine) dyes are a large class of dyes including different families as mono-, tri-, penta- and heptamethine cyanines, styryl cyanines, squaraine and croconium dyes, and mero- and apocyanines. Styryl cyanine dyes are one of the most important families of functional polymethine dyes.[19] Almost all polymethine dyes are capable of spontaneous self-association to dimers as well as more complex aggregates[20] which defines their vast application. Some of the applications include media for optical recording in laser discs, as flexible dyes, laser dyes, as optical sensitizers in dye-sensitized solar cells (here the aggregation plays a major role) as well as dyes with non-linear optical properties.[19] Doubtless, bio-labelling and biomedicinal analysis are nowadays among the most promising and widely spread applications.[21] In the last mentioned field the self-association of the cyanine dyes is capable seriously to disturb or to modify the binding ability to different bio objects.

Understanding the structure dependent self-association of the investigated dyes in water would facilitate choosing the most appropriate representatives for further complexation with DNA and RNA as well as the relevant systems to model these interactions. Different spectroscopic methods are used for this purpose including UV–Vis, fluorescence and NMR spectroscopy.[22] The former two benefit from the high sensitivity to study low concentrations of the investigated solutions (up to 4 orders of magnitude lower than NMR). However, the NMR spectroscopy is capable of investigating the geometry of the stack (the relative orientation of the stacked molecules to one another) in addition to obtaining information about the thermodynamics of the process and the self-association constants. Different (mostly ^{1}H) NMR techniques are used to investigate the process of self-association including concentration and temperature dependent ^{1}H NMR spectra[23–25], diffusion ordered (DOSY) spectroscopy[26], relaxation[27] as well as NOE based experiments like NOESY and ROESY[24,28]. ^{1}H NMR spectra recorded as a function of concentration reveal differences in the chemical shifts of the dye molecules related to changes in the chemical environments influenced to a different degree by the ring current effect from the neighboring molecules at dilution.[23,25,26] Following these changes it is possible to determine the self-association constant and the number of the stacked molecules.[24] The same is valid recording concentration dependent ^{1}H DOSY NMR spectra, however, following the changes in the diffusion coefficient.[26] Temperature dependent ^{1}H NMR spectra provide information about the thermodynamic parameters of the self-association process related to Van't Hoff's analysis.[29] NOE related NMR experiments provide information about the spatial organization of stacked molecules based on dipolar contacts between protons in neighboring molecules. Both main variants NOESY and ROESY in solution as well as in the solid state and methods based on single quantum-double quantum correlation like BaBa (Back-to-Back)[30] in the solid state are widely applied to investigate stacking. [1]H relaxation studies provide further information about the dynamics of the dye molecules at different temperatures and concentrations.[31]

Here we present the synthesis of three novel and two known [32] styryl dyes (Scheme 1). Slight changes in the chemical structure result in significant differences in the stability in aqueous environment. Thiazole analogues are stable in the 4.5 – 9.2 pH range. The substitution of benzo[d]oxazolium end group of the chromophore with oxazolo[4,5-b]pyridinium functionality improves the stability at basic pHs due to better charge distribution. The styryl cyanine dyes form stacks in water due to π-π interactions. The self-association constants as well as the thermodynamic parameters of the process have been determined. The most hydrophobic derivative with two methyl functions in the benzothiazole ring is characterized by the highest self-association constant (k_a = 299 L mol^{-1}) and the lowest Gibbs energy (ΔG = -

14 kJ mol^{-1}). The average number of the molecules in the stack in the investigated concentration range has been calculated. The **3a** and **3c** analogues exist predominantly as dimers while the **3d** analogue is mostly in its monomeric form in water solutions. The **3b** and **3e** compounds exist in a both states (monomer : dimer ≈ 1 : 1). ^{1}H ROESY NMR experiments allow studying the organization in the stack.

2. Experimental

2.1. General

All solvents were HPLC grade or anhydrous where necessary. Fresh deuterated solvents were used for preparing the NMR samples. The chemical reactions were conducted under argon atmosphere. Mass spectrum acquisitions were conducted on an Advion expression compact mass spectrometer (CMS) with atmospheric pressure chemical ionization (APCI) at high temperature and low fragmentation regime. All spectra were acquired in the positive ion reflection mode, *m/z* range from 10 to 1000 *m/z*, and acquisition speed 10000 *m/z* units s^{-1}. The obtained spectra were analyzed by using Advion CheMS Express software version 5.1.0.2. Field desorption (FD) MS spectra were recorded on a Thermo Scientific Double Focusing Sector Field (DFS) Mass Spectrometer operated by Thermo Xcalibur 2.2 SP1.48 acquisition and interpretation software. The spectra were recorded in FD/LIFDI/FI positive mode, *m/z* from 100 to 1000. The melting points were measured on a Melting point meter Kruss, M5000, Germany. DC Aluminiumfolien, Kieselgelschicht, ALUGRAM SIL G UV254, 4x8 cm, Machery-Nagel TLC plates were used for first check of the purity of the target quaternary compounds in 5 mL eluent system methanol : dichloromethane = 0.5 : 4.5 mL. The purification of the target compounds was performed by fractional recrystallization or by column chromatography on Kieselgel 60, 0,063–0,2 mm, Machery-Nagel in eluent system methanol/dichloromethane with gradually increasing polarity.

2.2. Synthesis

2-methylbenzooxazole (**1a**), 2-Methylbenzothiazole (**1b**), 2,5,6-thrimethylbenzothiazole (**1c**) and 2-methylbenzoselenazole (**1d**) were purchased from TCI Europe, Co., Ltd and used without further treatment. 2-Methyloxazolo[4,5-b]pyridine (**1e**) was prepared by a known procedure.[33] **1e**: ^{1}H NMR (400.31 MHz, DMSO d_6, δ ppm): δ 2.67 (3H, s, CH$_3$), 7.38 (1H, dd, *J* = 8.1 Hz, CH), 8.10 (1H, d, *J* = 8.1 Hz, CH), 8.46 (1H, d, *J* = 6.3 Hz, CH). ^{1}H NMR (400.31 MHz, CDCl$_3$, δ ppm): δ 2.61 (3H, s, CH$_3$), 7.14 (1H, dd, *J* = 8.3 Hz, CH), 7.66 (1H, d, *J* = 8.3 Hz, CH), 8.40 (1H, d, *J* = 6.3 Hz, CH). The quaternization of all 2-methyl substituted N-heterocycles except **1e** was performed in anhydrous acetone solution at room temperature according the literature.[34,35] The target compounds were synthesized by a modified reaction procedure.[32,36]

Quaternization of 2-methyloxazolo[4,5-b]pyridine (**1e**) to prepare 2,4-dimethyloxazolo[4,5-b]pyridin-4-ium iodide **2e**

- Procedure A

1 mmol of intermediate **1e** was dissolved in 20 mL anhydrous acetone and 1.1 mmol methyl iodide was added. The reaction mixture was stirred vigorously at room temperature for 72 h under argon, in a dark. The formed precipitate was suction filtered and dried in a vacuum oven (45 °C) and stored in a desiccator. The ^{1}H NMR spectrum of the raw reaction product is demonstrated in the *SI* part. **2e**: Yield: 61%. ^{1}H NMR (400.31 MHz, DMSO d_6, δ
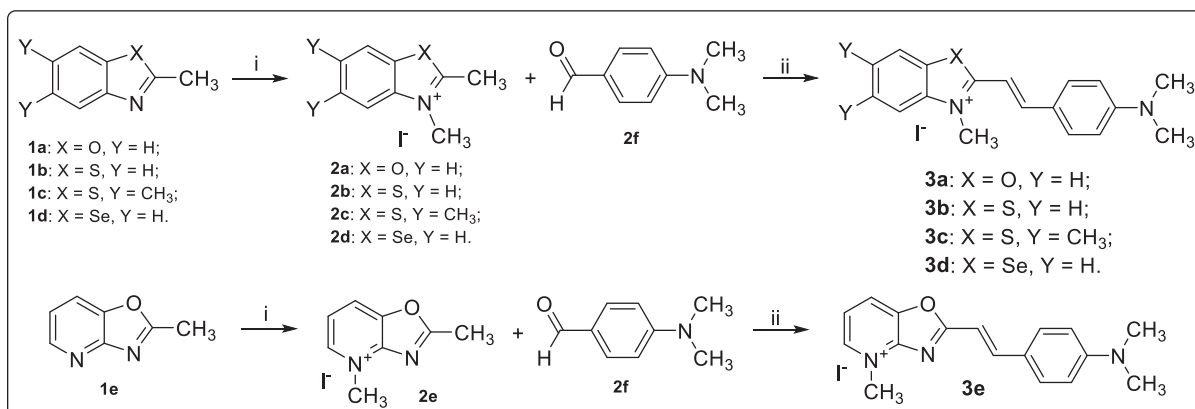
Scheme 1. Synthesis of dyes **3a-3e**. *Reactants, conditions, yields*: **i)** **1a** − **1e**, methyl iodide, acetone, 48 h r.t. Yields: **2a**: 68%, **2b**: 92%, **2c**: 95%, **2d**: 91%, **2e**: 77%. **ii)** **2a** − **2e**, **2f**, ethanol (acetic anhydride for **3a**), cat. piperidine, reflux 1 h, precipitation from ethanol : ethyl acetate 1:3. Yields: **3a** (47%); **3b** (73%); **3c** (79%); **3d** (74%); **3e** (62%).

ppm): δ 2.19 (3H, s, CH$_3$), 4.11 (3H, s, CH$_3$), 7.82 (1H, brs, CH), 7.97 (1H, brs, CH), 8.51 (1H, brs, CH).

- Procedure B

1 mmol of **1e** was dissolved in 20 mL anhydrous THF and 1.1 mmol methyl iodide was added. The reaction mixture was stirred vigorously at room temperature for 72 h under argon, in a dark. The formed precipitate was suction filtered and dried in a vacuum oven and stored in a desiccator. Yield: 78%. The ^{1}H NMR spectrum of the crude reaction product is showed in the *SI* part. **2e**: ^{1}H NMR (400.31 MHz, CDCl$_3$, δ ppm): δ 2.89 (3H, s, CH$_3$), 4.63 (3H, s, CH$_3$), 8.09 (1H, dd, *J* = 8.1 Hz, *J* = 6.3 Hz, CH), 8.66 (1H, d, *J* = 8.1 Hz, CH), 9.52 (1H, d, *J* = 6.3 Hz, CH).

- Procedure C

1 mmol of **1e** was dissolved in 20 mL anhydrous THF and 1.1 mmol methyl iodide was added. The reaction mixture was heated at 100 °C in a sealed tube and stirred vigorously for 4 h under argon, in a dark. After cooling the formed precipitate was suction filtered and dried in a vacuum oven at the before mentioned conditions and stored in a desiccator. Yield: 80%. The ^{1}H NMR spectrum of the raw reaction product is demonstrated in the *SI* part. **2e**: ^{1}H NMR (400.31 MHz, CDCl$_3$, δ ppm): δ 2.87 (3H, s, CH$_3$), 4.62 (3H, s, CH$_3$), 8.08 (1H, dd, *J* = 8.3 Hz, *J* = 6.1 Hz, CH), 8.71 (1H, d, *J* = 8.3 Hz, CH), 9.47 (1H, d, *J* = 6.1 Hz, CH).

2.3. Synthesis of dyes **3a-3e**

1 mmol of the quaternary onium salt 2,3-dimethylbenzo[*d*]oxazol-3-ium iodide (**2a**) or 2,3-dimethylbenzo[*d*]thiazol-3-ium iodide (**2b**), or 2,3,5,6-tetramethylbenzo[*d*]thiazol-3-ium iodide (**2c**), or 2,3-dimethylbenzo[*1,3-d*]selenazol-3-ium iodide (**2d**), or 2,4-dimethyloxazolo[*4,5-b*]pyridin-4-ium iodide (**2e**) and 1.2 mmol p-dimethylamino benzaldehyde (**2f**) were mixed and finely ground in a mortar. The mixture was transferred quantitatively in a 50 mL round bottom flask equipped with a reflux condenser and an electromagnetic stirrer and 10 mL ethanol (acetic anhydride instead of ethanol for dye (**3a**). Two drops of piperidine were added in every case. The mixture was refluxed and stirred vigorously for 1 h. Addition of 20 mL ethyl acetate to the hot reaction solution afforded precipitation of the product. After cooling the red residues were suction filtered and consecutively washed with 10 mL ethanol, 20 mL diethyl ether and 20 mL ethyl acetate. The analytical samples were obtained by fractional recrystallization from ethanol or

flash column chromatography with mixture of dichloromethane : methanol = 4.5 : 0.5 as eluent.

<u>(*E*)-2-(4-(dimethylamino)styryl)-3-methylbenzo[*d*]oxazol-3-ium iodide (**3a**):</u> Red powder; Yield: 47%; Mp = 221.0–221.5 °C; ^{1}H NMR (400.31 MHz, DMSO d_6, δ ppm): 3.11 (6H, s, CH$_3$), 4.07 (3H, s, CH$_3$), 6.85 (2H, d, *J* = 8.7 Hz, CH), 7.35 (1H, d, *J* = 15.3 Hz, CH), 7.64 – 7.67 (2H, m, CH), 7.91 (2H, d, *J* = 8.7 Hz, CH), 7.94 – 7.96 (2H, m, CH), 8.23 (1H, d, *J* = 15.3 Hz, CH); ^{13}C NMR (100.67 MHz, DMSO d_6, δ ppm): 32.1, 97.0, 112.3, 112.5, 113.9, 121.5, 127.5, 128.1, 131.9, 133.5, 147.3, 151.5, 154.3, 163.5. ^{15}N NMR (40.56 MHz, DMSO d_6, δ ppm): −229.3, −312.5.

<u>(*E*)-2-(4-(dimethylamino)styryl)-3-methylbenzo[*d*]thiazol-3-ium iodide (**3b**):</u> Violet needles; Mp = 250.6 °C; ^{1}H NMR (400.31 MHz, DMSO d_6, δ ppm): δ 3.11 (6H, s, CH$_3$), 4.22 (3H, s, CH$_3$), 6.84 (2H, d, *J* = 8.5 Hz, CH), 7.62 (1H, d, *J* = 15.4 Hz, CH), 7.68 (1H, dd, *J* = 7.8 Hz, *J* = 7.1 Hz, CH), 7.78 (1H, dd, *J* = 7.8 Hz, *J* = 7.1 Hz, CH), 7.91 (2H, d, *J* = 8.5 Hz, CH), 8.06 (1H, d, *J* = 15.4 Hz, CH), 8.09 (1H, d, *J* = 8.1 Hz, CH), 8.29 (1H, d, *J* = 8.1 Hz, CH); ^{13}C NMR (100.67 MHz, DMSO d_6, δ ppm): 36.1, 106.7, 112.4, 116.4, 121.9, 124.2, 127.3, 127.9, 129.3, 133.3, 142.4, 150.6, 154.0, 171.8. ^{15}N NMR (40.56 MHz, DMSO d_6, δ ppm): −208.3, −311.7. APCI-MS (*m/z*): Calc. 281.11, Found 281.10; FD-MS (*m/z*): Calc. 295.13, Found 295.23.

<u>(*E*)-2-(4-(dimethylamino)styryl)-3,5,6-trimethylbenzo[*d*]thiazol-3-ium iodide (**3c**):</u> Violet-greenish powder; Mp = 275.0–275.3 °C; ^{1}H NMR (400.31 MHz, DMSO d_6, δ ppm): δ 2.40 (3H, s, CH$_3$), 2.44 (3H, s, CH$_3$), 3.10 (6H, s, CH$_3$), 4.20 (3H, s, CH$_3$), 6.83 (2H, d, *J* = 8.7 Hz, CH), 7.60 (1H, d, *J* = 15.4 Hz, CH), 7.88 (2H, d, *J* = 8.7 Hz, CH), 7.93 (1H, s, CH), 8.01 (1H, d, *J* = 15.4 Hz, CH), 8.04 (1H, s, CH) ; ^{13}C NMR (100.67 MHz, DMSO d_6, δ ppm): 20.13, 20.40, 36.00, 106.95, 112.38, 116.51, 121.95, 123.75, 124.55, 132.97, 137.73, 139.06, 140.90, 149.58, 153.73, 170.64. ^{15}N NMR (40.56 MHz, DMSO d_6, δ ppm): −209.4, −311.7. APCI-MS (*m/z*): Calc. 309.14, Found 309.2.

<u>(*E*)-2-(4-(dimethylamino)styryl)-3-methylbenzo[*1,3-d*]selenazol-3-ium iodide (**3d**):</u> Violet powder; Mp = 257.1–257.6 °C; ^{1}H NMR (400.31 MHz, DMSO d_6, δ ppm): δ 3.11 (6H, s, CH$_3$), 4.19 (3H, s, CH$_3$), 6.84 (2H, d, *J* = 8.9 Hz, CH), 7.60 (1H, dd, *J* = 8.1 Hz, *J* = 7.2 Hz, CH), 7.66 (1H, d, *J* = 15.0 Hz, CH), 7.73 (1H, dd, *J* = 8.1 Hz, *J* = 7.2 Hz, CH), 7.93 (2H, d, *J* = 8.9 Hz, CH), 8.04 (1H, d, *J* = 8.1 Hz, CH), 8.11 (1H, d, *J* = 15.0 Hz, CH), 8.33 (1H, d, *J* = 8.1 Hz, CH); ^{13}C NMR (100.67 MHz, DMSO d_6, δ ppm): 37.17, 109.75, 112.46, 117.87, 122.35, 127.28, 127.65, 128.49, 128.96, 133.47, 143.82, 152.62, 154.03, 179.82. ^{15}N NMR (40.56 MHz,

DMSO d_6, δ ppm): − 205.3, − 310.6. APCI-MS (*m/z*): Calc. 329.06, Found 329.10; FD-MS (*m/z*): Calc. 343.07, Found 343.26.

(*E*)-2-(4-(dimethylamino)styryl)-4-methyloxazolo[*4,5-b*] pyridin-4-ium iodide (**3e**): Red needles; Mp = 246.0–246.4 °C; ^{1}H NMR (400.31 MHz, DMSO d_6, δ ppm): δ 3.07 (6H, s, CH_3), 4.35 (3H, s, CH_3), 6.79 (2H, d, *J* = 8.7 Hz, CH), 7.19 (1H, d, *J* = 15.8 Hz, CH), 7.78 (2H, d, *J* = 8.7 Hz, CH), 7.75–7.85 (2H, m, CH), 8.14 (1H, d, *J* = 15.8 Hz, CH), 8.68 (1H, d, *J* = 7.8 Hz, CH), 8.73 (1H, d, *J* = 6.2 Hz, CH); ^{13}C NMR (100.67 MHz, DMSO d_6, δ ppm): 41.80, 104.59, 112.37, 120.55, 121.78, 124.78, 132.32, 139.79, 146.64, 149.40, 152.28, 153.50, 171.73. ^{15}N NMR (40.56 MHz, DMSO d_6, δ ppm): −204.3, −316.5, −241.5. APCI-MS (*m/z*): Calc. 266.13, Found 265.09; FD-MS (*m/z*): Calc. 280.14, Found 280.24.

2.4. NMR spectroscopy

All NMR spectra were recorded on a Bruker Avance DRX 400 NMR spectrometer (Bruker Biospin GmbH, Rheinstetten, Germany) at a ^{1}H frequency of 400.31 MHz, ^{13}C frequency of 100.66 MHz and ^{15}N frequency of 40.56 MHz using a commercial Bruker 5 mm inverse 2 channel probe head equipped with z-gradients. The structure elucidation was performed in DMSO d_6 due to the very good solubility of all dyes. For all ^{1}H spectra 32 scans were averaged using 2 s recycle delay. All ^{1}H COSY (correlation spectroscopy) NMR spectra were measured using pulsed field gradients for coherence selection. The experiments were conducted recording 1024 data points in the direct dimension with 512 increments in the indirect dimension and 1 scan per increment with 2 sec recycle delay. The ^{13}C spectra were recorded with power gated decoupling averaging 1 k scans. All ^{1}H–^{13}C HSQC (heteronuclear single quantum correlation) NMR experiments were recorded using the *hsqcetgp* sequence with 256 increments, 32 transients, a 2 s recycle delay, sweep widths of 20 and 180 ppm and offsets of 5.5 and 80 ppm for the ^{1}H and ^{13}C dimension resp. The sequence was optimized for 145 Hz couplings. The data was processed using qsine windows functions in both dimensions of total 1024 (F2) and 512 (F1) points. The ^{1}H–^{13}C HMBC (heteronuclear multiple bond correlation) NMR spectra were recorded using the *hmbcgplpndqf* pulse sequence with 256 increments, 32 transients, 2 s recycle delay, sweep widths of 20 and 240 ppm and offsets of 5.5 and 110 ppm for the ^{1}H and ^{13}C dimensions resp. The sequence was optimized for couplings of 10 Hz, which is a common compromise for long range [1]H–[13]C couplings. The data was processed using sine windows functions in both dimensions of total 1024 (F2) and 512 (F1) points. ^{1}H–^{15}N HMBC experiments were measured with 256 increments, 32 transients, 2 s recycle delay, sweep widths of 12 and 500 ppm and offsets of 5.5 and 180 ppm for the ^{1}H and ^{15}N dimensions resp. The sequence was optimized for couplings of 6 Hz, which is a common compromise for long range [1]H–[15]N couplings. The data was processed using sine windows functions in both dimensions of total 1024 (F2) and 512 (F1) points.

The ^{1}H NMR dilution spectra studying aggregation as well as all the experiments related to complex formation and dynamic studies were measured in D_2O at pH of 7.2. The pH was adjusted using phosphate buffer prepared from 137 mg KD_2PO_4, 175 mg K_2DPO_4 and 10 mL D_2O. Prior to the experiments, all samples were sonicated for 5 min. The ^{1}H NMR dilution experiments were measured averaging 32 scans with 2 s recycle delay.

The ^{1}H ROESY (rotating frame Overhauser enhancement spectroscopy) spectra were conducted recording 1024 data points in the direct dimension with 512 increments in the indirect dimension and 16 scan per increment with 2 s recycle delay. The spin lock pulse duration was set to 200 ms.

Stimulated echo sequence with bipolar gradient pulses and a longitudinal eddy current delay was used for the ^{1}H diffusion ordered spectroscopy (DOSY) experiments. The gradient strength was incremented in 16 steps from 2 % to 95 % of the maximum gradient strength. The diffusion time and the gradient pulse length for all dyes were 100 ms and 2.8 ms with 2 s recycle delay, respectively. After Fourier transformation and baseline correction, the diffusion dimension of the 2D DOSY spectra was processed using the Topspin 1.3 software package (2007, patchlevel 8, Bruker Biospin GmbH, Rheinstetten, Germany). The diffusion analysis was performed using the Topspin T_1/T_2 relaxation package.

All ^{1}H and ^{13}C NMR spectra were referenced using the solvent lock (^{2}H) signal in accordance with the IUPAC recommended secondary referencing methods.[37] All ^{15}N spectra were referenced to external nitromethane + 10% $CDCl_3$ at 0 ppm.

3. Results and discussion

Synthesis, electronic effects related to the structure and chemical stability

The key intermediate 2-methyloxazolo[*4,5-b*]pyridine (**1e**) (Scheme 1) was synthesized by a known procedure.[33] The starting quaternary compounds **2a** − **2e** were freshly synthesized due to their hygroscopic properties and low chemical stability. The quaternization reaction of heterocyclic compounds **1a** − **1d** was performed in mild conditions in anhydrous acetone at room temperature according to the literature.[34,35] The quaternization of 2-methyloxazolo[*4,5-b*]pyridine (**1e**) was performed using three different procedures. The standard procedure in acetone at room temperature afforded only a moderate reaction yield. Using anhydrous tetrahydrofuran as medium at high temperature and pressure instead of acetone increased the yields (see experimental part). The synthesis of the target dyes we did by a modified reaction procedure.[32,36] The modification consists of addition of twenty percent molar excess of the p-dimethylamino-benzaldehyde to achieve a maximum degree of conversion with subsequent dilution with double excess of ethyl acetate. The proposed conditions facilitate the purification of the target dyes **3a** − **3e** and afford chromatographically (TLC) pure compounds. Further silica flash column chromatography (dichloromethane : methanol = 4.5 : 0.5) with subsequent recrystallization from ethanol/dichloromethane were used to obtain the analytical samples.

The synthesis of the dyes **3a** and **3b** has been previously reported.[32] The analogues **3c** and **3d** to the best of our knowledge are novel. We have earlier described a procedure for the synthesis and quaternization of 4-methyl-2-methylthio-oxazolo[*4,5-b*]pyridin-4-ium methyl iodide.[38] In the case of 2-mercapto-oxazolo[*4,5-b*]pyridine as a starting compound we proved that the quaternization reaction proceeds selectively to the pyridine nitrogen atom[38] because of the mesomeric effect of the S-atom from the mercapto group on the second position in the oxazolo [*4,5-b*]pyridinium core. The significant batochromic shift (almost 90 nm) of the visible absorption band of the oxazolopyridine dyes in comparison with the benzooxazole analog (Oxazole yellow) is an unambiguous proof for the proposed mechanism.[38] In a Japanese patent from 2006 Nakamura et al proposed that the quaternization of 2-methyloxazolo[4,5-b]pyridine with methyl iodide in boiling acetone results in attachment of the methyl group to the nitrogen from the pyridine core, however, with no clear evidence for the proposed mechanism.[39] In the current contribution, we prove spectroscopically this result with the reaction being conducted at ambient conditions.

Our previous studies revealed also that the dyes with oxazolopyridine end groups could be successfully used for fluorescence labelling of nucleic acids[40] and visualization of mitochondria.[41] This provoked the quest for novel analogues with good solubility in water and high chemical stability. The

structures of the synthesized dyes (*Table S1*) with the respective chemical shifts *(Tables S2, S3 and S4)* as well as a detailed description of the structure elucidation are presented in the *Supporting Information*.

3.1. Stability at different pHs

It is known that oxazoles and their derivatives undergo ring opening reactions under basic conditions[42] as well as hydrolytic ring opening reactions in acidic media.[43] Thiazoles and their derivatives are more stable under the same conditions compared to their oxazole analogues.[43] The nucleophilic attack of the base occurs at the quaternary carbon atom, which is flanked by oxygen and nitrogen to form an imine as intermediate and an ester as main product.[43]

The stability of the oxazole dye compounds **3a** and **3e** at acidic (pH = 4.5) and basic (pH = 9.2) conditions (Table S2) was further investigated recording pH-dependent ^{1}H NMR spectra at 299 K. The spectra were recorded directly after addition of the buffer, in two days and in a week. For the **3e** derivative the spectra are presented in Fig. 1.

Clearly, the **3e** analogue is stable over a period of one week under acidic conditions. The same is valid also for the **3a** analogue. The reason is related to the mechanism of the acidic ring opening reaction which includes the protonation of the nitrogen atom in the oxazole.[43] In this case, however, this position is already methylated and a protonation cannot occur for both **3a** and **3e** analogues.

Contrary to the stability under acidic conditions, both analogues undergo ring opening at basic pH. For the **3a** analogue the reaction takes place so fast, that upon addition of the basic buffer system the color disappears immediately. In the case of **3e** the reaction also takes place, however, significantly slower. On addition of a basic buffer system the ^{1}H NMR spectrum of the **3e** compound reveals the formation of a small amount of a second species (mechanism proposed by Holmes et al.[43] in Fig. 2a). The ^{1}H resonances related to this species grow further in a week. The change in the color of an acidic and a basic solution of **3e** after one week is presented in *Figure S1*. The loss of color is related to the decrease in the length of the conjugated aromatic system which shifts the absorption in the UV spectral region (Fig. 2b).

The kinetics of the basic ring opening reaction in the case of the **3e** analogue was investigated by ^{1}H NMR spectroscopy; all experiments being recorded with the same number of scans and receiver gain. The time between the consecutive experiments was

Fig. 1. ^{1}H NMR spectra of the compound **3e** at pH 9.2 after 0, 2 and 7 days and at pH 4.5 at 0, 2 and 7 days.

Δt = 600 s. To determine the rate constant of the hydrolysis the equation for a kinetic process of pseudo first order[53,54] is used:

$$A(t) = A_0 e^{-kt} \tag{1}$$

In this equation, $A(t)$ is the observed intensity for the peak of proton H-5' at the time t, A_0 is the intensity of the peak of proton H-5' at the beginning of the experiment, k is the rate constant and t is the time. The change in the intensity of the resonance for H-5' versus the time is presented in *Figure S2*. The rate constant for the hydrolysis of **3e** was determined to be $(7.9 \pm 0.3) \ 10^{-3}$s.

3.2. Self-association constant

Many aromatic molecules like benzene, naphthalene and acenes[44] as well as cyanine dyes[45] are known to form dimers at high concentrations in solution due to π-π-stacking[24,25,28]. The intermolecular distances in such dimers are in the range 0.3–0.4 nm.[24] The aromatic ^{1}H and ^{13}C chemical shifts of the nuclear spins in a conjugated aromatic system are influenced by the ring currents of the neighboring aromatic system in the dimer. This influence is expressed in a high field shift of the resp. resonances. Diluting the solution leads to destabilization of the dimers and formation of monomeric species. In systems characterized by a monomer–dimer (oligomer) equilibrium, the observed NMR shifts are often an average of the shifts of the monomer and the dimer (oligomer) due to chemical exchange in the fast tumbling regime. The change in the chemical shift at various concentrations gives information about the self-association (aggregation) of the investigated dye molecules. The isotropic shifts can be determined only for very dilute samples, which has the disadvantage of long measuring times. It is also possible to obtain values for the shifts of the monomeric form by a simplex algorithm, varying the chemical shifts until a minimum in the fit accuracy is reached. The procedure is described in detail in the *Supporting Information*.

The dissociation of an oligomer (M_n) consisting of n stacked molecules to a product with one monomeric unit less (M_{n-1}) is an equilibrium process:

$$M_n \overset{k}{\rightleftharpoons} M_{n-1} + M \tag{2}$$

with rate constants k and k^{-1} for the forward and reverse process respectively. In such equilibrium processes, both starting (M_n) and end product/s (M_{n-1} and M) are present in concentration, which remains unchanged in time.

If cyanine dyes form dimers (in the concentration range of 2.6 – 4.9 mmol), the equation of an equilibrium process related to the dissociation of a dimer D to two monomers M is:

$$D \overset{k}{\rightleftharpoons} 2M \tag{3}$$

Assigning with c_2 the concentration of the dimer and with c_1 the one of the monomer dye molecule, the following equation is valid [44]:

$$K_d = \frac{c_2}{c_1^2} \tag{4}$$

where K_d is the self-association (aggregation) constant.

Models like the isodesmic model[44] or the semi-isodesmic model[46] could be used to describe extended π-π-stacked dye molecule systems. According to the isodesmic model (described mathematically in detail in *Supporting Information*) every monomer addition to the growing stack is governed by a single equilibrium constant K[22,44]. The latter is related to the observed changes in the chemical shift upon dilution.

Fig. 3a presents the concentration dependent ^{1}H NMR spectra of **3e** in a concentration range 2.6–4.9 mmol L^{-1}. At lower concentrations all proton resonances shift downfield which indicates a shift
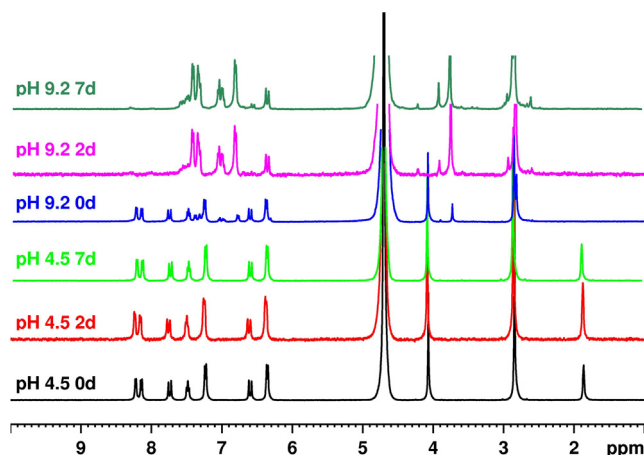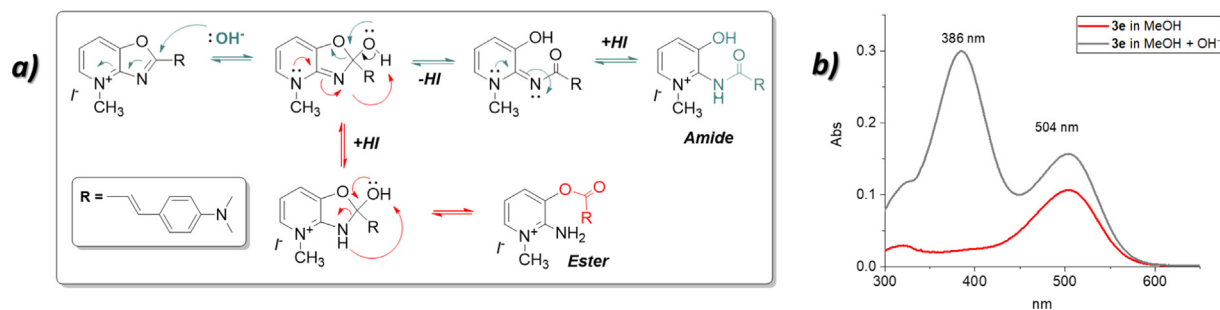
Fig. 2. Fig. 2a Proposed mechanism for the basic hydrolysis of **3e**; Fig. 2b. UV–Vis spectrum of the degradation products. The appearance of the strong absorption at 386 nm is related to the decrease of the length of the conjugated aromatic system because of the hydrolysis at basic pH.
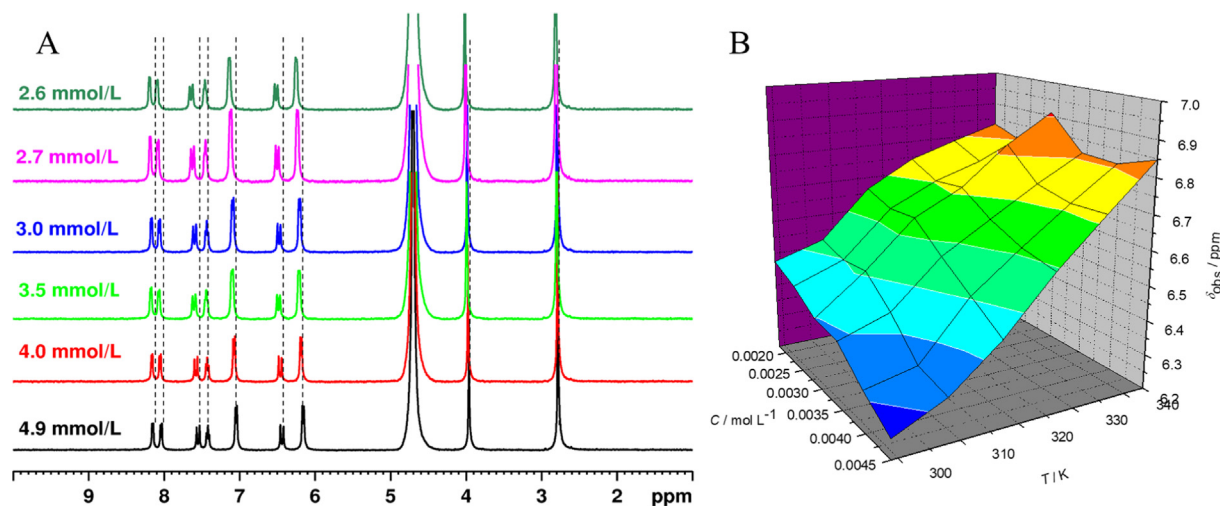
Fig. 3. *A*. Concentration dependent ^{1}H NMR spectra of **3e** from $2.6 - 4.9$ mmol L^{-1} at 299 K in D$_2$O phosphate-buffer. *B*. Change in the chemical shift for the proton H-2́ of **3e** as a function of temperature and concentration in D$_2$O phosphate-buffer.

of the equilibrium to the monomeric form. The same trend is observed increasing the temperature. The temperature dependent spectra (in the range 299–344 K) for each concentration show a deviation from the ideal increase in the chemical shift above 324 K. This behavior is exemplary presented in *Figure S3* for the proton H-2́ of the **3e** analogue. Clearly, the temperature dependent shifts develop exponentially only at the lowest measured concentrations. Increasing the concentration, a temperature dependent maximum in the shift is observed at a concentration of 3.0 mmol L^{-1}. Further temperature increase leads to weaker hydrogen-bonding interactions with the solvent molecules. Such changes may have a significant influence on the shielding parameters.[47]

Varying the values for the δ_m (isotropic shift for the monomer) and δ_d (isotropic shift for the dimer) (Table 1) in the equation:

$$\delta_{obs} = \delta_m + (\delta_d - \delta_m)\left(1 + \frac{1 - \sqrt{8K_d c_T + 1}}{4K_d c_T}\right) \quad (5)$$

allows obtaining the association constant K_d for all studied compounds at different temperatures (Table 2).

The three dimensional plot for the fit accuracy, dependent on the chemical shifts of the monomer and dimer is depicted on *Figure S3* while the dependence of the association constant on the fit accuracy is presented in *Figure S4*.

The obtained values for temperature dependent K_d and δ_d and δ_m for all dyes as a function of temperature are summarized resp. in Table 1 and Table 2. The values are determined based on equation (5) at 2.6–4.9 mmol L^{-1} concentration in a phosphate buffer solution. The effect of the structural changes on the self-association and the thermodynamic parameters of the process is further discussed comparing the **3a/3e**, **3a/3b/3d** and **3b/3c** dye analogues.

In the pair **3a/3e** where the C5 atom in the **3a** analogue is substituted with a nitrogen atom in the **3e** analogue, the self-association constants in aqueous environment decrease from 258 L mol^{-1} for **3a** to 106 L mol^{-1} for **3e** (Table 2). On one hand, nitrogen is slightly more electronegative than carbon, which leads to a change in the electron density distribution in the molecule. On the other, the nitrogen atom in the pyridine ring increases the solubil-

Table 1
The values for monomer isotropic shift (δ_m) and dimer isotropic shift (δ_d) are determined at a concentration range between 4.9 and 2.6 mmol L^{-1} for the H-2́ proton of the dyes **3a** – **3e** using eq. (5).

dye	**3a**	**3b**	**3c**	**3d**	**3e**
δ_m [ppm]	7.1	6.3	7.2	7.8	7.0
δ_d [ppm]	5.2	5.1	4.8	6.8	5.1

Table 2

Temperature dependent self-association constants K_d [L mol^{-1}] of the investigated cyanine dyes in D_2O phosphate-buffer and the resp. monomer and dimer chemical shifts (CS).

T, [K]	3a K_d [L mol^{-1}]	3b K_d [L mol^{-1}]	3c K_d [L mol^{-1}]	3d K_d [L mol^{-1}]	3e K_d [L mol^{-1}]
299	258 ± 7	104 ± 5	299 ± 17	4 ± 0	107 ± 2
304	218 ± 4	69 ± 2	245 ± 12	–	94 ± 3
314	146 ± 3	17 ± 2	165 ± 4	–	58 ± 2
324	103 ± 2	11 ± 1	130 ± 6	–	40 ± 1

ity in polar solvents due to the participation of its lone electron pair in hydrogen-bonding interactions.

The self-association constants for the **3a**, **3b**, and **3d** cyanine dyes containing resp. **O**, **S** and **Se** atoms in the same position of the molecule in the same solvent decrease from 258 L mol^{-1} (**3a**) to 103 L mol^{-1} (**3b**) and 4 L mol^{-1} (**3d**) in this row. This implies that the change of the heteroatom in the hetroaromatic system plays a significant role in the association process most probably due to the heteroatoms' different electronegativity. Oxygen is the second most electronegative element after fluorine according to the Pauling scale. It attracts electron density leaving the conjugated aromatic system electron deficient. The overall positive charge in the aromatic system is increased. This corresponds well with the finding that electron deficient rings prefer stacking interactions over electron rich ones which is in good agreement with the electrostatic model of Hunter and Sanders.[13] Thus, the stacking interaction of the oxazoles is expected to be the strongest in the row **3a**, **3b**, **3d** and the self-association constant the highest. Sulfur is slightly more electronegative than selenium, which explains the higher self-association constant of the thiazole containing aromatic system compared to the selenazole one. The electronegativity of selenium is equal to the one of carbon. Therefore, the exchange of the X-1 atom with selenium makes no difference from the point of view of electronegativity. Thus, the positive charge compensation of the dicationic dyes is in this case the least. However, the atomic radius of selenium is the highest in the row **3a**, **3b**, **3d**, which probably hinders stacking due to repulsion and resp. inefficient orbital overlap. This explains the very small (and close to zero) self-association constant of the **3d** analogue. Furthermore, the ^{1}H NMR spectra of the latter do not show a significant change in the chemical shift upon dilution. This leads to the conclusion that the **3d** cyanine derivative exists as a monomer in the solution within the investigated concentration range. Fig. 4 displays the dependence of the self-association constant on the electronegativity and the atomic radius for the **3a**, **3b** and **3d** analogues. Based on

the experimental data it is hard to determine which of these factors (the changes in electronegativity or atomic radius) dominates with regard to the changes in the self-association constants as both act simultaneously. Also, an important role in the process of self-association plays the participation of the unpaired electron pairs of the heteroatoms under discussion in the conjugated aromatic system. The electron donating properties and respectively the strength of the positive mesomeric effect increase from **3a** to **3d**. The electron charge mobility increases in the same way ensuring better electron charge distribution from **3a** to **3d** in the π-conjugated system of the presented dyes and consequently higher electron charge delocalization.

The self-association constant for the **3c** homologue is (ca. 299 L mol^{-1}) is nearly three times higher compared to the one for **3b** (103 L mol^{-1}). In this case (**3c**), the positive charge in the conjugated aromatic system is compensated to some extent from the donating methyl groups. However, it is not surprising that the most hydrophobic **3c** homologue is characterized by the highest self-association constant in aqueous environment.

The interplay between charge distribution in the π-conjugated aromatic system, hydrophilicity and the solvent effects determines the strength of the stacking interaction, which changes depending on the structure of the cyanine analogues.

The process of self-association can also be investigated by diffusion ordered spectroscopy (DOSY).[46,48] In this NMR experiment a series of 1D spectra are measured varying the strength of the gradient pulse. The resulting reduction of the signal intensity with increasing the strength of the gradient pulse is consequently fitted to determine the diffusion coefficient D. The latter is described by the Stokes-Einstein equation:

$$D = \frac{k_B T}{6 \pi \eta R_H} \tag{6}$$

where k_B is the Bolzman constant, T is the temperature [K], η is the viscosity [Pa s] and R_H is the hydrodynamic radius [m].

Clearly, a dimer would diffuse more slowly compared to a monomer, thus being characterized by a lower diffusion coefficient. Diluting a concentrated sample containing stacked molecules leads to a shift of the monomer–dimer equilibrium towards the monomeric form and resp. to a change in the diffusion coefficient. Thus, the thermodynamic parameters of the process of self-association can also be determined based on the changes in the diffusion coefficient upon dilution. In this case, however, not the chemical shifts but the diffusion coefficients of the monomer molecule and the oligomer are averaged in the fast tumbling regime. The disadvantage here is the long measuring time at low concentrations and for this reason we have performed the DOSY experiments only at a concentration of 4.9 mol L^{-1}. It should also be noted that the concentration dependence of the viscosity might lead to (systematic) errors when determining the self-association constant. This problem could be circumvented using an internal standard (a molecule, which does not participate in the association process) as a reference for the diffusion coefficient.[49] Nevertheless, one can find a relation between the self-association constant and the diffusion-coefficient.

The diffusion coefficients D [m^2 s^{-1}] from the DOSY experiment conducted on the dyes in D_2O and DMSO d_6 (Table 3) were
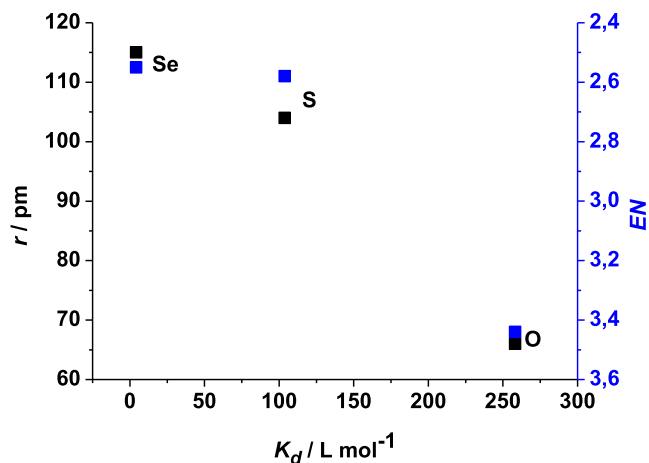

Fig. 4. Experimental self-association constants (L mol^{-1}) vs. the theoretical atomic radii of oxygen (**3a**), sulfur (**3b**) and selenium (**3d**) (left axis) and electronegativity of these heteroatoms according Pauling (right axis).

Table 3

Diffusion coefficients and hydrodynamic radii of dyes **3a** - **3e** in D$_2$O and DMSO d_6 solutions with a concentration of 4.9 mol L^{-1}.

Dye	M [g mol^{-1}]	D [10^{-10} m^2 s^{-1}] (DMSO d_6)	R_H [nm] (DMSO d_6)	D [10^{-10} m^2 s^{-1}] (D$_2$O)	R_H [nm] (D$_2$O)
3a	275	2,4 ± 0,0	0,4 ± 0,0	2,4 ± 0,0	0,9 ± 0,1
3b	295	2,2 ± 0,0	0,5 ± 0,0	3,5 ± 0,1	0,6 ± 0,0
3c	323	2,2 ± 0,1	0,5 ± 0,0	5,0 ± 0,8	0,4 ± 0,1
3d	342	2,2 ± 0,0	0,5 ± 0,0	3,6 ± 0,1	0,6 ± 0,0
3e	280	2,4 ± 0,0	0,4 ± 0,0	3,2 ± 0,8	0,7 ± 0,2

obtained from a fit of the exponential decay of the signal intensity versus the gradient field strength in consecutive experiments. Consequently, all hydrodynamic radii R_H of the dyes/dye aggregates could be extracted from the Stokes − Einstein equation for spherical particles. As long as the structures of all investigated molecules are very comparable no further correction of the diffusion coefficients related to the shape was performed.[50b]

The measured diffusion coefficients for the dyes in DMSO d_6 are in the range from 2,2 to 2,4 [10^{-10} m^2 s^{-1}] with the resp. hydrodynamic radii ranging from 0,4 to 0,5 nm. These comparable D and R_H values nicely correlate with the good solubility of all compounds in DMSO d_6. In D$_2$O, however, no such correlation is found. Most of the determined hydrodynamic radii are significantly larger compared to the values in DMSO d_6. This is related to the lower solubility in water, which results in aggregates formation due to π - π stacking of the conjugated aromatic systems. The D and R_H values for three of the investigated styryl hemicyanine dyes **3b**, **3d** and **3e** are comparable and in the range of 3,2 – 3,6 [10^{-10} m^2 s^{-1}] and 0,6 – 0,7 nm respectively. The analogue **3c** shows a comparable hydrodynamic radius to the one determined in DMSO d_6. This clearly indicates that no stacking is present in the selenazole derivative in both DMSO d_6 and D$_2$O. Possible reasons could be the out-of-plane mobility of the two methyl groups which hinders aggregate formation combined with the better charge delocalization in the aromatic system and the larger atomic radius of selenium. The hydrodynamic radius of the **3a** derivative is the highest from the studied dyes. It should be noted that the translational diffusion of the molecules is related not only to the aggregate formation but also to the whole hydration shell around the molecule/s. Due to the highest electronegativity of the oxygen atom compared to sulfur and selenium the benzooxazole ring possesses the highest positive charge, which might lead to a larger hydration shell. In addition, the exchange rate at these conditions might be different in the different cases regarding the time scale of the diffusion experiment.

3.3. Thermodynamics of the self-association

To better understand the cyanine dyes self-association, the thermodynamic parameters ΔH, ΔS and ΔG of the process are determined based on the temperature dependent self-association constants. The relation between K_d and ΔG is given by the Van't Hoff equation:

$$K_d = e^{-\frac{\Delta G}{RT}} \tag{7}$$

where R is the universal gas constant (8.314 J mol^{-1} K^{-1}) and T the absolute temperature [K].

To determine the values for ΔH and ΔS the Gibbs-Helmholtz-equation is applied:

$$\Delta G = \Delta H - T\Delta S \tag{8}$$

In this equation ΔG [kJ mol^{-1}] is the Gibbs free energy, ΔH [kJ mol^{-1}] the enthalpy change and ΔS [J mol^{-1} K^{-1}] the entropy change of the association process.

The plot of the logarithms from the self-association constant against the reverse temperature (the Van't Hoff plot) for the compounds **3a**, **3b**, **3c** and **3e** is displayed in Fig. 5. From this plot one can determine the ΔH (the slope = - ΔH / R) and the ΔS (the intercept = ΔS / R).

The tilt in the curves in the Van't Hoff plot (Fig. 5) confirms that the self-association including π-π-interactions of aromatic systems of the investigated cyanine dyes is an exothermic process.[51] Exothermic processes are characterized by negative enthalpy and entropy values respectively.[24] The main interaction arises due to dispersive van der Waals forces between the chromophores of the dye molecules. The values for ΔH, ΔS and the Gibbs free energy ΔG for the cyanine analogues at 299 K are summarized in Table 4.

As seen from the Van't Hoff plot the self-association of the **3a** and **3e** dyes is driven by enthalpy in the investigated temperature region. The derived enthalpies in aqueous environment for the **3a** and **3e** analogues at 299 K differ by only ca. 3 kJ mol^{-1} (ca. 30 kJ mol^{-1} for **3a** vs 33 kJ mol^{-1} for **3e**). The slightly more negative value for the enthalpy in the case of **3e** arises mainly from the attractive interaction between the electron poor oxazolopyridine and the electron rich N,N'-dimethylaniline-system.[2] The entropy is more negative for the **3e** compound by around 17 J mol^{-1} K^{-1}. This is hardly surprising as the solubility of the **3e** analogue is higher due to hydrogen bond formation with the water molecules with the participation of the unpaired electron pair of the nitrogen atom in the oxazolopyridinium ring. Thus, the dissociation of the **3e** dimer is slightly more favored compared to the **3a** one at the same conditions. The Gibbs free energy is comparable for both **3a** and **3e** compounds. The negative sign implies that the dimerization process is spontaneous for both compounds at the same conditions, however, slightly more favored for the **3a** analogue.

The **3d** analogue does not form dimers at ambient conditions in aqueous solutions (the self-association constant is close to zero). Thus, no thermodynamic parameters have been determined for this compound. For the **3a** and **3b** analogues the self-association is enthalpy driven in the temperature range 298 – 328 K. Both the enthalpy and the entropy for the **3b** analogue have higher
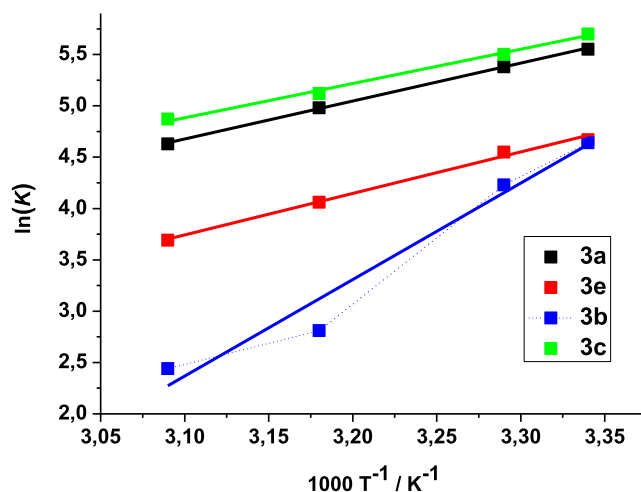

Fig. 5. Van't Hoff plot for the compounds **3a, 3b, 3c** and **3e**.

Table 4
Calculated thermodynamic parameters for the cyanine dyes **3a, 3b, 3c,** and **3e.** *a: Due to low K$_d$ of **3d** even at 299 K, there were no thermodynamic parameters calculated since the compound is dominantly present in the monomeric state at these conditions.

dye	3a	3b	3c	3d	3e
ΔH [kJ mol^{-1}]	-(30 ± 1)	-(77 ± 6)	-(27 ± 1)	a	-(33 ± 2)
ΔS [J mol^{-1} K^{-1}]	-(55 ± 3)	-(219 ± 35)	-(44 ± 4)	a	-(72 ± 7)
ΔG [kJ mol^{-1}]	-(14 ± 1)	-(12 ± 5)	-(14 ± 1)	a	-(12 ± 2)

absolute values compared to those of the **3a** analogue: enthalpy (ca. −78 vs −30 kJ mol^{-1}) and entropy (ca. −219 vs −55 J mol^{-1}). It is known, that the increase in the polarizability of a heteroatom leads to stronger dispersive Van der Waals interactions.[15] This is related to the enthalpy since the sulfur containing compound has an absolute value 44 kJ mol^{-1} higher than oxygen containing analogue. The higher absolute entropy indicates that the monomer form of **3b** is stronger favored at high temperatures. Thus, for the **3b** analogue the enthalpy becomes more favorable and the entropy more unfavorable as the electronegativity of the heteroatom decreases, indicating stronger enthalpy–entropy compensation. It is also possible to present the thermodynamic process of self-association of the **3b** analogue as consisting of three different processes (Fig. 5 *dotted line*) in the different studied temperature intervals as observed from the Van't Hoff plot. All three association processes are enthalpy favorable: (ΔH = -(62) kJ mol^{-1}, ΔS = -(169) J mol^{-1} K^{-1}, ΔG = -(12) kJ mol^{-1} at 298 – 303 K; ΔH = -(108) kJ mol^{-1}, ΔS = -(321) J mol^{-1} K^{-1}, ΔG = -(13) kJ mol^{-1} at 303 – 313 K and ΔH = -(34) kJ mol^{-1}, ΔS = -(85) J mol^{-1} K^{-1}, ΔG = -(9) kJ $^{-1}$ at 313 – 323 K. In the lower and the higher temperature range (298 – 303 K and 313–323 K) the incline of the curve is comparable to the plots of the other compounds presented in Fig. 5, i.e. the value for the enthalpy change is comparable to those for **3a, 3c,** and **3e** dyes. In the intermediate temperature range, a steeper slope is observed which is related to more pronounced change in the strength of the intermolecular interaction.

The enthalpies of the association of **3b** and **3c** differ by around 49 kJ mol^{-1} in favor of **3c**. The entropy is more negative for the compound **3b** (-(219 ± 35) J mol^{-1} K) compared to **3c** (-(44 ± 4) J mol^{-1} K). The Gibbs free energy is more negative for the compound **3c**, which suggests in a more stable dimer. The lowest absolute values for both, ΔH and ΔS are found for the self-association process in **3c**. The low enthalpy value is related to the repulsive interaction of the aromatic systems as the electronic density is increased due to the positive inductive effect of the two methyl groups. Supposedly, the highest absolute values in the Gibbs free energy and the self-association constant arise mainly from the hydrophobic nature of the **3c** molecule. The formation of a stacked dicationic dimer molecule should be favored in a polar solvent like D$_2$O, which is related to the entropy term.

3.4. Number of stacked molecules

The average number of stacked molecules N in an aggregate for all studied dyes (considering an equilibrium process association – dissociation) is calculated based on equation (9)[52] and presented for four temperatures in the range 299–324 K in Table 5.

$$N = \frac{1}{2}\left(1 + \sqrt{4K_d c_T + 1}\right)$$
(9)

A value close to 2 indicates that the compound is predominantly found in the dimeric state while a value close to 1 indicates the presence of only the monomer at concentration 4.5 mmol L^{-1}. At a value of 1.5 both (the monomer and the dimer forms) are present in a ratio 1:1.

Since the number of the stacked molecules N is proportional to K_d the number of stacked molecules decrease as a function of temperature as well, as the self-association constant does. From Table 5 it can be seen, that **3d** is already at ambient temperatures dominantly present in the monomeric form.

Fig. 6A presents the number of stacked molecules as a function of the concentration at 299 K. A line nearly parallel to the *x*-axis is observed for the **3d** analogue. This indicates, that even at high concentrations, no stacking takes place. The compounds **3a** and **3c** seem to form dimers at concentrations in the range of 0.01 mol L^{-1}.

By using equation 15 (*Supporting Information*) it is possible to determine the molar fractions α$_{mon}$ and α$_{aso-\pi}$. The intercept of the two functions indicates a 1 : 1 monomer–dimer equilibrium (equal amount of monomers and dimers are present in solution at this concentration). Fig. 6B shows the molar fraction of the dimeric and monomeric state of **3e** as a function of the concentration at 299 K in phosphate buffer. The 1 : 1 equilibrium was found at a concentration of 5.7 mmol L^{-1}. This is in a good agreement with equation (9) since the number of stacked molecules in a concentration range between 4.9 and 2.6 mmol L^{-1} is with a value of 1.38 below the 1 : 1 (monomer:dimer) value of 1.5.[52]

3.5. Organization in the stack

To determine the organization of the dye molecules in the stack one needs to measure concentration dependent ^{1}H spectra and plot the change in the chemical shift versus the concentration.[25]

As mentioned above, the ^{1}H chemical shifts of a molecule are influenced by the ring current of the aromatic systems of neighboring molecules provided that a π-π interaction exists. Thus, a proton in a molecular stack may experience to a higher degree the ring current at higher concentrations and respectively resonate at higher fields. Diluting the sample would shift the monomer–dimer equilibrium to the monomeric state thus inducing a low field shift.

As presented in Fig. 7, the ^{1}H shifts of the protons of the N,N'-dimethylaniline ring (H-2′ and H-3′) and of the double bond (H-10 and H-11) are the most influenced upon dilution, while the proton shifts in the oxazolopyridine-system are less affected. The smallest change was observed for the methyl protons H-5′, while the methyl protons H-8′ experience a somewhat more pronounced change in the chemical shift.

Table 5
Average number of molecules per stack at a concentration 4.5 mmol L^{-1}.

Temperature, K	3a	3e	3b	3d	3c
299	1.73	1.38	1.37	1.02	1.81
304	1.65	1.34	1.26	–	1.71
314	1.48	1.23	1.07	–	1.53
324	1.37	1.17	1.05	–	1.44
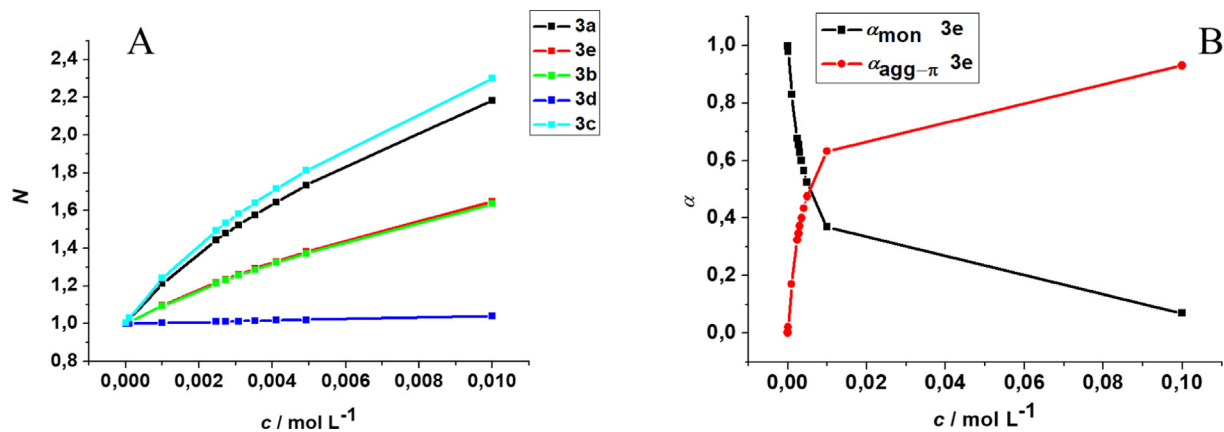
Fig. 6. *A.* Concentration dependence of the number of stacked molecules at 299 K. *B.* Molar fraction of the monomer and the aggregate as a function of concentration at 299 K for the compound **3e.**
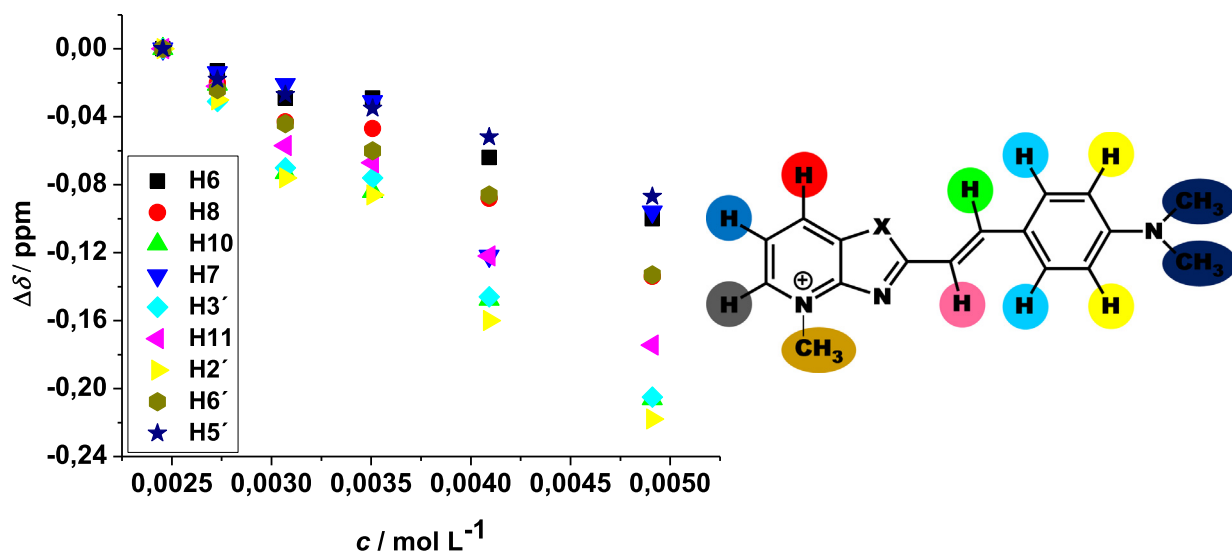
Fig. 7. Changes in the chemical shift of **3e** protons as a function of concentration in D_2O-phosphate-buffer (left) with the chemical structure (right).
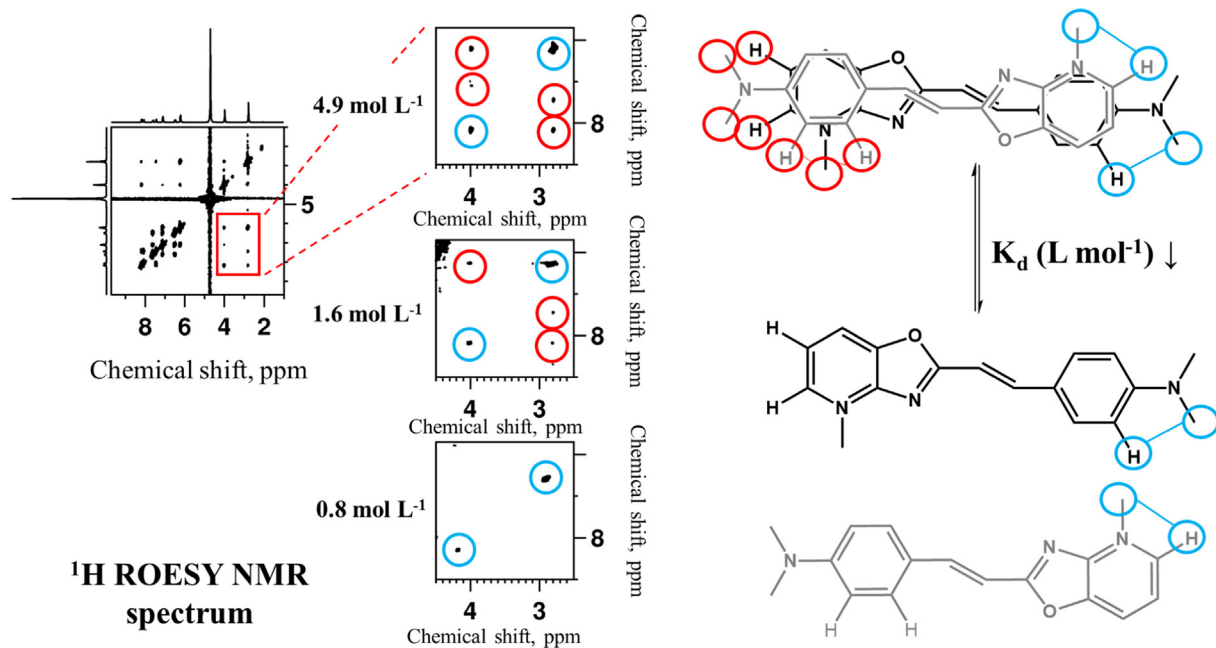
Fig. 8. ^1H ROESY spectrum for the compound **3e** at different concentrations with the proposed geometry of two stacked molecules.

NMR experiments based on the nuclear Overhauser effect (NOE) like NOESY and ROESY would facilitate probing the organization within the stack. At higher concentrations these experiments would reveal dipolar contacts between two (or more) stacked molecules.[46] Diluting the sample would result in a loss of such contacts due to the shift of the equilibrium to the monomeric form.

A number of possible orientations of the dye molecules in a stack exist; the common dimer geometry being with parallel or antiparallel orientation of the stacked molecules. Additionally, the molecules may experience a shift along one of the molecular axes.

To probe the organization in the dimers concentration dependent ^{1}H ROESY experiments were performed (Fig. 8). The most informative part of the spectra is related to contacts of the methyl protons and part of the aromatic protons. Clearly upon dilution, the cross peaks between the methyl group protons H-8' and the protons H-2' and H-3' as well as the cross peaks between the methyl groups protons H-5' and the protons H-6, H-7 and H-8 (red circles) of neighboring molecules disappear. At the same time the intramolecular dipolar contacts observed in the presented spectral region, i.e. between the methyl protons H-5' and the aromatic H-2' as well as those between the methyl H-8' and H-6 (blue circles) remain. This leads to the conclusion that the formed dimers are in an antiparallel arrangement, since the protons of the methyl groups from the N,N'-dimethylaniline show dipolar contacts with the protons of the oxazolopyridine-system. Fig. 8 shows the proposed stacking in the dimer. Furthermore, in this arrangement the positively charged nitrogen atom N-5 is localized close to the N,N'-dimethylaniline (possessing high electron density) from the neighboring stacked molecule.

The ^{1}H ROESY spectra recorded for **3a** analogue at the same conditions show the same cross peaks as in the **3e** case. The compounds **3b** and **3c** precipitate when recording the ^{1}H ROESY spectra, which correlates well with the determined thermodynamic parameters.

4. Conclusions

The interplay between charge distribution and hydrophilicity governs the self-association of styryl hemicyanine dyes in aqueous solutions. The investigated dyes organize as dimers due to the electrostatic interaction between the positively charged oxazole or thiazole ring and the π-system of the phenyl ring. The selenazole derivative exists in its monomeric form in the investigated concentration and temperature ranges due to the higher electron charge delocalization in the conjugated aromatic system. The analogue containing two (electron donating) methyl groups in its structure is, however, the most hydrophobic and is characterized resp. by the highest self-association constant (k_a = 299 L mol^{-1}). The substitution of the benzooxazolium with oxazolopyridium function in the oxazole derivative allows better solubility, which decreases the effect of the π-π interaction.

The self-association in the investigated temperature range for the styryl hemicyanine dyes (apart the selenazole analogue) is an exothermic process characterized by both negative enthalpy and entropy terms. The relative strength of the self-organization related to the change of the Gibbs free energy (ΔG) is highest for the most hydrophobic analogue. On the other hand the more polar and better soluble benzooxazole derivative is characterized by smaller, however, comparable ΔG = -(14 ± 1) kJ mol^{-1}. The **3b** and **3e** analogues show values in the range of −12 kJ mol^{-1} for the change in the Gibbs free energy. The difference is the high entropy gain for the **3b** derivative, resp. destabilization of the dimer, on temperature increase.

The thiazole derivatives are stable in the pH range 4.5 – 9.2. The oxazole derivatives are stable at lower pH values, however, experience ring opening at basic conditions. The substitution of benzoox-azolium with oxazolopyridium function improves the solubility and the stability in water and makes this new class of compounds very perspective for DNA/RNA labelling.

The demonstrated method for screening the solubility and self-aggregation of new dyes facilitates the rational molecular design of novel organic compounds for bio applications.

Declaration of Competing Interest

The authors declare that they have no known competing financial interests or personal relationships that could have appeared to influence the work reported in this paper.

Contribution

C. Haese conducted the NMR experiments and the fitting procedure; M. Boecker conducted the dilution ^{1}H NMR experiments; A. Vasilev synthesized the investigated compounds and wrote the synthetic part of the manuscript; M. Mondeshki initiated the study and wrote the paper excluding the synthesis.

Appendix A. Supplementary material

Supplementary data to this article can be found online at https://doi.org/10.1016/j.molliq.2022.118678.

References

[1] M. Egli, Structure and Function 112 (2010) 177.
[2] C. Martinez, B. Iverson, Chem. Sci. 3 (2012) 2191.
[3] a) P. Yakovchuk, E. Protozanova, M. D. Frank-Kamenetskii, *Nucleic acids research* **2006**, *34*, 564; b) V. Bloomfield, D. Crothers, I. Tinoco, *Nucleic acids. Structures, properties, and functions* / V. A. Bloomfield, D. M. Crothers, I. Tinoco, Jr., *with contributions from J. E. Hearst [et al.]*, University Science Books, Sausalito, Calif., United Kingdom, **2000**.
[4] a) D. Zhao, Y. Kong, S. Zhao, H. Xing, *Topics in current chemistry (Cham)* **2020**, *378*, 41; b) L. Doll, J. Lackner, F. Rönicke, G. U. Nienhaus, H.-A. Wagenknecht, *Chembiochem : a European journal of chemical biology* **2021**, *22*, 2561
[5] a) G. Silva, V. Ediz, D. Yaron, B. Armitage, *Journal of the American Chemical Society* **2007**, *129*, 5710; b) A. L. Benvin, Y. Creeger, G. W. Fisher, B. Ballou, A. S. Waggoner, B. A. Armitage, *Journal of the American Chemical Society* **2007**, *129*, 2025; c) Colier C., *Cell Biochemistry and Biophysics* **2000**, *33*, 323; d) G. Patony, J. Salon, J. Sowell, L. Strekowski, *Molecules* **2004**, *9*, 40; e) J. P. Jacobsen, J. B. Pedersen, L. F. Hansen, D. E. Wemmer, *Nucleic acids research* **1995**, *23*, 753; f) H. Zipper, H. Brunner, J. Bernhagen, F. Vitzthum, *Nucleic acids research* **2004**, *32*, e103; g) H. Ihmels, K. Faulhaber, D. Veraldi, F. Dall'Aqua, G. Viola, *Photochemistry and Photobiology* **2005**, *81*, 1107
[6] a) Y. Takashima, A. Harada, Journal of Inclusion Phenomena and Macrocyclic Chemistry 87 (2017) 313;
b) G. Yu, X. Chen, Theranostics 9 (2019) 3041;
c) H.-J. Schneider, Angew. Chem. INt. Ed. Eng. 30 (1991) 1417.
[7] M. Yang, K. Cao, L. Sui, Y. Qi, J. Zhu, A. Waas, E.M. Arruda, J. Kieffer, M.D. Thouless, N.A. Kotov, ACS nano 5 (2011) 6945.
[8] Q. Jiang, Q. Zhang, X. Wu, L. Wu, J.-H. Lin, *Nanomaterials (Basel, Switzerland)* **2020**, *10*.
[9] C.-P. Lee, C.-T. Li, K.-C. Ho, Mater. Today 20 (2017) 267.
[10] V. Joseph, K.R.J. Thomas, S. Sahoo, M. Singh, D.K. Dubey, J.-H. Jou, ACS Omega 3 (2018) 16477.
[11] M. Gsänger, E. Kirchner, M. Stolte, C. Burschka, V. Stepanenko, J. Pflaum, F. Würthner, JACS 136 (2014) 2351.
[12] R. Zhou, Modeling of Nanotoxicity, Springer International Publishing, Cham, 2015.
[13] C.A. Hunter, J.K.M. Sanders, JACS 112 (1990) 5525.
[14] a) C.A. Hunter, Angewandte Chemie International Edition Eng. 32 (1993) 1584;

b) C.A. Hunter, Chem. Soc. Rev. 23 (1994) 101;

c) E.C. Lee, B.H. Hong, J.Y. Lee, J.C. Kim, D. Kim, Y. Kim, P. Tarakeshwar, K.S. Kim, JACS 127 (2005) 4530.

[15] H.-J. Schneider, Acc. Chem. Res. 2015 (1815) 48.

[16] P. Mignon, S. Loverix, F. de Proft, P. Geerlings, The Journal of Physical Chemistry A 108 (2004) 6038.

[17] X. Mei, C. Wolf, The Journal of organic chemistry 70 (2005) 2299.

[18] a) A.J. Goodman, E.C. Breinlinger, C.M. McIntosh, L.N. Grimaldi, V.M. Rotello, Org. Lett. 3 (2001) 1531;

b) M.J. Rashkin, M.L. Waters, JACS 2002 (1860) 124.

[19] T. Deligeorgiev, A. Vasilev, S. Kaloyanova, J.J. Vaquero, Color. Technol. 126 (2010) 55.

[20] A. Mishra, R.K. Behera, P.K. Behera, B.K. Mishra, G.B. Behera, Chem. Rev. 2000 (1973) 100.

[21] a) J. Steinmeyer, F. Rönicke, U. Schepers, H.-A. Wagenknecht, *ChemistryOpen* **2017**, *6*, 514; b) S. M. Yarmoluk, V. B. Kovalska, K. D. Volkova, *113*, 161; c) V. P. Tokar, M. Y. Losytskyy, T. Y. Ohulchanskyy, D. V. Kryvorotenko, V. B. Kovalska, A. O. Balanda, I. M. Dmytruk, V. M. Prokopets, S. M. Yarmoluk, V. M. Yashchuk, *Journal of fluorescence* **2010**, *20*, 865; d) P. R. Bohländer, H.-A. Wagenknecht, *Methods and applications in fluorescence* **2015**, *3*, 44003.

[22] P. Thordarson, Chem. Soc. Rev. 40 (2011) 1305.

[23] A.S. Shetty, J. Zhang, J.S. Moore, JACS 118 (1996) 1019.

[24] D.B. Davies, L.D. Djimant, A.N. Veselkov, J. Chem. Soc. Faraday Trans. 92 (1996) 383.

[25] H. Sun, Y. Zhao, Z. Huang, Y. Wang, F. Li, The journal of physical chemistry. A 112 (2008) 11382.

[26] A. Fernandes, N.F. Brás, N. Mateus, V.d. Freitas, New J. Chem. 39 (2015) 2602.

[27] S.S. Petrova, A.A. Schlotgauer, A.I. Kruppa, T.V. Leshina, Zeitschrift für Physikalische Chemie 231 (2017) 7594.

[28] A. Pérez, D. de Saá, A. Ballesteros, J. L. Serrano, T. Sierra, P. Romero, *Chemistry (Weinheim an der Bergstrasse, Germany)* **2013**, *19*, 10271.

[29] D.J.W. Grant, M. Mehdizadeh, A.-H.-L. Chow, J.E. Fairbrother, Int. J. Pharm. 18 (1984) 25.

[30] a) C. Ochsenfeld, S.P. Brown, I. Schnell, J. Gauss, H.W. Spiess, JACS 123 (2001) 2597;

b) W. Pisula, M. Kastler, D. Wasserfallen, M. Mondeshki, J. Piris, I. Schnell, K. Müllen, Chem. Mater. 18 (2006) 3634;

c) M.M. Elmahdy, X. Dou, M. Mondeshki, G. Floudas, H.-J. Butt, H.W. Spiess, K. Müllen, JACS 130 (2008) 5311;

d) S.P. Brown, H.W. Spiess, Chem. Rev. 101 (2001) 4125.

[31] Y. Inoue, Annu. Rep. NMR Spectrosc. 27 (1993) 59.

[32] V. Kovalska, D. Kryvorotenko, A. Balanda, M. Losytskyy, V. Tokar, S. Yarmoluk, Dyes Pigm. 67 (2005) 47.

[33] M.J. Myllymäki, A.M. Koskinen, Tetrahedron Lett. 48 (2007) 2295.

[34] A. Kurutos, N. Gadjev, T. Šmidlehner, S. Minkovska, I. Piantanida, T. Deligeorgiev, Molbank 2016 (2016) M889.

[35] A. Vasilev, T. Deligeorgiev, S. Kaloyanova, S. Stoyanov, V. Maximova, J.J. Vaquero, J. Alvarez-Builla, Color. Technol. 127 (2011) 69.

[36] M.I. Kandinska, S.M. Kitova, V.S. Videva, S.S. Stoyanov, S.B. Yordanova, S.B. Baluschev, S.E. Angelova, A.A. Vasilev, Beilstein journal of organic chemistry 15 (2019) 1096.

[37] R. Harris, E. Becker, S. de Menezes, R. Goodfellow, P. Granger, Pure Appl. Chem. 73 (2001) 1795.

[38] A. Vasilev, T. Deligeorgiev, N. Gadjev, K.-H. Drexhage, Dyes Pigm. 66 (2005) 135.

[39] K. Nakamura, H. Fukunaga, PCT/JP2006/306049.

[40] a) V. B. Kovalska, V. P. Tokar, M. Y. Losytskyy, T. Deligeorgiev, A. Vassilev, N. Gadjev, K.-H. Drexhage, S. M. Yarmoluk, *Journal of biochemical and biophysical methods* **2006**, *68*, 155; b) A. Zarkov, A. Vasilev, T. Deligeorgiev, S. Stoynov, M. Nedelcheva-Veleva, *Molecular Imaging* **2013**, *12*, 7290.2012.00018.

[41] I. Crnolatac, L.-M. Tumir, N.Y. Lesev, A.A. Vasilev, T.G. Deligeorgiev, K. Mišković, L. Glavaš-Obrovac, O. Vugrek, I. Piantanida, ChemMedChem 8 (2013) 1093.

[42] a) M. I. El-Sheikh, A. Marks, E. R. Biehl, *Journal of Organic Chemistry* **1981**, *46*, 3256; b) D. Xu, W. Wang, C. Miao, Q. Zhang, C. Xia, W. Sun, *Green Chemistry* **2013**, *15*, 2975; c) J. Joseph, J. Y. Kim, S. Chang, *Chemistry (Weinheim an der Bergstrasse, Germany)* **2011**, *17*, 8294; d) I. J. Turchi, M. J. S. Dewar, *Chemical reviews*, *75*, 389.

[43] G.A. Holmes, K. Rice, C.R. Snyder, J Mater Sci 41 (2006) 4105.

[44] Z. Chen, A. Lohr, C.R. Saha-Möller, F. Würthner, Chem. Soc. Rev. 38 (2009) 564.

[45] W. West, Sandra Pearce, The Journal of Physical Chemistry 1965 (1894) 69.

[46] M. Bogdan, C.G. Floare, A. Pîrnau, J. Phys. Conf. Ser. 182 (2009) 12002.

[47] N. Muller, R.C. Reiter, The Journal of Chemical Physics 42 (1965) 3265.

[48] R. Ferrazza, B. Rossi, G. Guella, J. Phys. Chem. B 118 (2014) 7147.

[49] E. Cabrita, S. Berger, Magn. Reson. Chem. 39 (2001) S142–S148.

[50] a) A. Macchioni, G. Ciancaleoni, C. Zuccaccia, D. Zuccaccia, Chem. Soc. Rev. 37 (2008) 479;

b) A. Macchioni, G. Ciancaleoni, C. Zuccaccia, D. Zuccaccia, Chem. Soc. Rev. 37 (2008) 479.

[51] A.N. Veselkov, R.J. Eaton, V.I. Pakhomov, L.D. Djimant, D.B. Davies, J. Struct. Chem. 42 (2001) 193.

[52] Z. Chen, V. Stepanenko, V. Dehm, P. Prins, L. D. A. Siebbeles, J. Seibt, P. Marquetand, V. Engel, F. Würthner, *Chemistry (Weinheim an der Bergstrasse, Germany)* **2007**, *13*, 436.

[53] J. Baran, S. Penczek, Hydrolysis of Polyesters of Phosphoric Acid. 1. Kinetics and the pH Profile, Macromolecules 28 (1995) 5167–5176.

[54] Y. Yang C., L. Szafraniec L., W. Beaudry T., R. Way J., Kinetics and Mechanism of the Hydrolysis of 2-Chloroethyl Sulfides, J. Org. Chem. 53 (1988) 3293–3297.

Charge transport in protic ionic liquids: Effect of protonation state in 1-methylimidazolium – acetate/trifluoroacetate mixtures

Johannes Sutter, Constantin Haese, Robert Graf, Johannes Hunger [*]

Max Planck Institute for Polymer Research, Ackermannweg 10, 55128 Mainz, Germany

ABSTRACT

Despite the potential to overcome slow charge transport in ionic liquids by decoupling charge transport from mass transport in protic ionic liquids (PILs), the average proton distribution and the contribution of proton conduction to the overall charge transport in PILs has not been fully established. To elucidate the predominant underlying molecular species in the PILs and the molecular dynamics of the PILs, we study the dipolar response and conductivity using dielectric relaxation (DR) spectroscopy and the nucleis chemical environment and molecular mobility using nuclear magnetic resonance (NMR) spectroscopy of prototypical PILs based on 1–methylimidazolium as Brønsted base. To elucidate the effect of the acidity of the Brønsted acid we gradually vary the composition of the PILs from 1–methylimidazolium acetate [MimH][AcO] to 1–methylimidazolium trifluoroacetate [MimH][TFA]. Both, ^{15}N-NMR chemical shifts and the sample conductivities suggest that in neat [MimH][AcO] electro-neutral molecular species dominate, consistent with earlier findings. The dipolar response of these molecular species as detected via the DR spectra is stronger than what one would expect based on the molecular dipole moments estimated from density functional theory calculations, which points to the formation of an extended hydrogen-bonded network. Upon addition of [MimH][TFA], this dipolar response is reduced as the degree of protonation of 1–methylimidazolium gradually increases, which is apparent from the conductance and ^{15}N chemical shifts. Interestingly, diffusion ordered NMR spectroscopy indicates protons to become more mobile than the constituting acid and base molecules, consistent with Grotthuss-like proton transport. To vary the immediate environment of the PILs, we study solutions of the PIL mixtures in aprotic dimethylformamide (DMF) and protic methanol (MeOH) as two limiting cases. We find that [MimH][AcO] exclusively forms electroneutral species in DMF, as evident from the negligible conductivity, while with increasing TFA content the fraction of charged molecular species increases. Although these ionic species give rise to a finite conductivity, demonstrating the presence of mobile ions, a large fraction of these ions is bound in [MimH][TFA] ion-pairs, as detected in the DR spectra. Yet, temperature dependent ^{1}H-NMR linewidths of the acidic proton signals suggest proton exchange to occur on the NMR timescale, presumably between [MimH][+] and [Mim]. Conversely, in MeOH we find no evidence for the presence of ion-pairs, while the high conductivity of these solutions shows that MeOH can efficiently solvate ions and may participate in proton transfer. Together, our results highlight the sensitivity of protonation equilibria to the immediate environment and of proton dynamics to these protonation equilibria. Our results show that tuning these equilibria using PIL mixtures can provide routes to tailor the contribution of proton transport to charge transport in PILs.

1. Introduction

Over the last decades ionic liquids (ILs) have attracted substantial interest due to their unique properties, such as their high thermal stability, low vapor pressure, and large electrochemical window.[1–6] Consisting solely of ionic species with a melting point below 100 °C, ILs are also known as molten salts. The almost unlimited number of possible

combinations of cations and anions that form ILs leads to vast structural variations and widely tunable properties.[7–9] Therefore ILs are a promising material class for diverse applications, such as green solvents in synthesis,[2,10] pharmaceutical ingredients,[11–13] or electrolytes for fuel cells and batteries.[4,14–18] However, low ionic conductivities due to high viscosities of aprotic ionic liquids limit possible applications in e.g. energy-storage technologies.[19] In principle, protic ionic liquids

(PILs) could overcome these limitations,[20] as PILs form via reversible proton transfer between Brønsted acids and Brønsted bases.[21] Due to such proton transfer equilibria, PILs can form extended hydrogen-bonded networks,[22–25] and it is possible to decouple charge transport from the (slow) diffusive mass transport to enable high ionic conductivities.[8].

Although several studies have attempted to elucidate the underlying molecular-level dynamics and proton distributions, charge transport in PILs is not yet fully understood.[26–30] One prominent example for a PIL is 1–methylimidazolium acetate [MimH][AcO]. Previous studies have suggested that [MimH][AcO] consists predominantly of neutral species as the acidity of acetic acid is moderately low: Raman and potentiometric measurements have suggested that neutral species, acetic acid ([AcOH]) and 1–methylimidazolium ([Mim]), dominate in [MimH][AcO].[26,31] Consistent with this notion, molecular dynamics (MD) simulations with a 30 % degree of protonation could reproduce experimental dynamics.[32] The low degree of protonation has been further supported by density functional theory calculations, which have shown that a complex of the neutral species is more stable than a pair of charged molecules.[26] These studies have further suggested that the environment, such as the continuum solvent used for the computations, can facilitate proton transfer and shift protonation equilibria towards ion-pairs.[26] Yet, for other acid base mixtures NMR experiments have revealed a continuous transition between these extreme scenarios, hydrogen-bonded neutral species and ion-paired charged molecules. [33,34] This may explain why the ^{1}H-NMR experiments on [MimH] [AcO] have suggested that more than 90 % of [Mim] is protonated [35,36] with a marked decrease in ionicity upon addition of polar solvents, such as dimethylsulfoxide.[36] Altogether, these previous studies point towards the protonation states of [MimH][AcO] being very sensitive to various factors. As such, thermal fluctuations could give rise to fluctuations in the protonation states and consequently to a marked contribution of proton transfer to the overall conductivity. In fact, the relatively high ionic conductivity of [MimH][AcO] seems to support this notion[21,26,37] and comparison of the activation energies for translational and rotational diffusion has indicated that a Grotthuss-like charge transport takes place in [MimH][AcO].[38] It has been further suggested that increasing the acidity of the anion by replacing acetic acid by trifluoroacetic acid, results in a shift of the protonation equilibria to the fully protonated species, which goes along with a change in the proton conduction mechanism from proton hopping to vehicle transport.[39] Yet, experimentally information on proton transport in these PILs has been only indirectly inferred. Molecular dynamics simulations can directly visualize proton transport and it has been shown that a multitude of proton transfer channels exist in [MimH][AcO].[37] Yet, to allow for proton mobilities that markedly exceed the mobilities of the ionic species, cf. Grotthuss-type conduction, chain-like structures of neutral acetic acids are required.[37] Therefore, the conductivity of the PIL relies on the subtle balance between charged and neutral species, which can act as proton donors and acceptors. The sensitivity of conductivity to this balance implies that the transport properties can be tuned by altering the ratio of charged and electro-neutral species, which can be readily tuned via variation of the acidity of the Brønsted acid.

Here, we explore the effect of this balance on the transport properties, by studying mixtures of partly ionized [MimH][AcO], and 1–methylimidazolium trifluoroacetate ([MimH][TFA]) with a high ionicity.[39] We explore the dynamics in these mixtures using DR spectroscopy, which can detect the dynamics of dipolar species, in particular ion-pairs.[40,41] Additionally, DR spectroscopy provides information on the mobility of ions via the conductivity.[42,43] We complement this information using NMR, which can reveal information about structure and dynamics of the investigated ionic liquids. In particular, the ^{15}N chemical shifts provide information on the degree of protonation of the Brønsted base and diffusion ordered spectroscopy (DOSY) allows for assessing molecular mobilities. The combination of both experimental techniques provides the average proton distribution

in equilibrium and their dynamics and allows for gaining insight into the charge transport in these PILs. We study the neat PIL mixtures and explore the influence of the chemical environment on the PIL mixtures using protic and aprotic solvents. Our results demonstrate that increasing acidity of the Brønsted acid increases the iconicity and may result in decoupling of the proton transport from ionic diffusion. Our results further indicate that in aprotic dimethylformamide, aggregation of the PIL is enhanced resulting in a reduction of the conductivity. In turn, addition of the protic solvent methanol suppresses the formation of electro-neutral aggregates resulting in a marked enhancement of the conductivity.

2. Materials and Methods

2.1. Materials

1–methylimidazole (Mim, 99 %, ACROS), acetic acid, (AcOH, > 99.5 %, Alfa Aesar), and trifluoroacetic acid (99.5 %, VWR) were purified via distillation prior to use. All substances were stored and handled in an Ar-filled glovebox. 1–methylimidazolium acetate [MimH][AcO] and 1–methylimidazolium trifluoroacetate [MimH][TFA] were synthesized by stepwise addition of small portions of acetic acid and trifluoroacetic acid, respectively, to Mim under a nitrogen atmosphere to obtain an equimolar ratio of both reactants. The reaction mixture was cooled using an ice bath to avoid evaporation. After complete addition of the acid, the reaction solution was stirred at 65 °C under reflux for 6 h. The products [MimH][AcO] and [MimH][TFA] were stored in an Ar-filled glove box. The products were characterized by ^{1}H- & ^{13}C-NMR-spectroscopy (Figures S1 – S5, Supporting Information, SI).

N,N-dimethylacetamide (DMA, VWR, 99 %) and *N,N*-dimethylformamide (DMF, ACROS, 99.8 %), used for calibration of the dielectric reflectometer and for preparation of the IL solutions, were used without further purification. Methanol (MeOH, VWR, HPLC gradient grade) was dried over molecular sieve (3 Å) prior to use. Deuterated solvents, methanol-d_4 and dimethylsulfoxide-d_6 (DMSO-d_6, 99.95%) were purchased from Deutero GmbH and *N,N*-Dimethylformamide-d_7 (DMF-d_7, > 99.5 %) from Sigma Aldrich. Deuterated NMR solvents for preparation of the RTIL solutions (DMF-d_7, MeOH-d_4) were dried over molecular sieves (4 Å).

To study the effect of the acidity of the Brønsted acid we prepared [MimH][AcO]/[MimH][TFA] mixtures with molar fractions of [MimH] [AcO] $\chi(\text{Ac}) = 0 - 1$ at increments of 0.1 by weight using an analytical balance. We found [MimH][TFA] to be solid at room temperature, consistent with a reported melting point of $\sim 338 \, \text{K},$[31] although other studies,[44,45] based on synthetic routes involving water-containing reaction mixtures, have suggested [MimH][TFA] to be liquid at room temperature.[44,45] Also [MimH][AcO]/[MimH][TFA] mixtures were partly solid at room temperature, which limited the composition range for the [MimH][AcO]/[MimH][TFA] mixtures to mole fractions of acetate, $\chi(\text{Ac}) \leq 0.6$. For [MimH][AcO]/[MimH][TFA] dissolved in DMF and MeOH at a constant total ionic liquid concentration of 1 M, we studied the entire composition range $\chi(\text{Ac}) = 0 - 1$. These solutions were prepared by weighing the appropriate amounts of [MimH][AcO] and [MimH][TFA] into volumetric flasks and adding the respective solvent.

2.2. Dielectric relaxation spectroscopy (DRS)

The dielectric spectra were measured as a function of field frequency, ν, with a vector network analyzer (Anritsu MS4647A) using the signal reflected from coaxial probes. Frequencies at $0.13 \leq \nu/\text{GHz} \leq 9.5$ and at $9.5 \leq \nu/\text{GHz} \leq 54$ were covered using open-ended coaxial probes based on 1.85 mm and SMA connectors.[46,47] Frequencies at $54 \leq \nu/\text{GHz} \leq 125$ were covered using an open-ended probe, connected to an external frequency convertor (Anritsu 3744A mmW) via 1 mm connectors.[48] The sample temperature was controlled to 298 K by placing the sample

in a silicon oil bath, connected to a thermostat (Julabo F12-ED). The reflection coefficient at the coaxial-probe/sample interface was calibrated using air, conductive silver paint, and a third calibration standard (DMA for neat PILs, DMF and MeOH for PILs in solution).[49,50]

2.3. NMR

To monitor the composition of the synthesized PILs, ^{1}H- & ^{13}C-NMR spectra of the PILs in CDCl$_3$ were acquired using a Bruker 300 MHz AVANCE III spectrometer. Proton experiments were measured with 16 scans and a recycle delay of 1 s. Carbon experiments were measured with 1024 scans and a recycle delay of 2 s. [1]H spectra were referenced to the signal of residual CHCl$_3$ at 7.26 ppm.[51] Signals at 77.1 ppm in the ^{13}C spectra were assigned to CDCl$_3$.[51]

Diffusion ordered and temperature dependent ^{1}H-NMR spectra were recorded using a Bruker 700 MHz Avance III spectrometer equipped with a four channel inverse detection probe head (QXI:[1]H, ^{19}F, ^{13}C, ^{15}N). Proton single pulse spectra were measured with 8 scans and a recycle delay of 8 s. DOSY experiments were performed using a bipolar gradient stimulated echo pulse sequence with simultaneous ^{19}F depolarization in order to reduce transient heteronuclear nuclear Overhauser phenomena in TFA containing samples. Each DOSY measurement consists of 32 PFG-SE experiments with a linear variation of the gradient strength, 16 scans per experiment, and a recycle delay of 8 s. For field locking and shimming of the spectrometer, a capillary containing DMSO-d_6 was added to the NMR tube and the ^{1}H spectra were referenced to the signal of residual DMSO-d$_5$h$_1$[51] at 2.54 ppm.

To determine chemical shifts of the rare ^{15}N nuclei, ^{1}H-^{15}N–HMBC-NMR spectra were acquired using a Bruker 850 MHz spectrometer equipped with a four channel inverse detection (QXI: [1]H, ^{31}P, ^{13}C, ^{15}N) probe head with pulsed z-gradients of 0.5 T/m. ^{1}H-^{15}N–HMBC-NMR spectra were acquired with 16 scans, 256 increments in the indirect dimension, and a recycle delay of 1.5 s. The ^{15}N chemical shift values δ were referenced to the external reference nitromethane.

2.4. Auxiliary measurements

Sample viscosities were determined using a ball viscometer (Anton Paar, Lovis 2000 M) with a measurement distance of 99.88 mm in a capillary with a diameter of 1.59 mm. To determine molar concentrations of TFA, c_{TFA}, acetic acid, c_{Ac}, and Mim, c_{Mim}, sample densities for all liquid PIL mixtures at 25 °C were determined using a DM40 density meter (Mettler Toledo).

2.5. DFT calculations

Electrical dipole moments were calculated using density functional theory (DFT) with the ORCA program package (version 4.0.1.2).[52] Geometry optimizations were performed at the B3LYP[53,54]/def2-TZVP[55] level of theory. Closed-shell self-consistent field calculations were set to tight convergence. All calculations were performed using a conductor-like polarizable continuum model assuming the dielectric properties of dichloromethane as representative for the liquid environment. We note that the effect of the exact value of the permittivity of the medium on the calculated dipole moments is negligible (see SI). To directly compare dipole moments of ionic species to the relaxation strengths of DR experiments, the center of charge should be at the pivot. While for rotation in the gas-phase the center of mass is the appropriate pivot, in the liquid phase frictional forces govern molecular motion and the center of hydrodynamic stress is the appropriate reference point. [56,57] We approximate the center of hydrodynamic stress by the centroid ($\sum_{i=1..k} x_i/k$, with x_i the coordinates of all k atoms of an ion). The dipole moments were calculated using the optimized atomic coordinates and the CHELPG[58,59] charges of the atoms. Dipole moments calculated based on the different centers of charge and based on the full electron density with the center of mass as center of charge are

compared in the SI (Table S1). Optimized geometries are shown in Figure S6 (see SI).

3. Results and discussion

In this work we study the effect of the protonation state of the PIL and of the addition of solvents on the dynamics and transport properties of methylimidazolium based PILs. To systematically vary the protonation state of Mim, that is the ratio [Mim]/[MimH]$^+$, we vary the acidity of the Brønsted acid by studying binary mixtures of [MimH][AcO] and [MimH][TFA].[60] To elucidate the effect of added solvent, we investigate the dynamics of [MimH][AcO]/[MimH][TFA] mixtures in the aprotic solvent DMF, which barely dilutes the acid/base molecules, and in MeOH, which can act as proton acceptor and donor and can therefore contribute to a Grotthuss-type proton conduction.[61] The paper is structured as follows: we first study the dynamics using DR spectroscopy to obtain insights into ions' translational and dipolar rotational dynamics.[62–64] Secondly, we use NMR chemical shift experiments to deduce the protonation state,[65] diffusion ordered NMR spectroscopy to detect correlations between the mobility of the individual molecular species,[66] and the NMR linewidths to evidence chemical (proton-) exchange. We conclude with the joint discussion of the findings.

3.1. Dielectric relaxation spectroscopy

3.1.1. Neat PIL mixtures

To investigate the impact of TFA on the dipolar response and the conductivity of the ionic liquid mixtures we use DR spectroscopy, which probes the macroscopic polarization dynamics of a sample as a response to an externally applied oscillating electric field. The measured polarization is usually expressed as complex permittivity $\widehat{\varepsilon}(\nu)$: [63].

$$\widehat{\varepsilon}(\nu) = \varepsilon'(\nu) - i\varepsilon''(\nu) + \frac{\kappa}{2\pi i \nu \varepsilon_0} \tag{1}$$

With the real part $\varepsilon'(\nu)$ representing the dielectric permittivity and the imaginary part $\varepsilon''(\nu)$ representing the dielectric loss. The last term of equation (1) accounts for the contribution of translational dynamics of charged molecules, typically expressed in terms of the conductivity. Here, we assume the conductivity, κ, to be real and independent of frequency (i.e. the d.c. conductivity). ε_0 is the permittivity of free space. Typically, polarization dynamics due to rotation of dipolar species (e.g. dipolar molecules or ion-pairs) give rise to dispersions in $\varepsilon'(\nu)$ and peaks in $\varepsilon''(\nu)$. We note that by assuming κ to be constant and real, $\varepsilon'(\nu) - i\varepsilon''(\nu)$ contains all frequency dependent polarization dynamics, irrespective of being due to ion translations or dipolar rotations. As such, also a frequency dependent conductivity (e.g. due to spatially confined translation of ions) will contribute to $\varepsilon'(\nu) - i\varepsilon''(\nu)$. In fact, molecular dynamics simulations have suggested that ions' translations contribute to the polarization response of ionic liquids. Yet, for ionic liquids with small, rather spherical ions these translational dynamics are minor at MHz-GHz frequencies and this spectral window is dominated by dipolar rotations.[62,67] For less spherical ions – such as acetate containing ionic liquids – MD simulations have suggested that translational and rotational contributions can be similar in magnitude [32]. Yet, the separation of translational and rotational contributions depends on the choice of the center of charge and the center of mass is typically assumed as pivot (see also Methods section) in MD analysis. For diffusive rotation with the center of hydrodynamic stress as pivot, the balance between translational and rotational contributions differs and our calculated dipole moments suggest that rotational contributions are underestimated (translational contributions are overestimated) in particular for the acetate anion, where center of mass and center of hydrodynamic stress markedly differ (see Table S1, SI). Neglecting translational contributions, the magnitude of the dielectric amplitudes of the $\varepsilon'(\nu) - i\varepsilon''(\nu)$ spectra is a measure for the density and magnitude of dipoles in the samples, while the conductivity κ reports on the number density and

mobility of mobile charges (i.e. ions).

In Fig. 1(a) we show the dielectric spectra for the [MimH][AcO]/[MimH][TFA] mixtures at 298 K. As commonly observed for ionic liquids,[43,68] the spectra appear rather broad and featureless. Consistent, with earlier studies,[38,39] the spectrum of [MimH][AcO] is dominated by a loss peak centered at ∼ 0.5 GHz, which is asymmetrically broadened towards higher frequencies. With increasing TFA content, the magnitude of this relaxation at ∼ 0.5 GHz decreases, whereas the spectral range at > 10 GHz is rather insensitive to an increased fraction of TFA. Additionally, the frequency of the peak maximum of the imaginary part somewhat shifts to lower frequencies. We note that we observe similar trends at an elevated temperature of 333 K, at which the samples are liquid over a wider composition range (except $\chi(Ac) < 0.2$, see SI, Figure S7).

To quantify these changes to the spectra, we use a relaxation model consisting of three relaxation modes:

$$\widehat{\varepsilon}(\nu) = \frac{S_1}{1+(2\pi i\nu\tau_1)} + \frac{S_2}{1+(2\pi i\nu\tau_2)} + \frac{S_3}{1+(2\pi i\nu\tau_3)} + \varepsilon_\infty + \frac{\kappa}{2\pi i\nu\varepsilon_0} \quad (2)$$

With S_j and τ_j representing the relaxation amplitudes and relaxation times, respectively. The high frequency limit of the permittivity, ε_∞, contains all polarization dynamics, which are not accessible in the frequency range covered in this work. From these fits we find the three relaxations to be centered at ∼ 0.5 GHz, at ∼ 4 GHz, and ∼ 25 GHz (fit parameters are listed in Table S2, SI). Previous work on ionic liquids indicated that the lower frequency relaxations can be predominantly ascribed to cation reorientation, while the intermediate relaxations predominantly originate from the rotation of dipolar anions,[43,69,70]

which is also in broad agreement with what has been found for different ionic liquids based on molecular dynamics simulations.[62] Yet, given the complexity of the present samples with anticipated contributions from different anions, electro-neutral acids, protonated cations ([MimH]$^+$) and electro-neutral [Mim], such assignment is challenging for the present mixtures. Therefore, we consider the relaxation model merely as a formal description of the experimental spectra and only discuss the overall trends in relaxation parameters: We calculate the total relaxation amplitude $S_{tot} = \sum_{i=1}^{3} S_i$, that represents the strength of all relaxation dynamics in the PILs, and the amplitude-weighted average relaxation time $\tau_{tot} = \sum_{i=1}^{3} S_i\tau_i / \sum_{i=1}^{3} S_i$, which are shown in Fig. 1(b). The relaxation times τ_{tot} are somewhat insensitive to the addition of TFA with a minor decrease with increasing mole fraction of TFA, which is indicative of an acceleration of the overall dynamics. For diffusive rotational relaxation of uncorrelated molecules, this relaxation is expected to scale with the molar volume of the rotating species and the samples' microscopic viscosity.[71] Given the comparable molecular volume of all molecular species ([Mim], [MimH]$^+$, [AcO]$^-$, [AcOH], and [TFA]$^-$) and the increasing viscosity (Fig. 1(d)) with increasing molar fraction of TFA, the insensitivity of τ_{tot} to $\chi(Ac)$ may be surprising. However, the data in Fig. 1(b) point at correlated dynamics within the PILs (see below): for correlated dynamics, dipole–dipole correlations can markedly alter the observed relaxation time.[72] The presence of such correlations is consistent with the hydrogen-bonded structure of the PILs and upon addition of [MimH][TFA] breaking of the hydrogen-bonded structure results in altered (reduced) dynamic correlations of the molecular dynamics.

As already apparent from the raw spectra in Fig. 1(a), the total
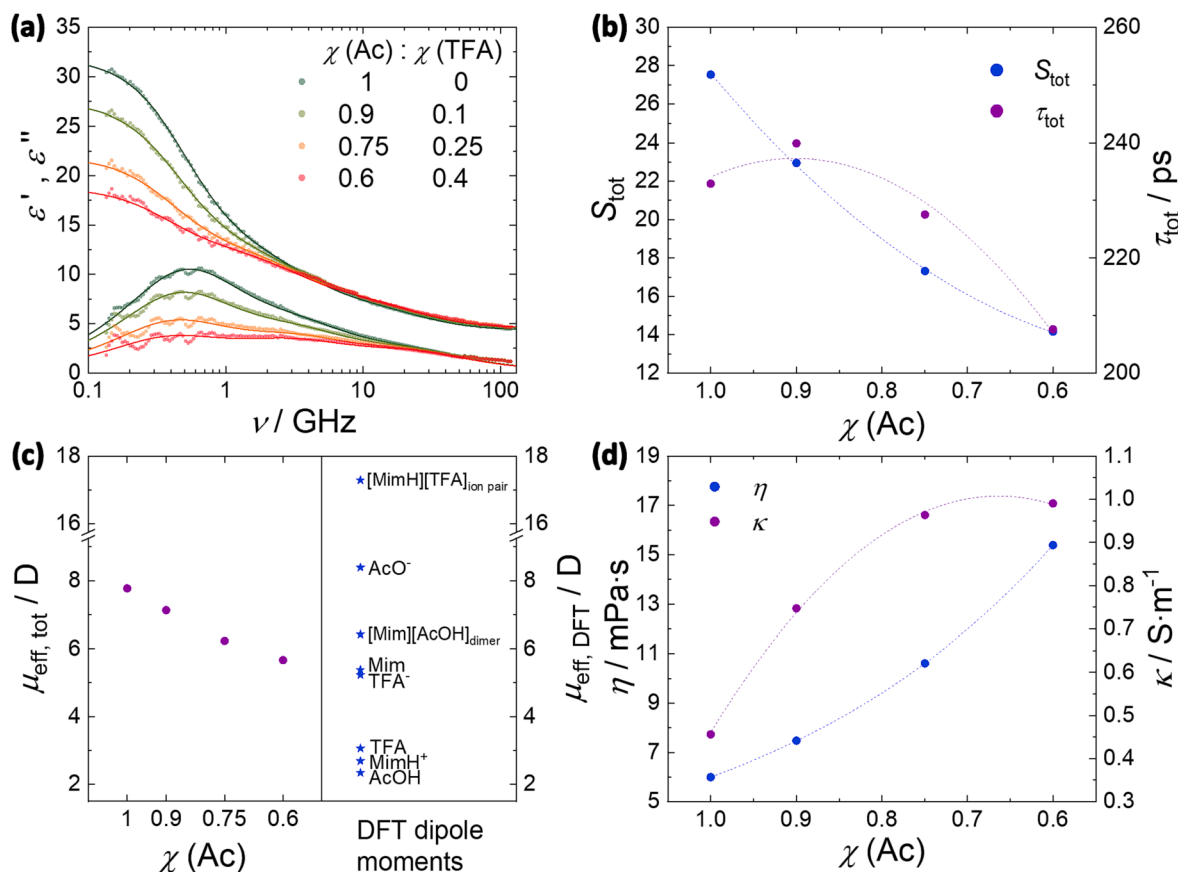
Fig. 1. (a) Complex permittivity spectra of neat PIL mixtures at 298 K. Symbols show experimental data, solid lines represent the fits of equation (2) to the data. Note the last terms of equations (1) and (2) have been subtracted for visual clarity. (b) Total relaxation amplitude, S_{tot}, and amplitude-weighted relaxation time τ_{tot} as a function of $\chi(Ac)$. Symbols represent parameters from the fit, dotted lines are a guide to the eye. (c) Left: total effective dipole moment $\mu_{eff, tot}$, obtained from experimental total amplitudes S_{tot} as a function of $\chi(Ac)$. Right: Molecular dipole moments based on DFT calculations. For ionic species the centroid is taken as the center of charge. (d) Viscosity η and dc conductivity κ as a function of $\chi(Ac)$. Symbols represent experimental data, dotted lines are a guide to the eye.

relaxation strength, S_{tot}, decreases with increasing TFA content (Fig. 1 (b)). Assuming only a single dipolar species giving rise to the observed relaxation dynamics, the dielectric amplitude S_j can be related to the effective dipole moment $\mu_{eff, j}$ of this species and its concentration c via [73]:

$$\frac{2\varepsilon_s + 1}{\varepsilon_s} S_j = \frac{N_A c_j}{k_B T \varepsilon_0} \mu_{eff, j}^2 \qquad (3)$$

where is $\varepsilon_s = S_{tot} + \varepsilon_\infty$, N_A the Avogadro constant, k_B the Boltzmann constant, and T the thermodynamic temperature. To relate the dipolar response to the dipole moment of molecular species, without discriminating between the individual molecular species, we calculate the total electrical dipole moment $\mu_{eff, tot}$, from S_{tot} by assuming $c_{tot} = c_{Mim} + c_{Ac} + c_{TFA}$, as determined from the sample compositions and the measured density. We note that this approach exclusively assumes dipolar contributions to the spectra and neglects translational polarization dynamics.

We find $\mu_{eff, tot}$ to decrease from ~ 8 D for $\chi(Ac) = 1$ to ~ 5.5 D for $\chi(Ac) = 0.6$ as $\chi(Ac)$ decreases (Fig. 1(c)). Similar trends are observed, when restricting the analysis to the lowest frequency relaxation (see Figure S8, SI). The DFT-calculated dipole moments $\mu_{eff, DFT}$ of the individual electro-neutral or ionic molecules range from 2.34 D for [AcOH] to 8.39 D for [AcO]$^-$ (Fig. 1(c)). The calculated dipole moments are listed in Table S1 (see SI) and the optimized molecular geometries are displayed in Figure S6 (see SI). The comparison of the calculated values to $\mu_{eff, tot}$ indicates that the $\mu_{eff, DFT}$ values of the individual molecular species are closer to the experimental values than those of the dimers, hence, rotational contribution of acid-base dimers to the spectra are rendered unlikely. It is worth noting, that the DFT calculations suggest that for two limiting cases that substitution of AcOH by TFA does (i) not alter the overall ionicity or (ii) TFA is fully ionized an moderately decreasing or constant $\mu_{eff, tot}$ would be expected if the observed relaxations are due to uncorrelated ionic/molecular rotations: For scenario (i) a moderate decrease of $\mu_{eff, tot}$ with decreasing $\chi(Ac)$ would be expected, as $\mu_{eff, DFT}([TFA]^-) \langle \mu_{eff, DFT}([AcO]^-)$ and $\mu_{eff, DFT}([TFA]) > \mu_{eff, DFT}([AcOH])$. This decrease would be consistent with the experimentally observed decrease of $\mu_{eff, tot}$, however, given the significant difference in acidities of AcOH (pK_a of 4.75) and TFA (pK_a of 0.5), constant iconicity seems rather unlikely. In scenario (ii) $\mu_{eff, tot}$ should be rather independent of TFA content, as $\mu_{eff, DFT}([MimH]^+) \approx \mu_{eff, DFT}([AcOH])$ and $\mu_{eff, DFT}([Mim]) \approx \mu_{eff, DFT}([TFA]^-)$. As such, this simplified consideration of only isolated dipoles with their dipole moments estimated from DFT calculations giving rise to the experimental dielectric response cannot explain the observed decrease of $\mu_{eff, tot}$ with decreasing $\chi(Ac)$. In turn, the higher values of $\mu_{eff, tot}$ relative to $\mu_{eff, DFT}$ of the individual molecular species may point to the presence of dynamic correlations to $\mu_{eff, tot}$. In this case, the decreasing $\mu_{eff, tot}$ with decreasing $\chi(Ac)$ can be rationalized by a TFA induced reduction of the dipolar correlations, e.g. TFA weakens the correlations imposed by the hydrogen-bonded structure of [MimH][AcO]. Yet, also translational contributions to the observed dynamics may explain these differences and molecular dynamics simulations would be required to fully disentangle these different contributions.

Remarkably, the determined conductivities indicate that, despite the increase of the viscosity with increasing TFA content (Fig. 1(d)), κ markedly increases. In light of previous studies,[21,26,37] which indicate that in neat [MimH][AcO] neutral species ([Mim] and [AcOH]) dominate and form an extended hydrogen-bonded network, the observed increase of conductivity can be explained by an increasing fraction of ionic species upon substitution of AcOH by TFA: Based on the higher acidity of TFA with a pK_a of 0.5 as compared to the weaker acid acetic acid with a pK_a of 4.75 the fraction of ions in the PIL mixtures is expected to increase with addition of TFA.[31] Apparently, the increasing ion density can outnumber the viscosity induced decrease in

the ions' mobility. Yet, also a contribution of more mobile charge carriers (e.g. Grotthuss-type transport of protons) may contribute to the observed increase in conductance.

3.1.2. PILs in solution

We proceed with discussion of the dielectric response of 1 M [MimH] [AcO]/[MimH][TFA] in DMF, for which effects of altered viscosities are reduced. The dielectric spectra for [MimH][AcO]/[MimH][TFA] mixtures in DMF in Fig. 2(a) are dominated by a relaxation centered at ~ 15 GHz, which can be assigned to the orientational relaxation of DMF.[49] For $\chi(Ac) = 1$ the experimental spectra of the PIL solution are shifted to lower frequencies, as compared to neat DMF, and also appear asymmetrically broadened (see Fig. 2(a)).[49] With decreasing $\chi(Ac)$ a contribution at low frequencies (~1.5 GHz) emerges, indicative of the formation of dipolar species. To quantify these spectral contributions, we use a combination of two Debye-type relaxations, to model the dominant DMF relaxation and the lower-frequency dynamics associated with the PIL:

$$\widehat{\varepsilon}(\nu) = \frac{S_{PIL}}{1 + (2\pi i \nu \tau_{PIL})} + \frac{S_{DMF}}{1 + (2\pi i \nu \tau_{DMF})} + \varepsilon_\infty + \frac{\kappa}{2\pi i \nu \varepsilon_0} \qquad (4)$$

with S_{PIL} and τ_{PIL} the relaxation strength and time of the lower frequency relaxation, respectively. S_{DMF} and τ_{DMF} are the strength and time of the higher frequency relaxation. Given the similarity of the relaxation parameters of the higher frequency relaxation to those of neat DMF we assign this relaxation to be dominated by the orientational dynamics of DMF (fit parameters are listed in Table S3, SI). Conversely, the lower frequency relaxation is attributed to stem from the PIL. We note that these fits somewhat deviate from the experimental data at higher frequencies (Fig. 2(a)), which is presumably due to an additional fast relaxation process, which is also present in neat DMF,[49] yet not fully covered by the present frequency range.

In all mixtures we find τ_{DMF} to be longer than in neat DMF[49] (Fig. 2 (a)) and, τ_{DMF} slightly increases with decreasing $\chi(Ac)$. This minor slow-down in orientational dynamics of the DMF molecules can most likely be attributed to an increase in viscosity due to the addition of PIL and decreasing $\chi(Ac)$, respectively. In accordance with equation (3), the decrease in amplitude S_{DMF} compared to S_{DMF} in neat DMF[49] is due to the lower concentration of DMF molecules and kinetic depolarization [74,75] in the solutions of the PILs.

The parameters of the lower frequency relaxation allow for obtaining information on the state of the PIL in the solvent. The relaxation time τ_{PIL}, which is associated with the dynamics of the PIL solute, increases with decreasing $\chi(Ac)$, which points towards an increase of the samples' viscosities or to an increase in the molecular volume of the underlying dipolar species with increasing TFA content (Fig. 2(b)). To elucidate the underlying molecular species, we calculate from the relaxation strengths S_{PIL}, which also gradually increase with decreasing $\chi(Ac)$ (Fig. 2(b)), the corresponding effective dipole moment $\mu_{eff, PIL}$ (eq (3), $c_{PIL} = c_{Mim} = c_{Ac} + c_{TFA}$), which also exhibits a marked and gradual increase with decreasing $\chi(Ac)$. For $\chi(Ac) = 0$ the thus obtained value of $\mu_{eff, PIL} \approx 20$ D is close the dipole moment for an isolated [MimH][TFA] ion-pair of ~ 17 D as obtained from the DFT calculations (see Fig. 1(c)). As such, our results suggest that at high TFA concentrations, ion-pairs are the dominant underlying molecular level species. Conversely, at $\chi(Ac) = 1$ $\mu_{eff, PIL}$ is twice as high as the calculated value for a hydrogen-bonded [Mim][AcOH] dimer (see Fig. 1(c)). The observation that the experimental dipole moment exceeds the value expected for a hydrogen-bonded [Mim][AcOH] dimer suggests that also for $\chi(Ac) = 1$ ion-pairs (with markedly higher dipole moments) partially exist, in line with the partially ionized character of neat [Mim][AcOH]. Yet also other molecular aggregates such as acetic acid selfdimers[76–78] (with distorted symmetry) or larger aggregates consisting of multiple acetic acid molecules and a [Mim] base,[79] which allow for a larger charge separation and thus result in higher dipole moments, may be formed. In this context it is important to note that the samples conductivity at $\chi(Ac) = 1$
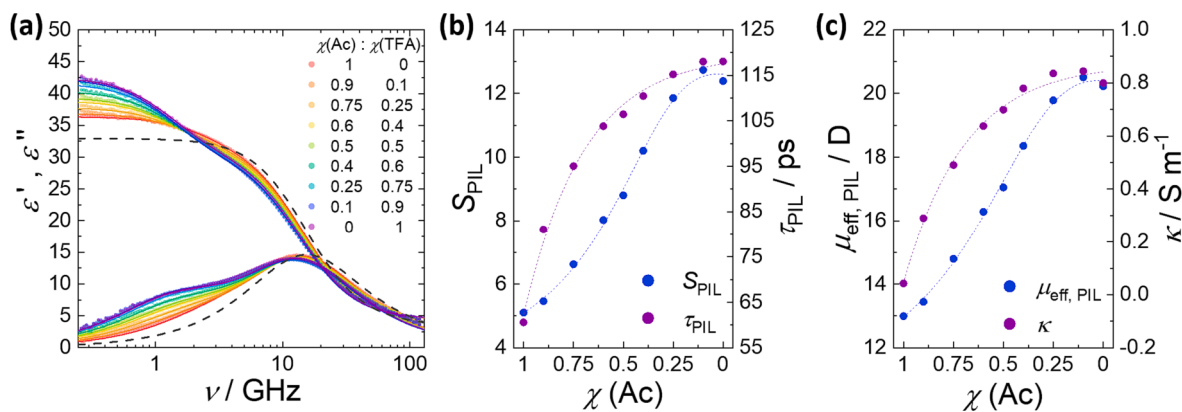
Fig. 2. (a) Complex permittivity spectra of PIL mixtures (1 M) in DMF at 298 K. Symbols represent experimental data, solid lines represent the fit (eq. (4)). The grey dotted line represents the literature spectrum of DMF,[49] scaled by a factor of 0.88. For visual clarity the Ohmic loss (last term of equation (2) & (4)) has been subtracted. (b) Dielectric amplitude S_{PIL} and relaxation times τ_{PIL} of the PIL relaxation (low frequency mode) as a function of the composition of the PIL mixture. Dotted lines are a guide to the eye. (c) Effective PIL dipole moment $\mu_{eff, PIL}$ calculated from S_{PIL} and dc conductivity κ of PILs in DMF as a function of $\chi(Ac)$. Dotted line is a guide to the eye.

is negligibly small, which demonstrates that aggregates in solution are predominantly electro-neutral (see Fig. 2(c)). With decreasing $\chi(Ac)$ the conductance increases (see Fig. 2(c)), demonstrating that in the presence of TFA mobile ions are partially present.

Conversely, the trends of the dielectric spectra of the PIL mixtures in hydrogen-bonding MeOH (Fig. 3(a)), differ from the trends of the PILs in DMF: Irrespective of PIL composition, the experimental spectra are dominated by a relaxation centered at ~ 3 GHz, similar to the spectrum of neat MeOH.[80] While the overall spectral amplitude decreases with decreasing $\chi(Ac)$, the shape of the spectra is rather insensitive to the PIL composition. To quantify the spectral contributions, we model the spectra using a combination of three Debye-type relaxation modes (eq. (2), analogously to the neat PIL mixtures and to the spectra for neat MeOH.[80].

A relaxation mode at low frequencies associated to PIL species can be fitted to the experimental spectra (Table S4, see SI). As this PIL relaxation overlaps with the MeOH relaxation (~3 GHz) resolving[81] the PIL contribution is challenging and correlations of the fit parameters of the two overlapping modes does not allow for a meaningful interpretation. [81] Therefore, we determine the total relaxation amplitude S_{tot}, representing contributions of both MeOH and PIL species to the dielectric spectra, and the amplitude weighted average relaxation time τ_{tot} from the obtained parameters (see Fig. 3(b), parameters are listed in Table S4, SI). The value of τ_{tot} represents the amplitude weighted average of both,

PIL relaxations and methanol relaxations and is therefore lower than τ_{PIL} found for mixtures with DMF, which is associated with PIL dynamics. As already apparent from the insensitivity of the spectral shape of the raw spectra to $\chi(Ac)$, the overall dynamics as determined from τ_{tot} hardly vary with PIL composition and only moderately increase at high TFA concentrations. This is further supported by the normalized dielectric loss spectra (see SI, Figure S9), which confirm that the spectral shape does not vary with composition. As such, the data show that the characteristic timescales of the PILs' (and methanol) contributions to the spectra do not drastically change with PIL composition.

The total dielectric amplitude S_{tot} markedly decreases with decreasing $\chi(Ac)$. Such decrease, commonly referred to as depolarization, can have different origins, including dilution of dipoles, solvation, and kinetic depolarization.[74,75] For the present samples, kinetic depolarization – the coupling between (ionic) translational currents and (dipolar) rotational currents – can quantitatively describe the reduction of S_{tot} as a function of $\chi(Ac)$ (see SI, Figure S10). The fact that the experimental decrement agrees with the reduction due to the expected kinetic dielectric decrement for MeOH implies that the dynamic correlations of MeOH[82] are little affected by the PIL. This may be somewhat surprising as such correlations can be readily reduced by ions.[83] Most importantly, the experimental amplitude S_{tot} differs by a constant offset from the amplitude estimated for the contribution of methanol, corrected for kinetic depolarization (see SI, Figure S10). This constant
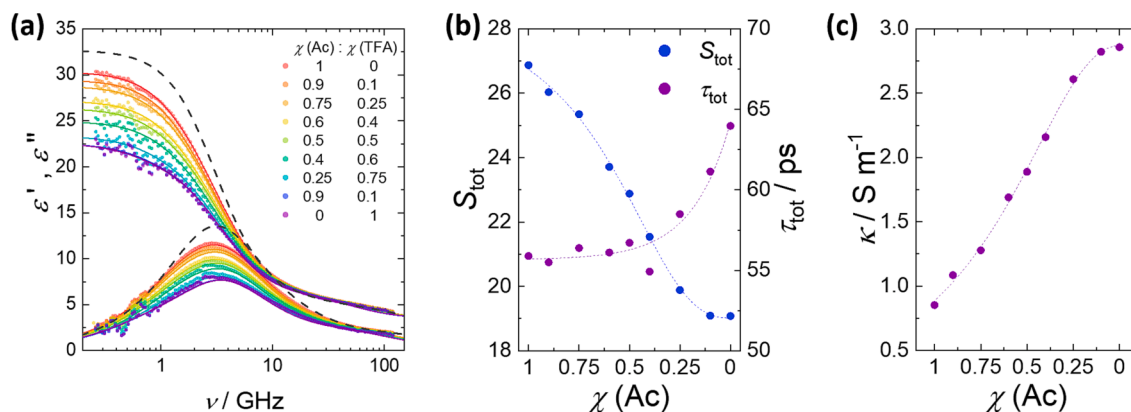
Fig. 3. (a) Complex permittivity spectra of PIL mixtures (1 M) in MeOH at 298 K. Symbols represent experimental data, solid lines represent the fit. The grey dashed line represents the spectrum of MeOH, taken from ref.[80], scaled by a factor of 0.95. (b) Total dielectric amplitude S_{tot} and relaxation times τ_{tot} as a function of the composition of PIL mixture. Symbols represent parameters from the fit, dotted lines are a guide to the eye. (c) dc conductivity κ of PILs in MeOH as a function of the composition. Symbols represent parameters from the fit, dotted lines are a guide to the eye.

offset – irrespective of χ(Ac) – demonstrates that contributions of the PIL to the total amplitude do not vary with PIL composition. As such the underlying dipolar species (e.g. ions, electro-neutral species, ion-pairs, …) giving rise to the PILs' contributions do not vary with χ(Ac). Hence, and in contrast to our findings for solutions in DMF, we find no evidence for a transition from the presence of isolated molecules/ions to the formation of highly dipolar ion-pairs in MeOH.

Despite the negligible effect of the PIL mixtures on the dipolar dynamics of MeOH, the conductance of the PILs in MeOH (Fig. 3(c)) exceeds the conductivity of the neat PIL mixtures (Fig. 1(d)) and of the PIL solutions in DMF (Fig. 2(c)). This elevated conductivity demonstrates the presence of mobile charge carriers in the solutions and the increase of κ with decreasing χ(Ac) (Fig. 3(c)) suggests that the number density of these charge carriers increases upon substitution of AcOH by TFA. This trend may be explained by an increasing formation of ionic species, e.g. increasing protonation of [Mim] upon addition of TFA but could also stem from MeOH forming together with [Mim] and TFA an extended hydrogen-bonded network allowing for a Grotthuss-type charge transport in solution. Conversely, in the mixtures with DMF such Grotthuss-type transport is not possible and the macroscopic conductivity is reduced (as compared to the neat PILs, Fig. 1(d)) and vanishes for solutions of [MimH][AcO] (Fig. 2(c)). Irrespective of the exact molecular-level conduction mechanism, comparison of the neat PIL mixtures and the PILs dissolved in DMF and MeOH demonstrates that the immediate environment of the PIL, like the nature of the solvent, can profoundly affect protonation equilibria and – possibly – proton transport within the PIL.

3.2. NMR experiments

3.2.1. ^{15}N chemical shift

To further elucidate the contribution of ions and protons to charge transport in the PILs and their mixtures we investigate the protonation state of the [Mim] base in these samples. As the protonatable site of [Mim] is located at the non-methylated nitrogen atom (referred to as N1; while N2 represents the methylated nitrogen atom), we determine the chemical environment of these nuclei as reflected by their ^{15}N chemical shift.

The corresponding ^{15}N chemical shifts of the neat PILs and their solutions in methanol-d_4 and DMF-d_6 are shown in Fig. 4. For all samples we find the chemical shift of N1 decreases with increasing TFA
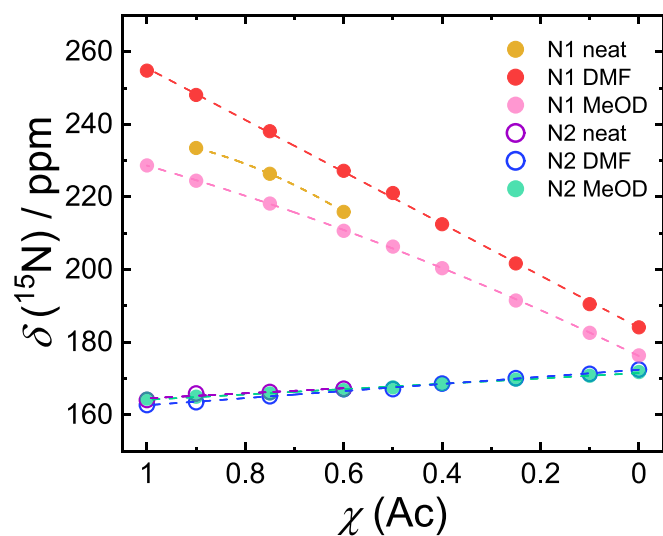
concentration. Conversely, N2 only slightly shifts down-field with decreasing χ(Ac). Given that these chemical shifts are the motionally averaged signals of all Mim molecular species ([Mim] and [MimH]$^+$), these results imply that the fraction of protonated [MimH]$^+$ increases [84] in all samples with decreasing χ(Ac), irrespective to the (solvent) environment. Yet, the absolute chemical shift values for N1 depend on the environment for χ(Ac) = 1, whereas the chemical environment of N2 is rather insensitive to the solvent. Upon decreasing χ(Ac), the chemical shifts of N1 for solutions in DMF-d_6 and methanol-d_4 become more similar. The different values for the two solvents can be attributed to the hydrogen-bond donor/acceptor properties of both solvents:[85] While the aprotic solvent DMF-d_6 is a hydrogen-bond acceptor and can stabilize [MimH]$^+$, but cannot donate a hydrogen-bond to [Mim], the protic solvent methanol-d_4 can accept and donate a H-bond from [MimH]$^+$ and to [Mim], respectively, which helps rationalizing the higher sensitivity of N1 to the solvent as compared to N2.

It is interesting to note, that for the neat ionic liquid the N1 signal for χ(Ac) = 1 cannot be resolved. Taking our dielectric results into account, which suggest that at χ(Ac) = 1 neutral species dominate in solution, the absence of the N1 signal in the spectra may point towards a very short dephasing time, which leads to peak broadening, such that the signals cannot be resolved. We speculate that hydrogen-bond formation of acetic acid to the N1 atom together with the high viscosities in the neat PILs restrict the rotational degrees of freedom of the [Mim]/[MimH]$^+$ molecules. Such reduced mobility can cause a reduction of the dephasing time.[86] Apparently, upon increasing TFA content, the hydrogen-bonds between [Mim] and acetic acid break, and the dephasing time becomes longer, making the N1 signals to be readily detectable.

The ^{15}N chemical shift experiments demonstrate that, despite the vastly different polarization dynamics detected for the neat PILs and their solutions, the effect of the Brønsted acidity on the protonation state of the Mim base is rather similar in the neat PILs and the solutions in DMF and methanol. Therefore, the different charge transport dynamics cannot stem from vastly different degrees of protonation but must have different molecular origins.

3.2.2. DOSY NMR

To study the transport dynamics of the different molecular species in the PILs and their solutions we use pulse-field gradient spin echo (PFGSE) NMR experiments, often referred to as diffusion ordered spectroscopy (DOSY).[66,87] In a DOSY experiment a series of spin echo spectra is recorded applying different pulsed field gradient strengths. The use of inhomogeneous magnetic fields can provide spatially resolved information. Based on the decay of the signals, the mobility (diffusivity) of the different molecular species with spectrally resolved NMR signals can be obtained. For samples containing TFA, ^{19}F depolarization was applied to reduce transient heteronuclear nuclear Overhauser contributions. The irradiation frequency, especially for the acidic proton, was adjusted to reduce off-resonant biases. For the present samples we discriminate the following four different species: [Mim]/ [MimH]$^+$ via their aromatic proton signals, [AcOH]/[AcO]$^-$ via the motionally averaged CH$_3$ signal, [TFA]/[TFA]$^-$ via the CF$_3$ signals, and the acidic proton H$^+$, which can be separately detected via its proton NMR signal in the range between 13 and 17 ppm, depending on the concentration of the acids. The PFGSE-determined diffusion coefficients, D, for these different species are shown in Fig. 5(a) for the neat PILs and in Fig. 5(b) for solutions of the PILs in DMF-d_6. Note, that we did not determine the diffusivities for solutions of the PILs in methanol-d_4 as the exchange of deuterons will interfere with the other ^{1}H exchange processes in the PILs and cause oscillatory results depending on the different exchange rates and the duration of the spatial encoding pulses as discussed elsewhere.[88]

Overall, for both the neat PIL mixtures and the solutions in DMF-d_6, the diffusion coefficients decrease with decreasing χ(Ac), which can be explained by the increasing viscosity. For the neat PIL mixtures, the mobility of the acidic species ([AcO]$^-$/[AcOH] or [TFA]$^-$/[TFA]) is

Fig. 4. ^{15}N chemical shifts as a function of χ(Ac) for the methylated nitrogen atom N2 and non-methylated nitrogen atom N1 for neat PILs and for PILs in solution. Symbols represent experimental data, dotted lines serve as a guide to the eye.
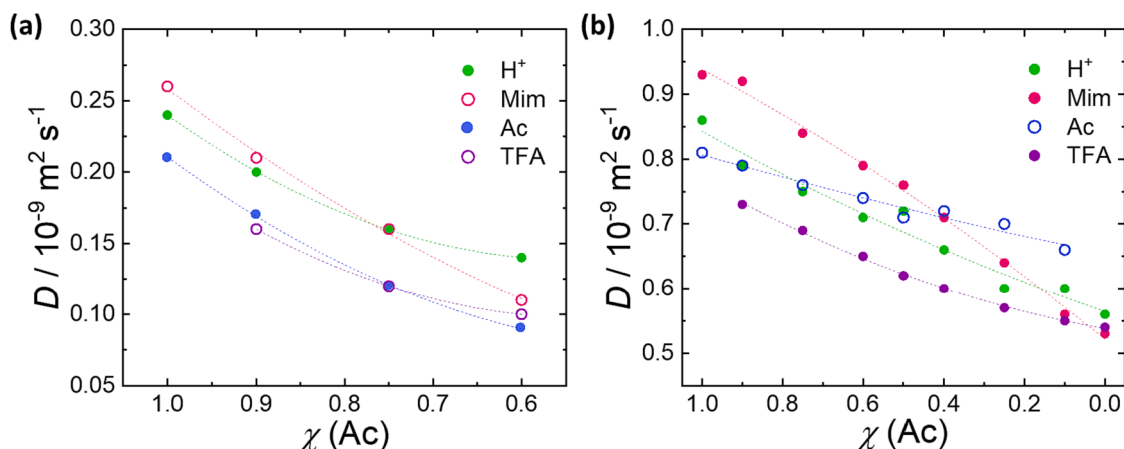
Fig. 5. (a) Diffusion coefficients as a function of χ(Ac) of neat PILs measured at room temperature. Symbols represent experimental data, dotted lines serve as a guide to the eye. (b) Diffusion coefficients as a function of χ(Ac) of PILs in DMF measured at room temperature. Symbols represent experimental data, dotted lines serve as a guide to the eye.

consistently lower than the mobility of [Mim]/[MimH]$^+$, which may be explained by the different molecular volumes or stronger interaction with the immediate environment. Additionally, self-aggregation[89] of the acids could result in a fraction of larger aggregates with a higher molecular volume (slower diffusivity). At χ(Ac) = 1, the mobility of the acidic proton lies between the mobility of [AcO]$^-$/[AcOH] and [Mim]/[MimH]$^+$, which one may expect for vehicular transport[90] of the proton with either [AcO]$^-$ or [Mim] as 'vehicle'. The fact that the proton mobility neither coincides with the mobility of the acid nor the base suggests that the proton is partially transferred between both molecular entities. Remarkably, with decreasing χ(Ac) the retardation of the proton diffusivity is less pronounced than the slow-down of the other molecular entities. In fact, at χ(Ac) = 0.6 the acidic proton shows the highest diffusivity amongst all species. Apparently, the acidic protons diffuse faster than the potentially available molecular vehicles, which points at a Grotthuss-type transport for this composition.

For solutions of the PILs in DMF-d_6 (Fig. 5(b)), the diffusion coefficients are generally higher than in the neat PILs due to the reduced viscosities.[91,92] At χ(Ac) = 1 the trend in mobilities is comparable to the neat PIL: D([AcO]$^-$/[AcOH]) < D(H$^+$) < D([Mim]/[MimH]$^+$). This observation implies that exclusive formation of [MimH][AcO] aggregates can be ruled out at χ(Ac) = 1, as in that case the diffusivities of all species would coincide. Conversely, upon decreasing χ(Ac) the diffusivities of [Mim]/[MimH]$^+$, H$^+$, and TFA converge to virtually the same value at χ(Ac) = 0, consistent with [MimH][TFA] aggregates (cf. ion-pair formation discussed above) dominating at this composition. The significantly higher diffusivity of [AcO]$^-$/[AcOH] at low χ(Ac) implies that acetic acid is not entirely bound in PIL aggregates.

Together, the diffusivities suggest that with increasing TFA content, the mobilities of molecular species become more correlated in the neat PILs, while the proton motion somewhat decouples. For solutions in DMF-d_6, only the motion of [TFA]/ [TFA]$^-$, H$^+$, and [Mim]/[MimH]$^+$ become highly correlated (in line with ion-pair formation), while the mobility of [AcO]$^-$/[AcOH] seems to decouple from these transport dynamics.

3.2.3. Temperature dependent proton linewidths

Analysis of the DOSY spectra revealed indications for a Grotthuss–type proton conduction in the PILs. To further support this observation, we analyze thermal effects on the chemical shift and the linewidth of the NMR signal of the acidic proton at 13–17 ppm in more detail. Here, we focus on PILs in DMF-d_6 as for neat PILs with χ(Ac) < 0.6, the viscosity increases in the accessible temperature range to such an extent that the chemical shift resolution in the NMR measurements is lost. For the temperature dependent studies, we focus on the two neat

PILs ([MimH][AcO] (χ(Ac) = 1) and [MimH][TFA] (χ(Ac) = 0)) and an equimolar PIL mixture.

Fig. 6(a) shows the ^{1}H chemical shift values of the acidic proton as a function of the inverse temperature for the three investigated PIL mixtures. For χ(Ac) = 0 the chemical shift is rather insensitive to temperature variations, indicating that the average electronic environment of H$^+$ is not altered. For χ(Ac) = 0.5 and χ(Ac) = 1, the chemical shift values decrease with increasing temperature. This decrease is most pronounced for χ(Ac) = 1, where the chemical shift values vary by about 2 ppm between T = 263 K and T = 400 K. This change in chemical shift is indicative of a change in the electronic surrounding of the acidic proton and, as such, of altered chemical equilibria in the samples. Considering that for χ(Ac) = 1, and to a lesser extent for χ(Ac) = 0.5, mostly electroneutral species are present in solution (as evidenced by the negligible conductivity, Fig. 2(c)) the variation of the chemical environment suggests temperature induced variations of the hydrogen-bonded structure: hydrogen-bonds of [AcOH] to [Mim], DMF, or other [AcOH] molecules (AcOH selfdimers) can be broken and result in a redistribution of the H-bonded species. These altered equilibria in turn result in a marked variation of the detected chemical environment.

The temperature dependent linewidths of these signals (Fig. 6(b)) provide evidence for chemical exchange dynamics on a millisecond timescale in the presence of TFA: At χ(Ac) = 1 the linewidth of the acidic proton becomes continuously narrower with increasing temperature. This behaviour is common to systems with a temperature-independent chemical environment, for which enhanced thermal fluctuations lead to enhanced averaging of local heterogeneities and, as such, longer dephasing times.[86] In turn, for χ(Ac) = 0.5 and χ(Ac) = 0 the thermally induced narrowing is only observed at reduced temperatures. At elevated temperatures the signals become broader with increasing temperature resulting in a marked minimum of the linewidth at $T \approx 350$ K for χ(Ac) = 0 and at $T \approx 320$ K for χ(Ac) = 0.5. Such thermally induced broadening can be explained by thermal shifts of chemical equilibria resulting in dynamic exchange processes. While the chemical shift values indicate variations of the chemical environment of the acidic proton with temperature for χ(Ac) = 1 and, to a lesser extent, for χ(Ac) = 0.5, the chemical shift of the acidic proton is constant for χ(Ac) = 0. Yet, we observe an increasing linewidth at high temperatures for χ(Ac) = 0. This clearly points to the onset of a dynamic process, which leaves the chemical environment unchanged. This suggests, together with the high degree of protonation of the Mim molecules for χ(Ac) = 0 deduced from the ^{15}N chemical shift data, that the dynamic process at high temperature is most likely related to proton hopping between [MimH$^+$] and [Mim] species. For χ(Ac) = 0.5 an increase in linewidth can also be observed at elevated temperatures but to a lesser extent, as compared to
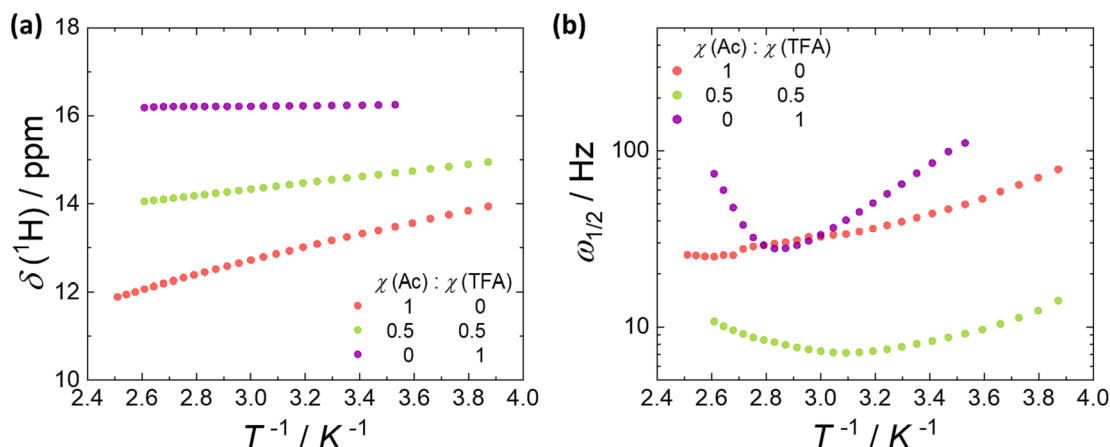
Fig. 6. (a) Temperature dependence of the ^{1}H chemical shift and (b) linewidth of the acidic proton for the two limiting cases χ(Ac) = 1 and χ(Ac) = 0 and the equimolar PIL mixture in DMF.

χ(Ac) = 0. This observation indicates that such proton dynamics might also occur at lower TFA concentrations. Complete analysis of the thermal activation of this dynamic process, however, is beyond the scope of this study and the examples given here only serve to support the results presented above.

4. Conclusion

In the present study we investigate molecular-level dynamics in Mim-based PILs using DR and NMR spectroscopy. For [MimH][AcO] we find the total dielectric amplitude, S_{tot}, to exceed the amplitude that would be expected for uncorrelated reorientation of molecular-level dipoles, with the molecular dipole moments estimated using DFT calculations. This enhanced dipolar relaxation amplitude indicates the presence of dynamic dipolar correlations, typical for the dipolar response of hydrogen-bonded liquids. The finite conductivity, κ, evidences the existence of mobile ions, although the ^{15}N-NMR chemical shifts demonstrate a moderate degree of protonation of the [Mim] base. Diffusion ordered ^{1}H-NMR spectra show that the diffusion coefficients of the acidic proton at 13–17 ppm is somewhat higher than the diffusion coefficient of the acetic acid species, yet, lower than the mobilities of the species associated with the [Mim] base. These mobilities are consistent with a partial proton transfer from AcOH to [Mim], and suggest charge transport to be dominated by vehicular dynamics. Yet, also self-aggregation of AcOH and the formation of acetic acid chains – pertinent to Grotthuss transport – could result in a reduced mobility of the acid. Upon substitution of AcOH by TFA, we find an increasing fraction of [MimH]$^+$, as apparent from the marked decrease of the ^{15}N chemical shift of the N1 nitrogen atom and an increase of the sample conductivity – despite the increase in the viscosity of the PIL. Simultaneously, the dipolar amplitude S_{tot} decreases, which implies that the increasing presence of ionic species partly reduces dynamic dipolar correlations. Diffusion ordered ^{1}H-NMR spectra indicate that with decreasing χ(Ac) the diffusivities of the acidic protons decrease less, as compared to the other molecular species, and at χ(Ac) = 0.6 the diffusion coefficient of the acidic proton exceeds those of the molecular species (D(H$^+$) > D ([Mim]/[MimH]$^+$) > D([TFA]/[TFA]$^-$) > D([AcOH]/[AcO]$^-$)). This enhanced proton mobility suggests a Grotthuss-type mechanism contributing to charge transport in the PIL.

Our findings further show that the nature of the solvent in PIL solutions critically affects chemical equilibria: [MimH][AcO] forms in DMF nearly exclusively electro-neutral molecular species/aggregates, which virtually supresses the macroscopic conductivity, consistent with a low degree of protonation of the [Mim] base as deduced from the ^{15}N chemical shifts. Nevertheless, the ^{1}H-NMR determined mobility of the acidic proton is somewhat higher than the mobility of [AcOH]/[AcO]$^-$

species, yet lower than the mobility of [Mim]/[MimH]$^+$, which again points at partial deprotonation of AcOH or self-aggregation of AcOH. Upon increasing TFA content, the conductivity increases, evidencing the formation of mobile ([MimH]$^+$, [TFA]$^-$) ions. Yet, the emergence of the PIL associated lower-frequency dielectric relaxation suggests that a large fraction of the ions is bound in [MimH][TFA] ion-pairs. Temperature dependent linewidths of the ^{1}H NMR signal of the acidic proton demonstrate that these protons can chemically exchange on the NMR timescale. The presence of ion-pairs and free ions is consistent with the enhanced degree of protonation of [Mim], as detected via the ^{15}N chemical shifts. In fact, these chemical shifts exhibit similar trends for the neat PILs, solutions in DMF, and solutions in MeOH, which suggests similar trends in protonation upon substituting AcOH by TFA. Yet, in methanol the PIL solutes do not form highly dipolar aggregates and the conductivity of all PIL solutions in methanol exceeds those of the neat PILs and PIL solutions in DMF. This high charge mobility in MeOH demonstrates efficient solvation of the free ions and is consistent with methanol and the PIL forming an extended hydrogen-bonded network, which may also allow for a Grotthuss-type transport of protons.

In general, our results show that protonation equilibria and dynamics in these PILs are highly sensitive to the immediate environment. In particular, altering proton acceptors and proton donors, e.g. by substitution of AcOH by TFA, offers opportunities to engineer these equilibria and dynamics such that charge transport and the electrochemical performance can be optimized.

Author Contributions

The manuscript was written through contributions of all authors. All authors have given approval to the final version of the manuscript.

Declaration of Competing Interest

Data availability

Data will be made available on request.

Acknowledgements

This project has received funding from the Deutsche Forschungsgemeinschaft (DFG) – project HU 1860/9-1.

Appendix A. Supplementary data

Supplementary data to this article can be found online at https://doi.org/10.1016/j.molliq.2023.122975.

References

[1] C. Austen Angell, Y. Ansari, Z. Zhao, Ionic Liquids: Past, present and future, Faraday Discuss. 154 (2012) 9–27, https://doi.org/10.1039/c1fd00112d.
[2] R.D. Rogers, K.R. Seddon, Ionic Liquids - Solvents of the Future? Science 302 (2003) 792–793, https://doi.org/10.1126/science.1090313.
[3] J.P. Hallett, T. Welton, Room-Temperature Ionic Liquids: Solvents for Synthesis and Catalysis. 2, Chem. Rev. 111 (2011) 3508–3576, https://doi.org/10.1021/cr1003248.
[4] H. Niedermeyer, J.P. Hallett, I.J. Villar-Garcia, P.A. Hunt, T. Welton, Mixtures of ionic liquids, Chem. Soc. Rev. 41 (2012) 7780–7802, https://doi.org/10.1039/c2cs35177c.
[5] P. Hapiot, C. Lagrost, Electrochemical reactivity in room-temperature ionic liquids, Chem. Rev. 108 (2008) 2238–2264, https://doi.org/10.1021/cr0680686.
[6] M.J. Earle, J.M.S.S. Esperança, M.A. Gilea, J.N.C. Lopes, L.P.N. Rebelo, J. W. Magee, K.R. Seddon, J.A. Widegren, The distillation and volatility of ionic liquids, Nature. 439 (2006) 831–834, https://doi.org/10.1038/nature04451.
[7] F. Pena-Pereira, J. Namieśnik, Ionic liquids and deep eutectic mixtures: Sustainable solvents for extraction processes, ChemSusChem. 7 (2014) 1784–1800, https://doi.org/10.1002/cssc.201301192.
[8] Z. Wojnarowska, M. Paluch, Recent progress on dielectric properties of protic ionic liquids, J. Phys. Condens. Matter. 27 (2015), https://doi.org/10.1088/0953-8984/27/7/073202.
[9] N.V. Plechkova, K.R. Seddon, Applications of ionic liquids in the chemical industry, Chem. Soc. Rev. 37 (2008) 123–150, https://doi.org/10.1039/b006677j.
[10] F. Endres, S. Zein El Abedin, Air and water stable ionic liquids in physical chemistry, Phys. Chem. Chem. Phys. 8 (2006) 2101–2116, https://doi.org/10.1039/b600519p.
[11] J. Stoimenovski, P.M. Dean, E.I. Izgorodina, D.R. MacFarlane, Protic pharmaceutical ionic liquids and solids: Aspects of protonics, Faraday Discuss. 154 (2012) 335–352, https://doi.org/10.1039/c1fd00071c.
[12] N. Chieng, T. Rades, D. Saville, Formation and physical stability of the amorphous phase of ranitidine hydrochloride polymorphs prepared by cryo-milling, Eur. J. Pharm. Biopharm. 68 (2008) 771–780, https://doi.org/10.1016/j.ejpb.2007.09.001.
[13] Z. Wojnarowska, K. Grzybowska, L. Hawelek, A. Swiety-Pospiech, E. Masiewicz, M. Paluch, W. Sawicki, A. Chmielewska, P. Bujak, J. Markowski, Molecular dynamics studies on the water mixtures of pharmaceutically important ionic liquid lidocaine HCl, Mol. Pharm. 9 (2012) 1250–1261, https://doi.org/10.1021/mp2005609.
[14] W. Xu, C.A. Angell, Solvent-free electrolytes with aqueous solution-like conductivities, Science. 302 (2003) 422–425, https://doi.org/10.1126/science.1090287.
[15] A. Lewandowski, A. Świderska-Mocek, Ionic liquids as electrolytes for Li-ion batteries-An overview of electrochemical studies, J. Power Sources. 194 (2009) 601–609, https://doi.org/10.1016/j.jpowsour.2009.06.089.
[16] J.-P. Belieres, D. Gervasio, C.A. Angell, Binary inorganic salt mixtures as high conductivity liquid electrolytes for >100 °C fuel cells, Chem. Commun. 111 (2006) 4799–4801, https://doi.org/10.1039/B611150E.
[17] T. Frömling, M. Kunze, M. Schönhoff, J. Sundermeyer, B. Roling, Enhanced lithium transference numbers in ionic liquid electrolytes, J. Phys. Chem. B 112 (2008) 12985–12990, https://doi.org/10.1021/jp804097j.
[18] S. Menne, R.S. Kühnel, A. Balducci, The influence of the electrochemical and thermal stability of mixtures of ionic liquid and organic carbonate on the performance of high power lithium-ion batteries, Electrochim. Acta. 90 (2013) 641–648, https://doi.org/10.1016/j.electacta.2012.12.042.
[19] F. Béguin, V. Presser, A. Balducci, E. Frackowiak, Carbons and electrolytes for advanced supercapacitors, Adv. Mater. 26 (2014) 2219–2251, https://doi.org/10.1002/adma.201304137.
[20] S. Menne, J. Pires, M. Anouti, A. Balducci, Protic ionic liquids as electrolytes for lithium-ion batteries, Electrochem. Commun. 31 (2013) 39–41, https://doi.org/10.1016/j.elecom.2013.02.026.
[21] T.L. Greaves, C.J. Drummond, Protic ionic liquids: properties and applications, Chem. Rev. 108 (2008) 206–237, https://doi.org/10.1021/cr068040u.
[22] H. Weingärtner, A. Knocks, W. Schrader, U. Kaatze, Dielectric spectroscopy of the room temperature molten salt ethylammonium nitrate, J. Phys. Chem. A. 105 (2001) 8646–8650, https://doi.org/10.1021/jp0114586.
[23] K. Fumino, A. Wulf, R. Ludwig, The potential role of hydrogen bonding in aprotic and protic ionic liquids, Phys. Chem. Chem. Phys. 11 (2009) 8790–8794, https://doi.org/10.1039/b905634c.
[24] K. Fumino, V. Fossog, P. Stange, D. Paschek, R. Hempelmann, R. Ludwig, Controlling the subtle energy balance in protic ionic liquids: Dispersion forces compete with hydrogen bonds, Angew. Chemie Int. Ed. 54 (2015) 2792–2795, https://doi.org/10.1002/anie.201411509.

[25] S. Zahn, J. Thar, B. Kirchner, Structure and dynamics of the protic ionic liquid monomethylammonium nitrate ([CH3NH3][NO3]) from ab initio molecular dynamics simulations, J. Chem. Phys. 132 (2010) 124506, https://doi.org/10.1063/1.3354108.
[26] H. Doi, X. Song, B. Minofar, R. Kanzaki, T. Takamuku, Y. Umebayashi, A new proton conductive liquid with no ions: Pseudo-protic ionic liquids, Chem. - A Eur. J. 19 (2013) 11522–11526, https://doi.org/10.1002/chem.201302228.
[27] M. Shen, Y. Zhang, K. Chen, S. Che, J. Yao, H. Li, Ionicity of protic ionic liquid: Quantitative measurement by spectroscopic methods, J. Phys. Chem. B. 121 (2017) 1372–1376, https://doi.org/10.1021/acs.jpcb.6b11624.
[28] T.L. Greaves, C.J. Drummond, Protic ionic liquids: evolving structure-property relationships and expanding applications, Chem. Rev. 115 (2015) 11379–11448, https://doi.org/10.1021/acs.chemrev.5b00158.
[29] O. Hollóczki, F. Malberg, T. Welton, B. Kirchner, On the origin of ionicity in ionic liquids. Ion pairing versus charge transfer, Phys. Chem. Chem. Phys. 16 (2014) 16880–16890, https://doi.org/10.1039/c4cp01177e.
[30] J. Stoimenovski, E.I. Izgorodina, D.R. MacFarlane, Ionicity and proton transfer in protic ionic liquids, Phys. Chem. Chem. Phys. 12 (2010) 10341–10347, https://doi.org/10.1039/c0cp00239a.
[31] R. Kanzaki, H. Doi, X. Song, S. Hara, S.I. Ishiguro, Y. Umebayashi, Acid-base property of N-methylimidazolium-based protic ionic liquids depending on anion, J. Phys. Chem. B. 116 (2012) 14146–14152, https://doi.org/10.1021/jp308477p.
[32] F. Joerg, C. Schröder, Polarizable molecular dynamics simulations on the conductivity of pure 1-methylimidazolium acetate systems, Phys. Chem. Chem. Phys. 24 (2022) 15245–15254, https://doi.org/10.1039/d2cp01501c.
[33] P.M. Tolstoy, J. Guo, B. Koeppe, N.S. Golubev, G.S. Denisov, S.N. Smirnov, H. H. Limbach, Geometries and tautomerism of OHN hydrogen bonds in aprotic solution probed by H/D isotope effects on 13C NMR chemical shifts, J. Phys. Chem. A. 114 (2010) 10775–10782, https://doi.org/10.1021/jp1027146.
[34] I.I. Schuster, C. Dyllick-Brenzinger, J.D. Roberts, Nitrogen-15 nuclear magnetic resonance spectroscopy. Effects of hydrogen bonding and protonation on nitrogen chemical shifts of pyrazoles, J. Org. Chem. 44 (1979) 1765–1768, https://doi.org/10.1021/jo01325a003.
[35] K. Chen, Y. Wang, J. Yao, H. Li, Equilibrium in protic ionic liquids: The degree of proton transfer and thermodynamic properties, J. Phys. Chem. B. 122 (2018) 309–315, https://doi.org/10.1021/acs.jpcb.7b10671.
[36] J. Zhang, J. Yao, H. Li, Solvent effect on the ionicity of protic ionic liquid: 1-methylimidazolium-acetic acid, J. Phys. Chem. B. 126 (2022) 2279–2284, https://doi.org/10.1021/acs.jpcb.2c00973.
[37] J. Ingenmey, S. Gehrke, B. Kirchner, How to harvest grotthuss diffusion in protic ionic liquid electrolyte systems, ChemSusChem. 11 (2018) 1900–1910, https://doi.org/10.1002/cssc.201800436.
[38] H. Watanabe, T. Umecky, N. Arai, A. Nazet, T. Takamuku, K.R. Harris, Y. Kameda, R. Buchner, Y. Umebayashi, Possible proton conduction mechanism in pseudo-protic ionic liquids: A concept of specific proton conduction, J. Phys. Chem. B. 123 (2019) 6244–6252, https://doi.org/10.1021/acs.jpcb.9b03185.
[39] H. Watanabe, N. Arai, Y. Kameda, R. Buchner, Y. Umebayashi, Effect of Brønsted acidity on ion conduction in fluorinated acetic acid and N-methylimidazole equimolar mixtures as pseudo-protic ionic liquids, J. Phys. Chem. B. 124 (2020) 11157–11164, https://doi.org/10.1021/acs.jpcb.0c07706.
[40] A. Stoppa, J. Hunger, R. Buchner, G. Hefter, A. Thoman, H. Helm, Interactions and dynamics in ionic liquids, J. Phys. Chem. B. 112 (2008) 4854–4858, https://doi.org/10.1021/jp800852z.
[41] Y. Marcus, G. Hefter, Ion pairing, Chem. Rev. 106 (2006) 4585–4621, https://doi.org/10.1021/cr040087x.
[42] A. Stoppa, J. Hunger, R. Buchner, How ideal are binary mixtures of room-temperature ionic liquids? J. Mol. Liq. 153 (2010) 46–51, https://doi.org/10.1016/j.molliq.2009.05.001.
[43] J. Hunger, A. Stoppa, S. Schrödle, G. Hefter, R. Buchner, Temperature dependence of the dielectric properties and dynamics of ionic liquids, ChemPhysChem. 10 (2009) 723–733, https://doi.org/10.1002/cphc.200800483.
[44] M. Dabiri, M. Baghbanzadeh, E. Arzroomchilar, 1-Methylimidazolium triflouroacetate ([Hmim]TFA): An efficient reusable acidic ionic liquid for the synthesis of 1,8-dioxo-octahydroxanthenes and 1,8-dioxo-decahydroacridines, Catal. Commun. 9 (2008) 939–942, https://doi.org/10.1016/j.catcom.2007.09.023.
[45] G. Zhao, T. Jiang, H. Gao, B. Han, J. Huang, D. Sun, Mannich reaction using acidic ionic liquids as catalysts and solvents, Green Chem. 6 (2004) 75–77, https://doi.org/10.1039/b309700p.
[46] D.V. Blackham, R.D. Pollard, An improved technique for permittivity measurements using a coaxial probe, IEEE Trans. Instrum. Meas. 46 (1997) 1093–1099, https://doi.org/10.1109/19.676718.
[47] W. Ensing, J. Hunger, N. Ottosson, H.J. Bakker, On the orientational mobility of water molecules in proton and sodium terminated nafion membranes, J. Phys. Chem. C. 117 (2013) 12930–12935, https://doi.org/10.1021/jp312623p.
[48] V. Balos, H. Kim, M. Bonn, J. Hunger, Dissecting Hofmeister effects: Direct anion-amide interactions are weaker than cation-amide binding, Angew. Chemie Int. Ed. 55 (2016) 8125–8128, https://doi.org/10.1002/anie.201602769.
[49] J. Barthel, R. Buchner, B. Wurm, The dynamics of liquid formamide, N-methylformamide, N,N-dimethylformamide, and N,N-dimethylacetamide. A dielectric relaxation study, J. Mol. Liq. 98–99 (2002) 51–69, https://doi.org/10.1016/S0167-7322(01)00309-9.
[50] R.M. Shirke, A. Chaudhari, N.M. More, P.B. Patil, Temperature dependent dielectric relaxation study of ethyl acetate - alcohol mixtures using time domain technique, J. Mol. Liq. 94 (2001) 27–36, https://doi.org/10.1016/S0167-7322(01)00239-2.

[51] H.E. Gottlieb, V. Kotlyar, A. Nudelman, NMR chemical shifts of common laboratory solvents as trace impurities, J. Org. Chem. 62 (1997) 7512–7515, https://doi.org/10.1021/jo971176v.

[52] F. Neese, F. Wennmohs, U. Becker, C. Riplinger, The ORCA quantum chemistry program package, J. Chem. Phys. 152 (2020), 224108, https://doi.org/10.1063/5.0004608.

[53] A.D. Becke, Density-functional thermochemistry. III. The role of exact exchange, J. Chem. Phys. 98 (1993) 5648, https://doi.org/10.1063/1.464913.

[54] C. Lee, W. Yang, R.G. Parr, Development of the Colle-Salvetti correlation-energy formula into a functional of the electron density, Phys. Rev. B. 37 (1988) 785–789, https://doi.org/10.1103/PhysRevB.37.785.

[55] F. Weigend, R. Ahlrichs, Balanced basis sets of split valence, triple zeta valence and quadruple zeta valence quality for H to Rn: Design and assessment of accuracy, Phys. Chem. Chem. Phys. 7 (2005) 3297, https://doi.org/10.1039/b508541a.

[56] J.L. Dote, D. Kivelson, Hydrodynamic rotational friction coefficients for nonspheroidal particles, J. Phys. Chem. 87 (1983) 3889–3893, https://doi.org/10.1021/j100243a020.

[57] J. Barthel, H. Hetzenauer, R. Buchner, Dielectric relaxation of aqueous electrolyte solutions II. Ion-pair relaxation of 1:2, 2:1, and 2:2 electrolytes, Ber. Bunsenges. Phys. Chem. 96 (1992) 1424–1432, https://doi.org/10.1002/bbpc.19920961015.

[58] T. Lu, F. Chen, Multiwfn: A multifunctional wavefunction analyzer, J. Comput. Chem. 33 (2012) 580–592, https://doi.org/10.1002/jcc.22885.

[59] J. Zhang, T. Lu, Efficient evaluation of electrostatic potential with computerized optimized code, Phys. Chem. Chem. Phys. 23 (2021) 20323–20328, https://doi.org/10.1039/d1cp02805g.

[60] M. Yoshizawa, W. Xu, C.A. Angell, Ionic liquids by proton transfer: vapor pressure, conductivity, and the relevance of Delta pKa from aqueous solutions, J. Am. Chem. Soc. 125 (2003) 15411–15419, https://doi.org/10.1021/ja035783d.

[61] E.S. Stoyanov, I.V. Stoyanova, C.A. Reed, IR Spectroscopic Properties of $H(MeOH)_n^+$ Clusters in the Liquid Phase: Evidence for a Proton Wire, Chem. - A Eur. J. 14 (2008) 3596–3604, https://doi.org/10.1002/chem.200701746.

[62] C. Schröder, M. Haberler, O. Steinhauser, On the computation and contribution of conductivity in molecular ionic liquids, J. Chem. Phys. 128 (2008), 134501, https://doi.org/10.1063/1.2868752.

[63] R. Buchner, G. Hefter, Interactions and dynamics in electrolyte solutions by dielectric spectroscopy, Phys. Chem. Chem. Phys. 11 (2009) 8984–8999, https://doi.org/10.1039/b906555p.

[64] J. Hunger, A. Stoppa, R. Buchner, G. Hefter, From ionic liquid to electrolyte solution: dynamics of 1-N-butyl-3-N-methylimidazolium tetrafluoroborate/dichloromethane mixtures, J. Phys. Chem. B. 112 (2008) 12913–12919, https://doi.org/10.1021/jp8045627.

[65] M. Alei, L.O. Morgan, W.E. Wageman, T.W. Whaley, The pH dependence of nitrogen-15 NMR shifts and coupling constants in aqueous imidazole and 1-methylimidazole. Comments on estimation of tautomeric equilibrium constants for aqueous histidine, J. Am. Chem. Soc. 102 (1980) 2881–2887, https://doi.org/10.1021/ja00529a002.

[66] M. Zanatta, V.U. Antunes, C.F. Tormena, J. Dupont, F.P. dos Santos, Dealing with supramolecular structure for ionic liquids: a DOSY NMR approach, Phys. Chem. Chem. Phys. 21 (2019) 2567–2571, https://doi.org/10.1039/C8CP07071G.

[67] A. Szabadi, P. Honegger, F. Schöfbeck, M. Sappl, E. Heid, O. Steinhauser, C. Schröder, Collectivity in ionic liquids: a temperature dependent, polarizable molecular dynamics study, Phys. Chem. Chem. Phys. 24 (2022) 15776–15790, https://doi.org/10.1039/D2CP00898J.

[68] H. Weingärtner, Understanding ionic liquids at the molecular level: facts, problems, and controversies, Angew. Chemie Int. Ed. 47 (2008) 654–670, https://doi.org/10.1002/anie.200604951.

[69] D.A. Turton, J. Hunger, A. Stoppa, G. Hefter, A. Thoman, M. Walther, R. Buchner, K. Wynne, Dynamics of imidazolium ionic liquids from a combined dielectric relaxation and optical Kerr effect study: evidence for mesoscopic aggregation, J. Am. Chem. Soc. 131 (2009) 11140–11146, https://doi.org/10.1021/ja903315v.

[70] J. Hunger, A. Stoppa, R. Buchner, G. Hefter, Dipole Correlations in the Ionic Liquid 1-N-Ethyl-3-N-methylimidazolium ethylsulfate and its binary mixtures with dichloromethane, J. Phys. Chem. B. 113 (2009) 9527–9537, https://doi.org/10.1021/jp9024574.

[71] J. Hunger, A. Stoppa, A. Thoman, M. Walther, R. Buchner, Broadband dielectric response of dichloromethane, Chem. Phys. Lett. 471 (2009) 85–91, https://doi.org/10.1016/j.cplett.2009.02.024.

[72] P.H. Fries, J. Richardi, H. Krienke, Dielectric and structural results for liquid acetonitrile, acetone and chloroform from the hypernetted chain molecular integral equation, Mol. Phys. 90 (1997) 841–854, https://doi.org/10.1080/002689797172183.

[73] E.A.S. Cavell, P.C. Knight, M.A. Sheikh, Dielectric relaxation in non aqueous solutions. Part 2. —Solutions of tri(n-butyl)ammonium picrate and iodide in polar solvents, Trans. Faraday Soc. 67 (1971) 2225–2233, https://doi.org/10.1039/TF9716702225.

[74] V. Balos, M. Bonn, J. Hunger, Anionic and cationic Hofmeister effects are non-additive for guanidinium salts, Phys. Chem. Chem. Phys. 19 (2017) 9724–9728, https://doi.org/10.1039/C7CP00790F.

[75] V. Balos, B. Marekha, C. Malm, M. Wagner, Y. Nagata, M. Bonn, J. Hunger, Specific ion effects on an oligopeptide: bidentate binding matters for the guanidinium cation, Angew. Chemie Int. Ed. 58 (2019) 332–337, https://doi.org/10.1002/anie.201811029.

[76] Y. Fujii, H. Yamada, M. Mizuta, Self-association of acetic acid in some organic solvents, J. Phys. Chem. 92 (1988) 6768–6772, https://doi.org/10.1021/j100334a054.

[77] M. Lim, R.M. Hochstrasser, Unusual vibrational dynamics of the acetic acid dimer, J. Chem. Phys. 115 (2001) 7629–7643, https://doi.org/10.1063/1.1404144.

[78] K. Heyne, N. Huse, J. Dreyer, E.T.J. Nibbering, T. Elsaesser, S. Mukamel, Coherent low-frequency motions of hydrogen bonded acetic acid dimers in the liquid phase, J. Chem. Phys. 121 (2004) 902–913, https://doi.org/10.1063/1.1762873.

[79] C. Malm, H. Kim, M. Wagner, J. Hunger, Complexity in acid-base titrations: Multimer formation between phosphoric acids and imines, Chem. - A Eur. J. 23 (2017) 10853–10860, https://doi.org/10.1002/chem.201701576.

[80] J. Barthel, K. Bachhuber, R. Buchner, H. Hetzenauer, Dielectric spectra of some common solvents in the microwave region. Water and lower alcohols, Chem. Phys. Lett. 165 (1990) 369–373, https://doi.org/10.1016/0009-2614(90)87204-5.

[81] R. Buchner, C. Hölzl, J. Stauber, J. Barthel, Dielectric spectroscopy of ion-pairing and hydration in aqueous tetra-n-alkylammonium halide solutions, Phys. Chem. Chem. Phys. 4 (2002) 2169–2179, https://doi.org/10.1039/b110361j.

[82] P. Petong, R. Pottel, U. Kaatze, Dielectric relaxation of H-bonded liquids. Mixtures of ethanol and n-hexanol at different compositions and temperatures, J. Phys. Chem. A. 103 (1999) 6114–6121, https://doi.org/10.1021/jp991046l.

[83] K.F. Rinne, S. Gekle, R.R. Netz, Ion-Specific Solvation Water Dynamics: Single Water versus Collective Water Effects, J. Phys. Chem. A. 118 (2014) 11667–11677, https://doi.org/10.1021/jp5066874.

[84] M. Alei, W.E. Wageman, 15N NMR shifts for imidazole and 1-methyl imidazole in CH_2Cl_2 relative to aqueous solution, Tetrahedron Lett. 20 (1979) 667–670, https://doi.org/10.1016/S0040-4039(01)93540-3.

[85] A. Duereh, R.L. Smith, Strategies for using hydrogen-bond donor/acceptor solvent pairs in developing green chemical processes with supercritical fluids, J. Supercrit. Fluids. 141 (2018) 182–197, https://doi.org/10.1016/j.supflu.2017.11.004.

[86] D. Besghini, M. Mauri, R. Simonutti, Time domain NMR in polymer science: From the laboratory to the industry, Appl. Sci. 9 (2019) 1801, https://doi.org/10.3390/app9091801.

[87] V. Mazan, M. Boltoeva, Insight into the ionic interactions in neat ionic liquids by diffusion ordered spectroscopy nuclear magnetic resonance, J. Mol. Liq. 240 (2017) 74–79, https://doi.org/10.1016/j.molliq.2017.05.021.

[88] A. Chen, J. Johnson, M. Lin, M.J. Shapiro, Chemical exchange in diffusion NMR experiments, J. Am. Chem. Soc. 120 (1998) 9094–9095, https://doi.org/10.1021/ja9809410.

[89] D. Lengvinaite, K. Aidas, L. Kimtys, Molecular aggregation in liquid acetic acid: Insight from molecular dynamics/quantum mechanics modelling of structural and NMR properties, Phys. Chem. Chem. Phys. 21 (2019) 14811–14820, https://doi.org/10.1039/c9cp01892a.

[90] J. Lin, C. Korte, Influence of the acid-base stoichiometry and residual water on the transport mechanism in a highly-Brønsted-acidic proton-conducting ionic liquid, RSC Adv. 10 (2020) 42596–42604, https://doi.org/10.1039/d0ra08969a.

[91] P.S. Nikam, S.J. Kharat, Density and viscosity studies of binary mixtures of N,N-dimethylformamide with toluene and methyl benzoate at (298.15, 303.15, 308.15, and 313.15) K, J, Chem. Eng. Data. 50 (2005) 455–459, https://doi.org/10.1021/je040012q.

[92] W. Qian, Y. Xu, H. Zhu, C. Yu, Properties of pure 1-methylimidazolium acetate ionic liquid and its binary mixtures with alcohols, J. Chem. Thermodyn. 49 (2012) 87–94, https://doi.org/10.1016/j.jct.2012.01.013.